Lecture Notes in Physics

D. Lemke M. Stickel K. Wilke (Eds.)

ISO Surveys of a Dusty Universe

Proceedings,
Ringberg Castle,
Tegernsee,
Germany 1999

Springer

Lecture Notes in Physics

Springer
Berlin
Heidelberg
New York
Barcelona
Hong Kong
London
Milan
Paris
Singapore
Tokyo

Physics and Astronomy ONLINE LIBRARY
http://www.springer.de/phys/

The Editorial Policy for Proceedings

The series Lecture Notes in Physics reports new developments in physical research and teaching – quickly, informally, and at a high level. The proceedings to be considered for publication in this series should be limited to only a few areas of research, and these should be closely related to each other. The contributions should be of a high standard and should avoid lengthy redraftings of papers already published or about to be published elsewhere. As a whole, the proceedings should aim for a balanced presentation of the theme of the conference including a description of the techniques used and enough motivation for a broad readership. It should not be assumed that the published proceedings must reflect the conference in its entirety. (A listing or abstracts of papers presented at the meeting but not included in the proceedings could be added as an appendix.)

When applying for publication in the series Lecture Notes in Physics the volume's editor(s) should submit sufficient material to enable the series editors and their referees to make a fairly accurate evaluation (e.g. a complete list of speakers and titles of papers to be presented and abstracts). If, based on this information, the proceedings are (tentatively) accepted, the volume's editor(s), whose name(s) will appear on the title pages, should select the papers suitable for publication and have them refereed (as for a journal) when appropriate. As a rule discussions will not be accepted. The series editors and Springer-Verlag will normally not interfere with the detailed editing except in fairly obvious cases or on technical matters.

Final acceptance is expressed by the series editor in charge, in consultation with Springer-Verlag only after receiving the complete manuscript. It might help to send a copy of the authors' manuscripts in advance to the editor in charge to discuss possible revisions with him. As a general rule, the series editor will confirm his tentative acceptance if the final manuscript corresponds to the original concept discussed, if the quality of the contribution meets the requirements of the series, and if the final size of the manuscript does not greatly exceed the number of pages originally agreed upon. The manuscript should be forwarded to Springer-Verlag shortly after the meeting. In cases of extreme delay (more than six months after the conference) the series editors will check once more the timeliness of the papers. Therefore, the volume's editor(s) should establish strict deadlines, or collect the articles during the conference and have them revised on the spot. If a delay is unavoidable, one should encourage the authors to update their contributions if appropriate. The editors of proceedings are strongly advised to inform contributors about these points at an early stage.

The final manuscript should contain a table of contents and an informative introduction accessible also to readers not particularly familiar with the topic of the conference. The contributions should be in English. The volume's editor(s) should check the contributions for the correct use of language. At Springer-Verlag only the prefaces will be checked by a copy-editor for language and style. Grave linguistic or technical shortcomings may lead to the rejection of contributions by the series editors. A conference report should not exceed a total of 500 pages. Keeping the size within this bound should be achieved by a stricter selection of articles and not by imposing an upper limit to the length of the individual papers. Editors receive jointly 30 complimentary copies of their book. They are entitled to purchase further copies of their book at a reduced rate. As a rule no reprints of individual contributions can be supplied. No royalty is paid on Lecture Notes in Physics volumes. Commitment to publish is made by letter of interest rather than by signing a formal contract. Springer-Verlag secures the copyright for each volume.

The Production Process

The books are hardbound, and the publisher will select quality paper appropriate to the needs of the author(s). Publication time is about ten weeks. More than twenty years of experience guarantee authors the best possible service. To reach the goal of rapid publication at a low price the technique of photographic reproduction from a camera-ready manuscript was chosen. This process shifts the main responsibility for the technical quality considerably from the publisher to the authors. We therefore urge all authors and editors of proceedings to observe very carefully the essentials for the preparation of camera-ready manuscripts, which we will supply on request. This applies especially to the quality of figures and halftones submitted for publication. In addition, it might be useful to look at some of the volumes already published. As a special service, we offer free of charge LaTeX and TeX macro packages to format the text according to Springer-Verlag's quality requirements. We strongly recommend that you make use of this offer, since the result will be a book of considerably improved technical quality. To avoid mistakes and time-consuming correspondence during the production period the conference editors should request special instructions from the publisher well before the beginning of the conference. Manuscripts not meeting the technical standard of the series will have to be returned for improvement.

For further information please contact Springer-Verlag, Physics Editorial Department II, Tiergartenstrasse 17, D-69121 Heidelberg, Germany

Series homepage – http://www.springer.de/phys/books/lnpp

D. Lemke M. Stickel K. Wilke (Eds.)

ISO Surveys of a Dusty Universe

Proceedings of a Ringberg Workshop
Held at Ringberg Castle, Tegernsee,
Germany, 8-12 November 1999

Springer

Editors

D. Lemke
M. Stickel
K. Wilke
Max-Planck-Institut für Astronomie
Königstuhl 17
69117 Heidelberg, Germany

Library of Congress Cataloging-in-Publication Data applied for.

Die Deutsche Bibliothek - CIP-Einheitsaufnahme

ISO surveys of a dusty universe : proceedings of a Ringberg Workshop, held at Ringberg Castle, Tegernsee, Germany, 8 - 12 November 1999 / D. Lemke ... (ed.). - Berlin ; Heidelberg ; New York ; Barcelona ; Hong Kong ; London ; Milan ; Paris ; Singapore ; Tokyo : Springer, 2000
(Lecture notes in physics ; 548)
(Physics and astronomy online library)
ISBN 3-540-67479-9

ISSN 0075-8450
ISBN 3-540-67479-9 Springer-Verlag Berlin Heidelberg New York

Typesetting: Camera-ready by the authors/editors
Cover design: *design & production*, Heidelberg

Printed on acid-free paper
SPIN: 10720791 55/3144/du - 5 4 3 2 1 0

Preface

Many of the ISO observers who assembled for this workshop at Ringberg castle met for the third time in the Bavarian Alps. At two previous meetings in 1989 and 1990 surveys were only a minor topic. At that time we were excited by the discoveries of the IRAS survey mission and wanted to follow it up with pointed observations using an observatory telescope equipped with versatile instruments. With the rapid development of detector arrays and stimulated by ISO's Observing Time Allocation Committee, however, surveys eventually became an issue for the upcoming mission. In a review paper on "Infrared Surveys - the Golden Age of Exploration" given at an IAU meeting in 1996, Chas Beichman already mentioned that there are ISO surveys. They were at the bottom of his hit list, while the winners were future space missions (Planck, SIRTF, etc.) and ground-based surveys in preparation (Sloan, 2MASS, DENIS, etc.). He organized his table according to the relative explorable volume, calculated from the solid angle covered on the sky and the maximum distance derived from the detection sensitivity. Clearly, with this figure of merit, ISO, as a pointed observatory, is rated low.

Applying the classical definition of a survey, i.e. to search in as large a volume as possible for new or rare objects and/or study large numbers of objects of various classes in order to obtain statistical properties, ISO was indeed limited. As is usual in an observatory mission, hundreds of observers competed with hundreds of proposals, therefore only limited samples of certain objects could be allocated to individuals.

However, if we extend the definition of a survey to include the investigation of reasonable samples of similar objects, then ISO was indeed a great survey mission. For the first time on a cooled space mission, the observatory offered several unique capabilities:

- Mid-infrared deep imaging with unprecedented sensitivity.
- 200 μm mapping with a spatial resolution comparable to that of IRAS at 100 μm.
- Similar sensitivity to COBE but much higher spatial resolution for exploration of the far-infrared extragalactic background.
- High and low spectral resolution capabilities over the wide wavelength range of 2 – 200 μm.
- Far-infrared polarization studies.

- Complementary surveys performed with "no cost" of observing time in parallel to the main instrument or during slews or to fill small gaps in the scheduled observations.

The ISOCAM surveys at 15 μm and the ISOPHOT surveys at 170 μm have revealed many new sources in the distant universe. This has impressively demonstrated that even with a 60-cm telescope, if cooled, important cosmological questions, such as star formation history in the young universe, can be addressed. The infrared is a key region for this research because many of these young galaxies are dust-enshrouded. In addition, ISO has delivered many template spectra for luminous galaxies such as ULIRGs, starbursters, and AGNs throughout the whole infrared wavelength region. ISO data already place serious constraints on the galaxy evolution models and are stimulating many follow-up observations to explore fully the nature of the sources discovered.

The 170 μm Serendipity Survey presented its first galaxy catalogue at this workshop. It is the largest one so far beyond the IRAS limit and already provides significant statistical answers to questions on the dust content of galaxies. Moreover, it has identified interesting "cold" galaxies to follow up. The success of the four parallel, serendipity and filler surveys should encourage ESA to proudly publicize this fact, as expressed by Michael Rowan-Robinson, the chairman of the relevant session.

The very positive response to the call for this Ringberg workshop has been an indication that the topic "ISO Surveys of a Dusty Universe" was exactly right at this time, 1 1/2 years after boil off of the helium. Large survey databases, with entries often close to the noise limits and requiring the elimination of unwanted components in the signals, need more analysis time than individual observations. Mike Hauser, who presented his important extragalactic background results from COBE/DIRBE after many years of careful analysis, has reminded us that quality is more important than speed.

With the now unlimited access to ESA's data archive of the whole ISO mission, several survey projects can increase their number of objects. Others, such as the CAM parallel survey, have just lifted the veil of a huge database still to be explored. Within the next few years, ISO surveys will certainly become a treasure trove for targets of the upcoming infrared missions SIRTF, SOFIA, and FIRST.

Because of the multi-wavelength character of various related topics such as AGN contributions to the IR sky, we enjoyed several exciting non-ISO reviews presented by Günther Hasinger, Chas Beichman, and David Schlegel. We acknowledge the support of our colleagues in the scientific organizing committee (C. Beichman, C. Cesarsky, T. Henning, M.F. Kessler, K. Mattila, M. Rowan-Robinson) who set up an excellent scientific programme. The local organizing committee (supported by U. Klaas and L. Schmidtobreick) prepared and ran the workshop smoothly. We thank them and the staff of the MPG meeting place "Schloss Ringberg" for the comfortable stay in the

inspiring atmosphere experienced that week. We are indepted to the Max-Planck Society and to Deutsches Zentrum für Luft- und Raumfahrt (DLR) for supporting this meeting.

Heidelberg
April 2000

D. Lemke (SOC chair)
M. Stickel (LOC chair)
K. Wilke (LOC)

Contents

The ISO* Mission and Its Surveys

Martin F. Kessler

ISO Data Centre, Astrophysics Division, Space Science Department of ESA,
Villafranca del Castillo, P.O. Box 50727, 28080 Madrid, Spain.

Abstract. The European Space Agency's Infrared Space Observatory (ISO) was an infrared space-borne observatory open to the general astronomical community. It provided sensitive and flexible imaging, photometric, polarimetric and low-medium-high resolution spectroscopic capabilities over a wide wavelength range from 2.5–240 μm. During its highly-successful operational lifetime, it made some 30000 individual pointed observations. All data are now in the public domain and can be retrieved from the ISO Data Archive at `'www.iso.vilspa.esa.es'`. A summary of the mission –including some of its highlights– is presented, followed by a description of current activities designed to help the community exploit the ISO archive.

1 Introduction

ISO's history stretches back to a proposal made to ESA in 1979. The project was selected in 1983, the instruments chosen in 1985, the initial observing programme determined in 1994, the satellite launched in November 1995 and operated in orbit until May 1998. It was the world's first true orbiting infrared observatory. Equipped with four highly-sophisticated and versatile scientific instruments, ISO provided astronomers with a facility of unprecedented sensitivity and capabilities for a detailed exploration of the universe at infrared wavelengths from 2.5–240 μm. The satellite was a great success with most of its sub-systems operating far better than specifications and with its scientific results impacting practically all fields of astronomy. At a wavelength of 12 μm, ISO was one thousand times more sensitive and had one hundred times better angular resolution than its predecessor, the all-sky-surveying IRAS. During its routine operational phase, which lasted almost a year longer than specified, ISO successfully made some 30000 individual observations (scientific and calibration) ranging from objects in our own solar system right out to the most distant extragalactic sources. The ISO archive opened to the community in December 1998. ISO is now in a post operations phase designed to maximise the scientific exploitation of its unique data set and to leave behind a homogeneous archive as a legacy to future generations of astronomers.

* ISO is an ESA project with instruments funded by ESA Member States (especially the PI countries: France, Germany, the Netherlands and the United Kingdom) and with the participation of ISAS and NASA.

D. Lemke, M. Stickel, and K. Wilke (Eds.): LNP 548, pp. 3–10, 2000.

2 Mission Description

2.1 Satellite

The ISO satellite [10], [8] consisted of a 'payload module', the upper cylindrical part in Fig. 1, and a 'service module'. Overall, it was 5.3 m high, 2.3 m wide with a mass of approximately 2500 kg at launch. The service module included the solar array mounted on the sun shield, and subsystems for thermal control, data handling, power conditioning, telemetry and telecommand, and attitude and orbit control. The last item provided the three-axis stabilisation to an accuracy of around an arc second, and also the raster pointing facilities needed for the mission. The downlink bit rate was 32 kbit/s, of which 24 kbit/s were dedicated to the scientific instruments.

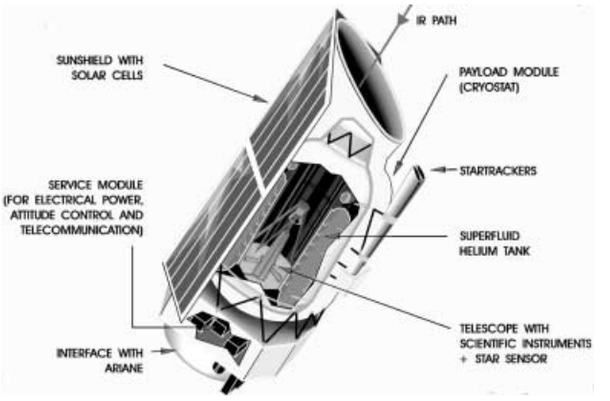

Fig. 1. Cut-away schematic of the ISO satellite

The payload module was essentially a large cryostat. Cooling of the telescope and the instruments to close to absolute zero practically eliminated their thermal emission –an undesirable 'foreground' radiation source– and enabled observations to be made at high sensitivities. Inside the vacuum vessel was a toroidal tank, which at launch was filled with over 2300 litres of superfluid helium. The longer-wavelength infrared detectors were directly coupled to the helium tank and were held at a temperature below 2 K. Cold boil-off gas from the liquid helium cooled the telescope and the scientific instruments (to temperatures of around 3 K) as well as the optical baffles and three radiation shields, before being vented to space. Mounted on the outside of the vacuum vessel at the entrance of the telescope was a sunshade, which prevented direct sunlight from entering the cryostat.

Suspended in the middle of the tank was the telescope, a Ritchey-Chrétien configuration with an effective aperture of 60 cm. The optical quality of its mirrors was designed to be adequate for diffraction-limited performance at

a wavelength of 5 μm. Stringent control over straylight, necessary to ensure that the system's sensitivity was not degraded, was accomplished by means of the sunshade, the Cassegrain and main baffles, and a light-tight shield around the instruments. Additional straylight control was provided by constraining ISO from observing too close to the Sun, Earth and Moon.

2.2 Scientific Instruments

The scientific payload consisted of four instruments: a camera, ISOCAM [3], [2]; an imaging photopolarimeter, ISOPHOT [11], [12]; a long wavelength spectrometer, LWS [4], [5]; and a short wavelength spectrometer, SWS [6], [7]. Each instrument was built by an international consortium of scientific institutes and industry, headed by a Principal Investigator, using national funding. Although developed separately, the four instruments were designed to form a complete, complementary and versatile common-user package.

Photometry was possible in broad and narrow spectral bands across its entire wavelength range of 2.5 to around 240 μm. A variety of apertures, ranging from 5 to 180″, was selectable out to 120 μm. For spectroscopy, resolving powers ranging from 50 to 30,000 were available in the wavelength range from 2.5 to nearly 200 μm. ISO was capable of direct imaging in broad and narrow spectral bands across the complete wavelength range at spatial resolutions ranging from 1.5″ (at the shortest wavelengths) to 90″ (at the longer wavelengths). Mapping could be carried out using sequences of pointings.

In addition to the main observing modes, there were three auxiliary modes, which have provided significant quantities of data highly suitable for present and future survey work. When the camera and the long wavelength spectrometer were not the main instruments, they were generally used in a parallel mode to image adjacent areas of sky. Whenever possible, the long-wavelength channel of the photometer was used during satellite slews, leading to a partial sky survey at wavelengths around 200μm, a spectral region not covered by the IRAS survey. Additionally, serendipitous data was taken during slews by the long wavelength spectrometer in ten narrow spectral intervals from 45 – 180 μm.

2.3 Orbit and Operations

ISO's operational orbit had a period of just under 24 hours, an apogee height of 70600 km and a perigee height of around 1000 km. In this orbit two ground stations were needed to provide visibility of the satellite from the ground for the entire scientifically-useful part of the orbit. ESA provided one ground station. The second ground station plus associated resources was contributed by the National Aeronautics and Space Administration (NASA), USA and the Institute of Space and Astronautical Science (ISAS), Japan. Operations of ISO [9], [8]; were conducted from ESA's Villafranca Satellite Tracking Station (VilSpa), located near Madrid in Spain. Due to its limited lifetime, the severe

sky coverage constraints, the complexity of the scientific instruments, and the necessity to make many short observations, ISO was operated in a service observing mode with each day's observations being planned in detail and finalised up to 3 weeks in advance.

3 Observing Programme and Surveys

Approximately 45% of ISO's time was reserved for those parties contributing to the development and operation of the scientific instruments and the overall facility; the other 55% was distributed to the general community via 'Calls for Observing Proposals'. ISO successfully made over 26,000 scientific observations belonging to some 1000 research programmes led by about 600 different Principal Investigators. The total time used was approximately 10,000 hours. Overall, about 10% of ISO's time was used for solar system studies, 23% for the ISM, 29% on stellar and circumstellar topics, 27% for extragalactic observations and 11% for cosmology.

In total, the ISO Data Archive contains over 100,000 data sets, including the scientific and calibration observations, engineering pointings and data from the parallel and serendipity modes. With all the data having entered the public domain by August 1999, the archive provides many opportunities for construction of new samples for "archival surveys".

Table 1. The largest ISO observing programmes, each with 1% or more of ISO's observing time and together amounting to 15% of the total time available.

Programme	Principal Investigator
European Large Area ISO Survey	Rowan Robinson
Spectroscopy of Bright Galactic Nuclei	Genzel
ISOCAM Survey of the Inner Galaxy	Omont
ISOCAM Deep Survey Programme	Cesarsky
ISM of Normal Galaxies	Helou
Dust Debris Around Solar Mass Stars	Becklin
Exploring the Full Range of Quasar/AGN Properties	Wilkes
Structure of FIR Background	Puget

When setting up the observing programme, there was no specific provision for surveys. Each programme was treated on its scientific merits and considerations of technical feasibility. It is interesting to note that results from the majority of the 8 largest programmes (Table 1) were presented at this meeting on surveys.

Other rich sources of survey material from ISO include the data from the auxiliary modes, see papers in this volume by Stickel et al. (ISOPHOT serendipity, [16]), Siebenmorgen et al. (ISOCAM parallel, [15]) and Lim (LWS parallel and serendipity, [13]). Furthermore, to maximise scheduling efficiency, there was the concept of 'filler' programmes, which were set up with lots of relatively short observations of targets roughly uniformly distributed over the sky. The basic idea was that whenever there was a short gap in the schedule where no other higher priority observation would fit, it could be filled by one of these observations of a nearby target. The main filler programme (Lonsdale, this volume) received some 65 hours of time.

4 Highlights

ISO was a great technical, operational and scientific success. Due to excellent engineering and a fortunate combination of circumstances at launch, the liquid helium supply lasted over 10 months longer than the specified 18 months. The extra lifetime not only led to many more observations but also made it possible to observe the Taurus/Orion region – inaccessible in the nominal mission. By a combination of very good in-orbit performance, detailed analysis on the ground and a variety of tune-ups, the accuracy of the pointing system was improved to the arc second level. The absolute pointing error was reduced to around $1''$, ten times better than specified and the short term jitter was about five times better than the specification of $2.7''$ (2σ, half cone, over a 30 second period of time). The optical performance of the telescope and baffle system was excellent, with straylight being too low to measure.

All the scientific instruments, including many delicate cryogenic mechanisms, performed extremely well and returned large quantities of high quality data, although compared to pre-launch predictions, there was a sensitivity loss for three of them. All elements of the ground segment also performed excellently, leading to an overall availability of the system during routine phase of 98.3% of the time scheduled for science. Taking into account all possible reasons for failure, only 4% of observations were lost. The mission planning systems produced schedules with an average efficiency of 92% and over 98% of the highest-priority observations were successfully executed.

Scientifically, as demonstrated by the papers at this conference and others as well as by the still-increasing publication rate in the refereed literature, ISO results are significantly impacting almost all fields of astronomical research, almost literally from cosmology to comets. Some highlights include:

- making deep cosmological surveys at all its wavelengths, the results from which show: early star formation hidden by dust; the need for evolutionary models; resolution of part of the cosmic infrared background (CIB) into discrete sources; and detection of fluctuations in the CIB,
- distinguishing between central engines and starbursts as the energy sources for ultra-luminous infrared galaxies,

- detailed investigations of star-forming regions in our own and external galaxies, including detections of pre-stellar cores and determinations of initial mass functions showing substantial numbers of objects in the brown dwarf mass range,
- demonstrating for solar system studies, with its wealth of discoveries, the worth of a relatively-small telescope in Earth orbit even in the age of remote exploration,
- opening up many new new fields of study such as:
  - water vapour in the cosmos, via measuring a wealth of water vapour transitions in objects such as Mars, Titan, the giant planets, comets, shocks, the cold interstellar medium, circumstellar envelopes and in the ultra-luminous galaxy Arp 220,
  - the first detections of the lowest pure rotational lines of H_2 plus detections of HD,
  - detailed investigations of interstellar solid state features, e.g. CO_2 ices,
  - crystalline silicates, showing inter alia a link between interplanetary and interstellar dust,
- some specific discoveries:
  - first detection of a fluorine-bearing molecule (HF) in interstellar space,
  - discovering the OH absorption feature at 35 μm, which had long been predicted to provide the excitation and line inversion responsible for powering this galaxy's megamaser emission.

5 The ISO Data Archive and Current Activities

A network of data centres, grouped around the institutes which contributed to the instruments and operations, has been set up to maximise the scientific return of the mission by helping the community in its effective and widespread exploitation of the data and by preparing the best possible final archive to leave as ISO's legacy. Users of ISO data are strongly advised to take advantage of the expertise available from the centres involved in this effort, namely:

- ISO Data Centre, ESA, Villafranca, Spain
- Five Specialist National Data Centres:
  - French ISO Centres, SAp/Saclay and IAS/Orsay
  - ISOPHOT Data Centre, MPIA, Germany
  - Dutch ISO Data Analysis Centre, Groningen
  - ISO Spectrometer Data Centre, MPE, Germany
  - UK ISO Data Centre, RAL, Chilton
- ISO Support Center, IPAC, USA.

The ESA ISO Data Centre (e-mail: `helpdesk@iso.vilspa.esa.es`) is responsible for the archive, the general off-line processing ("pipeline") software, the global instrumental cross-calibration and supporting the European user

community. The National Data Centres are responsible for the instrument-specific aspects (including calibration, data reduction software and expertise) and for supporting their local and national user communities. IPAC is responsible for supporting the US community and provision of some software.

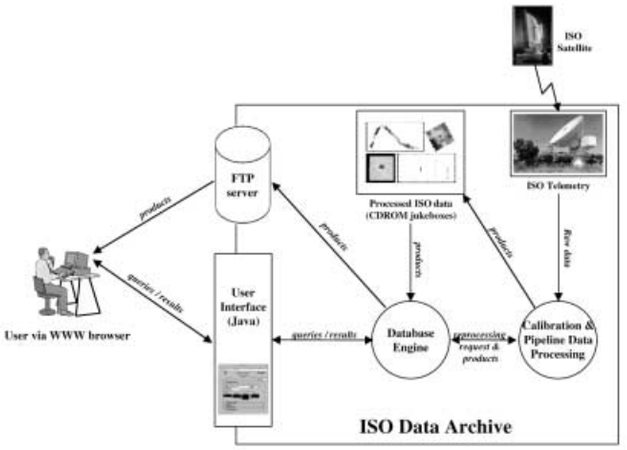

Fig. 2. A schematic representation of the ISO Data Archive.

After exhaustion of ISO's liquid helium supply and the end of the in-orbit mission, all data were reprocessed with the then-current calibration and algorithmic knowledge to populate the ISO 'interim' archive. In December 1998, community access started via the WWW (`'www.iso.vilspa.esa.es'`) to this archive (cf. Fig. 2 and [1]), which includes three levels of 'browse' products designed to give a quick but accurate impression of the scientific content of each observation. The Java-based user interface provides a wide range of search capabilities for both general and expert users. Additional capabilities, aimed at instrumentally-expert users were added in August 1999. Version 3 (December 1999) was a major enhancement for general users, providing links between observations and the refereed literature in which they have appeared, more sophisticated manipulation of the browse products, and direct access to relevant IRAS data. It also added functionality so that other archives (e.g. Simbad) can serve ISO browse data products. The archive is intensively used by the community, with the equivalent of 10 – 30% of the total number of scientific observations being retrieved each month.

A 'library' of explanatory documents to help users get the best out of the data is also accessible via the web. During 2000, this will be further expanded to contain the six-volume set of ISO Handbooks, the definitive stand-alone guide to all ISO data products. Software tools to reduce and analyse the data interactively are also available for download.

The processing software and calibration files for each instrument are upgraded approximately annually. So that users can take advantage of the improved processing, the default retrieval from the archive now reprocesses the requested data with the latest system prior to making them available to the user via ftp. A second bulk re-processing of all the data is foreseen in mid-2001 to populate a 'legacy' archive, which will be available to the community before the end of 2001.

6 Conclusions

The ISO mission has been an outstanding technical, operational and scientific success, with results impacting almost all field of astronomy from cosmology to comets. The publication rate in the refereed literature continues to increase. All data have been processed with the 'end-of-mission' pipeline and made available to the community via a WWW- and Java-based interface to the ISO Data Archive. Over the next 2 years, the calibration of, and reduction algorithms for, the date will be further refined and additional functionality will be added to the state-of-the-art archive. All data will be re-processed in mid-2001 to populate the 'Legacy Archive', which will support future generations of astronomers.

References

1. Arviset, C. and Prusti, T. 1999, ESA Bulletin, 98, 133.
2. Cesarsky C.J. 1999, Proc. Universe as Seen by ISO, ESA SP-427, Cox, P. and Kessler, M.F. (Eds), 45.
3. Cesarsky C.J., Abergel, A., Agnèse, P. et al. 1996, A&A, 315, L32.
4. Clegg P.E. 1999, Proc. Universe as Seen by ISO, ESA SP-427, Cox, P. and Kessler, M.F. (Eds), 39.
5. Clegg P.E., Ade P.A.R., Armand C. et al. 1996, A&A, 3.5, L38.
6. de Graauw Th. 1999, Proc. Universe as Seen by ISO, ESA SP-427, Cox, P. and Kessler, M.F. (Eds), 31.
7. de Graauw Th., Haser, L.N., Beintema, D.A. et al. 1996, A&A, L49.
8. Kessler, M.F., 1999, Proc. Universe as Seen by ISO, ESA SP-427, Cox, P. and Kessler, M.F. (Eds), 23.
9. Kessler, M.F., Clavel, J. and Faelker, J. 1998, ESA Bulletin, 95, 87.
10. Kessler, M.F., Steinz, J.A., Anderegg, M., et al. 1996, A&A, 315, L27.
11. Lemke D. and Klaas, U. 1999, Proc. Universe as Seen by ISO, ESA SP-427, Cox, P. and Kessler, M.F. (Eds), 51.
12. Lemke D., Klaas, U., Abolins, J. et al. 1996, A&A, 315, L64.
13. Lim et al., this volume
14. Lonsdale et al., this volume
15. Siebenmorgen et al., this volume
16. Stickel et al., this volume

A New Population of Faint Starburst Galaxies Revealed by 15 μm ISOCAM Deep Surveys

Catherine J. Cesarsky[1,2,3]

[1] On behalf of the ITGES consortium: D. Elbaz, D. Fadda, H. Aussel, F.X. Désert, A. Franceschini, H. Flores, M. Harwit, J.L. Puget, J.L. Starck, L. Danese, D.C. Koo, and R. Mandolesi.
[2] CEA Saclay - Service d'Astrophysique, Orme des Merisiers, 91191 Gif-sur-Yvette CEDEX, France
[3] European Southern Observatory, Karl-Schwarzchild-Strasse, 2 D-85748 Garching bei Muenchen, Germany *(email: ccesarsk@eso.org)*

Abstract. We present the counts derived from the five mid-IR 15 μm (12-18 μm LW3 band) ISOCAM Guaranteed Time Extragalactic Surveys performed in the regions of the Lockman Hole and Marano Field, the HDF-North and South (plus flanking fields) and the lensing cluster A2390 at low fluxes and IRAS at high fluxes. We cover four decades in flux from 50 μJy to $\sim$0.3 Jy. The roughly 1000 sources detected with ISOCAM, 600 of which have a flux above the 80 % completeness limit, guarantee a very high statistical significance for the integral and differential source counts from 0.1 mJy up to $\sim$5 mJy. The slope of the differential counts is very steep ($\alpha = -3.0$) in the flux range 0.4-4 mJy, hence much above the Euclidean expectation of $\alpha = -2.5$. When compared with no-evolution models based on IRAS, our counts show a factor $\sim$ 10 excess at 400 μJy, and a fast convergence, with $\alpha = -1.6$ at lower fluxes.

Multiwavelength studies of a subsample of the ISOCAM sources indicate that they are intrinsically bright galaxies (Luminous Infrared Galaxies, LIRGs), with median redshift 0.7. These galaxies, despite their low surface density, are responsible for a large part of star formation at $z < 1$ and contribute substantially to the cosmic infrared background at 140 μm.

1 Introduction

The understanding of galaxy evolution is a key problem for cosmology, and number counts appear to be a strong constraint on the models, which does not suffer from the exotic behaviour of individual galaxies. Most of the energy released by local galaxies is radiated in the optical-UV range [30]. If this were to remain true over the whole history of the universe, then one could follow the comoving star formation rate of the universe as a function of redshift by measuring the optical-UV light radiated by galaxies [20] [21]. This scenario changed considerably after the detection of a substantial diffuse cosmic IR background (CIRB) in the 0.1 – 1 mm range from the COBE-FIRAS data [26] [16] [17] [12] [19] and at 140 – 240 μm from the COBE-DIRBE data [17] [19]. Surprisingly the mid-IR/sub-mm extragalactic background light is at

D. Lemke, M. Stickel, and K. Wilke (Eds.): LNP 548, pp. 11–20, 2000.

least as large as that of the UV/optical/near–IR background [9] [19], which implies a stronger contribution of obscured star formation at redshifts larger than those sampled by IRAS ($z > 0.2$). To understand the exact origin of this diffuse emission and its implications for galaxy evolution, we need to identify the individual galaxies responsible for it and the best way to do that consists of observing directly in the IR/sub-mm range.

In the mid-IR, IRAS has explored the local universe ($z < 0.2$). With a thousand times better sensitivity and sixty times better spatial resolution, ISOCAM [6], the camera onboard ISO [18], provides for the first time the opportunity to perform cosmologically meaningful surveys.

We have performed several such surveys with ISOCAM, ranging from large area-shallow surveys to small area-ultra deep surveys. This paper presents the source counts obtained with the LW3 filter centred at 15 μm (12-18 μm). Including the surveys over the two Hubble deep fields, almost 1000 sources with flux densities ranging from 0.1 mJy to 10 mJy were detected, allowing us to establish detailed source count diagrams.

2 Description of the Surveys and Data Reduction

The five ISOCAM Guaranteed Time Extragalactic Surveys ([6], Table 1) are complementary. They were carried out in both the northern (Lockman Hole) and southern (Marano Field) hemispheres, in order to be less biased by large-scale structures. These two fields were selected for their low zodiacal and cirrus emission and because they had been studied at other wavelengths, in particular in the X-ray band, which is an indicator of the AGN activity of the galaxies. Only one of the 'Marano' maps was scanned at the exact position of the original Marano Field [22], while the 'Marano FIRBACK' (MFB) Deep and Ultra-Deep surveys were positioned at the site of lowest galactic cirrus emission, because they were combined with the FIRBACK ISOPHOT survey at 175 μm [27] [8]. Indeed the importance of the Galactic cirrus emission in hampering source detection is much larger at 175 μm than at 15 μm, but the quality of the two 15 μm ultra deep surveys in the Marano Field area is equivalent. In addition, very deep surveys were taken with ISOCAM over the areas of the HDF North [29] and HDF South.

The transient behaviour of the cosmic ray induced glitches, which makes some of them mimic real sources, is the main limitation of ISOCAM surveys. We have developed two pipelines for the analysis of ISOCAM surveys in order to obtain two independent source lists per survey and improve the quality of the analysis. PRETI (Pattern REcognition Technique for ISOCAM data), developed by Starck et al. [31], is able to find and remove glitches using multi-resolution wavelet transforms. The "Triple Beam-Switch" (TBS) technique, developed by Désert et al. [7], treats micro-scanning or mosaic images as if they resulted from beam-switching observations. All the surveys have been independently analysed using both techniques. Monte Carlo simulations were

Table 1. ISOCAM 15 μm surveys sorted by increasing depth.

Survey Name	N_{obs}	Area (am^2)	$S_{80\%}$ (mJy)	t_{int} (min)	# gal	Slope
(1)	(2)	(3)	(4)	(5)	(6)	(7)
Lockman Shallow[(a)]	3	1944	1	3	80	-2.1 ± 0.2
Lockman Deep[(a)]	6	510	0.6	11	70	-2.4 ± 0.3
MFB Deep[(a)]	18	710	0.4	15.4	144	-2.4 ± 0.2
Marano UD[(a)]	75	70	0.2	114	82	-1.5 ± 0.1
MFB UD[(a)]	75	90	0.2	114	100	-1.5 ± 0.2
HDF North[(b)]	64	27	0.1	135	44	-1.6 ± 0.2
HDF South[(a)]	64	28	0.1	168	63	-1.4 ± 0.1
A2390[(c)]	100	5.3	0.05	432	31	-1.2 ± 0.6

Comments: Col.(1) Survey name with reference: (a) Elbaz et al. [10], (b) Aussel et al. [2], (c) Altieri et al. [1]; Col.(2) maximum number of pointings on the same sky position (redundancy); Col.(3) the total area covered in square arcminutes; Col.(4) the flux at which the survey is at least 80% complete; Col.(5) the corresponding integration time per sky position (in minutes); Col.(6) the number of galaxies whose flux is over the 80% completeness threshold; Col.(7) the slope of the fit to the integral $\log N - \log S$. A2390 completeness limit includes the corrections for lensing magnification.

performed by taking into account the completeness and the photometric accuracy to correct for the Eddington bias and to compute error bars in the number count plots.

3 The ISOCAM 15 μm Source Counts

Figures 1 and 2 show respectively the integral and the differential number counts obtained in the five independent guaranteed time surveys conducted in the ISOCAM 15 μm band, as well as the HDF surveys. The contribution of stars to the 15 μm counts was corrected. It is negligible at fluxes below the mJy level as confirmed by the spectro-photometric identifications in the ISOHDF-North (1 star out of 44 sources), South (3 stars over 71 sources), and CFRS 1415+52 (1 star over 41 sources ranging from ~ 0.3 mJy to ~ 0.8 mJy). In the Lockman Shallow Survey ($S_{15\,\mu m} > 1$ mJy), about 12 % of the sources were classified as stars from their optical-mid IR colours (using the Rayleigh-Jeans law). We have also represented the counts from the ISOHDF-North (from [2]), ISOHDF-South, and, at the lowest fluxes, the counts obtained from the A2390 cluster lens (down to 50 μJy, including the correction for lensing magnification; [1], see also [24]). We have only included the flux bins where the surveys are at least 80 % complete, according to the simulations.

The first striking result of these complementary source counts is the consistency of the eight 15 μm surveys over the full flux range. Some scatter

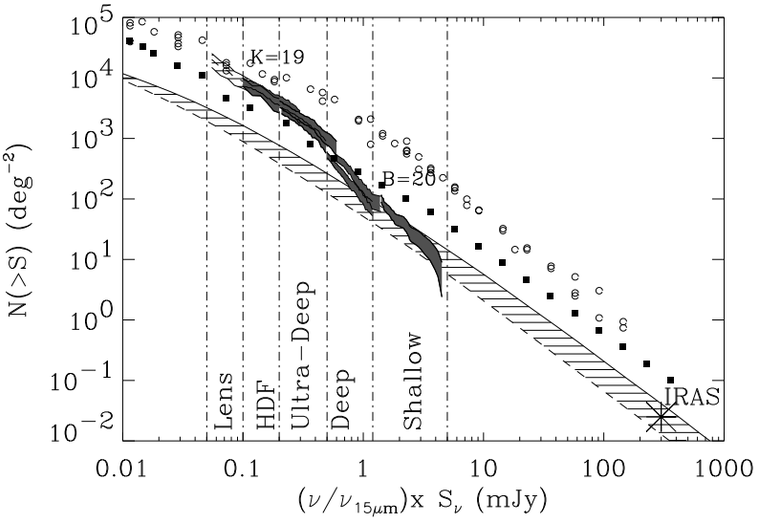

Fig. 1. Integral counts, i.e. the number of galaxies, N, detected at 15 μm above the flux S(mJy), with 68 % confidence contours. K counts (Gardner et al. [15]) and B counts (Metcalfe et al. [23]),multiplied by the ratio ν/ν_{15} to represent the relative energy densities at high fluxes, are overplotted with open circles and filled squares, respectively. The hatched area materialises the range of possible expectations from models assuming no evolution and normalised to the IRAS 12 μm local luminosity function (LLF). The upper limit was calculated on the basis of the LLF of Rush, Malkan & Spinoglio [28], as Xu et al. [33] and shifted from 12 to 15 μm with the template SED of M82; the lower limit uses the LLF of Fang et al. [11] and the template SED of M51.

is nevertheless apparent; given the small size of the fields surveyed, we attribute it to clustering effects. The two main features of the observed counts are a significantly super-Euclidean slope ($\alpha = -3.0$) from 3 to 0.4 mJy and a fast convergence at flux densities fainter than 0.4 mJy. In particular, the combination of five independent surveys in the flux range 90-400 μJy shows a turnover of the normalised differential counts around 400 μJy and a decrease by a factor $\sim$ 3 at 100 μJy. We believe that this decrease, or the flattening of the integral counts (see the change of slope in col(7) of Table 1) below $\sim$400 μJy, is real. It cannot be due to incompleteness, since this has been estimated from the Monte-Carlo simulations (see section 2). The differential counts can be fitted by two power laws by splitting the flux axis in two regions around 0.4 mJy. In units of mJy^{-1} deg^{-2}, we obtain, by taking into

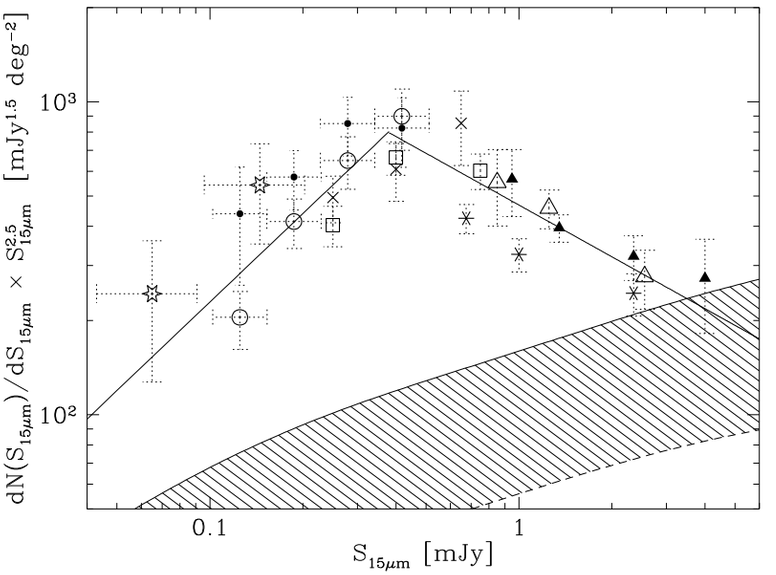

Fig. 2. Differential Number Counts of 15 μm Galaxies, with 68% error bars. The counts are normalised to a Euclidean distribution of non-evolving sources, which would have a slope of $\alpha = -2.5$ in such a universe. Data points: A2390 (open stars), ISOHDF-North (open circles), ISOHDF-South (filled circles), Marano FIRBACK (MFB) Ultra-Deep (open squares), Marano Ultra-Deep (crosses), MFB Deep (stars), Lockman Deep (open triangles), Lockman Shallow (filled triangles). The hatched area materialises the range of possible expectations from models assuming no evolution (see Fig. 1).

account the error bars (S is in mJy):

$$\frac{dN(S)}{dS} = \begin{cases} (2000 \pm 600)\ S^{(-1.6\pm0.2)} \ \ldots\ 0.1 \leq S \leq 0.4 \\ \\ (470 \pm 30)\quad S^{(-3.0\pm0.1)} \ \ldots\ \ 0.4 \leq S \leq 4 \end{cases} \tag{1}$$

In the integral plot, the curves are plotted with 68 % confidence contours based on our simulation analysis. The total number density of sources detected by ISOCAM at 15 μm down to 100 μJy (no lensing) is (2.4 ± 0.4) arcmin^{-2}. It extends up to (5.6 ± 1.5) arcmin^{-2}, down to 50 μJy, when including the lensed field of A2390 [1].

4 Nature of the ISOCAM Galaxies

In Fig. 1, we have overplotted the integral counts in the K [15] and B [23] bands, in terms of νS_ν. For bright sources, with densities lower than 10 deg^{-2},

these curves run parallel to an interpolation between the ISOCAM counts presented here and the IRAS counts; the bright K sources emit about ten times more energy in this band than a comparable number of bright ISOCAM sources at 15 μm. But the ISOCAM integral counts present a rapid change of slope around 1-2 mJy, and their numbers rise much faster than those of the K and B sources. The sources detected by ISOCAM are a sub-class of the K and B sources which harbour activity hidden by dust, they have nothing to do with the faint blue galaxies which dominate the optical counts at z$\sim$0.7.

Deep surveys have been carried out on small fields containing sources well known at other wavelengths: the HDF North ([29], [2], [3], [7]) and the CFRS 1452+52 field ([13]). This has yielded a small but meaningful sample of sources (83 galaxies) with a positional accuracy better than 6", sufficient for most multiwavelength studies. Most of these sources can easily be identified with bright optical counterparts ($I_C < 22.5$) with a median redshift of $z \simeq 0.7 - 0.8$ imposed by the k-correction ([2], [3], [13]). In both samples, the proportion of bonafide, spectroscopically confirmed, active nuclei among ISOCAM galaxies is very low. The majority of the galaxies have optical colours comparable to those of Sbc and Scd spirals, and do not even exhibit strong OII lines: it is really dust enshrouded star formation that we are witnessing, and which can only be revealed by infrared (ideally complemented by radio) observations. This is also confirmed by near infrared spectroscopy on a sample of HDF-S ISOCAM sources, yielding detections of Hα emission (Rigopoulou et al., Flores et al, these proc.).

Despite the fact that the SED of these galaxies is not known, Aussel et al., using various templates, estimate their bolometric luminosities as being in the range several 10^{10} to 10^{12} $L_\odot$[3]. Flores et al. use the far infrared-radio correlation to estimate the infrared flux, and reach similar conclusions [13]. Note that there are constraints on the far infrared flux of the ISOCAM galaxies: they cannot be too high, otherwise they enter in contradiction with counts at other wavelengths and with the measurements of the infrared background (see section 6). We show in Fig. 3 the SCUBA counts at 850 μm, together with the ISOCAM counts. The hatched areas correspond to predictions for these counts if the ISOCAM sources have (a) a starburst-like SED, based on the spectrum of M82, (b) an ULIRG-like SED, based on the spectrum of Arp 220. It is clear that starburst-like spectra are required.

5 Interpretation of the Counts

The differential counts (Fig. 2), which are normalised to $S^{-2.5}$ (the expected differential counts in a non expanding Euclidean universe with sources that shine with constant luminosity), present a turnover around $S_{15\,\mu m}$=0.4 mJy, above which the slope is very steep ($\alpha = -3.0 \pm 0.1$). No evolution predictions were derived assuming a pure k-correction in a flat universe ($q_0 = 0.5$), including the effect of Unidentified Infrared Bands emission in the galaxy

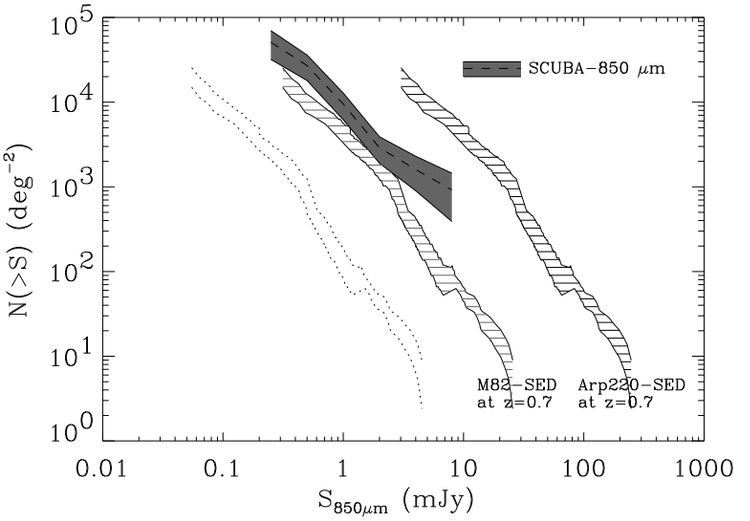

Fig. 3. Integral counts at 850 μm from SCUBA [4]. From the 15 μm ISOCAM counts (dotted lines), one can extrapolate the contribution of the ISOCAM galaxies at 850 μm for a given redshift distribution and spectral energy distribution (SED). Two examples are shown here using SEDs of M82 and ARP 220, and assuming that all ISOCAM galaxies have the same redshift, $z = 0.7$, corresponding to their median redshift in the HDF and CFRS fields.

spectra. In the figures 1 and 2, the lower curve is based on the Fang et al. IRAS 12 μm local luminosity function (LLF), using the spectral template of a quiescent spiral galaxy (M51) [11]. The upper curve is based on the Rush, Malkan & Spinoglio IRAS-12 μm LLF [28], translated to 15 μm using as template the spectrum of M82, which is also typical of most starburst galaxies in this band. More active and extinct galaxies, like Arp220, would lead to even lower number counts at low fluxes while flatter spectra like those of AGNs are less flat than M51. In the absence of a well established LLF at 15 μm, we consider these two models as upper and lower bounds to the actual no-evolution expectations; note that the corresponding slope is ~ -2. The actual number counts are well above these predictions; in the 0.3 mJy to 0.6 mJy range, the excess is around a factor 10: clearly, strong evolution is required to explain this result (note the analogy with the radio source counts, [32]).

Franceschini et al. have modelled the counts, invoking the presence of a strongly evolving starburst population superimposed to that of normal and active galaxies [14]. Assuming that the local fraction of the evolving starburst population is only several per cent of the total, they find a good match to the differential counts(see Fig. 4) if the comoving density of starbursts increases

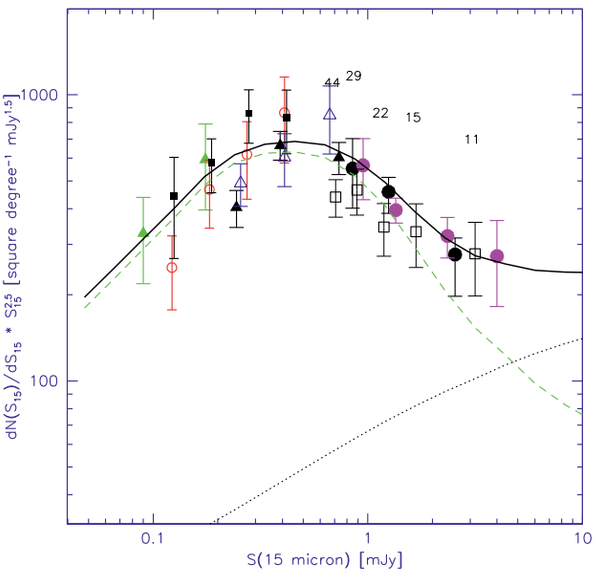

Fig. 4. Differential source counts at 15 μm normalized to the Euclidean law ($N[S] \sim S^{-2.5}$). The data come from an analysis of the GITES surveys by Elbaz et al. [10]. The differential form of the counts is such that all data points in the figure are statistically independent. The dotted line corresponds to the expected counts for a population of non-evolving spirals. The dashed line comes from the population of starbursting galaxies modelled by Franceschini et al. [14]

as $n(L,z) = n_0(L_0,z) \times (1+z)^6$ and, at the same time, an increase of the luminosities as $L(z) = L_0 \times (1+z)^3$.

This fast evolution should turn over at $z \sim 0.8-0.9$ to match the redshift distributions obtained in HDF-N and in the CFRS field.

6 Contribution of ISOCAM Sources to Global Star Formation and the Infrared Background

Flores et al. estimate, from their sample of 41 sources in a CFRS field, that accounting for the IR light from star forming galaxies leads to a global star formation rate which is 2 to 3 times larger than estimated from UV light only [13]. This implies that the ISOCAM galaxies account for at least half of the star formation over the major part of the life of the universe.

In Fig. 5 we display the SED of the cosmic background from the UV to mm waves. We have also represented the 15 μm background contributed by the ISOCAM sources, which at this point can only be compared to (and is comfortably lower than) upper limits of this background derived from observations of high energy gamma ray sources. It is clear from this figure that

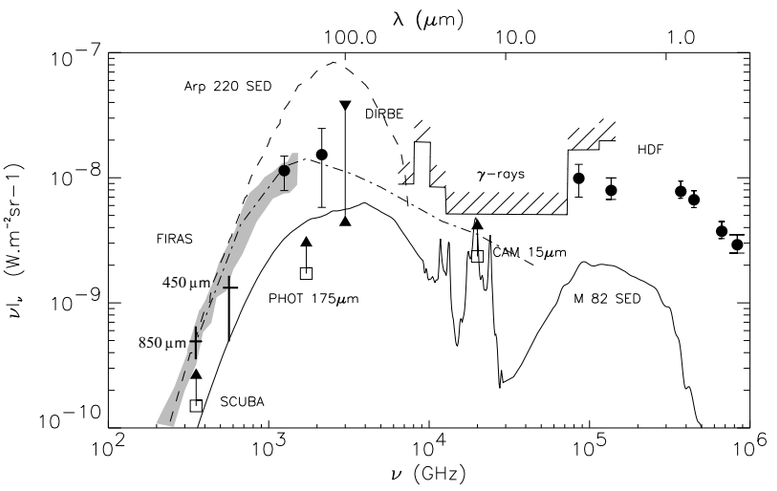

Fig. 5. Cosmic background from UV to mm. Open squares give the lower limit from ISO (ISOCAM-15 μm and ISOPHOT-175 μm) and SCUBA-850 μm (the two tick crosses correspond to the recent values at 450 and 850 μm from [4]. The optical–UV points are from [25]. The COBE FIRAS (grey area) and DIRBE 140 and 240 μm (filled circles) data are from [19]

the ISOCAM sources contribute a sizeable part of the infrared background at 140 μm: about 30 % if their SED is like that of M82. It is also apparent from this figure that the ISOCAM galaxies cannot have ratios of fluxes (FIR/MIR) as high as Arp 220, otherwise they would much overproduce the FIR background.

7 Conclusion

We have presented the 15 μm differential and integral counts drawn by several complementary ISOCAM deep surveys, with a significant statistical sampling (993 galaxies, 614 of which have a flux above the 80 % completeness limit) over two decades in flux from 50 μJy up to 5 mJy. These counts reveal the presence of a new population of galaxies, whose rate of evolution surpasses that of any known type of objects. Detailed studies of small samples of these galaxies indicate that they are LIRGs, unrecognisable from their optical colours; and that they account for an important part of the infrared background and of the global star formation in the universe.

References

1. Altieri B., Metcalfe L., Kneib J.P., 1999, A&A 343L, 65
2. Aussel H., Cesarsky C., Elbaz D. et al., 1999a, A&A 342, 313
3. Aussel H., Elbaz D., Désert F.X. et al., 1999b, in Cox, P., Kessler, M.F. (eds.), *The Universe as seen by ISO*, ESA SP-427, p. 1023
4. Blain, A.W., 1999, MNRAS 309, 955
5. Cesarsky C., Abergel A., Agnèse P. et al., 1996, A&A 315, L32
6. Cesarsky C.J., Elbaz D., 1996, IAUS, M. C. Kafatos, Y. Kondo (eds.), Kluwer Acad. Pub., Dordrecht, vol. 168, 109.
7. Désert F.X., Puget J.L., Clements D. et al., 1999, A&A 342, 363
8. Dole H., Lagache G., Puget J.L. et al., 1999, in Cox, P., Kessler, M.F. (eds.), *The Universe as seen by ISO*, ESA SP-427, p. 1031, astro-ph/9902122
9. Dwek E., Arendt R., Hauser M. et al., 1998, ApJ 508, 106
10. Elbaz,D., Cesarsky,C.J., Fadda,D.,Aussel,H. et al.(1999) A&A, 351, L37
11. Fang F., Shupe D., Xu C., Hacking P., 1998, ApJ 500, 693
12. Fixsen D.J., Dwek E., Mather J.C. et al., 1998, ApJ 508, 123
13. Flores H., Hammer F., Thuan T. et al., 1999, ApJ 517, 148
14. Franceschini A., Hasinger G., Miyaji T., et al., 1999, MNRAS 310L, 5
15. Gardner J.P., Cowie L.L., Wainscoat R.J., 1993, ApJ 415, L9
16. Guiderdoni B., Bouchet F, Puget J.L. et al., 1997, Nat 390, 257
17. Hauser M.G., Arendt R.G., Kelsall T., 1998, ApJ 508, 25
18. Kessler M., Steinz J., Anderegg M. et al., 1996, A&A 315, L27
19. Lagache G., Abergel A., Boulanger F. et al., 1999, A&A 344, 322
20. Lilly S., Le Fèvre O., Hammer F. et al., 1996, ApJ 460, L1
21. Madau P., Ferguson H., Dickinson M. et al., 1996, MNRAS 283, 1388
22. Marano, B., Zamorani, G., Zitelli, V., 1988, MNRAS 232, 111
23. Metcalfe N., Shanks T., Fong R. et al., 1995, MNRAS 273, 257
24. Metcalfe L., Altieri B., McBreen B. et al., 1999, in Cox, P., Kessler, M.F. (eds.), *The Universe as seen by ISO*, ESA SP-427, p. 1019
25. Pozetti L., Madau P., Zamorani G., Fergusson H.C., Bruzual G.A., 1998, MNRAS 298, 1133
26. Puget J.L., Abergel A., Bernard J.P. et al., 1996, A&A 308, L5
27. Puget J.L., Lagache G., Clements D. et al., 1999, A&A 345, 29
28. Rush B., Malkan M.A., Spinoglio L., 1993, ApJS 89, 1
29. Serjeant S., Eaton N., Oliver S. et al., 1997, MNRAS 289, 457
30. Soifer B.T., Neugebauer G. 1991, AJ 101, 354
31. Starck J.-L., Aussel H., Elbaz D. et al., 1999, A&AS 138, 365
32. Windhorst R.A., Fomalont E.B., Partridge R.B., Lowenthal J.D., 1993, ApJ 405, 498
33. Xu C., Hacking P., Fang F. et al., 1998, ApJ 508, 576

Mid-Infrared Properties of Distant Cluster Galaxies as Revealed by ISOCAM

Dario Fadda[1], David Elbaz[1], Pierre-Alain Duc[1], Hector Flores[1], and Catherine Cesarsky[2]

[1] CEA Saclay - Service d'Astrophysique, Orme des Merisiers, 91191 Gif-sur-Yvette Cédex, France
[2] European Southern Observatory, Karl-Schwarzchild-Strasse, 2 D-85748 Garching bei München, Germany

Abstract. Several distant galaxy clusters have been observed by the Infrared Satellite Observatory ISO in the mid-infrared. We present preliminary analyses of mid-IR properties and optical follow-ups of ISOCAM sources detected in Abell 1689 and Abell 2390, two clusters at a redshift of $z = 0.2$, and of J1888 and 3C330, two clusters at high redshift ($z = 0.6$).

Galaxies detected at 6.75 μm , which correspond to the brightest optical sources, always exhibit a central concentration. In contrast to that, galaxies emitting in the 15 μm band, which is more sensitive to hot dust, are more frequent in the outskirts than in the central parts of clusters. Optical colors of 6.75 μm sources do not differ significantly from the median color of cluster galaxies. In contrast, galaxies detected at 15 μm are bluer than the main population of cluster galaxies and most of them correspond to the blue outliers of the color-magnitude relation for clusters which are responsible for the Butcher-Oemler effect. Moreover, galaxies which are optically classified as dust-obscured starburts are all detected at 15 μm .

1 Introduction

Galaxy clusters may be seen as cosmic laboratories where we can study the evolution of galaxies at different stages by looking at different redshifts. Butcher & Oemler first noted an increase of the blue fraction of galaxies in clusters as a function of redshift [3]. Other signs of evolution have recently been discovered by considering the morphology (increase in the proportion of spirals versus S0 [5]) and the spectral properties (increase in the proportion of star-forming or post-starburst galaxies [6]). These studies have also shown that the Butcher-Oemler effect is not due to the bulk population of the cluster but rather to some galaxies which deviate from the color-magnitude relation of the cluster. These galaxies lie mainly in the outskirts of the clusters (see, e.g., [10]) and a large part of them appear to be involved in dynamical interactions and mergers [4]. From a theoretical point of view, phenomena like galaxy interactions, infall of galaxies, galaxy harassment, ram pressure stripping by the intracluster medium (ICM), and group-cluster or cluster-cluster merging can affect the star-formation and the morphology of galaxies in clus-

D. Lemke, M. Stickel, and K. Wilke (Eds.): LNP 548, pp. 21–27, 2000.

Cluster Name	RA(2000)	DEC(2000)	z	Filter	Field (sq. arcmin)	N_{fr}	T_{int} (sec)	PFoV	T_{tot} (min/pix)
A1689*	13:11:31.25	-1:20:21.6	0.18	LW3	6×6	9	5	$6''$	5.5
A1689*				LW3	6×6	9	10	$6''$	7.6
A1689*				LW2	6×6	9	10	$6''$	8.2
A1689				LW3	5×5	16	10	$6''$	11.0
A1689				LW2	5×5	16	10	$6''$	13.5
A2390	21:53:36.80	17:41:43.0	0.23	LW2	5×5	25	5	$6''$	4.8
A2390				LW3	5×5	25	5	$6''$	4.8
J1888	00:56:56.86	-27:40:29.3	0.56	LW2	15.2×3.4	4×25	5	$6''$	4×7.3
J1888				LW3	15.1×3.4	4×25	5	$6''$	4×11.5
3C330	16:09:36.52	65:56:43.0	0.55	LW3	15.9×3.4	4×25	5	$6''$	4×13.6

Table 1. ISOCAM Observations presented in the paper. N_{fr} is the number of frames in the raster observation, T_{int} the integration time per readout, and T_{tot} the total integration time per sky pixel. Asterisks mark observations during the calibration phase.

ters, although it is not yet clear what combination of effects has to be at play in order to explain the observational results.

The study of the MIR emission from galaxy clusters can be an interesting complement to the optical study, in order to understand better the effects of environment on the galaxy evolution. The MIR emission is in fact able to unveil the presence of star formation activity hidden by dust. We know, for instance, that a large part of star formation in interacting galaxies is visible only in the MIR and completely obscured in optical (see the case of the Antennae [8]). Moreover, galaxies which are optically classified as dust-obscured starbursts constituting more than 50% of VLIR galaxies in the FIR are expected to emit in the MIR [9].

Previous studies on galaxy clusters have been conducted with IRAS, but they have mainly concentrated on the overall emission from clusters and on the detection of dust in the ICM. Only some nearby clusters have been observed. In these nearby clusters, almost only "IR-normal" galaxies have been detected, in contrast to the field where at least 20% have FIR luminosity greater than 10^{11} $L_{\odot}$ [2]. The improved sensitivity and resolution of ISOCAM allows one to observe more distant clusters and search for environmental and evolution effects on cluster galaxies. In this context, we have observed several rich clusters at medium and high redshifts with ISO in order to investigate the nature of galaxies emitting in IR, the amount of star-formation hidden by the dust in clusters, and to compare these results to analogous studies for galaxies in the field. Here we present preliminary results for 4 clusters, two of them at a redshift of z=0.2 (A1689 and A2390) and the other two at z=0.6 (J1888 and 3C330).

2 Observations and Data Analysis

The clusters have been observed with ISOCAM in the two broad bands (LW2 and LW3), which cover the spectral regions 5–8 μm and 12–18 μm , respec-

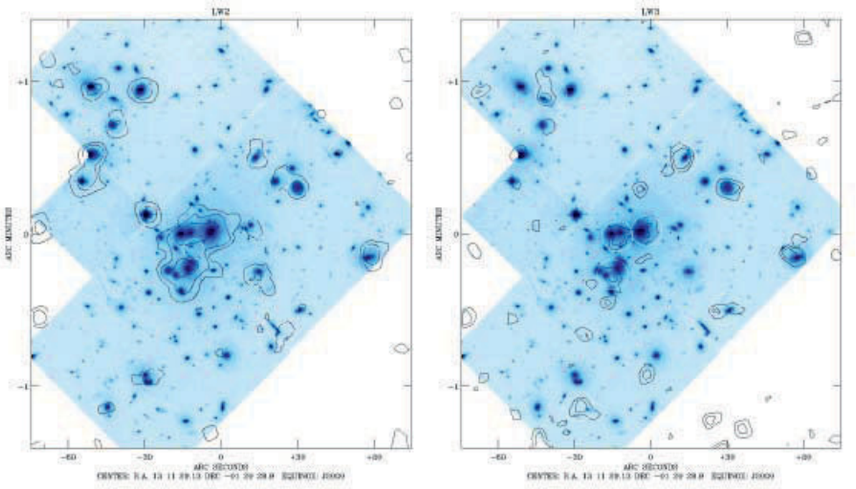

Fig. 1. Contours of the 6.75 μm (left) and 15 μm (right) ISO images of A1689 on a HST image. The median offset between ISO sources and optical counterparts is 1.5″.

tively, and which are centered at 6.75 μm and 15 μm (see Table 1). Data have been reduced using the CIA software package for ISOCAM analysis and the PRETI package [11] for the detection of faint sources. To coadd several images relative to the same fields, the astrometry of each image has been corrected by using the positions of optical sources which are present in the field. Finally, to calibrate fluxes measured on ISO images, we have done several simulations by putting fake sources with different fluxes in positions which are free of real sources. We have added these sources to the original data cube taking into account all the effects which enter in the real signal (dark current, flat-field, transients, PSF and camera distortions) and we have reanalyzed the cube in exactly the same way used with real data to measure fluxes of fake sources. Optical counterparts of ISO sources are identified following Flores et al. who compute the probability for rejecting the identification by considering for each source the candidates within a certain distance and their optical fluxes [7]. Photometric and spectrophotometric follow-up observations of ISO sources have been done using public databases and observations realized with different telescopes (NTT, 2.2m at ESO, and the Italian National Telescope Galileo).

3 Discussion

The sources detected in mid-IR bands generally have clear counterparts (see e.g. figure 1). In A1689 and A2390, the two median redshift clusters for which

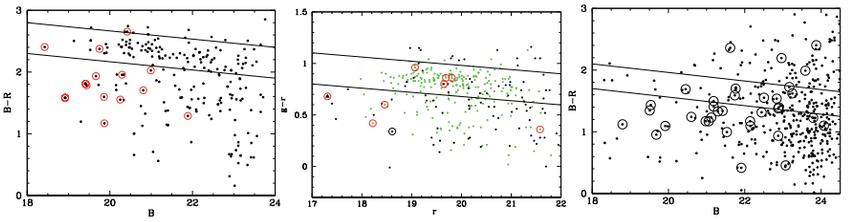

Fig. 2. Color-magnitude diagram for galaxies (black dots) of A1689 (left), A2390 (center) and J1888 (right). Open circles mark sources detected at 15 μm . The CM relation, which is evident for closest clusters and polluted from field galaxies for J1888, is shown by two parallel lines. Most of the ISO sources lie out of this relation.

we have spectroscopical follow-up observations, almost 80% of ISO sources with known redshift belong to the clusters. This is apparently in contrast with the results for the core of A2390 of Altieri et al. who detect almost only background sources [1]. In their case, only a small central region of the cluster was deeply observed. Thus, the number of expected galaxy members in LW3 filter is lower because we are looking for spiral galaxies or dust-obscured starburst which are more common in the outskirts than in the core of the cluster.

We can state that galaxies seen at 6.75 μm correspond to brightest optical objects. In order to study the nature of mid-IR emitters we have examined optical colors and spectral features of these galaxies. The colors of 6.75 μm sources do not differ significantly from the mean color of the cluster galaxies. In contrast, 15 μm sources are on average bluer than the bulk of galaxies ($\Delta_{B-V} = 0.3$mag) in the cluster and most of them correspond to blue outliers of the color-magnitude relation for the clusters (see figure 3).

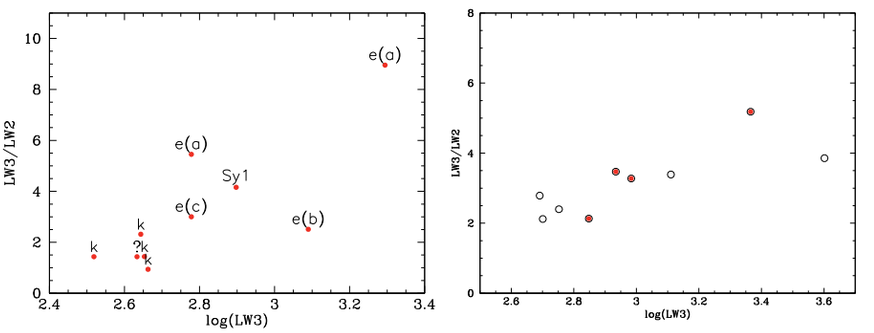

Fig. 3. The relation between LW3/LW2 color and the LW3 flux for A1689 (left) and A2390 (right). Spectral types are reported for A1689. This relation could be linked to activity.

We find a relation between the color LW3/LW2 and the LW3 flux at least for A1689 and A2390 (see figure 3). For J1888 this relation is not clear, maybe because of the contamination by field galaxies. The forthcoming spectroscopical follow-up observations will answer this question. For A1689 and A2390 we have been able to classify galaxies within the scheme based on spectra features proposed by Dressler et al. [6]. While most of 6.75 μm sources are classified as k galaxies (old elliptical-like), the brightest sources detected at 15 μm are mainly active galaxies (spiral-like, e(c), starbursts, e(b), dust-obscured starbursts, e(a) and AGNs). Interestingly, among the galaxies observed in the A1689 field, all the e(a) (dust-obscured starbursts) are detected at 15 μm . Figure 3 shows that the color LW3/LW2 correlates with the LW3 flux and that in the case of A1689, more active spectral types have higher LW3 fluxes. Therefore, since we believe a) that an important fraction of galaxies detected at 15 μm correspond to dusty galaxies which enshroud a high star-formation (or AGN) activity and b) that they correspond to the brightest blue galaxies which are responsible for the so-called Butcher-Oemler effect, this effect is probably enhanced in the mid-IR with respect to the optical.

Finally, if we consider the distribution of ISO sources in the clusters, we notice that in A1689 most of the brightest LW2 sources are concentrated in the central region while LW3 sources seem to be brighter in the outskirts than in the center (see figure 4).

In the two distant clusters we also find evidence for an increase in the number density of 15 μm sources with the radius, while 6.75 μm sources appear more concentrated in the central region, just as in the optical case (see figure 5).

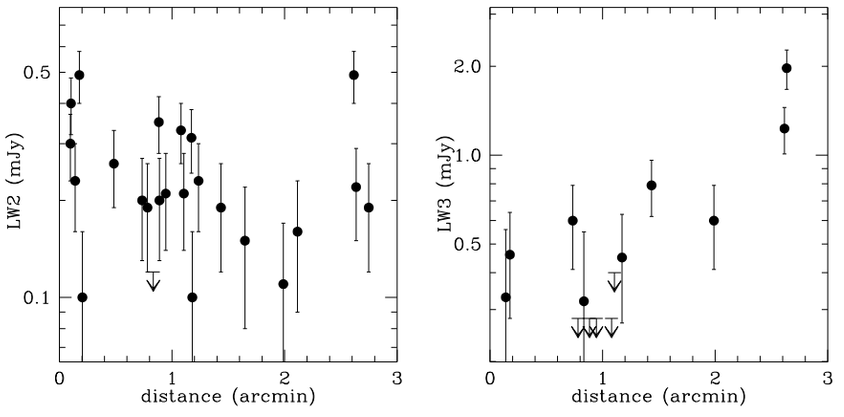

Fig. 4. Distribution of fluxes versus distances for galaxies members of A1689 cluster: LW2 on the left and LW3 on the right. Most of the bright LW2 sources are concentrated within one arcminute from the cluster center, while LW3 fluxes seem to increase with the distance from the cluster center.

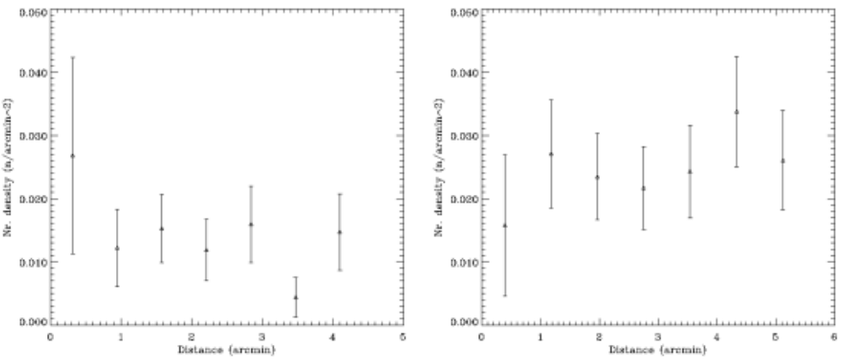

Fig. 5. Density of sources versus distance for J1888. LW2 sources (left) show a peak in the first arcminute, while LW3 source density (right) seems to increase with the distance from the cluster center.

These two facts agree with the similar known behaviour of the distribution of starburst galaxies in clusters and of the proportion of spiral galaxies as function of the distance from the cluster center.

4 Conclusions

We have presented the observations of four rich galaxy clusters at medium and high redshift observed in the mid-IR with the ISO satellite. We have shown that galaxies detected at 6.75 μm follow the bulk of optical emission while galaxies detected at 15 μm are bluer than the main population of galaxies in the clusters. Most of these galaxies correspond to blue outliers of the color-magnitude relation for the clusters. For the two clusters at medium redshift for which we have spectroscopical follow-up observations, we note that starburst-like galaxies with absorption signatures are all detected at 15 μm , which is in agreement with the study of Poggianti & Who about the detection of dusty-starbursts in the far-IR [9]. Since the emission at 15 μm is linked to hidden star-formation – as proved by the correlation between LW3 emission and LW3/LW2 color as well – and since most of the galaxies detected at 15 μm are bluer than the median color of the cluster galaxies, we are probably unveiling a hidden part of the Butcher-Oemler effect.

Finally, while 6.75 μm sources appear brighter and more concentrated in the central region rather than in the outskirts of the cluster, the number density of 15 μm sources seems to increase with the radius, as well as the flux of the detected sources. These two facts are probably related to the change of morphological type ratio with radius and with the fact that starburst galaxies lie mainly in the outskirts of clusters.

Acknowledgements

The data presented in this paper have been analyzed using CIA software. CIA is a joint development by the ESA Astrophysics Division and the ISOCAM Consortium. The ISOCAM Consortium is led by the ISOCAM PI, C. Cesarsky, Direction des Sciences de la Matiere, C.E.A., France.

References

1. Altieri B., Metcalfe L., Kneib J.P. et al., 1999, A&A, 343, L65
2. Bicay M. D. & Giovanelli R., ApJ, 321, 645
3. Butcher, H. & Oemler, A., 1978, ApJ, 219, 18
4. Couch W. J., Barger A. J., Smail I. et al., 1998, ApJ, 497, 188
5. Dressler A., Oemler A. JR., Couch W. J. et al., 1997, ApJ, 490, 577
6. Dressler A., Smail I., Poggianti B.M. et al., 1999,ApJS,122,51
7. Flores H., Hammer F., Thuan T.X., 1999, ApJ, 517, 148
8. Mirabel I. F., Vigroux L., Charmandaris V. et al., 1998, A&A, 333, L1
9. Poggianti B. M. & Who H., 1999, ApJ in press, astro-ph/9908180
10. Rakos K., Odell A. & Schombert J., 1997, ApJ, 490, 194
11. Starck J.L., Aussel H., Elbaz D., Fadda D. & Cesarsky C., 1999, A&AS,138,365

The European Large Area ISO Survey (ELAIS): Latest Results

Seb Oliver[1,5], Steve Serjeant[1], Andreas Efstathiou[1], Hans Crockett[1], Carlotta Gruppioni[2], Fabio La Franca[3], and the ELAIS Consortium[4]

[1] Astrophysics Group, Blackett Laboratory, Imperial College of Science Technology & Medicine, Prince Consort Rd., London. SW7 2BW, England
[2] Osservatorio Astronomico di Bologna, Bologna, Italy
[3] Dipartimento di Fisica, Universita degli Studi "Roma TRE", Roma, Italy
[4] 23 additional institutes as detailed on http://athena.ph.ic.ac.uk/
[5] Astronomy Centre, CPES, University of Sussex, Brighton, BN1 9QJ, England email: S.Oliver@sussex.ac.uk

Abstract. We present some recent results from the European Large Area ISO Survey (ELAIS). This survey was the largest non-serendipitous ISO field survey. A preliminary reduction has recently been completed and catalogues of sources released to the community. Early results show strongly evolving source counts. A comprehensive identification programme is underway and a number of extremely luminous objects have already been discovered. This survey provides an exciting legacy from the ISO mission and (amongst many goals) will allow us to provide important constraints on the obscured star-formation history of the Universe.

1 Introduction

The European Large Area ISO Survey (ELAIS [1]) was the largest non-serendipitous ISO [2] field survey, utilising 377 hours of the Open-Time programme. The project is a collaborative venture between 26 institutes from 11 countries, almost exclusively European. ELAIS is the major project supported by the TMR network programme "ISO Surveys".

The survey covers around 12 square degrees and has observations in four bands covering much of the ISO wavelength window, $6.7, 15, 90$ and 175μm, using both *ISO-CAM* [3] and *ISO-PHOT* [4].

As with any field survey the goals are varied and include the following:

- Obscured star formation history of the Universe
- Ultra-luminous Infrared Galaxies at high redshifts
- Dusty tori around AGN
- Dust in Normal Galaxies
- Dust emission from halo stars
- Detection of new classes of objects
- Investigation of populations making up the FIR background

D. Lemke, M. Stickel, and K. Wilke (Eds.): LNP 548, pp. 28–35, 2000.

A more detailed description of the principal intended goals can of the ELAIS survey can be found in Oliver et al. 2000 (ELAIS [1]) though pre-defined goals will not anticipate the full range of possibilities that the data affords.

For a number of the goals we require statistically significant samples of galaxies at high redshifts ($z \sim 0.5$) compared to e.g. IRAS but relatively modest compared to some deep surveys. It was this requirement that drove the survey area to be of order 10 square degrees. Not only does a large area produce larger samples of galaxies, reducing the Poisson errors, it also reduces the cosmic variance, which would otherwise be significant at these redshifts. Fig. 1 illustrates the minimum survey area required to measure a global quantity (e.g. mean galaxy density) with a given cosmic variance.

This illustrates that ELAIS is complimentary to smaller area deeper surveys ISO such as the HDF [5] which study similar populations at higher redshift but cannot address these populations at lower redshift.

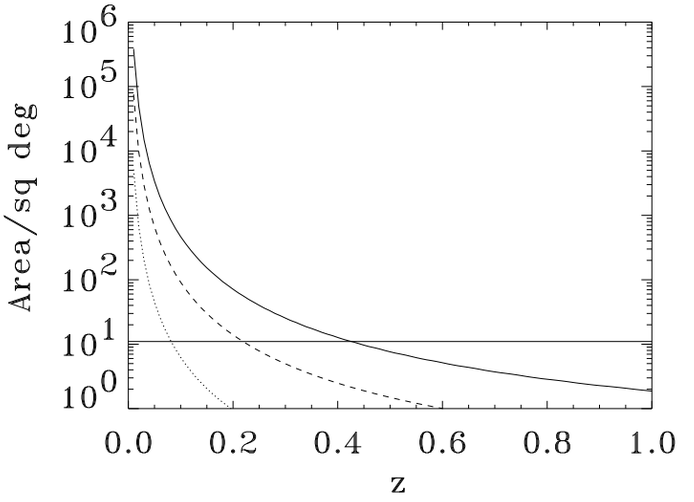

Fig. 1. The minimum area of a survey required to measure mean densities in populations visible to a given redshift such that the systematic errors due to large-scale structure are: $\sigma = 0.1$ - solid line, $\sigma = 0.2$ - dashed line, $\sigma = 0.5$ - dotted line. The nominal area of the *ELAIS* survey is over-plotted. This plot assumes that the survey area is split into four independent survey areas as is the case for *ELAIS*.

2 ISO Observation Summary

ELAIS comprised four major fields N1-3, S1 and 7 smaller fields S2, X1-6 (three of which were chosen on the basis of known objects and so are not

true field surveys). A summary of the area of each field covered in each band is present in Table 1

Table 1. Survey Fields covered at least once. Areas are given in square degrees. The 175μm observations in N1 have been carried out by the FIRBACK team (PI J-L Puget, see Dole et al. [6]) and are included in this table to illustrate the complete *ISO* coverage of the *ELAIS* fields. N1-3, S1-2 and X1-3 are unbiased survey fields, while X4-X6 are centred on known objects so should not be included with the other fields for statistical purposes.

Field	Wavelength/μm			
	6.7	15	90	175
N1		2.67	2.56	2
N2	2.67	2.67	2.67	1
N3	1.32	0.88	1.76	
S1	1.76	3.96	3.96	
S2	0.12	0.12	0.11	0.11
X1		0.16	0.19	
X2		0.16	0.19	
X3		0.16	0.19	
	5.87	10.78	11.63	3.11
X4		0.09	0.11	
X5		0.09		
X6		0.09	0.11	

3 ELAIS Data Products

In order to provide source lists and maps for rapid follow-up we pursued a two phase strategy for the data processing. During the mission we decided on a "Preliminary" data reduction pipe-line. This processing has been carried out on the complete survey data, producing source lists both for follow-up campaigns and for preliminary scientific analysis. An important stage in the "Preliminary" data reduction for both PHOT and CAM data was that at least two observers examined the time-lines of candidate sources before acceptance. This extremely labour intensive activity ensured that the sources lists are highly reliable. Subsets of the "Preliminary Analysis Catalogues" were released to world via our WWW page (http://athena.ph.ic.ac.uk/) concurrent with the release of data in August 1999. Table 2 shows the number of sources in subsets of the catalogues.

The second ("Final Analysis") phase in the data reduction, which involves reprocessing the entire data sets, using the best post-mission knowledge is now nearing completion. "Final" catalogues will be available withing the *ELAIS* consortium early in 2000 and to the world shortly thereafter.

Table 2. Numbers of objects in "Preliminary" Analysis catalogues as released via the WWW and in the entire catalogues. The released CAM catalogues had a hard flux limit imposed, approximate limiting fluxes are given for other samples.

Cat.	Band μm	No.	Flux mJy
PA-WWW	7	273	4
	15	484	4
	90	98	150
PA	15	600	2
	90	300	60

4 Results from the ISO Data

The first results to be extracted from the *ELAIS* data naturally come from the *ISO* data alone. Much more detailed insight will be forthcoming when the data are combined with follow-up observations and surveys at other wavelengths.

The galaxy number counts have been determined at 6.7, 15 and 90μm. The 15μm counts [7], illustrated in Figure 2, have been shown to agree with many strongly evolving population models [8], [9], [10] based on *IRAS* counts, while being inconsistent with at least one non-evolving model [10]. The 90μm counts [11], Figure 3, are also consistent with similar strong evolution models. The 6.7 and 15μm fluxes of morphologically classified stars were in general consistent with model photospheres and, as expected, the 6.7 and 15μm fluxes provide a good discriminant between stars and galaxies, Figure 4 [12].

5 Follow-Up Programme

An extensive follow-up programme is being undertaken, utilising a vast battery of telescopes around the world, and also a number of satellites. The current coverage of the *ELAIS* fields in un-biased surveys across the electromagnetic spectrum is summarised in Table 3.

The spectroscopic follow-up has not progressed as rapidly as we would have liked. The largest sample of spectra we have come from the S1 field taken in one hour of 2dF time, snatched from an otherwise cloudy night. Another cloudy night on the 2dF produced a second exposure, though this has yet to be analysed.

Since the Ringberg meeting two surveys using XMM to study the *ELAIS* fields and a La Palma International Time Programme have been awarded time. The XMM surveys will provide both deeper and wider hard X-ray coverage than is indicated in Table 3 (which refers only to the Chandra and BeppoSax surveys). The International Time is around three weeks on La Palma telescopes, primarily this will be used to obtain spectra for our *ISO* sources, but will also provide deeper optical and NIR imaging.

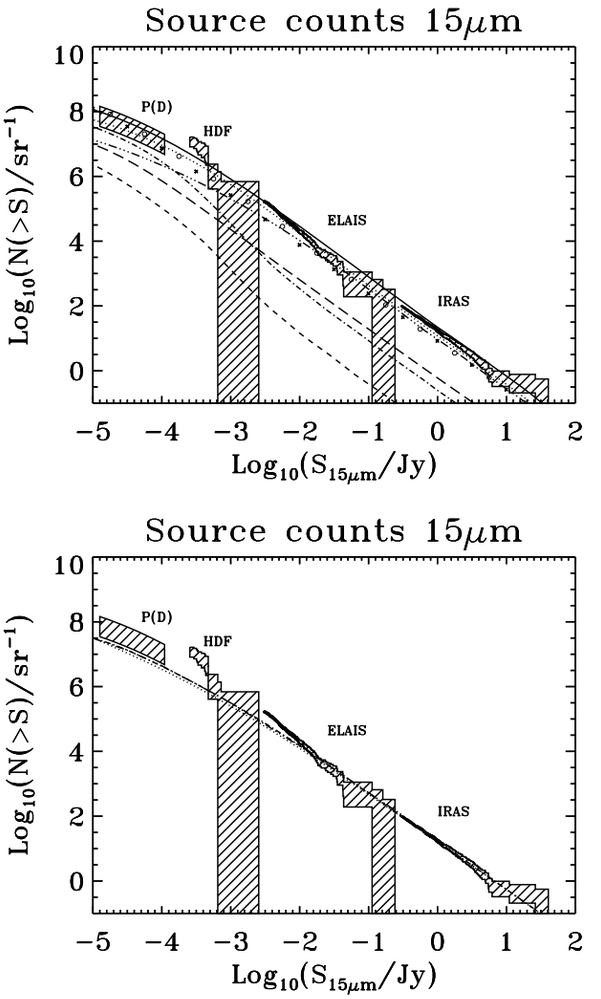

Fig. 2. Integral ELAIS extragalactic source counts at 15μm. Flux densities are quoted in Jy. Shaded regions show the ranges spanned by $\pm 1\sigma$ uncertainties. Also shown are the source counts and P(D) analysis from the Hubble Deep Field [13], [14]. The IRAS counts are estimated from the 12μm counts.
The upper panel has the Franceschini et al. source count model [8] over-plotted. The model spiral contribution is shown as a dotted line, ellipticals as a dashed line, S0 as a dash-dot line, star-bursts as a dash-dot-dot-dot line and AGN as a long dashed line. The total population model is shown as a full line. Also plotted are the Guiderdoni et al. [15] models A and E, as small filled crosses and small open circles respectively. The lower panel shows all available no-evolution models. Franceschini et al. (in prep.) is over-plotted as a dash-dot-dot-dot line. The Xu et al. [10] models are shown with and without the MIR spectral features (dash-dot and dotted respectively). All three no-evolution models have been renormalised to match the IRAS counts, by a factor of 0.8 for the Franceschini et al. models, and 1.8 in the case of the Xu et al. [10] models.

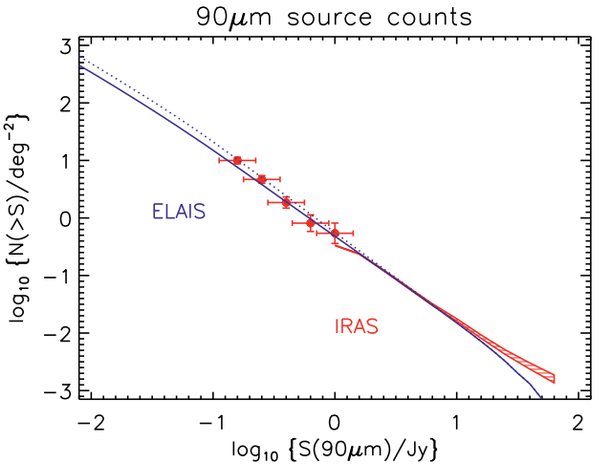

Fig. 3. *ELAIS* and *IRAS* 90μm source counts. The solid line and dotted lines are the counts predicted by the models A and E (respectively) of Guiderdoni et al. [15]

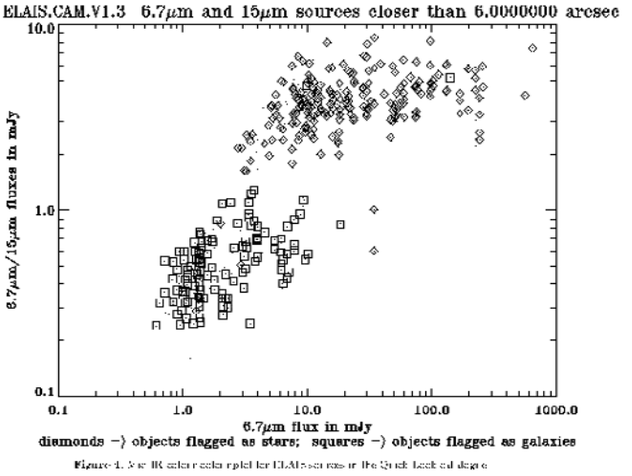

Fig. 4. Mid-IR colour-colour diagram for ELAIS sources in the Preliminary Catalogue. Diamonds indicate sources classified as "stars" on the basis of the morphology of their apparent counterparts on the DSS plates; squares indicate sources classified as "galaxies"; isolated dots indicate sources which were too faint for a clear morphological classification. constant effective temperatures indicated. The dashed line corresponds to effective temperatures of about 6000K, typical of F8V to G2V stars.

Table 3. Multi-wavelength field surveys within the main *ELAIS* fields, the vast majority carried out as part of the *ELAIS* collaboration. Areas are in square degrees. Some sub-fields within these go to greater depth. The X-ray and sub-mm surveys are yet to be completed.

Band	2-10keV	u, g, r, i, z	H	K	6.7	15	90	175	850	21cm
Depth Units	CGI	mag	mag	mag	mJy	mJy	mJy	mJy	mJy	mJy
			N1							
Area	0.07	9	0.5	0.4		2.6	2.6	2	0.05	1.54
Depth	10^{-14}	23.3,24.2,23.5, 22.7,21.1	19.5	18.0	1	3	100	100	8	0.1-0.4
			N2							
Area	0.07	2	0.5	0.4	2.7	2.7	2.7	1	0.05	1.54
Depth	10^{-14}	22.5,24.2,23.5, 22.7,21.1	19.5	18.0	1	3	100	100	8	0.1-0.4
			N3							
Area		1,1,2.3,1,0	1		1.32	0.9	1.76			1.14
Depth		22.5,23,23,	19.5		1	3	100			0.1-0.4
		23,0								
			S1							
Area	2	1.2,0,4,3,0			1.8	4	4			4
Depth	10^{-13}	23,0,23.5, 23,0			1	3	100			0.24

6 Early Results from Follow-Up Programme

The limited spectroscopy we have been able to obtain to date has allowed us to determine redshifts for around 300 *ISO* and radio sources. A couple of the *ISO* sources are at redshifts $z > 3$, and many sources have ultra high luminosities. From these spectra we are also able to present a very preliminary classification, Table 4. All the types of objects that we expected from studies of local *IRAS* samples are seen, it is too early to say whether the populations are found in the proportions expected as the selection effects in these highly incomplete spectroscopic samples need to be modeled carefully.

7 Conclusion

The *ELAIS* sample is clearly going to provide a major legacy from the *ISO* mission. A preliminary catalogue has already been released to the community and a final analysis is in progress. Source counts show strong evolution, and with forthcoming optical spectroscopy in 2000 ELAIS will provide exceptional constraints on the cosmic star formation history.

Table 4. Provisional spectral classifications of *ISO* and 21cm selected sources in the Southern *ELAIS* field S1. Spectra come from a one hour 2dF exposure and a number of nights on the ESO 3.6m and NTT telescopes.

Class	21cm		*ISO*	
	2dF	ESO	2dF	ESO
Absorption	48		15	6
Star-burst	9	3	22	52
Hα	5	2	26	
OII	10		4	
OIII	1			
AGN/QSO	6	2	20	19
AGN/Sy1	2	1	3	
AGN/Sy2	8	3	8	8
AGN/BLLac			2	
Stars	1		8	3
Too Faint	60	3	41	

References

1. Oliver S., et al. 2000 MNRAS, in press
2. Kessler, M. F., et al. 1996 A&A, 315, L27
3. Cesarsky, C.J., et al. 1996, A&A, 315, L32
4. Lemke, D., et al. 1996, A&A, 315, L64
5. Serjeant S., et al., 1997, MNRAS289, 457
6. Dole H. et al. 1999 *In 'The Universe as seen by ISO', eds. P. Cox and M.F. Kessler, 1999, UNESCO, Paris, ESA Special Publications series* ISBN 92-9092-708-9 p. 1031
7. Serjeant et al. 2000, MNRAS, in press
8. Franceschini, A., Mazzei, P., De Zotti, G. & Danese, L. 1994, ApJ, 427, 140
9. Pearson, C. & Rowan-Robinson, M. 1996, MNRAS, 283, 174
10. Xu, C., et al., 1998, ApJ, 508, 576
11. Efstathiou A., et al. 2000 MNRAS, submitted
12. Crockett H., et al. 2000 MNRAS, in prep.
13. Oliver S., et al., 1997, MNRAS, 289, 471
14. Aussel, H., Cesarsky, C.J., Elbaz, D., Starck, J.L., 1999, A&A, 342, 313
15. Guiderdoni, B., Hivon, E., Bouchet, F. R. & Maffei, B. 1998, MNRAS, 295, 877

The European Large Area ISO Survey: ISOPHOT Final Analysis - Number Counts

Christian Surace[1], Andreas Efstathiou[1], Philippe Héraudeau[2], Dietrich Lemke[2], Seb Oliver[1], Michael Rowan-Robinson[1], and the ELAIS Consortium[3]

[1] Imperial College of Science Technology and Medecine, London SW7 2BZ - UK
[2] MPIA Heidelberg , Königstuhl 17, D-69117 Heidelberg Germany
[3] European consortium involving 19 countries

Abstract. The European Large Area ISO Survey is a consortium of 26 institutes whose goal is to study the Infra-red objects and Infra-red background in 4 main areas of the sky using ISO. In this paper, we present the final analysis pipeline of the ISOPHOT data and will show the latest results extracted from the pipeline. We also present and discuss the number counts extracted from the ELAIS areas that extend the IRAS number count by an order of magnitude.

1 ELAIS

The European Large Area ISO Survey (hereafter ELAIS) has provided Infrared observations of 4 main regions of the sky with ISO. Seven smaller fields, six of which are centered on specific high redshift objects, have also been observed. See [8](ELAIS paperI), [7][9] for a complete description of the ELAIS survey. Refer also to the ELAIS WEB page (*http://athena.ph.ic.ac.uk/*) for a complete status of the survey follow-up programmes. Around 2000 Infrared sources have been detected altogether at 7 and 15 μm (with ISOCAM), 90 and 175 μm(with ISOPHOT) over 13 square degrees of the sky. To process the large amount of data, several data extraction pipelines have been set up at Imperial College (London)[11],[5] (ELAIS paper III), IAS and CEA (Paris)[2] and MPIA (Heidelberg)[13]. This paper will focus on the ISOPHOT data extraction pipeline for 90 μm observations and discuss the first results extracted from the final analysis.

2 Observations

We observe the ELAIS fields at 90 μm using ISOPHOT [3]. We used the P22 observational mode. Because of the compromise between the large coverage (which allows cosmological variance to be removed) and integration time (which allows observations further into space) the integration time has first been set up to 20s and each area has been covered by a 20×10 raster map with and/or without overlapping.

D. Lemke, M. Stickel, and K. Wilke (Eds.): LNP 548, pp. 36–39, 2000.

3 ISOPHOT Pipeline

3.1 Raw Data Extraction

The raw data have been analyzed using the isoPhot Interactive Analysis tool ([4]) (PIA[1] Version 7.3). We use PIA to reduce the raw data from the "Edited Raw Data (ERD)" level to the "Auto Analysis Product (AAP)" level, keeping the integrated values during the ISO slewing mode.

3.2 Data Analysis

The non overlapping mapping mode makes the detection of the sources difficult using only the reconstructed maps. Indeed, a pixel affected by an uncorrected glitch could be detected as a source. Thus, the detection of the ISOPHOT sources is based directly on the time sequence analysis of the AAP files. The eye-balling step of the time line data is crucial for confirming the real sources.

We use the FCS measurements to calibrate the data. The calibration was checked using dedicated measurements (see section 3.3). We used dedicated routines ([12]) to reduce the pixel-to-pixel response fluctuations and to derive the final surface brightness values and fluxes of the objects.

The detections are visually inspected by 5 different people and classified in 5 groups from (1: clear detection to 5: spurious detection). A final classification is given to the detections. In the following we will only consider the detections belonging to the classes 1, 2 and 3. These detections represent approximatively 10% of the total number of detections.

3.3 Calibration

We checked out the quality of the FCS calibration of the survey by observing several times calibration stars and sources detected in the ELAIS survey. We then compared the fluxes obtained in these measurements with theoretical values [15]. We found that the fluxes derived in our pipeline were in relatively good agreement for the point-like sources (the fluxes derived using the FCS calibratiton and the theoretical values agree within 15% of the total fluxes)

3.4 Maps

The maps have been created using a dedicated software [14]. The background values have been compared to COBE and IRAS values. The median background values agree to within 10 %. For each ISOPHOT raster we built brightness, sources, background, internal noise and sky noise maps. All the sources previously detected have been extracted and we computed the fluxes using aperture photometry.

[1] PIA is a joint development by the ESA Astrophysics Division and the ISOPHOT consortium

4 Number Counts

The 90 μm number counts extracted from the ELAIS survey fields extend the IRAS number counts by an order of magnitude in flux [5]. To extract the source counts, we have determined the area over which the survey is sensitive to as a function of flux. The counts are normalized by the area over which each source was found. The resulting integral counts and the IRAS counts are shown in Fig. 1.

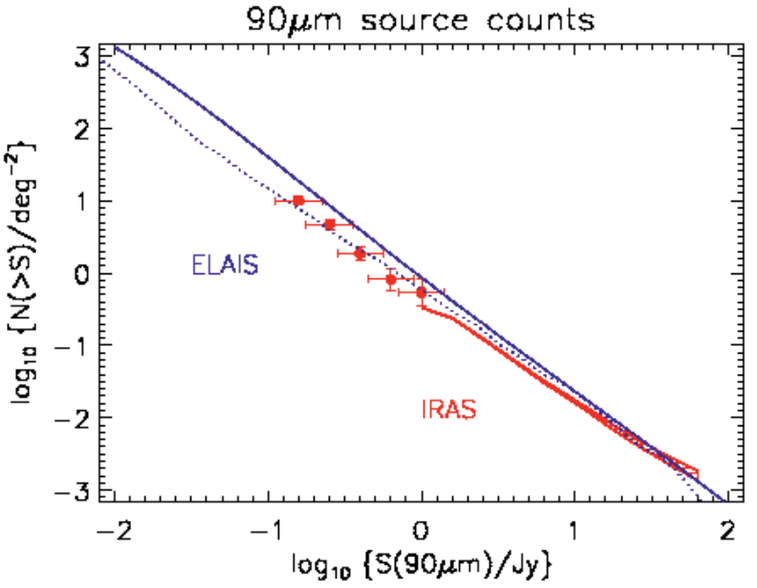

Fig. 1. *Number counts of the 90 μm, with the models of RR99 and AF99*

The counts have been compared with four models, two of which are overplotted in the previous figure (RR99 [10] and AF99[6]). The counts predicted by the different models vary by a factor of 8 at around 100 mJy. The counts seem to favour the AF99 model which assumes that the extragalactic population is composed of a non evolving population and a strong evolving starburst population with peak emissivity around z=0.8. The RR99 model assumes a star formation history of the Universe described by an analytic formula. The SFR of the universe is supposed to evolve due to pure luminosity evolution. However, both models agree to introduce a strong evolution in order to fit the data.

A more detailed analysis appears in ELAIS paper III [5].

5 Conclusion

The final analysis of the ELAIS ISOPHOT data has provided maps and a list of around 300 sources detected at 90 μm.

From the maps we derived the position and fluxes of the ELAIS ISOPHOT detections. These positions and fluxes are crucial to define observations for ground based and space telescopes. The extensive wavelength coverage of the ELAIS fields ensures that the 90 μm sources will be extensively studied and will therefore be ideal tools to provide new insight on dust-enshrounded galaxies. We derived number counts and compared them with two models RR99 and AF99. The counts seem to favour the AF99 model.

A more detailed analysis on the implications of the observational strategy on the next IR surveys and a deeper number counts will appear in a forthcoming paper [14].

References

1. C.J. Cesarsky et al. 1996, A&A, 315, L32
2. D. Elbaz, H. Aussel C.J. Cesarsky et al. 1999, Proceedings of the Conference "The Universe as seen by ISO", Eds. P. Cox and M.F. Kessler, ESA SP-427, 999-1006
3. D. Lemke et al., 1996, A&A, 315, L64
4. Gabriel C. et al., 1996, PIA Users Manual, available from ESA/ISO Ground Observatory VILSPA or MPIA Heidelberg
5. A. Efstathiou et al., 2000, MNRAS, submitted
6. A. Francceschini et al., 2000 in prep.
7. Oliver, S., and the ELAIS consortium, 2000, these proceedings
8. Oliver, S., and the ELAIS consortium, 2000, MNRAS, accepted
9. M. Rowan-Robinson, 1999, Proceedings of the Conference "The Universe as seen by ISO", Eds. P. Cox and M.F. Kessler, ESA SP-427, 1011
10. M. Rowan-Robinson, 1999, MNRAS in press (ASTRO-PH/9906308)
11. Serjeant, S. Oliver, M. Rowan Robinson et al., 2000, MNRAS accepted
12. Surace C., Abraham P., Herbstmeier U., ' New flatfielding correction method for ISOPHOT C100/C200 detector', June 1997, ISOPhot Interactive Analysis reports
13. C. Surace, P. Héraudeau, D. Lemke, A. Efstathiou, S. Oliver, M. Rowan Robinson Proceedings of the Conference "The Universe as seen by ISO", Eds. P. Cox and M.F. Kessler, ESA SP-427, 1059
14. C. Surace, P. Héraudeau, D. Lemke, A. Efstathiou, S. Oliver, M. Rowan Robinson and the ELAIS consortium, 2000, MNRAS, submitted
15. Schultz, B., private communication

Japanese Deep Surveys with ISO

Haruyuki Okuda[1,2]

[1] The Institute of Space and Astronautical Science, 3-1-1 Yoshinodai, Sagamihara, Kanagawa 229-8510, Japan,
[2] Gunma Astronomical Observatory, Gunma 377-0702, Japan

Abstract. We have made deep surveys of the Lockman Hole, the lowest HI column density area in the sky, using ISOCAM and ISOPHOT onboard the ISO satellite. The observations were very successful and provided valuable data on star forming activity and galaxy evolution. Model calculations indicate that there was an intense star formation period that peaked at around $z = 0.7$.

1 Introduction

When we were given an opportunity to participate in the ISO project and guaranteed time for observation as well, we decided to make the deepest survey possible to search for protogalaxies using the full capabilities of ISO. However, we were very anxious about its success because we were quite unfamiliar with ISO and its instruments: neither did we know the details of their operational characteristics and observational capabilities, nor did we know what detection limits would be achievable under the influence of severe cosmic ray effects in the detector material and the limited flatfield accuracy. In spite of these anxieties, we decided to invest a substantial fraction (one third) of our guaranteed time in the deep survey.

To optimize the success of our observations, we have made every effort to make the observational conditions as good as possible. For the observational wavelengths, we chose mid-infrared and far-infrared bands by using ISOCAM and ISOPHOT. For the ISOCAM observations, we selected the LW2 filter with a central wavelength of about $7\,\mu$m, which should be most sensitive to the stellar light component. It was also expected that this band would be least affected by background radiation and therefore would provide us with the lowest detection limit for ISOCAM observations. For the ISOPHOT observations, we selected the C_90 and C_160 filters centered at $90\,\mu$m and $170\,\mu$m, respectively. These bands should be the ones which are most sensitive to dust emission. The reason for selecting two different bands was that they would be useful for cross checking of the observational data in case it was heavily contaminated by cosmic ray events. Also, observations in two different filters could possibly be used for a rough estimation of the redshift. As a target, we chose the Lockman Hole, where the HI column density is lowest in the sky, in order to minimize contamination by cirrus emission. This was particularly important for the observations in the far-infrared. For the

D. Lemke, M. Stickel, and K. Wilke (Eds.): LNP 548, pp. 40–48, 2000.

ISOPHOT observations, we chose two fields, LHNW and LHEX, of about $40' \times 40'$ square each, avoiding bright stars or bright infrared objects; the latter overlaps with the ROSAT deep field. Both have HI column densities of about $4 \times 10^{19}\,\mathrm{cm}^{-2}$. The ISOCAM field of about $3' \times 3'$ square was positioned in the center of LHNW. At a later stage, we added the SSA13 area to the ISOCAM targets, since this area had been observed extensively at various wavelengths with a variety of techniques: by HST, the Keck telescope and other ground based telescopes, as well as by VLA radio telescope.

2 Observations

Our observations were made in a relatively early phase of the ISO mission and hence served as a pilot observation for the subsequent similar surveys. The observational logs are summarized in Table 1. The total observing time was 80 hours, one third of the Japanese guaranteed time.

Table 1. Observational logs of Japanese deep surveys

ISOCAM			LW2		
	LHNW	$3' \times 3'$	14h		May 1996
	SSA13	$4' \times 4'$	23h		May/June 1997
ISOPHOT			C_90	C_160	
	LHEX	$40' \times 40'$	7.5h	10h	May/June 1996
	LHNW	$40' \times 40'$	7.5h	10h	May/June 1996

Since the observations were the first trials for surveys in the ISO programs, the data analysis was made by trial and error in close collaboration with the ISO operation team in VILSPA and the instrument teams. This laborious work was mostly done by K. Kawara and Y. Sato staying at VILSPA as ISO supporting team members and they have done excellent jobs.

3 Results and Discussion

The original data suffered badly from cosmic ray glitches as well as from sensitivity drifts or sensitivity variations. We have carefully performed deglitching and drift corrections, details of which have been reported previously [1] [2] [3]. In principle, however, there was no means to distinguish the real signals from the spurious noises such as those due to the cosmic events, or statistical fluctuations from the observed data alone, particularly in a single band observation.

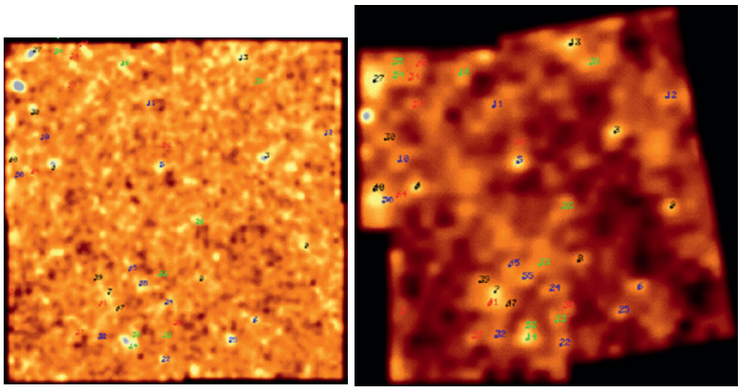

Fig. 1. 90 μm(left) and 170 μm images for LHNW. 170 μm sources extracted by DAOPHOT [6] are also marked, showing excellent coincidence of source positions between two images

For the ISOCAM observations in the Lockman Hole, we have taken H/K images by using the 88″ telescope of the University of Hawaii for comparison. As was reported previously [1], there is a fairly good positional correspondence between the two images. From this correspondence, we grew confident about our observation and its data analysis. In fact, several sources were later observed spectroscopically by the Keck telescope, which succeeded in determining their redshifts, ranging from $z = 0.2 - 1.1$. This implies that our observations are fairly reliable and have reached to cosmological distances as far as $z = 1$. No further observations of the same targets have been made and the nature of the observed sources is not yet clear. Recently, this field was selected for the submillimeter observations at 850 μm by JCMT [4]. A bright submillimeter source has been found in it, but no corresponding ISOCAM source is present within the error box.

The data analysis of the SSA13 area has recently been completed [3]. An excellent correspondence with the H/K image has again been found similar to that seen in the Lockman Hole observation. As mentioned before, numerous observational data sets are available for this area. In view of their morphological similarity, 22 extended sources are identified: 10 spirals, 8 ellipticals and 2 irregular/merger galaxies, while 2 are identified as field stars from comparison with the H/K image taken by the Keck telescope. The redshifts of the HST sources have been observed using Keck telescopes, among which 15 sources have correspondences to the ISOCAM sources. The redshifts of the identified sources are distributed from $z = 0$ to 1.5.

The number density of the ISOCAM sources are countable down to fluxes as low as 30 μJy, and the position on the $\log N / \log S$ diagram is consistent with the other observations [5].

The original data of ISOPHOT observations were seriously contaminated by cosmic ray events. The latter were carefully removed, we also applied corrections for the drift of the detector sensitivity [2]. Despite the complexity of the data analysis, the final results obtained look fairly reliable. This is assured by the fact that the images at 90 μm and 170 μm show very good correlation [6]. The images for LHNW are shown in Fig. 1 as an example.

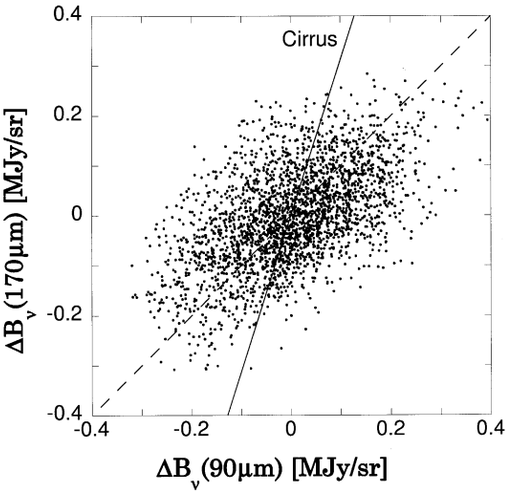

Fig. 2. Point-to-point comparison between the 90 μm and the 170 μm sky brightness in the Lockman Hole. The brightness is not an absolute one, but is offset from the median brightness. In order to avoid error due to the difference of the beam size between the two bands, the 90 μm images are convoluted with the 170 μm beam profile. The IR cirrus color vector [7], approximately 16K gray-body with an emissivity proportional to λ^{-2}, is also shown(*solid line*)

Both images show excellent correspondence w.r.t. the bright and the faint sources, even the general pattern of the intensity distribution is more or less the same. It can also be shown that more sources than expected from a coincidence by chance are identified as the radio sources detected by VLA observations [6]. Cirrus effects should be almost negligible (since we selected the Lockman Hole), which has been confirmed by the power spectrum analysis [9]: The amplitude of the cirrus fluctuation is negligibly small, and the fluctuation power spectrum shows a much flatter spectrum than that of the cirrus component. It is also interesting to note that the 170 μm / 90 μm color of the background emission (slope of the correlation = 1) shows different behavior from that of the cirrus ($\simeq$ 3) as shown in Fig. 2 [8].

All these considerations indicate that observed images must be real and dominated by extragalactic sources. The nature of these sources, however,

cannot be specified from the observations alone. Various observations using ground based (Kiso Schmidt, KPNO 0.9m, UH 2.2m, Subaru 8.2m) and submillimeter telescopes (IRAM 30m, CSO 10m) as well as radio observations (VLA) have been tried to identify the sources, but no definite results have been obtained, either due to the insufficient sensitivities or the poor positional accuracy of the ISOPHOT observations. In the meantime, we can discuss the nature of the sources only from the number density and its dependence on flux, i.e., the $\log N/\log S$ information.

The $\log N/\log S$ diagrams for $90\,\mu$m and $170\,\mu$m bands are shown in Fig. 3. As seen in the figures, the number density rises very steeply with decreasing flux density. The former has also been estimated by fluctuation analysis and extended to lower flux densities [9]. It connects smoothly to the source counts results as shown in the figures.

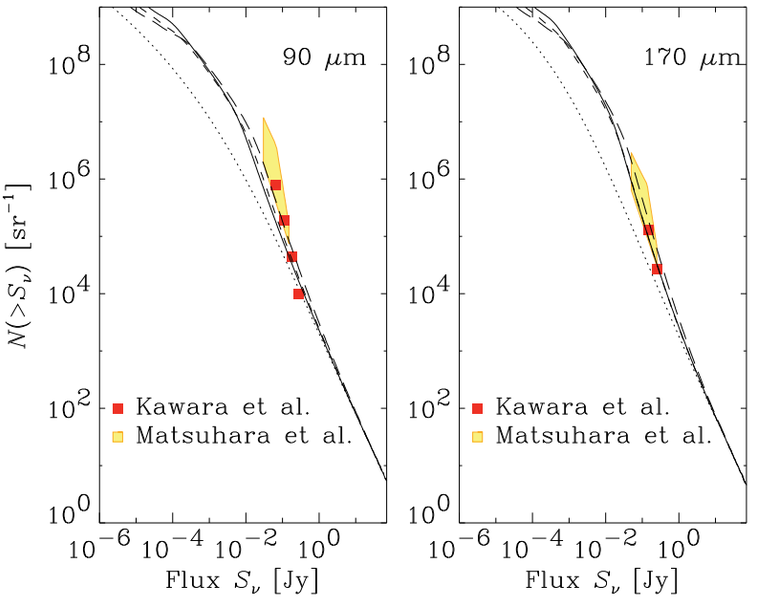

Fig. 3. The $\log N/\log S$ diagrams for far-infrared sources in the Lockman Hole: $90\,\mu$m counts on the left and $170\,\mu$m ones on the right. Direct source counts with the correction for the source confusion [6] are shown by red squares, while the constraints given by the fluctuation analysis [9] are shown by yellow regions. Model counts [11] with no evolution (*dotted line*), luminosity evolutions shown in Fig. 4 (case 1: *long-dashed line*, case 2: *short-dashed line*, case 3: *solid line*) are shown for comparison

In order to explain the observed $\log N/\log S$ behaviors, T. Takeuchi and his collaborators have made a model calculation under the following assumptions [10] [11]:

- The luminosity function of the sources is assumed to be the same function as inferred from the IRAS results [12] but multiplied by a certain factor to account for evolutionary effects.
- The SED of the sources is assumed to be similar to the standard spectrum of the ULIRGs.
- The evolutionary effect is included in the luminosity function by a stepwise form which is a function of redshift z.

In addition, the high z cut-off of the luminosity evolution is chosen to reconcile with the limit of the cosmic far-infrared background radiation recently estimated from COBE observations [13] [14] [15]. If we assume a higher level of activity in high z region, it will give a more excessive flux of the background radiation than the estimated one.

Based on the assumptions given above, $\log N/\log S$ curves have been calculated and compared with the observed results in Fig. 3. Three cases of the luminosity evolution are assumed, as is shown in Fig. 4 (cases 1,2,3). Among them, the first case of the luminosity evolution can fit best of all to the observed counts. This means that the star formation rate should have increased very rapidly with z and reached ten to several ten times higher values at around $z = 0.7$ than in the local universe, but it rapidly decreased beyond $z = 1$. Since sources at a distance of $z > 1$ are rather insensitive to our observations, no detailed information is available from these number counts. The same model can also explain the results in the $7\,\mu$m and $15\,\mu$m bands [10] [11].

A number of models have been proposed to explain the observational results by the European groups [16] [17] [18] [19] [20] [21] and reached similar conclusions [22] [23] [20].

Since no information other than the number counts is available in the far-infrared surveys, it is difficult to discuss the nature of the detected sources. Presumably, they are ULIRGs or active star burst galaxies, as discussed by many authors. However, we would like to point out that the lifetime of star burst activity of an individual galaxy (10Myr) is much shorter than the active period of the luminosity evolution (>1Gyr) as estimated above. The questions are then how the star formation is activated, why it occurred in this particular period, what is the nature of the ancestors and descendants of these galaxies, and where and how they can be observed. Moreover, the question arises whether any of these galaxies experienced the active phase of star formation. It should be taken into account that the observed excess in the number counts cannot be solely explained by a density evolution model without conflict with the far-infrared background radiation [10] [11]. Recently, many papers have been written on the evolutional trends of the galaxies based on UV, optical, and infrared data, as well as submillimeter observations, from which

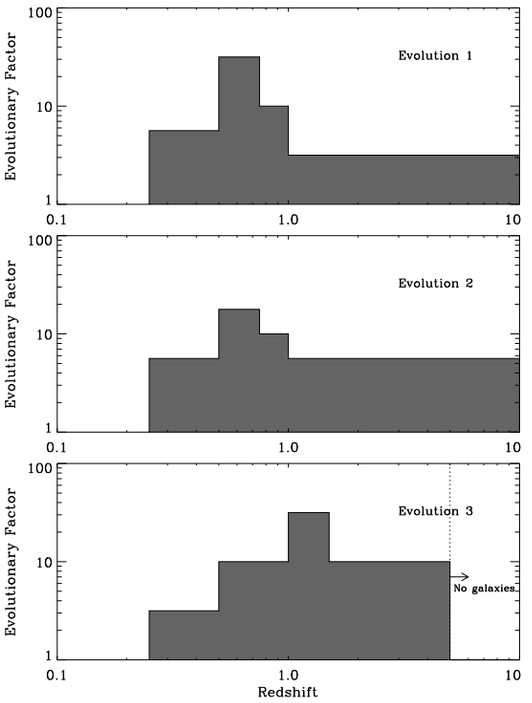

Fig. 4. The evolutionary factors of galaxy luminosity as a function of redshift, used in the number count models [11]

a similar evolutional trend has been proposed [24] [25] [20] [26] [27] (see [28] for summary). Ultimately, it is essential to disclose the interrelation among those components, such as normal galaxies, AGNs, ULIRGs etc. These are very interesting problems to be investigated in the future.

4 Conclusions

From the above discussion, we have reached the following conclusions:

- The deep surveys made by ISOCAM and ISOPHOT in the Lockman Hole were very successful. They have provided valuable data of the galaxies in deep space and hence they are useful for study of the evolution of galaxies.
- By selecting the Lockman Hole area, the cirrus effects could be minimized, thus the observed sources should be real and dominated by galactic component.

- The survey at 7 μm by ISOCAM was generated using the longest integration times; it reached the deepest space regions or the faintest flux density observed so far. The evolutionary effect is relatively less sensitive to the number counts but the observed number density is consistent with the enhancement of the star formation rate inferred from the far infrared survey.
- The surveys at 90 μm and 170 μm have succeeded in reaching infrared galaxies much more distant than those observed by IRAS. Their number densities show much steeper gradients than could be expected from the non evolutionary model of the galaxy luminosity.
- Model calculations indicate that there must have been a time when starburst activity in galaxies was dramatically enhanced, by a factor of several tens or more than the present level. This activity was concentrated in a relatively short period around $z = 0.7$.
- For detailed discussion, however, identification by high resolution telescopes should be made and be followed by morphological and spectroscopic observations to clarify the genuine nature of the sources. For this purpose, near-infrared and submillimeter observations by large ground based telescopes, radio observations with VLA techniques, as well as far-infrared and submillimeter observations in space should be used to the full.
- The deep surveys by ISO have opened a new age for studies of the galaxy formation in the universe.

Acknowledgements

We are very happy that we have been given an opportunity to participate in the ISO project. We are also grateful to the people involved in the development, operation and data analysis of ISO for their extensive collaboration. This is a Japan/US joint project and this report is based on their collaborated work. The model calculation refers to the work by Tsutomu Takeuchi and his collaborators. I appreciate all their effort.

References

1. Taniguchi, Y., Cowie, L.L. et al. (1997) A&A 328, L9-L12
2. Kawara, K., Sato, Y. et al. (1998) A&A 336, L9-L12
3. Sato, Y., Cowie, L.L. et al. (1999) A Mid-infrared Deep Galaxy Survey in the SSA13 Field. In: Cox, P., Kessler, M.F. (Eds.) Proceedings of the conference "The Universe as seen by ISO" at Paris, France, October 20-23, 1998. ESA SP-427, 1055-1057
4. Barger,A.T., Cowie, L.L. et al. (1998) Nature 394, 248-251
5. Oliver, S.J., Goldschmidt, P. et al. (1997) MNRAS 289, 471-481
6. Kawara, K., Sato, Y. et al. (1999) in this volume.
7. Kawada, M., Bock, J.J. et al., (1994) ApJ, 425, L89 – L93

8. Matsuhara, H., Kawara, K. et al. (2000) in preparation.
9. Matsuhara, H., Kawara, K. et al. (1999) in this volume.
10. Takeuchi, T.T. et al. (1999) Exploring Galaxy Evolution from Infrared Galaxy Number Count. In: Proceedings of Star formation 99 Workshop at Nagoya, Japan. 61-62
11. Ishii, T.T., Takeuchi,T.T. et al. (2000) Cosmic Star Formation History Required from Infrared Galaxy Number Count: Future Prospect for Infrared Imaging Surveyor(IRIS). In: Favata, F., Kaas, A.A., Wilson, A. (Eds.) Star Formation from the Small to the Large Scale, 33rd ESLAB Symp. at ESTEC, Noordwijk, The Netherlands, November 2 - 5, 1999. ESA SP-445, in press
12. Soifer, B.T., Sanders, D.B. (1987) ApJ 320, 238-257
13. Puget, J.L., Abergel, A. et al. (1996) A&A 308, L5-L8
14. Hauser, M.G., Arendt, R.G. et al. (1998) ApJ 508, 25-43
15. Fixsen, D.J., Dwek, E. et al. (1998) ApJ 508, 123-128
16. Elbaz, D., Cesarsky, C.J. et al. (1999) A&A 351, L37-L43
17. Oliver, S. et al. (1999) in this volume.
18. Puget, J.L., Lagache, G. et al. (1999) A&A 345, 29-35
19. Aussel, H., Cesarsky, C.J. et al. (1999) A&A 342, 313-336
20. Rowan-Robinson, M., Oliver, S. et al. (1999) The European Large Area ISO Survey: ELAIS. In: Cox, P., Kessler, M.F. (Eds.) Proceedings of the conference "The Universe as seen by ISO" at Paris, France, October 20-23, 1998. ESA SP-427, 1011-1014
21. Dole, H., Lagache, G. et al. (1999) FIRBACK Far Infrared Survey with ISO: Data Reduction, Analysis and First Results. In: Cox, P., Kessler, M.F. (Eds.) Proceedings of the conference "The Universe as seen by ISO" at Paris, France, October 20-23, 1998. ESA SP-427, 1031-1035
22. Franceschini, A., Aussel, H. et al. (1997) Source-Counts and Background Radiation. In: Wilson, A. (Ed.) The Far Infrared and Submillimetre Universe, Noordwijk, The Netherlands, ESA SP-401, 159
23. Guiderdoni, B., Hivon, E. et al. (1998) MNRAS 295, 877-898
24. Madau, P., Ferguson, H.C. et al. (1996) MNRAS 283, 1388–1404
25. Tan, J.C., Silk, J. et al. (1999) ApJ 522, 579-589
26. Cesarsky, C.J. (1999) in this volume.
27. Sanders, D. (1999) A New View of Galaxy Evolution from Submillimeter Surveys with SCUBA. In: Toward a New Millennium in Galaxy Morphology, Kluwer, the Netherlands(astro-ph/9910028)
28. Genzel, R., Cesarsky, C.J. (2000) Ann. Rev. Astron. Astrophys. in press.

ISO Deep Far-Infrared Survey in the Lockman Hole

Kimiaki Kawara[1], Yasunori Sato[2], Hideo Matsuhara[2], Yoshiaki Taniguchi[3], Haruyuki Okuda[2], Yoshiaki Sofue[1], Toshio Matsumoto[2], Ken-ichi Wakamatsu[4], Lennox L. Cowie[5], Robert D. Joseph[5], and David B. Sanders[5]

[1] Institute of Astronomy, University of Tokyo, Mitaka 181-8588, Japan
[2] ISAS, Sagamihara 229-8510, Japan
[3] Astronomical Institute, Tohoku University, Sendai 980-8578, Japan
[4] Department of Physics, Gifu University, Gifu 501-1193, Japan
[5] Institute for Astronomy, University of Hawaii, Honolulu, HI 96822, USA

Abstract. Two $44' \times 44'$ fields in the Lockman hole have been surveyed at 95 and 175μm with ISOPHOT. The raw data were reduced by PIA up to AAP products and then the responsivity drift was corrected by the median filter technique. IRAF DAOPHOT was used to extract point sources from the maps. Simulations generating artificial objects show the effect of source confusion is significant in the flux range below 200 mJy. The differential and cumulative source number density vs flux relations were derived after correction for the confusion effect. The number densities have excess over the models by Guiderdoni et al. by a factor of 10 - 50. The slopes of the number densities are similar at the both wavelengths, implying far-infrared sources are at low redshift. Comparisons with radio and X-ray sources indicate most of far-infared sources are star-forming galaxies.

1 Introduction

As part of the Japan/UH cosmology program using the ISAS guaranteed time, a 95 μm and 175 μm survey was conducted in the Lockman Hole to search for obscured infrared galaxies. The first results and discussion were presented by Kawara et al. (1998) [1] with details of the observations, image processing, and flux calibration. This article presents point source extraction, source counts, and discussion on the nature of far-infrared sources. The effect of the IR cirrus confusion is fully examined by Matsuhara et al.(1999) [2] as well as the source number density - flux relations derived from the power spectrum analysis. The astrophysical implications are discussed by Okuda et al. [3] by comparing with the models for source counts.

2 The Survey

The observations in the Lockman hole began in March 1996, less than two months after the start of the ISO routine phase, and ended in June 1996. The total survey area covered in two $44' \times 44'$ fields, called LHEX and LHNW, is

D. Lemke, M. Stickel, and K. Wilke (Eds.): LNP 548, pp. 49–53, 2000.

approximately 1 sq. deg. at the 95 and 175 μm bands. Each field is made up of four sub-fields having an approximately $22' \times 22'$ area.

3 Point Source Extraction

The PHT Interactive Analysis (PIA) version 7.3 was used with the default settings to reduce the edited raw data to the AAP(Astronomical Analysis Processing) products. At this level of image-processing, the astronomical signals especially at 95 μm are buried under the predominant noise that is caused by drift in the responsivity of the detectors. The responsivity drift was successfully corrected by using the MEDIAN filter routine developed by Kawara et al. (1998) [1]. The drift corrected maps of the four sub-fields are rebinned into $2.3''$/pixel at 95μm or $4.6''$/pixel at 175μm, and then mosaiced into the $44' \times 44'$ maps of LHEX and LHNW. Finally, the IRAF gauss routine was applied with sigma = 6 for smoothing the images.

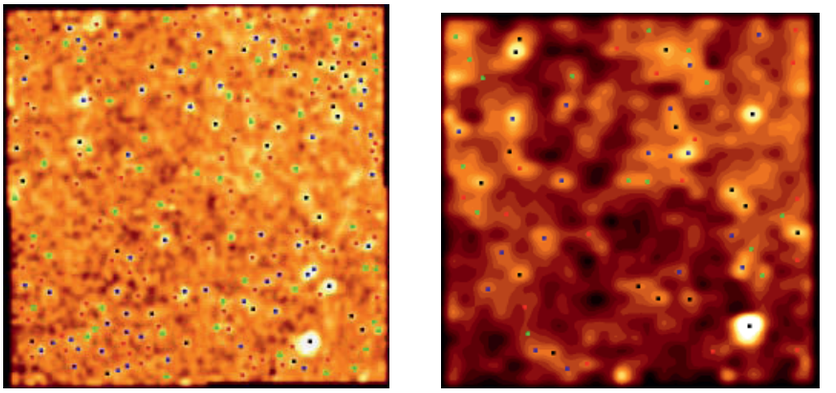

Fig. 1. Sources extracted by DAOPHOT are plotted on the LHEX 95μm map on the left and the 175μm map on the right. The brightest source is F10507+5723 which is the only IRAS source in the survey fields.

IRAF DAOPHOT is likely to be the unique tool to extract source in the maps by the following reasons; (1) as shown in Fig. 1, the maps are very crowded and (2) FWHM measurements of profiles of bright sources indicate all of them are not significantly extended and are point sources. DAOPHOT has indeed been developed to perform stellar photometry in crowded fields [4]. The point spread function to be fed to DAOPHOT was created by using several brightest sources in LHEX.

4 Confusion Analysis and Source Counts

The effect of the source confusion to the completeness of the source counts has been examined by means of simulations in which several artificial sources were added to the maps, and detections and measurements were made with the same set of DAOPHOT parameters. The simulations were repeated with changing the object positions until the sufficient number of objects had been obtained in each flux level which ranges from 70 to 280 mJy. The flux levels were set in such a way that the flux creases in each level by a factor of $\sqrt{2}$. A simulation with artificial 140 mJy objects in the LHEX 175μm map is shown in Fig. 2. The simulations indicate that the source confusion makes more than one faint sources detected as a single bright source, and this effect is significant. For example, 80% of artificial 100 mJy objects at 95μm are detected and the mean observed flux is 135 mJy, and at 175μm only 50% of 140 mJy objects are detected with a mean observed flux of 205 mJy.

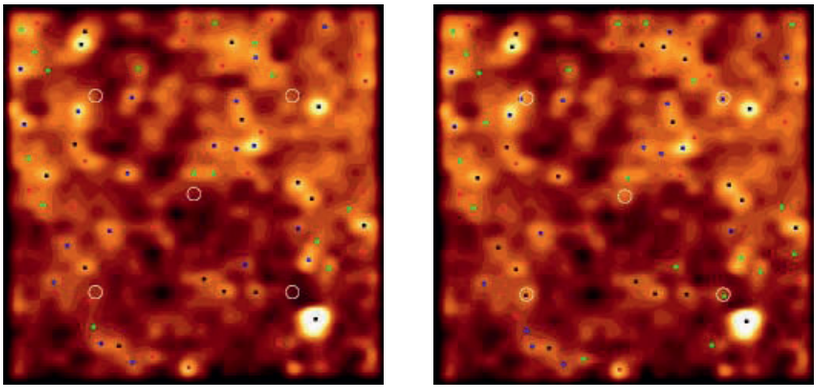

Fig. 2. A simulation with artificial 140 mJy objects for LHEX 175μm map is shown. The map on the left is without objects. The map on the right is with 140 mJy objects which were added at the center of the white circles. Notice that the object added at the center of the map were missed in DAOPHOT detection, and the SNRs depend on the brightness distribution at which the objects were added.

The effect due the source confusion can clearly be seen in Fig. 3, and the effect should be corrected in the flux range below 200 mJy.

5 Nature of ISO Far-Infrared Sources

The slopes of the number-flux function in Fig. 3 are quite similar at the both wavelengths. This can be expected if the magnitudes of K-correction brightening are similar in the both wavelengths. If this is the case, the sources are in low redshift such as $z \sim 0.5$. The differential counts clearly indicate a large

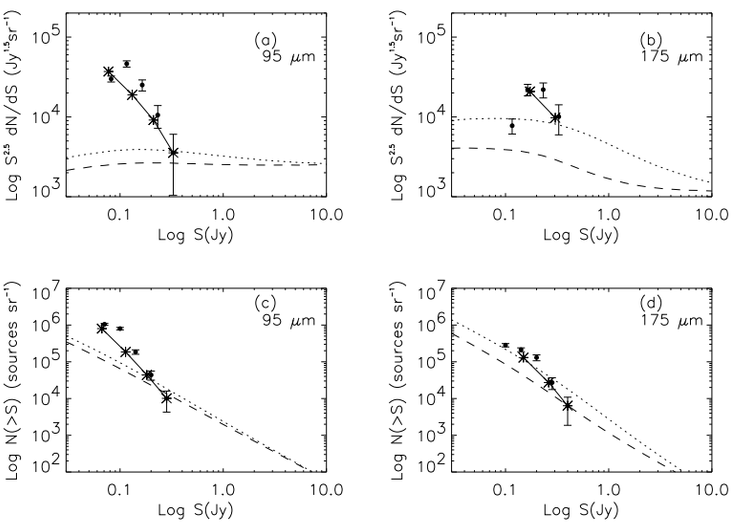

Fig. 3. The number versus flux-density relations for ISO sources in the Lockman Hole. a.- Differential surface number densities of 95 μm sources. b. - Same as (a) but for 175 μm. c.- Cumulative surface number densities of 95 μm sources. d. - Same as (c) but for 175 μm. The dots represent the cumulative or differential numbers without the correction for the source confusion. The bars are statistical errors only (i.e., $\sqrt{N}$). The asterisks show the cumulative or differential numbers with the correction for the source confusion. The dashed and dotted lines denotes model A and model E by Guiderdoni et al.(1998) [5].

excess of far-infrared sources by a factor of 10 - 50 over the models by Guiderdoni et al.(1998) [5] that were developed to account for the cosmic infrared background radiation derived by Puget et al. (1996) [6] from the analysis of the COBE/FIRAS residuals. The excess especially at 95μm over the models is so large that there would be a strong excess in the volume density of far-infrared sources at low redshift in such a way that such high volume density will violate the constraint from the cosmic infrared background radiation if it does not decrease at high redshift [3].

Fig. 4 compares the LHEX 95μm map with VLA 20cm continuum sources [7] and ROSAT X-ray sources [8]. The positional correlation with radio sources is much better than that with X-ray sources. It is considered that the radio observations looked at non-thermal emission from supernova remnants in star-forming galaxies except for bright radio sources that would be radio galaxies or AGNs, while ROSAT X-ray sources are mostly AGNs. Thus, the correlations in Fig. 4 indicate that ISO far-infrared sources are mostly star-forming galaxies.

Our number density at 175μm is consistent with the results by Puget et al. (1999) [9]. On the other hand, the 95μm number density is much higher than that by Rowan-Robinson et al. (1999) [10], and the difference is a factor of 10 at 70 mJy. The origin is not clear.

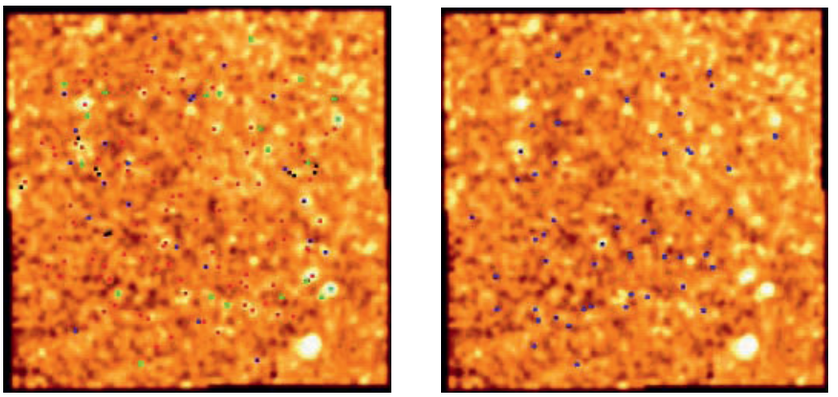

Fig. 4. The figure on the left shows VLA 20cm continuum sources plotted on the LHEX 95μm map. The right shows ROSAT X-ray sources on the same map.

References

1. Kawara, K., Sato, Y. et al. (1998) A&A **336**, L9–L12.
2. Matsuhara et al. 1999 in this volume.
3. Okuda et al. 1999 in this volume.
4. Stetson, P. (1987) PASP **99**, 191–222.
5. Guiderdoni, B., Hivon, E., Bouchet, F.R., & Maffei, B. MNRAS **295**, 877–898.
6. Puget J.L., Abergel, A. et al. A&A **308**, L5–L8.
7. de Ruiter, H.R., Zamorani, G. et al. A&A, **319**, 7–17.
8. Hasinger, G., Burg, R. et al. 1998 A&A **329**, 482–494.
9. Puget, J. L., Lagache, G. et al. 1999 A&A **345**, 29–35.
10. Rowan-Robinson, M., Soliver, S. et al. 1999 in 'The Universe as Seen by ISO', ed. by Cox, P. & Kessler, M., 1011–1015.

FIRBACK Source Counts and Cosmological Implications

Hervé Dole[1], Richard Gispert[1], Guilaine Lagache[1], Jean-Loup Puget[1], Hervé Aussel[2,3], Francois R. Bouchet[4], Paolo Ciliegi[5], David L. Clements[6], Catherine Cesarsky[7], Francois-Xavier Désert[8], David Elbaz[2], Alberto Franceschini[3], Bruno Guiderdoni[4], Martin Harwit[9], Rene Laureijs[10], Dietrich Lemke[11], Richard McMahon[12], Alan F.M. Moorwood[7], Seb Oliver[13], William T. Reach[14], Michael Rowan-Robinson[13], and Manfred Stickel[11]

[1] Institut d'Astrophysique Spatiale, Orsay, France
[2] Service d'Astrophysique, CEA/DSM/DAPNIA Saclay, France
[3] Osservatorio Astronomico di Padova, Italy
[4] Institut d'Astrophysique de Paris, France
[5] Osservatorio Astronomico di Bologna, Italy
[6] Cardiff University, UK
[7] ESO, Garching, Germany
[8] Laboratoire d'Astrophysique, Observatoire de Grenoble, France
[9] 511 H.Street S.W., Washington, DC 20024-2725
[10] ISOC ESA, VILSPA, Madrid, Spain
[11] MPIA, Heidelberg, Germany
[12] Institute for Astronomy, University of Cambridge, UK
[13] Imperial College, London, UK
[14] IPAC, Pasadena, CA, USA

Abstract. FIRBACK is a one of the deepest survey performed at 170 μm with ISOPHOT onboard ISO, and is aimed at the study of the cosmic far infrared background sources. About 300 galaxies are detected in an area of four square degrees, and source counts present a strong slope of 2.2 of the integral "logN-logS" plot, which cannot be due to the effect of the cosmological evolution if no K-correction is present. The resolved sources account for less that 10% of the Cosmic Infrared Backgound at 170 μm. In order to understand the nature of the sources contributing to the CIB, and to explain deep source counts at other wavelengths, we have developped a phenomenological model, which constrains in a simple way the luminosity function evolution with the redshift, and fits all the existing deep source counts from the mid-infrared to the submillimetre range.

1 Introduction

The Cosmic Infrared Background (CIB), due to the accumulation of all galaxies emissions at every redshift on the line of sight in an instrument beam, is a powerful tool for studying galaxy evolution. FIRBACK ([19],[5]), one of the deepest survey performed at 170 μm, is aimed at the study of the CIB, in two complementary ways:

- study the resolved sources (this paper)

D. Lemke, M. Stickel, and K. Wilke (Eds.): LNP 548, pp. 54–61, 2000.

- study the background fluctuations ([13], [14])

Throughout this paper we use a cosmology with $h = 0.65$, $\Omega = 1$ and $\Lambda = 0$.

2 The FIRBACK Survey

FIRBACK, is a survey of 4 square degrees in 3 high galactic latitude fields, choosen to have as low HI column-density as possible, typically $N_H \simeq 10^{20} cm^{-2}$, and if possible multiwavelength coverage. Observations were carried with the ESA's Infrared Space Observatory (ISO, [12]) with the ISOPHOT photometer [16] in raster mode (AOT P22) with the `C200` camera and `C_160` broadband filter centered at $\lambda = 170\,\mu m$. A detailed description of the reduction, data processing, and calibration will be discussed in [15], whereas the analysis of the complete survey will be discussed in [6].

3 Source Counts at $170\,\mu m$

Preliminary FIRBACK integral source counts at $170\,\mu m$ (Fig. 1), not corrected for uncompleteness, show a strong slope of 2.2 between 120 and 500 mJy. This strong slope is not explained by the effect of the K-correction or cosmological evolution alone: both must be present; the K-correction is the ratio, at a given wavelength, of the emitted flux over the redshifted flux.
Non (or low) evolution scenarii, or extrapolation of IRAS counts, are not able to reproduce the observed counts. For illustration, we plotted in Fig. 1 the non evolution model from [9] and the evolution model A from [11]. On the other hand, evolutionary models from [9] and from [11] (model E: evolution + ULIRGs) give a better agreement. At this wavelength, FIRBACK sources account only for 3% of the background.

4 Modelling the Evolution of Galaxies

4.1 Method

Our philosphy is to make a simple phenomenological model that explains all the observed deep source counts and reproduces the CIB in the mid-IR to submillimetre range. One way to do it is to constrain the evolution with the redshift of the luminosity function (LF) in the infrared, given:

- templates of galaxy spectra
- the energy density available at each redshift

For the first point, we used template galaxy spectra based on IRAS colors [18] modified to account for recent ISO observations, in particular the absorption feature near $10\,\mu m$ at high luminosity; PAH features are present in the mid-infrared [4], even if their strength seems larger than the observations: this is

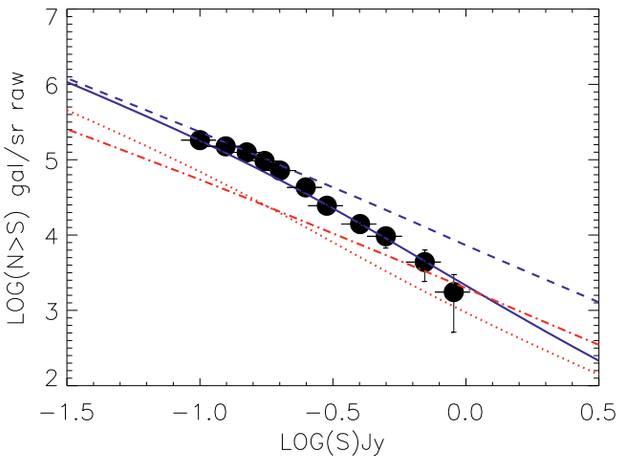

Fig. 1. FIRBACK integral source counts at 170 μm not corrected for uncompleteness. Models from [11]: A (dot) with evolution, E (solid) with evolution + ULIRGs. Models from [9]: without evolution (dot-dash), with evolution (dash).

not a problem because the right amount of energy is present in each peak, and we convolve the spectrum by the filter spectral response (Fig. 2). For the second point, we used the inversion of the CIB spectrum by [10] and [20], which gives with a good accuracy the energy density available at redshifts between 1 and 3. This energy density is the integral of the luminosity function at each redshift, but there is not a unique solution for the LF shape.

4.2 Evolving Luminosity Function

The question is: how do evolve the LF with redshift ?
Fig. 3 represents the LF of [21] at a redshift z=0, renormalized for $h = 0.65$ and for having the same integral than [23]. Our constrain for the LF redshift variation is the energy density available at each redshift [10]. Usually, authors apply a pure density evolution to the LF in function of the redshift (that is a vertical shift), or a pure luminosity evolution (an horizontal shift). It does not work for FIRBACK source counts: there is no alternative than adding the evolution into one part of the LF only. This part is constrained by IR and submm observations: this is the bright end of the LF. Fig. 3 represents our decomposition of the local LF in 2 parts:

- left part: "normal" galaxies
- right part: ULIRG's, centered on a luminosity $L_{ULIRG} = 1.3 \times 10^{11} L_{\odot}$, where L_{ULIRG} is the free parameter; we get the same value as [24]

In our model, without evolution means that the local LF (Fig. 3a) is taken, and is the same at every redshift. In the evolution scenario, only the ULIRG

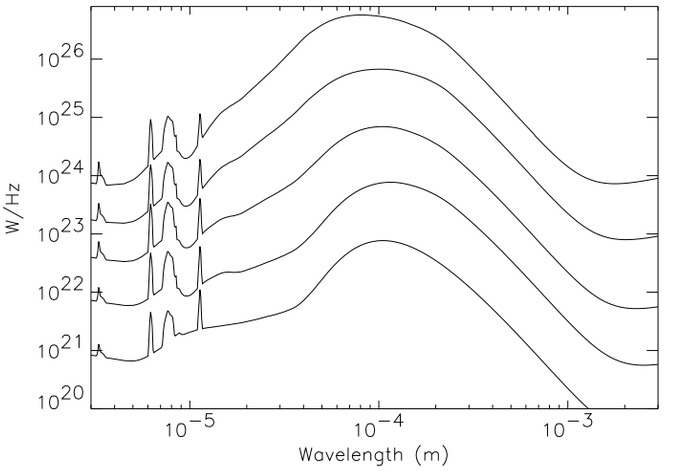

Fig. 2. Template spectra used for simulating source counts; from bottom to top: $L = 10^9$, 10^{10}, 10^{11}, 10^{12}, $10^{13}\, L_\odot$.

part moves, in such a way that the integral of the LF equals the constraint given by the CIB inversion at each redshift. The maximum is reached at $z \simeq 2.5$, and Fig. 3b represents the LF at this redshift. We neglect at this stage the evolution of "normal" galaxies, which do not play a crucial role in the mid-infrared to submillimetre wavelength range.

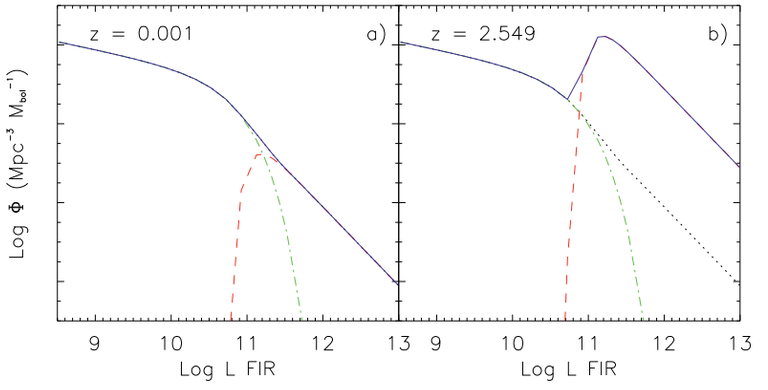

Fig. 3. a: Luminosity Function at z=0 in solid line; normal galaxy (dot-dash) ULIRG (dash-dash). b: Luminosity Function at z=2.5 in solid line; normal galaxy (dot-dash) ULIRG (dash-dash) and local LF (dot).

4.3 Model of Source Counts at 170 μm

Models at 170 μm, together with our data, is presented in Fig. 4. The brightest point of the observed counts is compatible with all our models, in particular the non-evolution scenario, which is expected for local sources. We also show the effect of the K-correction, which steepens the integral source counts slope. Our evolution scenario fits within the error bars the data. Most of the background will be resolved into sources when we will be able to detect sources at the mJy level. This wavelength, at which evolution effects are particulary important and where there is a good ability to detect higher redshift sources because of the K-correction, is nowadays probably the best-suited for probing galaxy evolution from space in the far-infrared range.

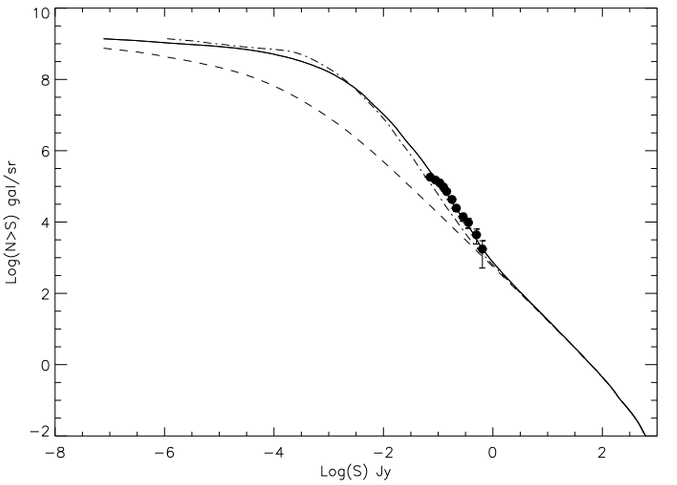

Fig. 4. Models at 170 μm with (solid line) and without (dashed line) evolution and observed counts. Model with evolution and without K-correction is the dot-dash line.

4.4 Models of Source Counts at Other Wavelengths

Data at 15 μm [7], 90 μm [8] and 850 μm [2], with our models are presented in Fig. 5, Fig. 6 and Fig. 7 respectively.
At 15 μm, both the slopes and the little "waves" in the counts appear in the models with the combined effects of the K-correction and the evolution. At 90 μm, the K-correction do not emphasize the differences between the scenarii of evolution or non-evolution. At 850 μm, the "non smooth" appearance of our model is due to the discretization of the LF.

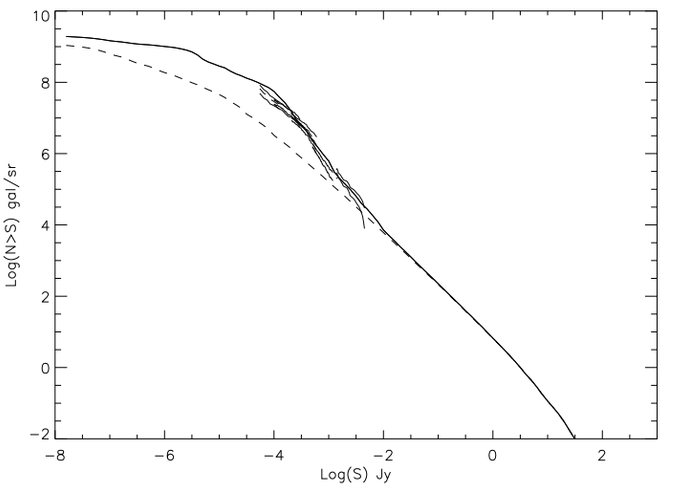

Fig. 5. Models at 15 μm with (solid line) and without (dashed line) evolution, and observed counts from Elbaz et al. [7] (thin lines).

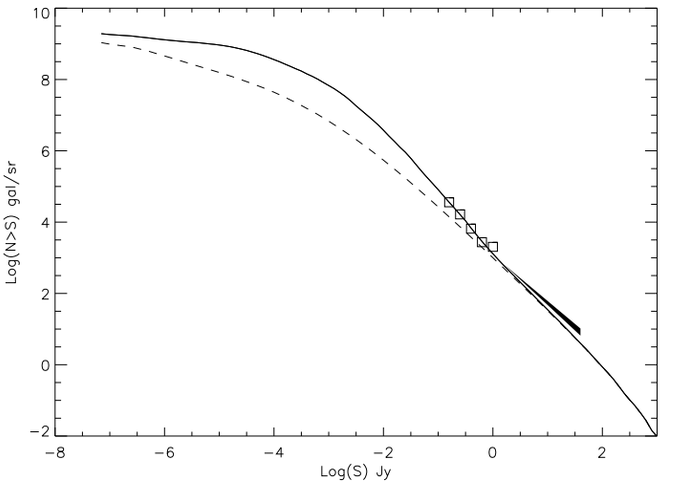

Fig. 6. Models at 90 μm with (solid line) and without (dashed line) evolution, and observed counts from Efstathiou et al. [8] (squares) and IRAS counts [8] (solid area)

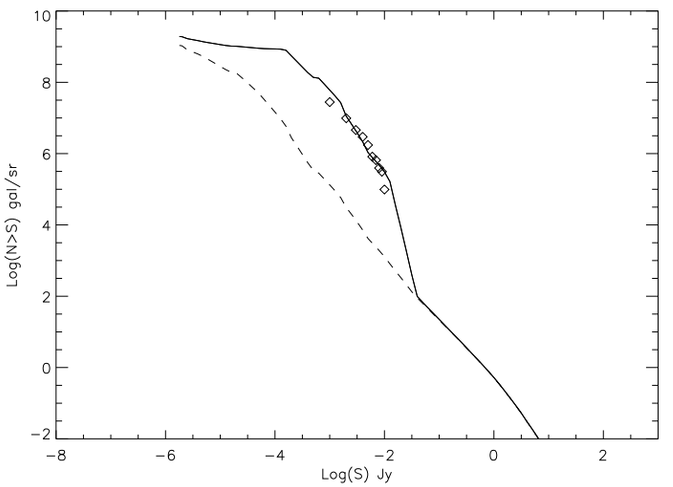

Fig. 7. Models at 850 μm with (solid line) and without (dashed line) evolution, and observed counts from Barger et al. [2] (losanges).

5 Discussion

5.1 The Bright End Luminosity Function Evolution Model

Our model, in the evolving LF scenario, fits most of the existing deep survey data from space (mid and far infrared) and ground (submillimetre). It is also compatible with the observational estimation of the LF in [17]. The strong observational constrain of multiwavelength source counts is thus explainable by a simple evolution law of the LF: the Bright End Luminosity Function Evolution (BELFE) model. One simple model is in agreement with all up-to-date observables and reproduces the background.

5.2 Redshift and Nature of the Sources

Another crucial observational test for our model is the predicted vs observed redshift distribution. Although the statistics is low, we have some evidence that most of the ISOCAM sources lie at redshift between 0 and 1.4 with a median at 0.8 [1], and that most of the SCUBA sources lie at redshifts greater than 2 [2]. Our predicted redshift distributions at these two wavelengths are in agreement with the existing observations.
What about FIRBACK 170 μm sources ? Our predicted redshift distribution shows that most of the sources lie at redshifts below 1.5, with a comparable median as for ISOCAM sources; that means that we are sensitive both to local and above-redshift-1 sources. All the FIRBACK sources with known redshift (less than 10) [3], [22] are in this range: 2 submillimetre sources at $z > 1$, and few visibles sources are at $z \simeq 0.2$.

It is difficult to adress the question of the difference of nature between PHOT and CAM sources, because their redshift distributions (respectively expected and observed) are similar, but about half of 170 μm sources have 15 μm counterparts.

6 Conclusion

We presented results from the FIRBACK survey, one of the biggest ISO programs, dealing with resolved sources of the CIB: our source counts at 170 μm show a strong evolution. This evolution is explained by a simple evolution law in redshift of the luminosity function, different from pure density or luminosity evolution: the "Bright End Luminosity Function Evolution" model. This strong evolution model fits all the existing source counts at 15, 90, 170 and 850 μm, and also predicts a redshift distributions in agreement with the (sometimes rare) observations. This powerful tool, based on observational constraints coming for the CIB spectrum inversion and the local Luminosity Function, and on assumed template galaxy spectra, not only agrees with existing data but also is able to make useful predictions in terms of source counts or CIB fluctuations for the scientific preparation of forthcomming major telescopes such as SIRTF, Planck, FIRST and ALMA. All these FIRBACK materials are available at: `http://wwwfirback.ias.fr`.

References

1. Aussel, H., 1999, PHD Thesis Université Paris VII
2. Barger A.J., Cowie L.L., Sanders, D.B., 1999 ApJ, 518, L5
3. Dennefeld, M., 1999, Private Communication
4. Désert, F-X., Boulanger F., Puget, J.L., 1990, A&A, 237, 215
5. Dole H., Lagache G., Puget J-L., Gispert R., et al., 1999, ESA/SP-427, p1031, astro-ph/9902122
6. Dole H., Gispert R., Lagache G., Puget J-L., et al., 2000, in preparation
7. Elbaz D., et al., 1999, A&A, 351, L37
8. Efstathiou A., et al., 1999, MNRAS, submitted
9. Franceschini A., et al., 1998, MNRAS, 296, 709
10. Gispert R., Lagache G., Puget J-L., 2000, A&A, submitted
11. Guiderdoni B., et al., 1998, MNRAS, 295, 877
12. Kessler M. F., et al., 1996, A&A, 315, L27
13. Lagache G., and Puget J-L., 1999, A&A, in press, astro-ph/9910255
14. Lagache G., et al., 1999, this volume
15. Lagache G., and Dole, H., 2000, in preparation
16. Lemke D., et al., 1996, A&A, 315, L64
17. Lilly, Ss.J., et al, 1999, ApJ, 518, L641
18. Maffei B., 1994, PHD Thesis Université Paris-Sud
19. Puget J-L., et al., 1999, A&A, 345, 29
20. Puget J-L., et al., 1999, this volume
21. Sanders D.B., and Mirabel I.F., 1996, ARAA, 34, 749
22. Scott D., et al, 2000, A&A, in press, astro-ph/9910428
23. Soifer B.T., and Neugeubauer G., 1991, AJ, 101, 354
24. Tan J.C., Silk J., Balland C., 1999, ApJ, 522, 579

Deep Far Infrared ISOPHOT Survey in "Selected Area 57"

Michael J.D. Linden-Vørnle[1,2,3], Hans Ulrik Nørgaard-Nielsen[2], Henning E. Jørgensen[1], Leif Hansen[1], Martin Haas[4], Ulrich Klaas[4], Peter Ábrahám[4], Dietrich Lemke[4], Ib L. Rasmussen[2], and Herbert W. Schnopper[5]

[1] Niels Bohr Institute for Astronomy, Physics and Geophysics, Astronomical Observatory, Juliane Maries Vej 30, DK–2100 København Ø, Denmark
[2] Danish Space Research Institute, Juliane Maries Vej 30, DK–2100 København Ø, Denmark
[3] Tycho Brahe Planetarium, Gl.Kongevej 10, DK–1610 København V, Denmark
[4] Max-Planck-Institut für Astronomie (MPIA), Königstuhl 17, D–69117 Heidelberg, Germany
[5] Harvard-Smithsonian Center for Astrophysics, 60 Garden Street, Cambridge, MA 02138, USA

Abstract. We present here the results of a deep survey in a 0.4 deg^2 blank field in Selected Area 57 conducted with the ISOPHOT instrument aboard ESAs Infrared Space Observatory (ISO[1]) at both 60 μm and 90 μm. We describe our data reduction and analysis scheme with special emphasis on source extraction and flux calibration. With a formal signal to noise ratio of 6.75 we have source detection limits of 90 mJy at 60 μm and 50 mJy at 90 μm. To these limits we find cumulated number densities of 5±3.5 deg^{-2} at 60 μm and 14.8±5.0 deg^{-2} at 90 μm. These number densities of sources are found to be lower than previously reported results from ISO but the data do not allow us to discriminate between no-evolution scenarios and various evolutionary models.

1 Introduction

It is widely accepted that a significant part of the evolution of galaxies is hidden from UV/optical studies due to internal absorption by dust grains, and that the absorbed radiation is re-emitted in the infrared.

The IRAS All Sky Survey has revealed more than 25.000 galaxies, of which only half were already known at optical wavelengths (Soifer et al. [20]). The vast majority of these are local late-type spirals while ellipticals and S0 galaxies were rarely detected. Only a few very luminous infrared galaxies were detected at significant redshifts.

A first indication of a possible evolution of the population of infrared sources at the IRAS detection limit was found by Hacking & Houck [8].

[1] Based on observations with ISO, an ESA project with instruments funded by ESA member states (especially the PI countries: France, Germany, the Netherlands, and the United Kingdom) and with the participation of ISAS and NASA.

D. Lemke, M. Stickel, and K. Wilke (Eds.): LNP 548, pp. 62–69, 2000.

Analysing the Hacking & Houck [8] data, Hacking et al. [9] found a significant excess of their 60 μm number density below 100 mJy, if no evolution out to $z \approx 0.2$ is assumed. They fit the number densities with simple models assuming a power law in $(1 + z)$ either as pure density or pure luminosity evolution, but are not able to distinguish between these two types of models. Following the pioneering work by Hacking & Houck [8] several other deep IRAS surveys have been published e.g. Gregorich et al. [6] and Bertin et al. [3].

2 The ISOPHOT Observations

As part of the Infrared Space Observatory (ISO, Kessler et al. [13]) Central Programme, we have performed a deep ISOPHOT survey of a ~ 0.4 deg^2 area within Selected Area 57 (e.g. Stebbins et al. [21]). We have chosen this area because it is close to the North Galactic Pole and thus has a low far infrared sky background and it is relatively clean with respect to cirrus emission.

We have performed the observations using the ISOPHOT C100 detector array, both at 60 μm and at 90 μm producing three 16×16 arcmin^2 and ten 10×10 arcmin^2 PHT32 raster maps in each wavelength band. One of the large raster maps is observed twice in each band in order to facilitate consistency checks. The total area covered is 0.40 deg^2 in each band. As an extension to this work we have also included and reanalysed the deep ISOPHOT survey at 90 μm of a 1.1 deg^2 area in the Lockman Hole (Kawara et al. [12]).

3 Data Reduction

We here present a very brief outline our data reduction, source extraction and calibration scheme. For a full description please see Linden-Vørnle et al. [15]. The backbone of the reduction is PIA version 7.3.1(e) where we have used batch processing from ERD- to AAP-level using the processing steps listed in Table 1. We have employed our own non-PIA IDL routine to remove

Table 1. Processing steps used in the PIA batch reduction from ERD- to AAP-level

Level	Processing step
ERD	Two-threshold deglitching
ERD→SRD	1. order pol. fit to ramps
SRD	Reset interval correction
SRD	Signal deglitching
SRD	Orbital dependent dark current subtraction
SRD→SCP	No drift handling
SCP→AAP	Actual responsivity flux-calibration
	using only FCS1 in the FCS-measurement
	following the science raster

the baseline drift at the AAP-level. After drift is removed PIA is used to produce individual raster maps. Coadded maps are shown in Fig. 1.

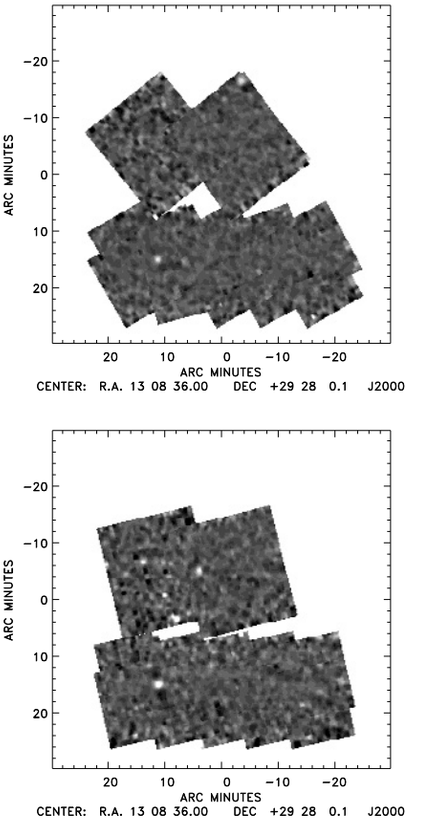

Fig. 1. Coadded maps at 60 μm (top) and 90 μm (bottom)

In order to detect individual sources we have employed the SExtractor software, verion 1.2 (Bertin & Arnouts [2]) optimizing the extraction parameters by investigating the parameter space for the source extraction for the repeated large rasters which have almost 100% area overlap. With the chosen SExtractor parameters the detected sources have a formal signal to noise ratio, SNR ≥ 6.75.

For a source detection to be classified as reliable we set the requirement that in areas where the raster maps are overlapping a detection must be confirmed in the individual overlapping raster map(s) observed in the same band within an error-ellipse with radius 10 arcsec. Non-confirmed sources

in overlapping areas are presently considered to be dubious detections. In areas without any overlap we must rely on the robustness of the extraction parameters chosen. Due to the increasing noise at the edges of the maps detections closer than 45 arcsec to the edges are however rejected.

Our flux calibration is done using the internal Fine Calibration Sources (FCS). We find that the resulting sky brightnesses are in agreement with the COBE DIRBE (Hauser et al. [10]) annual average values within about 25%.

In order to correct the source signal found within the detection area to obtain the total flux, we have simulated the PHT32 mapping procedure assuming a linear response and then used it on the point spread functions for C100 with C_60 and C_90 filters, taken from the calibration file PC1FOOTP.FITS.

To calibrate the source signals found by SExtractor to an absolute flux scale we have used observations of α Aql (C_60) and HR 1654 (C_90), observed with nearly the same instrument parameters as the HUNNSA57 raster maps. Model fluxes for the two stars have been established as part of the ISO calibration ground-based preparatory programme (GBPP, Jourdain de Muizon & Habing [11] and van der Bliek et al. [22]) for α Aql and by Cohen et al. [4] and Cohen private communication for HR 1654.

In order to obtain these model fluxes from our observed source signals of the standard stars, using the correction for source signal lying outside the detection area, we find a factor of 2.51 for C_60 and 1.41 for C_90 has to be applied.

Based on the detection criteria and the empirical calibration factors established above our source detection limit with a formal SNR = 6.75 is 90 mJy for C_60 and 50 mJy for C_90.

Two of the sources are IRAS Faint Sources with good 60 μm fluxes (IRAS quality flag 3). We find that our ISOPHOT fluxes agree with the IRAS fluxes within $\sim 10\%$ with the ISOPHOT values tending to be lower than IRAS. One of the IRAS sources also has a good 100 μm flux but unfortunately this source lies just outside our C_90 raster maps prohibiting an independent check of our 90 μm calibration.

We are thus confident that we have established a reliable calibration which yields a sky brightness in agreement with COBE DIRBE results and point source fluxes consistent with IRAS FSC at least for 60 μm. Based on the agreement with DIRBE and the scatter of source fluxes from independent maps we estimate that our photometric uncertainty for point sources is about 25%.

As mentioned in Sect. 2 we have included the ISOPHOT observations of a 1.1 deg^2 blank field in the Lockman Hole area (Kawara et al. [12]) in this work. We have reduced the C_90 data using the same batch processing steps as outlined in Table 1 and also removed drift at the AAP-level using median filtering. Source extraction is also performed using SExtractor.

Regarding calibration we find that the sky brightness in the C_90 data resulting from the ISOPHOT FCS calibration yields a sky background which

is about 30% brighter than the DIRBE annual average value. This is in fairly good agreement with our findings for the HUNNSA57 data. Regarding point sources, we have simulated the PHT22 mapping mode again assuming a linear response in order to establish the relation between the observed flux and the detection area. After using this relation to correct the source signals found by SExtractor to obtain the total flux we have applied our empirical C_90 calibration factor of 1.41 obtained from the standard star observations. One of the Lockman Hole sources has also been detected by IRAS with an IRAS 100 μm flux of 1218 mJy. With the calibration established in this work this flux is underestimated by 63%. Kawara et al. [12] use this IRAS source to calibrate their point source fluxes and therefore fluxes and flux limits presented by Kawara et al. [12] have to be corrected by a factor of $(1.0 + 0.63)^{-1} = 0.61$ in order to allow comparison with our results.

4 Discussion

We have in our HUNNSA57 survey detected seven sources at 90 μm brighter than 68 mJy and two sources at 60 μm brighter than 236 mJy. Only one of the sources, HUNNSA57_1, is detected in both bands yielding a flux ratio, $\frac{f_\nu(90\mu\mathrm{m})}{f_\nu(60\mu\mathrm{m})} = 0.7$. For the observations of the Lockman Hole the number of reliably detected sources amounts to eight down to 165 mJy which is somewhat more conservative than the result of 36 sources down to 90 mJy reported by Kawara et al. [12]. Based on our experience with the redundant HUNNSA57 data we are however – at this stage – not confident about detections below our limit of 165 mJy. Furthermore Kawara et al. [12] do not in detail describe their criteria for finding sources. Note that the flux limit reported Kawara et al. [12] is 150 mJy which here has been corrected by a factor of 0.61 in order to match our calibration as described in Sect. 3.

As mentioned in Sect. 2 the total area is 0.40 deg^2 in both bands for the HUNNSA57 survey. This also takes into account the area lost by rejecting sources at the edges. For the Lockman Hole data the area is 1.1 deg^2. The cumulative number counts at 90 μm down to 150 mJy are 14.8 per deg^2 and at 60 μm 5 per deg^2 down to 90 mJy. Compared to the number counts coming from the Guiderdoni et al. [7] no-evolution model i.e. no evolution of neither source density nor luminosity and a cosmology with $h = 0.5$ and $\Omega_0 = 1$ our number counts indicate a number density which is higher by a factor of 1.8 ± 0.6 for 90 μm but are inconclusive for 60 μm.

In Fig. 2 and Fig. 3 the number density of 60 μm and 90 μm sources from our HUNNSA57 survey respectively are plotted together with previously published counts and evolutionary models.

From Fig. 2 it can be seen that even though our 60 μm data are quite sparse they do not deviate substantially from the general trend outlined by other data sets and evolutionary models. With our 60 μm detection limit of 90 mJy at the formal SNR of 6.75 it is noteworthy that we do not find any

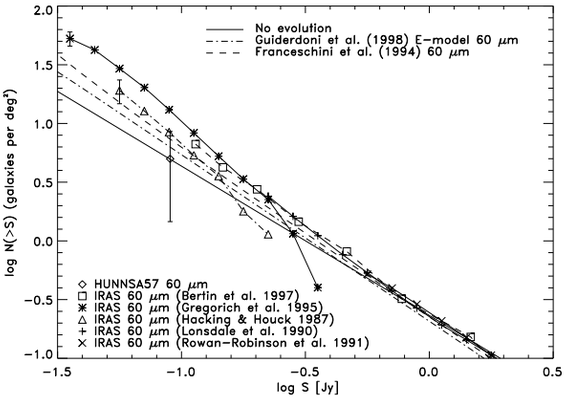

Fig. 2. Cumulative 60 μm number counts for HUNNSA57 along with previously published source counts and models. Our data are plotted with with error bars representing Poissonian uncertainties whereas the previously published source counts are plotted without error-bars except for the faintest bin of the Hacking & Houck [8] and Gregorich et al. [6] data

sources in the flux range from 236 mJy to 90 mJy. This situation is probably a result of the small survey area by chance missing out fainter sources.

For the 90 μm data in Fig. 3 the combined HUNNSA57 and Lockman Hole number densities are in line with evolutionary models by Guiderdoni et al. [7], Pearson & Rowan-Robinson [18] and Franceschini et al. [5] without being able to discriminate between them. Also the no-evolution scenario is not ruled out by the data even though there is an indication of evolution at least at 150 mJy. If this single data point is higher just by chance, no-evolution would be the most obvious match to the data.

When comparing our 90 μm source counts with the Hacking & Houck [8] 100 μm source counts (note that these counts are *not* an independent sample and furthermore heavily contaminated by cirrus) and the empirically scaled 60 μm counts (see caption for Fig. 3 for an explanation of this scaling) there seems to be a fairly good agreement between our results and the results obtained by Hacking & Houck [8], Bertin et al. [3], and also the number densities found by Gregorich et al. [6]. It is seen that the curve for our cumulated source counts is flattening below a flux of 150 mJy. This effect might be a result of incompleteness below this level but it could also indicate that the number density of sources below this level is actually leveling out. At the brighter end the number density falls of somewhat more steeply than Bertin et al. [3] which probably is due to the low probability of finding sources this bright in an area of only a few deg^2. This trend is also seen in the Hacking & Houck [8] 100 μm number counts.

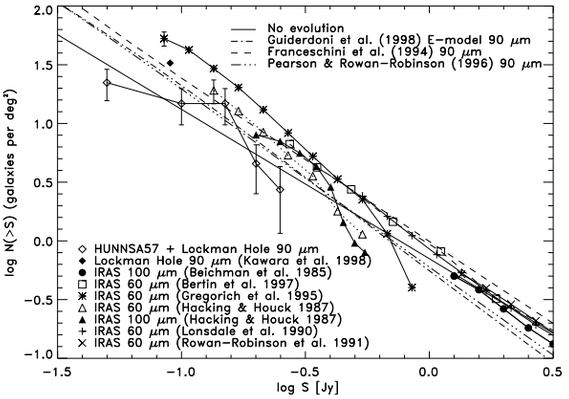

Fig. 3. Cumulative 90 μm number counts for HUNNSA57 + Lockman Hole data along with previously published counts and models. Except for the IRAS 100 μm data from Beichman et al. [1] and Hacking & Houck [8] the previously published counts are actually the 60 μm counts presented in Fig. 2 with the flux scale multiplied by a factor of 2.4. This factor has been established as the flux factor between the IRAS 60 μm and 100 μm point source counts at $|b| > 50^\circ$ and we have verified that this scaling is valid at least for low redshift galaxies ($z \leq 0.5$) with dust temperatures in the range 30-40 K and an emissivity indices ranging from 1 to 2. As in Fig. 2 our data are plotted with error bars representing Poissonian uncertainties whereas the previously published source counts are plotted without error bars except for the faintest bin of the Hacking & Houck [8] and Gregorich et al. [6] data. Note that the flux limit of the Kawara et al. [12] data has been corrected as discussed in Sect. 3 in order to match up with our calibration

5 Conclusion

Using the ISOPHOT C100 detector we have conducted a deep survey at 60 μm and 90 μm in a small part of Selected Area 57 near the North Galactic Pole. We have established a calibration which is in line with both the COBE DIRBE annual average sky background and IRAS point sources to within about 25% at least at 60 μm.

Cumulative source counts based on the combined source detections both in our HUNNSA57 data and our reduction of the Lockman Hole 90 μm survey indicate that evolution as given by the models of Guiderdoni et al. [7] (E-model) and Franceschini et al. [5] is consistent with our data. Our data do however not permit us to discriminate between these models and do furthermore not rule out no-evolution scenarios even though there is an indication of evolution at least at 150 mJy.

Our 90 μm source counts are in line with Hacking & Houck [8] 100 μm source counts and the empirically scaled 60 μm results from Bertin et al. [3],

Hacking & Houck [8] not precluding the number densities found by Gregorich et al. [6].

Acknowledgements

The ISOPHOT data presented in this paper were partly reduced using PIA Version 7.3.1(e), which is a joint development by the ESA Astrophysics Division and the ISOPHOT Consortium. We would like to thank Bruno Guiderdoni (IAP, France) and Alberto Franceschini (University of Padova, Italy) for providing us their evolutionary models. Finally we would like to thank the Phot Instrument Dedicated Team (ESA/VILSPA, Madrid) and especially Bernhard Schulz and Carlos Gabriel for their help and support.

References

1. Beichman, C.A. et al. (1985) Infrared Astronomical Satellite (IRAS), Catalogs and Atlases, Explanatory Supplement, GPO, Washington DC
2. Bertin, E., Arnouts, S. (1996) A&AS 117, 393
3. Bertin, E. et al. (1997) A&A 323, 685
4. Cohen, M. et al. (1996) AJ 112, 2274
5. Franceschini, A. et al. (1994) ApJ 427, 140
6. Gregorich, D.T. et al. (1995) AJ 110, 259
7. Guiderdoni, B. et al. (1998) MNRAS 295, 877
8. Hacking, P., Houck, J.R. (1987) ApJS 63, 311
9. Hacking, P. et al. (1987) ApJ 316, L15
10. Hauser, M.G. et al. (1997) COBE Diffuse Infrared Background Experiment (DIRBE) Explanatory Supplement, version 2.1, COBE Ref. Pub. No. 97-A, Greenbelt, MD: NASA/GSFC
11. Jourdain de Muizon, M., Habing, H.J. (1992) In: Infrared astronomy with ISO, Les Houches series, Nova science publishers Inc.
12. Kawara, K. et al. (1998) A&A 336, L9
13. Kessler, M.F. et al. (1996) A&A 315, L27
14. Koo, D.C. et al. (1986) PASP 98, 285
15. Linden-Vørnle, M.J.D. et al. (1999) Submitted to A&A
16. Lonsdale, C.J. et al. (1990) ApJ 358, 60
17. Moshir, M. et al. (1992) Explanatory Supplement to the IRAS Faint Source Survey, Version 2, JPL D-10015 8/92
18. Pearson, C., Rowan-Robinson, M. (1996) MNRAS 283, 174
19. Rowan-Robinson, M. et al. (1991) MNRAS 253, 485
20. Soifer, B.T. et al. (1987) ARA&A 25, 187
21. Stebbins, J. et al. (1950) ApJ 112, 469
22. van der Bliek, N.S. et al. (1996) The Messenger 70, 28

A Deep 12 μm Survey with ISO

David L. Clements[1,2]

[1] Dept. Physics and Astronomy, Cardiff University, PO Box 913, Cardiff, CF2 3YB, UK
[2] Institut d'Astrophysique Spatiale, Université de Paris XI, Bâtiment 121, F-91405 Orsay Cedex, France

Abstract. I present results from a deep 12μm extragalactic survey conducted with the ISOCAM instrument. The survey covers about 0.1 sq. deg. in four fields and reaches a 5σ flux limit of $\sim$500μJy. 50 sources are identified to this flux limit. Of these, 37 are classified as galaxies on the basis of optical/mid-IR colours using identifications from the USNO-A photographic survey. Number counts for these objects exceed those predicted for no-evolution models in simple models. However, these conclusions are somewhat dependent on the assumed K-corrections. For this reason, and to better determine the nature of the evolution of this population, followup observations are required to determine redshifts, broadband optical-IR colours, and optical morphologies. The first results from these followups are presented. Images and optical/IR photometry for one of the four fields is discussed, and I also present the first results from optical spectroscopy. The highest redshift for the sample so far is z=1.2 for a broad-line object.

1 Introduction

Our view of the universe was fundamentally changed when the IRAS satellite revealed the importance of the mid- and far-IR parts of the spectrum in the light output of normal galaxies. About 1/3 of the luminosity of normal spirals is emitted in the mid- to far-IR [1]. Perhaps more surprising was the discovery of a class of objects with very high luminosities, $> 10^{12} L_{\odot}$, which is almost entirely emitted in the mid- to far-IR (eg. [2]; [3], and references therein). Such objects are known as Ultraluminous Infrared Galaxies, and have been the targets of intense study in the local universe (eg. Genzel, these proceedings). The issue of evolution in the ULIRG and broader IR luminous populations has always been of interest. However, it was not possible to observationally tackle this issue until recently since our main database on such objects, the IRAS catalogues, were dominated by relatively low redshift sources. Two instruments have now changed this situation — ISO, and SCUBA. SCUBA provides excellent possibilities for deep surveys in the submm, allowing us to look for high redshift counterparts to local ULIRGs (eg. [4] and references therein). ISO allows deeper surveys in the mid- and far-IR, boosting our capabilities relative to IRAS by up to 1000 times. The whole issue of far-IR evolution has also been made more urgent by the discovery of a cosmological infrared background (eg. Lagache, Puget contributions in this volume).

D. Lemke, M. Stickel, and K. Wilke (Eds.): LNP 548, pp. 70–77, 2000.

There are numerous mid- and far-IR surveys underway, many of which are discussed in this volume. The two instruments on ISO that permit such surveys are ISOCAM, operating in the mid-IR [5], and ISOPHOT, operating in the far-IR [6]. There are arguments both for and against the use of both instruments and surveys have been undertaken with both (see eg. Dole, Cesarsky, Oliver contributions in this volume). We here discuss the results from a survey conducted with ISOCAM using the LW10, 12μm filter.

2 Why a 12 μm Survey?

By far the bulk of the surveys conducted with ISOCAM have been made at 7 or 15μm. Such surveys cover larger areas of the sky (eg. ELAIS, Oliver, this volume) and go deeper (eg. ULTRADEEP, Cesarsky, this volume) than the present work. One might then ask why we should bother with a 12μm survey. The answer to this lies in two directions. Firstly, the LW10 filter broadly matches the IRAS 12μm passband. Our current survey can thus act as a bridge between the shallower all-sky surveys from IRAS with the deeper, smaller area surveys at 7 and 15μm conducted with ISO. Secondly, the mid-IR emission of galaxies contains a complex mix of different emission mechanisms. These include the unidentified infrared bands (eg. at 7.7 and 11.3μm), various emission line species (eg. NeII at 12.7μm), absorption lines (principally the silicate feature at 9.7μm), and contributions from very hot dust grains at $\sim$200K (see eg. [7]). When this complex spectral energy distribution (SED) is combined with the effects of redshift and specific observational filters, there is the potential for substantial colour(K)-corrections to any survey. The broader the observational filter, the less subject to K-corrections the resulting survey becomes. Since we do not know, and, until SIRTF observations arrive, will not be able to determine, the underlying mid-IR SED of any given galaxy in a mid-IR survey, this can lead to significant uncertainties in scientific conclusions. This is especially true when the redshifts of the sources are unknown. Xu et al. have shown that both the average K-corrections for a 12μm ISO survey and the uncertainties in those corrections for any individual object are significantly smaller than for 15μm observations [8]. The present observations will thus be easier to interpret thanks to both the smaller K-corrections, and the copious amounts of IRAS 12μm data available.

3 The ISO Deep 12 μm Survey: A Happy Accident

The data for the 12μm survey were not originally acquired for this purpose. They were originally obtained for a search for comet trails associated with comet 7P/Pons-Winnecke, and were part of a larger project (see [9]). The original aim was to image four fields with ISOCAM raster maps in regions 1^o ahead and 0.5^o, 1^o and 2^o behind the nucleus of the comet. Each raster was 11x7 pointings, with 6" pixel-field-of-view, and 60" by 48" spacing. Each

position on the sky was thus visited 12 times, providing good redundancy to the data. Total integration time per position is about 300s. Unfortunately, the observations were scheduled one day later than assumed in the ephemeris calculations for the comet, ensuring that the comet trails will lie at or beyond the bottom of each image. No trace of the trails is in fact seen in the reduced data, so we are left with four fields at high galactic latitude (typically $b = -53$) with deep mid-IR imaging — ideal for a cosmological survey. The data were reduced using the IAS dual-beamswitch method [10]. Further details of the data reduction are discussed in [11].

4 Survey Results

A total of 148 verified sources are detected to 3σ in the survey, down to a flux limit of 300μJy. For number count purposes we restrict ourselves to those sources detected at $> 5\sigma$ for a number of reasons. Firstly a number of uncertainties remain in the identification of the weakest sources, and secondly the problems of Malmquist bias are most easily controlled in samples detected at $> 5\sigma$. 50 objects are detected at $> 5\sigma$. We obtain optical identifications for these objects from the USNO-A catalogue, which includes B and R band magnitudes. We remove stars from this catalogue on the basis of optical-IR colours (see Fig. 1), and then plot the integrated number counts for the galaxies alone (Fig. 2).

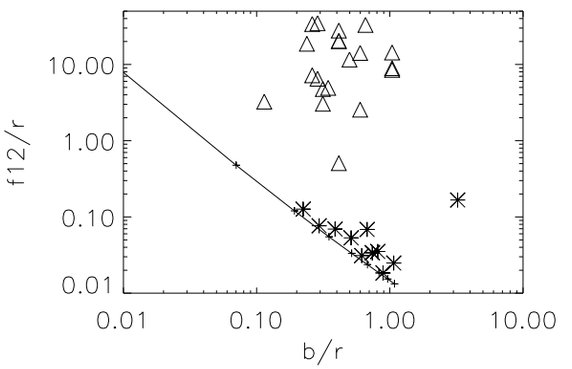

Fig. 1. Optical-IR Colour-Colour Diagram
Triangles are 12μm galaxies, stars are objects identified as stars on the basis of their optical-IR colours. The line shows where a pure Rayleigh-Jeans spectrum object would lie. The star on the far right of the plot is a merged pair of stars in the 12μm data.

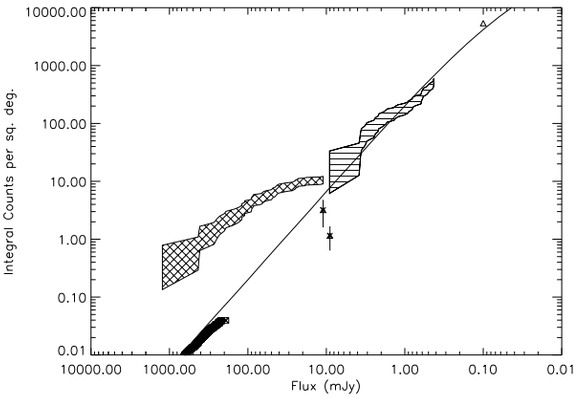

Fig. 2. 12μm Integrated Number Counts
Single hatched region are the number counts from the present data, double hatched are counts from the deepest IRAS 12μm survey [12] which is dominated by stars, dark line to the bottom are counts from the IRAS galaxy survey [13]. Triangles in the middle of the diagram are galaxies from Hacking & Houck survey ([12], lower) and Gregorich et al. ([14]). Triangle to upper right are the 15μ counts from the ISOHDF [15]. Solid line is a strong evolution model from Clements et al. [11].

The number counts from this plot can be compared to evolving and non-evolving models. We find that simple non-evolving models are excluded by this data at the 3.5σ level. However, uncertainties in the K-corrections mean that this conclusion is not final. For that, we need further data including redshifts.

5 Optical/IR Colours and Imaging

As part of the UKIRT mini-survey and the INT Wide Field Survey programme, much of the first of the four 12μm fields was imaged at UBVRIJ and K. This multicolour imaging allows us to examine both the morphologies and optical/IR SEDs of these objects. We include in this study not only those objects detected at $> 5\sigma$ but also those detected at $> 3\sigma$ with believable optical counterparts. The issue of any blank field 12μm sources, ie. those detected at $> 3\sigma$ but with no optical counterpart, will be discussed elsewhere. We find that the optical/near-IR colours of the 12μm sources are largely unexceptional (see Fig. 3). Only one source has an unusually large B-I colour (later spectroscopy shows this object to be an M-type star). The rest of the sources largely have colours typical of the bulk of the population seen in this field. One must then ask why these objects have become luminous at 12μm. The optical images perhaps provide a clue to this (Fig 4). Inspection

of these reveals that 77% of the 12μm galaxies have companions or disturbed morphologies. This compares with a rate of $\sim$ 10% for low luminosity IRAS galaxies [16], and suggests that interactions or mergers may be involved in triggering the 12μm activity of these sources.

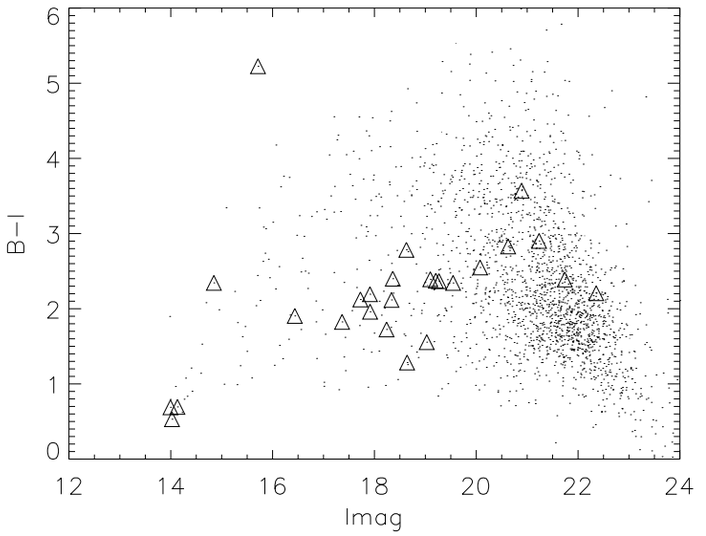

Fig. 3. B-I Colour Magnitude Diagram
Triangles are 12μm sources, the brightest of which are stars. Dots are all the optically selected objects in the field. Note that the 12μm sources, with one exception, are not unusually red, indicating that the optical emission of these objects is not heavily obscured by dust. The one unusually red object turns out to be an M star.

6 Optical Spectroscopy

Of the 12μm sources identified in this survey, only one had a previously known redshift (z=0.11 [17]). We must obtain redshifts for the whole sample, or complete subsamples, to properly test evolutionary models. Optical spectroscopy for these sources is thus a high priority. We have so far had two runs at the ESO 3.6m telescope using EFOSC-2 for this part of the programme. The first of these runs suffered from poor weather conditions and instrument failures. In contrast, the most recent of these runs, shortly after the Ringberg meeting of which these are the proceedings, went very well. We now have secure redshifts for at least 25 objects, with redshifts ranging from

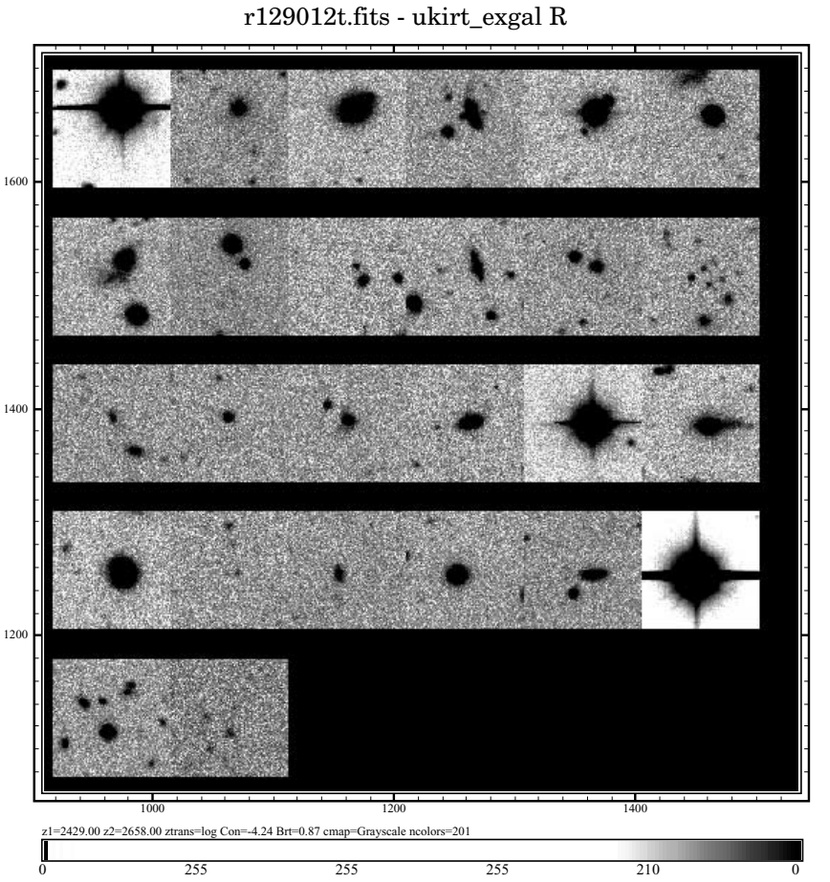

Fig. 4. R band images for the 26 12μm sources found in Field 1
Images are 37" across with 0.37" pixels.

0.037 to 1.2. We have also found that one or two of the objects previously identified as galaxies turn out to be M-stars. Their SEDs appear to be galaxy like in the optical-mid-IR colour-colour diagram because of the large molecular absorption bands reducing their optical emission below Rayleigh-Jeans levels. As well as redshift determination, we will use these spectra to classify the nature of the ionising source in the objects. It already appears that the majority of these sources are powered by star formation, since they have HII region-like spectra. Several, though, show signs of an AGN contribution, including our highest redshift object which has a broad line spectrum (Fig. 5).

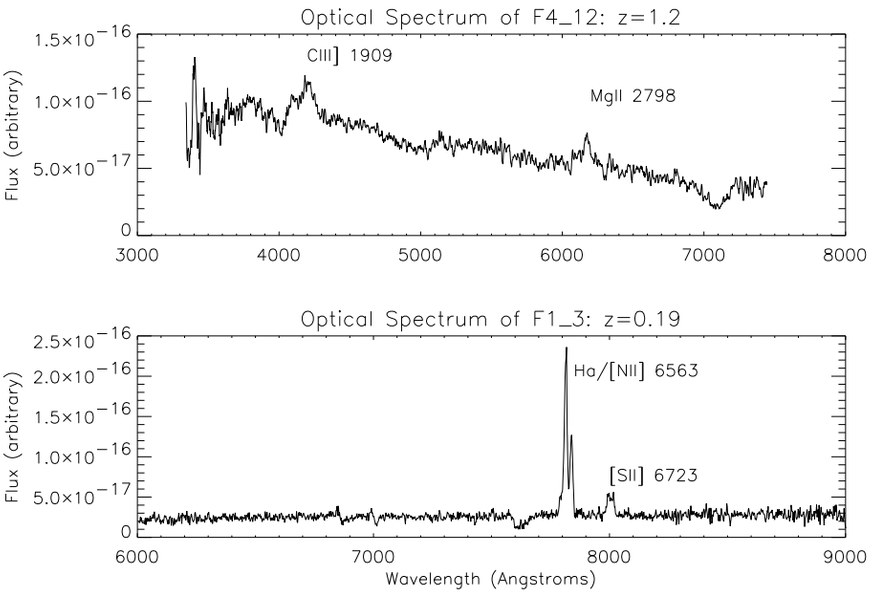

Fig. 5. Example spectra for two sources in the 12μm survey

7 Conclusions

I have presented results from a deep 12μm survey with ISO. The survey data themselves suggest that strong evolution is taking place in this population, but additional followup observations are needed to confirm this. The followup programme is now well underway, with optical/IR imaging for one of the four survey areas in hand, and optical spectra complete for the brighter objects in the sample. The next stage will be to construct luminosity functions for the spectroscopic subsample and to compare this with IRAS data on nearby objects. With the sad demise of the WIRE spacecraft, the present work is likely to be the deepest 12μm survey available until the NGST era. As such it represents an important link between the IRAS surveys and the deeper, smaller area ISO surveys at 7 and 15μm. It is thus an important resource for the future of mid-IR cosmology.

Acknowledgements

It is a pleasure to thank my collaborators on this project: Xavier Desert, Alberto Franceschini, Bill Reach, Amanda Baker, John Davies and Catherine Cesarsky. I am also very grateful to Steve Warren, Scott Croom and the UKIRT Minisurvey team for providing the optical/IR imaging data. Thanks also to ESA and ESO for the use of their facilities. This work was supported by EU TMR network and PPARC postdoctoral posts.

References

1. Soifer, B.T., & Neugebauer, G. (1991) The properties of infrared galaxies in the local universe. AJ 101:354
2. Joseph R.D., & Wright, G.S. (1985) Recent star formation in interacting galaxies. II - Super starburst in merging galaxies. MNRAS 241:87
3. Sanders, D.B., & Mirabel, I.F. (1996) Luminous Infrared Galaxies ARAA 34:749
4. Eales, S.A., et al. (1999) The Canada-UK Deep Submillimeter Survey: First Submillimeter Images, the Source Counts, and Resolution of the Background. ApJ 515:518
5. Cesarsky, C., et al. (1996) ISOCAM in flight. A&A 315:L32
6. Lemke, D., et al. (1996) ISOPHOT - capabilities and performance. A&A 315:L64
7. Aussel, H. et al. (1999) ISOCAM observations of the Hubble Deep Field reduced with the PRETI method. A&A 342:313
8. Xu, C., et al. (1998) Emission Features and Source Counts of Galaxies in the Mid-Infrared. ApJ 508:576
9. Davies, J.K., et al. (1997) ISOCAM Observations of the Comet P/Kopff Dust Trail. Icarus 127:251
10. Desert, F-X., et al. (1999) A classical approach to faint extragalactic source extraction from ISOCAM deep surveys. Application to the Hubble Deep Field. A&A 342:363
11. Clements, D.L., et al. (1999) A deep 12 micron survey with ISO. A&A 346:383
12. Hacking, P., & Houck, J.R., (1987) A very deep IRAS survey at l = 97 deg, b = 30 deg. ApJS 63:311
13. Rush, B., et al. (1993) The extended 12 micron galaxy sample. ApJS 89:1
14. Gregorich, D.T., et al. (1995) Study of Deep IRAS Fields at 60 micron. AJ 110:259
15. Oliver, S.J., et al. (1997) Observations of the Hubble Deep Field with the Infrared Space Observatory - III. Source counts and P(D) analysis. MNRAS 289:471
16. Lawrence, A., et al. (1988) High-luminosity IRAS galaxies. I - The proportion of IRAS galaxies in interacting systems. MNRAS 240:329
17. Clements, D.L., et al. (1996) Optical imaging of ultraluminous IRAS galaxies: how many are mergers?. MNRAS 279:477

The Extragalactic Background and Its Fluctuations in the Far-Infrared Wavelengths

Guilaine Lagache[1], Jean-Loup Puget[1], Alain Abergel[1], Francois-Xavier Désert[2], Hervé Dole[1], Francois R. Bouchet[3], Francois Boulanger[1], Paolo Ciliegi[4], David L. Clements[5], Catherine Cesarsky[6], David Elbaz[6], Alberto Franceschini[7], Richard Gispert[1], Bruno Guiderdoni[3], L. Matthew Haffner[8], Martin Harwit[9], Rene Laureijs[10], Dietrich Lemke[11], Alan F.M. Moorwood[12], Seb Oliver[13], William T. Reach[14], Ronald J. Reynolds[8], Michael Rowan-Robinson[13], Manfred Stickel[11], and Stephen L. Tufte[14]

[1] Institut d'Astrophysique Spatiale, Orsay, France
[2] Laboratoire d'Astrophysique, Observatoire de Grenoble, France
[3] Institut d'Astrophysique de Paris, France
[4] Osservatorio Astronomico di Bologna, Italy
[5] Cardiff University, UK
[6] Service d'Astrophysique, CEA/DSM/DAPNIA Saclay, France
[7] Osservatorio Astronomico di Padova, Italy
[8] Astronomy Department, University of Wisconsin, Madison, USA
[9] 511 H.Street S.W., Washington, DC 20024-2725
[10] ISOC ESA, VILSPA, Madrid, Spain
[11] MPIA, Heidelberg, Germany
[12] ESO, Garching, Germany
[13] Imperial College, London, UK
[14] IPAC, Pasadena, CA, USA
[15] Department of Physics, Lewis & Clark College, Portland, USA

Abstract. A Cosmic Far-InfraRed Background (CFIRB) has long been predicted that would trace the initial phases of galaxy formation. It has been first detected by [1] using COBE data and has been later confirmed by several recent studies [2], [3], [4]. I will present a new determination of the CFIRB that uses for the first time, in addition to COBE data, two independent gas tracers: the HI survey of Leiden/Dwingeloo [5] and the WHAM H_α survey [6]. We will see that the CFIRB above 100 μm is now very well constrained. The next step is to see if we can detect its fluctuations. To search for the CFIRB fluctuations, we have used the FIRBACK observations. FIRBACK is a deep cosmological survey conducted at 170μm with ISOPHOT [7]. We show that the emission of unresolved extra-galactic sources clearly dominates, at arc-minute scales, the background fluctuations in the lowest galactic emission regions. This is the first detection of the CFIRB fluctuations.

D. Lemke, M. Stickel, and K. Wilke (Eds.): LNP 548, pp. 81–87, 2000.

1 Determination of the CFIRB Above 100 μm: Another Approach

In very diffuse parts of the sky (no molecular clouds and HII regions), the far-IR emission can be written as the sum of dust emission associated with the neutral gas, dust associated with the ionized gas, interplanetary dust emission and the CFIRB (and eventually the cosmological dipole and CMB). In previous studies [1], [2], [3], dust emission associated with the ionized gas which was totally unknown has been either not subtracted properly or neglected.

We have detected for the first time dust emission in the ionized gas [4] and shown that the emissivity (which is the IR emission normalized by unit of hydrogen column density) of dust in the ionized gas was nearly the same as that in the neutral gas. This has consequences on the determination of the CFIRB. Following this first detection, we have combined HI and WHAM H_α data [6] with far-IR COBE data in order to derive the dust properties in the diffuse ionized gas as well as to make a proper determination of the CFIRB. Technically, after a careful pixel selection (see [8] for more details) we describe the far-infrared dust emission as a function of the HI and H^+ column density by:

$$IR = A \times N(HI)_{20cm^{-2}} + B \times N(H^+)_{20cm^{-2}} + C \quad (1)$$

where $N(HI)_{20cm^{-2}}$ and $N(H^+)_{20cm^{-2}}$ are the column densities normalized at 10^{20} H cm^{-2}. The coefficients A, B and the constant term C are determined simultaneously using regression fits. We show that about 25% of the IR emission comes from dust associated with the ionized gas which is in very good agreement with the first determination [4]. The CFIRB spectrum obtained using this far-infrared emission decomposition is shown in Fig. 1 together with the CFIRB FIRAS determination of [4] in the Lockman Hole region. We see a very good agreement between the two spectra. These determinations are also in good agreement with [2].

At 140 and 240 μm, the values obtained for the CFIRB are 1.13±0.54 MJy/sr and 0.88±0.55 MJy/sr respectively For each selected pixel, we compute the residual emission, R = IR - A×N(HI) - B×N(H^+). Uncertainties of the CFIRB have been derived from the width of the histogram of R (statistical uncertainties derived from the regression analysis are negligible). The obtained CFIRB values, although much more noisy (due to the small fraction of the sky used), are in very good agreement with the determination of [3]. At 140 μm, the CFIRB value of [4] is smaller than that derived here since the assumed WIM dust spectrum were overestimated (the WIM dust spectrum was very noisy below 200 μm and the estimated dust temperature was too high).

At 100 μm, assuming an accurate subtraction of the zodiacal emission, our decomposition gives: $I_{CFIRB}(100)$= 0.78±0.21 MJy/sr. This is the first

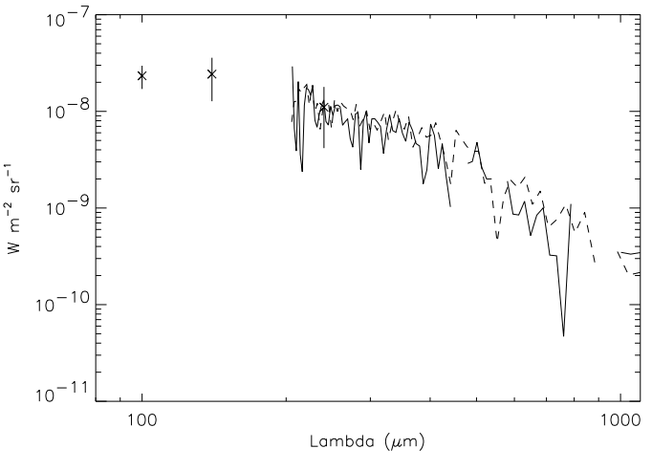

Fig. 1. CFIRB spectra obtained from the decomposition of the far-infrared sky (continuous line) and determined on the Lockman Hole region (dashed line) by [4]. Also reported are DIRBE values at 100, 140 and 240 μm.

time that two independent gas tracers for the HI and the H^+ have been used to determine the background at 100 μm. One has to note that methods based on the intercept of the far-IR/HI correlation for the determination of the CFIRB are dangerous. For example, for our selected parts of the sky, this intercept is about 0.91 MJy/sr, which is quite different from the value of the CFIRB (0.78 MJy/sr). The CFIRB value of 0.78 MJy/sr can be compared to the non-isotropic residual emission found by [3]. The average on three regions of the residual emission, equal to 0.73±0.20 MJy/sr, is in very good agreement with our determination.

So we see, using different approaches, that we are now converging on the shape and level of the CFIRB above 100 μm. The next step is to see if we can detect its fluctuations and study them.

2 Why Searching for the CFIRB Fluctuations?

The CFIRB is made of sources with number counts as a function of flux which can be represented, for the present discussion, by a simple power law:

$$N(>S) = N_0 \left(\frac{S}{S_0}\right)^{-\alpha}$$

. Obviously, these number counts need to flatten at low fluxes to ensure a finite value of the background. Thus, we assume that α=0 for $S < S^*$.

For the simple Euclidean case (α=1.5), the CFIRB integral is dominated by sources near S^* and its fluctuations are dominated by sources which are just below the detection limit S_0. It is well known that strong cosmological evolution, associated with a strong negative K-correction, could lead to a very steep number count distribution (see for example [9] and [10]). In the far-IR present observations show a very steep slope of α=2.2 [7]. In this case, the CFIRB integral is still dominated by sources near S^* but its fluctuations are now also dominated by sources close to S^*. Thus, it is essential to study the extra-galactic background fluctuations which are likely to be dominated by sources with a flux comparable to those dominating the CFIRB intensity.

To see if we can detect the CFIRB fluctuations, we need wide field far-IR observations with high angular resolution and very high signal to noise ratio. The FIRBACK project, which is a very deep cosmological survey with ISOPHOT at 170 μm [7], sustains all these conditions. To search for CFIRB fluctuations, we have first used the so-called "Marano1" field because it is made of 16 independent coadded maps which allow us to determine very properly the instrumental noise. In this field, we have a signal to noise ratio of about 300 and we detect 24 sources [11] that we remove from the original map. We then extend our first analysis to the other FIRBACK fields. Details on the data reduction and calibration can be found in [12].

Source subtracted maps show background fluctuations which are made of two components that we want to separate, galactic cirrus fluctuations and if present the extra-galactic ones.

3 Extragalactic and Galactic Background Fluctuations Separation: Detection of the CFIRB Fluctuations

Our separation of the extra-galactic and galactic fluctuations is based on a power spectrum decomposition. This method allows us to discriminate the two components using the statistical properties of their spatial behavior. Fig. 2 shows the power spectrum of the "Marano1" field. In the plane of the detector, the power spectrum measured on the map can be expressed in the form:

$$P_{map} = P_{noise} + (P_{cirrus} + P_{sources}) \times W_k \quad (2)$$

where P_{noise} is the instrumental noise power spectrum measured using the 16 independent maps of the Marano1 field [13], P_{cirrus} and $P_{sources}$ are the cirrus and unresolved extra-galactic sources power spectra respectively, and W_k is the footprint power spectrum. For our analysis, we remove P_{noise} from P_{map}.

We know from previous works that the cirrus far-infrared emission power spectrum, P_{cirrus}, has a steep slope in $\sim k^{-3}$ [14], [15], [16], [17], [18]. These

observations cover the relevant spatial frequency range and has been recently extended up to 1 arcmin using very diffuse HI data [19]. The extra-galactic component is unknown but certainly much flatter (see the discussion in [13]). We thus conclude that the steep spectrum observed in our data at k<0.15 arcmin^{-1} (Fig. 2) can only be due to the cirrus emission. The break in the power spectrum at k$\sim$ 0.2 arcmin^{-1} is very unlikely to be due to the cirrus emission itself which is known not to exhibit any preferred scale [20]. Thus, the normalization of our cirrus power spectrum P$_{cirrus}$ is directly determined using the low frequency data points and assuming a k^{-3} dependence.

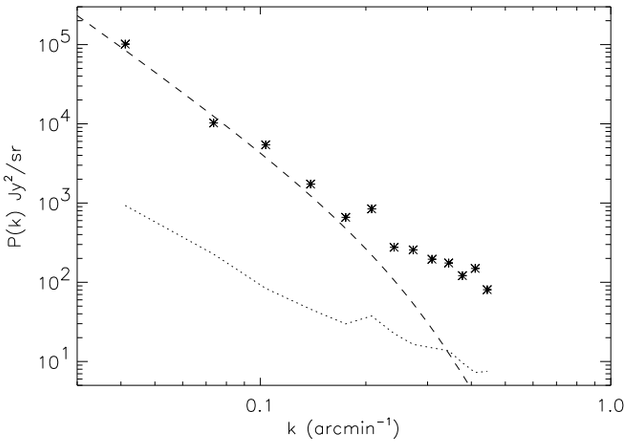

Fig. 2. Power spectrum of the source subtracted "Marano1" field (∗). The instrumental noise power spectrum (dotted line) has been subtracted. The dashed line represents the cirrus power spectrum, multiplied by the footprint one.

We clearly see in Fig. 2 an excess over P$_{cirrus}$ between k=0.25 and 0.6 arcmin^{-1} which is more than a factor 10 at k=0.4 arcmin^{-1}. Any reasonable power law spectrum for the cirrus component multiplied by the footprint leads, as can be easily seen in Fig. 2, to a very steep spectrum at spatial frequency k>0.2 arcmin^{-1} which is very different from the observed spectrum. Moreover, the excess is more than 10 times larger than the measured instrumental noise power spectrum. Therefore, as no other major source of fluctuations is expected at this wavelength, the large excess observed between k=0.25 and 0.6 arcmin^{-1} is interpreted as due to unresolved extra-galactic sources. This is the first detection of the CFIRB fluctuations.

The Marano1 field cannot be used to constrain the clustering of galaxies due to it rather small size. However, the extra-galactic source power spectrum mean level can be determined. We obtain $P_{sources}$ = 7400 Jy^2/sr, which is in very good agreement with the one predicted by [21]. This gives CFIRB rms fluctuations around 0.07 MJy/sr (for a range of spatial frequency up to 5 arcmin^{-1}). These fluctuations are at the $\sim$9 percent level, which is very close to the predictions of [22].

The same analysis can be done for the other and larger FIRBACK fields. From Eq. 2, we deduce:

$$P_{sources} = (P_{map} - P_{noise})/W_k - P_{cirrus}$$

Fig. 3 shows the extra-galactic fluctuation power spectrum ($P_{sources}$) obtained for the FIRBACK/ELAIS N2 field. It is very well fitted with a constant CFIRB fluctuation power spectrum of about 5000 Jy^2/sr, which is in good agreement with that obtained in the "Marano1" field. We obtain also exactly the same extra-galactic fluctuation power spectrum in the FIRBACK N1 field with a value of about 5000 Jy^2/sr.

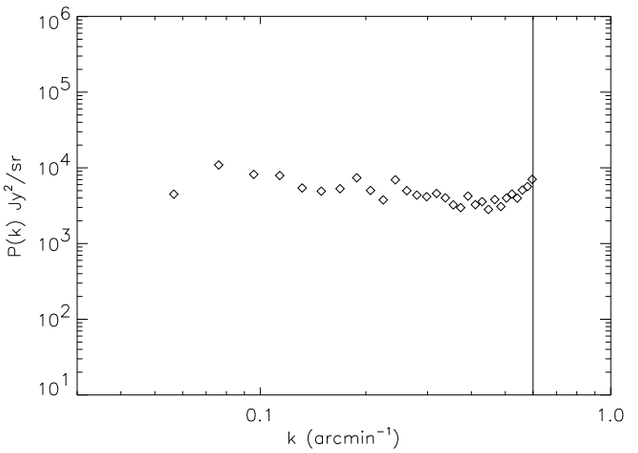

Fig. 3. Extra-galactic sources power spectrum of the FIRBACK/ELAIS N2 field. The vertical line shows the cut of the angular resolution.

4 Conclusions

We have shown in the FIRBACK fields that extra-galactic background fluctuations are well above the instrumental noise and the cirrus confusion noise.

The observed power spectrum shows a flattening at high spatial frequencies which is due to extra-galactic unresolved sources. The level of the extra-galactic power spectrum fluctuations is nearly the same in all FIRBACK fields. The next step consists of removing the cirrus contribution using independent gas tracers (the H_α and the 21cm emission lines) to isolate the extra-galactic fluctuation brightness and try to constrain the IR large scale structures.

References

1. Puget J.L., Abergel A., Bernard J.P., et al. 1996, A&A 308, L5
2. Fixsen D.J., Dwek E., Mather J.C., et al. 1998, ApJ 508, 123
3. Hauser M.G., Arendt R.G., Kelsall T., et al., 1998, ApJ 508, 25
4. Lagache G., Abergel A., Boulanger F., et al., 1999, A&A 344, 322
5. Hartmann D., Burton W.B., Atlas of Galactic neutral Hydrogen, Cambridge University Press, 1997
6. Reynolds R.J., Tufte S.L., Haffner L.M., et al., 1998, PASA 15, 14
7. Dole H., et al., this proceeding
8. Lagache G., Haffner L.M., Reynolds R.J., Tufte S.L., A&A, in press (Astroph/9911355)
9. Guiderdoni B., Hivon E., Bouchet F., Maffei B., 1998, MNRAS 295 , 877
10. Franceschini A., Andreani P., Danese L. 1998, MNRAS 296, 709
11. Puget J.L., Lagache G., Clements D.L. et al., 1999, A&A 354, 29
12. Lagache G., Dole H., to be submitted to A&A
13. Lagache G., J.-L. Puget, A&A, in press (Astroph/9910255)
14. Gautier T.N.III, Boulanger F., Pérault M., Puget J.L., 1992, AJ 103, 1313
15. Kogut A., Banday A.J., Bennett C.L., et al., 1996, ApJ 460, 1
16. Herbstmeier U., Abraham P., Lemke D., et al., 1998, A&A 332, 739
17. Wright E.L., 1998, ApJ 496, 1
18. Schlegel D.J., Finkbeiner D.P., Davis M., 1998, ApJ 500, 525
19. Miville-Deschênes M.A., PhD thesis, Paris XI University
20. Falgarone, E. in "Starbursts: triggers, nature and evolution", Les Houches School, 1998, Ed. B. Guiderdoni & A. Kembhavi
21. Guiderdoni B., Bouchet B., Puget J.L., et al., 1997, Nature 390, 257
22. Haiman Z., Knox L., 1999, ApJ in press (Astroph/9906399)

Cosmic Infrared Background: ISOPHOT FIR Source Counts at 90, 150 and 180 μm

Mika Juvela[1], Kalevi Mattila[1], and Dietrich Lemke[2]

[1] Helsinki University Observatory, Helsinki, Finland
[2] Max-Planck-Institut für Astronomie, Heidelberg, Germany

Abstract. Far-infrared maps obtained with ISOPHOT have been searched for point-like sources. The majority of the 55 sources is believed to be extragalactic and in most cases no previously known sources can be associated with them. Based on the far-infrared spectral energy distributions it is likely that dust-enshrouded, distant galaxies form a significant fraction of the sources.

We estimate the number densities of extragalactic sources at 90μm, 150μm and 180μm wavelengths and at flux density levels down to ∼100 mJy. The counts are compared with models of galaxy evolution. The counts exceed the predictions of current models, even those with strong evolution, and no-evolution models are rejected at a high confidence level.

Comparison with recent results from COBE mission indicates that at 90μm the detected sources correspond to $\gtrsim$20% of the extragalactic background light. At longer wavelengths the corresponding fraction is 10%.

1 Introduction

In the far-infrared the cosmic infrared background (CIRB) consists of radiation emitted by galaxies, intergalactic gas and dust, photon–photon interactions (γ-ray vs. CMB) and, possibly, by decaying relic particles. A large fraction of the energy released in the universe since the recombination epoch is contained in the CIRB. An important aspect is the balance between the UV-optical and the infrared backgrounds. With recent observations at infrared and sub-mm wavelengths it has become obvious that star formation efficiencies in the early universe derived from optical and UV observations are underestimated (e.g. Madau et al. [18]; Steidel et al. [24]).

The analysis of the data from the COBE DIRBE (Hauser et al. [7]) and FIRAS (Fixsen et al. [3]) indicated a FIR CIRB flux at a surprisingly high level of ∼1 MJy sr^{-1} between 100 and 240 μm. Similar results had been obtained already by Puget et al. [19] and Schlegel et al. [22]. Because of the great importance of the FIR CIRB for cosmology these results require confirmation by independent measurements.

The final goal of the ISOPHOT CIRB project is the determination of the FIR CIRB flux level. First steps are the measurement of the CIRB fluctuations and the detection of the bright end of FIR point source population. The

D. Lemke, M. Stickel, and K. Wilke (Eds.): LNP 548, pp. 88–95, 2000.

Table 1. The studied fields. The columns are: name of the field, coordinates of the centre of each field, area of the map, name of the ISOPHOT filter used in the observations, number of raster positions observed, step between adjacent raster positions in the staring mode mapping and integration time. The distance of adjacent scans was in all cases identical to the raster step used along the scan line

Field	Map Centre		Area	Filter	Rasters	Step	t_{int}
	RA(2000)	DEC(2000)	(sq.degr.)			($''$)	(s)
VCN	15 15 21.7	+56 28 58	0.030	C_90	10×4	90	46
				C_135	10×4	90	46
				C_180	10×4	90	46
VCS	15 15 53.1	+56 19 30	0.023	C_90	21×2	90	46
				C_135	21×2	90	46
				C_180	21×2	90	46
NGPN	13 43 53.0	+40 11 35	0.27	C_90	32×4	180	23
				C_135	32×4	180	27
				C_180	32×4	180	27
	13 42 32.0	+40 29 06	0.53	C_180	15×15	180	32
NGPS	13 49 43.7	+39 07 30	0.27	C_90	32×4	180	23
				C_135	32×4	180	27
				C_180	32×4	180	27
EBL22	02 26 34.5	-25 53 43	0.19	C_90	32×3	180	23
				C_135	32×3	180	27
				C_180	32×3	180	27
EBL26	01 18 14.5	01 56 40	0.27	C_90	32×4	180	23
				C_135	32×4	180	23
				C_180	32×4	180	23

ISOPHOT CIRB project has potential advantages over the DIRBE analysis: (1) with the much smaller f.o.v. ISOPHOT is capable of looking at the darkest spots between the cirrus clouds; (2) in spite of the smaller f.o.v. ISOPHOT's sensitivity surpasses that of DIRBE in the important FIR window at 120 – 200 μm; (3) with the good spatial and spectral sampling the galactic cirrus can be separated.

We have mapped four low-cirrus regions at high galactic latitude at the wavelengths of 90, 150, and 180 μm. Here we report on the point sources (galaxies) found in the FIR maps. The FIR source counts are important for the study of the star formation history of the universe and for the testing of models of galaxy evolution.

The point source extraction is based on the fitting of the detector footprint to spatial data. The method is different from those used in most previous studies (Kawara et al. [11]; Puget et al. [20]; Efstathiou et al.[2]) where the source detection has been based on the analysis of the detector signal as a function of time. Our analysis is therefore independent of and complementary to previous results.

2 Observations

The observations were performed with the ISOPHOT (Lemke at el. [14]) aboard ISO (Kessler et al. [12]). The maps were made in the PHT22 staring raster map mode (see Table 1). The area covered is ∼1.5 square degrees. The fields have low surface brightness and in some cases there is some redundancy i.e. the observed pixel rasters partly overlap each other.

The data were processed with PIA (PHT Interactive Analysis) versions 7.1 and 7.2. The flux density calibration was made using the FCS (Fine Calibration Source) before and after each map. The accuracy of the absolute calibration is expected to be better than 30% (Klaas et al. [13]).

Data reduction from the ERD (Edited Raw Data) to SCP (Signal per Chopper Plateau) was performed using the pairwise method (Stickel [25]). Instead of making linear fits to the ramps consisting of the detector read-outs one examines the distribution of the differences between consecutive read-outs. The mode of the distribution is estimated with myriad technique (Kalluri & Arce [10]) and is used as the final signal for each sky position. The pairwise method is robust against glitches and the analysis was based on the data reduced with this method.

3 Detection Procedure

The source detection was performed in two steps using data processed to the AAP (Astrophysical Applications Data) level with PIA and the pairwise method. The data consists of surface brightness values with error estimates. Flat fielding was performed with custom routines.

Each surface brightness value was compared with the mean of the region within a radius of ∼three times the size of the detector pixel. Values more than 0.7σ above the local background were considered as potential point sources. A model consisting of a point source and a constant background was fitted into each region surrounding a candidate position. Footprint matrices were used to calculate the contribution of the point source to the observed surface brightness values. The free parameters of the fit were the source flux density, the two coordinates of the source position, and the background surface brightness. The formal errors are used to calculate the probability, P, that the detection is not caused by background noise.

The completeness of the source detection and the number of false detections were studied with simulations. The results were used to adjust the probability level that was used for discarding uncertain detections. The ratio ρ between the source flux density and the background rms noise, $\sigma_{\mathrm{b}g}$, was used as a criterion to discard uncertain sources. Since ρ is not directly related to the probability obtained from the footprint fit it can be used as an additional safeguard against false detections.

The actual source list consists of sources detected at two or three wavelengths with a spatial distance between detections of less than $80''$. The expected number of co-incidental associations is no more than $\sim$10% and does not significantly affect the source counts.

4 Source Counts

The surface density of sources is estimated by dividing the number of detected sources at a given flux density level with the corresponding 'effective' map area.

As the first approximation the effective area corresponding to a given flux density level was taken to be the sum of those maps where sources with equal or lower flux densities were detected. The cumulative source densities obtained at 90μm, 150μm and 180μm are shown as histograms in Fig. 2. Two sets of sources were used. The first set consists of all detections (dotted line) while in the second set there are only sources detected at more than one wavelength (solid line). The results are similar for 150μm and 180μm and significant differences are seen only at 90μm. This is expected, since sources seen at 150μm are likely to be seen also at 180μm (and vice versa) while more of the 90μm sources remain unconfirmed at the longer wavelengths.

A third estimate for the cumulative source densities (dashed lines in Fig. 2) was obtained by selecting sources based on the ratio ρ (see Sect. 3). For each flux density level sources with $\rho > \rho_0$ were selected and no confirmation at other wavelengths was required. The effective area was obtained by integrating the total area where the rms noise was below $1/\rho_0$ times the source flux density. The values of ρ_0 were selected based on simulations. At the bright end the results agree with earlier histograms since no sources are rejected and the corresponding areas converge towards the total area mapped.

At very low flux density levels the small number of sources leads to large uncertainties. The values obtained below 150 mJy for 150μm and 180μm are probably only indicative.

5 Discussion

5.1 Cirrus Confusion

We have checked the probability that some of the sources detected are small scale cirrus structures (cirrus knots). Results of Herbstmeier et al. [8] show that at the scale of the C100 beam size, $d \sim 45''$, the expected cirrus fluctuation amplitude is below 10 Jy sr$^{-1/2}$ for all our 90μm maps. According to Gautier et al. [5] this corresponds to a flux density of 4 mJy which is clearly below the flux densities of the faintest 90 μm detections. Therefore, cirrus is not likely to be a significant contaminant in the source counts although, because of the non-gaussian nature of the cirrus fluctuations (Gautier et al. [5]), our source list may still contain a few cirrus knots.

5.2 Comparison with Galaxy Spectra

In Fig. 1 we compare the average of the source spectra with the spectra of the galaxies Arp 193 and NGC 4418. In the sample of luminous infrared galaxies presented by Lisenfeld, Isaak & Hills [16] Arp 193 has the lowest and NGC 4418 the highest estimated dust temperature.

In the rest frame the SEDs of luminous infrared galaxies reach maxima between 60μm and 100μm (Silva et al. [23]; Devriendt, Guiderdoni & Sadat [1]; Lisenfeld, Isaak & Hills [16]). The spectra of our FIR sources are flat in the observed wavelength range and the emission peak is typically above 90μm. This is consistent with most sources being at redshifts $0.5 \lesssim z \lesssim 1$.

The FIR emission maximum of normal spiral galaxies is also located close to 100μm (e.g. Silva et al. [23]). However, in the case of a spiral galaxy a FIR detection at the level of 0.1 Jy would correspond to a visual magnitude brighter than 16 and the optical counterpart should be readily visible. The lack of clear visual counterparts indicates that most of our sources are likely to be more distant and luminous infrared galaxies.

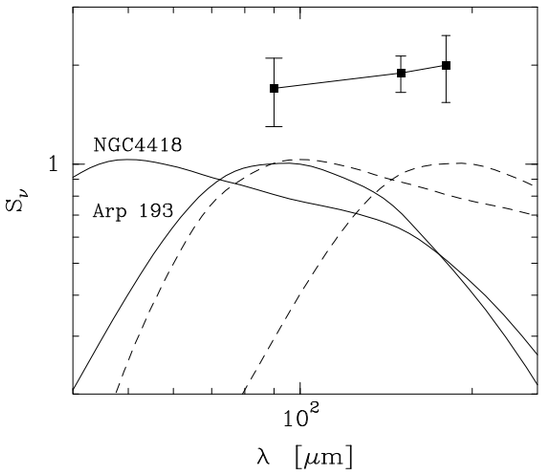

Fig. 1. The average of the source spectra and the model spectra of Lisenfeld et al. ([16]) for the luminous infrared galaxies Arp 193 and NGC 4418. The dashed lines show the spectra of the two galaxies shifted to z=1.0. The flux density scale is arbitrary

5.3 Comparison with Previous Source Counts

From Fig. 2 we obtain lower limits of $9\times10^4\,\mathrm{sr}^{-1}$, $2\times10^5\,\mathrm{sr}^{-1}$ and $2.2\times10^5\,\mathrm{sr}^{-1}$ for the cumulative source counts $\geq$100 mJy at 90 μm, 150 μm and 180 μm,

respectively. Similarly, above 200 mJy the source densities are $1.3\times10^4\,\mathrm{sr}^{-1}$, $6\times10^4\,\mathrm{sr}^{-1}$ and $7\times10^4\,\mathrm{sr}^{-1}$. The dotted histogram, which lies mostly between the two other curves, gives at 100 mJy values $1.4\times10^5\,\mathrm{sr}^{-1}$, $2.5\times10^5\,\mathrm{sr}^{-1}$ and $3.5\times10^5\,\mathrm{sr}^{-1}$ at 90 μm, 150 μm and 180 μm.

Kawara et al. [11] have performed similar counts using ISOPHOT observations of the Lockman Hole. The cumulative source counts were $1.1\times10^5\,\mathrm{sr}^{-1}$ and $1.3\times10^5\,\mathrm{sr}^{-1}$ at 95 μm and 175 μm, respectively, for sources $S_\nu > 150$ mJy. At 90 μm our results are close to their values. Our lowest estimates that were based on detections at two or three wavelengths are, however, lower by more than a factor of two. This could indicate that the requirement of having detections at more than one wavelength does indeed underestimate the counts.

Latest results from the ELAIS survey (Efstathiou et al. [2]), covering an area of 11.6 square degrees at 90μm, are similar to the preliminary results reported by Rowan-Robinson et al. [21]. At ∼150 mJy level the source density is $3.3\times10^4\,\mathrm{sr}^{-1}$ i.e. a factor of three lower than Kawara et al. [11]. The result is close to our lowest estimate as shown in Fig. 2.

Linden-Vørnle et al. [15] have performed source counts in a 0.4 square degree field at 60μm and 90μm. At 90μm the results are at 100 mJy level similar to the ELAIS counts but are lower at other flux density levels. Also in their re-analysis of the Lockman Hole field they found significantly lower source densities than reported by Kawara et al. [11].

Puget et al [20] have published source counts based on 175μm ISOPHOT observations of the Marano field covering ∼0.25 square degrees. The source densities (e.g. $\sim4\cdot10^5\,\mathrm{sr}^{-1}$ at 120 mJy) are slightly higher than our counts.

The source counts obtained in these different ISOPHOT studies are mainly within a factor of ∼2 from each other but direct comparison is made difficult by the differences in the source flux calibration adopted by the different authors. We have found a ∼30% difference between the DIRBE surface brightness values and our data calibrated with PIA version 7.3 (Juvela et al. [9]). This uncertainty is indicated in Fig. 3 by the horizontal lines that are used to represent our source counts. At 90μm the DIRBE calibration results in lower flux densities and at 150μm and 180μm in higher flux densities. These values are better for the comparison with e.g. the results of Efstathiou et al. [2] at 90μm since they used DIRBE as the basis of their calibration.

5.4 Comparison with Galaxy Models

The source counts at 150μm and 180μm are much higher than predicted by no-evolution models (e.g. Franceschini et al. [4]). At 180 μm the difference is a factor of five and these models can be safely rejected. Our results indicate that the luminosity or the number of galaxies must evolve strongly with z.

Guiderdoni et al. [6] have presented semi-analytic models for the galaxy evolution. In their model E (which predicts the highest source counts) both the 'burst' mode of star formation rate and the relative number of ultraluminous IR galaxies (ULIRGs) increase with z; at $z = 5$ half of all galaxies are

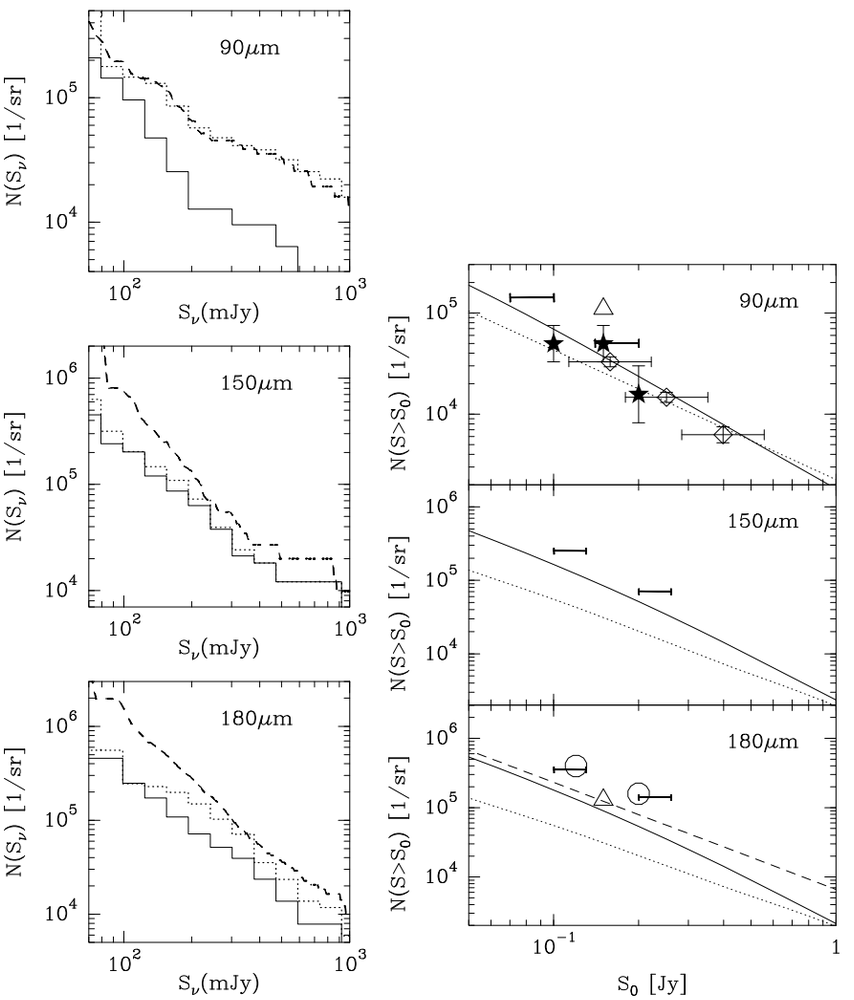

Fig. 2. (left) Cumulative source counts at 90μm, 150 μm and 180μm. The dotted line gives all sources detected and the solid line sources detected at more than one wavelength. Areas were estimated according to the faintest source detected in a map. The dashed curves represent cases in which both the the source selection and the area determination were based on the local background fluctuations (see text).

Fig. 3. (right) Comparison with other ISOPHOT counts and models of galaxy evolution. Our source counts at 100 mJy and 200 mJy are shown together with the results of Puget et al. [20] (circles), Kawara et al. [11] (triangles), Efstathiou et al. [2] (diamonds) and Linden-Vørnle [15] (stars). We present our results as horizontal lines that indicate the difference between the DIRBE calibration and the adopted ISOPHOT calibration (see text). The predictions of model E of Guiderdoni et al. [6] are shown with solid lines and the evolutionary model of Franceschini et al. [4] with a dashed line. Dotted lines show predictions of no-evolution models (90μm: Guiderdoni et al. [6]; 150μm and 180μm: Franceschini et al. [4])

ULIRGs. The model is in good agreement with extragalactic background light measurements in both optical and infrared. The model predicts source counts of $\sim 1.7\times10^5\,\mathrm{sr}^{-1}$ and $\sim 1.8\times10^5\,\mathrm{sr}^{-1}$ for sources brighter than 100 mJy at 150 µm and 180 µm, respectively. The number of sources found in this study clearly exceeds these predictions.

Franceschini et al. [4] have presented similar models which include contributions from two galaxy populations: dust-enshrouded formation of early-type galaxies and late-type galaxies with enhanced star-formation at lower redshifts. The predicted source counts at 170µm are higher than in the model of Guiderdoni et al. [6] and thus in better agreement with our results.

In Fig. 3 we show the predictions of these two models together with counts from other references. For this plot we have selected from Fig. 2 the values of the dotted histogram.

References

1. Devriendt, J.E.G., Guiderdoni, B., Sadat, R. (1999), A&A, in press
2. Efstathiou A., Oliver S., Rowan-Robinson M. et al. (1999) in preparation
3. Fixsen, D.J., Dwek, E., Mather, J.C. et al. (1998) ApJ 508, 123
4. Franceschini, A., Andreani, P., Danese, L. (1998) MNRAS 296, 709
5. Gautier, C., III, Boulanger, F., Perault, M., Puget, J.L. (1992) AJ 103, 1313
6. Guiderdoni B., Hivon E., Bouchet F.R., Maffei. B. (1998) MNRAS 295, 877
7. Hauser M.G., Arendt R.G., Kelsall T. et al. (1998) ApJ 508, 25
8. Herbstmeier, U., Abraham, P., Lemke, D., et al. (1998) A&A 332, 739
9. Juvela M., Mattila K., Lemke D. (1999) Cirrus Spectra of Low Surface Brightness Regions. In: Proceedings of the Meeting ISO Beyond Point Sources, ESA-SP
10. Kalluri S., Arce G.R. (1998) IEEE Transactions on Signal Processing Vol. 46, 2, 322
11. Kawara, K., Sato, Y., Matsuhara, H., et al. (1998) A&A 336, L9
12. Kessler M.F., Steinz J.A., Anderegg M.E. et al. (1996) A&A 315, L27
13. Klaas U., Laureijs, R.J., Radovich, M., Schulz, B. (1998) 'ISOPHOT Calibration Accuracies', http://www.iso.vilspa.esa.es/manuals/PHT/accuracies/pht_accuracies20/
14. Lemke, D., Klaas, O., Abolins, J., et al. (1996) A&A 315, L64
15. Linden-Vørnle M.J.D., Norgaard-Nielsen H.U., Jorgensen H.E. et al. (1999), submitted to A&A
16. Lisenfeld U., Isaak K.G., Hills R. (1999), MNRAS, in press, astro-ph/9907035
17. Low, F.J., Cutri R.M. (1994), Infrared Phys. Technol. Vol. 35, No 2/3, 291
18. Madau, P., Ferguson, H.C., Dickinson, M.E., et al. (1996) MNRAS 283, 1388
19. Puget, J.-L., Abergel, A., Bernard, J.-P. et al. (1996) A&A 308, L5–L8
20. Puget, J.-L., Lagache, G., Clements, D.L., et al. (1999) A&A 345, 29
21. Rowan-Robinson, M., Oliver, S., Efstathiou, A., et al. (1999) In: Proceedings of "The Universe as seen by ISO", Paris, ESA SP-427, p. 1011
22. Schlegel D.J., Finkbeiner D.P., Davis M. (1998) ApJ 500, 525
23. Silva L., Granato G.L., Bressan A., Danese L. (1998), ApJ 509, 103
24. Steidel C.C., Adelberger K.L., Giavalisco M. et al. (1999) ApJ 519, 1
25. Stickel, M. (1999) personal communication

Near Infrared Extragalactic Background

Toshio Matsumoto[1], Martin Cohen[2], Minoru M. Freund[1], Mitsunobu Kawada[3], Mark Lim[1], Shuji Matsuura[1], Hiroshi Murakami[1], Manabu Noda[4], and Masahiro Tanaka[1]

[1] Institute of Space and Astronautical Science, Kanagawa 229-8510, Japan
[2] Radio Astronomy Laboratory, University of California, Berkeley, Berkeley CA94702, USA
[3] Department of Physics, Nagoya University, Nagoya 464-8602, Japan
[4] Nagoya Science Museum, Nagoya 453-0037, Japan

Abstract. We searched for the near infrared extragalactic background light (IREBL) in the data from the Near Infrared Spectrometer (NIRS) on the Infrared Telescope in Space (IRTS). After subtracting the contribution of faint stars and zodiacal component based on the model, significant isotropic emission is detected whose in-band flux amounts to ~ 30 nWm^{-2}sr^{-1}. This brightness is consistent with upper limits of COBE/DIRBE, but is much brighter than the integrated light of faint galaxies at the H and K bands. A significant fluctuation of the sky brightness was also detected that can not be explained by known foreground emission components. 2-point correlation analysis indicates that the fluctuation has a characteristic spatial frequency at $1 \sim 2 \times 10^2$ arcmin. These results indicate that the detected isotropic emission is cosmological in origin, and is new observational evidence for the study of the formation and evolution of galaxies.

1 Introduction

The infrared extragalactic background light (IREBL) has been thought to be an important clue to the understanding of the early universe and the evolution of galaxies. In the near infrared, redshifted star light from high z galaxies constitutes the background, while dust emission causes the far infrared and submillimeter background. Both emission components are thought to be important parameters to understand the energy generation during the galaxy formation era. Detection of the IREBL, however, is not so easy due to strong foreground emission. Prominent airglow and thermal emission of the atmosphere make it impossible to observe the EBL from ground. Even in space, zodiacal light (scattered sunlight), zodiacal emission, interstellar dust emission, etc. remain to be bright foreground emission sources.

It is thought that the near infrared (1 – 5 μm), and far infrared / submillimeter (100 – 300 μm) regions are useful wavelength bands to detect the EBL, since any sky brightness will be very low. Several observations with sounding rockets have been made to search for near infrared EBL [1] [2], but a significant EBL has not yet been detected.

Puget et al. (1996) [3] and Fixsen et al. (1998) [4] reported a significant detection of the submillimeter EBL from the COBE/FIRAS data. Further,

D. Lemke, M. Stickel, and K. Wilke (Eds.): LNP 548, pp. 96–105, 2000.

Hauser et al. (1998) [5] claimed the detection of the EBL at 120 and 240 μm from COBE/DIRBE, but obtained only upper limits in the near infrared wavelength bands. Difficulty in the DIRBE observation of near infrared EBL is mainly due to the relatively large beam size of 0.7° that caused serious confusion by the foreground stars.

In this paper, we present the detection of near infrared EBL with the data of IRTS/NIRS.

The Near InfraRed Spectrometer (NIRS) is one of the focal plane instruments of the InfraRed Telescope in Space (IRTS), and was optimized to observe the spectra of the diffuse background [6]. The NIRS covers the wavelength range from 1.4 μm to 4.0 μm with a spectral resolution of 0.13 μm. The beam size is 8 arcmin. square, considerably smaller than DIRBE.

The IRTS is one of the mission experiments of the small space platform, SFU, that was launched on March 18, 1995. During its one month observation period, IRTS produced the high quality spectra of the infrared sky [7].

Due to shortage of observed sky coverage and observation period, it was impossible to estimate zodiacal component with NIRS data itself. However, a recent physical model of interplanetary dust [8] enables us to estimate absolute brightness of the zodiacal light and zodiacal emission. This paper describes the new analysis to search for isotropic emission and its spatial fluctuation in IRTS/NIRS data.

2 Observation and Selection of the Data

The IRTS observation lasted for about 30 days, and 7% of the sky was surveyed [7]. During the observation period, many bright stars were observed, and absolute calibration and measurement of the beam pattern was satisfactorily attained with the flight data [9].

In the initial phase of the observation, NIRS observed the environmental OH emission in the southern hemisphere, which had a peak at about 2.8 μm. Passage of the South Atlantic Anomaly (SAA) and incidence of lunar radiation into the telescope tube also caused serious effects on the detectors. To avoid these effects, only the data for the last 5 days, those of orbits that did not pass the SAA and that did not suffer from lunar radiation, and those of northern sky were used for this analysis.

Further, in order to reduce the contribution from the faint stars, the sky at high galactic latitudes ($b > 40°$) is chosen. The highest galactic latitude is 58°, and the ecliptic latitude ranges from 12° to 71° in the selected data.

The data were taken with a 5 sec integration during which no distinguishable stars and no hits of cosmic rays were detected in any wavelength band. This procedure resulted in an effective beam size of 8 arcmin. × 20 arcmin. due to the scanning effect. Finally, full spectra of the sky at 1010 positions were obtained.

3 Subtraction of Foreground Emission

3.1 Contribution of Faint Stars

One of the superior characteristics of the NIRS observation is that fainter stars can be identified and subtracted due to less confusion owing to the smaller beam size than COBE/DIRBE.

The first step to subtract the stellar component is to obtain number density of stars ($logN/logS$ relation). Fortunately, NIRS detected several tens of thousands stars during the IRTS mission period, and a complete catalog is being prepared. Although this catalog is not so deep (completeness at 2.24 μm is $\sim$ 7.5mag), we constructed $logN/logS$ relation to 20 mag. for all wavelength bands based on a model Galaxy [10]. Uncertainty of $logN/logS$ relation is $\sim$ 10%.

The second step is to find out the contribution of stars that are too faint to be identified in the acquired data. We define the cut-off magnitudes as the brightest stars in the acquired data which are obtained with stellar fluxes that correspond to the noises with same spatial frequency as beam pattern. The cut off magnitude at 2.24μm thus obtained is 10.5 mag. Uncertainties are $\pm$0.5 mag for all wavelength bands.

With $logN/logS$ relations and cut off magnitudes, we calculated the surface brightness due to faint stars at $b = 42°, 45°$, and $48°$ along the scan path. We regard these three data sets as representative values for the sky regions at $40° < b < 42.5°$, $42.5° < b < 47.5°$, $47.5° < b$, respectively. The difference of the brightness in three positions is about 10%, and errors are 5 $\sim$ 10%, depending on the wavelength bands. The contribution of faint stars in the 2.24 μm band is about 10% of the observed sky brightness at high ecliptic latitude.

Integrated light of the faint stars for each wavelength band is subtracted from observed sky brightness. This "star subtracted data" is used for the further analysis.

3.2 Subtraction of Zodiacal Component

Recently the COBE/DIRBE team constructed a physical model of the interplanetary dust (IPD) using the seasonal variation of the zodiacal light and emission [8]. Based on this physical model, we calculated the brightness of the zodiacal light and emission corresponding to our wavelength bands and observed data. We tried to subtract this model brightness from the "star subtracted data".

Fig.1 shows ecliptic latitude dependence of the "star subtracted data", model zodiacal component, and residual emission after subtracting the stars and zodiacal component from the observed brightness at 2.24 μm. Other wavelength bands show essentially same features. Model brightness of the zodiacal component is calculated for all observed positions but the results

show no dependence on ecliptic longitudes. Therefore, the model brightness in Fig.1 looks like continuous curve.

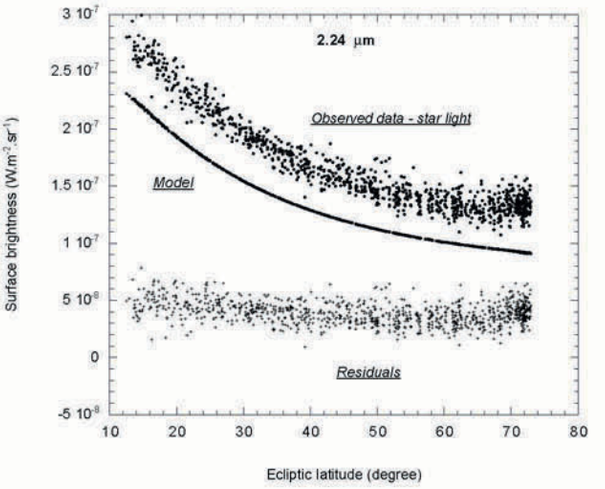

Fig. 1. Dependence on the ecliptic latitude for the data at 2.24 μm. Dots, solid lines, and crosses indicate "star subtracted data", IPD model, and residual brightness after subtracting the stars and zodiacal component from the observed sky brightness.

Fig.1 clearly shows that there remains a fairly isotropic residual emission after subtracting the faint stars and zodiacal component. Fig.2 indicates the correlation between "star subtracted data" and model brightness at 2.24 μm. The correlation is excellent for all bands, but slopes at long wavelength bands are a little steeper than 1.0, which implies that the model is not perfect in the long wavelength region. To attain a minor correction to the model, we made a linear fit for Fig.2 leaving the slopes to be free parameters. The isotropic emission is defined as the brightness where model brightness is zero. Errors are estimated by taking into account fitting errors, uncertainties of the cut off magnitudes, models of the Galaxy and IPD and systematic errors of the calibration. Fitting errors are small compared with other errors, and the major source of error is the uncertainty of the IPD model that is estimated by interpolating the uncertainties of the original model brightness, those are 15, 6, 2.1, and 5.9 $\mathrm{nWm^{-2}sr^{-1}}$ for the J, K, L and M bands, respectively [8].

Fig.3 shows the spectrum of the observed isotropic emission compared with upper limits of DIRBE [5], integrated light of galaxies [11] [12], and other observations. Fig.3 shows the obtained isotropic emission is consistent with DIRBE upper limits but considerably higher than the integrated light of galaxies. The spectrum of the isotropic emission is stellar like, and no clear band feature is found. In-band energy of the isotropic emission amounts to

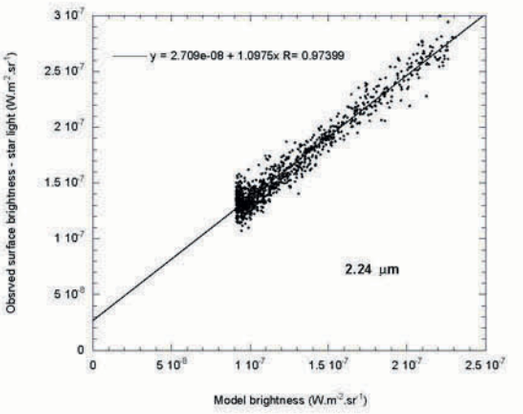

Fig. 2. Correlation diagram between star subtracted brightness and the model brightness at 2.24 μm.

$\sim$ 30 nWm^{-2}sr^{-1}, that can be compared with $\sim$ 12 nWm^{-2}sr^{-1} for the far infrared and submillimeter EBL.

The isotropic emission is consistent with Dwek and Arendt (1998) [13] who claimed a significant detection at 3.5 μm based on the correlation between the K and L bands. Gorjian et al. (1999) [14] recently reported a significant detection in the K and L bands by subtracting foreground stars from DIRBE data, that is fairly consistent with ours (filled circles in Fig.3).

4 Fluctuation Analysis

Fluctuation of the extragalactic background light is another important clue in the study of the formation and evolution of the galaxies. The beam size of 8 arcmin. $\times$ 20 arcmin. is an adequate scale to investigate the clustering of galaxies at high redshift [20].

For the fluctuation analysis with the NIRS data, we constructed the "fluctuation data set" by extracting the fluctuating component from the star subtracted data. We adopted a baseline obtained by fitting the ecliptic latitude dependence (Fig.1) to third order polynomials to avoid the incompleteness of the IPD model on the large scale structure. The standard deviations are obtained assuming a Gaussian distribution shown by filled circles in Fig.4.

Fluctuation due to faint stars is estimated by Monte-Carlo simulation with cut off magnitudes and the model Galaxy, where a random distribution is assumed. The read out noises are obtained from the fluctuation of signals when shutter was closed. It was found that observed fluctuation consists of read out noise on the longer wavelength side, but there remains an unknown fluctuation component in short wavelength side. In Fig.4, open circles indicate

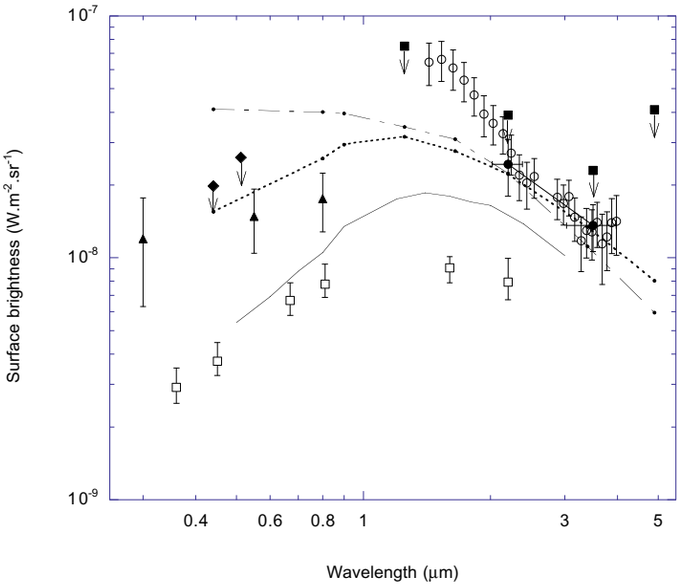

Fig. 3. Spectrum of observed isotropic emission is shown by open circles. Filled squares indicate upper limits by COBE/DIRBE [5]. Filled circles show the detection of EBL reported by Gorjian et al. (1999) [14]. Open squares represent integrated light of galaxies [11] [12]. Upper limits of the optical EBL by Dube et al. (1979) [15] and Toller et al. (1983) [16] are shown by filled diamonds, while the recent detection of EBL by Bernstein et al. (1999) [17] is indicated by filled triangles. Solid line represents prediction by Yoshi and Takahara (1988) [18]. The recent theoretical model by Jimenez and Kashlinsky (1999) [19] for two cases (dashed line : $z_f = 10, H_0 = 80$, and dot-dashed line : $z_f = 3, H_0 = 80$) is also shown.

the residual fluctuation that was obtained by subtracting the fluctuation due to stars and read out noise in quadrature.

There exists a clear correlation between wavelength bands. The correlation analysis for the fluctuation data set indicates that the color of the fluctuating component is very similar to the spectrum of the isotropic emission in section 3. This implies that the observed excess fluctuation has same origin as the isotropic emission, in other word, the isotropic emission fluctuates keeping same spectral shape.

The zodiacal component can not explain this fluctuation. The fluctuation of zodiacal emission has not been detected in the mid infrared region and is less than 1 % for various beam sizes (IRAS [21], COBE [8], ISO [22]). The upper limits thus obtained are much smaller than observed fluctuating component, that is, 1/4 of isotropic emission and 1/20 of the total sky brightness. Since it is unlikely that the scattering component has a much larger fluctuation than that of the thermal part, it is difficult to attribute

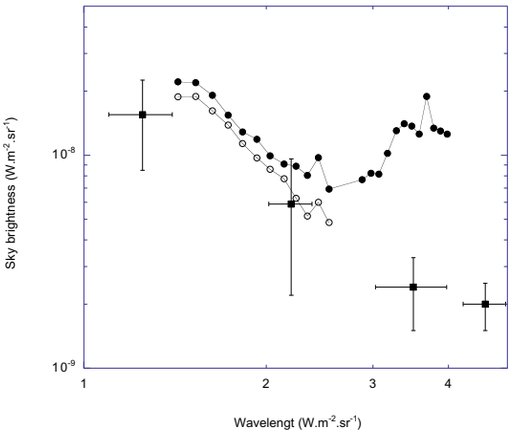

Fig. 4. Spectrum of 1 sigma fluctuation observed by the IRTS is shown by filled circles. Open circles indicate the excess fluctuation after subtracting read out noise and stellar fluctuation. Squares are rms fluctuation obtained by Kashlinsky et al. (1999) [20].

the excess fluctuation to zodiacal light. The fact that the fluctuation of the residual emission in Fig.1 has no dependence on the ecliptic latitude is more evidence that the observed fluctuation is not IPD in origin.

The contribution of faint stars to the fluctuation is not so clear since the spatial distribution of stars may not be random. Furthermore, it is difficult to confirm this, since infrared star catalog deep enough for this purpose is not yet available. However, in order to interpret the observed excess fluctuation as due to faint stars, fluctuation due to faint stars must be three to four times of that of the simulation. Considering that the contribution of the faint stars is over estimated in our analysis, it is hard to explain the observed excess fluctuation with faint stars.

In Fig.4 the recent fluctuation analysis of the DIRBE data by Kashlinsky et al.(1999) [20] is shown by squares. Although error bars are fairly large, good agreement is found between the two independent analyses. Fig.4 implies that the origin of the observed excess fluctuation is not stellar, and that the angular scale of the fluctuation could be comparable or larger than the DIRBE beam (0.7°).

In order to investigate the nature of the fluctuation, two point correlation analysis is crucial. To obtain a definite result, we defined the "wide band brightness" by integrating the brightness of short wavelength bands from 1.43 μm to 2.14 μm. Rms fluctuation of the "wide band brightness" was found to be 6.6 nWm^{-2}sr^{-1} of which read out noise amounts to 1.5 nWm^{-2}sr^{-1}, and fluctuation due to faint stars is estimated to be 2.1 nWm^{-2}sr^{-1}.

The two point correlation function is defined as $C(\theta) =< \delta F(x+\theta)\delta F(x) >$, where $\delta F(x)$ is fluctuating component of the "wide band brightness", θ is the

angular distance in arcmin. between two points, and x are the coordinates of the observed points. The left of Fig.5 shows the two point correlation function thus obtained. Error bars are indicated for selected points. The increase at the left end could be due to a proximity effect since some data points overlap on the scale of the beam size. Correlation at large angular scales ($\theta > 800$) is not adopted since large scale structure is seriously affected by uncertainty of the base line used to extract the "fluctuating component". On the other hand, structure around 100 arcmin. is statistically significant. Simulation with random data does not show fluctuation with this scale, that is, sampling effect is not the case.

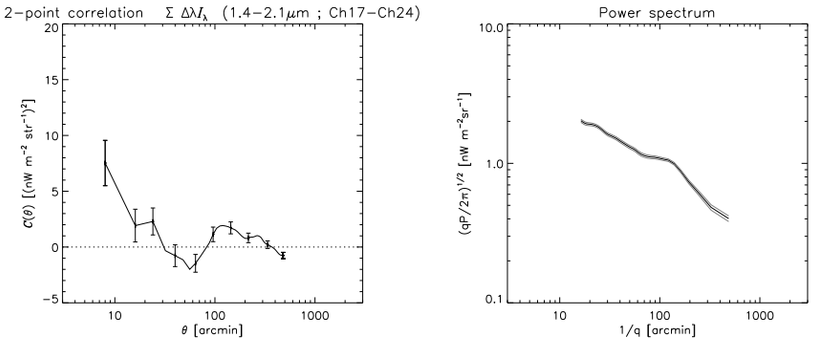

Fig. 5. Left: Two point correlation function is shown as a function of angular distance, θ. Right: Power spectrum $(qP(q)/2\pi)^{1/2}$ is shown as a function of $1/q$.

The two points correlation function can be converted to the power spectrum, $P(q)$, where q is wavenumber in unit of arcmin.$^{-1}$. Here, we adopted a one dimensional Fourier transformation with θ, since data points lie on the narrow belt and beam pattern is elongated along the scan path. The result is shown in the right of Fig.5 where $(qP(q)/2\pi)^{1/2}$ is plotted as a function of $1/q$. As expected, a clear hump at 100-200 arcmin. is found.

5 Discussion

The extragalactic background light has attracted strong interest of theoreticians, and many estimations have been made. These works are based on the present day luminosity function and scenarios of evolution. In all cases, the EBL brightness obtained is less than 1 nWm^{-2}sr^{-1} that is a few times lower than the isotropic emission obtained by us. This indicates a new energy source or a much stronger evolution effect are needed to explain the observed isotropic emission as extragalactic in origin.

The recent observational progress, however, has provided a new scope on the EBL study. One is the discovery of metals in Lyman α clouds which

suggests there was additional energy generation that was not considered in previous theories. Another important evidence is high star formation rate at high redshift, although evaluation of this depends on the estimation of the reddening.

Recent significant detection of EBL in the far infrared and submillimeter region [3] [4] [5] is brighter than that previously estimated, which also requires more energy generation at high redshift.

Fall et al. (1996) [23] first presented estimation based on these new observational evidences. They assumed a few types of models of star formation history at high redshift, and found that a bright near infrared EBL must exist to interpret the far infrared EBL.

Jimenez and Kashlinsky (1999) [19] made a detailed calculation with more realistic models. Their estimation depends on the model parameters, however, the prediction shows a much brighter EBL than previous models. Two typical cases of their result are shown by dashed line ($z_f = 10, H_0 = 80$) and dot-dashed lines ($z_f = 3, H_0 = 80$) in Fig.3.

As for the energetics, isotropic emission observed by us is not so far from recent model estimations but the spectral energy density (SED) is a little strange. Theoretical calculation is obtained by superposing SEDs of galaxies with different colors and redshifts, which results in flatter spectrum for the EBL than individual galaxies. The observed isotropic emission, however, has steeper spectrum than expected. In Fig.3, the recent observation of optical EBL by Bernstein et el. (1999) [17] is also shown. If their observation is correct, there must be a spectral break at around $\sim 1\mu m$.

Another piece of important observational evidence is a significant detection of fluctuations. The observed rms fluctuation level is fairly large ($\sim 1/4$ of isotropic emission) and the fluctuating component has a same spectral shape as that of the isotropic emission. On the other hand, detected two point correlation and PSD show typical angular scales of $1^\circ \sim 2^\circ$ whose scale and amplitude are marginally consistent with the model by Jimenez and Kashlinsky (1999) [19].

These observational results suggest that the isotropic emission originates in a short period at high redshift. Observed fluctuation may reflect clustering at that epoch.

At present, the origin of the observed isotropic emission is not clear, but this result will bring new observational evidence to investigate the formation and evolution of galaxies.

References

1. Matsumoto, T., Akiba, M. & Murakami, H. (1988) A Search for the near-infrared extragalactic background light. Astrophys. J. 332, 575-595
2. Noda, M. et al. (1992) Rocket observation of the near-infrared spectrum of the sky. Astrophys. J. 391, 456-465

3. Puget, J.-L, et al. (1996) Tentative detection of a cosmic far infrared background. Astron. Astrophys. 308, L5-L9
4. Fixen, D. J. et al. (1998) The spectrum of the extragalactic far-infrared background from the COBE/FIRAS observation. for the cosmic infrared background I. Limits and detections. Astrophys. J., 508, 123-128
5. Hauser, M.G. et al. (1998) The COBE diffuse infrared background experiment search for the cosmic infrared background I. Limits and detections. Astrophys. J., 508, 25-43
6. Noda, M. et al. (1994) Near infrared spectrometer on the Infrared Telescope in Space. Astrophys. J. 428, 363-369
7. Murakami, H. et al. (1996) The IRTS mission. Pub. Astron. Soc. Japan 48, L41-L47
8. Kelsall, T. et al. (1998) The COBE diffuse infrared background experiment search for the cosmic infrared background II. Astrophys. J. 508, 44-73
9. Noda, M., et al. (1996) Flight performance of the near-infrared Ssectrometer. SPIE 2817, 248-256
10. Cohen, M. (1997) Observation of late type stars. in Diffuse Infrared Radiation and the IRTS, ed. Okuda, H., Matsumoto, T. & Roellig, T. L. (New York, AIP), ASP Conf. Series, 124, 61-66
11. Patric, M., et al. (1998) Deep H-Band galaxy counts and half light radii from Hubble Space Telescope/NICMOS parallel observations. Astrophys. J. 503, L19-L22
12. Pozzetti, M., et al. (1998) High-redshift galaxies in the Hubble Deep Field. , Mon. Not. R. Astron. Soc. 298, 1133-1144
13. Dwek, E. and Arendt, R. G. (1998) A tentative detection of the cosmic infrared background at $3.5\mu m$. Astrophys. J. 508, L9-L12
14. Gorjian, V., Wright, E.L. and Charry, R. R. (1999) Tentative detection of the cosmic background at $2.2\mu m$ and $3.5\mu m$ using ground base and space observation. astroph 9909428
15. Dube R. R., Wickes, W. C. and Wilkinson, D. T. (1979) Upper limits on the extragalactic background light. Astrophys. J. 232, 333
16. Toller, G.N. (1983) The extragalactic background light at 4400 A. Astrophys. J. 266, L79-82
17. Bernstein, R. A., Freenman, W. L. and Modore, B.F. (1999) The HST/LCO measurement of the mean flux of the optical extragalactic background. preprint
18. Yoshii, Y. and Takahara, F. (1988) Galactic evolution and cosmology : Probing the cosmological deceleration parameter. Astrophys. J. 326, 1-18
19. Jimenez, R. and Kashlinsky, A. (1999) Galaxy evolution, deep counts, and the near-infrared cosmic infrared backgorund. Astrophys. J. 511, 16-33
20. Kashlinsky, A., Mather, J. C., and Odenwald, S. (1999) Clustering of the diffuse infrared background from COBE DIRBE maps. III. Astrophys. J. submitted
21. Vrtilek, J. M. and Hauser, M. G. (1995) IRAS measurement of diffuse solar System radiation : Annuak sky brightness variation and geometry of the interplanetary dust cloud. Astrophys. J. 455, 677-692
22. Abraham, P. et al (1998) Zodiacal light observation with ISOPHOTO. in The Universe as seen by ISO, ed. Cox, P. and Kessler, M. F. ESA, SP-427, 145-145
23. Fall, S. M., Charlot, S. and Pei, Y. (1996) Cosmic Emissivity and Background Intensity from Lyman-Alpha galaxies. Astrophys. J. 464, L43-L46

Power Spectrum Analysis of Far-Infrared Sky Brightness in the Lockman Hole

Hideo Matsuhara[1], Kimiaki Kawara[2], Yasunori Sato[1], Yoshiaki Taniguchi[3], Haruyuki Okuda[1], Toshio Matsumoto[1], Yoshiaki Sofue[2], Ken-ichi Wakamatsu[4], Lennox L. Cowie[5], Robert D. Joseph[5], and David B. Sanders[5]

[1] The Institute of Space and Astronautical Science, 3-1-1 Yoshinodai, Sagamihara, Kanagawa 229-8510, Japan
[2] Institute of Astronomy, The University of Tokyo, 2-21-1 Osawa, Mitaka, Tokyo 181-8588, Japan
[3] Astronomical Institute, Tohoku University, Aoba, Sendai 980-8578, Japan
[4] Faculty of Engineering, Gifu University, Gifu 501-1193, Japan
[5] Institute for Astronomy, University of Hawaii, 2680 Woodlawn Drive, Honolulu, HI 96822, USA

Abstract. We investigate the characteristics of far-infrared brightness fluctuations at 90 μm and 170 μm in the Lockman Hole which were surveyed with ISO, using power spectrum analysis over the spatial frequency range of $0.05 \ldots 1$ arcmin^{-1}. The power spectra are found to be rather flat at low spatial frequencies ($f \leq 0.1\,\mathrm{arcmin}^{-1}$), and tend to decrease slowly towards the higher frequencies. The latter – unlike the power-law ones – are seen in the IR cirrus fluctuations, and are well explained by randomly distributed point sources. We conclude that the fluctuations due to the IR cirrus are not dominant in the Lockman Hole and are most likely due to faint galaxies. We also give constraints on the galaxy number counts, which indicate the existence of strong evolution in the counts.

1 Introduction

A large portion of star formation activity in the universe may be hidden by dust, prohibiting optical and near-infrared studies due to the enormous extinction. Thus, surveys at far-infrared and submillimeter wavelengths are essentially important to reveal the complete picture of the star formation history of the universe. However, the detectivity of 1m-class space-borne far-infrared telescopes is likely to be limited by the noise due to the fluctuation of the IR cirrus [1] even at high Galactic latitude [2] [3].

In this paper we investigate the characteristics of far-infrared brightness fluctuations in the Lockman Hole, a region with a uniquely low HI column density [4], therefore the IR cirrus contribution to the fluctuation is expected to be minimal. Moreover, the fluctuation analysis can provide unique information on the number counts of faint galaxies even below the source-confusion limit.

The far-infrared images of the Lockman Hole have been obtained by the ISAS guaranteed time observations with ISO. The first results have already

D. Lemke, M. Stickel, and K. Wilke (Eds.): LNP 548, pp. 106–112, 2000.

been presented in Paper I [5]. The source extraction and the source counts are described by another contribution presented in this workshop [6]. Details of the fluctuation analysis will be described in Paper II [7]. The astrophysical implications of the source counts and the fluctuation analysis are also discussed in a review paper of Japanese deep surveys [8] by comparison with source count models.

2 The Survey Data

Two $44' \times 44'$ fields, LHEX and LHNW, were mapped in two wavebands: 90 μm and 170 μm. Each of the two fields is made up of 4 sub-fields. Each sub-field map was produced from the edited raw data by the PHT Interactive Analysis (PIA) versions 7.1 and 7.2 [9]. To correct the drift in the responsivity of the detectors, we applied the MEDIAN filter routine (Paper I). As was done in Paper I, the flux scale was calibrated based on the fluxes of the brightest source in the LHEX images(IRAS F10507+5723). The statistical instrumental noise in the final images is found to be negligible. In Fig. 1, the far-infrared images of LHEX and LHNW used for the fluctuation analysis are shown.

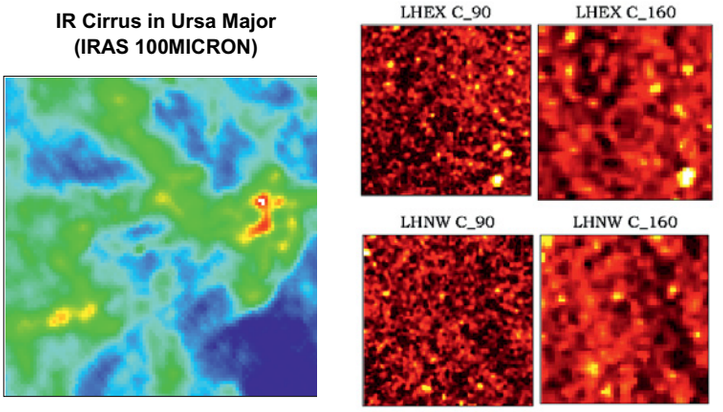

Fig. 1. Example of the IR cirrus image at 100 μm in Ursa Major is shown on the left, and the 90 μm and 170 μm images in the Lockman Hole are shown on the right. The cirrus image is about $2.5^\circ \times 2.5^\circ$ wide while each image in the Lockman Hole is about $40' \times 40'$ wide

3 Power Spectrum Analysis

For each image shown in Fig. 1, the two-dimensional angular correlation function $C(x, y)$ was calculated from the brightness distribution $B(x_0, y_0)$:

$$C(x, y) =< (B(x_0, y_0) - \bar{B})(B(x_0 + x, y_0 + y) - \bar{B}) > \quad (1)$$

where brackets $< >$ represent the average over the whole area in each image shown in Fig. 1, and $\bar{B} =< B >$. Then the coordinates were expressed in polar coordinates as $C(r, \theta)$, and the Fourier transforms in various radial directions were calculated (i.e., θ is fixed for each transform). The one-dimensional power spectral density (PSD) $P(f)$ is calculated from

$$P(f) = \frac{2}{N} \sum_{k=0}^{N-1} C_k cos(2\pi f r_k)\,, \quad (2)$$

where $f = 1/(Nr_{\rm pix}) \sim 1/(2r_{\rm pix})$ is the spatial frequency, $r_k \equiv r_{\rm pix}k$ ($k = 0, 1, \cdots, N-1$), $r_{\rm pix}$ is the pixel size of the map, $Nr_{\rm pix}$ is the largest angular size for which the angular correlation function is evaluated, and $C_k \equiv C(r = r_k,\ \theta)$. Note that the unit of the PSDs is the same as that of the angular correlation function: $\mathrm{Jy}^2/\mathrm{sr}^2$. Finally, the PSDs were averaged with respect to θ and are shown in Fig. 2. In order to check the contribution from bright sources, the PSDs are derived by masking circular regions with a 4×FWHM diameter around bright sources with fluxes above $S_{\rm max}$: $S_{\rm max}$ = 250 mJy at 170 μm, and $S_{\rm max}$ = 150 mJy at 90 μm. In the following discussion, the resulting PSDs are called "residual PSDs", and these are shown in Fig. 2 as well. Interestingly, the residual PSD for each image is more than half of the PSD of the corresponding original image with almost the same spectral shape, indicating that there remains significant contribution from randomly distributed point sources with fluxes below $S_{\rm max}$.

In Fig. 2, typical IR cirrus PSDs are also shown in order to check the contribution of the IR cirrus to the PSDs of the Lockman Hole. We examined several IRAS 100 μm maps of high-latitude clouds in Ursa Major ($l = 145°$, $b = 40°$), which are reproduced from the IRAS Sky Survey Atlas (ISSA) by reducing the brightness by a factor of 0.72, following the COBE/DIRBE calibration [10]. The average brightness of the cirrus is 2-3 MJy/sr. The cirrus fluctuation spectra show a power-law distribution, which is much different from those obtained for the Lockman Hole images. The latter exhibit rather flat spectra at low spatial frequencies. Contributions by the IR cirrus fluctuations in the Lockman Hole were estimated assuming that the cirrus PSD is proportional to B_0^3 [3], assuming a mean brightness B_0 of the IR cirrus in the Lockman Hole as B_0 = 0.32 MJy/sr at 90 μm and B_0 = 1.0 MJy/sr at 170 μm. The IR cirrus contributions to the PSDs in the Lockman Hole are negligible over all spatial frequencies $f \geq 0.05$.

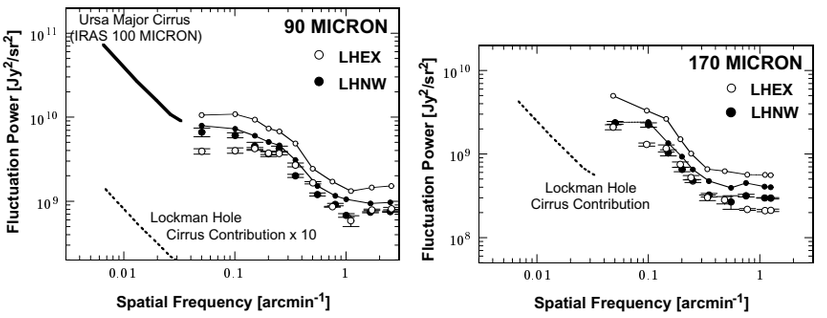

Fig. 2. Fluctuation power spectral densities (PSDs) of 90 μm (left) and 170 μm (right) images (*open circles*: LHNW, *filled circles*: LHEX). As well as the PSDs of the original images shown in Fig. 1 right (*circles with thin-solid lines*), the PSDs of the residual images ("residual PSDs"), where the pixels contain bright sources($\geq$ 150mJy at 90 μm or $\geq$ 250mJy at 170 μm) are masked, are also shown (*circles without lines*). An example of the IR cirrus PSD (*thick line*) is an average spectrum of several IR cirrus in Ursa Major, with 100 μm brightnesses of 2-3 MJy/sr. The cirrus contributions in the Lockman Hole (*dotted lines*) are estimated by assuming that the cirrus PSDs are proportional to B_0^3, where B_0 is mean brightness of the cirrus cloud.

4 Constraints on Number Counts

In order to interpret the residual PSDs in terms of source densities as a function of flux densities, a simulation was performed by creating artificial 90 μm and 170 μm images made up by galaxies with fluxes between $S_{\rm min}$ and $S_{\rm max}$ only, and calculating their PSDs. Here galaxies are treated as point sources with a PSF adjusted to the corresponding wavelength band of ISOPHOT. We used the image of the bright IRAS source (F10507+5723) seen in LHEX images for the determination of the artificial PSF. We ignored the spatial correlation between galaxies, and therefore the objects are randomly distributed in the images. The number of sources and their flux densities are controlled by the models of the source number counts. We evaluated the simulated PSDs for simple double power-law number count models:

$$N(>S) = N_{\rm max}\left(\frac{S}{S_{\rm max}}\right)^{-\beta_0} \quad \text{for } S_{\rm max} \geq S \geq S_{\rm crit}\,, \tag{3a}$$

$$N(>S) = N_{\rm crit}\left(\frac{S}{S_{\rm crit}}\right)^{-\beta_1} \quad \text{for } S_{\rm crit} \geq S \geq S_{\rm min}\,, \tag{3b}$$

where $N_{\rm crit} = N_{\rm max}(S_{\rm crit}/S_{\rm max})^{-\beta_0}$ and $0 \leq \beta_1 \leq \beta_0 \leq 3$. The uncertainty in $N_{\rm max}$ includes both Poisson uncertainties based on the total number of

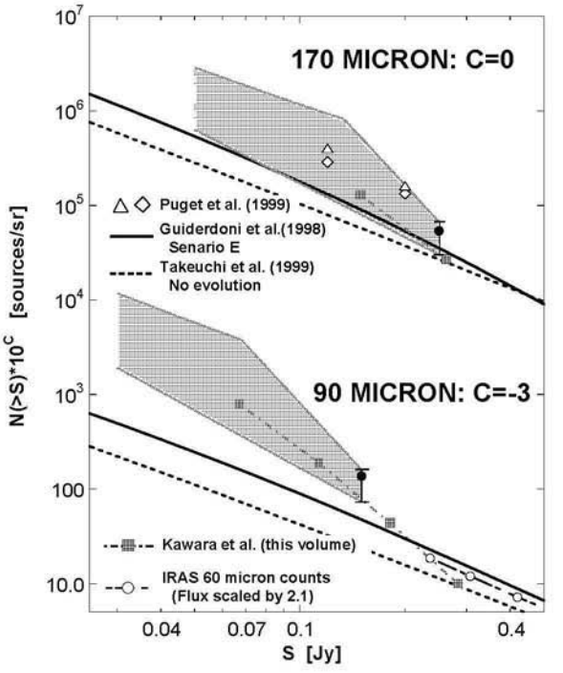

Fig. 3. The allowed regions for various number count models(*shaded areas*), which are consistent with the fluctuation power of the Lockman Hole images(the residual PSDs shown in Fig. 2) [7], together with observed number counts at $S_{\max}$(*filled circles*). The theoretical number count models [11] (scenario E, *solid lines*) and the no evolution model [12] (*dashed lines*) are compared. The observed(*open diamonds*) and incompleteness-corrected(*open triangles*) 170 μm source counts were obtained by the FIRBACK Marano 1 survey [13]. The IRAS 60 μm counts, in which the flux is scaled by the factor $S_\nu(90\,\mu\mathrm{m})/S_\nu(60\,\mu\mathrm{m}) = 2.1$ are also shown(*open circles with dash-dotted line*). The number counts with corrections for the source confusion [6] are also plotted(*filled squares on dash-dotted lines*)

extracted sources with flux above $S_{\max}$ in all images, and systematic ones originating from the incompleteness due to source confusion [6]. We found that the simulated PSDs match well with the residual PSDs over all spatial frequencies within $\pm 22\%$ for 90 μm PSDs and $\pm 17\%$ for 170 μm ones.

The allowed regions in the number count plots for the double power-law counts introduced above is shown in Fig. 3. The 90 μm counts below 30 mJy and the 170 μm counts below 50 mJy cannot be constrained well and are therefore not shown.

5 Discussion

The origin of the residual PSDs is not due to the IR cirrus fluctuations. We attribute it to the random distribution of faint point sources, most probably galaxies, which can no longer be identified as individual sources due to the source confusion. Another piece of evidence which supports this interpretation is the 170 μm/90 μm color of the far-infrared background emission, which is shown in Fig. 2 of the review paper [8]. The 170 μm/90 μm correlation with a slope of unity is consistent with the color of a star-forming galaxy located at $z \leq 1$ [7].

As shown in Fig. 3, we give constraints on the number counts down to 30-50 mJy which cannot be reached by the direct source counts due to the source confusion. As for the 170 μm counts, the allowed region is almost consistent with the scenario E model [11], and consistent with the counts at 120 mJy and at 200 mJy obtained from the FIRBACK Marano 1 survey [13]. On the other hand, the allowed region for 90 μm counts are far above those of any currently existing models. Since the 90 μm counts at 300 mJy are consistent with the ones derived from the non-evolution model, there must be a strong evolution below 300 mJy. The Impact of these results to the source count models is discussed in the review paper [8].

Finally, we mention the impact of our results on the present work in the field of the cosmic infrared background (CIB) obtained with COBE/DIRBE: an upper limit of 1.1 MJy/sr at 100 μm and a positive detection of CIB as 1.2 MJy/sr at 140 μm and 1.1 MJy/sr at 240 μm [14]. A detection of CIB at 100 μm as 0.78 ± 0.21 MJy/sr [15] is also reported. By summing up fluxes of all detected sources above 150 mJy, we obtained integrated brightness of 0.031 MJy/sr at 90 μm and 0.050 MJy/sr at 170 μm. If we consider the constraints on the number counts given in Fig. 3, then the integrated brightness amounts to 0.12-0.32 MJy/sr at 90 μm($S \geq$ 30mJy) and 0.07-0.23 MJy/sr at 170 μm($S \geq$ 50mJy). Hence, 10-30% of the CIB can now be attributed to the integrated light of discrete sources above 30 mJy or 50 mJy which are responsible for the fluctuations.

The authors would like to thank Hiroshi Shibai, Tsutomu Takeuchi, Hiroyuki Hirashita, and Chris P. Pearson for their extremely useful comments.

References

1. Low, F.J., Young, E. et al. (1984) ApJ **278**, L19-L22
2. Helou, G., Beichman, C.A. (1990) The Confusion Limits to the Sensitivity of Submillimeter Telescopes. In: Proceedings of the 29th Liége International Astrophysical Colloquium from Ground-Based to Space-Borne Sub-mm Astronomy, Liége, Belgium, July 3-5, 1990. ESA SP-314, 117-123
3. Gautier, T.N., Boulanger, F. et al. (1992) AJ **103**, 1313-1324
4. Lockman, F.J., Jahoda, K. et al. (1986) ApJ **302**, 432-449

5. Kawara, K., Sato, Y. et al. (1998) A&A **336**, L9 – L12 (Paper I)
6. Kawara, K., Sato, Y. et al. (1999) in this volume.
7. Matsuhara, H., Kawara, K. et al. (2000) in preparation. (Paper II)
8. Okuda, H. (1999) in this volume.
9. Gabriel, C., Acosta-Pulido, J. et al. (1997) In: Hugg, G., Payne,H.E. (Eds.) Astronomical Data Analysis Software and Systems VI, A.S.P. Conference Series, Vol. 125, 108
10. Wheelock, S., et al. (1994) IRAS Sky Survey Atlas Explanetary Supplement, JPL Publication 94-11, Pasadena: JPL
11. Guiderdoni, B., Hivon, E. et al. (1998) MNRAS **295**, 877-898
12. Takeuchi T.T, Hirashita, H. et al. (1999) PASP **111**, 288-305
13. Puget, J.L., Lagache, G. et al. (1999) A&A **345**, 29-35
14. Hauser, M.G., Arendt, R.G. et al. (1998) ApJ **508**, 25-43
15. Lagache, G., Abergel, A. et al. (1999) A&A **344**, 322-332

A Local Infrared Perspective to Deeper ISO Surveys

Dave M. Alexander[1] and Hervé Aussel[2]

[1] International School for Advanced Studies, SISSA, Trieste, Italy
[2] Osservatorio Astronomico di Padova, Padova, Italy

Abstract. We present new techniques to produce IRAS 12 μm samples of galaxies and stars. We show that previous IRAS 12 μm samples are incompatible for a detailed comparison with ISO surveys and review their problems. We provide a stellar infrared diagnostic diagram to distinguish galaxies from stars without using longer wavelength IRAS colour criteria and produce complete 12 μm samples of galaxies and stars. This new technique allows us to estimate the contribution of non-dusty galaxies to the IRAS 12 μm counts and produce a true local mid-infrared extragalactic sample compatible with ISO surveys. We present our initial analysis and results.

1 The Importance of the Local Infrared Picture

The recent ISO mission has produced a number of deep mid-infrared extragalactic surveys [1,2,3,4], many of which are presented elsewhere in these proceedings. In order to accurately evaluate the apparent source evolution found in these surveys, it is essential to have a stable and exact local infrared picture that is compatible with ISO surveys.

2 Previous Work and Problems

There have been a number of previous IRAS 12 μm extragalactic samples produced from either the Point Source Catalog, hereafter PSC, or the Faint Source Catalog, hereafter FSC. The FSC was constructed by co-adding the individual PSC scans and is consequently deeper at 12 μm by approximately one mag; the FSC is considered complete to $f_{12} > 0.2$ Jy. Due to the greater depth of the FSC only those samples constructed from it will be considered here [5,6 hereafter RMS and FSXH]. In essence none of these samples are truly compatible with the deeper ISO surveys because they apply longer wavelength IRAS colour selection criteria and do not objectively classify galaxies. Some of these samples additionally suffer from inaccurate source flux estimation, no correction for the overdensity due to large scale structure, and inaccurate K-correction. Due to the lack of space here these latter two points are not considered, although we refer the interested reader to [6,14] for excellent coverage of these problems.

D. Lemke, M. Stickel, and K. Wilke (Eds.): LNP 548, pp. 113–120, 2000.

2.1 The Colour Selection Problem

Selecting objects at 12 μm without colour selection will produce an abundance of stars over galaxies, due to the Jeans tail of stellar emission. Without exception every extragalactic 12 μm sample to date has had (the majority of) stars removed by applying longer wavelength IRAS colour criteria. This technique is clearly incompatible with ISO surveys, where no colour criterium is applied and will cause a bias towards dusty galaxies. This also means that every galaxy must have a longer wavelength flux, producing incompleteness even within the selection boundaries. For example, in RMS the primary selection is f_{12}>0.22 Jy but every galaxy must also have f_{60}>0.5f_{12} or f_{100}>f_{12}. However, due to the completeness of FSC (f_{60}>0.2 Jy and f_{100}>0.6 Jy) this sample cannot be complete for f_{12}<0.4 Jy or f_{12}<0.6Jy respectively.

2.2 The Classification Problem

To produce accurate extragalactic luminosity functions and understand the galaxy contributions to fainter source counts it is necessary to classify galaxies in an objective way; the most common technique is with optical line ratios [7,8]. To date the only classified 12 μm sample is RMS, although their classification was taken from various catalogues which differ in the definition of extragalactic type and completeness. As a comparison to this classification we have obtained line ratios from the literature for 349 of the 483 RMS galaxies with δ>0 degrees. This gives completenesses of 72%, 78% and 93% for objects f_{12}>0.22, 0.3 and 0.5 Jy respectively. Due to the spectroscopic incompleteness at lower fluxes and the colour selection incompleteness we only consider those of f_{12}>0.5 Jy here (see table 1); our classification follows that of [7,9].

Table 1. Extragalactic classification

	AGN	LINER	HII
RMS	13%	15%	-
AA	16%	24%	60%

All galaxies are found to show Hα emission, although for some galaxies W$_\lambda$(Hα)<1Åand they would appear as absorption line objects in lower resolution/signal to noise spectra. Of the HII galaxies, 50% show evidence for significant star formation (W$_\lambda$(Hα)>10 angstroms). RMS classified an object as an AGN if it is present in an AGN catalogue. We find a good agreement in classification for this object class, the principal reason for the construction of the RMS sample. LINERs were classified in the RMS sample if they were present in an AGN catalgoue and consequently this sample is thought to be incomplete. We confirm this here. RMS did not classify HII galaxies, although

they considered those galaxies not classified as a LINER or AGN, but with high infrared luminosities, to be starburst galaxies and all other objects to be normal galaxies.

2.3 The Source Flux Problem

The FSC detection algorithm has been optimised for unresolved sources, therefore fluxes for extended sources need to be calculated from the coaddition of scans (the ADDSCAN technique nowadays accessed via XSCANPI) [10]. However, if a source is unresolved, the flux calculation using this technique leads erroneously to a larger flux than the FSC flux [10]. Whilst FSXH carefully calculate the fluxes of extended and unresolved sources separately, RMS treat all sources as extended and consequently overestimate the fluxes of unresolved galaxies; due to the large beamsize of IRAS a large number of galaxies can be overestimated. The magnitude of this effect can be estimated from ISOCAM observations. Unfortunately only a few observations are available for the lw10 filter (the closest to the IRAS 12 μm band). Therefore in order to predict the IRAS 12 μm fluxes we have used observations in the lw2 (6.7 μm) and lw3 (14.3 μm) bands and a spectral decomposition technique similar to that described in [11]. In this simple model the mid-infrared emission is produced by two components: HII regions (using M17 [12]) and photo-dissociation regions (PDR) (using NGC7023 [13]). The ratio of HII to PDR is calculated from the ratio of lw2 to lw3 fluxes; a synthetic spectra is produced and the IRAS 12 μm flux is calculated. This technique will be somewhat imprecise due to the uncertainty of the CAM photometry and the ability of the model to reproduce the galactic spectrum. Overall we estimate an uncertainty of $\sim$20%, roughly equal to the worst error in the FSC photometry. In figure 1 we plot our predicted fluxes against the FSC and RMS fluxes divided by the predicted flux (i.e. the relative errors in flux).

Only those galaxies with z>2,500 kms^{-1} have been plotted, as they should all be unresolved in the IRAS beam. In general, a good agreement between the predicted flux and FSC flux is found, leading us to believe that the true fluxes for these objects are close to the FSC flux. Consequently RMS may be overpredicting the source flux for $\sim$50% of their objects. This will have the effect of shifting galaxies from faint flux/luminosity bins to higher bins, causing unpredictable effects in the source count and luminosity function determinations.

3 A New IRAS 12 μm Sample

Our new IRAS 12 μm sample aims to address these problems and create a local infrared sample that is compatible with ISO surveys. The sample definition is close to that of RMS: sources are taken from the FSC for those objects with |b|>25 degrees, f_{12}>0.2 Jy, and a moderate or good quality

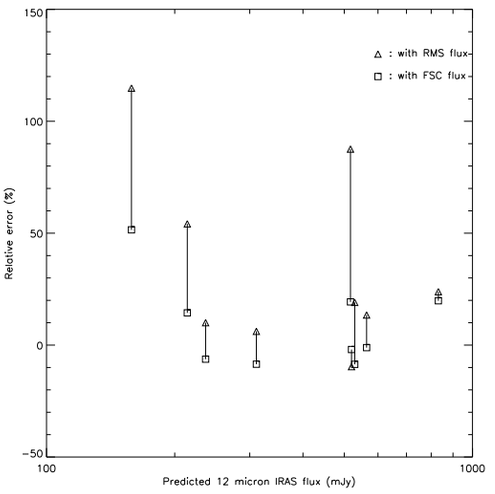

Fig. 1. 12 μm flux comparison

detection (S/N>3). This selection results in 31002 objects; by comparison the RMS colour selection bias produces ∼1100 objects.

Our sample provides an interesting complement to the PSC-z extragalactic survey [15], which selects those objects from the PSC with f_{60}>0.6 Jy. As with our sample, they do not apply colour selection criteria; stars are identified on Schmidt plates. In terms of the extragalactic objects we would expect many galaxies in common, although our sample should have a higher fraction of quasars and early type galaxies.

3.1 The Stellar Infrared Diagnostic Correlation

As a result of not applying colour selection to distinguish galaxies from stars, we have had to devise an alternative technique. The key assumption in our technique is that stars generally have predictable properties and therefore with the large and complete optical stellar databases currently available (in particular the Guide Star Catalogue [16], hereafter GSC) it is possible to find the majority of stars in our sample through positional cross correlation. An important factor here is the determination of the completeness of an optical stellar catalogue in an infrared sample, requiring an understanding of the general optical and infrared characteristics of stars.

To determine these characteristics for our stars we have used SIMBAD, which provides stellar classifications, and produced a large sample (∼9000 objects) of classified stars. When cross correlating to optical positions we consider a star correlated if its optical position falls within 5σ of the IRAS position (the mean major and minor error ellipse axes are 16.9" and 2.0" re-

spectively). The properties of our classified stellar sample are shown in figure 2. We have only plotted those stars for which there are at least 10 objects in a classified class and only a subset of these classes are shown here for clarity. A clear correlation between stellar type and flux ratio is found. The predicted black body colours for the different stellar types follows a straight line passing close to the A1V to K5III points. The interesting deviation observed for stars beyond type MOIII is *possibly* due to an increasing amount of stellar absorption in the V band.

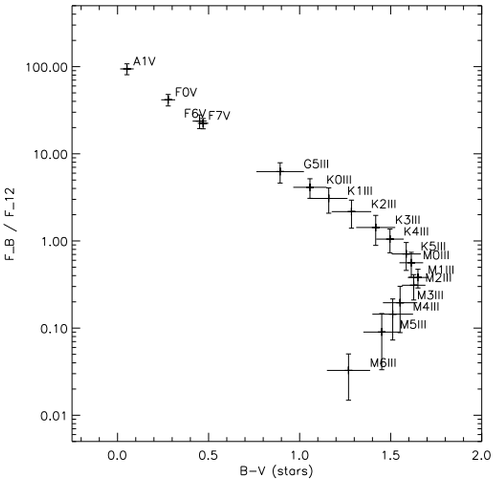

Fig. 2. Stellar infrared diagnostic diagram

These optical-infrared flux correlations provide an essential tool, the ability to predict the IRAS 12 μm flux of a star for a given spectral type or B-V colour. In the cases where we find an IRAS source associated with both a galaxy and a star we will be able to predict the flux from the star and therefore estimate the flux from the galaxy.

3.2 Cross Correlating Stars

The GSC is considered complete for 6<V<15 mags over the whole sky. Based on our stellar infrared diagnostic correlation this corresponds to a depth of f_{12}>0.2 Jy and therefore any stars earlier than a type M6III in our sample should be in the GSC. However, to accurately cross correlate the positions between the GSC and our sample requires accounting for proper motion. The Schmidt plates for the GSC were taken in 1975 and 1982; by comparison the mean IRAS observation epoch is 1983.5. By analysing a sub-sample of

Hipparcos stars (∼4000 objects, selected by sky area) we find a mean proper motion of 0.03"yr^{-1}, with a one σ maximum of 0.13"yr^{-1} (the maximum in the whole catalogue is 6"yr^{-1}). Taking into account the different observation epochs and the mean IRAS error ellipse, virtually all our stars should fall within 5σ of their GSC position.

We initially searched for associations by selecting all objects within 2' of the IRAS position (2' corresponds to $\sim 5\sigma$ of the mean positional uncertainty in the major axis direction), although we only consider a star cross-correlated if it falls within 5σ of an IRAS source. From this cross correlation we find that over 29000 of our IRAS sources are stars. Of these a small (∼0.5%), but significant, fraction show a considerable infrared excess ($f_{25}>f_{12}$) and warrant further study.

3.3 Cross Correlating Galaxies

Our extragalactic cross correlation is performed in a similar manner, although the problems associated with correlating galaxies are somewhat different. Proper motion is not a problem, although the extended size of galaxies is, as the peak mid-infrared position can vary from the peak optical position and therefore some positional uncertainty must be included when trying to correlate an infrared galaxy to an optical source. Although a 5σ positional uncertainty can correspond to 2' if the galaxy lies along the major axis of the IRAS error ellipse, it can also correspond to just 10" if the galaxy lies perpendicular to this direction. Therefore we only consider a galaxy cross correlated if it falls within 10σ of an IRAS source. Due to the often unknown incompleteness of extragalactic catalogues it is not possible to accurately determine the completeness of our sample in extragalactic catalogues and therefore we have simply used the largest (and most appropriate) databases. In the cross correlation presented here we have used the QIGC sample [17], which has just become available in electronic form, NED, SIMBAD and the FSC 25 μm sample [18].

Using these databases we find that over 700 of our sources, not confirmed as stars, fall within our 10σ threshold. From these confirmed galaxies we find that ∼50 are elliptical or S0 systems (not all are active galaxies), ∼150 have $f_{12}>f_{25}$ and are most probably PDR dominated galaxies. A number of galaxies have $f_{12} > 2 \cdot f_{60}$ and would therefore not be picked up by RMS. One of these galaxies is NGC 3115, a nearby bulge dominated galaxy of Hubble type S0. This galaxy is only detected at 12 μm, the 25, 60 and 100 μm fluxes are upper limits, although with a V band mag of ∼8.9 it is a bright optical galaxy. In terms of its B-V (1.0) and B/12 (2.5) colours it corresponds to a K0III star. As a comparison we have plotted a sample of our *normal* infrared galaxies, see figure 3.

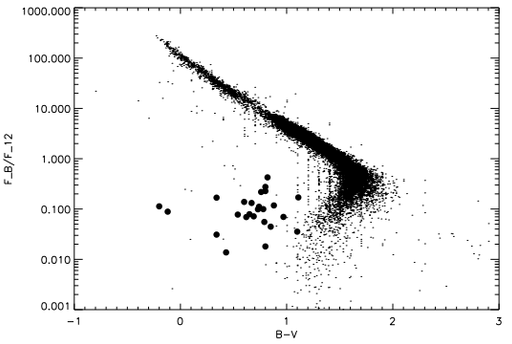

Fig. 3. Stellar and galactic colour plot. All confirmed stars are plotted as dots and a selection of normal infrared galaxies are plotted as filled circles. NGC 3115 is not plotted here but would correspond to the position of a K0III star, see figure 2

3.4 Further Improvements

Although our initial cross correlation has been successful, we have ∼500 objects for which we do not have an optical identification. These objects do not have IRAS Cirrus/Confused flags or low 12 μm fluxes, although approximately 75% have upper limit 60 μm IRAS fluxes. Visual inspection of a number of these objects with the Digital Sky Survey shows them to be nearby bright stars, suggesting incompleteness in the GSC at bright fluxes. However there is also probably a substantial population of stars not yet accounted for: those with V>15 mags (e.g. M7III and M8III stars), dark molecular clouds and planetary nebulae. We are currently compiling a list of additional stellar objects to cross correlate to our sample to allow us to produce a definitive list of unidentified extragalactic sources.

4 Further Work

Our primary aim is to construct complete 12 μm FSC selected samples of galaxies and stars. From this we will create accurate extragalactic source counts and classified luminosity functions with optical slit spectroscopy. As many of our extragalactic objects will be extended, we also intend to obtain integrated spectra to provide a classification which is compatible with the distant objects found in ISO surveys, where the observed slit spectra will be produced by most of the galaxy. With our stellar sample we wish to create a complete list of high galactic latitude stars and sources to help constrain galactic models and provide further diagnostics in distinguishing stars from galaxies in faint surveys (e.g. the Hubble Deep Field [3]). Both our galactic and stellar samples show objects that deviate from the norm (i.e. galaxies

with stellar colours and stars with galactic colours) and warrant further study in their own right.

Acknowledgements

We thank I.Matute for assistance in producing the initial catalogue and M.Moshir for fruitful discussions. We are grateful to O.Laurent and H.Roussel for providing the ISOCAM fluxes for some of the RMS sample sources. We acknowledge and thank the EC TMR extragalactic networks for postdoctoral grant support. This research has made use of the NASA/IPAC Extragalactic Database (NED) which is operated by the Jet Propulsion Laboratory, California Institute of Technology, under contract with NASA.

References

1. Elbaz, D., Cesarsky, C., Fadda, D., Aussel, H., Désert, F.-X., et al. (1999) A&A, 351, L37
2. Oliver, S., Rowan-Robinson, M., Alexander, D.M., Almaini, O., Balcells, M., et al. (1999), in press
3. Aussel, H., Cesarsky, C., Elbaz, D., Starck, J. (1999) A&A, 342, 313
4. Clements, D.L., Désert, F.-X., Franceschini, A., Reach, W.T., Baker, A.C., Davies, J.K., Cesarsky, C. (1999) A&A, 346, 383
5. Rush, B., Malkan, M.A., Spinoglio, L. (1993) ApJS, 89, 1 (RMS)
6. Fang, F., Shupe, D.L., Xu, C., Hacking, P.B. (1998) ApJ, 500, 693 (FSXH)
7. Baldwin, J.A., Phillips, M.M., Terlevich, R. (1981) PASP, 93, 5
8. Poggianti, B.M., Smail, I., Dressler, A., Couch, W.J., Barger, A.J., et al. (1999) ApJ, 518, 576
9. Ho, L., Filippenko, A.V., Sargent, W.L.W. (1997) ApJS, 326, 653
10. Moshir, M., et al. (1992) Explanatory Supplement to the IRAS Faint Source Survey, Version 2, Pasadena, JPL
11. Tran, Q.D. (1998) PhD thesis, University of Paris, Orsay, France
12. Cesarsky, D., Lequeux, J., Abergel, A., Perault, M., Palazzi, E., Madden, S., Tran, D. (1996) A&A, 315, L309
13. Cesarsky, D., Lequeux, J., Abergel, A., Perault, M., Palazzi, E., Madden, S., Tran, D. (1996) A&A, 315, L305
14. Xu, C., Hacking, P.B., Fang, F., Shupe, D.L., Lonsdale, C.J., et al. (1998) ApJ, 508, 576
15. Saunders, W., Oliver, S., Keeble, O., Rowan-Robinson, M., Canavezes, A., et al. (1997) in Maddox, S., Aragon-Salamanca, A., Wide Field Spectroscopy and the Distant Universe, World Scientific Press, Singapore
16. Lasker, B.M., Sturch, C.R., McLean, B.J., Russel, J.L., Jenker, H., Shara, M.M. (1990) AJ, 99, 2019
17. Lawrence, A., Rowan-Robinson, M., Ellis, R.S., Frenk. C.S., Efstathiou. G., et al. (1999) MNRAS, 308, 897
18. Shupe, D.L., Fang, F., Hacking, P.B., Huchra, J.P. (1998) ApJ, 501, 597

The Role of Luminous Infrared Galaxies at z $\sim$ 1 as Revealed by the 15 μm Extragalactic Background Light

David Elbaz

CEA-Saclay, SAp/DAPNIA/DSM, and UCSC, Physics Department, Santa Cruz, CA 95064, USA

Abstract. Deep mid-infrared sky surveys have revealed a strong excess, compared to the local universe, of faint but intrinsically bright galaxies at redshifts close to $z \sim 0.8$. A preliminary study of a sample of optical counterparts with spectroscopic redshifts in the Hubble Deep Field North (HDFN) and in one of the Canada-France Redshift Survey (CFRS) fields, indicates that they are massive ($M \sim 10^{11}\ M_{\odot}$) and bright (several $10^{11}\ L_{\odot}$) galaxies. The contribution of these galaxies, brighter than 50 μJy ($AB \sim 20$), to the 15 μm extragalactic background light (E.B.L.) is $2.2 \pm 0.8\ nW\ m^{-2}\ sr^{-1}$. This energy density is as high as 60% (30%) of the one produced by the 60 times more numerous galaxies detected in the HDFN in the B_{450}-band (I_{814}-band) down to $AB = 29$. The ratio of the energy radiated by luminous infrared galaxies at 15 μm over that radiated by all types of galaxies in the optical was therefore two orders of magnitude higher at $z \sim 0.8$ than today. Depending on their spectral energy distribution, these galaxies must produce more than 30 % of the 140 μm EBL, where the cosmic infrared background peaks. Hence, they produce a significant fraction of the overall energy radiated by galaxies during the hubble time, may it be due to nucleosynthesis or to accretion around a black hole.

1 Introduction

In a previous paper (Elbaz et al 1999 [5], hereafter Paper I, see also Cesarsky, in these proceedings), we have presented the results of the ISOCAM 15 μm extragalactic deep surveys in the form of number counts. Both the slope and the high normalization of these counts rule out the predictions based on the IRAS counts assuming no evolution of the galaxy population. In this paper, we propose to compare the integrated energy radiated by these individual galaxies to the one measured in the optical. We also take advantage of the redshift distribution of the faint sources detected in the HDFN (Aussel et al. 1999, 2000 [1,2]) and CFRS (Flores et al. 1999 [6]) to estimate the evolution of this energy density as a function of redshift.

2 Optical Counterparts to the 15 μm Galaxies

In spite of its small telecope diameter of 60 cm, the ISO satellite, with its mid-infrared camera ISOCAM, allowed us for the first time to find, with a

D. Lemke, M. Stickel, and K. Wilke (Eds.): LNP 548, pp. 121–126, 2000.

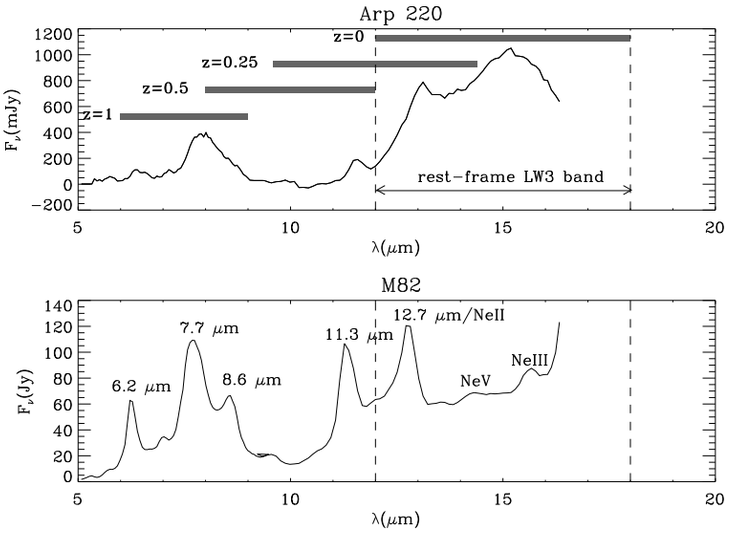

Fig. 1. ISOCAM CVF spectra of Arp 220 (upper plot) and M82 (lower plot). The 15 μm broadband (12-18 μm, LW3 filter) is redshifted from z=0 to z=1. Above $z \sim 1.5$, the dust emission becomes negligible and the galaxy becomes too faint to be detected by ISOCAM, unless the dust is heated to very high temperature by an AGN (high continuum below 5 μm). The right side of the spectra is dominated by a hot continuum due to very small grains of dust while the left side is dominated by aromatic features.

remarkable precision, some optical counterparts, and therefore spectroscopic redshifts, to a large number of luminous infrared galaxies ($L > 10^{11}\ L_\odot$) at redshifts up to $z \sim 1.2$ (while it is much more problematic in far-IR with ISOPHOT or in the sub-mm with SCUBA). The astrometric accuracy of the ISOCAM micro-scanning images is of the order of 2 arcsec and the final image pixels are of 3 arcsec, after over-sampling the 6 arcsec physical pixels. At 15 μm the FWHM of the PSF is $\sim$ 10 arcsec, hence an average of 5-6 optical sources lie in the error box for a field as deep as the HDF. However, in most cases (but not all), we find a single bright galaxy lying within 3 arcsec of the ISOCAM centroid. We have checked (see Aussel et al. 1999, 2000 [1,2], Flores et al. 1999 [6]) that this galaxy is also the one with the highest probability of association (in most cases), assuming that the optical sources follow a poissonian statistics, calculated with the following formula for the probability of a pure chance association of a given optical source (Flores et al. 1999 [6]):

$$P(d, I) = 1 - e^{-n(I)\pi d^2} \quad (1)$$

where $n(I)$ is the integrated surface density of sources of the magnitude I of the optical source and d is the distance between the optical source and the ISOCAM source. There is a reason why most optical counterparts to ISOCAM sources are obvious: due to k-correction, ISOCAM cannot detect galaxies above a redshift larger than ~ 1.5, above which the region of the spectrum due to dust emission exits from the 15 μm band (see Fig. 1).

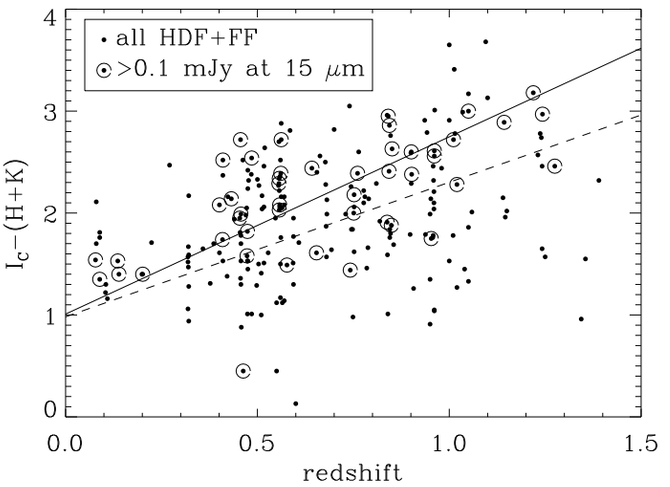

Fig. 2. I(Kron-Cousins)-(H+K) color (from Barger et al. 2000) versus redshift for field galaxies (dots) and galaxies detected above 0.1 mJy at 15 μm by ISOCAM (dots surrounded by circles), in the Hubble Deep Field North plus its Flanking Fields. Plain line: linear fit to the colors of ISOCAM galaxies. Dashed line: same for all galaxies.

The two fields where spectroscopic redshifts are already available, HDFN and CFRS, have yielded to the same conclusion in terms of redshift distribution: the 15 μm galaxies appear to be peaked around $z \sim 0.7 - 0.8$. This is very close to the mean redshift of the faint blue galaxies which dominate the optical light (z∼0.6, Pozzetti et al. 1998 [12]). However, the comparison of the colours of the optical counterparts to the 15 μm galaxies with the general colours of field galaxies in the HDFN indicates that the 15 μm galaxies are spread over the whole colour range and do not exhibit any significant signature (see Fig. 2).

The median colour of the HDF+FF galaxies is $I_C-(H+K) = 2$, while the sub-sample of galaxies brighter than 0.1 mJy at 15 μm have a median colour of I_C-(H+K)= 2.3. Hence, the mid-IR galaxies are slightly redder than the rest of the optical galaxies, but not enough to allow one to select them from their

optical colour only. The linear fit to the I_C-(H+K) versus redshift plot of the two samples of galaxies in Fig. 2 also shows a weak tendancy for the 'dusty' galaxies to redden slightly faster with increasing redshift than the natural (due to k-correction) reddening of the whole population of field galaxies.

From the full sample of 15 μm galaxies with known redshift and optical-near IR magnitudes, we find that these galaxies are massive ($\sim 10^{11}$ $M_\odot$, Franceschini et al. [8]). The assessment of their bolometric luminosity requires the assumption of a spectral energy distribution, which is largely uncertain since the ratio of the far-IR over mid-IR flux densities is highly variable among galaxies. However, no galaxy fainter than $\sim 10^{11}$ $L_\odot$, with a SED similar to local galaxies, could have been detected above 0.1 mJy at $z \sim 0.7$ in the HDFN. Hence most of them are at least LIRGs. They could also be ULIRGs, i.e. brighter than $\sim 10^{12}$ $L_\odot$, but if all of them where as extreme ULIRGs as Arp 220, then they would over-produce both the SCUBA 850 μm number counts and the DIRBE 140 μm EBL (see next Section).

3 Extragalactic Background Light

By integrating the differential number counts presented in the Fig.2 of Paper I, one can derive the 15 μm extragalactic background light (EBL) produced by these galaxies and use it as a lower limit to the total 15 μm EBL. We performed this calculation by taking into account a large number of surveys overlapping in flux density, hence including large scale fluctuations in the error bars, for a total of 614 galaxies in both the Northern (Lockman Hole, Hubble Deep Field-North, A2390) and Southern (Marano Field, HDF-South) hemispheres. We find that the sum of all galaxies brighter than $S_{15\,\mu m}$ =0.05 mJy produce a 15 μm EBL of: 2.2 ± 0.8 $nW\ m^{-2}\ sr^{-1}$ (see Fig. 3).

This is already as high as ∼60% of the B band EBL ($3.7^{+0.7}_{-0.5}$ $nW\ m^{-2}\ sr^{-1}$) and ∼30 % of the V or I EBL (respectively $6.7^{+1.2}_{-0.9}$ and $7.8^{+1.6}_{-0.9}$ $nW\ m^{-2}\ sr^{-1}$) measured in the HDF-N by Pozzetti et al. 1998 [12]. This result is even more striking when one considers that among 1000 galaxies brighter than the limiting magnitude of the HDF of I(AB)=29, only 3 are brighter than 0.1 mJy at 15 μm. This ratio can be compared to the one found by Soifer & Neugebauer (1991) [14] in the local universe (z<0.2) where the light radiated by galaxies in the full infrared range, from 8 to 1000 μm, makes only 30 % of the optical light, while about 10 % of the infrared light comes from mid-infrared range. If we consider only the infrared light coming from LIRGs, which are the only galaxies detected by ISOCAM at $z \sim 0.7 - 0.8$, then the ratio of the 8–1000 μm infrared over optical energy density becomes 2 % instead of 30 %, and ten times less for the mid-infrared light (in $\nu S\nu$). This implies that the ratio of the mid-infrared over optical light produced by LIRGs was two orders of magnitude higher at $z \sim 1$ than it is today at $z = 0$. Consequently, the luminous infrared galaxies discovered by IRAS (Sanders & Mirabel 1996 [13]) cannot anymore be considered as peculiar cases producing a tiny frac-

tion of the energy content of the universe. Even assuming a conservative SED for these galaxies, they must produce a significant contribution (of the order of 30 % in the case of M82, see Fig. 3) to the 140 μm EBL as measured by DIRBE (Lagache et al. 1999 [10], Hauser et al. 1998 [9]).

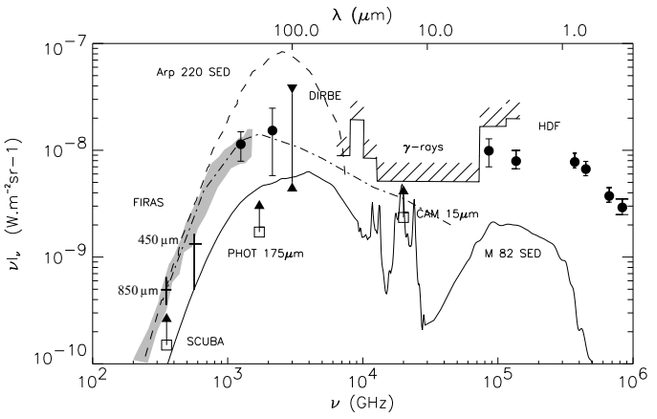

Fig. 3. Cosmic background from UV to mm. Open squares give the lower limits from ISO (ISOCAM-15 μm and ISOPHOT-175 μm) and SCUBA-850 μm (Blain et al. 1999 [4]). The optical-UV points are from Pozzetti et al. (1998) [12]. The COBE FIRAS (grey area) and DIRBE 140 & 240 μm (filled circles) data are from Lagache et al. (1999) [10]. Upper limit from the γ-ray emission of Mrk 501 (Stanev & Franceschini 1998) [15]. Dot-dashed curve: model from Franceschini et al. (1997) [7].

4 Discussion

The galaxies producing the strong evolution measured in the ISOCAM mid-IR number counts are very different from the galaxies producing the evolution seen in the optical-UV and used to calculate the redshift evolution of the star formation density per co-moving volume of the 'Madau' plot (Madau et al. 1996 [11]). Hence the star formation associated to these galaxies must be added to the one measured from the rest-frame UV light. Adopting a simple approach to this contribution based on energetic considerations, one finds that the IR side of the history of star formation must follow a very rapid evolution, as measured by the rapid increase of the ratio of infrared

over optical light from $z = 0$ to $z \sim 1$. The new picture drawn by the ISOCAM results is the one of a universe where most of the present-day stars are produced in a dust-enshrouded phase similar to what is observed in local LIRGs (Flores et al. 1999 [6]). Ground-based follow-ups are now necessary to understand the nature of these galaxies and compare different star formation indicators (UV; Hα, see Rigopoulou et al. in these proceedings; radio). The survey by Chandra and XMM of some of the ISOCAM fields in the hard X-ray will be crucial to determine the contribution of dusty AGNs to the ISOCAM sources.

References

1. Aussel H., Cesarsky C., Elbaz D., et al., 1999, A&A 342, 313
2. Aussel H., et al., 2000, in preparation
3. Barger, A., et al., 2000, submitted to AJ
4. Blain, A.W., Smail, I., Ivison, R., Kneib, J.P., To appear in 'The Hy-redshift universe', Astronomical Society of the Pacific Conference Series Volume 193, eds. A.J. Bunker & W.J.M. van Breugel
5. Elbaz, D., Cesarsky, C. J., Fadda, D., et al., 1999, A&A 351L, 37
6. Flores H., Hammer F., Thuan T., et al., 1999, ApJ 517, 148
7. Franceschini, A., Aussel, H., Bressan, A., et al., 1997, The Far Infrared and Submillimetre Universe. Edited by A. Wilson. Noordwijk, The Netherlands : ESA, 1997., p.159, astro-ph/9707080
8. Franceschini, A., et al., 2000, in preparation
9. Hauser M.G., Arendt R.G., Kelsall T., et al., 1998, ApJ 508, 25
10. Lagache G., Abergel A., Boulanger F., et al., 1999, A&A 344, 322
11. Madau, P., Ferguson, H.C., Disckinson, M.E., et al., 1996, MNRAS, 283, 1388
12. Pozzetti L., Madau P., Zamorani G., Ferguson H.C., Bruzual G.A., 1998, MNRAS, 298, 1133
13. Sanders D.B., Mirabel I.F., 1996, *Ann. Rev. Astron. Astrophys.* 34, 749
14. Soifer B.T., Neugebauer G., 1991, AJ 101, 354
15. Stanev, T., Franceschini, A., 1998, ApJ 494, L159

The Star Formation History of the Universe

Michael Rowan-Robinson

Astrophysics Group, Blackett Laboratory,
Imperial College of Science Technology and Medicine
Prince Consort Road, London SW7 2BZ

Abstract. A simple and versatile parameterized approach to the star formation history allows a quantitative investigation of the constraints from far infrared and submillimetre counts and background intensity measurements. A good fit to the counts, the 850 μm background and the star formation history can be found in an $\Omega_o = 1$ universe, but this model fails to account for even the lowest estimates of the 140-350 μm background by a factor of 2. Either the observed values are overestimated or we need a new population of submm sources. The problem is eased in a $\Lambda = 0$, $\Omega_o = 0.3$ or $\Lambda = 0.7$, $\Omega_o = 0.3$ universe.

1 Introduction

Many authors have attempted to model the star formation history of the universe (eg [4,24]) or equivalently the evolution of the starburst galaxy population (eg [10,11,12,2,23,14,5,3]). Most of these studies explore a small range of models designed to fit the available observations. In the present paper I report the results of a parameterized approach to the star formation history of the universe, which allows a large category of possible histories to be explored and quantified. The parametrized models can be compared with a wide range of source-count and background data at far infrared and submillimetre wavelengths to narrow down the parameter space that the star formation history can occupy.

A Hubble constant of 50 km/s/Mpc is used throughout, and $\Omega_o = 1$ (unless otherwise stated).

2 Parametrized Approach to Star Formation History

To study what constraints on the star formation history can be derived from source-counts and background intensity measurements at far infrared and submm wavelengths, I present here a parameterized approach to the problem, investigating a wide range of possible star formation histories.

The constraints we have on the star formation rate, $\dot{\phi_*}$(t) are that: (i) it is zero for t = 0, (ii) it is finite at $t = t_o$, (iii) it increases with z out to at least z = 1 (and from (i) must eventually decrease at high z).

A simple mathematical form consistent with these constraints is

$$\dot{\phi_*}(t)/\dot{\phi_*}(t_o) = \exp \mathrm{Q}(1\text{-}(t/t_o))\ (t/t_o)^P \quad (1)$$

D. Lemke, M. Stickel, and K. Wilke (Eds.): LNP 548, pp. 129–135, 2000.

where P and Q are parameters (P > 0 to satisfy (i), Q > 0 to satisfy (iii)). I assume that $\dot{\phi}_*(t) = 0$ for z > 10.

Equation (1) provides a simple but versatile parameterization of the star formation history, capable of reproducing most physically realistic, single-population scenarios.

Given an assumed (P,Q) I then determine the 60 μm luminosity function, using the IRAS 1.2 Jy sample [8].

I fit this with the form assumed by Saunders et al (1990) [33]

$$\eta(L) = C_*(L/L_*)^{1-\alpha} e^{-0.5[log_{10}(1+L/L_*)/\sigma]^2} \quad (2)$$

and find that the luminosity function parameters can be well approximated as follows:

σ = 0.765-0.04 W

$log_{10}L_*$ = 8.42 + 0.07 W - 2 $log_{10}(H_o/100)$

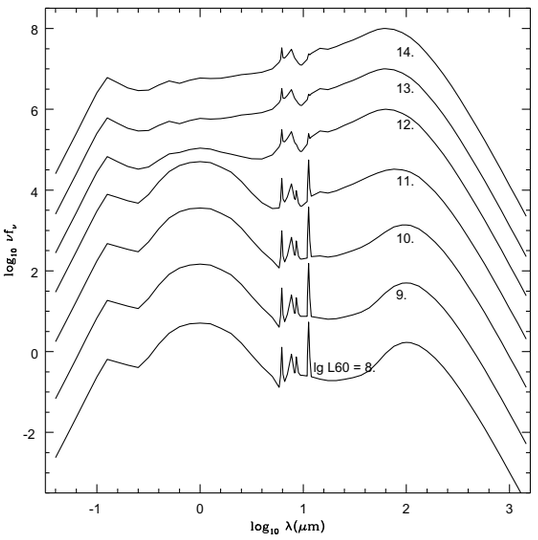

Fig. 1. Adopted spectral energy distributions for infrared galaxies based on a mixture of four components: cirrus, M82-starburst, A220-starburst (models from [7]), AGN dust torus (model from [29]), as a function of 60 μm luminosity, ranging from $log_{10}(L_{60}/L_\odot)$ = 8 to 14.

where W = 0.825 Q - P, and I have assumed fixed values for α = 1.09, C_* = 0.027 $(H_o/100)^3$. It is not clear that previous studies have correctly taken account of the need to change the 60 μm luminosity function as the rate of evolution is varied. The study of Guiderdoni et al (1998) [14] explicitly

violates the known constraints on the 60 μm luminosity function at the high luminosity end and as a result the models predict far too many high redshift galaxies at a flux-limit of 0.2 Jy at 60 μm, where substantial redshift surveys have already taken place.

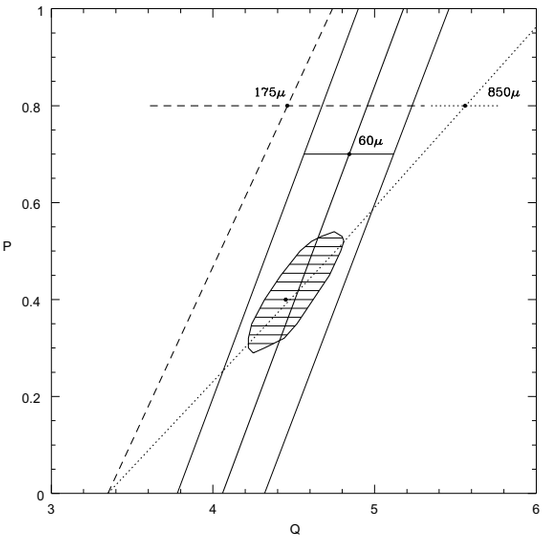

Fig. 2. P-Q diagram, with loci for models fitting 60 (solid curve), 175 (broken curve) and 850 μm counts (dotted curve). Counts loci correspond to N60(0.25Jy) = 2.0, N175(0.1Jy) = 39 [18], log N850(4mJy) = 900 per sq deg [17].

To transform this 60 μm luminosity function to other wavelengths I assume that the spectral energy distributions of galaxies are a mixture of four components, a starburst component, a 'cirrus' component, an Arp 220-like starburst, and an AGN dust torus (cf [28,31,29]), with the proportions of each depending on 60 μm luminosity. The normalization between far infrared and optical-uv components is determined by L(60μm)/L(0.8μm) = 0.28 for the cirrus component, 5 for the starburst component, and 50 for the Arp220 component. Note that the dust emission from the starburst model peaks at 60 μm while the cirrus model peaks at 200 μm, and there are distinct differences in the predicted PAH spectra. The starburst model is a good fit to multiwavelength data for M82 and NGC6092 [7], and also to far infrared and submillimetre data for luminous starburst [27].

The proportions of the four components (at 60 μm) as a function of luminosity have been chosen to give the correct mean relations in the S(25)/S12), S(60)/S925), S(100)/S(60) and S(60)/S(850) versus L(60) diagrams. The pro-

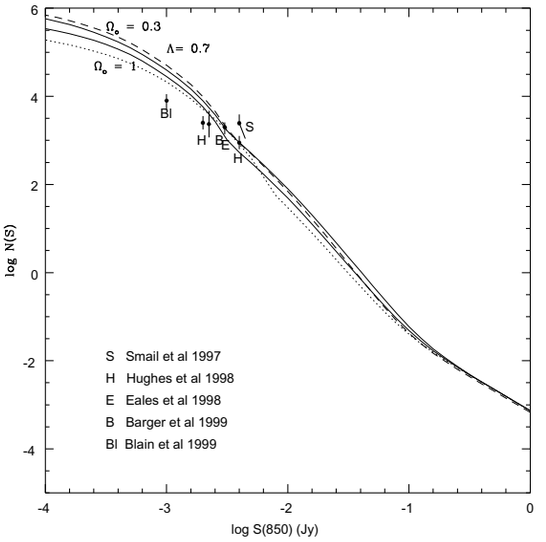

Fig. 3. Integral source counts at 850 μm. Data are from Hughes et al (1998) [17], Eales et al (1999) [6], Smail et al (1997) [35], Barger et al (1999) [1], Blain et al (1999) [2]. The 3 models shown are, for $\Omega_o = 1$ and (P,Q) = (0.4, 4.45) (dotted curve), for $\Omega_o = 0.3$, (P,Q) = (0.3, 5.1) (solid curve) and for $\Lambda = 0.7$, (P,Q) = (0.8, 6.4) (broken curve).

portion of galaxies containing AGN dust tori is assumed to increase from about 10% at lg L(60) = 11 to 50% at lg L(60) = 13. The resulting mean spectral energy distributions (sed) as a function of L(60) are shown in Fig 1.

I can now predict the counts and background intensity at any wavelength and by comparing with observed values, constrain loci in the P-Q plane. Fig 2 shows a number of such loci for the case of pure luminosity evolution in an Einstein de Sitter model ($\Omega = 1$). Figure 3, 4 shows integral counts at 850 and 175 μm. Figure 5 shows the spectrum of the integrated background radiation, compared with selected models. Because of the simplistic nature of the assumed optical seds, I have not attempted to show optical counts, but it is of interest to try to get roughly the correct balance of optical and far infrared/submm background radiation.

We see that models consistent with the far infrared and submillimeter counts can be found, eg (P,Q) = (0.4,4.45), and that such models also are consistent with the observed 850 μm background. However stronger evolution is required to fit the 140-350 μm background intensity, and such models are inconsistent with the observed counts.

An important constraint on the models is that the total mass of stars produced in galaxies should be greater than or equal to the mass of stars

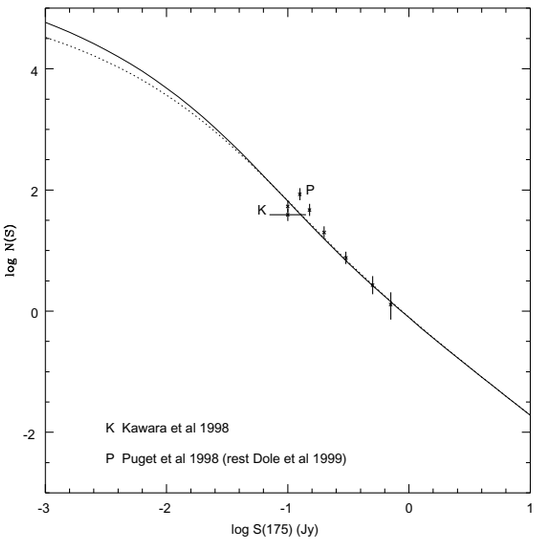

Fig. 4. Source counts at 175 μm. Data are from Kawara et al (1988) [18], Puget et al (1998) [26], Dole et al (1999). Models as for Fig 3 for $\Omega_o = 1$ and $\Omega_o = 0.3$.

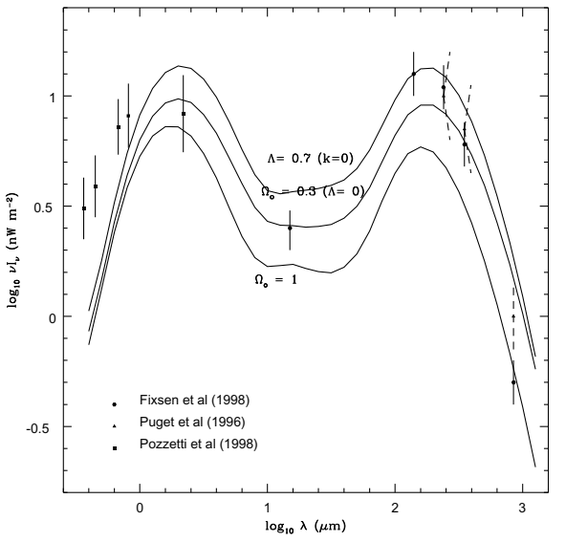

Fig. 5. Predicted spectrum of integrated background for same models as Fig 2. Data from Fixsen et al (1998) [9], Puget et al (1996) [26] (far ir and submm), Pozzetti et al (1998) [25] (opt and uv).

observed, $\Omega_* \geq 0.006 \pm 0.0018(H_o/50)^{-1}$ [19], and that it should be less than the total density of baryons in the universe, $\Omega_* \leq 0.05 \pm 0.01(H_o/50)^{-2}$ [36]. The models which fit the submm source-counts tend to require values for Ω_* significantly greater than the observed value for an assumed Salpeter IMF, possibly implying that the IMF is truncated at higher redshifts.

We might expect that the cosmological model could have a significant effect on the relationship between predicted counts and predicted background intensity, since the latter is sensitive to how the volume element and look-back time change with redshift.

To test this we have explored models with $\Lambda = 0$, $\Omega = 0.3$, and $\Lambda = 0.7$, $\Omega = 0.3$. Predicted counts and background spectra are shown for these models in Figs 3-5.

Thus within the framework of the types of star formation history considered in section 5, there is a clear sensitivity to cosmological parameters, with $\Omega_o = 0.3$ preferred to $\Omega_o = 1$. This not to say that more complex assumptions about the star formation history, for example the inclusion of a dust-enshrouded population not represented at low redshift as in Franceschini et al (1997) [12] , might not be consistent with $\Omega_o = 1$. The full dependence on cosmological parameters will be explored in later work.

References

1. Barger A.J., Cowie L.L., Sanders D.B., Fulton E., Taniguchi Y., Sato Y., Kawara K., Okuda H., 1998, Nat 394, 248
2. Blain A.W., Longair M.S., 1993, MN 264, 509
3. Blain A.W., Smail I., Ivison R.J., Kneib J.-P., 1999, MN 302, 632
4. Cole S., Aragon-Salamanca A., Frenk C.S., Navarro J.F., Zepf S.E., 1994, MN 271, 781
5. Dwek E., et al, 1998, ApJ 508, 106
6. Eales S., Lilly S.J., Gear W.K., Dunne L., Bond J.R., Hammer F., Le Fevre O., Crampton D., 1999, ApJL (in press), astro-ph/9808040
7. Efstathiou A., Rowan-Robinson M., Siebenmorgen R., 1999, MN (in press)
8. Fisher K.B., Huchra J.P., Strauss M.A., Davis M., Yahil A., Schlegel D., 1995, ApJS 100, 69
9. Fixsen D.J., Dwek E., Mather J.C., Bennett C.L., Shafer R.A., 1998, ApJ 508, 123
10. Franceschini A., Toffolatti L., Mazzei P., Danese L., De Zotti G., 1991, AAS 89, 285
11. Franceschini A., Mazzei, P., de Zotti, G., Danese, L., 1994, ApJ 427, 140
12. Franceschini A., Silva L., Fasano G., Granato G.L., Bressan A., Arnouts S., Danese L., 1998, ApJ 506, 600
13. Gregorich D.T., Neugebauer G., Soifer B.T., Gunn J.E., Herter T.L., 1995, AJ 110, 259
14. Guiderdoni B, Hivon E., Bouchet F.R., Maffei B., 1998, MN 295, 877
15. Hacking P.B. and Houck J., 1987, ApJS 63, 311
16. Hauser M.G., et al, 1998, ApJ 508,25

17. Hughes D.H., et al, 1998, Nat 394, 241
18. Kawara K., et al, 1998, AA 336, L9
19. Lanzetta K.M., Yahil A., Fernandez-Soto A., 1996, Nature 381, 759
20. Lonsdale C.J., Hacking P.B., Conrow T.P., Rowan-Robinson M., 1990, ApJ 358, 60
21. Lutz D., Spoon H.W.W., Rigopoulou D., Moorwood A.F.M, Genzel R., 1998, ApJ 505, L103
22. Madau, P., Ferguson, H.C., Dickinson, M.E., Giavalisco, M., Steidel, C.C., Fruchter, A., 1996, MNRAS 283, 1388
23. Pearson, C., Rowan-Robinson, M., 1996, MN 283, 174
24. Pei, Y.C., and Fall, S.M., 1995, ApJ 454, 69
25. Pozzetti L., Madau P., Ferguson H.C., Zamorani G., Bruzual G.A., 1998, MN 298,1133
26. Puget, J.-L., Abergal A., Bernard J.-P., Boulanger F., Burton W.B., Desert F.-X., Hartmann D., 1966, AA 308, 5
27. Rigopoulou D., Lawrence A., Rowan-Robinson M., 1996, MN 288, 1049
28. Rowan-Robinson M., and Crawford J., 1989, MN 238, 523
29. Rowan-Robinson M., 1995, MNRAS 272, 737
30. Rowan-Robinson, M., 1992, MN 258, 787
31. Rowan-Robinson, M., Efstathiou, A., 1993, MN 263, 675
32. Rowan-Robinson M. et al, 1997, MN 289, 490
33. Saunders, W., Rowan-Robinson, M., Lawrence, A., Efstathiou, G., Kaiser, N., Frenk, C.S., 1990, MN 242, 318
34. Schlegel D.J., Finkbeiner D.P., Davis M., 1998, ApJ 500, 525
35. Smail I., Ivison R.J., Blain A.W., 1997, ApJL 490, L5
36. Walker T.P., Steigman G., Schramm D.N., Olive K.A., Kang H.-S., 1991, ApJ 376, 51

Implications of the Cosmic Infrared Background for the Redshift Distribution of Infrared Galaxies

Jean-Loup Puget, Guilaine Lagache, and Richard Gispert

Institut d'Astrophysique Spatiale Université de Paris-Sud, Bâtiment 121, F-91405 Orsay Cedex, France

Abstract. The cosmic infrared background detected in the COBE data contains a surprisingly large fraction of the cosmic background due to distant galaxies. The spectrum of this background decreases at long wavelength with a slope much less steep than the one observed for individual infrared galaxies. Considering the variety of long wavelengths spectra observed for these galaxies we have explored the range of possible redshift evolution histories for these galaxies. We show that only a comoving production rate of far infrared radiation with strong evolution at low redshifts but little evolution between redshifts 1.5 and 3.5 is allowed by the cosmic background spectrum. The detailed low redshift evolution is much better constrained by the ISO deep surveys than by the background.

1 Introduction

The history of star formation in the Universe is one of key function in physical cosmology. It is closely linked to galaxy formation and evolution and controls the second most important contribution to the cosmic electromagnetic background after the Cosmic Microwave Background (CMB) generated at the time of recombination at a redshift around 1000. It has been pointed out many times in the past 30 years, that measurements of the cosmic background radiated by all galaxies over the history of the Universe would be extremely valuable for physical cosmology. It would strongly constrain models for Galaxy formation and evolution (see for example Peebles and Partridge 1967). This background is expected to be composed of three main components:
- the stellar radiation in galaxies concentrated in the ultra-violet and visible with a redshifted component in the near infrared
- a fraction of the stellar radiation absorbed by dust either in the galaxies or in the intergalactic medium and found in the far infrared and submillimeter
- the radiation from active galactic nuclei which has a broad spectral distribution including a high energy component.

The energy in the first two components is derived from nucleosynthesis in stars, the last one probably derived from gravitational energy of accreted matter onto massive black holes. In the last years the cosmic background at

D. Lemke, M. Stickel, and K. Wilke (Eds.): LNP 548, pp. 136–140, 2000.

visible, infrared and submillimeter wavelengths has been finally measured at the longest wavelengths and strongly constained by very deep source counts and upper limits on the diffuse isotropic emission at shorter wavelengths.

The far infrared radiation production rate as a function of redshift can be deduced from the spectrum of the cosmic background in the submillimeter range under relatively simple hypotheses. If the cosmic far infrared background is dominated by very luminous infrared galaxies as indicated by the ISO results reported at this conference ([1], [2], [3], [4], [6]) we know that these sources radiate the bulk of their energy between 60 and 100 μm and present at long wavelengths a spectrum much steeper than the spectrum of the cosmic background. It is easy to understand that in this case, sources filling the background at 150 μm must be relatively low reshift sources (z between 0.5 and 1.5) and these cannot fill the longer wavelength background with its relatively flat spectrum. The long wavelength part has to be filled with the emission from infrared galaxies at larger redshifts. Nevertheless the inversion allowing to derive the far infrared radiation production rate as a function of redshift is not unique if the spectrum of the sources is too broad. Furthermore even under the assumption that the submillimeter background is dominated by luminous infrared galaxies, the average spectral energy distribution (SED) of the population of infrared galaxies at redshift 1 or larger is not known and must be constrained from astrophysical considerations using the observations of such galaxies locally or at moderate redshifts.

2 Constraining the History of Far Infrared Radiation Production in the Universe

Considering the limitations given in the previous section, what can be done is:

- to establish the range within which the SED of luminous infrared galaxies should lie from astrophysical considerations
- make the assumption that the galaxy formation and evolution process leads to a smooth redshift history of the infrared production rate which can be thus represented with a small number of free parameters
- explore through a Monte-Carlo calculation the full range of these parameters for a set of reasonable SEDs and a set of cosmological models. In each case find the redshift distribution which optimises the fit to the data and finds the acceptable range around this best fit history which contains the fit within a given χ^2.

This was done by [7] and they show that even when allowing the emission peak wavelength of the SED to go from 75 to 140 μm, and changing the long wavelength emissivity index from 1.3 to 2 the far infrared radiation production rate between redshift 1.5 and 4 is strongly constrained.

This is illustrated in figure 1.

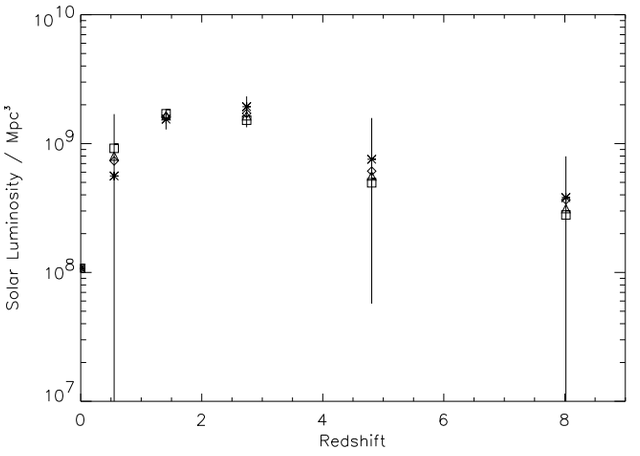

Fig. 1. Far infrared production rate (derived from the cosmic far infrared background determination of [5]) as a function of redshift for different long wavelength emissivity index (stars: α=2, diamonds: α=1.7, triangles: α=1.5, squares: α=1.3)

3 Analysis of the Results

The most striking result is the stability of the far infrared radiation production rate per comoving unit volume between redshift 1 and 4 which must be roughly constant at a value about 20 times the local value established by [8]. This result is shown to be almost independant of SED chosen as well as independant of the cosmological model adopted. This can be understood easily. If one makes the extreme assumption that the radiation of infrared galaxies is concentrated at a single wavelength, the spectrum of the background can be easily inverted to get the radiation production rate. If the production rate of infrared radiation per comoving volume element at a single frequency ν_o is $\phi_{\nu_o}(z)$, the resulting cosmic background in the simple case of Euclidean Universe will be given by:

$$\nu I_\nu = \int\int \phi_{\nu_o}(z) H_o^{-1} (\nu/\nu_o)^{5/2} \delta(z - \nu/\nu_o) d\nu dz$$

This integral can be easily inverted to extract the infrared production rate as a function of redshift:

$$\frac{\phi_{\nu_o}(z)}{L_\odot Mpc^{-3}} = 6.5\,10^7 \frac{\nu I_\nu}{10^{-8} W m^{-2} sr^{-1}} (\nu/\nu_o)^{-5/2}$$

For a simple approximation of the background with power laws

$$\nu I_\nu = 17\,10^{-8} (\nu/\nu_o)^{2.5} W m^{-2} sr^{-1}$$

valid between 200 μm and 500 μm, and

$$\nu I_\nu = 25\,10^{-8}(\nu/\nu_o)^3 W m^{-2} sr^{-1}$$

valid between 500 μm and 1.5 mm, ($\nu_o = 310^{12}$Hz), we deduce

$$\phi_{\nu_o}(z) = 1.1\,10^9 L_\odot Mpc^{-3}$$

for $1 < z < 4$ and

$$\phi_{\nu_o}(z) = 1.6\,10^9(1+z)^{-0.5}(\frac{\nu_o}{310^{12}Hz})^{0.5} L_\odot Mpc^{-3}$$

for $z > 4$.
There is *nodependance* of the energy production rate with ν_o for z between 1 and 4 because the slope of the background corresponds to the case of no evolution of the comoving radiation production rate.

The radiation produced is shifted in frequency and diluted by expansion by factors which depend only on redshift. If we express the production rate of energy per redshift interval, there is no dependance on the cosmological model. The cosmological model comes only when we express the energy production rate per unit time. It is thus not surprising that the cosmic infrared background, considering its spectrum, contrains very strongly the energy production rate as a function of redshifts above redshift 1. Going to large redshifts, the relevant part of the cosmic background spectrum is the very long wavelength part which becomes very noisy. Furthermore the spectrum of the galaxies at long wavelengths start to become a significant parameter. If luminous infrared galaxies at redshift 1 have flatter spectra in the millimeter range they will fill a larger fraction of the cosmic background reducing the fraction to be attributed to galaxies at larger redshifts. This can be seen in figure 1 when different spectral indexes are used. On the one hand, one can see that even taking an extreme value of the spectral index of 1.3, the production rate up to z=3 is barely affected. On the other hand, the production rate at larger z becomes more dependant on this long wavelength spectrum as expected.

4 Astrophysical Implications

The radiation produced by luminous infrared galaxies is produced either by starburst or by dust enshrouded active nuclei. In both cases the energy comes out in the far infrared with a peak emission around 100 μm. The submillimeter background alone which is the sum of the contributions from these two types of galaxies does not give any information about their respective contributions.

To identify the populations of galaxies making this strong background we need to break this background into sources through deep blind surveys.

This is difficult at wavelengths containing most of the energy (about 150 μm) because these wavelengths can be observed only from space and sensitivity would require both a cold and a large telescope. These requirements are difficult to fulfill simultaneously. ISO with its liquid helium cooled 60 cm telescope was not optimised for such observations which will be better done with FIRST and ALMA in the future. Nevertheless high luminosity sources can be detected with ISOPHOT up to redshifts of 1 or 2. The brightest sources filling about 5% of the background have been found at 170 μm in the FIRBACK survey ([9], [2]). The fluctuations of the extragalactic background at 170 μm dominated by the weaker sources have also been detected for the first time ([10], [11]).

References

1. Cesarsky C.J. et al., this volume
2. Dole H., Gispert R., Lagache G. et al., this volume
3. Elbaz D. et al., this volume
4. Genzel R. et al., this volume
5. Lagache G., Abergel A., Boulanger F. et al., 1999, A&A 344, 322
6. Oliver S. et al., this volume
7. Gispert R., Lagache G., Puget J.L., submitted to A&A
8. Soifer and Neugebauer, 1991, AJ 101, 354
9. Puget J.L., Lagache G., Clements D.L. et al., 1998, A&A 354, 29
10. Lagache G. and Puget J.L., 2000, A&A, in press
11. Lagache G., Puget J.L., Abergel A. et al., this volume

Models for the Infrared Emission from Starburst Galaxies

Andreas Efstathiou[1], Ralf Siebenmorgen[2], and Michael Rowan-Robinson[1]

[1] Imperial College, Blackett Lab, Prince Consort Rd, London SW7 2BW
[2] ISO Science Operations Centre, Astrophysics Division of ESA, Villafranca del Castillo, P.O.Box 50727, E-28080 Madrid

Abstract. We present illustrative models for the UV to millimeter emission of starburst galaxies which are treated as an ensemble of optically thick giant molecular clouds (GMCs) centrally illuminated by recently formed stars. The models follow the evolution of the GMCs due to the ionization-induced expansion of the HII regions and the evolution of the stellar population within the GMC according to the Bruzual & Charlot stellar population synthesis models. The effect of transiently heated dust grains/PAHs to the radiative transfer, as well as multiple scattering, is taken into account.

The expansion of the HII regions and the formation of a narrow neutral shell naturally explains why the emission from PAHs dominates over that from hot dust in the near to mid-IR, an emerging characteristic of the infrared spectra of starburst galaxies.

The models allow us to relate the observed properties of a galaxy to its age and star formation history. We find that exponentially decaying $10^7 - 10^8$ yrs old bursts can explain the IRAS colours of starburst galaxies. The models are also shown to account satisfactorily for the multiwavelength data on the prototypical starburst galaxy M82 and NGC6090, a starburst galaxy recently observed by ISO. In M82 we find evidence for two bursts separated by 10^7yrs. In NGC6090 we find that at least part of the far-IR excess may be due to the age of the burst (6.4×10^7yrs).

1 Introduction

As is well known a large fraction of the power emitted by galaxies (ranging from about 30% in normal galaxies to almost 100% in actively star forming galaxies or starbursts) lies in the infrared part of the spectrum as a result of reprocessing of starlight by dust. Extensive infrared observations of galaxies are therefore necessary in order to describe fully their energy output. With the advent of the Infrared Space Observatory (ISO) the spectra of a number of galaxies in the local Universe have been observed with unprecedented detail in the infrared. They invariably display a variety of absorption/emission features due to dust/molecules. It is clear that radiative transfer calculations in dusty media will be useful for the interpretation of these observations and a development of a better understanding of the origin of the infrared luminosity of galaxies.

Radiative transfer models for the infrared emission of starburst galaxies have been presented before by [1], [2], and [3]. These models used state

D. Lemke, M. Stickel, and K. Wilke (Eds.): LNP 548, pp. 141–148, 2000.

of the art codes for calculating the transfer of radiation in dusty media and incorporated a model for the composition and size distribution of grains in the interstellar medium. The basic assumption of previous starburst models is that a starburst is made up of an ensemble of compact HII regions similar to those found in our galaxy.

All of the above models assume that the cloud ensemble in the starburst consists of a number of identical systems. In this paper we present illustrative models for the evolution of giant molecular clouds (GMCs) induced by massive star formation at their centers and calculate their infrared spectra. In the radiative transfer code we use, the effect of transiently heated particles/PAHs as well as classical grains is included. We also follow the evolution of the stellar populations with the models of [4]. This approach allows us to relate the observed properties of a starburst to its age and its star formation history. We illustrate these models by comparison with the IRAS colours of starburst galaxies as a class and with the multiwavelength data on M82 and NGC6090.

A more extensive discussion of the models presented in this paper can be found in [5].

2 A New Starburst Model

The basic assumption of our model for a starburst galaxy is that star formation takes place primarily within optically thick molecular clouds. This is supported by an array of observational studies (e.g. [6]) which show that molecular clouds are associated with young stars.

The mass of molecular clouds in our Galaxy ranges between $10^2 - 10^7 M_\odot$ with a mass distribution approximately following $M^{-1.5\pm0.1}$ ([7], [8]). It follows that about 70% of molecular mass is associated with GMCs more massive than $10^6 M_\odot$. If the mass distribution in a starburst follows a similar form as the Galactic one, and GMCs are at least as likely to be the sites of massive stars as the less massive molecular clouds, then we would expect the bulk of the luminosity of the starburst to arise from GMCs with a fairly narrow range of mass. In fact low-mass molecular clouds, like the nearby Taurus and Ophiuchus clouds, are known to form predominantly low-mass stars.

An indirect argument that massive star formation in galaxies takes place in GMCs with roughly a power-law mass distribution comes from HST observations of starburst galaxies ([9], [10]) which reveal a population of super star clusters following a luminosity function of a power-law form $\phi(L) \propto L^{-2}$. A similar slope is found for systems of young clusters in other galaxies (e.g. [11]). This luminosity function is quite unlike that of globular clusters although it has been suggested that it could evolve into one ([10]). In our model these star clusters represent the evolved counterparts of star clusters forming within GMCs, with the mass spectrum given above, after they have dispersed their nascent molecular clouds.

In previous studies we assumed that a starburst is an ensemble of identical star forming complexes, which we approximate as spherical. Here we refine this model by considering the fact that, given the starburst takes place over a finite period of time, the star-forming complexes that constitute it are bound to be at different evolutionary stages. We therefore use a simple evolutionary model for HII regions to construct a family of models that predict the infrared spectrum of HII regions as a function of their age. The defining characteristic of this model is that the HII regions formed by the ionizing stellar radiation compress the neutral gas and dust in the GMC to a narrow shell. The family of evolving HII region models will then form the basis of our starburst models under our assumption that the latter are an ensemble of giant HII regions at different evolutionary stages. For more details about the assumed evolutionary scheme the reader is referred to [5].

In order to get a first impression of the characteristics of our models we have in this paper confined our attention to the spherically symmetric case. Clearly, highly non-spherical geometries can arise especially at the later stages of the evolution and we plan to explore these situations in future studies. The model we have assumed for the absorption/emission properties of the dust is an extension of the 'classical' grain model (e.g. [12] and references therein) to take into account the effects of small grains and molecules. The model is described in detail in [13] where it has been shown to account satisfactorily for the emitted spectra of dust in a number of environments (solar neighbourhood, planetary nebulae, star-forming regions).

The method of solution of the radiative transfer problem in dusty media is that used by [14] and [15]. The emission of the transiently heated particles is calculated according to the method of [13]. Proper treatment of the photodestruction of the PAHs and the sublimation of the large grains, at the inner part of the cloud, is taken into account.

3 Evolving HII Region Models

There are basically three free parameters in our model (the GMC total mass M_{GMC}, the efficiency of conversion of gas to stars η, and the initial GMC optical depth τ_V) which we fix by relating to observational constraints where available.

In Figure 1 we plot the spectral energy distributions of a GMC with assumed parameters $M_{GMC} = 10^7 M_\odot, \eta = 0.25$, and $\tau_V = 100$.

The SEDs of the GMCs vary significantly with age. In the early stages of the cloud's evolution its SED is predicted to be warmer and show little signs of PAH emission. This is partly because the stellar population is younger and the radiation field stronger. The main contributing factor though is that there is more hot dust inside the Stromgren sphere than at later times. The weakness of the PAH features is partly due to the stronger near to mid-IR

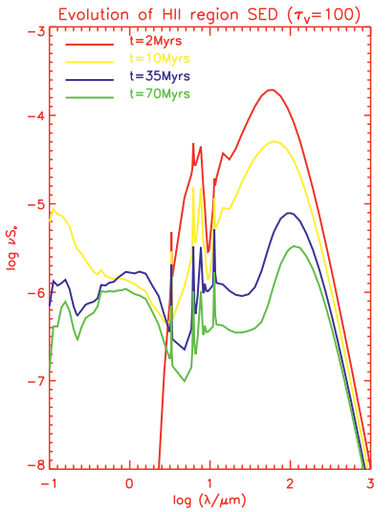

Fig. 1. Spectral energy distributions (right), of the GMCs at four representative ages of the HII region phase. The νS_ν scale is arbitrary but constatnt for all models

continuum emission from large grains and to the higher degree of photodestruction because of the stronger and harsher radiation field.

By 10Myrs the mid-IR spectrum is dominated by the PAH features and quasi-continuum and shows the characteristic shape that is observed in the spectra of starburst galaxies ([16], [17]). At t > 20Myrs the peak of the SEDs of the shells shifts to longer wavelengths and the SEDs become remarkably similar to those of the diffuse medium and cirrus clouds.

4 Evolving Starburst Models

To synthesize the spectral energy distribution from a burst of star formation from those of individual GMCs, let us assume that at time t after the onset of the starburst, the star formation rate (or in our case the number of GMCs forming stars instantaneously with efficiency η) is $\dot{M}_*(t)$. If we further assume that the ensemble of clouds is optically thin, i.e. they don't shadow each other, then the flux from the burst is given by

$$F_\nu(t) = \int_0^t \dot{M}_*(t') S_\nu(t - t') dt' \tag{1}$$

where $S_\nu(t - t')$ is the flux from a GMC $t - t'$ years after the onset of star formation at its centre.

A useful parameterization for the star formation rate in a starburst which has been extensively used (e.g. [18], [17]) is that of exponential decay, $\dot{M}_*(t') \sim e^{-t/\tau}$, where τ is some time constant.

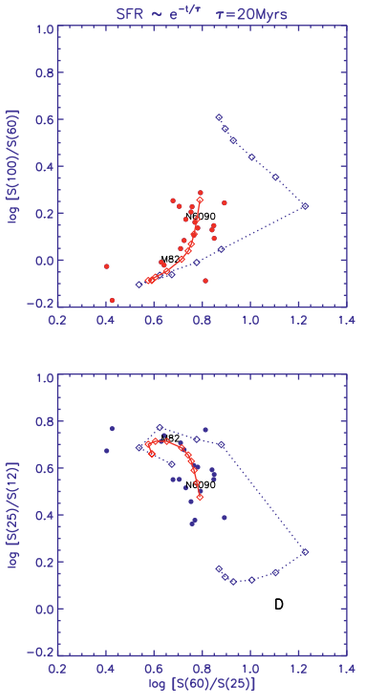

Fig. 2. IRAS colour-colour diagrams of starburst galaxies from the sample of [1] with models superimposed. The dotted line shows the colours of the sequence of GMCs. The ages indicated by open squares are (clockwise on the 25/12 versus 60/25 colour plot) 0, 1.7, 6.6, 10, 17, 26, 32, 37, 45, 57 and 72Myrs. The solid line shows the colours of a $\tau = 20 Myrs$ starburst at the same ages. The symbol D denotes the position of the 'Disc' component of [1]

In Figure 2 we plot the IRAS colours of the starburst galaxies in the sample of [1] (selected to have good quality fluxes in all four IRAS bands) and indicate the position of their disc component (D). Also indicated in Figure 2 are the positions of M82 and NGC6090 on the colour-colour diagrams. Disc galaxies cover the part of the colour-colour diagram between the starbursts and D, although there is some overlap with the starburst galaxies.

If we consider first the predicted colours of the sequence of GMCs (dotted line), we see that they span the entire range of observed galaxy colours. This suggests that a weighted sum of emission from such a family of GMCs (which is what equation (1) essentially is) may explain the observed galaxy colours. To test this we have computed the colours of a galaxy that experienced an exponentially decaying burst with $\tau = 20$Myrs (solid line). The predicted colours in the age range 0-72Myrs nicely match the spread in the colours of starburst galaxies. Furthermore, they predict a correlation of the

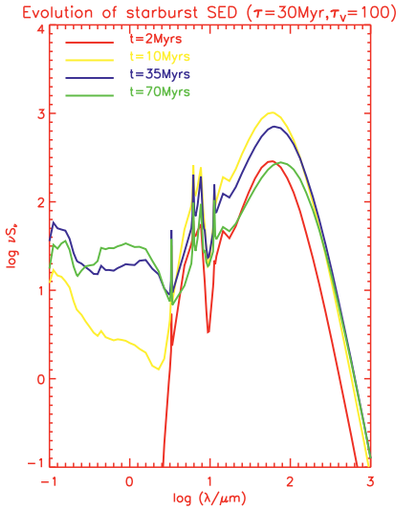

Fig. 3. Spectral energy distributions of a $\tau = 30 Myrs$ starburst at different ages. The assumed GMC parameters are $M_{GMC} = 10^7 M_\odot, \eta = 0.25, \tau_V = 100$. The vertical scale is arbitrary but constant for the four models. Note the bolometric luminosity of the starburst peaks at about 10-20Myrs.

100/60 ratio, and an anticorrelation of the 25/12 one, with age. The predicted mean age of starburst galaxies ($\sim$ 50Myrs) agrees remarkably well with other estimates from Brγ equivalent widths and CO indices ([19]) as well as ISO spectroscopy ([17]). The predicted colours are not very sensitive on the assumed value of τ. The colours for the constant star formation case, a scenario more appropriate for disc galaxies, also lie on the same track but are packed towards the M82 end. This may have significant implications for the origin of the far-IR luminosity of disc galaxies. The conclusion from this analysis is therefore that the age of the burst can account for some of the variation in IRAS galaxy colours attributed by [1] to mixing with a cirrus component.

In Figure 3 we give the SEDs of the starburst discussed above (τ = 30Myrs) for some representative ages. A number of features are worth highlighting: (1) there is a general tendency for the peak of the SED to shift to longer wavelengths with age. (2) The PAH features get stronger with age. (3) the 9.7μm silicate feature gets shallower with age. (4) while the optical/UV light of the youngest bursts is almost completely obscured, the oldest starbursts are predicted to emit significantly in the optical/UV. This illustrates the extent to which old diffuse (and therefore optically thin) GMCs dominate the emission of old bursts.

5 Models for the M82 and NGC6090 Starbursts

M82 being the nearest example of a starburst (D=3.25Mpc [20]) has received a lot of attention both observationally and theoretically. Our model fit, shown in Figure 4, assumes that M82 experienced two bursts of star formation. The first one occured 26.5Myrs ago and had a very steep exponential decay ($\tau = 2Myrs$). This burst is now responsible for most of the K band light and about half of the far-IR and submillimeter emission. The second burst occured 16.5Myrs ago and decayed more slowly ($\tau = 6Myrs$). The GMCs in both bursts are assumed to leak 20% of their starlight after 10Myrs which subsequently suffers a visual extinction of 1.5 magnitudes. The two bursts are predicted to contribute roughly equal amounts of UV flux.

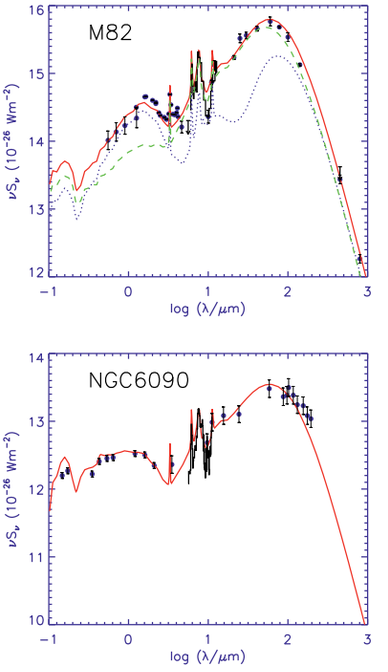

Fig. 4. Fits to the SEDs of M82 (top) and NGC6090 (botttom) with the starburst model. See text for model parameters

[18] presented ISO spectrophotometry and extensive multi-wavelength photometry for NGC6090. This galaxy is about 10 times more luminous than M82 and its optical image shows a disturbed morphology and signs of a recent interaction. The IRAS colours of NGC6090 show evidence for cold dust. It is therefore not surprising that the emission from an M82 type starburst

has to be supplemented by colder dust to fit the data for $\lambda > 120\mu m$ ([18]). We find that a good fit can be obtained with $t = 64$Myrs, $\tau = 50$Myrs.

6 Conclusions

We have presented models of the infrared emission of starburst galaxies which are treated as an ensemble of GMCs at different evolutionary stages. While useful constraints on the star formation history and stellar populations of galaxies can be obtained from this model, it will be of much interest to explore in the future the effect of deviations from spherical symmetry especially at the later stages of GMC evolution. Hydrodynamical simulations of the evolution of star-forming molecular clouds which take into account the effects of ionization, stellar winds and multi-supernova explosions in dense environments should also take high priority. Only then will we be able to take full advantage of the data ISO, SCUBA, SIRTF, NGST, VLT, FIRST, PLANCK, SOFIA, ALMA etc. are expected to yield over the next decade or so.

References

1. Rowan-Robinson, M., Crawford, J., 1989, MN 238, 523.
2. Rowan-Robinson, M., Efstathiou, A., 1993, MN 263, 675.
3. Krügel, E., Siebenmorgen, R., 1994, AA, 282, 407.
4. Bruzual, A & Charlot, S., GISSEL user guide.
5. Efstathiou, A., Rowan-Robinson, M., Siebenmorgen, R., 2000, MNRAS, astro-ph/9912252
6. Elmegreen, B.G., 1985, in Protostar and Planets II, p.33-58.
7. Dame, T.M., Elmegreen, B.G., Cohen, R.S., & Thaddeus, P., ApJ, 305, 892.
8. Solomon, P.M., Rivolo, A.R., Barrett, J., & Yahil, A., 1987, ApJ, 322, 101.
9. O'Connell, R.W., Gallagher III, J.S., Hunter, D.A., Colley, W.N., 1995, ApJ, 446, L1.
10. Meurer, G.R., Heckman, T.M., Leitherer, C., Kinney, A., Robert, C., Garnett, D.R., 1995, AJ, 110, 2665.
11. Whitmore, B.C., & Schweizer, F., 1995, AJ, 109, 960.
12. Mathis, J.S., 1990, ARAA, 28, 37.
13. Siebenmorgen, R., Krügel, E., 1992, AA, 259, 614.
14. Efstathiou, A., Rowan-Robinson, M., 1990, MN, 245, 275.
15. Efstathiou, A., Rowan-Robinson, M., 1995, MN, 273, 649.
16. Acosta-Pulido, J.A., *et al.*, 1996, AA, 315, 121.
17. Genzel, R., et al 1998, ApJ, 498, 579.
18. Rieke, G.H., Lebofsky, M.J., Thompson, R.I., Low, F.J., Tokunaga, A.T., 1980, ApJ, 238, 24.
19. Goldader, J.D., Joseph, R.D., Doyon, R., Sanders, D.B., 1997, ApJ, 474, 104.
20. Tammann, G.A., & Sandage, A., 1968, ApJ, 151, 825.

IR Surveys with the Infra Red Imaging Surveyor (IRIS)

Chris Pearson

Institute of Space and Astronautical Sciences, Yoshinodai 3-1-1, Sagamihara, Kanagawa 229, Japan

Abstract. ISO (like IRAS before) has significantly increased our awareness of the importance of large and/or deep surveys in the infrared in order to investigate, constrain, and ultimately understand the evolutionary and star formation history of the universe. Following the sucess of ISO, many new space borne telescope missions are planned in the coming decade (SIRTIF, FIRST, PLANCK, IRIS, HII/L2). Using the results and knowledge gained from the ISO IR surveys, what can we expect from the next generation of IR telescopes? Building on the legacy of IRAS and ISO, the IRIS ASTRO-F mission plans to undertake a large scale survey in the 50-150μm range down to fluxes of 20-50mJy covering almost the entire sky. Revised source count models, in the light of results from and dicussions stimulated by ISO, predict counts of the order of a few million galaxies.

1 The Infra Red Imaging Surveyor (IRIS)

The Infrared Imaging Surveyor (IRIS) is the second infrared astronomy mission of the Institute of Space and Astronautical Science (ISAS). The IRIS is a 70 cm cooled telescope dedicated for infrared sky surveys [1]. The IRIS telescope has a 70 cm aperture and is cooled to 6K using Stirling-cycle coolers and liquid helium. The primary and secondary mirrors are light-weight mirrors made of silicon carbide. The IRIS covers a wide wavelength range from K-band to 200μm. Two focal-plane instruments are installed. One is the Far-Infrared Surveyor (FIS, see Table 1) which will survey the entire sky in the wavelength range from 50 to 200 μm with angular resolutions of 30 - 50 arcsec using high sensitivity Ge:Ga detector arrays [2]. The other focal-plane instrument is the Infrared Camera (IRC, see Table 2). It employs large-format detector arrays and will take deep images of selected sky regions in the near and mid infrared range [3]. The field of view of the IRC is 10 arcmin and the spatial resolution is approximately 2 arcsec. The IRIS has much higher sensitivity than that of the IRAS survey. For example, the IRIS has 50 - 100 times higher sensitivity at 100 μm and more than 1000 times at mid-infrared wavelengths. The detection limits are 1-100 mJy in the near-mid infrared and 10 - 100mJy in the far infrared (Fig. 1). With the IRIS survey, great progress is expected in the research on evolution of galaxies, formation of stars and planets, dark matter, and brown dwarfs. The IRIS is now scheduled to be launched with ISAS's launch vehicle M-V, into a sun-synchronous polar orbit with an altitude of 750 km in mid 2003

D. Lemke, M. Stickel, and K. Wilke (Eds.): LNP 548, pp. 149–156, 2000.

Table 1. Far Infra-Red Surveyor Parameters

Channel	Wavelength Range	pixel size (Diffraction Beam)
60μm	$50-75\mu m$	$30''/Pixel(21.6'')$
Wide-S	$50-100\mu m$(FTS spectroscopy)	$30''/pixel(30'')$
Wide-L	$100-200\mu m$(FTS spectroscopy)	$50''/pixel(50'')$
170μm	$150-200\mu m$	$50''/pixel(60'')$

Table 2. Infra-Red Camera Parameters

Channel	Wavelength Bands	FOV (Pixel size)
IRC-NIR	K,L,M+$(1.25-2.5, 2-5.5\mu m$ grism)	$10'$x$10'(1.4''/pixel)$
IRC-MIR-S	$7, 9, 11\mu m(5-10\mu m$ grism)	$10'$x$10'(2.34''/pixel)$
IRC-MIR-L	$15, 20, 25\mu m(10-25\mu m$ grism)	$10'$x$10'(2.34''/pixel)$

2 Galaxy Source Count Predictions in the Infra-Red

Galaxy source counts are predicted by using an extended and improved evolution of the Pearson and Rowan-Robinson model [4]. The model consists of a 4 component parametrization including normal galaxy (IR cirrus like), starburst, ultraluminous and AGN (Seyfert) components. Components are distinguished via SED and luminosity class. The 60μm luminosity function of Saunders *et al.* [5] is used to represent the normal, starburst, and ULIRG galaxies, while the AGN luminosity function is defined at 12μm [6]. K-corrections are calculated using model SEDs for Normal [7] , starburst [8] and Seyfert (torus model) [9] galaxies. The major significant difference between the present and previous models is the introduction of Poly Aromatic Hydrocarbons (PAH) into the spectra [10] which are expected to affect the mid-IR source counts to some extent [11]. A comparison of the new and previous SEDs [12], [13] are shown in Fig. 2, 3. Simple luminosity evolution of the form $L(z) = L(0)(1+z)^{3.1}$ is incorporated into the starburst, ULIG, and AGN components. This form of evolution has been shown to provide a good fit at least at brighter fluxes to the source counts over a wide range in wavelength [14] although additional evolution is almost certainly needed to explain the faint 15μm ISOCAM source counts [15] and the SCUBA sub-mm data [16], [17] . For a general *first look* at the capabilities of IRIS, such evolution will suffice.

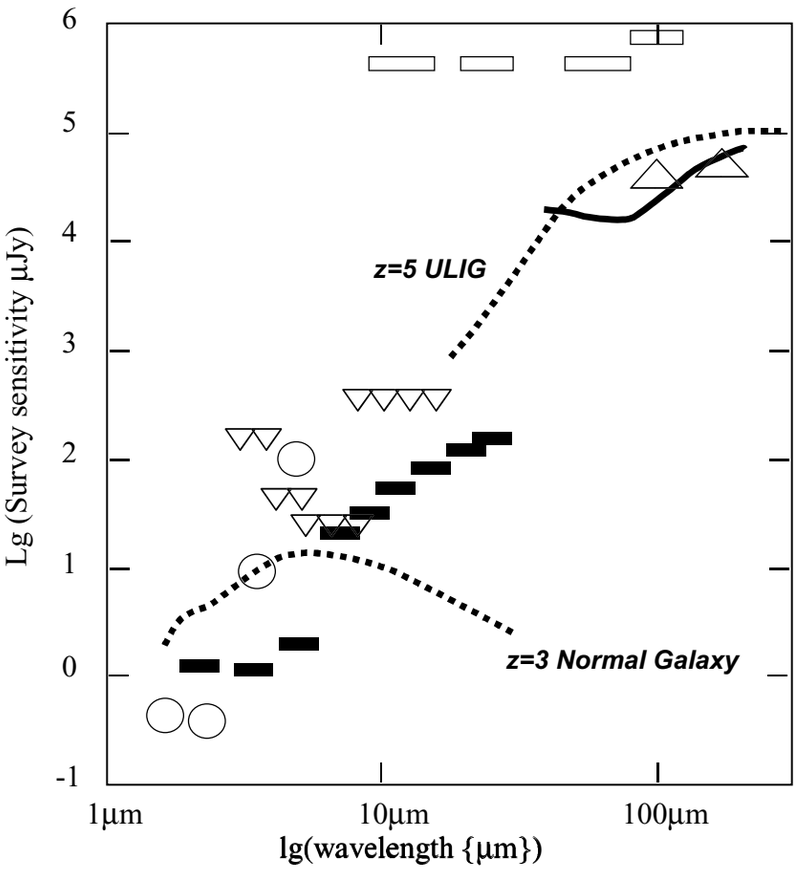

Fig. 1. IRIS survey sensitivities (5σ) in comparison with other IR detection limits. IRIS FIS and IRC (*solid line and filled boxes*), IRAS (*empty boxes*), ISOPHOT *large upward triangles*), ISOCAM deep survey (*small downward triangles*) and the Japanese Subaru telescope (*unfilled circles*).

3 Survey Strategy and Expectations

Three phases for the IRIS observing program are planned. During Phase 1 (the first 180 days), priority is given to the FIS which will carry out an all sky (>90%) far-IR survey in 4 bands from 50 to 200 μm. Pointing observations will be limited to approximately 2000 during this period. Phase 2 continues until the depletion of the liquid helium, possibly lasting around 300 days. Containing some 5000 pointing observations, the primary instrument will be the IRC with the FIS filling gaps in the all sky survey. During the third phase,

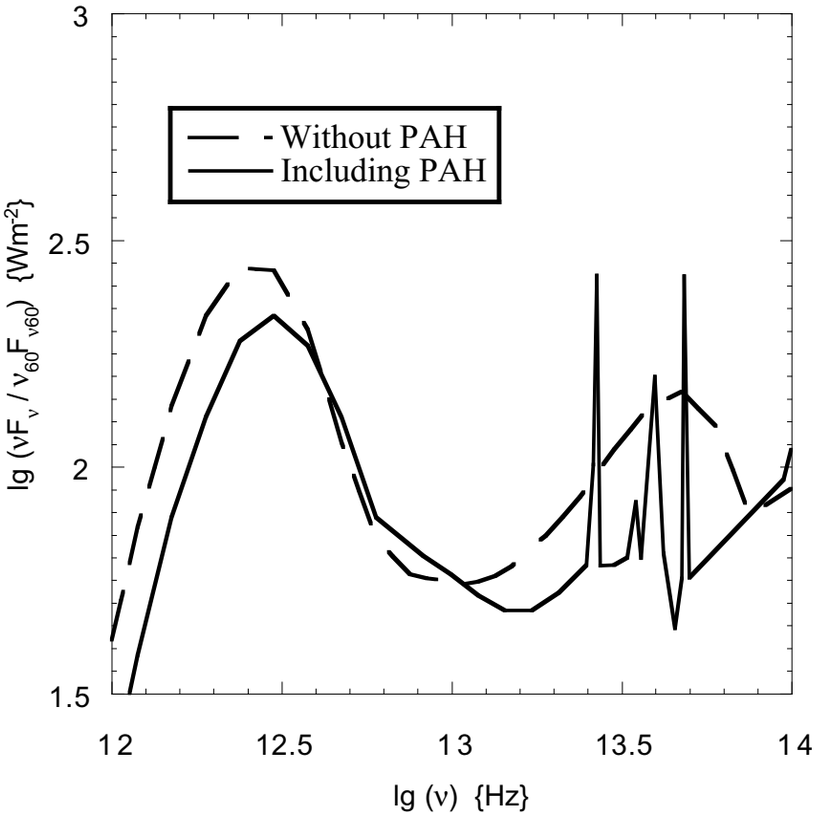

Fig. 2. Model normal galaxy (Cirrus) SED. Fluxes normalized at 60μm

only the NIR channel of the IRC can be operated. The length of phase 3 is limited only by the lifetime of the Stirling cycle cylinders. Source counts at IRIS wavelengths using the models decribed in the previous section are shown in Fig. 4 for the MIR wavebands and Fig. 5 for the FIR all sky survey wavebands respectively. Although the IRC's primary task will be pointed observations, an ultra-deep survey covering approximately 3200 square arcminutes around the North Ecliptic Pole is planned. The expected survey sensitivites and confusion limit due to extragalactic sources are included in Fig. 4. Note that any NIR or MIR observations would be expected to be detector noise limited. The corresponding survey sensitivities and source confusion limits for the all sky far-IR survey are shown in Table 3. Also shown are the expected number of sources at each wavelength assuming a survey area of 4π sr. The confusion limits are calculated using the classical criteria of 1 source per 40 beam areas of the observing instrument (see Table 1). At the longest Far-

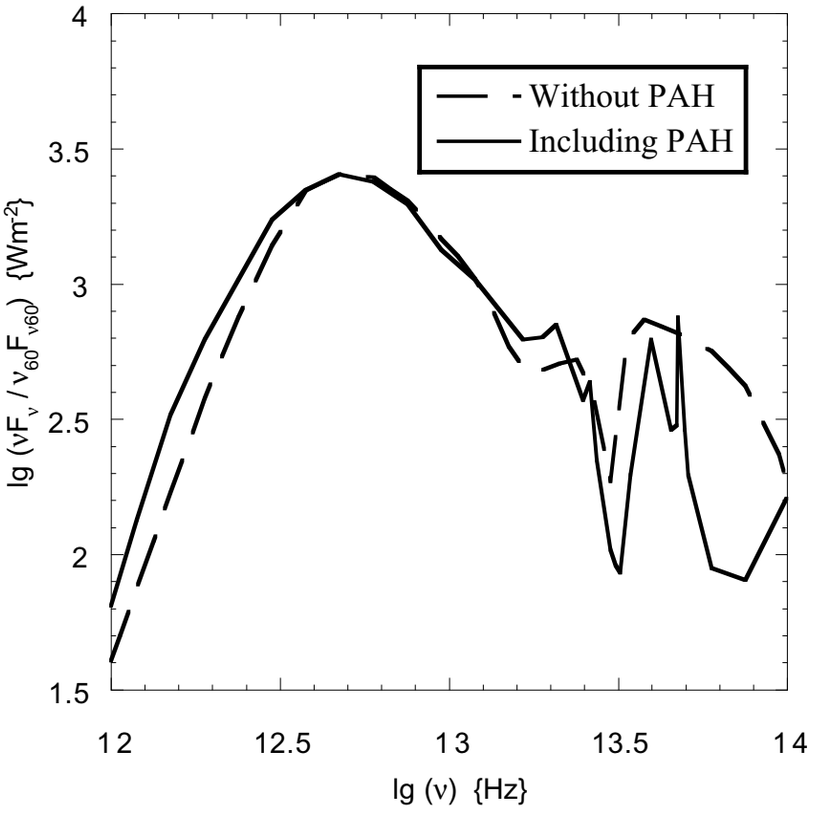

Fig. 3. Model starburst galaxy SED. Fluxes normalized at 60μm

IR wavelengths the survey sensitivities are expected to approach the limit of source confusion. The MIR-NEP survey would cover almost 1 square degree down to sensitivities of 10ths of μJy. In each waveband, more than 3000 sources would be expected to be roughly equally distributed between normal, starburst and Seyfert galaxies, between 1/3 and 1/2 being at redshift > 1 and a significant number of higher ($z > 2$) redshift objects. The FIS-FIR all sky survey would expect to detect the order of 2-4 million sources in each waveband. The longer wavelengths would preferentially detect starbursts, the majority of which would be at redshifts greater than 1. Further improvments in the model SEDs incorporated and evolutionary scenarios will further enhance the model predictions but it seems clear that IRIS has the potential to provide a scientific database complementing and surpassing that of IRAS and will also provide important information and results relevant to the SIRTF, FIRST and PLANK missions.

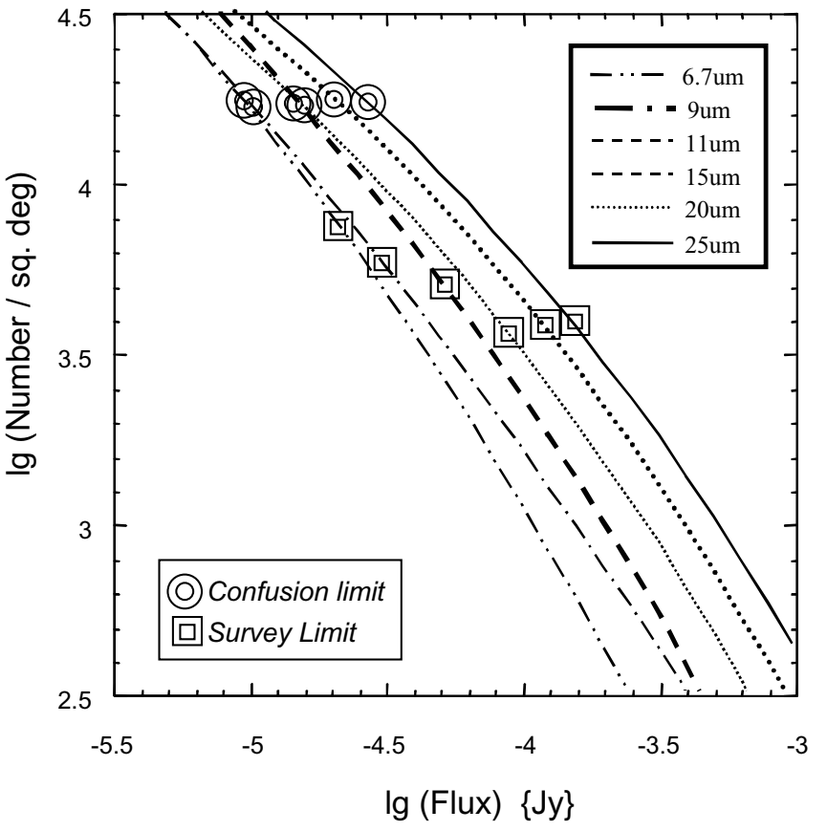

Fig. 4. Source counts at mid-IR wavelengths. Sensitivities given are for 3200sq.arcmin. IRIS survey around NEP using MIR-S 5-12μm and MIR-L 10-26μm IRC channels. Source confusion is met at the limit of 17000 sources per sq.deg., i.e., well below survey sensitivity limits.

Table 3. Far-IR Survey Survey Sensitivities and Source Confusion

wavelength	Confusion Limit	Survey Limit	Number of Sources
50μm	$3.8mJy$	$20mJy$	1.5x10^6
75μm	$8.3mJy$	$20mJy$	4.9x10^6
95μm	$13.2mJy$	$30mJy$	4.4x10^6
200μm	$42.7mJy$	$60mJy$	2.6x10^6

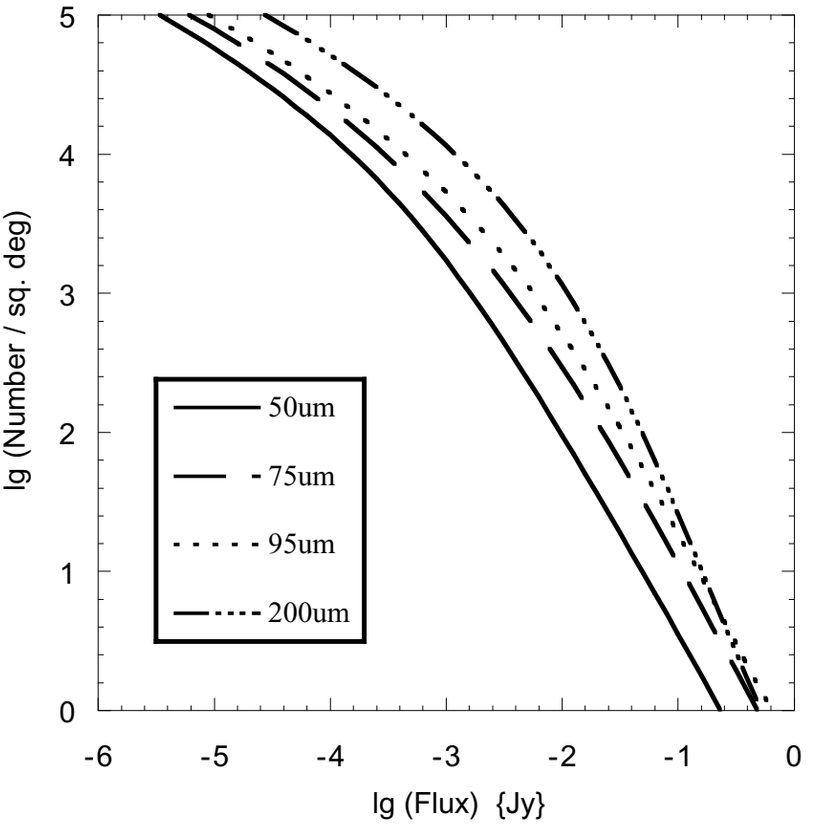

Fig. 5. Source counts at far-IR wavelengths

Acknowledgements

I would like to thank the organizers of the conference and staff at Ringberg castle for a thoroughly enjoyable conference. I would also like to thank Andreas Efstathiou for supplying SED data on short demand and my host Japanese researchers and especially Professor Okuda at ISAS for making this work possible. I acknowledge also a fellowship from the Japanese Society for the Promotion of Science (JSPS).

References

1. Onaka, T., Sugiyama, Y., Miura, S.(1998) Telescope system of the Infrared Imaging Surveyor (IRIS). In: Fowler,A. M. (Ed.)Infrared Astronomical Instrumentation, Proc. SPIE 3354

2. Kawada, M. (1998) FIS: Far-Infrared Surveyor onboard IRIS. In: Fowler, A. M. (Ed.)Infrared Astronomical Instrumentation, Proc. SPIE 3354
3. Matsuhara, H. (1998) IRC: An Infrared Camera onboard the IRIS In: Fowler,A. M. (Ed.)Infrared Astronomical Instrumentation, Proc. SPIE 3354
4. Pearson, C. P., Rowan-Robinson, M. (1996) Starburst Galaxy Contributions to Extragalactic Source Counts. MNRAS 283, 174
5. Saunders, W., Rowan-Robinson, M., Lawrence, A., Efstathiou, G., Kaiser, N., Ellis, R. S. (1990) The 60-micron and Far-Infrared Luminosity Functions of IRAS Galaxies. MNRAS 242, 318
6. Rush, B., Malkan, M., Spinoglio, L.(1993)The extended 12μm galaxy Sample. ApJSS 89, 1
7. Efsthiou, A., Siebenmorgen, R. (2000) MNRAS *in preperation*
8. Efsthiou, A., Rowan-Robinson, M., Siebenmorgen, R. (2000) Massive Starformation in Galaxies Radiative transfer models of the UV to mm emission of starburst galaxies. MNRAS *accepted*
9. Rowan-Robinson, M. (1995) A New Model for the Infra-Red Emission from Quasers. MNRAS 272, 737
10. Siebenmorgen, R., Krugel, E. (1992) Dust Models Containing Polycyclic Aromatic Hydrocarbons in Various Environments. AA 259, 614
11. Xu, C,*et al.*(1998)Emission Features and Source Counts of Galaxies in the Mid-Infrared. ApJ 508, 576
12. Rowan-Robinson, M., Efsthiou, A., Lawrence, A., Oliver. S., Taylor, A. (1993) The Ultraviolet to Radio Continuum of the Ultraluminous Galaxy IRAS F10214+4724. MNRAS 261, 513
13. Rowan-Robinson, M. (1992)Interstellar Dust in Galaxies. MNRAS 258, 787
14. Rowan-Robinson, M., *et al.* (1999) The European Large Area ISO Survey: ELAIS.astro-ph/9906273
15. Dole, H., *et al.* (1999) *These proceedings.*
16. Hughes, D., *et al.* (1998) Unveiling Dust Enshrouded Star Formation in the Universe: a Sub-mm Survey of the Hubble Deep Field. Nature 394, 241
17. Smail, I., Ivison, R. J., Blain, A. W. (1997)A Deep Submillimeter Survey of Lensing Clusters: A New Window on galaxy Formation and Evolution. ApJ 490, L5

The Effect of Dust Evolution on the Spectral Energy Distribution of Galaxies

Eli Dwek[1], Michel Fioc[2], and Frank Városi[3]

[1] Laboratory for Astronomy & Solar Physics, Code 685, NASA Goddard Space Flight Center, Greenbelt, MD 20771, USA, eli.dwek@gsfc.nasa.gov
[2] National Research Council Resident Research Associate, Code 685, NASA Goddard Space Flight Center, Greenbelt, MD 20771, USA
[3] Raytheon ITSS, Code 685, NASA Goddard Space Flight Center, Greenbelt, MD 20771, USA

Abstract. The spectral energy distribution of galaxies is strongly affected by the abundance, composition, and size distribution of their dust content. In addition, the morphology of a galaxy and the clumpiness of its interstellar medium play a crucial role in the attenuation of starlight and in its conversion to infrared emission. In this contribution we present simple models for the evolution of dust in normal spiral galaxies and pristine starburst regions, and examine how the dust affects the attenuation and spectral energy distribution of these systems.

1 Introduction

A primary objective of astrophysics is to understand the origin and evolution of the complex structures seen in the universe today. Recent observations suggest that a significant fraction of the cosmic star-formation activity was shrouded by dust and took place early on during the first billion years after the Big Bang (e.g. [1] and references therein). The formation of these structures was accompanied by the formation of stars and metals, and associated energy releases. However, the determination of their underlying physical properties, such as their star formation rate and metallicity, is greatly affected by the presence of dust.

In order to derive the history of structure, star, and metal formation in the universe from observations of various type galaxies and pregalactic objects, we must be able to infer their underlying physical properties from their spectral energy distribution (SED). Models for the evolution of their SED should include possible morphological changes due to collisions, mergers, or internal processes, as well as changes in their dust abundance, composition, and size distribution. All these factors play an important role in determining the attenuation properties and the UV to far–IR appearance of these systems.

In this contribution we will concentrate on radiative transfer and evolutionary effects in the dust abundance and composition on the SED in normal spiral galaxies, and in pristine starburst regions.

D. Lemke, M. Stickel, and K. Wilke (Eds.): LNP 548, pp. 157–165, 2000.

2 Dust Evolution

Following their injection into the interstellar medium (ISM), dust particles are subject to a number of physical processes that alter their abundances, composition, and size distribution ([7] – hereafter D98 – and references therein). These include grain formation in the various sources, grain destruction by thermal sputtering and grain–grain collisions in the general ISM, and grain growth by accretion and coagulation in molecular clouds. The overall opacity and IR emission from a galaxy depends on the abundance and nature of the dust, the stellar radiation field, the relative distribution of stars and dust, and the clumpiness of the ISM.

Of particular interest is the evolution of the carbon abundance in the ISM. Most of the carbon dust is made by stars in the 2–5 $M_{\odot}$ mass range, depending on the initial stellar metallicity. Its injection into the ISM is delayed by the time it takes these stars to evolve off the main sequence and form dust. Simplifying the more detailed model of D98, we will assume that grain destruction in the general ISM is exactly balanced by accretion in molecular clouds. In spite of this simplification, the abundance of the dust relative to that of the metals, and the relative abundance of silicate to carbon dust evolve with time as a result of the variations in the dust to metallicity yields in the various sources. Previous models (e.g. [16] and references therein; [3]) assumed that the dust to metallicity ratio, and the relative abundance of silicate and carbon dust remain constant with time.

In calculating the dust yield as a function of stellar mass, we must consider the separate contribution of the different types of mass loss that are responsible for the chemical enrichment of the ISM. These include fast winds from massive Wolf–Rayet stars, slow winds from low mass AGB stars, and the explosive ejecta from novae and Type II and Ia supernovae (SN). For example, chemical evolution models which assume that all elements are returned in gaseous form to the ISM do not need to make such distinction when calculating the total yields from massive stars that "instantaneously" recycle their ejecta into the ISM. However, the dust yield from such objects depends critically on whether a given condensible element has been ejected in the wind or in the explosion, since its condensation efficiency – and consequently the dust composition – depends on the the ejecta composition and physical conditions.

Figure 1 depicts the carbon and oxygen yields and the C/O number ratio in the quiescent outflows of low mass AGB stars, and massive Wolf–Rayet (WR) stars of different initial metallicity. We assumed that outflows in which the C/O ratio exceeds 1 form carbon dust, and those in which the C/O ratio is less than unity form silicate dust. No such restriction was imposed on SN ejecta, since the formation of CO does not totally deplete the C or O abundance in the ejecta ([7] and references therein; [5]). We also assumed that WR stars are only capable of forming carbon dust (provided the C/O ratio is >1) in the ejecta. The panels on the right of Figure 1 show the

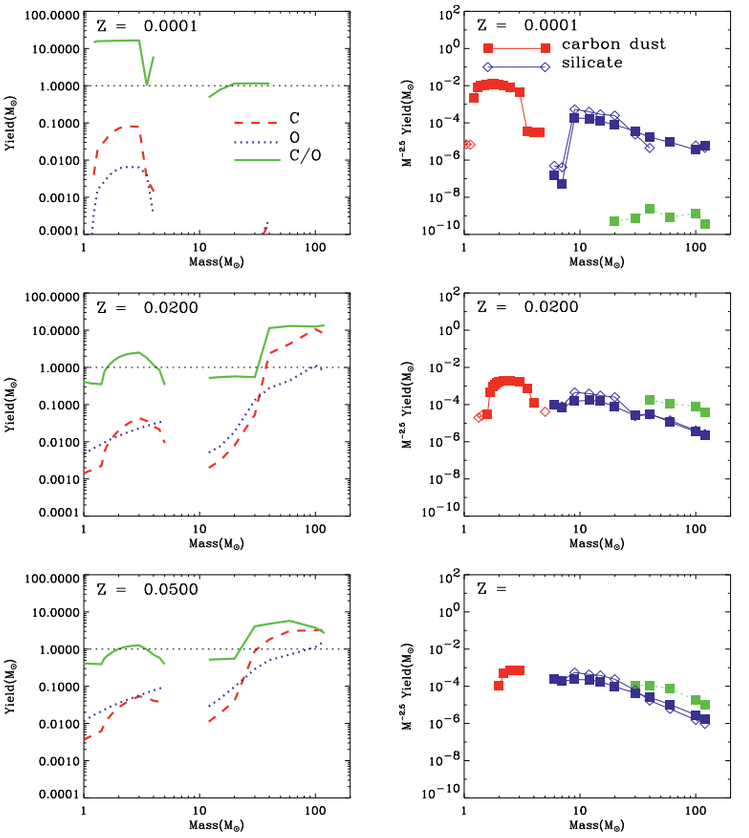

Fig. 1. Left column: the C, O mass yields and the C/O number ratio as a function of progenitor stellar mass for different initial stellar metallicities. Right column: graphite and silicate mass yields as a function of stellar mass for different initial stellar metallicities

corresponding silicate and carbon yields (weighed by a Salpeter initial mass function, IMF) in the winds and in the explosive ejecta at various initial stellar metallicities. At M > 6 $M_{\odot}$, the SN yields are indicated by solid lines, while WR yields are indicated by a dotted line. The prescription used to calculate the yields was presented in [7]. Dust condensation efficiencies were taken to be unity in the quiescent AGB outflows, 0.8 in the fast winds of WR stars, and 0.5 in explosive SN Type II and Ia ejecta. Stellar yields for the winds and explosive ejecta from massive stars were taken from [14] and references therein. Yields for stars in the 0.8 to 5 $M_{\odot}$ mass range were taken from [12].

The first dust in the universe is likely to be formed in the outflowing winds of massive Wolf–Rayet (WR) stars and SN explosions. However, Figure 1 shows that at low metallicities, the C/O ratio never exceeds unity in the stellar outflows from massive stars. The first dust in the universe is therefore dominated by SN condensates (instead of WC–type Wolf–Rayet stars). Some carbon dust is made in SN ejecta; however the bulk of the carbon dust is created in low mass stars and its injection into the ISM is delayed by ≥ 100 Myr, the lifetime of ≤ 5 $M_\odot$ stars. The figure also shows the relative decline in the production of carbon dust in low mass stars as a function of initial stellar metallicity.

In the following we will use these yields to calculate the evolution of the dust and its attenuation and reemission of starlight in normal spiral and starburst galaxies.

3 The Evolution of Spiral Galaxies

The chemical and spectral evolution of normal spiral galaxies was calculated using "typical" input parameters. The chemical evolution was described by a metal–free infall model with a timescale of 1 Gyr, and a star formation timescale of 5 Gyr. The stellar initial mass function (IMF) in the 0.1 to 120 $M_\odot$ mass range was adopted from [15]. The spectral evolution was calculated using the PÉGASE code ([9], [10], and references therein).

The dust injected into the interstellar medium ISM was assumed to have an $a^{-3.5}$ power law distribution in grain radii a, extending from 0.0025 to 0.25 μm for silicate grains and from 0.0010 to 0.25 μm for graphite grains. We also added a population of polycyclic aromatic hydrocarbon (PAH) molecules, commonly believed to be carriers of the broad near–IR emission lines observed in the general ISM of the Milky Way and external galaxies. The population of PAHs was smoothly joined (i.e., with the same power-law in particle mass) to the population of graphite grains, extending from 10 to 470 carbon atoms, the upper limit corresponding to a graphite radius of 10 Å. With this prescription, PAHs constitute $\sim 3\%$ of the carbon atoms locked up in the dust. The PAH emission spectrum in the 3 to 18 μm wavelength region was represented by the observed spectrum of NGC 7023 [2] [13]. Their UV–optical absorption cross section per carbon atom was assumed to be equal to that of very small graphite particles.

The stellar emission component was divided into Lyman continuum photons and non–H-ionizing photons. The ionizing photons were assumed to be locally absorbed by gas and dust in the surrounding H II region. We also assumed that PAHs do not survive in the ionized gas. Consequently, the reemitted IR emission from the H II gas lacks any PAH emission features.

The fraction of the stellar non-ionizing photons absorbed or scattered by the dust was calculated using a Monte–Carlo model for a simple slab geometry in which the stars and dust are uniformly mixed. The reradiated

IR spectrum was calculated using a stochastic heating model for the graphite and silicate dust [8]. The PAH emission spectrum was calculated by equating the total power they absorb in the UV–optical to their 3–18 μm emission.

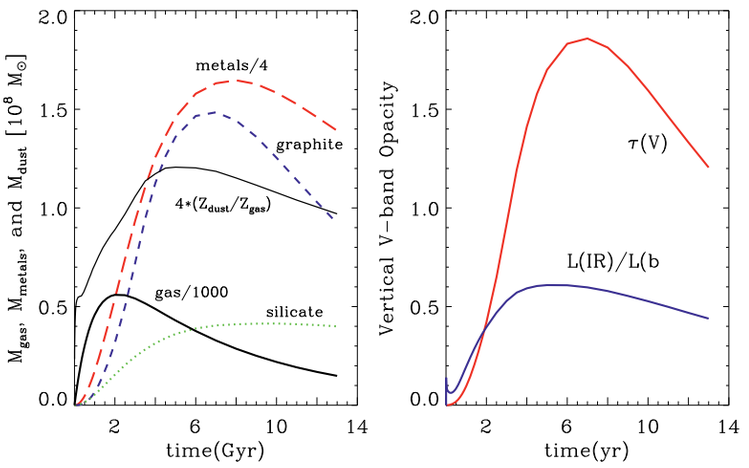

Fig. 2. Left panel: the evolution of the gas, metals, dust mass, and the dust–to–gas mass ratio in a spiral galaxy. Right panel: the evolution of the vertical V–band opacity and IR to bolometric luminosity

Figure 2 (left panel) shows the evolution of the gas, metals, and the dust (graphite and silicate) abundance. The dust–to–metallicity ratio slowly rises from an initial value of ~ 0.12 to a value of ~ 0.25. Also noticeable are the changes in the ratio of the carbon–to– silicate dust mass in the ISM. The model gives a rather high, ~ 2.5, value for this mass ratio at the present epoch (13 Gyr), compared with the ratio of ~ 0.7 in the local ISM. The reason for this overabundance of carbon dust stems from the internal inconsistency of the Portinari et al. [14] yields. Yields in the stellar winds were calculated for a normalized $R \equiv {}^{12}\mathrm{C}(\alpha,\gamma)/{}^{16}\mathrm{O}$ rate of unity, and augmented by the Woosley & Weaver [18] explosive yields which were calculated for a normalized rate of 1.7. The use of a value of $R = 1.7$ for calculating the wind composition would be more consistent with current constraints on this rate. The right panel of the figure depicts the evolution of the vertical V–band opacity and the IR to bolometric luminosity.

Figure 3 depicts the evolution of the UV to far–IR spectrum of the galaxy at various epochs. The thin solid line represents the unattenuated stellar spectrum, and the heavy solid line is the total spectrum of the galaxy. The dotted line represents the reradiated IR emission. At early epochs the stellar spectrum is dominated by ionizing UV photons. Consequently, the spectrum is

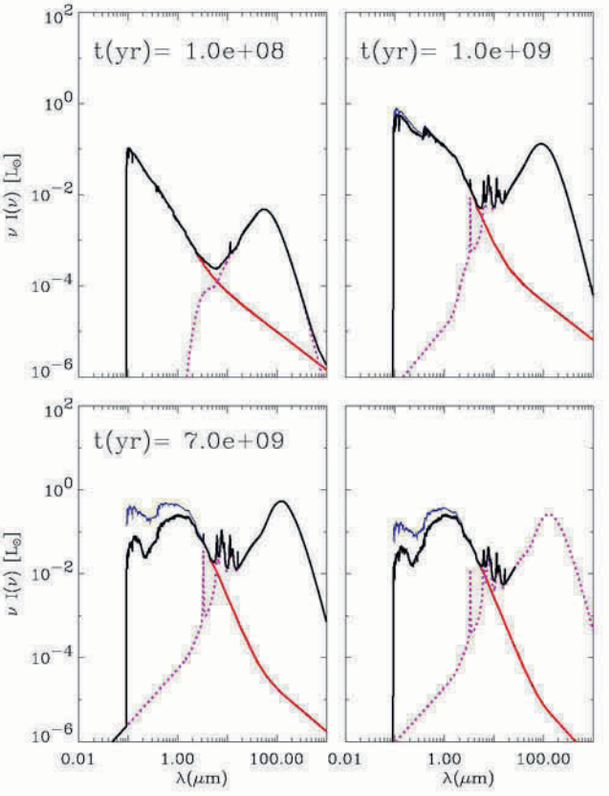

Fig. 3. The evolution of the SED of a normal spiral galaxy. Details in text

dominated by emission from dust in H II regions. The galaxy's SED therefore lacks any PAH features. As the stellar population ages (t > 100 Myr), the contribution of non–ionizing photons to the heating of the dust, and consequently that of the IR cirrus component, increases. This trend is easily observed in the later panels of the figure. Also noticeable is the presence of the 2175 Å absorption feature associated with the graphite extinction bump. Currently, there is no evidence to corroborate the presence of this feature in the SED of normal galaxies, and we have made no efforts to introduce additional model parameters to affect the strength of this feature. Overall, the model gives a galactic SED that is consistent with typical spiral galaxies. About 40% of the stellar output is reradiated by dust at IR wavelengths with a spectrum that peaks in the 100 – 140 μm wavelength regime.

4 The Evolution of Pristine Starbursts

The chemical and spectral evolution of the starburst (SB) was calculated for a constant birthrate of 100 $M_\odot$ yr^{-1}, lasting for a period of 100 Myr. The starburst region was assumed to be confined to a spherical volume with a radius of 200 pc, a clumpy ISM characterized by a clump–interclump density contrast of 250, a clump radius of 1.32 pc, and a clump volume filling factor of 12%. Our choice of ISM morphology was motivated by the observational constraints imposed by the near–IR line emission observed from M 82 [6].

The attenuation of starlight and the reradiated IR emission spectra were calculated with the analytical model CLUMPY, developed for calculating the transport of radiation via scattering, absorption, and IR emission through a dusty and clumpy medium [17]. The MODEL can accommodate several geometries, and has been extensively tested against Monte Carlo simulations for a wide range of model parameters. These include clump volume filling factors between 0.01 and 1.0, clump–interclump density contrasts between 1 and 10^3, clump radii (normalized to that of the emitting region) ranging from 0.01 to 0.10, and radial homogeneous optical depths between 0.1 and 40. The latter quantity is the radial optical depth if the dust was homogeneously distributed throughout the region.

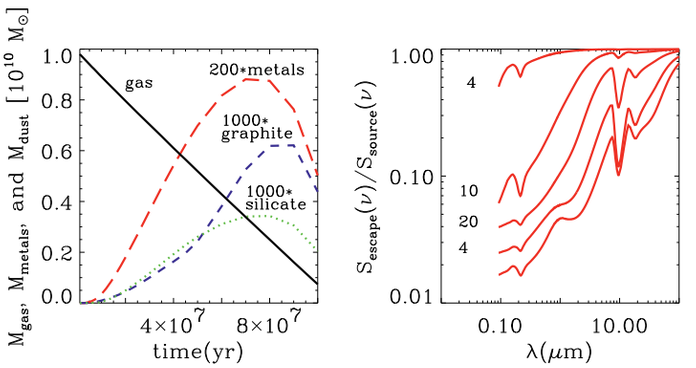

Fig. 4. Left panel: the evolution of the gas, metals, and dust mass in a pristine starburst. Right panel: the evolution of the attenuation, defined as the ratio between the escaping and intrinsic source spectrum. The curves are labeled by the epoch in Myr

Figure 4 depicts the ISM and the gas and dust metallicity as a function of time. The dust–to–metal mass ratio (not shown in the figure) evolves from a value of ~ 0.08 to a value of ~ 0.3 at 100 Myr. The relative abundance of silicate and graphite dust also changes as a function of time. The right panel of the figure depicts the evolution of the attenuation factor. Prominent

in the figure is the 2175 Å graphite extinction bump, in sharp contrast to the observed SB attenuation curves which do not exhibit this feature [4]. Our model confirms the conclusion previously reached by Gordon, Calzetti, & Witt that, in addition to clumpiness, interstellar processing of the small dust particles that give rise to this feature is needed to eliminate it from the SB attenuation curve [11].

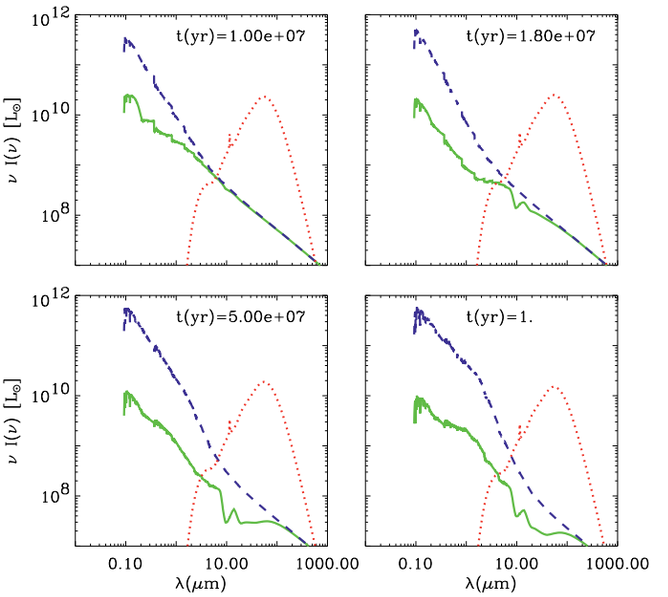

Fig. 5. The evolution of the SED of a pristine starburst. Details in the text

Figure 5 depicts the evolution of the starburst's SED. Noticeably absent in the spectrum are the PAH emission features. This is a direct consequence of our assumption that PAHs are only formed in the outflows of low-mass stars, which did not have time to evolve off the main sequence during the lifetime of the starburst. Pristine starbursts should therefore be characterized by the absence of the PAH emission features, unless PAHs are formed in the ISM by various grain processing mechanisms which were not included in the model.

Acknowledgements

M. Fioc acknowledges the support of the National Research Council Resident Research Associateship program. This research is partially supported by a grant from NASA's Theoretical Astrophysics Prgram NRA 97–OSS12.

References

1. Blain, A. W., Smail, I. et al. (1999) MNRAS, 302, 632–648
2. Boulanger, F., Boissel, P. et al. (1998) A&A, 339, 194–200
3. Calzetti, D., & Heckman, T. M. (1999) ApJ, 519, 27–47
4. Calzetti, D., Kinney, A. L., & Storchi-Bergmann, T. (1994) ApJ, 429, 582–601
5. Clayton, D. D., Liu, W., & Dalgarno, A. (1999) Science, 283, 1290–1292
6. Colbert, J. W., Malka, M. A. et al. (1999) ApJ, 511, 721–729
7. Dwek, E. (1998) ApJ, 501, 643–665
8. Dwek, E., Arendt, R. G. et al. (1997) ApJ, 475, 565–579
9. Fioc, M., & Rocca-Volmerange, B. (1997) A&A, 326, 950–962
10. Fioc, M., & Rocca-Volmerange, B. (2000) in preparation
11. Gordon, K., Calzetti, D., & Witt, A. N. (1997) ApJ, 487, 625–635
12. Marigo, P., Bressan, A., & Chiosi, C. (1996) A&A, 313, 545–564
13. Moutou, C. 1996, PhD Thesis, Université de Paris VI
14. Portinari, L., Chiosi, C., & Bressan, A. (1998) A&A, 334, 505–539
15. Rana, N. C., & Basu, S. (1992) A&A, 265, 499–503
16. Silva, L., Granato, G. L. et. al. (1998) ApJ, 509, 103–117
17. Városi, F., & Dwek, E. (1999) ApJ, 523, 265–305
18. Woosley, S. E., & Weaver, T. A. (1995) ApJS, 101, 181–235

The ISOPHOT View of Quasars and Radiogalaxies

Rolf Chini[1], Martin Haas[2], Ulrich Klaas[2], Ernst Kreysa[3], Dietrich Lemke[2], Klaus Meisenheimer[2], Sven Müller[1], and Manfred Stickel[2]

[1] Astronomisches Institut, Ruhr–Universität Bochum, D–44780 Bochum, Germany
[2] Max–Planck–Institut für Astronomie, Königstuhl 17, D–69117 Heidelberg, Germany
[3] Max–Planck–Institut für Radioastronomie, Auf dem Hügel 69, D–53121 Bonn, Germany

Abstract. We summarize the current status of the ISOPHOT Guaranteed Time Proposal on quasars and radio-galaxies. The ISO data from 4.8 to 200 μm, complemented by additional ground–based measurements at 1300 μm, yield spectral energy distributions that show two components of different strength: i) synchrotron emission that dominates the radio range and – depending on the spectral slope – may extend into the near infrared regime. ii) Thermal dust emission that dominates the infrared regime but may be masked – in extreme cases of flat spectrum radio quasars – by the synchrotron component. The spectral energy distributions exhibit different shapes that reflect the various contributions of the AGN and the star formation to the heating of the dust in the nucleus and the outer parts of the host galaxy. The relative contributions of synchrotron and dust emission and the broad range of dust temperatures support a picture where the observational appearance of quasars and radio-galaxies is determined by the dust morphology (circum–nuclear torus/individual dust clouds) and by different viewing angles (beamed radio emission/scattered blue emission) towards the source.

1 Introduction

Understanding the nature of the far–infrared (FIR) emission of quasars (QSOs) was one of the challenges that ISOPHOT ([1], [2]) offered to astronomers. The classical view that QSOs emit predominantly synchrotron radiation has been debated since the advent of FIR data by *IRAS* : The spectral energy distributions (SEDs) of radio–quiet QSOs increase from 12 to 100 μm suggesting a rapid fall off towards radio wavelengths [3]. Chini et al. performed 1300 μm observations of radio–quiet and radio–loud quasars that revealed a decline by several orders of magnitude of the flux densities between 100 and 1300 μm [4] [5]. From the spectral slopes that were too steep in the framework of classical synchrotron emission and from the common turnover point of the SEDs at around 100 μm Chini et al. suggested that thermal radiation may also play an important role in the most luminous objects of our universe. Nevertheless,

D. Lemke, M. Stickel, and K. Wilke (Eds.): LNP 548, pp. 169–176, 2000.

due to the small number of QSOs observed by *IRAS* the observational evidence for distinguishing between thermal and non–thermal components was too weak and their relative strengths could not be investigated. Furthermore, the issue of whether radio–loud and radio–quiet QSOs on one hand and radio-galaxies on the other hand are intrinsically similar objects remained unclear. In such a scenario where the non–thermal emission may be beamed due to magnetic fields, while visible radiation suffers from extinction, the objects may appear rather different depending on the viewing angle. In contrast, a circum–nuclear torus probably common to all object classes would manifest itself by isotropic thermal emission in all SEDs. Therefore, the FIR regime is ideal to address these questions.

2 Statistics

The Guaranteed Time (GT) proposal of the ISOPHOT consortium on quasars and radio-galaxies contains various classes of objects. They were chosen to address the emission mechanisms in QSOs and to testify to the unified scheme. The samples comprise QSOs and radio-galaxies from the 3C catalogue, other radio–loud QSOs and BL Lac objects, optically selected QSOs from the Palomar–Green sample and high redshifted QSOs. About 70% of the original proposal could be observed despite technical constraints like visibility during the flight, sensitivity and observing time. The statistics of the proposed samples $N_{\rm prop}$, the observations performed $N_{\rm obs}$ and the final detections $N_{\rm det}$ are summarised in Table 1.
Apart from high$-z$ QSOs the detection rate is $\geq 70\%$. It is mainly determined by the brightness of the background. With our observing mode and time typically about 1% of the background brightness could be reached. For faint cirrus areas this results for example in a limit at $60\,\mu$m of about 100 mJy. A "*detection*" does not necessarily imply that the object could be measured at all 11 wavelengths from 4.8 to $200\,\mu$m. Compared to IRAS numerous new detections were achieved; e.g. out of the 17 PG–QSOs eight sources were detected in the far–infrared for the first time.

Table 1. Statistics within the ISOPHOT GT Proposal on QSOs

Sample	$N_{\rm prop}$	$N_{\rm obs}$	$N_{\rm det}$	Det. [%]
3CR sources	36	21	16	76
r-l QSOs + BL Lacs	33	27	19	70
opt. sel. QSOs (PG)	25	17	14	82
high$-z$ QSOs	9	6	0	0
Total	103	71	49	69

3 Individual Sources

In the following we discuss a few representative objects from our samples; for a complete view of the sources reduced so far we refer to [6] and [7]. All observational data and corresponding results have been transformed to the rest frame of the QSOs in order to facilitate a comparison between objects at different redshifts.

PG 0050+124 – One of the template objects for the thermal origin of the FIR emission in radio–quiet QSOs is PG 0050+124. This source exhibits one of the most complete SEDs available to date (Fig. 1) and was already contained in the early studies by Neugebauer et al.[3] and Chini et al. [4]. The ISO data which are in excellent agreement with the *IRAS* measurements demonstrate that the emission increases until 100 μm and decreases steeply at longer wavelengths. The spectral index of $\alpha \approx 3$ between 200 and 1300 μm is a unique signature for dust emission. Fitting a modified Planck curve (with $\kappa_\lambda \propto \lambda^{-2}$) to this wavelength range one obtains a coldest temperature component of 27 K. This is very similar to the dust in star forming galaxies. In fact, the host galaxy of PG 0050+124 is a spiral with a circum–nuclear ring of HII regions. Hotter dust of up to several 100 K is required to match the observations until the NIR regime. Other examples for similar – i.e. thermal emission dominated – SEDs come e.g. from PG 1613+658 and PG 1634+706.

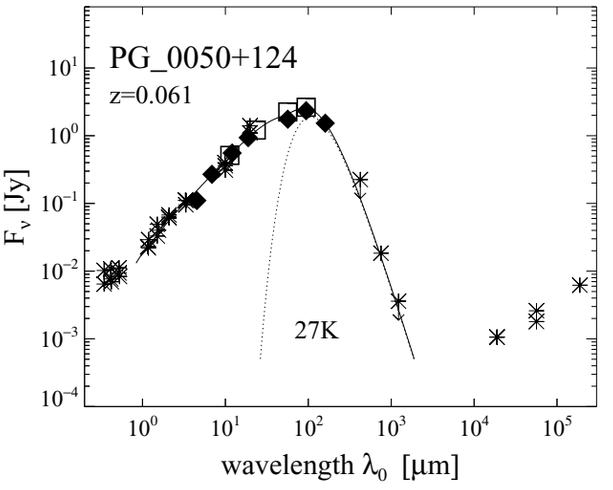

Fig. 1. The spectral energy distribution of PG 0050+124 in the rest frame of the quasar. The filled symbols denote our data from ISOPHOT, open squares come from *IRAS* and the asterisks are taken from the literature. A modified Planck curve has been fitted to the wavelengths between 200 and 1300 μm in order to estimate the temperature $T_{\rm d}$ of the coldest dust component

FR 0234+28 – The template object for a non–thermal origin of the FIR emission is the flat spectrum radio–loud QSO FR 0234+28 (Fig. 2). Again the ISO data exhibit a smooth (but much flatter) increase of the SED from optical to FIR wavelengths. However, beyond 100 μm the SED keeps rising until 1300 μm and remains flat within the radio regime. This spectral shape very probably originates entirely from synchrotron emission that extends from the radio into the visible regime. Other examples for similar, i.e. non–thermal emission dominated SEDs come e.g. from FR 2126-158 or 3C446.

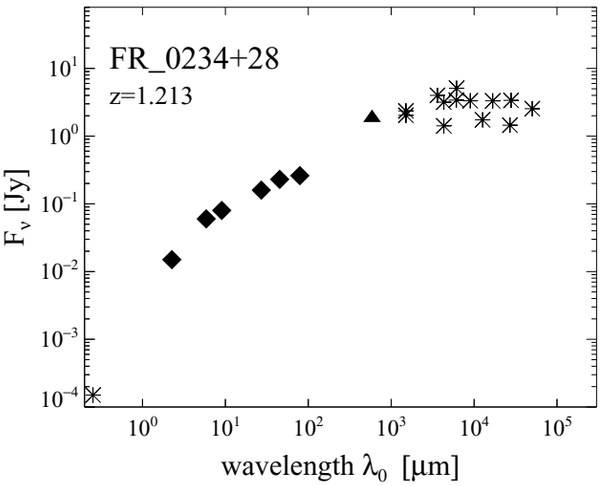

Fig. 2. The spectral energy distribution of FR 0234+28 in the rest frame of the quasar. The filled symbols denote our data from ISOPHOT and IRAM, the asterisks are optical and radio data from the literature

3C405 – The nucleus of this radio-galaxy (Cyg A) exhibits an SED (Fig. 3) that is a combination of the two previous cases. In the NIR and in the radio regime the emission of 3C405 has a comparable weak frequency dependence; this suggests a broad, underlying synchrotron component as indicated by the dashed line in Fig. 3. Between 7 and 300 μm there is emission in excess of this line; from 7 to 60 μm the SED increases and falls off steeply towards 200 μm. Both the turnover point and the following steep spectral slope lead us to interpret this excess as being dominated by thermal radiation sitting on top of the synchrotron emission. The coldest dust component is at a temperature of 53 K, but even hotter dust of 150 K is required to explain the SED until 7 μm; a similar SED can be found in 3C48.

3C279 – The SED of this archetypical flat spectrum radio–loud QSO (Fig. 4) is very similar to that of 3C405. As discussed in detail by Haas et al. [6], one

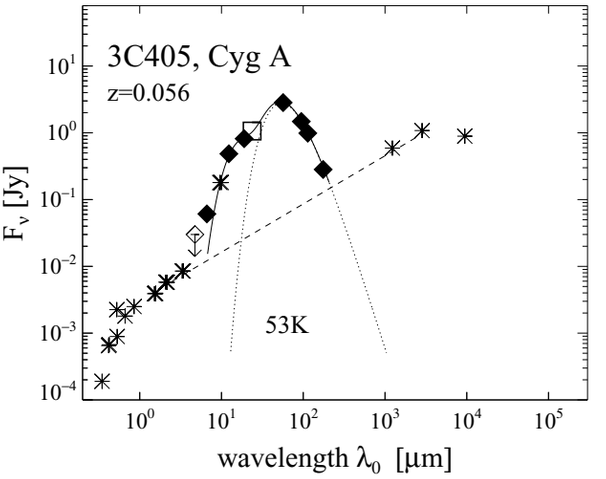

Fig. 3. SED of 3C405; same notation as Fig. 1

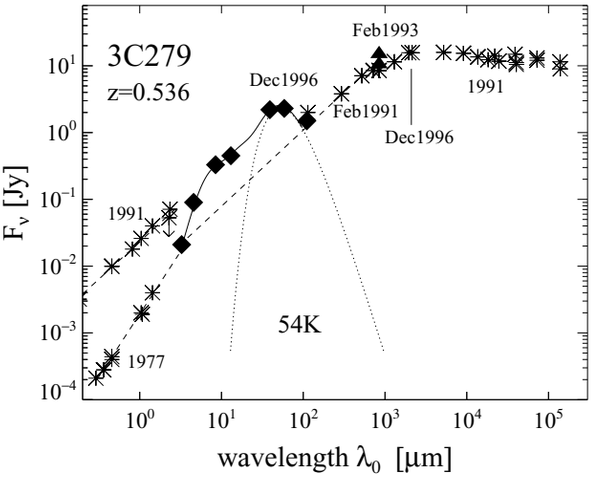

Fig. 4. SED of 3C279; same notation as Fig. 1

may decompose the observations into a synchrotron component that dominates from 0.3 to 5 μm and longward of 170 μm. The latter fact is corroborated by Klaas et al. [8], who observed variable polarised emission with ISOPHOT at 170 μm.

The ISOPHOT observations were performed at a stage of low non–thermal activity; the excess emission over the synchrotron interpolation (dashed line in Fig. 4) between 7 and 60 μm suggests the presence of thermal components of equal strength; the visibility of these components obviously depends on the

strength of the synchrotron component. Similar to 3C405 the coldest dust attains a temperature of 54 K.

PG 0044+030 – As seen in Fig. 5, PG 0044+030 is a radio–loud QSO whose non–thermal emission (or at least its extrapolation to shorter wavelengths) is fainter than the thermal component at FIR wavelengths. In this sense, the SED longward of its maximum is similar to that of the radio-galaxy Cyg A. At shorter wavelengths the shape of the SED differs from what we have seen so far: Instead of a power–law increase this source exhibits a three–level SED where the NIR, MIR and FIR levels are rather flat and separated from each other by discrete steps. The coldest dust is at a temperature of about 38 K or below that. Because mm/submm data are still missing, a corroboration of this interpretation has to await further data; the SED of PG 0052+251 seems to show similar behaviour (Haas et al. [7]).

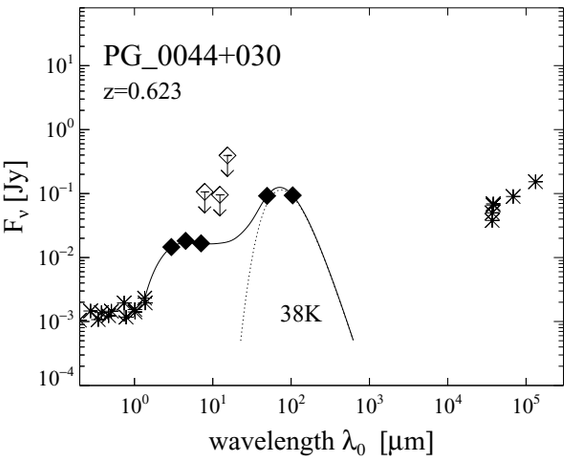

Fig. 5. The spectral energy distribution of PG 0044+030 in the rest frame of the quasar. A three–level SED short-ward of the maximum is indicated with rather flat levels at optical, NIR and FIR wavelengths

PG 1411+442 – This radio–quiet QSO shows a smooth increase of its SED from optical wavelengths to 10 μm and remains remarkably flat between 10 and 100 μm which definitely indicates a different type of SED. A similar FIR shape is found in PG 2112+059 (Haas et al. [7]). Interestingly, the archetype for such an infrared luminous SED is the QSO *IRAS* 13349+2438 (Beichman et al. [9] and Chini et al. [10]). Optical to NIR polarisation data suggest an inclined, thick, dusty disk, parallel to the plane of the host galaxy which absorbs most of the UV/optical light and reradiates it at infrared wavlengths (Wills et al. [11]).

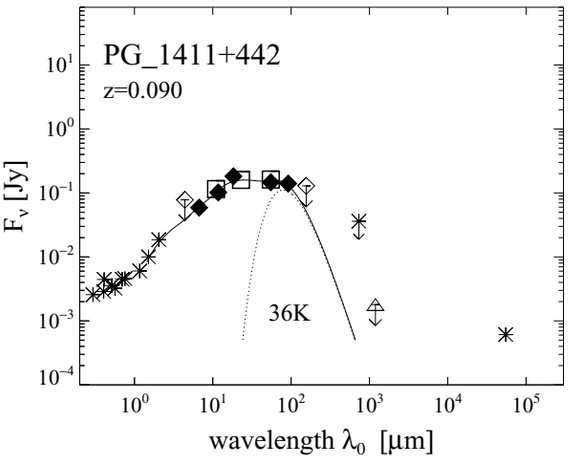

Fig. 6. The spectral energy distribution of PG 1411+442 in the rest frame of the quasar. A modified Planck curve has been fitted to the longest wavelengths of thermal emission in order to estimate the temperature $T_{\rm d}$ of the coldest dust component

4 The Nature of the FIR Emission

The results from the previous section have demonstrated that a broad thermal bump with a peak at around 60 μm is a common feature in the SEDs of most QSOs. Only in the rare cases of strong, flat spectrum radio QSOs can this thermal bump be masked by synchrotron radiation; as estimated by Chini et al. [5], even a considerably larger amount of dust (e.g. $10^9\,{\rm M}_\odot$ at 35 K) can easily be outshone by a corresponding non–thermal component. The broad range of temperatures, however, as witnessed by the various shapes of SEDs, have different energetic and spatial origins; furthermore, the emission components contribute with variable strength to the total luminosity.

The temperature of the coldest dust component in PG 0050+124 and other radio–quiet QSOs lies between 20 and 30 K and imply dust masses of $\approx 10^8\,{\rm M}_\odot$. These values are typical for the dust content of large spirals and indicate that the emission beyond 60 μm is dominated by cool dust powered by the interstellar radiation field in the disk of the host galaxy.

The analysis of the dust emission in radio–loud objects is difficult because of the strong underlying synchrotron radiation that is of comparable strength at FIR wavelengths and thus contaminates both the temperature and the mass estimates. Nevertheless, it seems that the coldest component in flat and steep radio spectrum QSOs (e.g. 3C279 and 3C48) and in radiogalaxies (e.g. 3C405) attains values between 34 and 54 K. The amount of dust associated with the radio-loud QSOs is of the order of several $10^8\,{\rm M}_\odot$ and thus comparable to the dust content in the host galaxies of radio–quiet QSOs. Temperatures between 30 and 40 K are generally found in active, starburst

dominated spirals. The temperature of the coldest dust in the radio-galaxy 3C405 is well constrained; the corresponding dust mass, however, is only about $5 \cdot 10^6\,M_\odot$ and thus a factor of 100 lower than in the host galaxies of QSOs; it is comparable to the dust content in elliptical galaxies.

Obviously, the SEDs shortward of $60\,\mu$m require additional dust components of higher temperatures. Their relative contributions reflect the influence of the dominant heating sources and the spatial distribution of the dust. For simplicity we compare three luminosities at 1, 10 and $100\,\mu$m corresponding to i) hot nuclear dust and stars (NIR), ii) warm circum–nuclear dust (MIR) and iii) cool dust from the host galaxy (FIR). Interestingly, for all but one object (PG 1411+442) the ratio $L_{\rm NIR}/L_{\rm FIR}$ ranges between 0.5 and 1, irrespective of the object class, i.e. including the synchrotron dominated sources. The ratio $L_{\rm MIR}/L_{\rm FIR}$ shows a larger scatter with values between 1 and 4 and thus seems to reflect intrinsic differences. Omitting, however, the synchrotron dominated sources this range decreases to 1 – 2 only.

PG 1411+442 deviates significantly from the above considerations with ratios $L_{\rm NIR}/L_{\rm FIR} = 5$ and $L_{\rm MIR}/L_{\rm FIR} = 10$! This result corroborates previous suggestions that a class of MIR–loud QSOs exists that might have escaped detection so far due to the selection criteria of optical and radio QSO surveys. The only similar object known so far is – as mentioned above – the radio–quiet QSO *IRAS* 13349+2438 with $L_{\rm NIR}/L_{\rm FIR} = 7$. In analogy, we interpret the MIR emission of PG 1411+442 as originating from a dense and hot circum–nuclear torus in which most of the UV photons are processed by dust grains into thermal MIR radiation. In contrast to *IRAS* 13349+2438, however, where the line of side towards the torus has been estimated to be at around 52° ($L_{\rm NIR}/L_{\rm FIR}$ is only 1.2), the torus of PG 1411+442 must be seen nearly face–on due to its relatively strong NIR luminosity.

References

1. Lemke D., Klaas U., Abolins et al. (1996) A&A 315, L64
2. Kessler M.F., Steinz J.A., Anderegg M.E., et al. (1996) A&A 315, L27
3. Neugebauer G., Soifer B.T., Miley G.K., Clegg P.E. (1986) ApJ 308, 815–828
4. Chini R., Kreysa E., Biermann P.L. (1989) A&A 219, 87–97
5. Chini R., Biermann P.L., Kreysa E., Gemünd H.-P. (1989) A&A 221, L3–L6
6. Haas M., Chini R. Meisenheimer K. et al. (1998) ApJ 503, L109–L113
7. Haas M., Müller S., Chini R. et al. (2000) A&A (accepted)
8. Klaas U., Laureijs R., Clavel J. (1999) ApJ 512, 157–161
9. Beichman C.A., Soifer B.T., Helou G. et al. (1986) ApJ 308, L1–L5
10. Chini R., Kreysa E., Salter C.J. (1987) A&A 182, L63–L65
11. Wills B.J., Wills D., Evans II N.J. et al. (1992) ApJ 400, 96–114

Infrared Properties of High Redshift and X-ray Selected AGN Samples

Belinda J. Wilkes[1], Eric J. Hooper[1], Kim K. McLeod[2], Martin S. Elvis[1], David H. Hughes[3], Chris D. Impey[4], Joanna K. Kuraszkiewicz[1], Carol S. Lonsdale[5], Matt A. Malkan[6], and Jonathan C. McDowell[1]

[1] Harvard-Smithsonian CfA, Cambridge, MA 02138 USA
[2] Wellesley College, Wellesley, MA 02481 USA
[3] INAOE, Puebla, Pue. Mexico
[4] Steward Observatory, Tucson, AZ 85721 USA
[5] IPAC, Caltech, Pasadena, CA 91125 USA
[6] UCLA, Los Angeles, CA 90095-1562 USA

Abstract. The NASA/ISO Key Project on active galactic nuclei (AGN) seeks to better understand the broad-band spectral energy distributions (SEDs) of these sources from radio to X-rays, with particular emphasis on infrared properties. The ISO sample includes a wide variety of AGN types and spans a large redshift range. Two subsamples are considered herein: 8 high-redshift ($1 < z < 4.7$) quasars; and 22 hard X-ray selected sources.

The X-ray selected AGN show a wide range of IR continuum shapes, extending to cooler colors than the optical/radio sample of [7]. Where a far-IR turnover is clearly observed, the slopes are < 2.5 in all but one case so that non-thermal emission remains a possibility. The highest redshift quasars show extremely strong, hot IR continua requiring $\sim 100 M_{\odot}$ of 500–1000 K dust with ~ 100 times weaker optical emission. Possible explanations for these unusual properties include: reflection of the optical light from material above/below a torus; strong obscuration of the optical continuum; or an intrinsic deficit of optical emission. A cosmology of (H_0, Ω_m, Ω_k, Ω_Λ) = (50 km s^{-1} Mpc^{-1}, 1, 0, 0) is assumed.

1 Introduction

Active galactic nuclei are among the broadest emission sources in nature, producing significant flux over a span > 9 decades in frequency, from radio to X-rays and beyond [7]. The various emission mechanisms involved are presumably ultimately powered by a central supermassive black hole [28].

A substantial fraction of the bolometric luminosity of many AGN emerges in the infrared, from synchrotron radiation and dust. Which of these is the principal emission mechanism is related to quasar type and is an open question in many cases [37]. Non-thermal emission is paramount in core dominated radio-loud quasars and blazars [19], although hot dust contributes in some cases [4]. The non-thermal component is likely related to radio and higher frequency synchrotron radiation, providing information about the relativistic plasma and magnetic fields associated with quasars. Other AGN classes

D. Lemke, M. Stickel, and K. Wilke (Eds.): LNP 548, pp. 177–184, 2000.

show evidence for a predominant dust contribution [6], particularly infrared-luminous radio-quiet quasars [15], or a mix of emission components [12]. Much of the dust emission is due to heating by higher energy photons from the active nucleus, and is therefore important for understanding the overall energy balance. The AGN thermal component may be an orientation-independent parameter, useful for examining unification hypotheses.

The nature of the foremost infrared emission source is ambiguous in many AGN with sparsely sampled spectral energy distributions (SEDs). Dust with smooth spatial and temperature distributions can mimic a power law spectrum [29,3], particularly in the absence of detailed measurements to reveal bumps from temperature and density inhomogeneities. Grain emissivity is characterized by a Planck function multiplied by a power law factor $\propto \nu^{1-2}$ [16], so spectral slopes in the Rayleigh-Jeans region of the coldest potential thermal component lie between $\alpha = 2$–4, depending on the grain properties and optical depth. Known synchrotron emitters have relatively flat sub-mm power-law spectra ($\alpha \leq 1.1; f_\nu \propto \nu^\alpha$) [10], and radio sources generally have spectra flatter than the canonical $\alpha = 2.5$ for a self-absorbed homogeneous synchrotron source [26]. Therefore, $\alpha = 2.5$ is a convenient partition to distinguish thermal emission from standard non-thermal models, and simple two-point spectral slopes and even lower limits to spectral indices may reveal the dominant mechanism. However, synchrotron models with a concave electron energy distribution [5,31], free-free absorption, or plasma suppression [32] can produce slopes steeper than $\alpha = 2.5$. While $\alpha = 4$ is observed in some milliarcsecond radio knots [24], thermal models offer the most consistent explanation for steep far-infrared (FIR) to mm slopes [15,1]. A thermal origin is considered to be the most likely explanation for sub-mm/FIR slopes $\alpha > 2.5$ in the present work.

Two large, complementary ISO AGN observing programs are opening up new wavelength windows in the FIR as well as improving the spatial resolution and sampling at shorter wavelengths: the ISO European Central Quasar Program [12,13]; and the NASA/ISO Key Project on AGN, discussed herein. The Key Project sample consists of 5–200 μm chopped and rastered ISOPHOT [22] observations of 73 AGN selected to incorporate a wide range of AGN types and redshifts. The data are reduced using a combination of the (ISO-) PHOT Interactive Analysis (PIA) [9] software plus custom scripts. Details of the reduction, difficulties encountered, and early results are discussed in [36,17,38,18]. These observations directly measure the FIR spectral slopes in low and moderate redshift AGN and provide better constraints on the emission mechanisms throughout the infrared region. Some of the fundamental questions being addressed with the new data include: the range of SEDs within each quasar type; differences between one type and another; the evolution of the SEDs; and correlations with fluxes at other wavebands, host galaxy properties, and orientation indicators. This paper focuses on two subsamples, hard X-ray selected AGN, and high-redshift quasars.

2 Hard X-ray Selected AGN

Infrared and X-ray data complement each other well and are important for understanding the overall AGN energy balance. Non-thermal infrared emission is possibly connected with the X-rays, either directly as a portion of a broad synchrotron component, or as part of a radio-infrared seed spectrum which Compton scatters to produce the X-rays. Infrared data from dust-dominated sources reveal the level of ultra-violet (UV) and soft X-ray radiation which has been reprocessed, and dust masses can be estimated assuming optically thin emission.

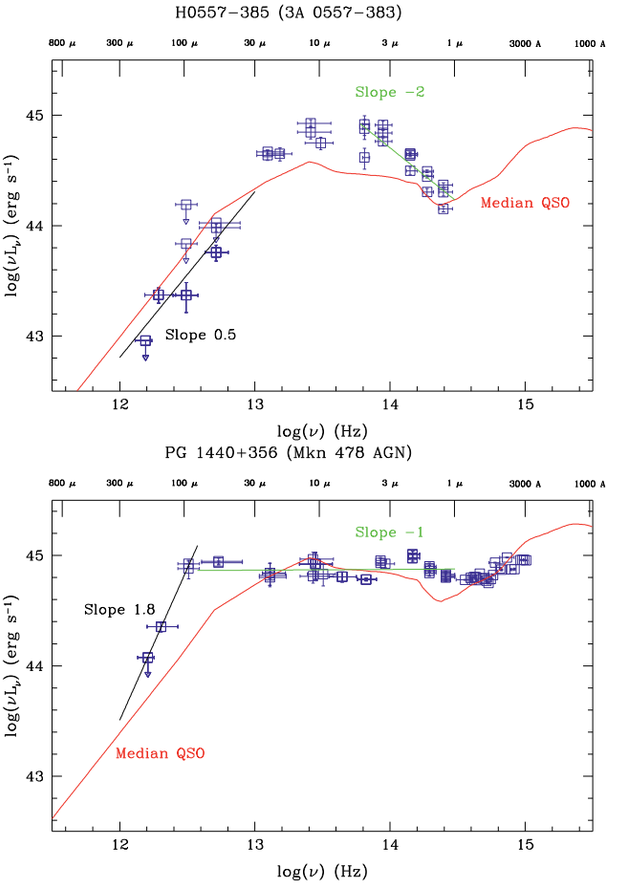

Fig. 1. *Spectral Energy Distributions (SEDs) of H0557-385 (top) and PG1440+356 (bottom) compared with the median SED for a low-redshift sample [7] illustrating the two extreme SED types present in this sample. The near-IR and far-IR cutoff slopes are indicated in both cases.*

Table 1. X-ray Selected Sample: IR SED Parameters.

Name	z	$L_{10-100\mu}$ 10^{44} erg s^{-1}	$L_{1-10\mu}$ 10^{44} erg s^{-1}	α_{IR}	α_{cut}
MKN 1152	0.052	6.3	2.4	−0.9	–
MKN 590	0.025	3.3	4.2	−0.9	–
H0235−52	0.045	4.5	2.6	−1.6	0.2
H0557−385	0.034	11.9	3.8	−2.1	0.7
PG0804+761	0.100	37.1	53.0	−1.9	0.6
H1039−074	0.674	450.	190.	–	–
NGC 3783	0.009	1.3	1.6	−1.4	1.4
TON 1542	0.064	8.3	15.9	−1.7	–
IR1321+058	0.201	210.	6.4	−2.8	1.8
MCG−6−30−15	0.008	0.6	0.4	−1.6	1.3
IC4329A	0.014	5.4	20.3	− 0.8	
H1419+480	0.072	15.5	7.2	−1.3	0.3
PG1440+356	0.077	18.1	17.5	−1.1	1.8
H1537+339	0.330	72.3	42.7	−1.1	–
KAZ1803+676	0.136	20.9	31.0	−1.3	0.2
E1821+643	0.297	720.	550.	−1.1	2.5
H1834−653	0.013	1.2	0.3	−1.9	1.6
MKN 509	0.035	11.4	20.3	−1.0	2.2
NGC 7213	0.006	1.0	0.6	–	–
MR2251−178	0.068	18.4	23.6	−0.9	3.7
MCG-2-58-22	0.048	13.0	10.0	−0.9	2.5

Most X-ray selected AGN to date have been observed in soft energy bands < 3.5 keV [33,35,14]. These surveys suffer obscuration biases similar to optical selection, due to the gas typically associated with dust. The absorption cross-section drops steeply with increasing energy [39], so hard X-ray selection is much less affected by intervening material. Surveys in hard X-rays arguably are the most efficient way to distinguish between accreting and stellar sources [8] as well as the optimal method for defining a representative sample of AGN [37]. A comparison between the UV/soft X-ray flux absorbed and the IR emission provides an estimate of the relative importance of accretion and stellar power in AGN. We randomly selected 23 ISO targets (of which 22 are reported in Table 1) from a 2–10 keV AGN sample derived from the A2 experiment onboard the HEAO 1 satellite [11,20]; 12 of these are also in the earlier Piccinotti sample [21,23,27] from the same experiment.

Figure 1 shows the IR−optical SEDs for two HEAO AGN illustrating the wide range of behavior present. H0557−385 shows a strong hot component with a steep near-IR slope ($\alpha_{ir} \sim -2$, $F_\nu \propto \nu^\alpha$) and a turnover which is relatively flat. PG1440+356 shows a very flat optical−near-IR continuum ($\alpha_{ir} \sim -1$), a strong cool component compared with the low-redshift median [7] and a steeper turnover ($\alpha_{cut} \sim 1.8$) which, however, still remains below the critical value of 2.5 indicating thermal emission. The range of IR continua in the sample overlaps but extends to redder continua than an opti-

cal/radio selected sample [7]. This is apparent in the low mean for the near-IR slope, $\alpha_{IR} \sim -1.4 \pm 0.5$ compared with the Median SED value of -1.0 ± 0.3 and also the extension to cooler values of the ratio of decade luminosities: $\mathrm{L}(1-10\mu)/\mathrm{L}(10-100\mu) = 0.8 \pm 0.5$ compared with the radio/optical sample: 1.0 ± 0.8. The latter is also illustrated by comparison of the histograms in Figure 2. However a Kolmogorov-Smirnov test does not indicate a significant difference in the samples (P=18%). If real, this trend is an interesting extension to the lack of bias against red optical/UV continua in these sources. Confirmation awaits more systematic comparisons in an upcoming paper.

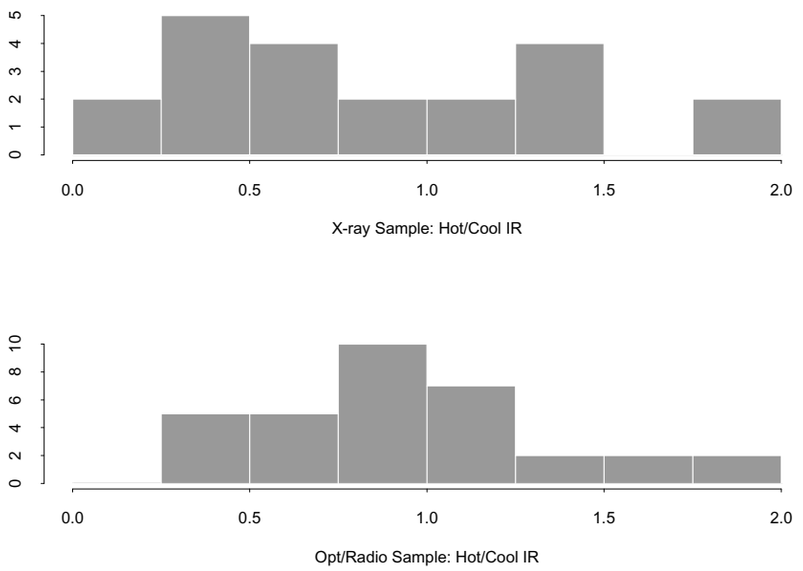

Fig. 2. *A comparison of the distribution of the ratio of hot to cool IR luminosities ($L(1-10\mu)/L(10-100\mu)$) for the HEAO sample with that of [7]. While a suggestive trend toward stronger cool luminosities is present in the HEAO sample, a KS test gives only an 18% probability that this is significant.*

3 High Redshift AGN

While skewed to low-redshift objects, due in part to lost sensitivity and changes in observing mode, the Key Project sample contains 8 quasars in the redshift range $1.0 \leq z \leq 4.7$. In order to cover the intrinsic FIR continuum in these sources, we also have an on-going sub-mm observing program at the JCMT.

The spectral energy distributions of these quasars vary widely. The highest redshift sources: 1202−0727 ($z = 4.69$); 1508+5714 ($z = 4.3$); and 1413+1143 ($z = 2.551$), are factors of 10–100 brighter in the near-IR than the low-z

median SED [7] (Figure 3). At lower redshifts, PG1407+265 ($z = 0.944$) and PHL5200 ($z = 1.981$) are a much closer match to the median, while PG1718+481 ($z = 1.084$) is > 5 times fainter throughout the IR. A much larger sample will be required to determine the underlying distribution of SEDs at moderate and high-z which is hinted at by the variety seen here.

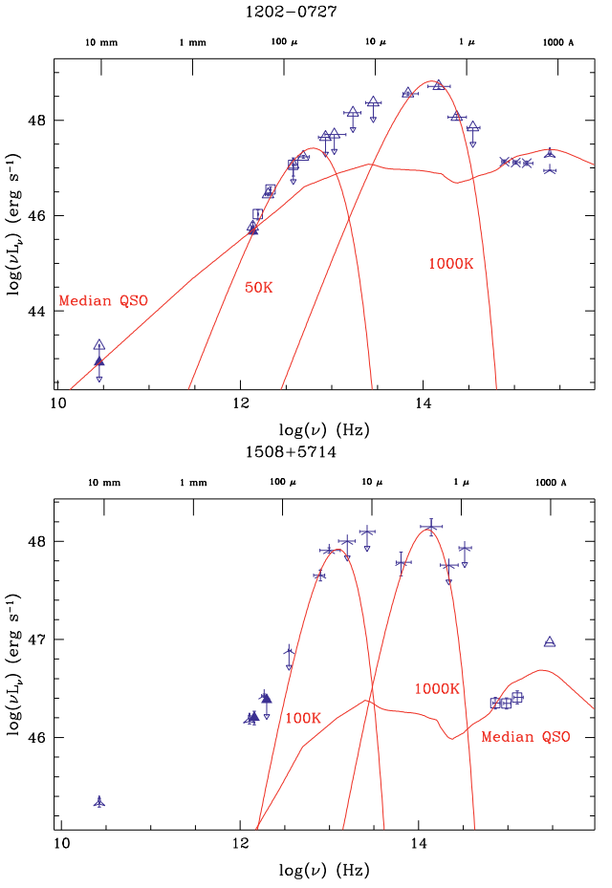

Fig. 3. *Spectral Energy Distributions (SEDs) of a) 1202−0727 and b) 1508+5714 compared with the median SED for a low-redshift sample [7] illustrating the extremely strong near-IR emission in both sources. Grey-body curves illustrating the minimum range of temperatures for purely thermal emission are also shown.*

The strong IR emission in the highest redshift quasars places them amongst the most powerful sources known. The range of temperatures is broad, 40–1000 K. Table 2 lists derived properties for two sources. The mass estimates assume optically thin gray dust with $\beta = 2$. The $40\,K$ component in 1508+5714 is based on only the observed 850 μm flux; it is likely to be an

upper limit, because the FIR slope is flattening at those wavelengths, indicating possible contamination by a high frequency extension of the non-thermal radio emission. These and other high-redshift AGN [1,15,25] contain large amounts of dust, which implies a substantial star formation rate (SFR). Average SFRs listed in Table 2 were calculated from the inferred mass assuming a 1% dust production efficiency [2] and an onset of star formation at $z = 10$. Estimates of the FIR luminosity due solely to this SFR, computed with a conversion of $2.2 \times 10^9\, L_\odot\, M_\odot^{-1}$ yr [30], are also listed. These are $\sim$ factor 10 below the observed luminosities, implying that the bulk of the FIR emission is driven by the AGN, or the sources are undergoing an intense starburst of $\geq 1000\, M_\odot\, \mathrm{yr}^{-1}$.

Both sources have large excesses over the median SED in a spectral region that corresponds to warm and hot dust emission. This emission cannot yet be conclusively attributed to a thermal source, but that is a strong possibility, since cool dust is clearly present in 1202−0727 and both objects show a sharp cutoff at wavelengths corresponding to the Wien region of dust near the sublimation temperature. The difficulty with a dust interpretation is the energy source to heat the material; the observed rest-frame optical and near-UV luminosity is clearly too low in both sources. Dust may obscure all but a small fraction $\sim$ 1% of the intrinsic blue bump luminosity. It is unlikely that we are directly viewing the extincted source, as broad emission lines are clearly visible on continua which do not appear heavily reddened [34]. The observed flux may be diminished by reflection off of a scattering surface positioned above a dust torus. Alternatively, if we are seeing the intrinsic output of the central engine in the optical and near-UV, then these AGN must be abnormally luminous in the far-UV and X-rays. There is an indication of a blue upturn in 1202−0727, but the requisite luminosity remains unobserved.

Table 2. Properties of two High-Redshift Sources

Name	z	Dust Mass ($M_\odot$)			$\overline{\mathrm{SFR}}$	FIR($\overline{\mathrm{SFR}}$)
		$40\,K$	$100\,K$	$1000\,K$	($M_\odot\,\mathrm{yr}^{-1}$)	($10^{45}\,\mathrm{erg\,s}^{-1}$)
1202−0727	4.690	1.5×10^9	$< 2.2 \times 10^7$	300	250	2.1
1508+5714	4.300	2.0×10^9	3.6×10^7	53	280	2.4

4 Summary

The principal points discussed in this paper are:

- The X-ray selected AGN show a broader, cooler range of IR continua than optical/radio selected AGN.
- The X-ray selected sample show no strong evidence (MR2251−178 excepted) for a steep, $\alpha_{cut} > 2.5$, far-IR turnover, which would rule out non-thermal emission. Sub-mm observations are necessary to confirm.
- $z > 4$ quasars show $\sim$100 times stronger near-IR emission than low-z AGN. This may be due to strong obscuration, orientation or a real deficit of optical emission in these sources.

- The strong cool IR emission in the high-z sources implies dust masses $> 10^9\,M_\odot$, which would require an average SFR of a few hundred $M_\odot\,\mathrm{yr}^{-1}$. This underproduces the observed FIR flux, so there is either a major AGN component, or the SFR at the time of observation is significantly larger, $\geq 1000\,M_\odot\,\mathrm{yr}^{-1}$.

References

1. Andreani, P., Franceschini, A., & Granato, G. 1999, MNRAS, 306, 161
2. Blain, A. W., et al. 1999, MNRAS, 302, 632
3. Bollea, D., & Cavaliere, A. 1976, A&A, 49, 313
4. Courvoisier, T. J.-L. 1998, A&ARv, 9, 1
5. de Kool, M., & Begelman, M. C. 1989, Nat, 338, 484
6. Edelson, R. A., Malkan, M. A. 1987, ApJ, 323, 516
7. Elvis, M. S., et al. 1994, ApJS, 95, 1
8. Fiore, F., et al. 1999, MNRAS, 306, L55
9. Gabriel, C., et al. 1998, Proc. of ADASS VII, ASP Conf. Ser., 145, 165
10. Gear, W., et al. 1994, MNRAS, 267, 167
11. Grossan, B. A. 1992, Ph.D. Thesis, MIT
12. Haas, M., et al. 1998, ApJ, 503, 109L
13. Haas, M., et al. 1999, A&A, submitted
14. Hasinger, G., et al. 1998, A&A, 329, 482
15. Hughes, D. H., et al. 1993, MNRAS, 263, 607
16. Hildebrand, R. H. 1983, QJRAS, 24, 267
17. Hooper, E. J., et al. 1999, in The Universe as Seen by ISO, 893
18. Hooper, E. J., et al. 1999, ASP Conf. Ser. 177, 153
19. Impey, C. D., & Neugebauer, G. 1988, AJ, 95, 307
20. Jahoda, K., & Mushotzky, R. F. 1989, ApJ, 346, 638
21. Kotilainen, J. K., et al. 1992, MNRAS, 256, 149
22. Lemke, D., et al. 1996, A&A, 315, L64
23. Malizia, A., 1999, ApJ, 519, 637
24. Matveyenko, L. I., & Witzel, A. I. 1999, Ast Let, 25, 643
25. McMahon, R. G., et al. 1999, MNRAS, 309, L1
26. O'Dea, C. P. 1998, PASP, 110, 493
27. Piccinotti, G., et al. 1982, ApJ, 253, 485
28. Rees, M. J. 1984, ARAA, 22, 471
29. Rees, M. J., et al. 1969, Nat, 223, 788
30. Rowan-Robinson, M. 1997, MNRAS, 289, 490
31. Schlickeiser, R., Biermann, P. L., Crusius-Wätzel, A. 1991, A&A, 247, 283
32. Schlickeiser, R., & Crusius, A. 1989, IEEE Trans Plas Sci, 17, 245
33. Stocke, J. T., et al. 1991, ApJS, 76, 813
34. Storrie-Lombardi, L. J., et al. 1996, ApJ, 468, 121
35. Thomas, H. C., et al. 1998, A&A, 335, 467
36. Wilkes, B. J. 1997, in Quasar Hosts, 136
37. Wilkes, B. J. 1999, in Quasars & Cosmology, ASP Conf. Ser. 162, 15
38. Wilkes, B. J., et al. 1999, in The Universe as Seen by ISO, 845
39. Zombeck, M. V. 1990, Handbook of Space Astron. & Astrophys., 2nd Ed., 198

A FIR Surveys of CSS and GPS Radio Galaxies

Francesca Pozzi[1], Carla Fanti[2,3], and Roberto Fanti[2,3]

[1] Dipartimento di Astronomia, Bologna, Italia
[2] Dipartimento di Fisica, Bologna, Italia
[3] Istituto di Radioastronomia, C.N.R., Bologna, Italia

Abstract. With ISOPHOT we have observed a sample of 17 CSS/GPS radio galaxies and a control sample of 16 extended radio galaxies spanning similar ranges in redshift ($0.2 \leq z \leq 0.8$) and radio luminosity ($P_{2.7GHz} \geq 10^{26} W/Hz$). The observations have been performed at $\lambda = 60, 90, 170, and 200\mu$m. The original purpose of these observations was to check whether CSS/GPS sources are associated with galaxies with an ISM different from that in extended radio sources.

By co–adding the data we have found no difference in the FIR properties of the ISM. So we have combined the two samples providing FIR information on a sample of radio galaxies at intermediate redshifts.

1 Introduction

Compact Steep Spectrum (CSS) and GHz Peaked Spectrum (GPS) radio sources are powerful extragalactic radio sources with radio emission confined well within their host galaxy/quasar. They are as powerful as the classical FRII radio sources but of much smaller physical size and yet with normal/steep radio spectra at GHz frequencies. Typically 25 % of a flux limited sample of steep spectrum radio sources belong to this class. For a review of the characteristics of these objects and related problems (see, e.g., [2] and [8]).
They could be either young objects (*youth* scenario) or sources which were born in an anomalous dense ISM which prevents them from growing to the hundreds of kpc of FRII radio sources (*frustration* scenario).
To distinguish between these two scenarios, a direct measure of the properties of the ISM is essential. Searches have been performed at optical, X-ray, MIR wavelengths, without any clear evidence that the ISM in CSS and GPS galaxies is different from that in galaxies associated with FRII radio sources. Here we give a preliminary report on FIR measurements, which probe the colder medium ($20K < T < 100K$) not investigated so far. A more detailed presentation will be given in a forthcoming paper (Fanti et al., submitted).

2 Sample and Observations

The sample is composed of 17 CSS/GPS radio galaxies in the red–shift range $0.2 < z < 0.8$ with radio sizes < 10 kpc (H_0=100 Km/(sec Mpc) and

D. Lemke, M. Stickel, and K. Wilke (Eds.): LNP 548, pp. 185–190, 2000.

q_0=0.5). A sample of 16 3CR radio galaxies with radio sizes > 20 kpc which spans a similar range in redshift and luminosity was selected for comparison purposes. The two samples are presented in tables 2 & 2.

Table 1. CSS/GPS sample

Source	z	LogP$_{2.7}$ (W/Hz)	LS kpc	Sample	Source	z	LogP$_{2.7}$ (W/Hz)	LS kpc	Sample
0108+38	0.67	26.79	0.023	PW	1607+26	0.47	26.92	0.18	PW
3C49	0.62	26.89	3.6	3CR	1622+66	0.20	25.66[a]	0.0013	Sn
3C67	0.31	26.30	6.8	3CR	3C343.1	0.75	27.24	1.3	3CR
0404+76	0.60	27.23	0.53	PW	1819+39	0.798[b]	27.23	3.4	PW
1244+49	0.21	25.63	5.7	San	1819+67	0.22	25.06	0.02	Sn
3C268.3	0.37	26.54	3.9	3CR	1829+29	0.60	26.96	9.3	PW
1323+32	0.37	26.75	0.18	PW	2342+82	0.74	27.25	0.66	PW
1358+62	0.43	26.81	0.16	PW	2352+49	0.24	26.18	0.15	PW
3C303.1	0.27	25.60	5.0	3CR					
median: $z = 0.43$ LogP$_{2.7GHz} = 26.79$ LS=1.0									

a): the spectrum of this GPS peaks at ≈3 GHz, and its $P_{2.7GHz}$ has been extrapolated from the spectrum at high frequencies. b) revised redshift from [13]. Sample – PW: Peacock and Wall [9]; 3CR: Laing et al. [7]; San: Sanghera [11]; Sn: Snellen [12].

The sources were observed with the ISOPHOT sub–instruments C100 & C200 at the wavelengths of 60, 90, 170 & 200 μm. Observations were made in rectangular chopping mode, with a chopper throw of 180", in order to have every few seconds (*chopper plateau*) an ON–source and an OFF–source measure of the same time length. The OFF data then have to be subtracted from the ON data in order to extract the source signal. The ON–source time ranges from 32 to 256 sec.

3 Data Reduction

The data analysis was carried out using mainly the PIA V7.2 (*ISO***P***hot* **I***nteractive* **A***nalysis*) software [5]. Some further software has kindly been made available to us by Dr. M. Haas from MPIA (Heidelberg) or has been written by ourselves.

In particular, we have estimated *the vignetting correction* for C200 from the data themselves, since, after running PIA, the (ON – OFF) fluxes were,

Table 2. Control Sample

Source	z	$\mathrm{LogP}_{2.7GHz}$ (W/Hz)	LS kpc	Source	z	$\mathrm{LogP}_{2.7GHz}$ (W/Hz)	LS kpc
3C 16	0.41	26.31	135	3C284	0.24	25.87	409
3C 19	0.48	26.77	20	3C295	0.46	26.51	20
3C 34	0.69	26.67	174	3C299	0.37	26.44	33
3C 42	0.40	26.51	85	3C330	0.55	27.18	192
3C 46	0.44	26.18	533	3C337	0.64	26.96	153
3C 79	0.26	26.32	212	3C401	0.20	26.12	40
3C274.1	0.42	26.52	470	3C441	0.71	27.03	117
3C277.2	0.77	26.92	214	3C459	0.22	26.18	20
median: $z = 0.43$ $\mathrm{LogP}_{2.7GHz} = 26.51$ LS=150							

on average, systematically negative, with a clear dependence on the background brightness.

The flux density for C100 has been computed by dividing the flux density falling onto pixel #5 by the appropriate value of f_{PSF}. For C200 the flux density has been obtained by summing the (ON–OFF) four matrix pixels and dividing the result by f_{PSF}.

The total flux density error σ_T on a source has been computed as:

$$\sigma_T = \sqrt{\sigma_n^2 + \sigma_{egc}^2 + \sigma_{cc}^2}$$

where σ_n is the individual source noise, σ_{egc} is the error due to the extragalactic confusion (which is the same in all fields at a given wavelength) and σ_{cc} the cirrus confusion noise appropriate for the specific source background.

The latter have been evaluated using IRSKY software by IPAC while σ_n has been derived, for each source, from the statistics of the (ON – OFF) sequence values. The software for this analysis is from M.Haas (private communication).

4 Individual and Average Detections

We considered detected the sources for which $S \geq 5 \times \sigma_T$ at least at one wavelength and possibly detected those for which $3 \times \sigma_T \leq S < 5 \times \sigma_T$. Only two sources, 1819+39 and 3C459, are clearly detected at least at one wavelength, while nine more sources (3C49, 1323+32, 3C303.1, 1622+663,

2352+49, 3C34, 3C79, 3C277.2 and 3C284) are possible detections. There are also a number of sources which have $3 \times \sigma_n \leq S < 3 \times \sigma_T$ at least at one wavelength. We have considered these just "formal" detections since it *does not mean* that we have *detected our target sources*, as extragalactic and/or cirrus confusion could cause spurious detections.

We have then co–added all measurements to look for an "average" emission from both the CSS/GPS sample and the control sample in order to search for a statistical difference between the two. By comparing the median values, we conclude that there is no statistical evidence that the FIR properties of galaxies associated with CSS/GPS are different from those of the galaxies associated with large size radio galaxies. This is a proof in favour of the youth scenario.
This will allow us to combine the two sets of data in the discussion.

5 Discussion

Given the same FIR properties, we have considered the two samples as a single sample of 33 radio galaxies at intermediate redshift, 0.2 <z< 0.8. In table 3, we report the mean and median FIR fluxes of the entire sample and the average FIR luminosities.

Considering also the data given in [3], we find that the dependence on frequency of the FIR flux can be described by a power law:

$$S(\nu) \propto \nu^{-1\pm0.2}$$

The MFIR average spectrum ($\lambda_{rest} \geq 20\mu$m) in nearby radio quiet ellipticals (Bregman 1996) is definitely steeper than that of our radio galaxies and of those given in [6]. The spectral index ($S(\nu) \propto \nu^{-\alpha}$) of the former is $\alpha_{RQE} \approx 2.3 \pm 0.2$, as compared to $\alpha_{us} \approx 1 \pm 0.2$ in our sample and $\alpha_{Knapp} \approx 1.2 \pm 0.2$ in [6]. This implies that the heating processes are different, with the one present in radio galaxies being more effective, probably due to an obscured quasar. This interpretation is further supported by the correlation between radio emission and MFIR emission [6] [4], with which our data are also consistent (fig. 1).

In the hypothesis that the dust is transparent at these wavelenghts, the FIR emission at a given temperature follows a modified Planck law given by

$$S(\nu_0) = \frac{\mu(\nu_e) B_{b.b.}(\nu_e) M_{dust}(1+z)}{D_L^2}$$

where ν_o and ν_e are the observed and emitted frequencies, μ the absorption coefficient, $B_{b.b.}$ the brightness of a black body at temperature T, M_{dust} the dust mass, D_L the luminosity distance and z the source redshift. We take $\mu(\lambda) = 10 \times (\lambda(\mu m)/250)^{-1}$ for $\lambda \leq 250\mu$. In order to fit our data, we have taken a simple two temperature approximation, with $T_1 = 80$ K and $T_2 = 25$ K with corresponding dust masses $M_1 \approx 5 \times 10^5\ M_\odot$ and $M_2 \approx 2 \times 10^8 M_\odot$.

Table 3. Average flux densities and FIR luminosities for the whole sample. Errors for both, mean and median, are 2 σ.

λ	mean			median	$L_{FIR}/L_{\odot}$	L_{FIR}
μm	mJy					erg s^{-1}
60	35	$\pm$	22	20^{+34}_{-13}	6×10^{10}	$\approx 2.4 \times 10^{44}$
90	29	$\pm$	16	32^{+15}_{-16}		
170	74	$\pm$	114	48^{+139}_{-37}	$\approx 10^{11}$	$\approx 5 \times 10^{44}$
200	256	$\pm$	112	232^{+123}_{-114}		

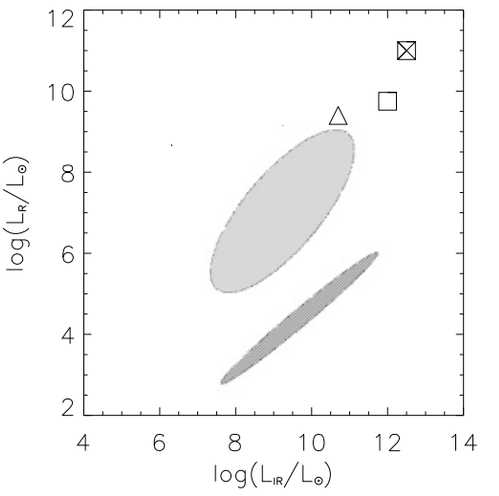

Fig. 1. Radio versus IR luminosity. Shaded areas represent the regions occupied by spirals and low power radio galaxies from [6]. The triangle marks the median values for the present sample of radio galaxies, while the empty and crossed squares are the low$-z$ and high$-z$ quasars respectively [3].

This range in temperatures is in agreement with the heating model of Sanders et al., which assumes an obscured AGN in the centre of the galaxies [10].

6 Conclusions

- We have presented ISOPHOT observations at $\lambda = 60, 90, 170, 200\mu$m of CSS/GPS radio galaxies and of a comparison sample of extended radio galaxies. A minority of objects is detected individually.
- From the data co–addition, we find no significant difference in the MFIR flux densities of the two samples. Thus we have combined the two samples for further analysis.
- The MFIR spectrum can be fitted by a single power law $\alpha_{us} \approx 1 \pm 0.2$. The average $L_{\rm FIR}$ are in the range $(0.5 - 1.0) \times 10^{11}$ L$_\odot$.
- We have fitted a two temperature ($T_1 = 80$ K and $T_2 = 25$ K) model to the IR spectrum and have derived dust masses of $M_1 \approx 5 \times 10^5$ $M_\odot$ and $M_2 \approx 2 \times 10^8 M_\odot$.
- Our observations are consistent with the MFIR luminosity in these powerful radio galaxies, being mostly powered by an obscured AGN - with a modest contribution from star formation in some objects.

References

1. Bregman J.N. et al., 1998, Ap.J., 499, 670
2. Fanti C. et al., 1995, A&A, 302, 317
3. Heckman T.M. et al., 1992, ApJ., 391, 39
4. Heckman T.M. et al., 1994, ApJ., 428, 65
5. Gabriel C. et al., 1997, Proc. of the ADASS VI Conf., ASP Conf. Ser, 125, 108
6. Knapp G.R. et al., 1990, AJ., 99, 476
7. Laing R.A. et al., 1983, MNRAS, 204, 151 (**3CR**)
8. O'Dea C.P., 1998, PASP, 110, 493
9. Peacock J.A. et al., 1982, M.N.R.A.S., 198, 843 (**PW**)
10. Sanders D.B. et al., 1989, Ap.J., 347, 29
11. Sanghera H.S. et al., 1995, A&A, 295, 629
12. Snellen I.A.G. et al., 1998, A&AS, 131, 435
13. Vermeulen R.C. et al., 1999, submitted to MNRAS

Seyfert Galaxies in the Far IR

José M. Rodríguez Espinosa[1] and Ana M. Pérez García[1]

Instituto de Astrofisica de Canarias
E-38200 La Laguna, Tenerife
Spain

Abstract. We show the results of a mid and far IR study of ISO data of the CfA Seyfert sample. These data allow a detailed study of the far IR Spectral Energy Distribution (SED) of these galaxies. We find that the mid and far IR SED of Seyfert galaxies can be explained solely through thermal reradiation of high energy photons by dust, and, that this thermal emission is made up of two or three different independent components, a warm, a cold and a very cold dust component. These thermal components have been explained as produced respectively by warm dust heated by either the active nucleus or by circumnuclear starburts, cold dust heated by star forming region in the galaxy disk, and very cold dust heated by the general interstellar radiation field.

1 Introduction

The origin of the IR emission from Seyfert galaxies has been debated since very early at the dawn of IR astronomy (e.g. Rieke & Low [1]; Stein [2]; Rieke [3]; Neugebauer [4], and others). The use of efficient instruments to observe at 10 μm, and especially the pioneering work at the far IR carried out from the Kuiper Airborn Observatory (KAO) showed the importance of the mid and far IR emission to quantify the bolometric luminosity of Seyfert galaxies ([5], [6]). However, the IRAS satellite that provided an extensive set of IR data for a large number of galaxies, was key to show that Seyfert galaxies are indeed strong far IR emitters ([7], [8], [9]). However the IRAS data alone are not sufficient to clarify the nature of the IR emission, as there are measurements only at a limited number of wavebands preventing a good definition of the shape of the Spectral Energy Distribution (SED) at mid and far IR wavelengths. A proper characterization of the mid and far SED is essential to understand the emission mechanisms that produce the high output of Seyfert galaxies in the IR.

Another important issue is the understanding of the differences between the two Seyfert types. According to the unified models, Seyfert 2 nuclei are intrinsically similar to Seyfert 1 nuclei, the differences observed being due solely to geometrical effects. In Seyfert 2, neither the broad line region nor the optical, UV and soft X ray continuum can be observed directly because the central region is obscured by intervening material in the line of sight. Some authors argue that this material forms a sort of disc or torus of molecular material, that is reponsible for the collimation of radiation and the observed

D. Lemke, M. Stickel, and K. Wilke (Eds.): LNP 548, pp. 191–198, 2000.

anisotropies, i.e., biconic structures in emission line images ([12], [13]) or highly collimated jets. It is expected that at sufficiently long wavelengths the optical depth of the torus would decrease and the differences between the two Seyfert types disappear. These obscuring tori have been theoretically modeled by Pier & Krolik [14] and Granato & Danese [15] among others, predicting that the mid IR optical depth is still considerable, thus it should be expected that Seyfert 1s are more luminous than Seyfert 2s in the mid IR.

In this paper we study the spectral energy distributions (SEDs) of Seyfert galaxies through ISO data of the entire CfA Seyfert sample ([16]) consisting of 25 Seyfert 1 and 22 Seyfert 2, plus a LINER.

2 Observations

Observations of the CfA Seyfert sample have been carried out with the Infrared Space Observatory (ISO; [17]) through filters at 16, 25, 60, 90 120, 135, 180 and 200μm. The ISOPHOT instrument ([18]) was used in the PHT-P and PHT-C configurations, with the P1, P2, C100 and C200 detectors. Integration times were calculated from the signal/noise ratio estimates produced by the ISOPHOT simulator based on interpolations and extrapolations of the IRAS data. The PHT-P observations were done in chopping mode through a 120 or 180 arcsec aperture depending on the size of the objects. The PHT-C observations were done in staring mode. In this case, to set the background level, an empty area adjacent to the source was observed prior to the actual source and with identical instrumental settings. For NGC 1068 we have done maps with C100, at 60 and 105 μm, moving by half a pixel (23") between two contiguous map positions. Four additional objects (NGC 3079, NGC 3227, NGC 4051 and NGC 4151) have been mapped at 90 μm with the C100 array. Details of the mapping observations of these four galaxies are given in Pérez García, Rodríguez Espinosa & Fuensalida [19].

3 Results

The Seyfert SEDs describe a well defined energy range with a steady increase from the near IR on to a maximum between 90 and 135μm and the start of a decline toward longer wavelengths.

However, instead of fitting the SEDs with an "ad hoc"number of black bodies, we have preferred to use an inversion method to analize the SEDs of the galaxies in the sample. This has the advantage that no assumptions have to be made as to the number or location of the sources responsible for the observed spectrum. In particular, we have used an Inverse Planckian Transform algorithm, that employs an emissivity ($\epsilon \propto \lambda^{-1.5}$) weighted Planck function kernel to switch from frequency space to the temperature domain, hence revealing the temperature distribution of the sources that originate the observed SEDs. The method applies Bayes theorem of conditional probability

and the Richardson-Lucy iteration algorithm which converges quickly to an optimum result. To increase the number of data points used in the inversion algorithm, whenever available, we have added IRAS data as given by Edelson, Malkan & Rieke [8]. Furthermore, to avoid boundary convergence problems in the inversion algorithm we have used 10 μm ground-based data from several authors ([3]; [8]; [21]), and 1.3 mm upper limit data from Edelson, Malkan & Rieke [8]. These additional data have been used solely for the purpose of constraining the inversion algorithm at the borders of the wavelength range of interest. Details of this method are given in Salas [22] and in Pérez García, Rodríguez Espinosa, & Santolaya Rey [23] and are not repeated here.

Fig 1 shows some examples of the results obtained after application of the Inverse Planckian Transform to the SEDs of the CfA Seyfert galaxies observed. For the objects shown, the upper pannel plots the ISO data (triangles) and the IRAS data (filled squares) and the best fit to the mid and far IR data (heavy solid line) with the different spectral components contributing to the fit printed in dashed lines; the bottom pannels show the temperature spectrum that produces these components. Similar results are obtained for the entire Seyfert sample, i.e., we recover three emission components that we have called warm, cold and very cold components. In a few cases only two components are found.

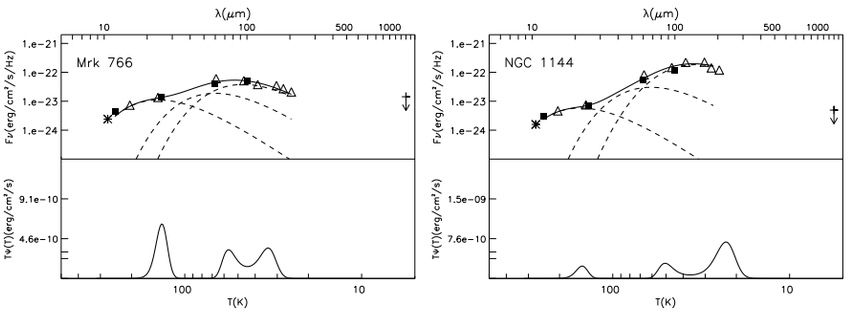

Fig. 1. Mid and far IR SEDs of several objects of the CfA Seyfert sample. For each object, the upper panel shows the ISO (triangles) and IRAS (filled squares) data and the best fit to the SED obtained with the Planckian inverse transform. The different thermal components contributing to the fit are printed in dashed lines. The bottom panel shows the temperature spectrum responsible for these components

The key point now is wheather these emission components obtained from the Inversion algorithm can be physically explained within a sensible scenario. In what follows we review the pieces of evidence that we have for explaining each of the components:

a) In a previous paper Rodríguez Espinosa & Pérez García [24] were able to use optical R band images of a subset of low redshift Seyferts of the CfA

sample to separate the fluxes from the central region from those of the galaxy disks. We found a very good correlation between the ratio of the extended to the compact R band fluxes and the ratio of the cold plus very cold component to the warm emission component. The conclusion was that the warm emission component is related to the central regions of the galaxies while the cold and the very cold emission originate in the disk of these galaxies.

b) A correlation has been found between the flux produced by the warm component and the flux in high ionization coronal emission lines like [OIV] λ25.9 and [NeV]λ14.3μm ([25]), indicating that the warm component must be heated by the nucleus of these galaxies.

c) In a recent paper, Pérez García, Rodríguez Espinosa & Fuensalida [19] have shown based on 90μm ISO maps of four nearby Seyferts, that the 90μm emission is physically extended up to radii similar or larger than those seen in optical images of these same galaxies. Furthermore, the extension of this 90μm emission has been characterized and its physical size, scale length and surface brightness profiles are typical of normal galaxy disks.

Based on the above, a scenario arises in which the warm component is associated with dust heated by radiation coming from the nuclear or circumnuclear regions of these galaxies, while the cold and very cold dust must be heated by processes occurring in the galaxy disk. Further support to this scenario comes from the following:

- Warm dust. Its characteristic peak temperature is in the range 120-170 K, a range of temperatures warmer than is normal of dust in typical star-forming regions. The nuclear origin of the radiation responsible for the heating of the warm dust was already indicated by Rudy (1984) who found a correlation between the [OIII]λ5007 emission line flux and the 10 μm emission for a sample of quasars, Seyfert galaxies and radiogalaxies. This author suggested that the dust responsible for the 10 μm emission is mixed with the ionized gas of the Narrow Line Region (NLR) that produces the [OIII]λ5007 emission line. Danese et al. [10] also conclude that the mid IR emission (10-25μm) is dominated by the nucleus or the circumnuclear region. More recently, Giuricin, Mardiossian and Mezzetti [11] support the idea of the nuclear heating of this warm dust, based on 10 μm small aperture observations of a sample of 100 galaxies. They found that the 10 μm emission correlates very well with the 25 μm IRAS emission, while the correlation is poor with the 60 μm emission. From a different perspective Heckmann et al. [26] have found in the Seyfert 2 galaxy Mrk 477 a strong starburst with very warm dust in an scale of a few hundred parsecs, that confirms the idea that the warm dust can also be heated by nuclear and circumnuclear starformation regions.
- Cold dust. Peak temperatures for this component range between 40 and 70 K, a range of temperatures that is typical of dust in regions of star-formation. Note that cold dust is present in mostly all classes of galaxies, including normal and starburst galaxies ([27]; [28]; [32]; [30]). In all

these galaxy types, the heating of the dust is produced by OB stars in star formation regions in the galaxy disks. The higher temperatures corresponding to higher recent starformation rates ([31])

- Very cold dust. Peak temperatures for this component range from around 15 to 25 K, temperatures that are normal of dust heated by the general interstellar radiation field. This very cold dust is tipically composed of big grains in thermal equillibrium with the interstellar radiation field and has been observed in normal spiral galaxies (see, e.g., [33]; [30]; [34]). For example, Cox, Kruger & Mezger [34] predict that the dust of the Galaxy is at a temperature of around 15-20 K, and Walterbos & Schwering [30] show that in the disk of M31 there is very cold dust at 21 K.

4 Anisotropy of the Warm Component

Recent studies of the mid IR emission from Seyfert galaxies claim that Seyfert 2 galaxies are weaker than Seyfert 1s ([35]; [21]; [11]; [36]). This result is interpreted within the framework of the unified models as an anisotropy, resulting from the presence of a molecular torus with a given optical thickness in the IR. To test this claim we have compared the fluxes of the warm component of the Seyfert SEDs to see if we find significant differences between Seyfert 1 and Seyfert 2s.

First, we refer to the ratios between the warm and total fluxes. The mean and standard deviations of these distributions are:

$$\langle F_{warm}/F_{IR}\rangle_1 = 0.42\ \sigma = 0.17$$
$$\langle F_{warm}/F_{IR}\rangle_2 = 0.28\ \sigma = 0.15$$

Figure 2 shows the flux ratio distributions. A KS test indicates that the distributions are different at the 99% level of significance. This result suggests that the Seyfert 1s emit fractionally more than the Seyfert 2s in the mid IR (warm component).

This is consistent, for example, with the models of circumnuclear tori of Pier & Krolik ([14]; [38]) and of Granato & Danese ([15], that predict anisotropy by absorption of nuclear emission in the mid IR. However this result should be taken with care, as it could indicate either that the nuclear emission is larger in the Seyfert 1s relative to their total FIR flux or that the contribution of the host galaxy is stronger in the Seyfert 2s. To discriminate between these two possible explanations we must normalize the infrared fluxes with an isotropic property of the galaxies in the sample, i.e., with fluxes emitted at long enough wavelengths that they are not suspect of suffering extinction and thus do not depend on the geometry of the sources. Other authors have used [OIII]λ5000 Å fluxes, hard X-ray fluxes or radio fluxes

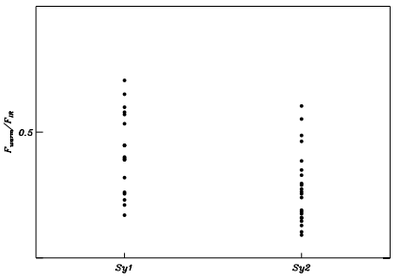

Fig. 2. Distribution of the ratio between the warm and the total fluxes of the CfA sample

(see, for example, Mulchaey et al. [36]). However, the [OIII] λ5000 Å fluxes can be affected by absorption due to dust in the NLR. We prefer to use 20 cm radio emission fluxes to normalize the IR flux, since the radio emission is not affected by selective extinction. We have used integrated radio data from Edelson [37]. These data consists of VLA observations at 1.46 GHz (20 cm) with a bandwidth of 45 MHz. The FWHM beamwidth used is 1.5 arcmin, directly comparable with our ISO data.

The distributions of the radio normalized warm IR fluxes show the following characteristics:

$$\langle log(F_{warm}/F_{20cm})\rangle_1 = 6.5\ \sigma = 0.3$$
$$\langle log(F_{warm}/F_{20cm})\rangle_2 = 6.1\ \sigma = 0.3$$

KS tests indicate that both distributions are different at a significance level of 99.9%. Therefore, the warm flux is indeed higher in Seyfert 1s than it is in Seyfert 2s, and it can be concluded that the warm emission from Seyfert 2s is affected by dust extinction to a larger extent that in the Seyfert 1 galaxies.

This result suggests that at shorter wavelengths (mid IR) the emission is still anisotropic, in agreement with the molecular torus models of Pier & Krolik ([14]; [38]) and Granato & Danese ([15]). These and others authors have proposed different models for the absorbing material. Pier & Krolik ([14]; [38]), Granato & Danese ([15]) and Efstathiou & Rowan-Robinson ([39]) have modeled the absorbing structures as axially symmetric tori. The models proposed by Granato & Danese ([15]) result in thin and extended tori with optical depths ranging from $\tau \approx 10$ to 300 in the UV band and maximum radii ranging from tens to hundreds of parsecs. On the contrary, the models proposed by Pier & Krolik ([38]) show thin and compact accretion disks with very large optical depths with values of $\tau \lesssim 1000$ in the UV band, and compact radii with dimension of a few pc. If we consider the Seyfert 1 as

canonical unobscured objects, and abscribe the differences found between the two Seyfert types to absorption by the obscuring torus we obtain a mid IR optical depth of $\tau_{IR} \approx 0.4$ or a $\tau_{UV} \approx 80$ (assuming $\tau_\lambda \propto 1/\lambda$) for the Seyfert 2 objects. This value is indeed very mild and within the range predicted for the thin and extended tori of Granato, Danese & Franceschini ([40]).

The validity of ratioing with the 20 cm radio flux has been however questioned based on the idea that Seyfert 2 galaxies may have more star formation in their disks than Seyfert 1s ([21]). This would affect the radio emission, and hence the warm to radio flux ratio. It remains to test wether the Seyfert 2 galaxies are indeed stronger emitters of extended far IR radiation. We consider for this test the ratio of the cold far IR component to 20 cm radio flux. For the two groups the values are:

$$\langle log(F_{cold}/F_{20cm})\rangle_1 = 6.7\ \sigma = 0.7$$
$$\langle log(F_{cold}/F_{20cm})\rangle_2 = 6.5\ \sigma = 0.5$$

These distributions are similar (60% probability) according to the KS test. Therefore, Seyfert 2s are not stronger emitters in extended IR radiation than Seyfert 1s, and there are no reasons to suspect that they should be stronger radio emitters based solely on the amount of star formation occurring in Seyfert 2s. It is also worth pointing out that the differences found between the type 1 and 2 Seyferts are restricted to the warm emission, while there are not differences regarding the cold and very cold emission, i.e.,the emission from their respective galaxy disks.

5 Conclusions

Mid and far IR ISOPHOT data for the CfA Seyfert sample have been acquired with ISO. these data allow the study of the Seyfert SEDs for which we find that they consist in most cases of three distinct dust emission components. we present a scenario in which the warm component is related to the nuclear region, thecold component to starforming regions in the galaxy disks, and the very cold component to the general interstellar radiation field. Further we show that there is anisotropy in the warm component between the Seyfert 1s and the type 2 Seyferts.

References

1. Rieke, G.H., Low, F.J., 1972, ApJ, 176, L95
2. Stein, W.A., 1975, PASP, 87, 5
3. Rieke, G.H., 1978, ApJ, 226, 550
4. Neugebauer, G., 1978, PhyS, 17, 149

5. Telesco, C.M., Harper, D.A., 1980, ApJ, 235, 392
6. Smith, M.A., Lada, C.J., Thronson, H.A., Glaccum, W., Harper, D.W., Loewenstein, R.F., Smith, J., 1983, ApJ, 274, 571
7. Rodríguez Espinosa, J.M., Rudy, R.J., Jones, B., 1987, ApJ, 312, 555
8. Edelson, R.A., Malkan, M.A., Rieke, G.H., 1987, ApJ, 321, 233
9. Spinoglio, I., Malkan, M.A., Rush, B., Carrasco, L., Recillas-Cruz, E., 1995, ApJ, 453, 616
10. Danese, L., Zitelli, V., Granato, G.L., Wade, R., De Zotti, G., Mandolesi, N., 1992, ApJ, 399, 38
11. Giuricin, G., Mardirossian, F., Mezzetti, M., 1995, ApJ, 446, 550
12. Simpson, C., Wilson, A.S., Bower, G., Heckman, T.M., Krolik, J.H., Miley, G.K., 1997, ApJ, 474, 121
13. Wilson, A.S., Braatz, J.A., Heckman, T.M., Krolik, J.H., Miley, G.K., 1993, ApJ, 419, L61
14. Pier, E.A., Krolik, J.H., 1992, ApJ, 401, 99
15. Granato, G.L., Danese, L., 1994, MNRAS, 268, 233
16. Huchra, J., Burg, R., 1992, ApJ, 393, 90
17. Kessler, M. F., Steinz, J.A., Anderegg, M.E., Clavel, J., Drechsel, G., Estaria, P., Faelker, J., Riedinger, J.R., Robson, A., Taylor, B.G., Ximenez de Ferran, S., 1996, A&A, 315, L27
18. Lemke, D., et al. 1996, A&A, 315, L64
19. Pérez García, A.M., Rodríguez Espinosa, J.M., Fuensalida ,J.J., 2000, ApJ (in press)
20. Prieto, M.A., Viegas, S.M., 2000, ApJ in press
21. Maiolino, R., Ruiz, M., Rieke, G.H., Keller, L.D., 1995, ApJ, 446, 101
22. Salas, L., 1992, ApJ, 385, 288
23. Pérez García, A.M., Rodríguez Espinosa, J.M., Santolaya Rey A.E., 1998, ApJ, 500, 685
24. Rodríguez Espinosa, J.M., Pérez García, A.M., 1997, ApJ, 487, L33
25. Prieto, M.A., Pérez García, A.M., Rodríguez Espinosa, J.M., 2000 (submitted)
26. Heckman, T.M., González-Delgado, R.M., Leitherer, C., Meurer, G.R., Krolik, J., Wilson, A.S., Koratkar, A., Kinney, A., 1997, ApJ, 482, 114
27. Knapp, G.R., Rupen, M.P., Fich, M., Harper, D.A., Wynn-Williams, C.G., 1996, A&A, 315, L75
28. Chini, R., Kruger, E., Kreysa, E., 1992, A&A, 315, 75
29. Klaas, U., Haas, M., Heinrichsenm, J., Schulz, B., 1997, A&A, 325, L21
30. Walterbos, R.A.M., Schwering, P.B.W., 1987, A&A, 180, 27
31. Young, J.S., Xie, S., Kenney, J.D.P., Rice, W.L., 1989, ApJS, 70, 699
32. Klaas, U., Haas, M., Heinrichsenm, J., Schulz, B., 1997, A&A, 325, L21
33. Walterbos, R.A.M., Greenwalt, B., 1996, ApJ, 460, 696
34. Cox, R., Kruger, E., Mezger, P.G., 1986, A&A,, 155, 380
35. Heckman, T.M., 1995, ApJ, 446, 101
36. Mulchaey, J.S., Koratkar, A., Ward, M.J., Wilson, A.S., Whittle, M., Antonucci, R.J.J., Kinney, A.L., Hurt, T., 1994, ApJ, 436, 658
37. Edelson, R.A., 1987, ApJ, 313, 651
38. Pier, E.A., Krolik, J.H., 1993, ApJ, 418, 673
39. Efstathiou, A., Rowan-Robinson, M., 1994, MNRAS, 212, 218
40. Granato, G.L., Danese, L., Franceschini, A., 1997, ApJ, 487, 147

The Nature of Ultra-Luminous Infrared Galaxies

Reinhard Genzel, Dieter Lutz, Alan F.M. Moorwood, Dimitra Rigopoulou, Henrik W.W. Spoon, Amiel Sternberg, Eckhard Sturm, and Dan Tran

Max-Planck-Institut für extraterrestrische Physik
Postfach 1603, 85740 Garching, Germany

Abstract. We review investigations with SWS, ISOPHOT-S, and ISOCAM-CVF of several samples of ultra-luminous infrared galaxies (ULIRGs) drawn from IRAS catalogs. The mid-IR data indicate that the majority of the local ULIRG population is predominantly powered by star formation but that AGN activity plays a significant role in many sources and dominates the most luminous ones. AGN and starburst activity is present in all phases of the ULIRG/merger evolution. There is no obvious trend for AGNs to be more predominant, or the molecular content to be lower in the late ULIRG phases. Star formation activity in ULIRGs likely occurs in short (10^7 years) phases terminated by the disruptive effects of superwinds and supernovae. Highly obscured AGNs dominating the total energy output may be hidden to the mid-infrared observations in a few cases but are not characteristic of the average ULIRG.

1 Introduction

The nature of ultra-luminous infrared galaxies (ULIRGs: $L_{8-1000\mu m} > 10^{12} L_\odot$) and their possible evolutionary connection to quasars has been the subject of intense debate since their discovery by IRAS one and a half decades ago (for a recent review see [19]). ULIRGs exhibit evidence for activity from both starbursts and active galactic nuclei (AGN: meaning accretion onto massive black holes). The question as to which generally dominates the luminosity has remained largely unsolved. This is mainly due to the large dust obscuration of their nuclear regions from which most of their luminosity emerges. Measurements in the visible, ultra-violet or soft X-ray bands thus are difficult and hard to interpret.

In the local Universe ULIRGs are a spectacular curiosity. They contribute only $\sim 1\%$ to the local infrared radiation field, and $\sim 0.3\%$ to the total bolometric emissivity [19]. The recent ISOCAM, ISOPHOT and SCUBA deep surveys (see elsewhere in this volume) show that this fraction increases dramatically (factor > 100) at higher redshift. ULIRGs contribute a significant fraction of the cosmic radiation density (and star formation rate) at $z > 1$. Understanding the nature and properties of the ULIRG population at low redshift is thus of essence.

D. Lemke, M. Stickel, and K. Wilke (Eds.): LNP 548, pp. 199–208, 2000.

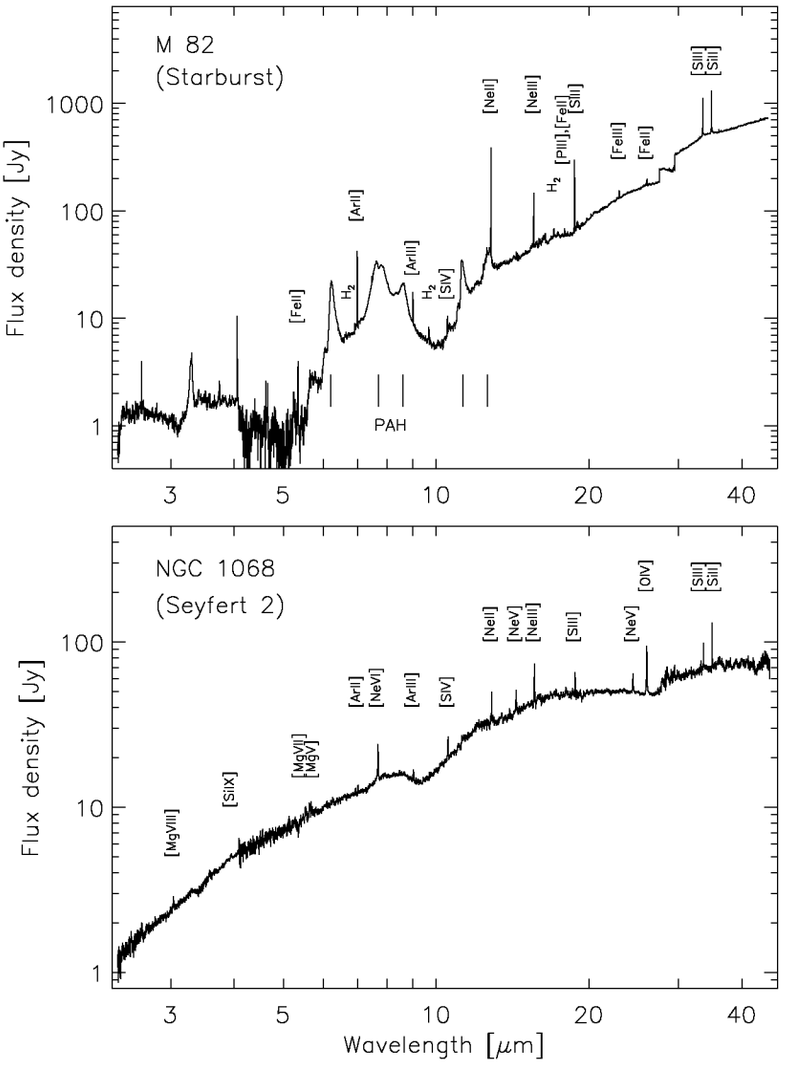

Fig. 1. Full 2.5 to 45 μm spectra of the starburst galaxy M82 (top) and the Seyfert 2 galaxy NGC 1068 (bottom). The mid-infrared spectra show a rich set of atomic fine structure lines and PAH features. (see text).

2 New ISO Diagnostics for the Power Source of IR Galaxies

With the advent of ISO, sensitive mid- (and far-) IR spectroscopy has become available as a new tool capable of penetrating the dust often obscuring galactic nuclei. Figure 1 and Figure 2 demonstrate some of the crucial features of mid-IR AGN and starburst spectra. The 2.5 to 180 μm spectral range accessible to the two spectrometers onboard ISO allowed observations of a wide range of atomic/ionic fine structure lines sampling excitation potentials of less than 10 to more than 300 eV. Comparison of the SWS/ISOPHOT-S spectra in Figures 1 and 2 shows the obvious qualitative differences that ISO sees between galaxies known to be powered by star formation and those by AGNs. Starbursts show very strong low excitation fine structure lines (e.g. [Ne II] 12.8μm) but only weak or no detectable high excitation lines (e.g.[O IV] 25.9μm, or [N eV] 14.3 μm). In contrast high excitation lines are strong in AGN spectra. This is in accordance with expectations from photoionization models. Only the ultra-violet/X-ray continuum radiation from the AGN accretion disk, corona and jet regions is hard enough to create the highly excited species in the mid-IR spectra. The low resolution ISOPHOT-S and ISOCAM-CVF spectra cover the mid-IR 6.2, 7.7, 8.6, and 11.3μm emission features (the infrared unidentified bands, or UIBs) often attributed to polycyclic aromatic hydrocarbons (PAHs). ISO data confirm ground-based observations of these and a companion at 3.3μm which first demonstrated that these features are strong in starburst galaxies but weak or absent in classical AGNs. The line to continuum ratio of the most prominent, 7.7μm, feature can thus be also used as an empirical discriminator between starburst and AGN activity in systems, such as ULIRGs, where the powering source(s) is highly obscured and not known.

3 Observations of ULIRGs: Starbursts or AGNs?

With the help of the diagnostic tools just discussed it is possible to investigate whether ULIRGs are predominantly powered by star formation or by AGNs. Figure 2 shows the prototypical ULIRG Arp 220 to be starburst-like in its mid-IR spectral diagnostics: There are no high excitation fine structure lines but strong PAH features. The results of fine structure line observations with SWS and observations of the PAH features with ISOPHOT-S, for a sample of 15 bright ULIRGs, are summarized in the ISO 'diagnostic diagram' of Figure 3 [6]. From this diagram ULIRGs appear to be composite objects located between pure AGNs and pure starbursts. Most are located close to starbursts (like Arp 220, 17208-0014, 23128-5919), especially when taking into account that the [OIV]/[NeII] line ratios are typically only upper limits. In the simple 'mixing' model shown in Figure 3, the SWS ULIRGs on average have a $< 30\%$ AGN contribution with $> 70\%$ coming from star formation. In

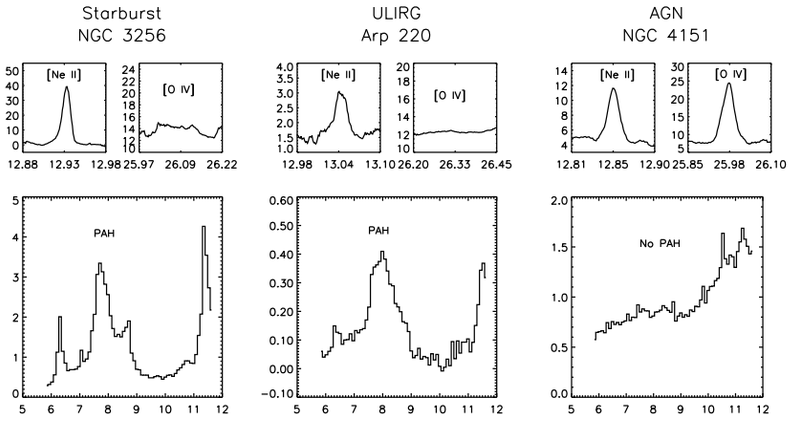

Fig. 2. Mid-IR fine structure lines and UIB/PAH features are new ISO tools to distinguish between star formation and AGN activity in ULIRGs (see text).

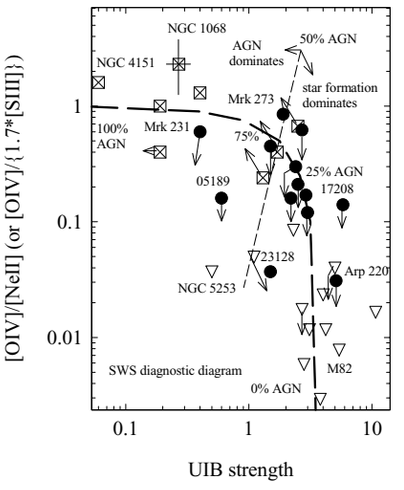

Fig. 3. Diagnostic diagram for ULIRGs (filled circles), based on ISO-SWS and ISOPHOT-S Observations (from Genzel et al 1998). The vertical axis measures the flux ratio of high excitation to low excitation mid-IR emission lines, the horizontal axis measure the strength (feature to continuum flux ratio) of the 7.7μm UIB/PAH feature. AGN templates are marked as rectangles with crosses, starburst templates as open triangles, UILRGs as filled circles. A simple "mixing curve" from 0% to 100% AGN is shown with long dashes.

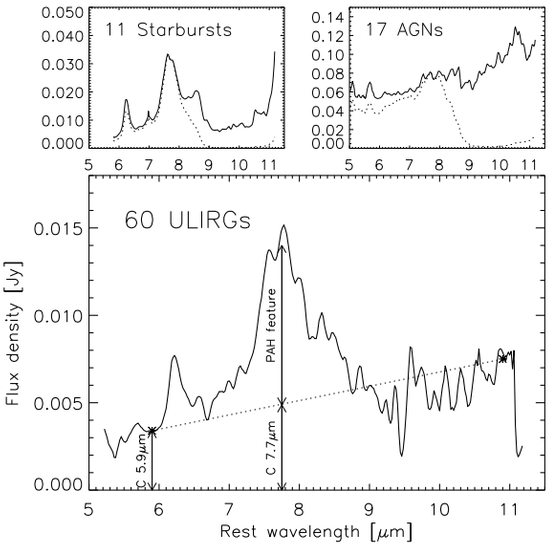

Fig. 4. Average ISOPHOT-S spectrum of 60 ULIRGs, individually scaled to S_{60}=1Jy. Average spectra of starburst galaxies and AGNs are added for comparison. The dashed lines represent these spectra after applying an additional A_V=50 foreground extinction (adapted from [9]).

4 of the 13 bright ULIRGs the data indicate an energetically significant AGN, either on the basis of a detection of strong high excitation lines (Mrk 273, NGC 6240), or on the basis of a low UIB/PAH strength (Mrk 231, 05189-2524). Recall again that predominance of one source of luminosity does not exclude presence of the other.

4 Trends with Luminosity and Evolutionary Status

The sample of 15 ULIRGs presented by Genzel et al. [6] is not large enough for detailed studies of trends within the class of ULIRGs. Using ISOPHOT-S and ISOCAM-CVF Lutz et al. [9], Rigopoulou et al. [16] and Tran et al. [25] have extended the local ULIRG sample to fainter sources, higher redshift and greater luminosity (totaling 75 sources to z∼0.4 and $10^{13}L_{\odot}$). The ISOPHOT-S sample is mainly drawn from the 1.2 Jy survey [5]. No infrared color criteria were applied to avoid biasing the sample in AGN content. The average of all 60 ISOPHOT-S ULIRG spectra, individually scaled to S_{60}=1Jy to give all sources equal weight, is shown in Figure 4. It clearly shows the PAH features at 6.2, 7.7, and 8.6μm but relatively weak continuum. Comparison with the starburst and AGN templates provides a first and direct indication

that ULIRGs as a class are starburst-like. More specifically the main findings of the spectroscopic studies are

- about 80% of all the ULIRGs are predominantly powered by star formation but the fraction of AGN powered sources increases with luminosity. Whereas according to the PAH criterion only about 15% of ULIRGs at luminosities below $2 \times 10^{12} L_{\odot}$ are AGN powered this fraction reaches about half at higher luminosity [9] [25],
- the PAH feature-to-continuum ratio is anticorrelated with the ratio of feature-free 5.9μm continuum to the IRAS 60μm continuum, confirming earlier suggestions that strong mid-IR continuum is a prime AGN signature. The location of starburst-dominated ULIRGs in such a diagram is consistent with the ISO-SWS spectroscopy which implies significant extinction even in the mid-IR [9],
- for those ULIRGs with mid-IR spectra and high resolution near-IR images [16], there is no correlation of AGN/starburst dominance with merger phase, as postulated by the classical evolutionary scenario of Sanders et al.[17]. Here the compactness of the near-IR (stellar) emission (separation of double nuclei etc.) is taken as a qualitative clock of the merger. This suggests that the dominance of AGN or starburst may depend on local and shorter term conditions determining the fuelling of the AGN in addition to the global state of the merger,
- starburst durations in ULIRGs are relatively short ($\sim 10^7$ years) and there may be several burst episodes during a merger [24]. In the framework of starburst models with a Salpeter initial mass function and upper mass cutoffs of 50 to 100 $M_{\odot}$, the ULIRG data are fit with burst ages/durations of ~ 8 to 80×10^6 years. In the case of NGC 6240 Tecza et al have directly determined the age of the most recent star formation activity ($t = (2 \pm 0.5) \times 10^7$ years) from the fact that the K-band light in both nuclei appears to be dominated red supergiants [24]. For that age and the measured (low) Br gamma equivalent width the duration of the burst has to be about $(5 \pm 2) \times 10^6$ years. This starburst age/duration is comparable to the dynamical time scale and time since the last perigalacticon, and much smaller than the time scale for complete merging (several hundred million years),
- there is also no dependence of luminosity and molecular gas mass on the merger phase [16]. In a simple, Schmidt-law parameterization of star formation, one would expect the most powerful starbursts in the very last stages of the merger [11], as the mean gas density is largest then. Likewise if the ULIRG phase were terminated when most of the gas is used up, late stage mergers are expected to have a lower gas content than early stage mergers. Again, the lack of of correlation suggests that the story is more complex, that global characteristics do not solely determine the evolution and that starbursts are terminated by the negative feedback

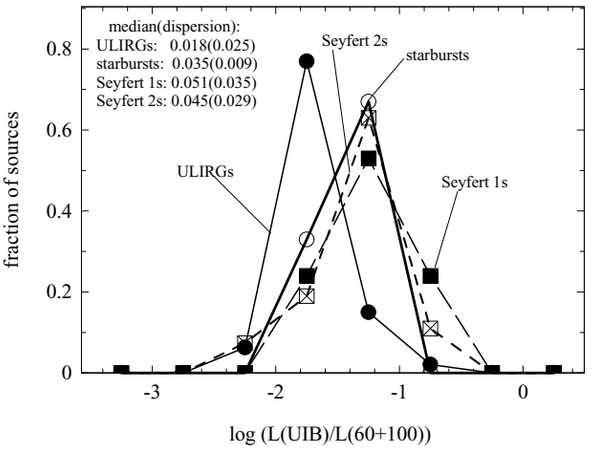

Fig. 5. Fraction of sources as a function of ratio of 7.7μm UIB/PAH luminosity to 60+100μm-band IRAS luminosity for ULIRGs (filled circles and thin continuous line), starbursts (open circles and thick line), Seyfert 2s (open rectangles and thick dashed) and Seyfert 1s (filled rectangles and thin long dashes) (data from [6], [16], [2]).

from the massive star formation and not by the exhaustion of the gas supply.

5 Are the ISO Source Classifications Reliable: Hidden AGNs?

Source classifications based on the ISO spectroscopy agree very well with those obtained from optical diagnostic line ratios. For 48 ULIRGs with ISOPHOT - S / ISOCAM data and good quality optical spectra the optical and ISO classifications of the individual galaxies agree very well if HII-galaxies and LINERs are both identified as starbursts [10]. All but one of 23 ISO star formation dominated ULIRGs are HII/LINER galaxies. 11 of 16 ISO AGNs are Seyferts. All but one of the Seyfert 1/2s are ISO AGNs. The identification of infrared selected optical LINERs as star formation dominated galaxies is quite plausible. The LINER spectra in ULIRGs are likely caused by shock excitation in large scale superwinds and not by circum-nuclear gas photoionized by a central AGN.

Yet the active regions of ULIRGs are veiled by thick layers of dust. From fine structure and recombination line ratios Genzel et al. (1998) [6] deduce

equivalent 'screen' dust extinctions in ULIRGs (and LIRGs) between A(V) 5 and 50. ISOPHOT-S and ground-based data confirm this evidence for high dust extinction [3] [9]. The most extreme case is Arp 220 where the ISO SWS data indicate A(V(screen)) $\sim$ 50 (A(25μm) $\sim$ 1), or an equivalent 'mixed model' extinction of 500 to 1000 mag in the V-band [23]. Soifer et al. find similar values from mid-IR imaging [21]. These large extinctions combined with a mixed extinction model solve the puzzle that starburst models based on near-IR/optical data cannot account for the far-IR luminosities in a number of ULIRGs. If the emission line data are instead corrected for the (much larger) ISO-derived extinctions, the derived L(IR)/L(Lyc) ratios are in reasonable agreement with starburst models. Submm/mm CO and dust observations imply yet larger column densities than the mid-IR data (N(H) $> 10^{24}$cm^{-2} or A(V) > 500 [15] [22]. Is it possible, therefore, that all ULIRGs contain powerful central AGNs that are missed by the mid-IR (and optical) data?

Hard X-rays penetrate to column densities $> 10^{24}$cm^{-2}. The ASCA satellite has observed a small sample of ULIRGs in the 2-10 keV band. About a dozen sources are common between ISO and ASCA [1] [8] [14] [12]. In Mrk 273, 05189-2524, NGC 6240 and 230605+0505 ASCA finds evidence for a hard X-ray source with $<$ L(X)/L(IR) $> > 10^{-3}$. BeppoSAX observations show that the AGN in NGC 6240 is attenuated by a Compton thick (N(H) 2×10^{24}cm^{-2}) absorber [26]. After correction for this absorption and depending on its filling factor the ratio of intrinsic AGN X-ray to IR luminosity is 2 to 6×10^{-2}. Both the AGN and the starburst can account for the entire far-IR luminosity of NGC 6240. In Mrk 231 a hard X-ray source is seen but it is weak ($<$ L(X)/L(IR) $> \sim 10^{-3.5}$). ISO finds evidence for significant AGN activity in all of these sources as well. In sources classified by ISO as starburst dominated (Arp 220, UGC 5101, 17208-0014, 20551-4250, 23128-5919) ASCA also finds no hard X-ray source. The limit to the hard X-ray emission in Arp 220 corresponds to 10^{-4} of the infrared luminosity. For comparison, in Seyfert 1 and Seyfert 2 galaxies $<$ L(X)/L(IR) $>$ is 10^{-1} and 10^{-2}, respectively. For radio quiet QSOs, the sample averaged SEDs of Sanders et al. and Elvis et al. give L(X)/L(IR) = 0.2 and L(X)/L(bol) $\sim$ 0.05 [19] [4]. Although the statistics is still relatively poor at this point, the hard X-ray data do not present evidence for powerful AGNs that are completely missed by the mid-IR observations.

There are exceptions to this reasonable agreement between IR and X-ray data. The nearby galaxy NGC4945 fulfills all criteria of a pure starburst at optical to mid-IR wavelengths ([13], Fig. 3: NGC4945 is the starburst to the bottom right of Arp 220 and top left of M82). There is no evidence for a narrow line region or any other AGN indicator at these wavelengths. The mid-IR [Ne III]/[Ne II] line ratio is small and indicates that the starburst is aging (Spoon, priv.comm.). Yet ASCA and BeppoSAX data show that at its center lurks a powerful AGN, attenuated by a Compton thick foreground absorber [7]. As in NGC 6240 both the AGN (from the X-ray data) as well

as the starburst (from the optical to IR data) can account for the entire bolometric luminosity of NGC4945. While NGC4945 is much less luminous than a ULIRG ($10^{10.1} L_{\odot}$) the case is puzzling and needs to be studied further.

If mid-IR continuum and PAH features suffer different obscurations, as in Seyfert 2 galaxies [2], the PAH strength criterion employed above looses its meaning. Instead it is necessary to directly compare the ratio of PAH-luminosity to total far-IR ($60 + 100\mu$m) luminosity even if this ratio depends on the mid-IR extinction. The PAH/FIR ratio in ULIRGs (Figure 5) is on average half of that in starbursts (and Seyferts). This suggests that at least half of the luminosity in the average ULIRG comes from star formation if the same PAH/FIR ratio holds as in other galaxies. Correction for extinction increases this fraction. If the average mid-IR extinction is A(V(screen)) $\sim$ 15 and A(7.7)/A(V) $\sim$ 0.04, the PAH/FIR ratio is fully consistent with that in starburst galaxies. The PAH strength criterion in ULIRGs thus tells qualitatively the correct story.

In summary then, extinction obviously plays an important role in ULIRGs at all bands between X-rays and the mid-IR. Still, optical and near-IR emission line diagnostics remain a useful qualitative diagnostic tool (in almost all cases). After extinction correction, mid-IR emission lines and UIB/PAH features can be used as a quantitative tool for estimating the relative contributions of AGN and star formation in (most) ULIRGs. Given the large extinctions, how can optical/near-IR tracers give the correct (qualitative) picture? The optical and IR emission line diagnostics rely on penetrating to the (less obscured) NLR, and not through the high column density, circumnuclear torus. The large scale ($> 10^2$ pc) obscuring material is likely very patchy and arranged in thin (and self-gravitating) disks (as in Arp 220 [20]). Radiation and outflows from a powerful AGN likely punches rapidly through the clumpy obscuring screen at least in certain directions.

Acknowledgements

We thank the other members of the MPE-ESO-Tel Aviv team studying galaxies with ISO: T. Alexander, N. Förster-Schreiber, D. Kunze, H. Netzer, and M. Thornley. This work is based on observations with ISO, an ESA project with instruments funded by ESA Member states and with the participation of ISAS and NASA. The SWS is a joint project of SRON and MPE. SWS and the ISOSDC at MPE are supported by DLR (formerly DARA). This work also has been supported by a grant from the German-Israeli Foundation.

References

1. Brandt, W.N., Fabian, A.C., Takahashi, K., Fujimoto, R., Yamashita, A., Inoue, H., Ogasaka, Y. 1997, MNRAS 290, 617
2. Clavel, J., et al. 1998, astro-ph 9806054

3. Dudley, C.C. and Wynn-Williams, C.G. 1997, Ap. J. 488, 720
4. Elvis, M. et al. 1994, Ap. J. Suppl. 95, 1
5. Fisher, K.B., Huchra, J.P., Strauss, M.A., et al., 1995, ApJS, 100, 69
6. Genzel, R., Lutz, D., Sturm, E., et al. 1998, ApJ, 498, 579
7. Iwasawa, K. et al. 1993, Ap.J. 409, 155
8. Kii, T., Nakagawa, T., Fujimoto, R., Ogasaka, T., Miyazaki, T., Kawabe, R. and Terashima, Y. 1997, In X-ray Imaging and Spectroscopy of Cosmic Hot Plasmas, eds. F. Makino, K. Mitsuda. Tokyo: Universal Academy Press, pp. 161
9. Lutz, D., Spoon, H.W.W., Rigopoulou, D. et al., 1998, ApJ, 505, L103
10. Lutz, D., Veilleux, S. and Genzel, R. 1999, Ap. J. 517, 13
11. Mihos, J.C. and Hernquist, L. 1996, Ap. J. 464, 641
12. Misaki, K., Iwasawa, K., Taniguchi, Y., Terashima, Y., Kunieda, H., and Watarai H., 1999, Adv.Space Res. 23 (5):1051
13. Moorwood, A.F.M., van der Werf, P.P., Kotilainen, J.K., Marconi, A. and Oliva, E. 1996, Astr.Ap. 308, L1
14. Nakagawa, T. et al.1999, In ULIRGs: Monsters or Babies, eds. D. Lutz and L.J. Tacconi, San Francisco: ASP Conf. Series. in press
15. Rigopoulou, D., Lawrence, A. and Rowan-Robinson, M. 1996, MNRAS 278, 1049
16. Rigopoulou, D. et al. 1999, A.J. in press
17. Sanders D.B., Soifer, B.T., Elias, J.H., et al. 1988, ApJ, 325, 74
18. Sanders, D.B., Phinney, E.S., Neugebauer, G., Soifer, B.T. and Matthews, K. 1989, Ap. J. 347, 29
19. Sanders, D.B. and Mirabel, I.F. 1996. Ann. Rev. Astr. Ap. 34, pp. 749
20. Scoville, N.Z. et al. 1998, Ap. J. Lett. 492, 107
21. Soifer, B.T. et al. 1999, Ap. J. 513, 207
22. Solomon, P.M., Downes, D., Radford, S.J.E. and Barrett, J.W. 1997, Ap. J. 478, 144
23. Sturm, E. et al. 1996, Astr. Ap. 315,133
24. Tecza, M. et al. 2000, Ap.J. in press
25. Tran, D., et al., 2000, in preparation
26. Vignati, P., et al. 1999, Astr.Ap.349, L57

ISO Spectroscopy of Active Galactic Nuclei

Dieter Lutz[1], Eckhard Sturm[1], Tal Alexander[2], Reinhard Genzel[1], Alan Moorwood[3], Amiel Sternberg[4], and Hagai Netzer[4]

[1] Max-Planck-Institut für extraterrestrische Physik, Postfach 1603, 85740 Garching, Germany
[2] Institute for Advanced Study, Olden Lane, Princeton, NJ 08540, USA
[3] European Southern Observatory, Karl-Schwarzschild-Straße 2, 85748 Garching, Germany
[4] School of Physics and Astronomy, Tel Aviv University, Ramat Aviv, Tel Aviv 69978, Israel

Abstract. Spectroscopy in the mid-infrared spectral range provides a number of unique diagnostics of active galactic nuclei which can now be used thanks to ISO's sensitivity and full wavelength coverage. Mid-infrared aromatic emission features are absent close to the AGN but can be strong on larger host galaxy scales, in particular if there is intense circumnuclear star formation. The rich fine structure and coronal line spectrum can be used to reconstruct the otherwise unobservable extreme ultraviolet emission of the AGN. We find evidence for 'big blue bump' emission from the accretion disk but also for neutral absorbers located inside the narrow line region. The ability of mid-infrared emission to penetrate dust allows to probe the structure of dusty narrow line regions, and to search for the obscured broad line region in Seyfert 2 galaxies.

1 Continuum and Features

With the exception of the brightest lines in the very brightest sources, mid-infrared spectroscopy of galaxies has been impossible to obtain from ground-based or airborne observations. Full wavelength coverage and high sensitivity of the ISO cryogenic space telescope have changed this situation, providing spectra of unprecedented detail in particular for the 2.4-45μm region covered by the short wavelength spectrometer SWS. Figure 1 compares the SWS spectra of the prototypical Seyfert 2 galaxies NGC 1068 and Circinus with those of starburst galaxies [18]. A first clear difference is the stronger and warmer mid-infrared continuum of the Seyferts, due to dust heated by the AGN.

In accordance with previous ground-based results, the aromatic emission features that dominate the mid-infrared spectra of starbursts are weaker or absent in many Seyfert spectra. Spatially resolved ISO spectra of NGC 1068, Cen A, and Circinus demonstrate even more convincingly that the aromatic 'PAH' features are not AGN related ([1],[9],[13],[15]): PAH emission is undetected in the nuclei but seen on larger scales, excited in a starburst or cirrus type situation. In the context of unified scenarios, these observations

D. Lemke, M. Stickel, and K. Wilke (Eds.): LNP 548, pp. 209–216, 2000.

are related to the finding that PAH equivalent widths of Seyfert 2's are larger than those of Seyfert 1's while the PAH fluxes of both categories are similar [5]. Such a behaviour can be explained if the PAH emission originates on larger scales and is emitted isotropically, while the AGN continuum is emitted anisotropically, changing significantly with angle between line of sight and axis of the putative dust torus.

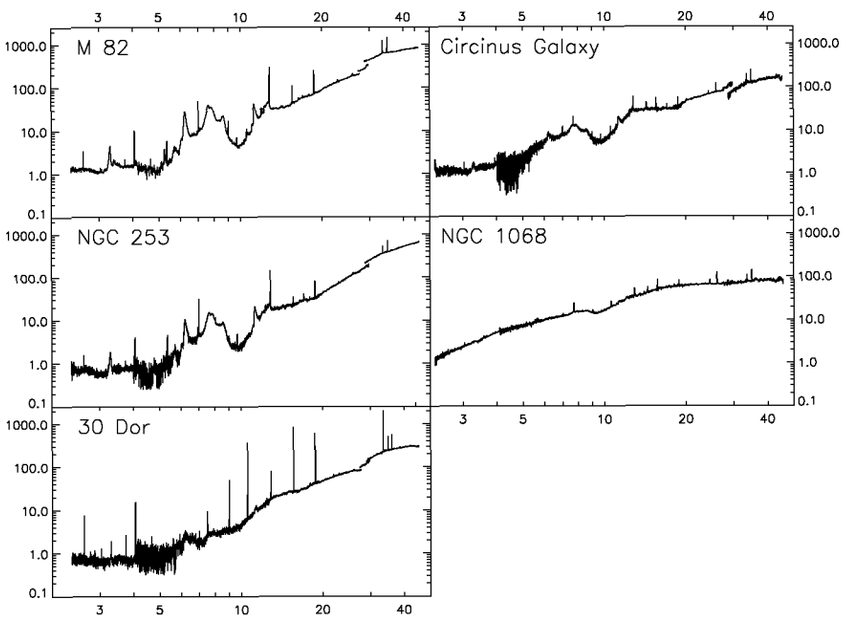

Fig. 1. ISO-SWS 2.4-45μm spectra of the Seyfert 2 galaxies Circinus and NGC 1068, along with comparison starburst spectra.

On detailed inspection of the SWS spectra of galaxies, new fainter features are seen in the 13-25μm range. Analogy to galactic sources suggests that they are most likely due to aromatic carriers just as the stronger shorter wavelengths ones [18]. While the main change from galaxy to galaxy is one of overall strength, there are also some features unique to individual sources e.g. in the 20μm region of Circinus. Given that galaxy spectra average over many different regions, this is surprising and may suggest a transient nature of some of the carriers.

2 Reconstructing the Extreme Ultraviolet Big Blue Bump

In the standard paradigm AGNs contain thin accretion disks that are expected to emit a quasi-thermal radiation of temperature a few times 10^5K. This emission will mainly be in the extreme ultraviolet which cannot be observed even from space, due to Galactic and intrinsic absorption. UV and soft X-ray studies of Seyfert 1s are generally consistent with the presence of an accretion-disk 'Big Blue Bump' in the unobservable EUV but suffer several limitations. A completely independent approach is to use infrared spectra to infer the EUV spectral energy distribution. Ionization energies of line emitting species in the narrow line region and coronal line region cover the EUV range. The emission line spectra will contain a signature of the intrinsic AGN continuum SED which can be reconstructed by photoionization modelling. The emission line spectrum will, however, not only depend on the shape of the ionizing continuum but in addition on other factors like NLR geometry and ionization parameter. SED reconstruction will hence be difficult and possible only with a large number of constraints. The rich mid-infrared fine structure line spectra of the brightest Seyferts are well suited for this task (e.g. Fig. 2). In addition, the fine structure line fluxes are quite insensitive to extinction and electron temperature variations, thus eliminating two additional elements of uncertainty.

Three nearby Seyferts have been analysed using this technique: Circinus [14],[2], NGC 4151 [2], and NGC 1068 [3]. A scored fitting approach has been used, evaluating photoionization models for a large number of SEDs representing all possible combination of fluxes at a number of pivot energies. The reconstructed EUV spectrum of Circinus is indeed found to exhibit an EUV bump peaking at about 70eV and containing about half of the AGN luminosity. For the small black hole mass of Circinus [12], the AGN must be radiating at high efficiency of greater than 10% of the Eddington luminosity, in accordance with standard expectations.

The SEDs derived for NGC 4151 and NGC 1068 appear quite different (Fig. 3). They fall sharply beyond the Lyman limit and then rise sharply again toward 100eV. Such a structured SED is not consistent with any accretion disk model and difficult to reconcile with any continuum emission mechanism. Alternatively, the deep minimum might be due to absorption by neutral hydrogen. Then, the narrow line region does not see the intrinsic SED of the AGN which will have a smoother UV continuum and perhaps even a Big Blue Bump. For NGC 4151, this interpretation is corroborated by independent evidence: the reconstructed (absorbed) SED does not contain enough UV photons to photoionize the BLR, i.e. it cannot be the intrinsic SED. Observations of UV Lyman absorption lines similary suggest a neutral absorber [8]. Column densities of the neutral absorbers inside the NGC 4151 and NGC 1068 NLRs are estimated around $5{\times}10^{19}\mathrm{cm}^{-2}$. While a significant range of SEDs and NLR geometries has been explored to confirm the robust-

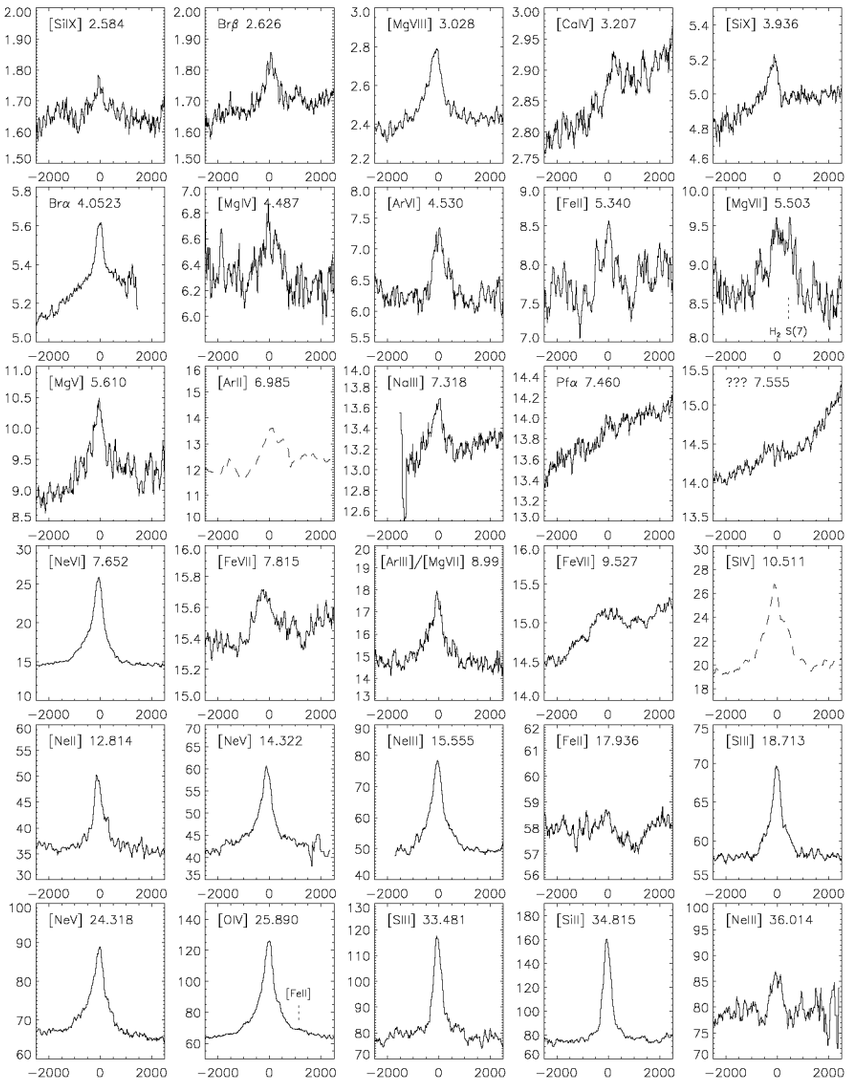

Fig. 2. ISO-SWS spectra of lines emerging in the ionized medium of NGC 1068. Flux densities in Jy are shown for a range of ±2500 km/s around systemic velocity. Line identifications and rest wavelengths in μm are given in each panel.

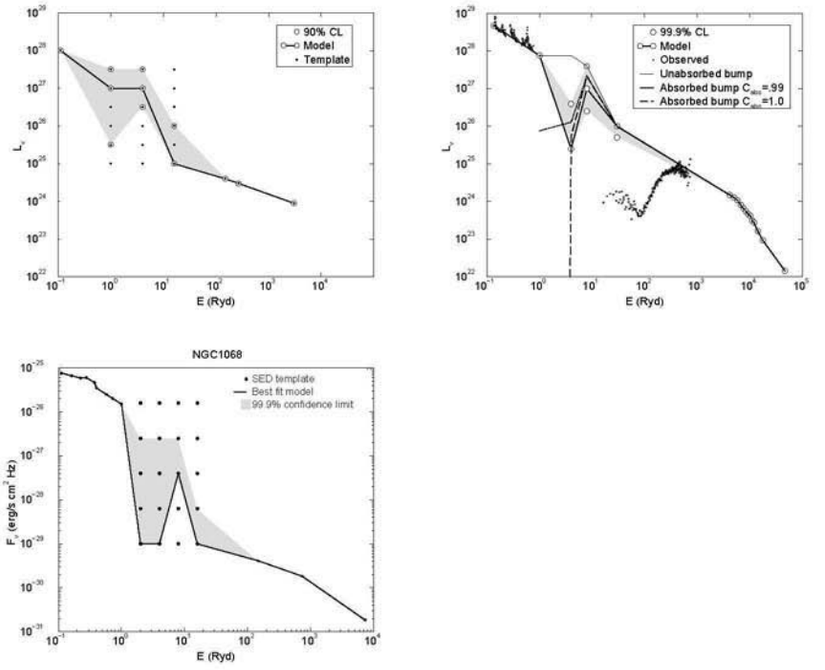

Fig. 3. Extreme ultraviolet SEDs of the Seyfert galaxies Circinus (top left), NGC 4151 (top right), and NGC 1068 (bottom) as inferred from photoionization modelling of the infrared and optical line emission. The energy scale is given in Rydberg units (=13.6eV). The gray shaded area indicates the confidence range. The spectra of NGC 4151 and NGC 1068 appear modified by a neutral absorber inside the NLR.

ness of the inferred SEDs, it is also possible to get good fits with simple power law continua if introducing significant additional free parameters like a variable ratio of specific matter bounded and radiation bounded clouds [4]. Our reconstructed SEDs that appear very unsual at first glance are again consistent with the standard AGN paradigm of thin accretion disks emitting a Big Blue Bump, assuming that the NLR sees a partially absorbed continuum.

3 Line Profiles and the Structure of the Narrow Line Region

Integrated emission line profiles are an (albeit indirect) tool to constrain the dynamical structure and extinction properties of the narrow line region. Optical Seyfert emission lines have often been found to show blue wings and a net blueshift with respect to systemic velocity [7]. In addition, correlations

of line width with ionization potential and/or critical density have been observed. Various explanations have been suggested, the most common ones assuming outflow in a dusty NLR. Comparisons of optical and infrared profiles are powerful tests of such scenarios - in the simplest case the infrared lines should be symmetric and centered on systemic velocity (Fig. 4 left). This case is cleary not observed for NGC 4151 where optical and IR profiles are very similar [17]. This might suggest an alternative scenario where part of the receding NLR regions are obscured by a small but optically highly thick screen or torus (Fig. 4 right). NGC 1068 appears to be intermediate in showing some extinction-related changes between optical and IR profiles but also a remaining blueshift of the IR lines [11]. Alternative to the presence of a small thick screen, the observations of both sources are also consistent with an intrinsic real asymmetry of the NLR. Testing this proposition would require infrared line profiles of a much larger sample of Seyfert galaxies, selected in an orientation-independent way.

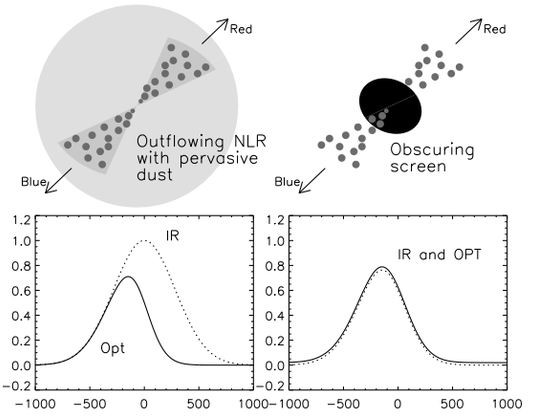

Fig. 4. Sketch indicating the effect of dust extinction on NLR line profiles. If the NLR is outflowing and embedded in pervasive dust of moderate optical depth, optical lines will be blueshifted with respect to systemic velocity while infrared lines will be not. In contrast, a highly optically thick screen obscuring part of the receding NLR regions will affect optical and infrared lines in the same way.

4 Searching for Obscured Broad Line Regions

'Unified' models assume that Seyfert 2 galaxies host a Seyfert 1–like BLR which is obscured towards our line of sight by a dusty torus, and have been highly successful in explaining several aspects of Seyfert galaxies. The key observational evidence supporting such models came from the spectropolarimetric dectection of broad hydrogen recombination lines, but direct detection

of the obscured BLR may be in principle possible at near- and mid-infrared wavelengths and can provide another route to studies of Seyfert unification, independent of the uncertain scattering efficiency entering the quantitative analysis of most spectropolarimetric data. Detections or limits for a significant sample of Seyfert 2s could be used to derive constraints on column densities and geometry of the putative tori, by studying detection rates and columns as a function of orientation. Different torus models in the literature reproduce photometric data equally well but differ widely in inferred properties and optical depth of the torus [6],[16].

Broad line components have been detected to near-infrared lines (mainly Paschen β) in several Seyferts, but these data tend to probe a population of relatively small obscuring column as inferred from X-ray data. There is hence a strong rationale for trying to detect longer wavelength recombination lines that are able of penetrating a larger column, and to extend searches to more difficult but more rewarding X-ray quiet targets. The major observational difficulties in attempts to detect broad mid-infrared recombination lines are (1) the rapid fall of intrinsic recombination line fluxes towards higher series, i.e. longer wavelengths; (2) the active galactic nucleus (AGN) dust continuum rising steeply towards longer wavelengths, leading to small line-to-continuum ratios vulnerable to systematic effects; and (3) the shape of the mid-infrared extinction curve which determines the wavelengths able of penetrating the highest obscuring column.

Observations of 2.62μm Brackett β, 4.05μm Brackett α and 7.46μm Pfund α in NGC 1068 were unable to detect broad components [10]. The limit of $A_V > 50$mag to the BLR is not yet significant enough to discriminate between different torus models. From a practical point of view, these data favour the use of Brackett α for future infrared BLR searches. 7.46μm Pfund α appears less favourable than assumed pre-ISO, both because the extinction at this wavelengths may be larger than assumed and because of the presence of nearby broad emission features which make continuum definition difficult.

5 Conclusions

High quality mid-infrared spectroscopy of active galactic nuclei has become possible for the first time with ISO. The central AGN emits a strong mid-infrared continuum on which emission features originating in the host galaxy may be superposed. Fine structure line emission from the Narrow Line Region allows a reconstruction of the otherwise unobservable EUV spectrum of the AGN. Results are consistent with an accretion disk as required by the AGN paradigm but also suggest neutral absorbers inside the NLR. High dust penetration of infrared lines tests structure and dust content of the NLR, and allows to probe for obscured broad line regions required by the unified scheme.

References

1. Alexander D.M., Efstathiou A., Hough J.H., Aitken D., Lutz D., Sturm, E., Roche P. (1999) MNRAS 310, 78
2. Alexander T. Sturm E., Lutz D., Sternberg A., Netzer H. Genzel R. (1999) Astrophys. J. 512, 204
3. Alexander T., Lutz D., Sturm E., Genzel R., Sternberg A., Netzer H. (2000) Astrophys. J., submitted
4. Binette L., Wilson A.S., Raga A., Storchi-Bergman T. (1997) Astron. Astrophys. 327, 909
5. Clavel J., Schulz B., Altieri B., Barr P., Claes P., Heras A., Leech K., Metcalfe L. (1998) astro-ph/9806054
6. Granato G.L., Danese L., Franceschini L. (1997) Astrophys. J. 486, 147
7. Heckman T.M., Miley G.K., van Breugel W.J.M., Butcher H.R. (1981) Astrophys. J. 247, 403
8. Kriss G.A., et al. (1992) Astrophys. J. 392, 485
9. Laurent O., Mirabel I.F., Charmandaris V., Gallais P., Vigroux L., Cesarsky C.J. (1999) in: The Universe as seen by ISO, eds. P.Cox, M.F.Kessler, ESA-SP427, p. 913
10. Lutz D., et al. (2000), Astrophys. J., in press
11. Lutz D., Sturm E., Genzel R., Moorwood A.F.M., Alexander T., Netzer H., Sternberg A. (2000) Astrophys. J., submitted
12. Maiolino R., Krabbe A., Thatte N., Genzel R. (1998) Astrophys. J. 493, 650
13. Mirabel I.F., et al. (1999), Astron. Astrophys. 341, 667
14. Moorwood A.F.M., Lutz D., Oliva E., Marconi A., Netzer H., Genzel R., Sturm E., de Graauw Th. (1996) Astron. Astrophys. 315, L109
15. Moorwood A.F.M. (1999) in: The Universe as seen by ISO, eds. P.Cox, M.F.Kessler, ESA-SP427, p. 825
16. Pier E.A., Krolik J.H. (1992) Astrophys. J. 401, 99
17. Sturm E., Alexander T., Lutz, D., Sternberg A., Netzer H., Genzel R. (1999) Astrophys. J. 512, 197
18. Sturm E., Lutz D., Tran D., Feuchtgruber H., Genzel R., Kunze D., Moorwood A.F.M., Thornley M.D. (2000) Astron. Astrophys., submitted

First Results of the ISO Photometry of 12 μm Active Galaxies ⋆

Luigi Spinoglio[1], Paola Andreani[2], and Matt Malkan[3]

[1] IFSI-CNR, Via Fosso del Cavaliere 100, I-00133 Roma, Italy
[2] Osservatorio di Padova, Vicolo dell'Osservatorio 5, I-35122 Padova, Italy
[3] UCLA Division of Astronomy & Astrophysics, Los Angeles, CA 90095-1562, USA

Abstract. We present the preliminary results of the ISOPHOT survey of the active galaxies belonging to the $12\mu m$ galaxy sample. Most of the observations have been collected in an ISO open time programme, while others have been extracted from the ISO archive. We present new ISOPHOT photometry of 50 galaxies, and include the literature data of 21 other galaxies. The total sample is distributed roughly equally among the three classes of Seyfert 1s, Seyfert 2s and high luminosity non-Seyfert galaxies. The ISO photometry together with the IRAS data are used to define color-color diagrams and energy distributions. It appears that – on average – thermal dust emission at two temperatures (one cold at 15-30K and one warm at 50-70K) are sufficient to fit the 60–200μm energy distributions. The far-IR spectra of active galaxies, longward of 100μm, are dominated by thermal emission from dust in the host galaxies with a wide range of temperature, down to 15K. With the present data the contribution of the active nucleus or of a dusty torus around it cannot be disentangled from that of the host galaxies. Seyfert 1s appear to have the flatter 12-120μm spectrum, as already indicated by the IRAS data.

1 Introduction

One of the main goals of selecting a complete sample of galaxies using the IRAS $12\mu m$ flux was the definition of a complete and largely unbiased sample of active galaxies in the local universe. This selection was done twice, with the first one producing a list of 26 Seyfert type 1 galaxies (hereinafter Seyfert 1s) and 32 Seyfert 2s [1] out of a sample of 390 galaxies from the IRAS PSC; the second one selecting 53 Seyfert 1s, 63 Seyfert 2s, two blazars, and 38 high-luminosity non-Seyferts (i.e. galaxies with $L_{IR} \geq 10^{44}$erg s^{-1} without a Seyfert type optical spectrum) out of a sample of 893 galaxies [2] from the IRAS FSC. What was found is that the $12\mu m$ flux is approximately a constant fraction ($\sim 1/5$) of the bolometric flux in active galaxies. Moreover, also for non-Seyferts (mostly spirals) $12\mu m$ selection is the closest available approximation to selection by a limiting bolometric flux, which is about 14

⋆ Based on observations with ISO, an ESA project with instruments funded by ESA Member States (especially the PI countries: France, Germany, the Netherlands and the United Kingdom) with the participation of ISAS and NASA

D. Lemke, M. Stickel, and K. Wilke (Eds.): LNP 548, pp. 217–223, 2000.

times νF_ν at $12\mu m$ [3]. It follows that deep surveys at $12\mu m$ will provide complete samples at different bolometric flux levels of normal and active galaxies, which will not suffer the strong selection effects present in both the optical-UV and far-infrared. A new selection of galaxies, again selected at $12\mu m$ from the IRAS database, is in progress [4] to provide a firm base for comparing the local universe "activity" with the properties and evolution observed in the recent ISO cosmological surveys [5].

ISOPHOT [6] data has been obtained for the open time proposal "IR energy distributions and imaging of the complete sample of $12\mu m$ active galaxies". In particular, we present here the PHOT P22 photometric results obtained with the C200 detector array in the spectral range 120-200μm on 36 objects belonging to the $12\mu m$ active galaxies sample. To increase the statistics, we have also included ISOPHOT archive data, that we analysed independently.

2 Observations and Results

The C200 ISOPHOT P22 observations were collected in chopped photometric mode in the five filters centered at 120, 150, 170, 180 and 200μm. The reduction has been performed using the PIA software, version 7.2 [7].

Because all the galaxies have good detections in the IRAS bands, we have constructed the spectral energy distributions using the new ISOPHOT data together with the IRAS data. A good agreement is always found between the two parts of the energy distributions. To increase statistics, we have included other C200 ISOPHOT P22 observations from the ISO Archive of 14 galaxies. Moreover, we compare our results with those published by [8], [9], [10], and in total we discuss 71 objects (21 Seyfert 1s, 26 Seyfert 2s, 10 high luminosity non-Seyferts, 14 normal galaxies).

In Fig. 1 we present the average energy distribution of our objects. The ISOPHOT flux densities have been corrected using the color correction (from the PIA [7]) correspondent to black-body functions with an emissivity law proportional to the inverse square of the wavelength at the temperaures of 20K for Seyfert 1s and normal galaxies, 25K for Seyfert 2s and 30K for high luminosity non-Seyferts. The dust temperature that we have assumed is the lowest color temperature that we derive from the [200 - 100] color of each class of galaxies (see Sect. 2.1).

The observed power νF_ν of each object was normalized to the $12\mu m$ power observed by IRAS, then a mean spectrum was computed for each class of galaxies. It can be seen from the figure that: *i)* Seyfert 1s have a flatter energy distribution, compared to all other classes of galaxies; *ii)* Seyfert 2s and high-luminosity non Seyfert galaxies have the same far-IR energy distribution; *iii)* the normal galaxies in the sample observed show a minimum at about $120\mu m$ and a knee beyond that wavelength, probably indicating the lack of dust at intermediate temperature. The class showing the widest difference from the

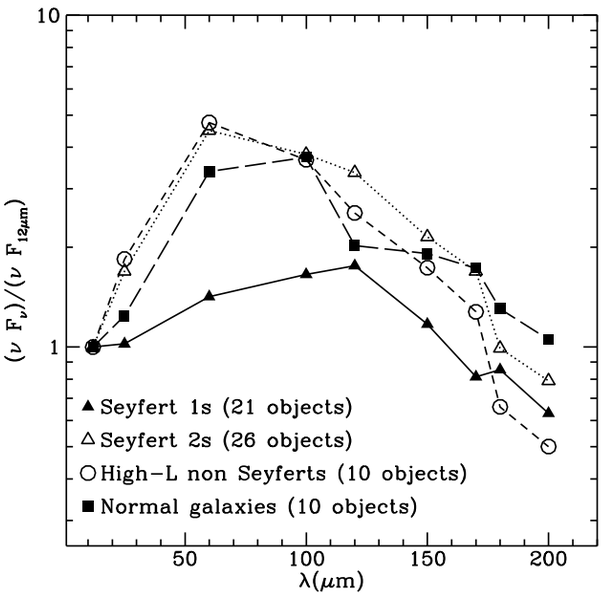

Fig. 1. The average energy distribution normalized to $12\mu m$ of galaxies belonging to the $12\mu m$ galaxy sample.

others is that of Seyfert 1s'. Their flatter energy distribution in the range 12-$120\mu m$ is probably related to the warmer dust heated by the active nucleus.

2.1 Far-Infrared Color-Color Diagram

To understand the origin of the far-infrared energy distributions observed, we constructed a color-color diagram: [200 - 100][1] versus [60 - 25]. We show this diagram separately for the Seyfert 1s, the Seyfert 2s and the high luminosity non-Seyfert galaxies together with the normal galaxies in Figs. 2, 3, and 4, respectively.

Most of the Seyfert 1s (Fig. 2) lie in a region that can be explained by the mixture of two black-bodies with a dust emissivity law proportional to the inverse square of the wavelength with T=22K and T=70K. We emphasize that flatter wavelength dependences of the dust emissivity law would not fit the [200 -100] color of most of the objects. This is a general finding, true for all classes of galaxies in the sample.

The three nearby CfA Seyfert 1s galaxies (NGC 3227, NGC 5033, NGC 4051) taken from [8] need lower temperatures. This can be merely due to a

[1] We define color $[\lambda_1 - \lambda_2] = \mathrm{Log}(F(\lambda_1)/F(\lambda_2))$

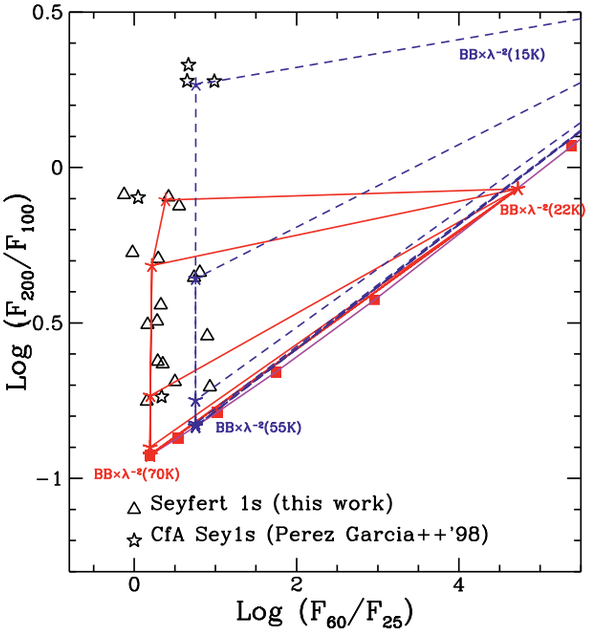

Fig. 2. The [200 -100] versus [60 - 25] color-color diagram of Seyfert type 1 galaxies belonging to the $12\mu m$ galaxy sample. The solid lines represent the models made of the mixture of two black-bodies at temperatures of 22K and 70K (with λ^{-2} dust emissivity). The dashed lines show the mixture of black-bodies at temperatures of 15K and 55K.

selection effect: the presence of faint emission associated to very cold dust can escape detection in objects lying at long distance, while it can be observed in these nearby objects.

The color-color diagram of Seyfert 2s (Fig. 3) shows that almost all these objects have a narrower temperature distribution in the range 25-65 K (with the usual dust emissivity), when compared to Seyfert 1s'. Again the two CfA Seyfert 2s' NGC 4388 and NGC 3982 [8] have lower temperature dust (T=18K).

High-luminosity non-Seyfert galaxies (Fig.4) show an even narrower range in temperatures: T=30-60K, while in the normal spirals belonging to $12\mu m$ galaxy sample and observed by [10] and by [9], dust at even lower temperature (15 K) is detected, confirming the previous finding of [9].

Comparing the three classes of galaxies, there appears to be a tendency showing that the most active objects (Seyfert 1s') have the coldest low temperature component (22K), together with the warmest high temperature one (70K); Seyfert 2s' are intermediate, while high-luminosity non-Seyferts have

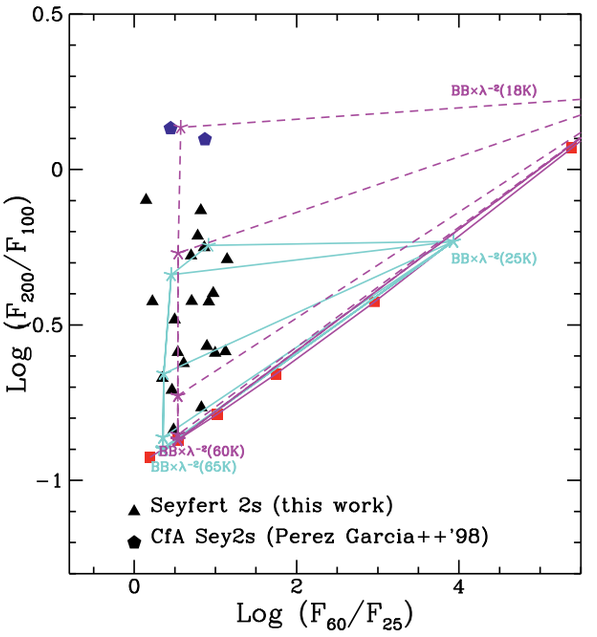

Fig. 3. The [200 -100] versus [60 - 25] color-color diagram of Seyfert type 2 galaxies belonging to the 12μm galaxy sample. The solid lines represent the models made of the mixture of two black-bodies (with λ^{-2} dust emissivity) at temperatures of 25K and 65K. The dashed lines show the mixture of black-bodies at temperatures of 18K and 60K.

the highest low temperature component (30K), together with the coldest high temperature one (60K).

A similar result has been found by [11] analysing the ISOPHOT data of the three interacting galaxies Arp 244, NGC 6240 and Arp 220: the increase of the highest dust temperature component is accompanied by the decrease of the lowest dust temperature component they detect. In four narrow-line Seyfert 1s [12] found that the lowest dust temperature is in the range 20-40K. The detection of very cold dust only in nearby objects could be explained with the very low surface brightness of its thermal emission. This dust component has been found by [9] to be surprisingly extended.

3 Conclusions

The preliminary results of the ISOPHOT photometry show that:

i) The 12-200μm energy distributions of active and normal galaxies in the local universe appear similar: the main differences are shown by Seyfert

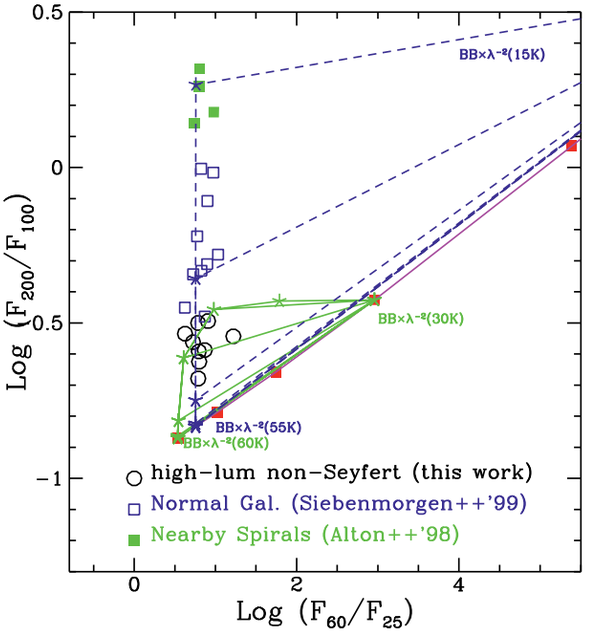

Fig. 4. The [200 -100] versus [60 - 25] color-color diagram of high luminosity non-Seyfert galaxies (open circles) and normal galaxies (squares) belonging to the $12\mu m$ galaxy sample. The solid lines represent the models made of the mixture of two black-bodies at temperatures of 30K and 60K (with λ^{-2} dust emissivity), which can fit the high luminosity non-Seyferts colors. The dashed lines show the mixture of black-bodies at temperatures of 15K and 55K (with λ^{-2} dust emissivity), fitting normal galaxies.

1s that have flatter spectra and by low luminosity normal galaxies, which show a knee in the distribution at about $120\mu m$, probably due to the lack of intermediate temperature dust.

ii) The [200 - 100] vs [60 - 25] color-color diagram shows that a mixture of two black-bodies with a warm and a cold component is able to fit all the data, only if we assume the dust emissivity law proportional to the inverse square of the wavelength.

iii) Comparing the three classes of galaxies, Seyfert 1s' show the larger range in temperature (22-70K), Seyfert 2s' are intermediate, while high-luminosity non-Seyferts have the narrower range in dust temperature (30-60K).

iv) Nearby normal spirals and CfA Seyfert galaxies show very cold dust components (15-18K).

References

1. Spinoglio L. & Malkan, M.A. 1989, ApJ 342, 83.
2. Rush B., Malkan M.A. & Spinoglio L. 1993, ApJSS 89,1.
3. Spinoglio L. et al. 1995, ApJ 453, 616.
4. Alexander D.M. et al. 1999, this conference.
5. Elbaz D. et al., A&A in press, astro-ph/9910406.
6. Lemke D. et al. 1996, A&A 315, L64.
7. Gabriel C. et al. 1997, Proc. of the ADASS VI Conf., ASP Conf. Ser., vol 125, p.108.
8. Perez-Garcia A.M. et al. 1998, ApJ 500, 685.
9. Alton P.B. et al. 1998, A&A 335, 807.
10. Siebenmorgen R., Krugel E., Chini R. 1999 A&A 351, 495
11. Klaas U., et al. 1997, A&A 325, L21.
12. Polletta M., Courvoisier T.J.-L., 1999, A&A 350, 765.

C II 158 μm Observations of a Sample of Late-Type Galaxies from the Virgo Cluster

Kieron J. Leech[1], Heinrich J. Völk[2], Ingolf Heinrichsen[1,2,4], Hans Hippelein[3], Leo Metcalfe[1], Daniele Pierini[2], Cristina C. Popescu[2,5], Richard J. Tuffs[2], and Cong Xu[4]

[1] ISO Data Centre, Astrophysics Division, ESA, Villafranca, Spain
[2] Max-Planck-Institut für Kernphysik, Saupfercheckweg 1, D-69117, Heidelberg, Germany
[3] Max-Planck-Institut für Astronomie, Koenigstuhl 17, D-69117, Heidelberg, Germany
[4] IPAC, Jet Propulsion Laboratory, Caltech 100-22, Pasadena, CA 91125, USA
[5] The Astronomical Institute of the Romanian Academy, Str. Cuţitul de Argint 5, 75212 Bucharest, Romania

Abstract. We have observed 19 quiescent Virgo cluster spiral galaxies with the Long Wavelength Spectrometer (LWS) onboard ESAs' Infrared Space Observatory (ISO), detecting 14 in the [CII] 157.741 μm fine structure line. Any influence of the Virgo cluster environment on the [CII] emission was found to be small compared with the strong dependence of the line emission on basic measurables such as morphology or bulk mass of the stellar component, as measured by the Near-IR (K′-band) luminosity. While the range of the [CII]-to-far-IR ratio is less than in other surveys, there is a good correlation between the strength of the [CII] line and the far-IR flux, as measured by IRAS. We find a trend of increasing [CII]-to-FIR flux ratio with increasing galaxy lateness. Moreover, the [CII]-to-K′-band flux ratio shows a two order of magnitude difference between RC3 type 0 and RC3 types later than 5. These two correlations express the relation between the mechanism of the [CII] emission and the massive star formation activity of the galaxy.

1 Introduction

The ISO (Kessler et al. [6]) Guaranteed Time programme VIRGO (Völk et al. *in prep*) is a photometric study of a complete volume-limited, unbiased sample of spiral, irregular and BCD galaxies from the Virgo cluster. Selecting galaxies from a cluster represents the most convenient way of ensuring completeness in a wide variety of intrinsic properties, embracing a large dynamic range in star-formation activity. In particular, the Virgo cluster was chosen for several reasons: the high level of completeness of the Virgo Cluster Catalogue (VCC) of Binggeli et al. [1], as described in Boselli et al. [2], to $B_T = 18$; at the distance to the cluster the typical angular sizes of the IR emitting regions are well matched to the angular resolution of ISO; and galaxies in the peripheral regions are thought to be freshly infalling from the field (Tully & Shaya [18]) and therefore less representative of the cluster environment.

D. Lemke, M. Stickel, and K. Wilke (Eds.): LNP 548, pp. 224–231, 2000.

While the VIRGO proposal is primarily photometric, we wished to observe many of these galaxies spectroscopically. Various constraints limited observations to the [CII] 157.741 μm cooling line, the most important gas cooling process in normal, i.e. non-starburst, late type galaxies, balancing the photoelectric heating from grains. It should probe photodissociation regions, e.g. Stacey et al. [16], associated with massive star formation, and also the diffuse components of the Interstellar Medium, e.g. Nakagawa et al. [11]. While in field galaxies the [CII] line has a luminosity of the order of 10^{-3} to 10^{-2} that of the total far-IR flux of a galaxy, e.g. Malhotra et al. [10], the Virgo sample galaxies are less active in star forming activity, even at the top end of the luminosity range observed.

At the distance of the Virgo cluster (taken to be 21 Mpc), the 70 arcsec diameter beam (Swinyard et al. [17]) of the LWS instrument (Clegg et al. [3]) covers an area of approximately 7 kpc in diameter. Optical images of the Virgo galaxies (Sandage et al. [14]) indicate that this will cover out to the observed spiral arms. In NGC 6946 the extended [CII] emission detected at this distance accounted for 70% of the total [CII] emission (Madden et al. [9]). Observation of Virgo galaxies with LWS will detect not only [CII] emission from the dense inner regions but, assuming Virgo galaxies are similar to NGC 6946, will primarily sample the [CII] emission from diffuse regions in and between the spiral arms.

This paper summarises the work of Leech et al. [7]. Pierini et al. [12] discusses the [CII] data and its relation to other measures of the star forming activity in more detail. Modelling of the relation between [CII] line emission and star formation history is deferred to Pierini et al. (*in prep*).

2 Sample Selection and Observations

The criteria for selecting the VIRGO sample from the VCC are discussed in Leech et al. [7]. The 18 spirals selected are earlier than Scd, come from both the cluster core and periphery, and are complete to $B_T = 12.3$ mag. They provide a sample of relatively quiescent galaxies in comparison to other of spiral galaxy samples selected for ISO observations e.g. Malhotra et al. [10]. One other optically faint but IR bright core galaxy, VCC 1326, was observed to serve as a LWS/ISOPHOT cross-calibration target. Reference fields were also selected to check for foreground [CII] emission from the Milky Way.

The observing mode used was standard LWS grating range scans (AOT 2's) centred on the redshifted [CII] line. All observations reached the same sensitivity limit per wavelength point. Sets of observations were used to observe several galaxies in sequence, with one sky background position used for each set. The observations were made between 30^{th} June and 15^{th} July 1996 with no instrumental or satellite problems reported.

Information on these galaxies and the observing log are given in Leech et al. [7].

3 Data Reduction and Results

The Auto Analysis Results from Off-Line Processing (OLP) version 7 were processed using the ISO Spectral Analysis Package (ISAP) version 1.6 by: discarding bad LWS data points; averaging scans for detector 8 (the one covering the 158 μm region); fitting the continuum; and finally fitting gaussians to any lines seen in the data to obtain flux and central wavelength.

Of the 19 galaxies observed, 14 were detected. Of the six background positions used, five had no detectable emission at galactic [CII] wavelengths and one was repointed to VCC 873, confirming the line flux and wavelength for that galaxy. In three galaxy observations (VCC 1110, 1326 and 1972) galactic [CII] emission was observed, and the data were fit with a line at the wavelength of galactic [CII] and one at the expected position of the Virgo [CII] emission.

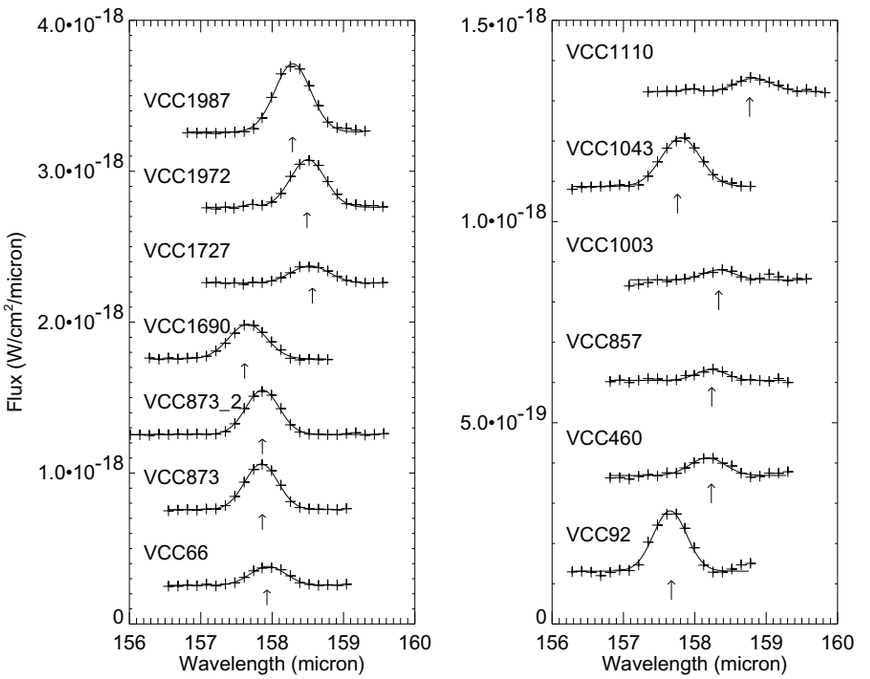

Fig. 1. Examples of Virgo galaxy observations. The baselines are arbitrary. The expected positions of the [CII] emission lines from optical observations are marked by arrows. Datapoints are marked by a '+', with the vertical size indicating the size of the systemic error when larger than the symbol size. Lines are fit to the data.

The [CII] line spectral region for example galaxies are shown in Figure 1. In this Figure the baselines used during plotting are arbitrary. The continuum is

quoted without subtracting any foreground emission from galactic emission. Note that the lines have not been resolved – linewidths are identical to the instrumental resolution (1100 km/s, Swinyard et al. [17]). Line fluxes, central wavelengths and continuum fluxes for all objects are given in Leech et al. [7].

4 Discussion

As already said in the Introduction, our sample of 19 VCC late type galaxies is biased toward low current star formation activity galaxies. In order to increase the range in current star formation activity, we add 5 low mass VCC galaxies observed by Smith & Madden [15].

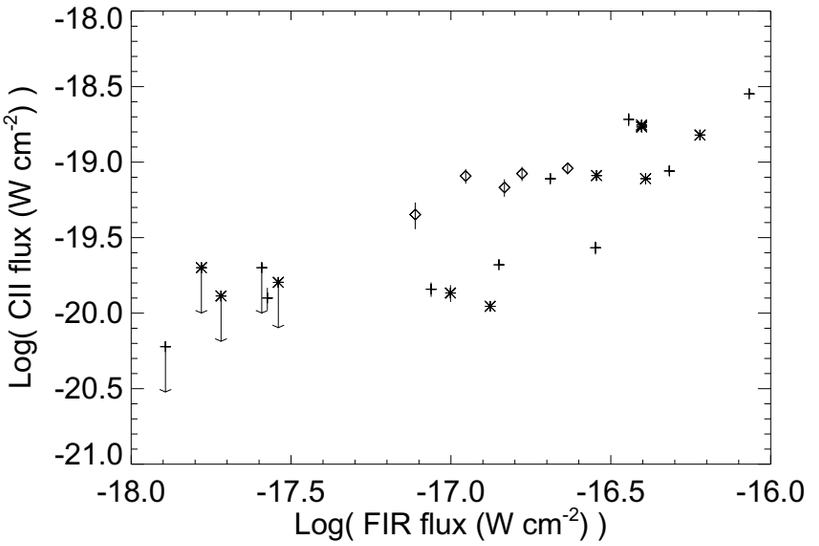

Fig. 2. [CII] flux against far-IR flux. Error bars are marked in the vertical, where they are larger than the symbol size, and upper limits are marked. Core galaxies are marked by '$*$', periphery by '$+$' and galaxies from Smith & Madden by diamonds.

4.1 The C[II] Flux Against Far-IR Flux

Figure 2 shows the relation between the [CII] flux and the far-IR flux (from IRAS, $FIR = 1.26 \times 10^{-18}(2.58 \times F_\nu(60\mu m) + F_\nu(100\mu m))Wcm^{-2}$, Helou et al. [4]). Despite the spatial mis-match between the LWS 70 arcsec diameter circular aperture and the larger IRAS square apertures, there is a good

correlation between these observed quantities within the approximately two orders of magnitude range in both quantities. We note that all the upper limits in the [CII] flux are found at the faint end of the far-IR emission.

When [CII] is detected, the [CII] to FIR ratio ranges from 0.1% to 0.5%. This covers the ranges expected for compact sources (0.2%), such as active star-forming regions, to the diffuse component on the ISM (0.6%) (Nakagawa et al. [11]). Galaxies observed by Stacey et al. [16] cover the range 0.15 – 0.6%, and in NGC 5713 the ratio is 0.7% (Lord et al. [8]).

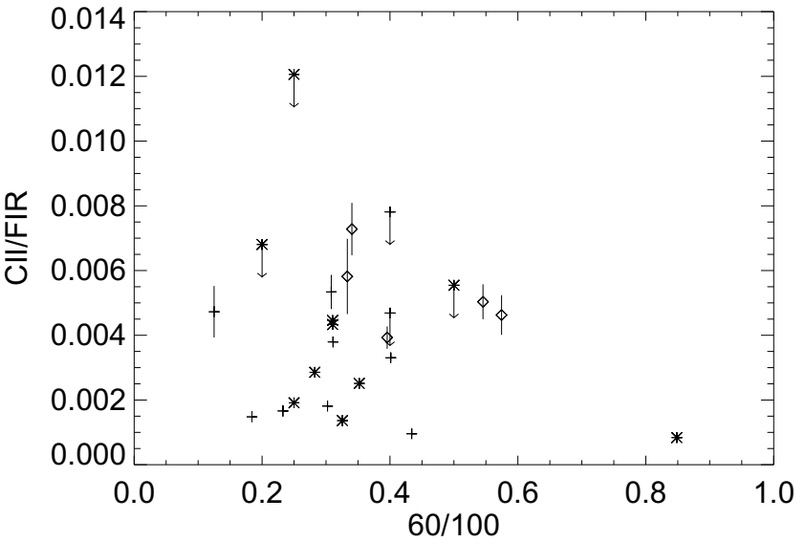

Fig. 3. [CII]/FIR ratio against dust temperature, indicated by 60/100 μm ratio. Error bars and upper limits are marked. Core galaxies are marked by '$*$', periphery by '+' and galaxies from Smith & Madden by diamonds. VCC 1326 lies at the edge of this diagram with a 60/100 ratio of 0.85 but an apparently anomalously low [CII]/FIR ratio of 0.09%, and may be a starburst galaxy.

4.2 Comparison with Dust Temperature

Figure 3 shows the [CII] to FIR ratio against the dust temperature, as measured by the ratio of the IRAS flux densities at 60 and 100 μm. The [CII]/FIR ratio is highest for galaxies with a 60 to 100 ratio of about 0.3 – 0.6, cf. Malhotra et al. [10].

4.3 C[II] and Morphological Type

Figure 4 shows the [CII]/FIR ratio against RC3 type. Ignoring the upper limits, there is marked difference between the ratio for RC3 types 0 – 3 against RC3 types later than 5. Galaxies with larger [CII]/FIR continuum ratios tend to have later Hubble types.

If the [CII] flux is normalised by K′-band ($\lambda = 2.1$ μm) flux, a measure of the number of old stars in the galaxy which constitute the bulk of the stellar mass component, c.f. Rix & Rieke [13], this difference with RC3 type is even more pronounced, as can be seen from Figure 5. This mass-normalization removes simple scaling effects in the relation between the [CII] and the K′-band luminosities (not shown).

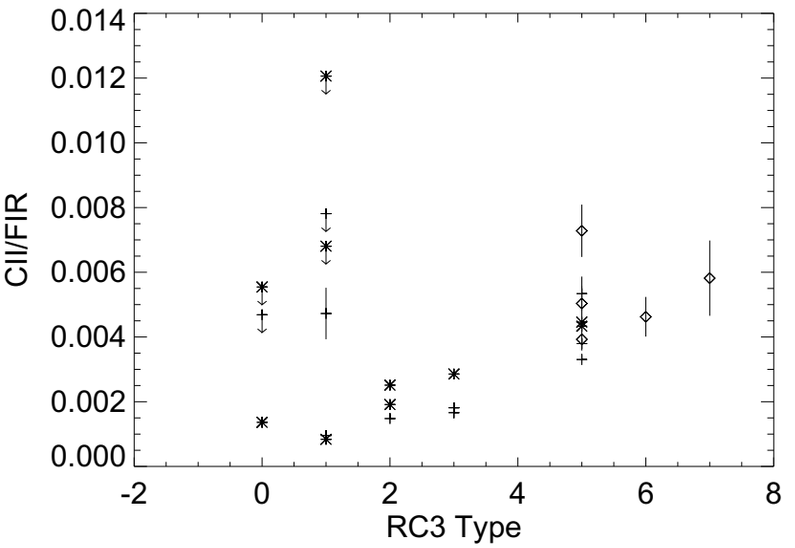

Fig. 4. [CII]/FIR ratio against RC3 Type. Error bars and upper limits are marked. Core galaxies are marked by '$*$', periphery by '+' and galaxies from Smith & Madden by diamonds.

Conversely, there is no apparent relation between the [CII] line properties and position in the cluster from Figures 2, 3, 4 and 5. Neither is there evidence for a relation between the [CII] line properties and disk HI mass surface density (within the LWS circular aperture), from Warmels [19], and therefore any relation of the [CII] emission to the diffuse HI component of the ISM is not obvious, at least for the central regions of the disks observed. This is interesting compared to the Madden et al. [9] results that find approximately

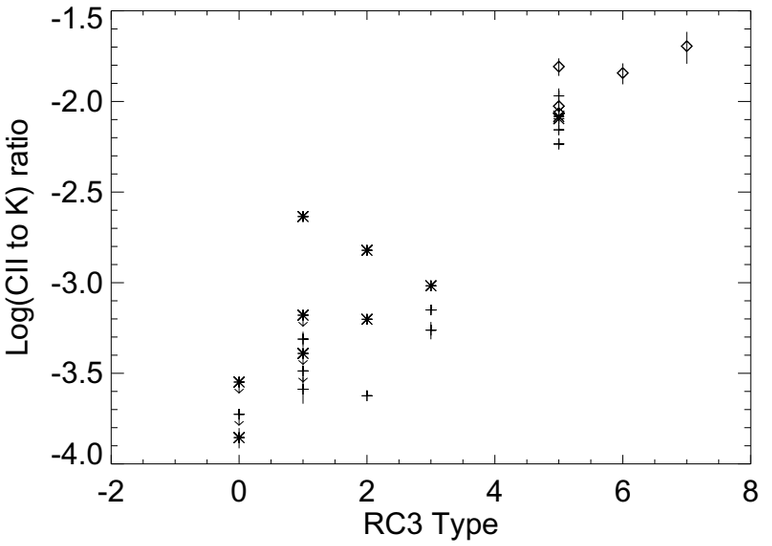

Fig. 5. [CII]/K′ flux ratio against RC3 Type. The difference between RC3 types 0 and 5 are more marked when the [CII] flux is normalised by a reliable estimate of the bulk of the galaxian stellar mass. Error bars and upper limits are marked. Core galaxies are marked by '∗', periphery by '+' and galaxies from Smith & Madden by diamonds.

70% of the total [CII] emission from NGC 6946 arises from diffuse components of the disk. The lack of a [CII]–HI correlation integrated over the disks of the Virgo spirals therefore may come as a surprise. One potential explanation is that the central HI mass surface density is not well correlated to any global properties of the sample galaxies, e.g. the Hubble Type or the central molecular gas surface density (Pierini et al. *in prep*). However, we caution that we only have HI data for 12 galaxies and that larger samples are needed to establish firm trends in view of the large intrinsic scatter of the HI emission from galaxies of given morphological types.

5 Conclusion

We have detected the [CII] fine structure line in fourteen late-type Virgo cluster galaxies. A good correlation is found between the [CII] strength and the FIR flux. Moreover, we find evidence for a dependence of the [CII]-to-FIR flux ratio on the galaxy morphology, with the [CII]/FIR ratio increasing with later Hubble types. A stronger correlation with lateness is found for the

[CII]-to-K′-band flux ratio, the K′ flux representing the bulk of the stellar mass content of the galaxy.

Why is the [CII] to FIR ratio highest for galaxies with a 60/100 ratio of about 0.3 – 0.6, as shown in Figure 3, higher than for starburst galaxies? And why is there a marked difference in the [CII]/FIR ratio between RC3 types 0 – 3 and types later than 5? We interpret both these in the following way. Quiescent galaxies have a larger proportion of dust heating from the old low mass stellar population, which produces little or no UV and hence little [CII] line emission. On the other hand, starburst galaxies produce copious hard-UV from their massive O stars which is very efficient at producing IR emission but is relatively inefficient at producing the [CII] line emission. Between these two extremes lie galaxies with a larger fraction of intermediate mass ($5 \leq M \leq 20\ M_{\odot}$) stars that are efficient at both IR and [CII] line emission production from soft UV. Since massive star formation activity increases with increasing lateness, e.g. Kennicutt et al. [5], this lead to the correlation in the [CII]/FIR ratio against RC3 type plot, (Figure 4). Note, however, that if the stars get too massive they become inefficient at producing the [CII] emission. This is discussed in more detail in Pierini et al. [12].

References

1. Binggeli B., Sandage A., Tamman G.A., 1985, AJ, 90, 1681
2. Boselli A., Tuffs R.J., Gavazzi G., Hippelein H., Pierini D., 1997, A&AS, 121, 507
3. Clegg P.E et al. , 1996, A&A, 315, L38
4. Helou G., Khan I.R., Malek L., Boehmer L., 1988, ApJS, 68, 151
5. Kennicutt R.C., Tamblyn P., Congdon C., 1994, ApJ, 435, 22
6. Kessler M.F. et al. , 1996, A&A, 315, L27
7. Leech, K.J. et al. , 1999, MNRAS, 310, 317.
8. Lord S.D. et al. , 1996, A&A, 315, L117
9. Madden S.C., Geis N., Genzel R., Herrmann F., Jackson J., Poglitsch A., Stacey G.J., Townes C.H., 1993, ApJ, 407, 579
10. Malhotra S., et al. , 1997, ApJ, 491, L27
11. Nakagawa T., et al. , 1998, ApJS, 115, 259
12. Pierini D., Leech K.J., Tuffs R.J., Völk, H.J, 1999, MNRAS, 303, L29
13. Rix H., Rieke M., 1993, ApJ, 418, 123
14. Sandage A., Binggeli B., Tammann G.A., 1985, AJ, 90, 395
15. Smith B.J., Madden S.C., 1997, AJ, 114, 138
16. Stacey G.J., Geis N., Genzel R., Lugten J.B., Poglitsch A., Sternberg A., Townes C.H., 1991, ApJ, 373, 423
17. Swinyard B., et al. 1998, In Proc. of SPIE Conference on Infrared Astronomical Instrumentation, Kona, Hawaii, SPIE Vol. 3354 pp 888-899
18. Tully R.B., Shaya E.J., 1984, ApJ, 281, 31
19. Warmels R.H., 1988, A&AS, 72, 427

Smoke in the "Smoke Rings": ISO Observations of Dust in Collisional Ring Galaxies

Philip N. Appleton[1], Vassilis Charmandaris[2], Cathy Horellou[3], I. Felix Mirabel[4], and Olivier Laurent[4]

[1] Iowa State University, Ames, Iowa 50011, USA
[2] Cornell University, Ithaca, NY 14853, USA
[3] Onsala Space Observatory, Sweden
[4] Service d'Astrophysique CEA/Saclay, France

Abstract. Collisional ring galaxies probably result from a head-on collision between a compact companion galaxy and a gas-rich disk system. We present a review of the discovery of warm dust in five collisional rings observed by ISO which range in total Far-IR luminosity from $10^{10} < L_{FIR} < 10^{11}$ L$\odot$. The results show that in most cases, the mid-IR (MIR) flux is often a significant fraction of the total energy budget of star formation activity in these galaxies (at least 10% even in the least powerful cases). We argue that the MIR emission, when combined with optical and radio observations, allows us to build a more complete picture of activity in these collisional systems. Although not as extreme as ULIRGs, these collisional systems provide low-redshift examples of the early effects of galaxy collisions on the ISM and may be relevant to the collisional assembly of galaxy disk components at high redshift.

1 Introduction

In this paper we review Infrared Space Observatory observations of ring galaxies. These galaxies are believed to represent the unusual class of collisional system in which one of the galaxies plunges through the center of a second larger disk system, creating radially driven waves which can trigger star formation in rings. Although the majority of the nearby examples do not significantly exceed far-IR luminosities of 10^{11} L$\odot$, a recent HST study of ultra-luminous far-IR galaxies by Borne et al. [7] shows many more distant examples of ring systems that exceed 10^{12} L$\odot$. Indeed, because of the rarity of rings in the nearby universe, large volumes of the universe need to be studied in order to build up a complete picture of the range of properties of these fascinating systems. These rare colliding galaxies have the advantage over more general collisional systems in that they are conceptually simple, symmetrical and the star formation around the ring is triggered almost simultaneously (see recent review by Appleton & Struck-Marcell [6]). Many of the nearby cases have been studied from the ground in considerable detail at many wavelengths.

D. Lemke, M. Stickel, and K. Wilke (Eds.): LNP 548, pp. 232–239, 2000.

This conference has highlighted the need to understand IR and sub-mm galaxy number counts, and the need for significant luminosity evolution in galaxies, especially at redshifts in excess of z = 0.5 to 1 where the luminosity evolution has to increase rapidly to fit these emerging data. Lavery et al. [13] has begun a major search of ring galaxies in deep HST archive images, and has found evidence for a large increase in the collision rate of these galaxies with redshift. It may not be surprising to find that the assembly of gas rich disk systems is a messy process, involving collisions between disk fragments at high velocity within loose galaxy potentials, creating high redshift analogs of these locally rare collisions. One challenge for the study of these systems is to understand the variety of ways in which gas is converted efficiently into stars, and what role, if any, is played by active nuclei in either hindering or encouraging the conversion of matter into luminous energy on both the small and large scales. The sample of galaxies discussed here ranges from examples of galaxies with little or no nucleus of any kind, to violently interacting ring galaxies containing high-speed gas flows and AGNs. In one case, NGC 985, ISOCAM imaging reveals new near-nuclear features not seen at shorter wavelengths, which may relate to the interaction of high-speed winds from the AGN with infalling gas from the galaxy on the kpc scale.

2 Observations

All the observations presented here were made with ISOCAM in various raster modes (usually 2 x 2 raster mapping) and typical integration times per filter of 10 minutes (see Table 1 for details and references to more detailed papers).

3 Low-Luminosity Ring Systems

Figure 1 shows an example of one classical "smoke ring" called VII Zw 466 observed with ISOCAM and detected in three filters (from [1]). This galaxy has been studied in considerable detail from the ground and comprises of an outer ring of powerful HII regions and fainter redder light which fills the interior of the ring (see Bransford et al. 1999a for further references). The likely intruder (the edge-on spiral to the south of the ring, G1 - see [2] for details) is also detected. Figure 2 displays how the IR emission follows loosely the distribution of optical emission-line sites, but that it is not a one to one correlation. Similarly, VLA radio observations, which trace thermal and non-thermal plasma compressed in the expanding ring, do not follow exactly the distribution of either the warm dust or the optical nebulae. Rather the radio emission tends to be concentrated on the inside-edge of the ring.

The results, which are discussed in much more detail by Appleton et al. [1], suggest that 10% of the available thermal uv luminosity is re-radiated in the MIR. Point-to-point variations in MIR emission from within the galaxy

Table 1. The Ring Galaxies Imaged by ISOCAM

Name	V_{Helio} ($km\,s^{-1}$)	Ring Type[a]	Filters[b]	$\log(\frac{L_{FIR}}{L_\odot})$	$\frac{L_{FIR}}{L_B}$
Cartwheel	8934	RN	LW2,3 (GT)[c]	10.14	1.0
VIIZw466	14335	RE	LW1,7,8,9 (GO)[d]	10.2	0.46
NGC 985	12950	RK (Sey1)	Lw1,3,7,8 (GO)[e]	10.98	0.71
Arp 10	9100	RN	LW2,3 (GT)[f]	–	–
Arp 118	8800	RN/K (Sey2)	LW2,3,CVF (GT)[f]	10.98	4.4

[a] Ring designations from Theys & Spiegel (1976)[17]
[c] Details on the ISOCAM filters can be found in the ISOCAM Observers Manual (*http://isowww.estec.esa.nl/manuals/iso_cam*)
[c] Charmandaris et al. (1999) [9], CAMACTIV GT Program
[d] Appleton et al. (1999) [1], NASA GO Program
[e] Appleton et al. in prep., NASA GO program
[f] Charmandaris et al. in prep., CAMACTIV GT program

compared with the underlying heat sources may be due to a number of effects–variations in dust filling factors and geometry–variations in the destruction rate of the small grains involved, as well as differences in the chemistry of the grains themselves. These sorts of variations, which are seen in other nearby galaxies, underline the difficulties that may ensue in trying to create a "standard galaxy" template for use in models that attempt to reproduce logN/logS diagrams for high-z galaxies. Care must especially be taken when K-corrections involve bands contaminated by mid-IR UIB features.

Figure 3 shows some early UKIRT J, H and K-band maps of the Cartwheel ring from Marcum, Appleton & Higdon [14]. Figure 4 shows the ISO detection of warm dust from the ring (from [9]), and emphasizes how different the near and mid-IR distributions are. In most cases, K- band imaging traces the stellar component (the recently formed star clusters) whereas the MIR emission is sensitive to warm dust heated by the uv from hot stars. The ISO observations show that the outer ring is more easily detected at shorter MIR wavelengths (where the emission is most likely dominated by UIB features around 6-7 microns), and is rather weak at longer wavelengths. One initial surprise was the detection of significant MIR flux from the inner regions of the Cartwheel where star formation activity is believed to be minimal. Horellou et al. [12] have recently obtained clear evidence for a large concentration of molecular material in the central regions of the Cartwheel. It now seems likely that low-level, but quite extended star formation may be occurring over the inner ring regions of the Cartwheel, perhaps a precursor to much more powerful activity in the near future. It is not yet clear whether this star

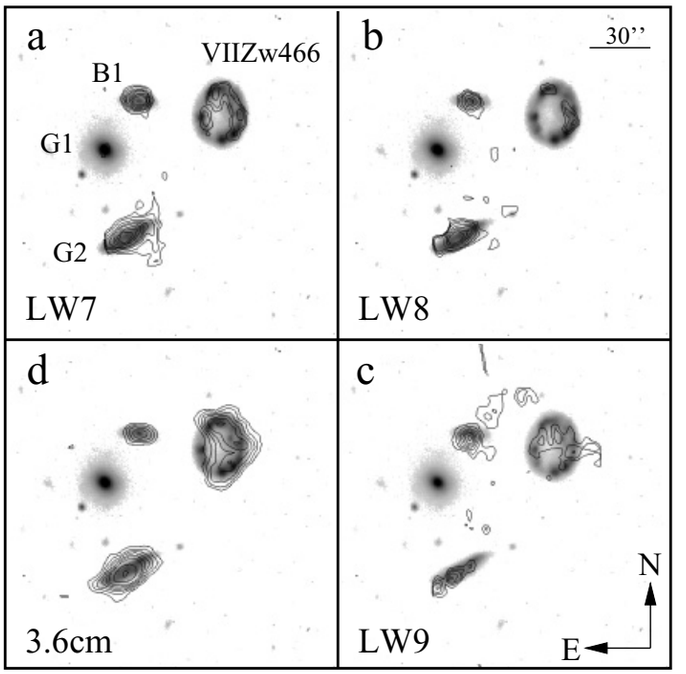

Fig. 1. ISO and VLA Observations of the VII Zw 466 Galaxy and Group

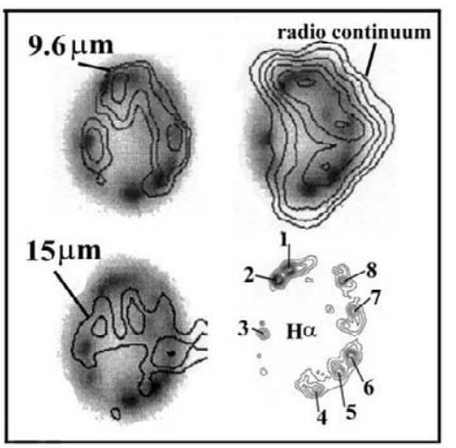

Fig. 2. Comparision with broad-band optical and Hα images

formation is triggered by infall from the outer disk, debris from the collision impacting the center, or just mild compression of the gas in the inner disk by passage through the second ring.

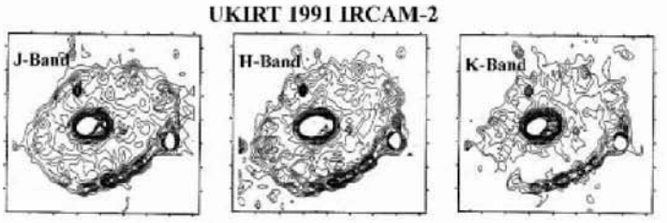

Fig. 3. J, H and K Near-IR Images of the Cartwheel from UKIRT

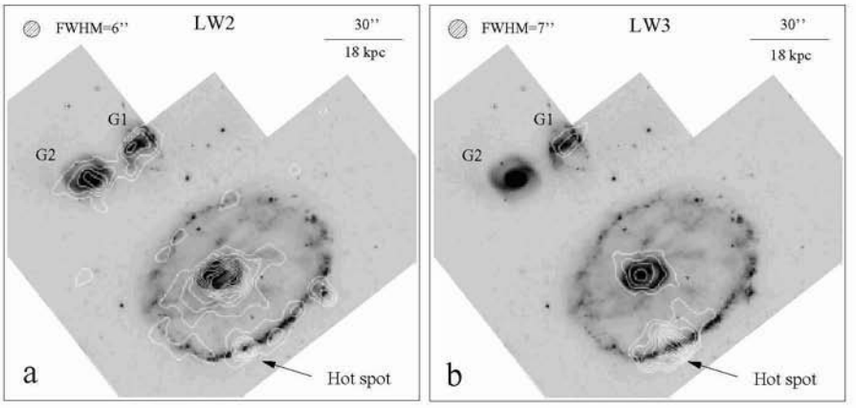

Fig. 4. ISO Imaging of the Cartwheel at 7 and 15 microns

4 Some Examples of More Violently Interacting Systems?

Two systems (NGC 985 and Arp 188 = NGC 1144/5) have FIR luminosities which are approaching those of ultra-luminous galaxies. Both have rings, AGNs, and neither is very simple in optical morphology. In the case of Arp 118 (Charmandaris et al., in preparation), the MIR emission originates from a bright featureless continuum source associated with the nucleus, and a very extended but bright concentrations of emission associated with a powerful

extra-nuclear HII regions. This latter emission is dominated by UIB spectral features (probably Polycyclic Aromatic Hydrocarborns), and emphasizes the composite nature of the MIR spectra of some Seyfert galaxies.

The galaxy NGC 985 is a ring galaxy with a bright "knot" embedded in the outer ring [16]. Optical and IR observations show that the "knot" is composed of two nuclei, a Seyfert-1 nucleus, and a second "spiral bulge" 3 arcsecs to the north-west of the Seyfert nucleus [15,3]. This has led to the conclusion that NGC 985 consists of two galaxies undergoing a merger; the AGN lying at the center of the nucleus of one galaxy, and the second nucleus corresponding to the other. If one of the nuclei is the original nucleus of the "target" galaxy, then it must be significantly displaced from the ring center. This suggests that we are viewing the early stages of a highly off-center merging collision, since dynamical friction would quickly center the collision if we were witnessing the event at a later time. This view is supported by the fact that the molecular gas is still quite extended in this system [11], unlike a well evolved merger, where the molecular gas is often concentrated in the nucleus.

Figure 5 shows a sequence of ISOCAM images of the galaxy in three bands (9.6, 11 and 15 microns). The off-center "bulge and nucleus" are easily detected (but not resolved) in all bands, as well as the brightest HII regions in the western edge of the ring.

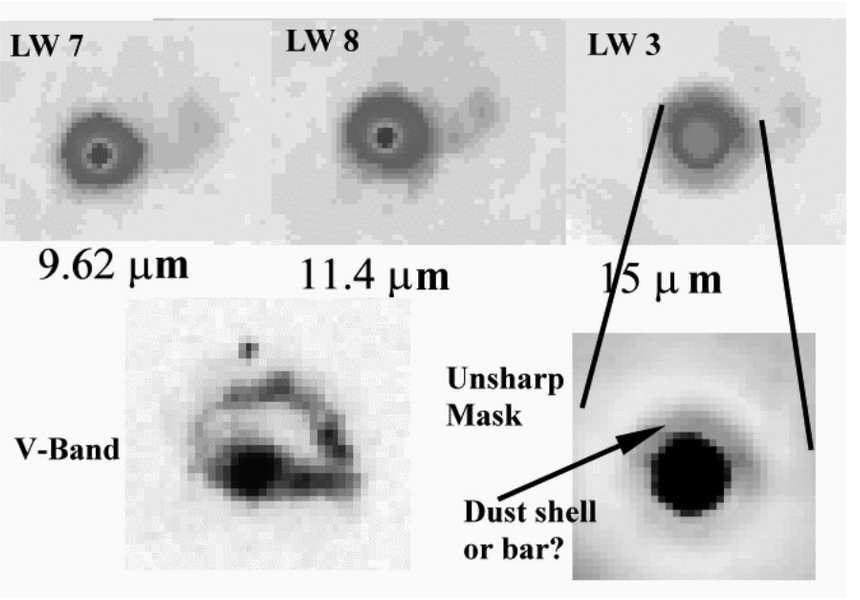

Fig. 5. ISOCAM Images of NGC 985 (Appleton et al. In Prep)

An unusual feature of the ISOCAM maps is seen when the images are further processed. For example, the inset shows the effect of applying an unsharp-masking technique to the image. The inset shows that a curved arc-like structure is seen about 5 arcsecs north-west of the Seyfert nucleus. The arc-feature does not correspond to the second nucleus seen in the early near-IR observations [3], but is a little beyond it. The structure is not an artifact of the unsharp-masking, since it is seen in the original data, and is also reproduced when a symmetrical gaussian profile is removed from the Seyfert nucleus. The structure, though strong at 15 microns (where the signal to noise ratio is highest), is also seen in both the LW7 and 8 filters, confirming its reality. One possible explanation for the structure is that is defines a cooling shock-front driven into infalling gas from the outer ring as it collides with a wind from the Seyfert nucleus. One attractive aspect of this picture is that it explains why the "arc" is not a complete shell around the nucleus. Models of collisions between galaxies which form off-center rings (e.g. [5]) predict that the strongest gaseous infall will occur on the side of the disk most strongly compressed in the collision. This is precisely the case here–the largest gas flows inwards are expected from material falling inwards from the N-W side of the ring where the ring is most sharply defined. Mid and far-IR spectroscopy of the "arc" feature would help to determine if the feature shows shock-excitation consistent with this simple hypothesis.

5 Conclusions

A mid-IR survey of collisional ring galaxies has yielded some interesting results. These are:

- The MIR flux is at least 10% of total thermal uv continuum, in even the low-luminosity examples of these galaxies. It is not yet known if this fraction depends on the degree of compactness of the collisional system, nor how this ratio changes in more distant ultra-luminous ring galaxies (e.g. [7]).
- A rough correspondence (but not always 1 to 1) between star formation sites and MIR emission regions is seen in most cases. Differences may reflect clumpy dust distributions, incomplete filling factors, thermal spiking (especially in UIB affected bands), and also possible variations in grain chemistry from region to region. Such variations suggest that creating "mean galaxy" templates for use in interpreting logN/LogS galaxy number counts may be unreliable, especially if some of the bands are dominated by UIB features.
- Near-nuclear emission is common in Seyfert ring galaxies. In Arp 118, the Seyfert nucleus is devoid of UIB features, but very powerful extra-nuclear starformation sites are dominated by UIB features. Such a galaxy, if viewed from a distance, would exhibit a composite MIR spectrum,

complicating the clear separation of AGN and starburst on the basis of MIR spectral features alone. In NGC 985, a dust arc is discovered in the MIR on the kpc–scale near the Seyfert 2 nucleus. This feature, which has not been seen at shorter wavelengths, may represent a shock wave driven into neutral or molecular gas by the AGN wind. The geometrical asymmetry of the "arc" might be expected on the grounds of asymmetric infall which is predicted in highly off-center ring galaxy collision models.

- In the Cartwheel, extended nuclear emission seen in MIR which was not expected based on optical imaging. This emphasizes the fact that ISO is can be sensitive to low-level distributed star formation which might but rather difficult to detect optically in dusty regions.

References

1. Appleton, P. N., Charmandaris, V., Horellou, C, Mirabel, I. F., Ghigo, F. D., Higdon, J. L. & Lord, S. 1999, ApJ, 527, 143
2. Appleton, P. N., Charmandaris, V. & Struck, C. 1996, ApJ, 468, 532
3. Appleton, P. N. & Marcum, P. M. 1993, ApJ, 417, 90
4. Appleton, P. N. & Struck-Marcell, C. 1987a, ApJ, 312, 566
5. Appleton P. N. & Struck-Marcell, C. 1987b, ApJ, 318, 103
6. Appleton, P. N. & Struck-Marcell, C. 1996, Fund. Cos. Phys, 16, 111
7. Borne, K. D., Bushouse, H., Colina, L. & Lucas, R. A.. 1999, BAAS, 31, 1304
8. Bransford, M. A., Appleton, P. N., McCain, C. F. & Freeman, K. C., 1999, ApJ, 525, 153
9. Charmandaris et al. 1999, A&A., 341, 69
10. Charmandaris et al. 2000 (in preparation)
11. Horellou, C., Casoli, F., Combes, F. & Dupraz, C 1995, A&A , 298, 743
12. Horellou, C., Charmandaris, V., Combes, F., Appleton, P. N., Casoli, F.; Mirabel, I. F 1998, A&A, 340, L51
13. Lavery, R. L., Seitzer, P, Suntzeff, N. B., Walker, A. R. & Da Costa, G. S. 1996, ApJL, 467, L1
14. Marcum, P. M., Appleton, P. N. & Higdon, J. L. 1992, ApJ, 399, 57
15. Perez-Garcia, A. M. & Roderigues Espinosa 1996, AJ, 112, 1863
16. Rodrigues-Espinosa, J. M. & Stanga, R. M. 1990, ApJ, 365, 502
17. Theys, J. C. & Spiegel, E. A. 1976, ApJ, 208, 650

NIR Spectroscopy with the VLT of a Sample of ISO Selected Hubble Deep Field South Galaxies

Dimitra Rigopoulou[1], Alberto Franceschini[2], Reinhard Genzel[1], Paul van der Werf[3], Hervé Aussel[2], Catherine Cesarsky[4], Michel Dennefeld[5], Seb Oliver[6], and Michael Rowan-Robinson[6]

[1] Max-Planck-Institut für extraterrestrische Physik, Postfach 1603, 85740 Garching, Germany
[2] Dipartimento di Astronomia, Viccolo Osservatorio 5 I-35122, Padova, Italy
[3] Leiden Observatory, PO Box 9513, 2300 RA, Leiden, The Netherlands
[4] European Southern Observatory, Karl-Schwarzschild-str. 2, 85740 Garching, Germany
[5] Institut d'Astrophysique de Paris - CNRS,98bis Boulevard Arago, 75014 Paris, France
[6] Imperial College of Science Technology and Medicine, Astrophysics Group, Blackett Laboratory, Prince Consort Rd., London, SW2 1BZ, U.K.

Abstract. A new population of faint galaxies characterized by an extremely high rate of evolution with redshift up to z∼1.5 has recently been discovered by ISO. These sources are likely to contribute significantly to the cosmic far-IR extragalactic background. We have carried out near-infrared VLT-ISAAC spectroscopy of a sample of ISOCAM galaxies from the Hubble Deep Field South. The rest-frame R-band spectral properties of the ISO population resembles that of powerful dust-enshrouded active starburst galaxies.

1 Introduction

IRAS observations show that about 30% of the total starlight emerges in the mid and far-infrared [30]. About 25% of the high mass star formation within 10 Mpc originates in dusty infrared luminous galaxies. IRAS counts indicate evidence for evolution at low flux levels in (Ultra)luminous Infrared Galaxies ((U)LIRGs, $L_{bol} > 10^{12}$ $L_{\odot}$ [23] [14]). However, the IRAS survey only sampled the local Universe (z<0.3), and the extrapolation of this evidence for cosmic evolution to higher redshifts is speculative. Since then, almost all information about high-z galaxies have relied on optical surveys. Although these surveys have been succesful in discovering distant galaxies (e.g., [29]) and constraining the star formation history of the Universe [24], they are only able to tell part of the story. The COBE detection of an extragalactic infrared background [28] with an integrated intensity similar or higher than that of optical light ([16], [20]) suggests that a significant part of the star formation in the Universe is obscured and has therefore been missed by the various optical surveys.

D. Lemke, M. Stickel, and K. Wilke (Eds.): LNP 548, pp. 240–247, 2000.

The advent of the Infrared Space Observatory (ISO) has had a very significant impact on the studies of high-z star forming galaxies. Operating in the mid-IR regime which is sensitive to dust and PAH emission, ISOCAM onboard ISO was more than 1000 times more sensitive than IRAS. It thus had the potential to study infrared bright galaxies at redshifts beyond $z = 0.5$. A number of cosmological surveys has been performed using ISOCAM ranging from large and shallow ones to pencil-beam deep ones reaching down to a few μJy sensitivities (see Cesarsky et al., this volume). The source counts from all ISOCAM surveys combined with those of IRAS are in good agreement with a no evolution model (α=-2.5) up to a flux level of 100 mJy. However, at fainter flux levels the situation changes rapidly: The counts lie an order of magnitude higher than the predictions of no-evolution models. This steepening in the log N–log S plot at $\sim$ 0.4 mJy implies that ISOCAM surveys have probably revealed a new population of strongly evolving galaxies ([11])

Among the deepest surveys performed by ISOCAM are the observations of the Hubble Deep Field North (N) and South (S) regions [32], resulting in the detection of $\sim$ 150 sources down to μJy levels. The next major step is to explore the nature of the ISOCAM population with optical/near-IR spectroscopy. The results we discuss in this work focus on a sample of galaxies taken from the ISOCAM survey of the HDF-S field. We present the results of near-infrared spectroscopic followup-observations carried out using the Very Large Telescope (VLT) in an attempt to characterize the nature of this new population.

2 ISOCAM Observations of HDF-S

The Hubble Deep Field S was observed by ISOCAM as part of the European Large Area ISO Survey (ELAIS, see Oliver et al., this volume). The observations were carried out at two wavelengths, LW2 (6.75 μm) and LW3 (15 μm). The data have been analysed independently by [26] and [3]. The latter analysis was carried out using the PRETI method [29] and resulted in the detection of 63 sources in the LW3 band. The results presented here are based on the analysis given in [3].

3 The VLT ISO-Hubble Deep Field-S Sample

The sample presented here was selected from the ISOCAM LW3 detections of the Hubble Deep Field-S (hereafter ISOHDFS sample). For the sample selection we imposed two criteria: a) a secure LW3 detection and b) a secure counterpart in the I-band image [6], or a counterpart in the K-band image (EIS Deep [5]). The latter was necessary because in a number of cases there were more than just one I-band counterparts for one ISOCAM candidate. We did not apply any selection based on colours. Our sample (hereafter

VLT ISOHDFS sample) is thus a fair representation of the strongly evolving ISOCAM population near the peak of the differential source counts [12].

Our VLT ISOHDFS sample contains about 25 galaxies. The LW3 flux ranges between 100–400 μJy. For the near-infrared observations, we used spectroscopic redshifts from optical spectroscopy (where available) for z<0.7 [6], or photometric redshift estimations based on the model PEGASE [7]. Our photometric redshift determination turned out to be accurate to $\pm$0.1 and provides a very powerful tool for ISAAC followup.

4 VLT Observations

The observations were carried out September 20-24, 1999 with the infrared spectrometer ISAAC [25] on ESO telescope UT1, on Paranal in Chile. For the observations we used the low resolution grism $R_s \sim 600$ and a slit of 1". The choice of filter was dictated by our aim to detect H_α line emission. Based on our spectroscopic and/or photometric redshift estimates, we chose the equivalent Z, SZ, J or H filter. To maximise the observing efficiency we positioned the slit (which had a $2'$ length) in such a way that at least two galaxies were traced at any given orientation.

We observed 13 galaxies, and H_α was succesfully detected in all but two of them. [NII] emission is also seen in some spectra. Finally, in some cases we also detected emission from the [SII] $\lambda\lambda$ 6717 6731 lines. The H magnitudes of the observed galaxies varied in the range 19-22 mag.

Most of the spectra were acquired with a 1hr on source integration time. With this integration time we were able to detect emission lines as well as continuum in almost all of the galaxies. Observations of spectroscopic standard stars were also performed to allow proper flux callibration of the galaxy spectra. The spectra were reduced in part using the ECLIPSE software [9] and standard IRAF routines.

Spectra of two of the galaxies observed are shown in Figures 1 and 2.

5 The Nature of the ISOCAM Faint Galaxies

Prior to our study, no near-infrared (rest-frame R-band) spectroscopy had been carried out for the ISOCAM population, primarily because of the faintness of the galaxies. Optical spectroscopy (rest-frame B-band) has been done for HDF-N [1] and the Canada France Redshift Survey (CFRS) field [8]. The ISOCAM HDF-N galaxies have been cross-correlated with the optical catalog from [4], resulting in 38 galaxies with confirmed spectroscopic redshifts. Flores et al. have identified 22 galaxies with confirmed spectroscopic information [8]. In both of these samples the median redshift is about 0.7. Our VLT ISOHDFS sample contains 1 galaxy with z<0.5, 6 galaxies 0.5<z<0.75 and 6 galaxies with 0.9<z<1.3. Thus our sample has a z-distribution very similar to the HDF-N [1] and CFRS [8] samples.

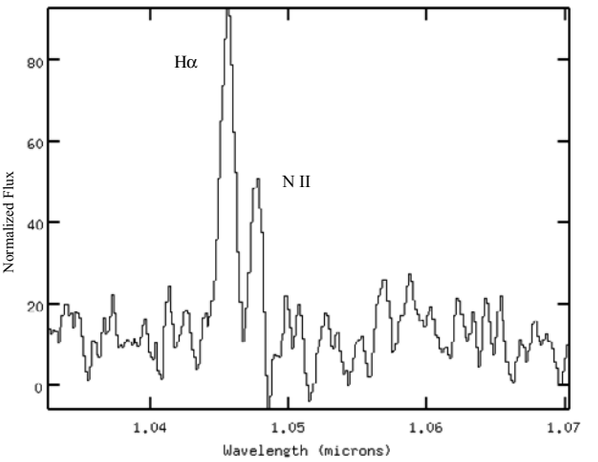

Fig. 1. Near-infrared spectrum of ISOHDFS 53, showing the clear detection of the H_α and NII emission line. The spectroscopic redshift of this object is $z = 0.58$.

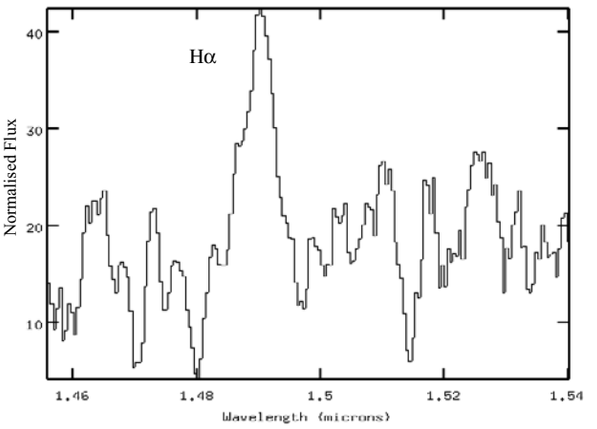

Fig. 2. Near-infrared spectrum of ISOHDFS 39, showing the clear detection of the H_α emission line. The spectroscopic redshift of this object is $z = 1.29$.

Rest-frame B-band spectra host a number of emission and absorption lines related to the properties of the starburst in a galaxy. Based on these features galaxies can be classified according to their starburst history. Strong H_δ Balmer absorption and no emission lines are characteristic of k+A galaxies. The presence of significantly higher level Balmer absorption lines implies the presence of a dominating A-star population. Such an A-star population may have been created in a burst 0.1–1 Gyr ago (post-starbursts). The simultaneous presence of Balmer absorption and moderate [OII] emission, known as e(a) or E+A galaxies, may be characteristic of somewhat younger, but still post-starburst systems or – alternatively – active but highly dust absorbed starbursts. As we will show, the ISOCAM galaxies are in fact powerful starbursts hidden by large amounts of extinction.

Despite the fact that the local mid-infrared luminosity function is dominated by AGNs [13], both Aussel et al. [1] and Flores et al. [8], find a large fraction of the ISOCAM galaxies to be predominantly powered by star formation. Based on spectrophotometric SEDs of 19 galaxies, Flores et al. deduce that the majority of the CFRS ISOCAM population exhibits post-starburst characteristics with the star formation occuring about 1 Gyr prior to the observed event.

5.1 ISOHDFS Galaxies Are Dusty Luminous Active Starbursts

As discussed in the previous section, k+A galaxies can be naturally explained as post-starbursts with a prominent burst 0.1–1.0 Gyr ago. E(a) (or E+A) galaxies would then equally naturally be explained as being somewhat younger systems. B-band spectra of local dusty starbursts such as M82 ($L\sim 10^{10}$ $L_\odot$, [18]), LIRGs ($L\sim 10^{11}$ $L_\odot$, [33]), and ULIRGs ($L\sim 10^{12}$ $L_\odot$, [21]), surprisingly enough, look like e(a), yet H_α is strong (typical for an HII or liner galaxy). The apparent discrepancy between these two signatures can be reconciled: differential dust extinction is at play.

Large amounts of dust exist within the HII regions where the H_α and [OII] line emission originates. [OII] emission is more affected than H_α, simply because of its shorter wavelength. The continuum is due to A-stars. This A-star signature comes from an earlier (0.1–1.0 Gyr) star formation epoch that is not energetically dominant; in fact it plays a small role once the dusty active starburst is dereddened. Such a scenario implies that these galaxies undergo multiple burst events: the less extincted population is due to an older burst while in the heavily dust enshrouded HII regions there is ongoing star formation.

A notable property of the e(a) galaxies appears to be their low EW(OII)/EW(H_α+NII) ratio. Such low ratios have already been observed in the spectra of distant clusters [10] and nearby mergers [27]. Similar behaviour is found among the dusty Luminous Infrared Galaxies (LIRGs) studied by Wu et al. [33] or the ULIRGs studied by Liu and Kennicutt [21]. The behaviour of the (OII)/(H_α+NII) ratio is shown in the EW(OII)–EW(H_α+ NII) diagram

(Figure 3): The majority of the points lie below the straight line, which represents a fit for normal field galaxies at low redshifts. Since for our ISOHDFS sample B-band spectra are not available yet, we use the values reported for the CFRS galaxies (median 20±15, [8]). It follows from Figure 3 that the ISOHDFS galaxies occupy the same region in the EQW(OII)/EQW(H_α+ NII) diagram as the LIRGs and ULIRGs.

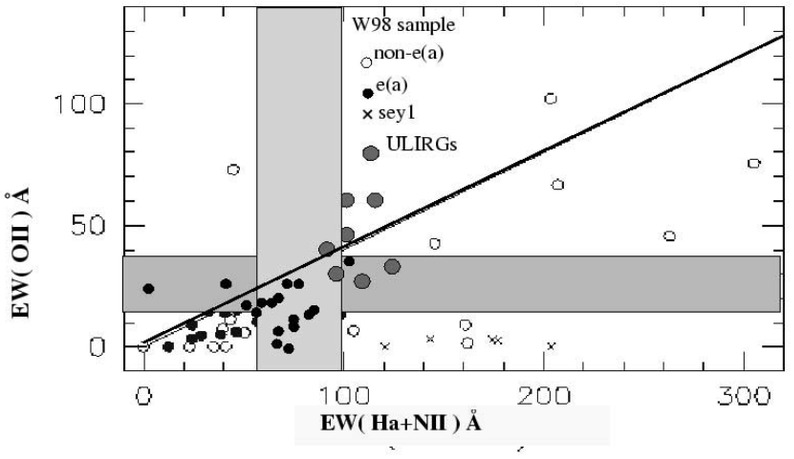

Fig. 3. EW(OII)–EW(H_α+ NII) diagram (from [27], filled circles e(a) galaxies, open circles non-e(a) galaxies, crosses Seyferts, grey filled circles ULIRGs). The shaded bars represent the area of the VLT ISOHDFS galaxies. The intersection of the two bars is the location of our galaxies, indistiguishable from the dusty luminous e(a) galaxies.

6 Star Formation Rates

In ionization bounded HII regions the Balmer emission line luminosities scale directly with the ionizing fluxes of the embedded stars. It is thus possible to use the Balmer emission lines to derive quantitative star formation rates in galaxies (e.g., [17]). Since H_α is typically the strongest of the Balmer lines, it fits our purposes best. However, beyond redshifts of $z \sim 0.2-0.3$, H_α redshifts into the near-IR which is not easily accessible with 4m class telescopes. Due to this constraint several scientists have relied on measurements of the [OII] λ3727 doublet as a star formation index for distant galaxies.

The conversion factor between ionizing flux and star formation rate (SFR) is usually computed using an evolutionary synthesis model. Only massive stars (> 10 $M_\odot$) with short lifetimes (a few million years) contribute significantly to the integrated ionizing flux. Based on our recent measurements of the H_α line strength and following the recipe of Kennicutt [19], the SF rate can be computed via

$SFR(M_\odot/yr) = 7.9 \times 10^{-42} L(H_\alpha)(\mathrm{erg\ s^{-1}})$.

Using this formula we estimate that the SFR rates in the ISOHDFS galaxies range between 10-40 $M_\odot$/yr, corresponding to total luminosities of $\sim$1–4×10^{11} $L_\odot$ (assuming $H_o = 75$ km/s/Mpc, Ω=1). These values imply that the ISOCAM galaxies would fall into the LIRG class. However, the present SFR estimates can be used only as an indication *lower limit* of the real SFR in these galaxies. An upward correction of a factor of 3 should be applied to correct for the extinction (assuming $A_V \sim 1.5$).

A preliminary calculation of SFR rates based on the LW3 fluxes ([15] shows indeed that the SFR is 3-4 times higher than estimated from H_α measurements.

7 Conclusions

We have presented first results of a followup program aiming to characterize the nature of the strongly evolving population discovered by the ISOCAM surveys. The detections of strong H_α emission and large EW in almost all of the galaxies we observed implies that these objects are active star-bursts. Our results imply as well that the star forming regions inside these galaxies are affected by differential extinction which is responsible for the low EW(OII)/EW(H_α) often observed in these galaxies. This result demonstrates that it is very dangerous to derive star formation rates using UV data only, since these wavelengths are subject to higher extinction. Thus a significant fraction of star formation may have been missed by optical surveys.

Using the observed H_α emission lines we estimate that the SFR rate in the VLT ISOHDFS galaxies ranges between 10 -40 $M_\odot$/ yr. This SFR rate serves as a lower limit to the true SFR in these galaxies. The SFR as derived from ISOCAM observations is about 3 times higher. We conclude that the ISOCAM surveys have unveiled a new population of active dusty starbursts which probabaly account for a substantial fraction of the FIR/submm background (see [12]).

References

1. Aussel, H., Cesarsky, C.J., Elbaz, D., Stark, J.L., (1999a) A&A 342, 313
2. Aussel, H., Elbaz, D., Cesarsky, C.J., Stark, J.L., (1999b) In The Universe as seen by ISO, eds. P. Cox, M.F. Kessler, ESA SP 47, 1023
3. Aussel, H., et al., 2000, in prep.

4. Barger, A.J., Cowie, L.L., Trentham, N., Fulton, et al., (1999) AJ 117, 102
5. DaCosta, et al., 1998, http://www.eso.org/science/eis/eis-rel/deep/HDF-Srel.html
6. Dennefeld, M., et al., 2000, in prep.
7. Fioc, M., Rocca-Volmerange, B., (1997), A&A 326, 950
8. Flores, H., Hammer, F., Thuan, T.X., Cesarsky, C., (1999) Ap.J., 517, 148
9. Devillard, N., 1997, Msngr 87
10. Dressler, A., Smail, I., Poggianti, B.M., Butcher, H., et al. (1999) astroph/9901263
11. Elbaz, D., Cesarsky, C.J., Fadda, D., Aussel, H., et al. (1999) A&A 351, L37
12. Elbaz, D., et al., (2000) in prep.
13. Fang, F., Shupe, D., Xu, C., Hacking, P., (1998) Ap.J., 500, 693
14. Franceschini, A., Danese, L., de Zotti, G., Xu, C. (1988) MNRAS 233, 175
15. Francheschini, A., et al., (2000) in prep.
16. Hauser, M.G., Arendt, R.G., Kelsall, T., 1998, ApJ 481, 49
17. Kennicutt, R.C., (1983) Ap.J., 272, 54
18. Kennicutt, R.C., (1992) Ap.J., 388, 310
19. Kennicutt, R.C., (1998) Ann. rev. Astr. Ap. 36, 189
20. Lagache, G., Abergel, A., Boulangerm F., Desert, F.X., Puget J-L., (1999), A&A 344, 322
21. Liu, C.T., Kennicutt, R.C., (1995) Ap.J., 450, 547
22. Lonsdale, C. J, Hacking, P., (1989) Ap.J. 339, 712-23
23. Lonsdale et al. (1990) Ap.J. 358, 60-82
24. Madau, P., Ferguson, H., Dickinson, M. et al., (1996), MNRAS 283, 1388
25. Moorwood, A.F.M., et al. (1998), Msngr 74, 7
26. Oliver, S., et al., (2000) in prep.
27. Poggianti, B.M., Wu, H., (1999) astroph/9908180
28. Puget, J-L., Abergel, A., Bernard J-P., Boulanger, F., Burton W.B., et al. (1996) A&A 308, L5
29. Starck, J.L., Abergel, A., Aussel, H., Sauvage, M., et al., (1999) A&AS 134, 135
30. Steidel, C.C., Giavalisco, M., Pettini, M., Dickinson, M., Adelberger, K.L. (1996) ApJ 462, L17
31. Soifer, B. T., Neugebauer, G. (1991) A.J. 101, 354-61
32. Williams, R.E., Blacker, B., Dickisnon, M., Dixon, W., (1996) AJ 112, 1335
33. Wu, H., Zou, Z.L., Xia, X.Y., Deng, Z.G., (1998) A&AS, 127, 521

ISOPHOT 170 μm Serendipity Sky Survey: The First Galaxy Catalogue ⋆

Manfred Stickel[1], Dietrich Lemke[1], Ulrich Klaas[1], Stephan Hotzel[1], L. Viktor Tóth[2], Martin F. Kessler[3], Rene Laureijs[3], Martin Burgdorf[3], Chas A. Beichman[4], Michael Rowan–Robinson[5], Andeas Efstathiou[5], Stefan Bogun[6], Gotthard Richter[7], and Michael Braun[7]

[1] Max–Planck–Institut für Astronomie, Königstuhl 17, D–69117 Heidelberg, Germany
[2] Department of Astronomy of the Loránd Eötvös University, Ludovika tér 2., H–1083 Budapest, Hungary
[3] ISO Science Operations Centre, Astrophysics Division, Space Science Department of ESA, Villafranca, P.O. Box 50727, E–28080 Madrid, Spain
[4] Infrared Processing and Analysis Center, JPL, California Institute of Technology, MS 100/22, Pasadena, CA 91125, USA
[5] Imperial College of Science, Technology and Medicine, The Blackett Laboratory, Prince Consort Road, London SW7 2BZ, United Kingdom
[6] Data Management and Operations Division, ESO, Karl-Schwarzschild-Str. 2, D-85748 Garching bei München, Germany
[7] Astrophysikalisches Institut Potsdam, An der Sternwarte 16, D–14482 Potsdam, Germany

Abstract. The ISOPHOT Serendipity Survey utilized the slew time between ISO's pointed observations with strip scanning measurements of the sky in the far-infrared at 170 μm. From the slew data with low ($I_{100\mu m} \leq 15$ MJy/sr) cirrus background, 115 well-observed sources with a high signal-to-noise ratio in all four detector pixels having a galaxy association were extracted. The integral 170 μm fluxes measured from the Serendipity slews have been put on an absolute flux level by using a number of calibrator sources observed with ISOPHOT's photometric mapping mode. For all but a few galaxies, the 170 μm fluxes are determined for the first time, which represents a significant increase in the number of galaxies with measured FIR fluxes beyond the IRAS 100 μm limit. The vast majority of the galaxies are morphologically classified as spirals. The large fraction of sources with a high $F_{170\mu m}/F_{100\mu m}$ flux ratio indicates that a very cold ($T < 20$ K) dust component is present in many galaxies. The typical mass of the coldest dust component is $M_{Dust} = 10^{7.5 \pm 0.5}\ M_{\odot}$, a factor 2 - 10 larger than that derived from IRAS fluxes alone. As a consequence, the gas-to-dust ratios are much closer to the canonical value of ≈ 160 for the Milky Way. By relaxing the selection criteria, it is expected that the Serendipity survey will eventually lead to a catalogue of 170 μm fluxes for ≈ 1000 galaxies.

⋆ Based on observations with ISO, an ESA project with instruments funded by ESA Member States (especially the PI countries: France, Germany, the Netherlands and the United Kingdom) and with the participation of ISAS and NASA. Members of the Consortium on the ISOPHOT Serendipity Survey (CISS) are MPIA Heidelberg, ESA ISO SOC Villafranca, AIP Potsdam, IPAC Pasadena, Imperial College London.

D. Lemke, M. Stickel, and K. Wilke (Eds.): LNP 548, pp. 251–258, 2000.

1 Introduction

The concept of a large scale survey covering a significant fraction of the sky has proven to be extremely successful for investigating the properties of large groups of objects and the discovery of new types of sources, particularly if a hitherto not observed wavelength band was to be used. The Infrared Space Observatory (ISO), dedicated largely to pointed observations, would have needed a prohibitively big fraction of its restricted lifetime to carry out a large scale sky survey at a wavelength $> 100\mu$m, as indicated by the telescope time put into surveys covering several square degrees such as the ELAIS (Oliver , these proceedings) or FIRBACK surveys (Dole, these proceedings).

With the capabilities of ISOPHOT to measure in a fast read-out mode beyond the IRAS 100 μm limit, a slew survey carried out during the movement of the ISO satellite from one target to the next was feasible, adding significantly to the scientific return from the ISO mission without requiring additional pointed telescope time. A broad band filter with a central of 170 μm had the prospect of delivering data serendipitously not only for cold point or marginally extended sources but also for extended cold FIR emitting material distributed on large scales in the Galaxy.

The implementation of the so-called Serendipity Survey was successfully tested during the Performance Verification Phase of ISO and has run smoothly and delivered data of the expected quality [1] throughout the whole ISO mission. Strong emphasis in the slew analysis has been put on the detection and extraction of point sources [4,5,6], the vast majority of which are late type galaxies. The analysis of the extended galactic cirrus emission, particularly cold regions or spots within molecular clouds is described by Tóth et al. [8], while the search for the coldest galactic objects is described by Hotzel et al. (these proceedings).

2 Observations and Data Reduction

Serendipity slew survey measurements were acquired with the ISOPHOT C200 detector [3], a 2×2 pixel array of stressed Ge:Ga with a pixel size of $89.4''$, which was used in conjunction with the C_160 broad band filter (central wavelength 170 μm, equivalent width 89 μm). The high dynamic range of brightnesses between the galactic plane and the galactic poles in conjunction with the slew speed of the telescope (max. $\approx 8'\mathrm{s}^{-1}$) required the fastest uncompressed read-out rate of the C200 camera of 1/8 s, during which four detector readouts took place. During the lifetime of the ISO mission, about 550 hours of measurements have been gathered with more than 12000 slews. The total slew length exceeds 150000° with a sky coverage of ≈ 15 %.

For each detector pixel, the raw detector voltages as a function of read-out time (ramps) are converted to signals per sky position by fitting a straight line to the integration ramps. The conversion to slew surface brightnesses

follows standard data reduction techniques within the ISOPHOT Interactive Analysis (PIA [1]) software package [2]. Surface brightnesses are derived from the fitted read-out ramp slopes either by using a measurement of the on-board Fine Calibration Source (FCS) preceding the slew observation, or, for short slews, the default C200 calibration.

The deglitched and background subtracted signals of the four detector pixels are phase-shifted according to the roll angle of the detector, and a signal-to-noise ratio weighted mean signal is derived. Regions of source candidates are selected by setting a cut of three times the local noise level on the background subtracted coadded surface brightness. This cut is varying along the slew due to crossing of the regions with different background levels such as the galactic plane. The ratio of the four peak fluxes to the highest flux among the four pixels is used in comparison with the expected ratios from a gaussian source model to estimate the minimal source distance perpendicular to the slew direction. The total source flux is then determined by a non-linear least-squares fit of a two-dimensional circular symmetric gaussian with fixed slew offset together with a tilted plane to the data from the four background subtracted data streams.

3 Calibration

The Serendipity point source fluxes are tied to an absolute level with dedicated photometric calibration measurements of 12 sources repeatedly crossed with varying impact parameters. Raster maps were obtained with the C200 detector and the C_160 broad band filter and fluxes derived using synthetic aperture photometry. The ratio of the Serendipity and the mapping fluxes as a function of the mapping fluxes is shown in Fig. 1. It indicates that for at least the brighter sources above $\approx$ 15 Jy, the slewing observation misses some signal. For the fainter sources the ratio shows a significantly increased scatter, which can be understood as the influence of the noise on the observed brightness distribution of the four detector pixels.

To correct for the signal loss during slewing, the raw Serendipity slew fluxes are scaled by the linear relationship shown as a dashed line in Fig. 1. This is a fit to all data points with serendipity to photometric flux ratios between 0.5 and 1.2, excluding the gross outliers. Its intercept is close to 0.9, which means that the faintest sources will not be scaled significantly. The scatter of the flux ratios in Fig. 1 indicates an accuracy of the corrected source fluxes of $\lesssim$ 40 %.

[1] The ISOPHOT data presented in this paper was reduced using PIA, which is a joint development by the ESA Astrophysics Division and the ISOPHOT Consortium. The ISOPHOT Consortium is led by the Max-Planck-Institute for Astronomy, Heidelberg

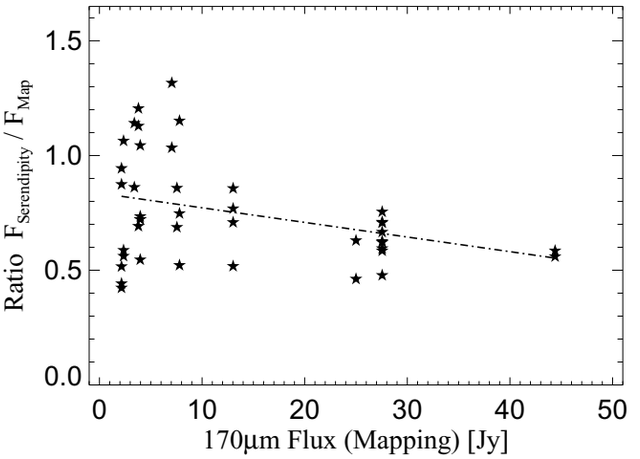

Fig. 1. The ratio of photometric mapping and Serendipity slew fluxes vs. the photometric flux for all crossings of the 12 calibration sources. For the brighter sources, the Serendipity slews miss some signal. At the faint end an increased scatter is noticable, most likely due to the influence of noise on the slew fluxes. The dashed line shows the linear relationship used to correct the source fluxes derived from the slews. Except for the faint end, the agreement between repeated slew observations is $\lesssim 40$ %.

4 Results

A first set of galaxies has been selected to demonstrate the scientific potential of the slew measurements and the immediate impact of early results on understanding the FIR emission of normal galaxies. This initial Serendipity source catalogue is intended to cover only the most reliable extragalactic sources off the galactic plane. It is not intended to represent a statistically complete sample, but is expected to represent an unbiased subset of all crossed extragalactic sources at high galactic latitudes. In the following, the sample properties of this initial Serendipity source list will be described. The complete source catalogue can be found in [7].

The Serendipity source candidate database was searched for sources at galactic latitudes $|b| > 15°$ with a signal-to-noise ratio of at least 5 in all 4 pixels and a fitted source width of $0.5' \leq \sigma \leq 1.25'$, which are located in an area where the 100 μm cirrus brightness does not exceed 15 MJy/sr. Only sources were considered where the extragalactic databases listed a galaxy with an optical diameter $< 6'$ within $3'$ from the Serendipity source position. These selection criteria lead to a list of 115 high quality Serendipity sources providing the first 170 μm fluxes for all but a few galaxies, and represents the largest set of galaxies with measured 170 μm fluxes to date. The red-

shift distribution shows that although the majority of the sources lies at low redshifts of z < 0.02, the Serendipity observations also detect galaxies with redshifts up to z ≈ 0.05.

The distribution of $F_{170\mu m}/F_{100\mu m}$ flux ratios (Fig. 2) shows that the majority of the galaxies has a flux ratio between ≈ 1 and 1.5, indicating that the FIR spectra are mostly flat between 100 μm and 200 μm. A downward trend in this wavelength range is seen only in very few galaxies, indicating that the coldest dust component in these objects is rather warm with $T \gtrsim 20$ K. Most important is the large fraction of more than 40 % of the sources which have $F_{170\mu m}/F_{100\mu m} > 1.5$, extending up to $F_{170\mu m}/F_{100\mu m} \approx 3$, indicating an up-turn in the SED beyond 100 μm similar to that seen in the Milky Way and M51. The new 170 μm fluxes allow a more accurate determination of the total FIR luminosities.

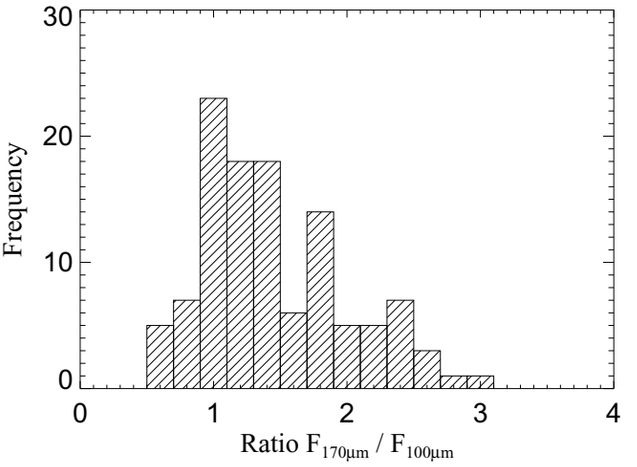

Fig. 2. The distribution of the ratio of Serendipity 170 μm and IRAS 100 μm fluxes.

The distribution of the $F_{170\mu m}/F_{100\mu m}$ flux ratios clearly indicates the presence of a cold dust component with dust color temperatures $T_D \lesssim 20$ K in a significant fraction of the galaxies. Since the IRAS as well as the ISOPHOT fluxes refer to a spectrum with νF_ν = constant, dust color temperatures were computed by iteratively correcting the tabulated IRAS 100 μm and Serendipity 170 μm fluxes in the two bandpasses for a modified blackbody (Planck) function

$$F_\nu = \nu^\beta B_\nu(T_D), \tag{1}$$

with a fixed emissivity index $\beta = 2$. The resulting distribution of dust color temperatures (Fig. 3) is centered at $T_D \approx 20$ K, with all but a few sources lying in the range 15 K $\leq T_D \leq$ 25 K.

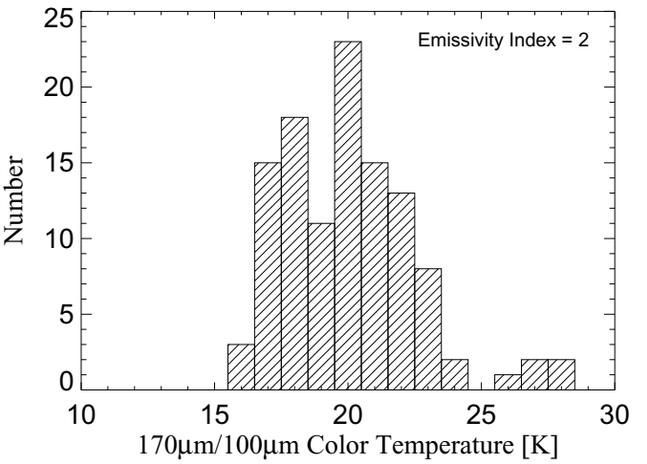

Fig. 3. The color temperature distribution, corrected for the ISOPHOT 170 μm and IRAS 100 μm bandpasses using an emissivity index of $\beta = 2$.

The luminosity of the coldest dust component mainly determines the bulk of the dust mass. Approximate total dust masses can thus be inferred from the dust color temperatures (Fig. 3) using a standard dust opacity for the case of optically thin dust emission (Fig. 4). The dust mass distribution peaks at $M_D = 10^{7.5 \pm 0.5}$ $M_\odot$, with a gradual decrease towards lower dust masses. These newly derived dust masses are larger by a factor 2 – 10 compared to those derived from IRAS fluxes alone. Moreover, these high values are reached without any very cold $T_D < 10$ K dust component usually inferred from sub-mm measurements.

Gas masses, mainly from HI measurements, are available for about half of the 115 Serendipity sources. The gas-to-dust ratios (Fig. 5) peaks at ≈ 250, close to the canonical value of ≈ 160 of the Milky Way. This indicates for the first time that the gas-to-dust ratio of the Milky Way can also be found in other external galaxies, and there is at least some justification in using this value to convert FIR measured dust masses to total gas masses. However, the range of gas-to-dust ratios covers the large range between 10 and 1000, much larger than expected from errors in FIR fluxes or HI masses, which on the other hand suggests that there is no fiducial gas-to-dust ratio applicable to all normal late type galaxies.

5 Concluding Remarks

The current set of sources was selected by using rather stringent criteria. It is anticipated that by relaxing these selection criteria, particularly the number of detector pixels showing a high signal, 170 μm fluxes for much larger

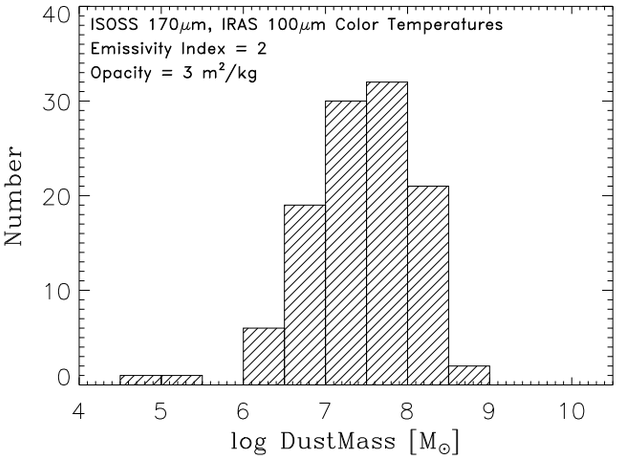

Fig. 4. The distribution of the dust mass, derived with an emissivity of $\beta = 2$ and a dust opacity of 3 m^2/kg. The asymmetric distribution peaks around $M_D \approx 10^{7.5\pm0.5} M_\odot$. The two sources at the lower end are the only galaxies unambiguously classified as irregulars.

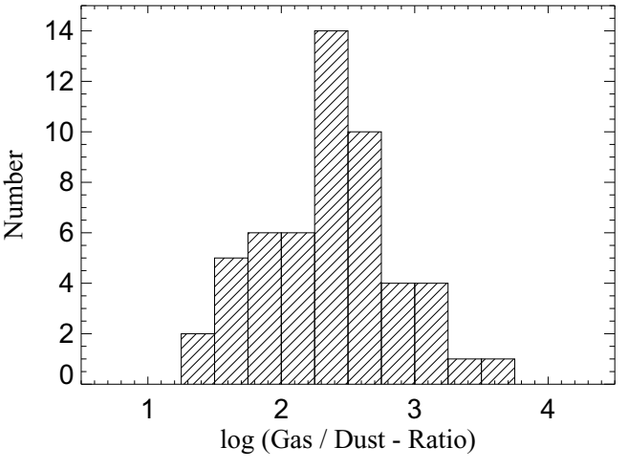

Fig. 5. The distribution of the gas-to-dust ratio peaks at ≈ 250, close to the canonical value for the Milky Way.

number of galaxies, possibly more than 1000 sources, will become available. This large database is expected to put the described initial results on a much broader basis. Particularly, the new 170 μm fluxes will allow a better statistical investigation of the total luminosity of galaxies.

In a further step, the requirement that a source should have a known galaxy association will be dropped. It is expected that quite a large number of compact cirrus knots will then show up in the selection. However, by inspecting the IRAS ISSA maps and the Digital Sky Survey, it should be possible to identify rare or even unknown classes of extragalactic FIR emitters.

Acknowledgements

Based on observations with ISO, an ESA project with instruments funded by ESA Member States (especially the PI countries: France, Germany, the Netherlands and the United Kingdom) and with the participation of ISAS and NASA.
The ISOPHOT project was funded by the Deutsche Agentur für Raumfahrtangelegenheiten (DARA, now DLR), the Max - Planck - Gesellschaft, the Danish, British and Spanish Space Agencies and several European and American institutes.
Members of the Consortium on the ISOPHOT Serendipity Survey (CISS) are MPIA Heidelberg, ESA ISO SOC Villafranca, AIP Potsdam, IPAC Pasadena, Imperial College London.
This research has made use of the Digitized Sky Survey, produced at the Space Telescope Science Institute, NASA's Astrophysics Data System Abstract Service, the Simbad Database, operated at CDS, Strasbourg, France, and the NASA/IPAC Extragalactic Database (NED) which is operated by the Jet Propulsion Laboratory, California Institute of Technology, under contract with the National Aeronautics and Space Administration.

References

1. Bogun S., Lemke D., Klaas U., et al. 1996, A&A 315, L71
2. Gabriel C., et al., (1997), Proc. of the ADASS VI Conference, eds. G. Hunt, H.E. Payne, pp. 108.
3. Lemke D., Klaas U., Abolins ., et al., 1996, A&A 315L, 64
4. Stickel M., Bogun S., Lemke D., et al. 1998, A&A 336, 116
5. Stickel M., Lemke D., Bogun S., et al. 1998, *"ISOPHOT far-infrared serendipity sky survey"*, Proc. SPIE 3349, p. 115
6. Stickel M., Lemke D., Bogun S., et al. 1999 *"ISOPHOT far-infrared serendipity sky survey"* in "The Universe as seen by ISO", ESA-SP 427, eds. P. Cox, M.F. Kessler, p. 839
7. Stickel M., Lemke D., Klaas U., et al. 2000, A&A, submitted
8. Tóth L.V., Hotzel S., Krause O., Lemke D., Stickel M., et al. 2000, in preparation

Chamaeleon's Cold Cloud Cores*

Stephan Hotzel[1], Dietrich Lemke[1], Oliver Krause[1], Manfred Stickel[1], and L. Viktor Tóth[1,2]

[1] Max-Planck-Institut für Astronomie, Königstuhl 17, D-69117 Heidelberg, Germany
[2] Department of Astronomy, Loránd Eötvös University, Pázmány Péter sétány 1, H-1117 Budapest, Hungary

Abstract. ISOPHOT Serendipity Survey (ISOSS) observations of the nearby interstellar medium towards Chamaeleon have revealed a number of cold cloud cores. Far-infrared colours have been studied using ISOSS and IRAS data. 10 very cold cores with colour temperatures $T_{\rm dust} \lesssim 13$ K have been found in an $11^\circ \times 8^\circ$ sized region. Comparing the FIR data with radio measurements, all of the very cold cores have high gas column densities, $N(\mathrm{H_2}) > 10^{21}$ cm^{-2}, and 7 out of 10 have low gas temperatures as indicated by $T_{\rm ex}(\mathrm{C^{18}O}) \approx 8$ K.

1 Introduction

The ISOPHOT Serendipity Survey (ISOSS) is a far-infrared survey at 170 μm, using the ISOPHOT C200 detector on board the ISO satellite [1,2]. ISOSS recorded the sky brightness during the slewing of the telescope between two pointed observations. Approximately 15 % of the sky is covered with an angular resolution (FWHM) of $2'$ [3]. This combination of wavelength and resolution makes the ISOPHOT Serendipity Survey an ideal tool not only for studying extragalactic sources [4], but also to study the distribution and characteristics of cold dust in the Milky Way [5].

Standard dust models lead to typical grain temperatures of between $\sim$ 15 K and 19 K, if an average interstellar radiation field is assumed. In Bok globules and dense molecular cloud cores even lower temperatures are predicted and have been reported in some individual cases. However, the preceding large area surveys have partially missed this kind of objects, because they are either too dense (for ^{12}CO), too small (for DIRBE) or too cold (for IRAS bands $\leq$ 60 μm). With ISOSS we are now able to detect and investigate these cores, which are believed to be widespread in the cold ISM, particularly in star forming regions. While the 60 μm IRAS data are still affected by the warmer very small grains, the far-infrared emission at 100 μm

* Based on observations with ISO, an ESA project with instruments funded by ESA Member States (especially the PI countries: France, Germany, the Netherlands and the United Kingdom) and with the participation of ISAS and NASA. Members of the Consortium on the ISOPHOT Serendipity Survey (CISS) are MPIA Heidelberg, ESA ISO SOC Villafranca, AIP Potsdam, IPAC Pasadena, Imperial College London.

D. Lemke, M. Stickel, and K. Wilke (Eds.): LNP 548, pp. 259–266, 2000.

originates from the big grains alone. Therefore, the comparison of the two bands at 100 μm (IRAS) and 170 μm (ISOSS) can determine the temperature of the dust, and the resolution of the IRAS Sky Survey Atlas ($\approx 5'$) is still high enough to resolve 0.2 pc sized dense molecular cloud cores in nearby galactic star forming regions.

Based on ISOSS, we have started a FIR analysis of the cold ISM. In the test region Chamaeleon, we have compared ISOSS measurements with IRAS, DIRBE and available CO survey data. We demonstrate that ISOSS can locate and characterize a lot of very cold spots in the Milky Way.

2 Data Analysis

ISOSS data were obtained with the ISOPHOT C200 detector, a 2×2 pixel array with a $3' \times 3'$ field of view. It was used in conjunction with the C_160 broad band filter, which has an effective wavelength of 170 μm. The fastest readout rate (1/8 sec) was chosen to achieve a dynamical range of 5 $\mathrm{MJy\,sr^{-1}} < I_{170} < 500\ \mathrm{MJy\,sr^{-1}}$ (see [3] for details). The raw (ERD level) ISOSS data were reduced using a batch processing routine based on the ISOPHOT Interactive Analysis[1] [6] software package.

The positional accuracy has been determined by comparing positions of point sources with positions of corresponding IRAS sources. An agreement of generally better than $1'$ has been found.

The photometric accuracy has been checked in three ways: First, ISOSS results have been compared with dedicated pointed raster maps (mode AOT PHT22), showing an agreement within $\pm$ 20 % in surface brightness. A second check has been made by comparing ISOSS with DIRBE data. We have created interpolated DIRBE 170 μm intensities from the 100 μm, 140 μm and 240 μm bands. An agreement between ISOSS and DIRBE calibration within 30 % has been found. Finally, the reproducibility of the ISOSS measurements has been tested by evaluating the slew crossing points in several regions. The root mean square of the relative brightness deviation at crossing points is $\lesssim 15\,\%$ (slightly dependent on the brightness level).

To find cold cores, the slews are searched individually for sources of high $I_{170}\,/\,I_{100}$ ratio. For this, the ISOSS slews are smoothed to $5'$ to match the IRAS resolution. Corresponding IRAS 100 μm intensities are extracted from the ISSA maps using a linear interpolation algorithm. Intensity peaks along the ISOSS slews are located by searching for local maxima in the second derivative of I_{170} as function of sky position. All peaks exceeding 2 $\mathrm{MJy\,sr^{-1}} (\approx 5\sigma)$ over the background are called *spots* and are selected as

[1] The ISOPHOT data presented in this paper was reduced using PIA, which is a joint development by the ESA Astrophysics Division and the ISOPHOT Consortium. The ISOPHOT Consortium is led by the Max-Planck-Institute for Astronomy, Heidelberg.

ISOSS source candidates for further analysis. The width of the source is defined from the I_{170} profile alone, and is assumed to be the same at 100 μm (see Fig. 1 (a)).

For each spot, a straight line is fitted to the I_{170} versus I_{100} data points, applying the ordinary least squares bisector algorithm. If the variation of background intensity is small and the source is optically thin in the FIR, the fitted line slope reflects the ratio of background corrected intensities. We denote this quantity as *colour parameter* (CP). The colour temperature of the source is derived from CP by assuming modified black body radiation with ν^2 emissivity law: $I_\nu \propto \nu^2 B_\nu(T_\mathrm{d})$ (see Fig. 1 (b)).

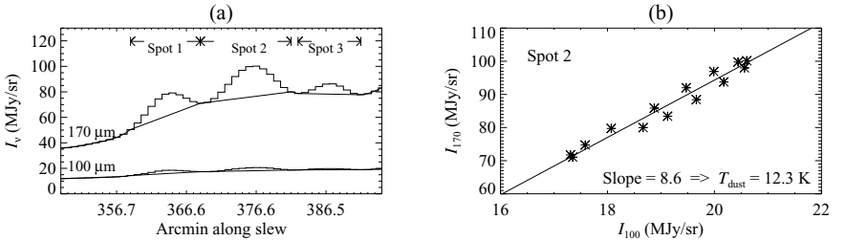

Fig. 1. (a) The sky surface brightness at 170 μm (convolved Serendipity data) and at 100 μm (extracted from ISSA maps) along a section of a slew. Here, 3 spots are found as indicated below the top axis. **(b)** I_{170} vs. I_{100} plot for the middle one of the peaks from (a). A straight line is fitted to the data points. The slope of the line corresponds to the colour temperature of the spot.

3 Results

We have located 709 spots with $I_{170}(\mathrm{peak}) > 2$ MJy sr^{-1}.The size and colour distributions are shown in Fig. 2. The sizes of the spots are similar to our angular resolution, indicating a linear size ≤ 0.1 pc for most of these objects, assuming a distance of 150 pc to the Chamaeleon clouds. The colour parameters have an asymmetric distribution. This is partly a result of the method being designed to find *cold* spots. The distribution has a median of CP = 3.6 and a prominent tail up to CP = 9, corresponding to dust temperatures of 15 K and 12 K respectively.

The CP < 4 spots show a random distribution, while the colder ones cluster at the main clouds Cha I, Cha II and Cha III. The spots with CP > 7 cluster into 10 groups, which reveal 7, 2, 1 very cold objects inside the Cha I, Cha II, Cha III molecular clouds respectively. For reasons discussed below, we call these objects *very cold cores* (VCCs). The parameters are listed in Table 1, where the columns are: (1) Core number, (2–3) equatorial coordinates, (4–6) major and minor diameters and position angle (PA) of the fitted

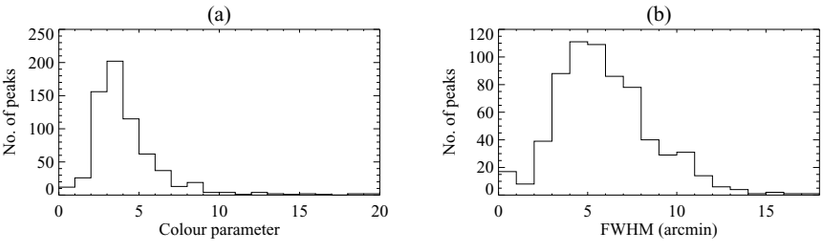

Fig. 2. Size and colour parameter distributions of the 170 μm peaks in Chamaeleon

Table 1. Positions and FIR parameters of the very cold cores in Chamaeleon

Core No.	R.A.(2000)	Dec.(2000)	Maj. (arcmin)	Min.	PA⋆ (deg)	CP	Opt. Ass.
(1)	(2)	(3)	(4)	(5)	(6)	(7)	(8)
1	$10^h49^m30^s$	$-77°05'00''$	10	5	150	18	DCld 296.2−15.8
2	10 54 55	−77 11 00	7	7	90	9	DCld 296.5−15.7
3	11 02 00	−77 15 00	7	4	120	6.5	
4	11 03 30	−77 59 00	7	7	90	7.5	
5	11 03 45	−77 48 30	10	6	45	8	DCld 297.1−16.1
6	11 06 30	−77 36 00	9	9	90	> 20	
7	11 10 15	−76 48 00	15	8	0	> 20	DCld 297.2−15.1
8	12 50 00	−76 55 00	8	8	90	9	DCld 302.9−14.1
9	12 56 00	−79 12 00	8	8	90	7	
10	12 59 15	−77 12 00	8	5	90	7.5	DCld 303.5−14.4

⋆ PA is the position angle of the major axis, measured anti-clockwise from north through east

ellipses, (7) colour parameter, (8) optical association [7]. The shape of the cores could not be determined from the 170 μm profile alone, because the smoothed slews are like one-dimensional cuts through the sources, and most of the cores have been crossed by not more than 2 slews. Therefore, columns (4–6) are based on eyeball checks of the 100 μm ISSA maps in conjunction with the 170 μm slew profiles. The positions and sizes of the VCCs of Cha I are shown in Fig. 3 (a).

All the CP > 7 spots have been checked carefully by hand to exclude artefacts and to have a highly reliable list of very cold cores. All except one (VCC no. 9) have been crossed and detected by at least 2 slews. The spots with CP < 7 have not been checked by eye systematically, but only in individual regions of interest (e.g. all the $C^{18}O$ cores discussed in Sect. 4).

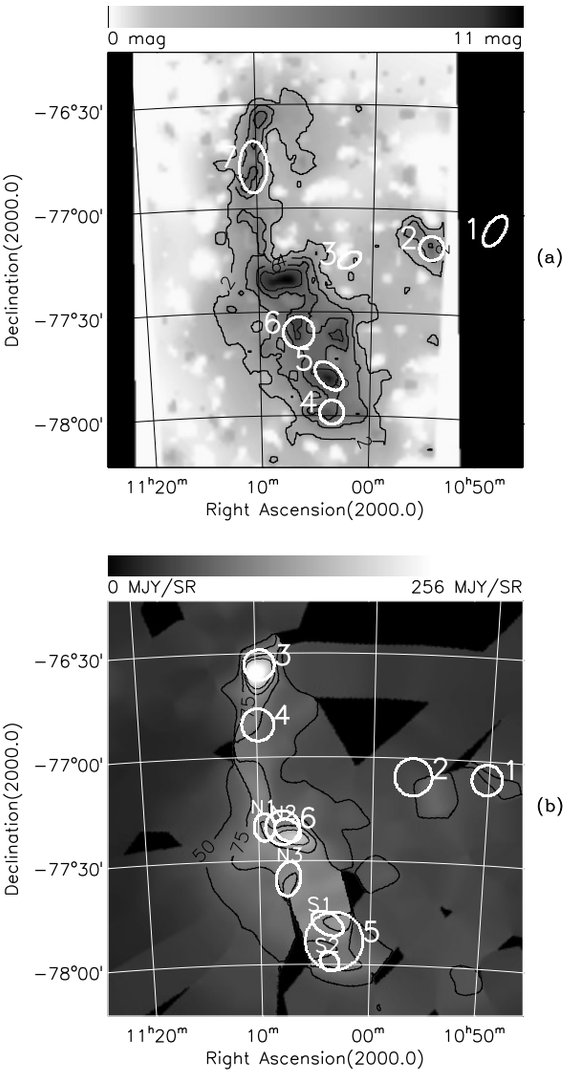

Fig. 3. **(a)** The visual extinction in Cha I. The map is based on NIR starcounts [10]. Contours are drawn at A_V = 2, 4, 6, 8 mag. The overlaid white ellipses are the positions of the VCCs, as given in Table 1. **(b)** ISOSS 170 μm slew composit map of Cha I, smoothed to the lower 5′ IRAS resolution. In the top part of the image, individual slews can still be seen; black regions are too far off the closest slews. Contours are drawn at I_{170} = 50, 75, 100, 125 MJy sr^{-1}. The overlaid white ellipses are the positions of C^{18}O cores. The numbering 1–6 and N1–S3 refers to the original papers [14] and [15] respectively.

4 Discussion

4.1 Dust Characteristics of Very Cold Cores

The positions of the VCCs have been compared with visual extinction and $C^{18}O$ data (see Fig. 3). The A_V map (Fig. 3 (a)) resolves the internal structure of the cloud, as the NIR star count method can trace the visual extintion up to 11 mag. All but one of the VCCs are associated with high extinction peaks ($A_V > 4$ mag, see also Table 2). Additionally, all the VCCs are associated with dense, molecular gas, as they all lie inside the 3.5 $K\,km\,s^{-1}$ contour of the ^{13}CO (J=1→0) line intensity [8]. Hence, our VCCs are indeed highly opaque molecular cloud cores.

We have estimated the physical parameters of the gas associated with the VCCs from ^{13}CO and $C^{18}O$ spectra [9], using the spectra nearest to the VCC centres and assuming LTE. The dust and gas parameters are compared in Table 2, where the columns are: (1) Core number as in Table 1, (2–3) average and peak visual extinction [10,11], (4) dust colour temperature, derived from column 7 of Table 1, (5) $C^{18}O$ excitation temperature, (6) optical depth of $C^{18}O$ (at line centre), (7) H_2 column density, derived from $C^{18}O$.

Table 2. Physical parameters of the very cold cores

Core No.	A_V (mag)	A_V^{max} (mag)	T_d (K)	$T_{ex}(C^{18}O)$ (K)	$\tau(C^{18}O)$	$N_{CO}(H_2)$ (10^{21} cm^{-2})
(1)	(2)	(3)	(4)	(5)	(6)	(7)
1	2.1*	2.3*	11	–	–	–
2	4.8	6.1	12.2	6.3	0.60	5.2
3	1.1	2.2	13.1	>20	0.02	0.23
4	5.0	7.8	12.7	6.4	0.96	11
5	8.0	10.3	12.5	7.3	0.78	12
6	6.8	9.2	<11	6.2	0.98	16
7	4.7	6.5	<11	–	<0.1	(7.6)
8	4.0	5.6	12.2	7.3	0.71	8.3
9	3.0	4.4	12.9	7.0	0.37	3.0
10	8.1	10.4	12.7	8.6	0.31	8.4

* based on B starcounts [12]

Seven of the ten VCCs have been found cold with $T_{ex}(CO) = 7.4\,K \pm 1.2\,K$. However, $T_{ex}(C^{18}O)$ can provide only a first order estimate of the kinetic temperature, since $C^{18}O$ is expected to be subthermal in dense cores. NH_3 is a better indicator of gas temperatures in dense cores. An ammonia survey of the VCCs would thus be necessary to confirm the low gas kinetic temperatures.

A general correlation is not expected between gas temperature and colour temperature of large dust grains. The heating and cooling mechanisms are different. Gas – dust interactions play a dominant role in the thermal balance only at high densities, and gas – dust encounters are most frequent between

molecules and the more abundant smaller dust grains. Correlations might however occur at high densities when the energy density of the interstellar radiation field is low. This is the case in those parts of the Chamaeleon clouds, where the shielding from the outside radiation is good and no star formation is taking place at present.

As it is seen from the molecular line measurements, the very cold cores have very low gas temperatures (Table 2). Assuming a grain size distribution $n(a) \propto a^{-3.5}$, a soft radiation field with low incident flux and a gas density of the order 10^4 cm^{-3}–10^5 cm^{-3}, theoretical calculations resulted in gas and dust temperatures in the range we found for our VCCs [13]. Hence, we regard our very cold spot finding method as an effective way to locate the coldest cloud cores in terms of gas temperature, too.

4.2 Very Cold Cores and $C^{18}O$ Cores

The distribution of $C^{18}O$ in Cha I was first shown by Haikala et al. [15], and dust temperatures were given for 2 cores inside the cloud (see Fig. 3 (b); cores N1, S1). Their cores S1, S2, N3 coincide with our VCCs no. 5, 4, 6 respectively (Fig. 3 (b)). Note that the $I_\nu(200\ \mu m)\ /\ I_\nu(150\ \mu m)$ colour temperature of S1 (13.5 K) is still in agreement with the dust temperature of VCC 5 (12.5 K). Core N1 has a FIR colour temperature of 16 K, while we find a spot of 15.1 K at the same position.

The $C^{18}O$ survey of Mizuno et al. [14] fully covers the three Chamaeleon main clouds with an angular resolution ($2.7'$) similar to ours. We have therefore used their list of 23 $C^{18}O$ cores to investigate the completeness of our method to locate cold cloud cores: 15 of the 23 cores have been crossed by ISOSS slews. All of these 15 cores have been detected. 9 (60 %) are cold with $T_{\rm dust} < 15$ K, 6 (40 %) are associated with VCCs.

The characteristics of the $C^{18}O$ cores differ in the three clouds. We therefore compare the gas and dust properties in the most densely covered Cha I region, where all 6 $C^{18}O$ cores have been crossed by ISOSS slews. The $C^{18}O$ cores no. 1, 2 and 4 have been identified as VCCs no. 1, 2 and 7 respectively; $C^{18}O$ core no. 5 contains the two separated VCCs no. 4 and 5 (Fig. 3). While these cores have colour temperatures < 14 K (Table 2) and $C^{18}O$ core no. 6 is associated with spots of $T_{\rm dust} \approx 14$ K, $C^{18}O$ core no. 3 has $T_{\rm dust} = 22$ K, i.e. it contains much warmer dust than all others (warm spots are not indicated in Fig. 3). The reason for this is a locally enhanced interstellar radiation field, as $C^{18}O$ core no. 3 is seen towards a peak in surface density of young stellar objects. It is worth noting that the gas properties of this core are not as outstanding as the dust temperature.

5 Conclusion and Outlook

We have presented a method for finding regions with very low FIR colour temperatures. Comparison of our ISOSS/IRAS results with earlier molecular

line surveys has proven that the very cold cores we find are indeed cold molecular cloud cores. In Chamaeleon we have detected 10 very cold cores and thus have demonstrated that ISOSS is very efficient in locating this kind of objects.

The sample we will obtain analysing the complete ISOSS database (15 % sky coverage) is much larger than any of the previous FIR air-borne, balloon-borne or sub-mm ground-based samples. The cold spot search will be extended to the giant molecular cloud complexes in Orion, Taurus, Cepheus, Cygnus and Ophiuchus. Extrapolating the results of our Chamaeleon survey, we expect to detect a large number of very cold cloud cores in the Milky Way. A series of follow-up measurements in mm and sub-mm wavelengths has been started in order to derive the physical properties of the gas in the very cold cores.

References

1. Kessler M. F., Steinz J. et al. (1996) A&A 315, L27
2. Lemke D., Klaas U. et al. (1996) A&A 315, L64
3. Bogun S., Lemke D. et al. (1996) A&A 315, L71
4. Stickel M., Bogun S. et al. (1998) A&A 336, 116
5. Tóth L. V., Hotzel S. et al. (2000) A&A submitted
6. Gabriel C., Acosta-Pulido J. et al. (1997) In: Hunt G., Payne H. E. (Eds.) ASP Conf. Ser. 125: Astronomical Data Analysis Software and Systems VI. Vol. 6, p. 108
7. Hartley M., Tritton S. B. et al. (1986) A&AS 63, 27
8. Mizuno A., Hayakawa T. et al. (1998) ApJ Lett. 507, L83
9. Mizuno A. (1999) Privat communication
10. Cambrésy L., Epchtein N. et al. (1997) A&A 324, L5
11. Cambrésy L. (1999) Ph.D. thesis, in preparation
12. Cambrésy L. (1999) A&A 345, 965
13. Krügel E., Walmsley C. M. (1984) A&A 130, 5
14. Mizuno A., Hayakawa T. et al. (1999) PASJ **51**, in press
15. Haikala L. K., Mattila K. et al. (1998) In: Yun J. L., Liseau R. (Eds.) ASP Conf. Ser. 132: Star Formation with the Infrared Space Observatory, p. 147

The ISO-IRAS Faint Galaxy Survey: ISOCAM Imaging and Optical Spectroscopy

Carol J. Lonsdale[1], Robert Hurt[1], Harding E. Smith[2], Deborah Levine[1], Chas Beichman[1], George Helou[1], Catherine J. Cesarsky[3], Dietrich Lemke[4], Ulrich Klaas[4], and David Elbaz[3]

[1] Infrared Processing & Analysis Center, Caltech/JPL, Pasadena, CA 91125 USA
[2] Center for Astrophysics & Space Sciences, University of California, San Diego, La Jolla, CA 92093-0424 USA
[3] Service d'Astrophysique, DSM, CEA–Saclay, F-91191, Gif-sur-Yvette Cedex, France
[4] Max-Planck-Institut für Astronomie, Königstuhl 17, D–69117 Heidelberg, Germany

1 The Sample and Observing Philosophy

The goal of the ISO-IRAS Faint Galaxy Survey was to obtain a sample of the most distant, highest luminosity infrared galaxies from the 0.75 million sources in the IRAS Faint Source Survey. The strategy involved providing a large sample of sources, selected to be faint, high-luminosity (hence high-redshift) infrared galaxies, that ISO could select from to fill short ($\sim$ 12 mins) schedule gaps. The initial observing program involved CAM LW10 imaging at 12μm plus PHT 90μm photometry (PHT22) in order to obtain SED information and to provide good positions and reliable identifications for optical spectroscopy and other follow-up observations.

The Survey Team provided ISO with an initial sample of 3776 IRAS 60μm sources from the Faint Source Survey with $f_{60} < 0.3$ mJy, $b^{II} > 30°$, $f_{60} > f_{25}\&f_{12}$, careful cirrus rejection, $f_{60}/f_{blue} > 10$ (from the IRAS OPTID database), to select the most luminous sources; the well-known correlation between infrared-to-optical color and infrared luminosity implies $L_{60} > 10^{10.5} L_{\odot}$.

Among the key questions which the IIFGS was designed to address are:

- Why does the SFR history decline so steeply since $z \sim 1$? Possible explanations include a decreasing merger rate as the co-moving space density of galaxies decreases; decreasing gas content of galaxies as the gas is used up by previous generations of star formation; or decreasing star formation efficiency.
- How is the evolution of merger-induced starbursts linked to that of QSOs?
- In a CDM scenario, does SF proceed largely in merger-induced, nuclear starburst events, as in local ULIRGs, or largely quiescently throughout disks?

D. Lemke, M. Stickel, and K. Wilke (Eds.): LNP 548, pp. 267–274, 2000.

- How do we explain the high luminosity SCUBA and ISO 15 & 175μm sources which account for a large fraction of the cosmic infrared background? This result is rather counter-intuitive to what would be expected in CDM models, in which smaller masses merge earlier. Can CDM models accommodate early mergers with such high SFRs?

2 ISO Observations

The IIFGS strategy was highly successful, particularly during the early phases of the ISO mission when higher-priority target lists had not yet been released. Initially observations were obtained both with ISOCAM and ISOPHOT, but following orbit 613 the PHT observations were abandoned in favor of increased CAM imaging integration time in order to allow more detailed analysis of source significance and 12μm flux-density. This resulted in a three-fold increase in on-target integration with ISOCAM and better resulting detector transient stability.

Table 1. IIFGS Observing Strategies

Phase 1 (Orbits 96–613)	Phase 2 (Orbits 614-866)
ISOCAM: LW10 ("IRAS" 12 μm) Filter	ISOCAM time increased
6″pixels, $\sim 3\times$ 3′ field of view	6″pixels, $\sim 3 \times 3'$ field of view
2 x 2 raster, 30″offsets	3 x 2 raster, 18 x 30″offsets
6 frames/raster, $T_{int} = 2.1$ sec/frame	20 frames/raster, $T_{int} = 2.1$ sec/frame
ISOPHOT: C90 (90μm) Filter	ISOPHOT observations suspended
Chopped PHT22 photometry	
64 sec on-source integrations	

2.1 Observation Status

In all, 521 FSS Fields were observed with ISOCAM (Pases 1 & 2) and 413 with ISOPHOT (Phase 1 only). All 413 Phase 1 CAM Fields have been processed. They were first reduced using ISO On-Line Processing (OLP) versions 6.0 and later and run through custom processing at IPAC. About a dozen PHT datasets were reduced manually. 108 Phase 2 Fields await processing employing a reduction pipeline using Cam Interactive Analysis package which is still under development. The longer observing times allow use of "standard" data reduction tools, and it is anticipated that these observations will allow better estimates of source significance for both datasets.

Optical spectroscopy, including redshifts, has been obtained for 121 galaxies from Lick and Palomar observatories. Optical imaging (g and r or i) has been obtained at Lick Observatory and ESO imaging has been obtained for Southern sources by P. Barthel et al.. UV and K band imaging for the more luminous, higher redshift systems is being obtained at UH 88 inch (J. Surace) and CO observations are being made at the OVRO in collaboration with M. Yun. Here I will concentrate on the Cam Phase 1 results and follow-up optical spectroscopy. Preliminary results for the first few IIFGS Sources were published in [3].

2.2 ISOCAM Data Reduction

The 413 Phase 1 ISOCAM observations were reduced in an IDL-based custom data pipeline developed at IPAC by R. Hurt. Starting with the standard-processed data (SPD) products, cosmic ray glitches were identified and masked. Owing to the small number of integrations allowed by the IIFGS observing strategy, the ISOCAM detectors were unable to stabilize fully during an integration and special care was needed in treating the detector transient response. Transient response correction was obtained by treating the background transient response as a polynomial baseline and subtracting it out. Individual frames were then averaged and rasters mosaiced. Sources were identified by both their brightness in the mosaic and the time-responses of the pixels. Detections were required in 4 different pixels in time domain to identify a source. The process was then iterated, excluding sources from transient fitting. This approach was necessary to filter out false detections caused by cosmic ray-induced changes in detector responsivity. All sources were then inspected by hand, and $\sim$ 120 sources resulting from detector glitches (which still made it through the source detection algorithms) were rejected. Source reliability was estimated from data simulations in which synthetic sources were introduced at a range of flux densities and then extracted using the above procedure. The final result was a total of 540 highly reliable CAM sources detected in 413 FSS fields with flux densities in the range $0.58 < f_{12} < 100$ mJy, with average and median flux densities 4.7 mJy and 3.4 mJy, respectively.

FSS-ISOCAM Source affiliation was determined using a Likelihood Ratio technique developed for the IRAS OPTID Project which compares the probability of a spatial match (determined by location with respect to the IRAS error ellipse) to the probability of a chance association of a background source of the appropriate magnitude (determined by 10μm background source counts) where $LR = P(trueID)/P(falseID)$ [4].

There are 387 FSS fields with 1 or more good CAM ID: a 94% detection rate. A large percentage of fields have > 1 detection (pairs) and these are frequently confirmed as interacting systems on direct images. In addition there are 59 "serendipitous sources" — CAM sources outside the IRAS error

circles and therefore probable background sources, including 3 QSOs with $0.17 < z < 0.90$.

3 New ULIRGs at Moderate Redshift

The IIFGS has very successfully selected LIRGs and ULIRGs; the identification rate of ISOCAM detections with strong emission line galaxies is over 90% - all LIRGs with $z \gtrsim 0.6$ and $L_{60} \gtrsim 10^{10.5} L_{\odot}$. Among the more than 120 galaxies for which spectroscopy is now available there are approximately 25 ULIRGs ($L_{60} > 10^{11.6}; H_0 = 75, \Omega = 1$), with redshifts $0.25 < z < 1.33$ and we therefore expect 100 to 125 in full ISOCAM sample.

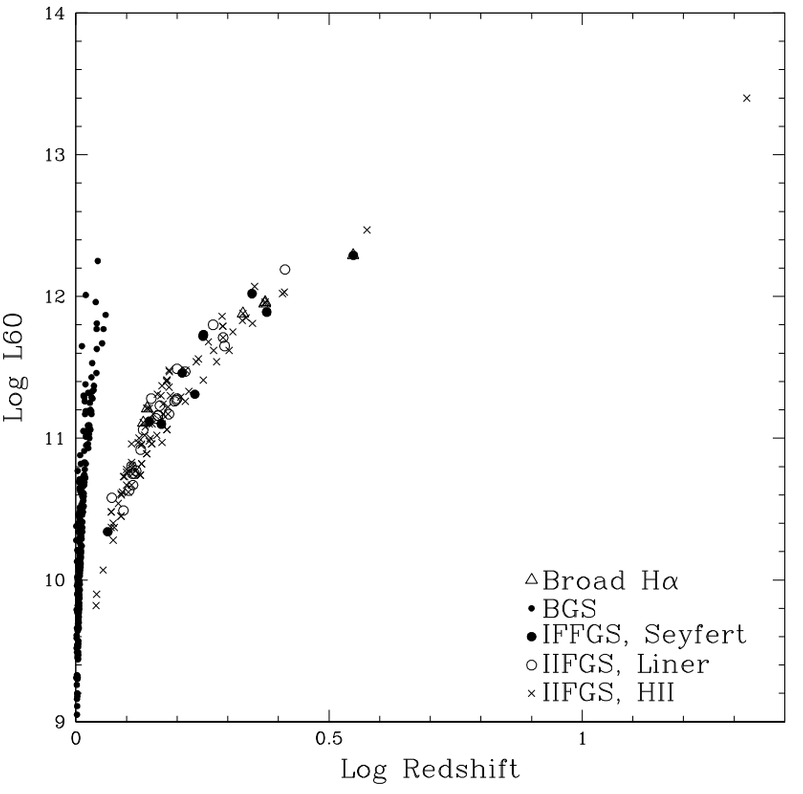

Fig. 1. Redshift distribution for the new sample, compared to the Bright Galaxy Sample from [6]. The new sample probes a narrow slice of L-z space

Comparison to some previous samples is given in Table 2 below:

Table 2. Comparison of ULIRG samples

Sample	# ULIRGs	F_{60} limit (Jy)	z-range
BGS (Soifer et al. [6])	10	> 5.34	$z < 0.1$
Leech et al. [2]	35	> 0.60	$0.1 < z < 0.3$
Clements et al. [1]	99	> 0.30	$0.06 < z < 0.44$
Kim & Sanders [5]	118	> 1.00	$0.04 < z < 0.27$
ven der Werf et al. [8]	6	> 0.20	$0.33 < z < 0.83$
Lonsdale et al. [4]	25+	$0.1 < f_{60} < 0.3$	$0.25 < z < 1.33$

It remains difficult to use the IIFGS for deriving space densities for evolution calculations. Because we selected a narrow range in f_{60} and a limited band in the L_{60} vs f_{60}/f_{blue} relation, the IIFGS represents a rather narrow slice in luminosity–redshift space. The combination of color selection and cirrus elimination, representing a further color selection, plus ISO scheduling translate into a complex selection function which we have not yet attempted to model. Furthermore, the low and variable SNR of the FSS 60μm sources makes Malmquist correction important, but difficult.

For now, the key use of the IIFGS will be as a new sample of distant ULIRGs for detailed study. How do they resemble or differ from local samples?

4 Spectroscopic Results

Follow-up spectroscopy at $\sim$ 5Åresolution has been obtained at Lick and Palomar Observatories for redshift determination and excitation analysis. Over 95% of IIFGS CAM identifications prove to be strong emission-line objects. Redshifts are currently available for over 120 fields and detailed spectroscopic analysis has been performed for about half that sample. Results are summarized in Table 3 below where we classify the galaxy excitation using the [OIII]/Hβ vs [NII]/Hα relation. In many cases the [OIII] and Hβ features are too weak to be measured leading to the ambiguous classifications listed in Table 3. We further segregate galaxies by the presence of a broad component ($\Delta\lambda \gtrsim$100Å) underlying the Hα/[NII] features.

Table 3. Optical Spectroscopic Classification

Excitation / line width Class	Broad Hα	No Broad Hα	Total
Seyfert	1	8	9
Liner	0	5	5
HII	2	10	12
HII/Liner	1	2	3
HII/Seyfert	0	9	9
Liner/Seyfert	0	10	10
HII/Liner/Seyfert	1	11	12

The results may be summarized as follows:

- Over 95% of the CAM identified objects are strong emission-line galaxies $0.05 \lesssim z \lesssim 0.6$; one object is a "hyperluminous" QSO with z = 1.3.
- 14 of 60–23% have clear AGN indicators.
- 10 galaxies – 17% are pure HII spectra with no broad lines (pure starburst).
- 17 galaxies – 28%, may be starbursts if the LINERS signature arises from starburst-driven superwind emission
- 30–50% cannot be classified unambiguously because only Hα and [NII] are visible; most of these fall on the LINER/AGN side of the excitation line for [NII]/Hα.

5 Colors and Luminosities

The IIFGS f_{60}/f_{blue} selection worked well at selecting Luminous Infrared Galaxies with $\log L_{60} > 10.5(L_{\odot})$; $0.06 \lesssim z \lesssim 1.4$. The z=1.325 QSO has a very low L_{60}/L_{blue} value.

There is a notable correlation between L_{60}/L_{blue} and L_{60}/L_{12} which extends in our sample from the BGS sample. An interesting result for this sample is a population of objects with extremely cool f_{60}/f_{12} infrared colors. These systems are not evident in the samples listed above and are not likely to be explained by k-correction effects. Such extreme objects in the earlier samples would have been undetectable at 12μm by IRAS (there are even some BGS galaxies undetected at 12μm). A careful analysis of selection effects and flux biases in our sample needs to be done before any conclusions are reached about this result.

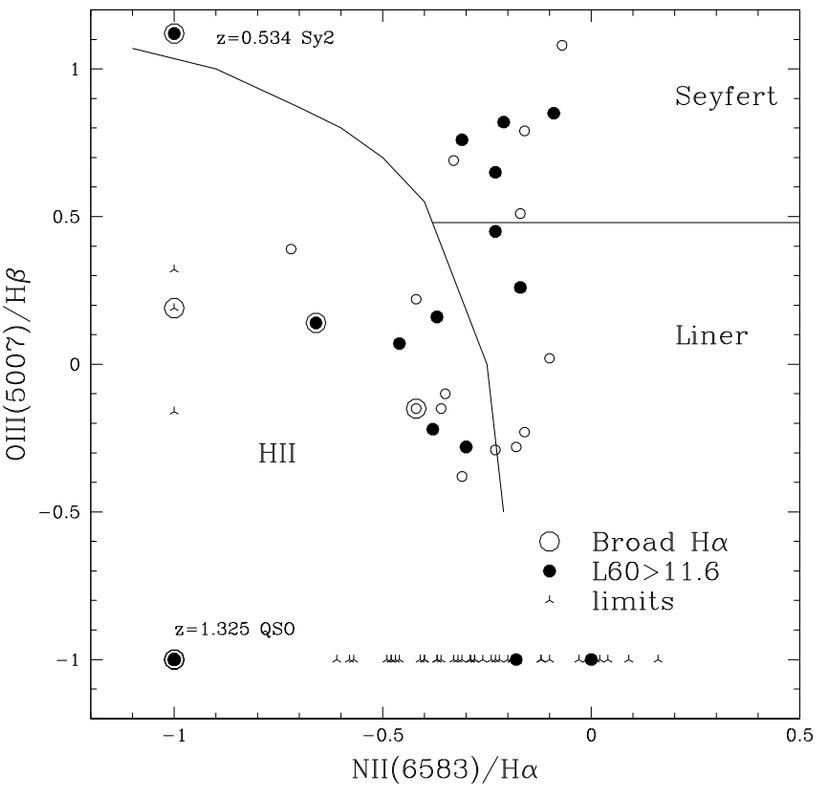

Fig. 2. Excitation diagram for 60 IIFGS galaxies with well-measured line strengths. As shown in Table 3, about 25% show clear AGN indicators — excitation or broad Hα and about 25% are starbursts in LINERS. For many objects only the [NII]/Hα ratio is measured; those objects are plotted along the bottom of the graph.

6 Conclusions

The IIFGS selection and observation techniques were highly successful, and a large new sample of 25 ULIRGs at $0.25 < z < 1.325$ has been obtained. This may increase by a factor of 4 to 5 with additional spectroscopy. The IIFGS is then an ideal sample for investigating the nature of moderate-z ULIRGs. For 30 galaxies with measured line ratios, roughly half have AGN excitation and half starburst, if LINERs are attributed to starbursts. These results resemble those for the highest luminosity objects in the Veilleux, Kim and Sanders 1 Jy sample [7]. The IIFGS sample extends to higher L_{60}, L_{60}/L_{blue} and L_{60}/L_{12} than the BGS; all of these quantities are intercorrelated. A

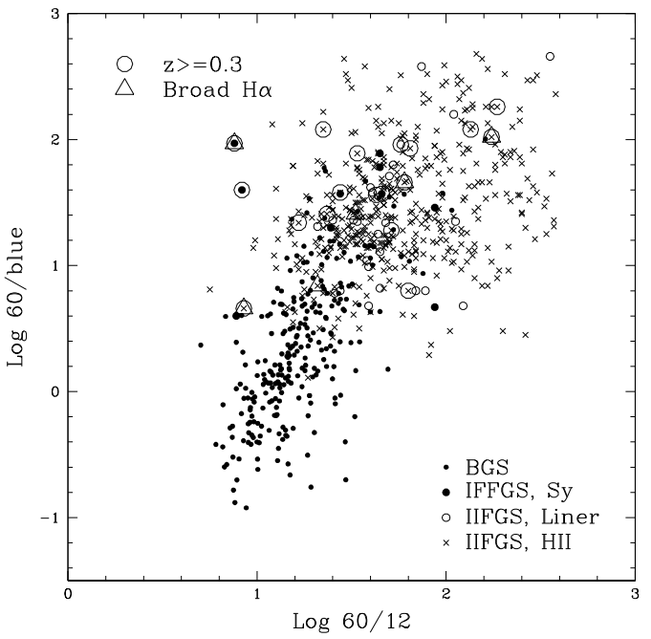

Fig. 3. Relationship between the f_{60}/f_{blue} vs f_{60}/f_{12} colors, showing a large spread to very cool f_{60}/f_{12} colors in the new sample.

sample of extremely cool L_{60}/L_{12} galaxies, present in this sample, may have been selected against in prior samples, but the IIFGS remains subject to uncertainties in flux bias and other selection effects, which require further evaluation.

This research has been supported in part by grants from NASA to IPAC and UCSD and by the US NSF to UCSD.

References

1. Clements, D. *et al.* 1999, *M.N.R.A.S.*, 302, 391
2. Leech, K. *et al.* 1994, *M.N.R.A.S.*, 267, 253
3. Levine, D., Lonsdale, C., Hurt, R. *et al.* 1998, *Ap.J.*, 504, 64
4. Lonsdale, C., Hurt, R., Smith, H. E. *et al.* 2000, *in preparation*
5. Kim, D-C. and Sanders, D. 1998, *Ap.J.S.*, 119, 41
6. Soifer, B. *et al.* 1987, *Ap.J.*, 320, 238
7. Veilleux, S., Kim, D.-C. & Sanders, D. 1999, *Ap.J.*, 552, 113
8. ven der Werf, P. *et al.*, 1999, *A&A*, 342, 665

The ISOCAM Parallel Mode*

Ralf Siebenmorgen[1], Norbert Schartel[2], and Stephan Ott[1]

[1] ESA/ISO Data Centre, Villafranca del Castillo, P.O. Box 50727, E-28080 Madrid
[2] ESA/ XMM Operation Centre, Villafranca del Castillo, P.O. Box 50727, E-28080 Madrid

Abstract. The mid infrared camera (ISOCAM) on board of the infrared space observatory (ISO) routinely exposed the sky during non prime observations. This so called ISOCAM parallel mode gives the largest data set of ISO. It represents more than 40% of all ISO observations. We present the calibration strategy of the ISOCAM parallel mode and discuss statistical properties of the extracted sources. Having analysed about 40% of the data we demonstrate that our point source catalogue should contain more than $\sim$ 50.000 sources at a limiting flux down to $\sim$ 3mJy, all found at a confidence level well above 95%. From the source catalogue we identified the asteroid Watsonia.

1 Introduction

During all pointed observations of ISO [2] when the infrared camera ISOCAM [1] was not the prime instrument it still routinely exposed to the sky. In the so called parallel mode, ISOCAM pointed, depending on the prime instrument, between 10' and 20' away from the prime target. Thus enabling to perform an effectively unbiased survey of limited areas of the infrared sky at high sensitivity [6]. Up today there are 42604 ISOCAM parallel mode observations in the ISO archive so that this survey amounts to about 40% of all observations performed during the ISO life time. In the parallel mode, ISOCAM was configured using the 6.7 μm broad band filter lw2 or 6.0 μm narrow band filter lw4, both at 6" pixel resolution giving a 180"$\times$180" total field of view. In addition during calibration revolutions the 14.3 μm broad band filter lw3 at 1.5" pixel scale was applied, which led to a 48"$\times$48" field of view. The spatial resolution of ISOCAM thus converts to about a 15 fold increase of angular resolution as compared to IRAS.

Compared to the ISO prime instrument, not the full telemetry rate of the satellite was available during parallel mode observations and a number of 12$\times$2.1s exposures have been co-added on-board so that every 25.2s a single exposure was down-linked to the ground segment. During one observation on a single sky position the typical (median) integration time is about 6 minutes.

* Based on observations with ISO, an ESA project with instruments funded by ESA Member States (especially the PI countries: France, Germany, the Netherlands and the United Kingdom) with the participation of ISAS and NASA.

D. Lemke, M. Stickel, and K. Wilke (Eds.): LNP 548, pp. 275–282, 2000.

In this article we present statistical properties of a first generation catalogue of point sources detected by ISOCAM in its parallel mode. The data analysed until now are 300 ISO revolutions, this represents about 40% of the total data available. During those 300 revolutions filters lw3 and lw4 have been configured about 13% each but filter lw2 was more frequently applied (74%). Therefore we restrict our statistical discussion here to lw2 observations.

2 Data Processing

We start calibration of the images from SPD level in the CIA [1] environment and apply basic calibration steps, consisting of dark correction, deglitching, co-addition of exposures on the same sky position, flat fielding and photometry conversion. (Principles on ISOCAM data are described by [5] However before calibration of images care has to be taken in the precision of the software which relates the ISO satellite time key to the ISOCAM instrument time key. Here we have been using an updated version of the standard off line processing system (OLP8). In addition already on raw data (ERD) level we check for saturated detector pixels. Those pixels have been flagged and are not considered for reliable source extraction still 10 minutes after pointing away from the saturation source. During observations a saturation avoidance procedure has been applied by the ISO operators so that only a small number of detector saturations occurred.

The most reliable deglitching is done by studying the time history of the signal of a single pixel. This limits us to analyse only data sets having more than 3 individual exposures. For cosmic ray suppression we applied an adaptive sigma-clipping method (Ott et al., this volume). The accuracy of the flat fields limits the faint source extraction. To improve the quality more than 100 different sky flats derived from suitable ISOCAM prime observations have been re-calibrated. This allows to group the flats of a single optical configuration into a number of different flat field families (Ott et al., this volume). Caused by the lens wheel jitter the most dramatic changes of the flats occurred at the outer parts on the array. Consequently we chose for each image the flat field which minimises the RMS at the boarder of the detector.

3 Extraction of Source Candidates

From the calibrated images we extract source candidates by considering the point spread function and the RMS image. We applied the multi wavelet

[1] CIA is a joint development by the ESA Astrophysics Division and the ISOCAM Consortium led by the ISOCAM PI, C. Cesarsky, Direction des Sciences de la Matiere, C.E.A., France. Contributing ISOCAM Consortium institutes are Service d' Astrophysique (SAp, Saclay, France) and Institute d' Astophysique Spatiale (IAS, Orsay, France)

transform algorithm by [7] and retrieve all source candidates for which the standard deviation of the noise is more than 4 σ and where the 1σ uncertainty of the location of the object on the array is smaller than 3 pixels. As second step we check the temporal signal behavior for each source candidate. For this we estimate the flux error for each exposure (σ_i), by assuming that the flux F_i to the next good flux estimate F_{i+1} is within $\sim 1\sigma_i$. All candidates where

$$2.5 \cdot (\sum_{i=1}^{N} \sigma_i^2)^{\frac{1}{2}} \leq \sum_{i=1}^{N} F_i - N \cdot B \tag{1}$$

are considered to be spurious and therefore rejected. Here $\sigma = \sqrt{\sum_{i=1}^{N} \sigma_i^2}$ and the background B is estimated by applying a 7×7 pixel median box filter over the image. As third step we apply a statistical analysis over all remaining source candidates, which is subject of the following Section.

4 Statistical Properties of the Source Catalogue

For each source candidate, retrieved with the procedure discussed in the previous section, we calculate a confidence level. The goal is to define *cut–of–parameters*, such as a limiting flux, which allows to extract sources at a confidence level above 95%.

As a first step we consider all sources observed in at least two pointings. This means we consider a source candidate S in pointing P_1 and select all pointings P_2 where candidate S should be re-observed. In P_2 we measure the distance D from the nominal position of S to all source candidates retrieved from image P_2. This we do for all our source candidates and plot the histogram of all those distances D. Such a plot we call from here on *coincidence histogram*. We expect three cases:

- If $D \leq 1$ pixel, the source candidate S was likely to be re-observed in P_2.
- If 1 pixel $\leq D \leq$ 2–3 pixels, the source candidate S was most likely re-observed, however caused by the lens wheel jitter the absolute astrometry of S is shifted relative to P_1.
- If $D > 3$ pixels, we measure the background.

The background at this point is of complicated structure, it contains:

1. True background sources, such as stars.
2. Spurious detections, such as residual cosmic ray hits of the detector not masked by our temporal deglitching method.
3. Variable targets, such as asteroids.

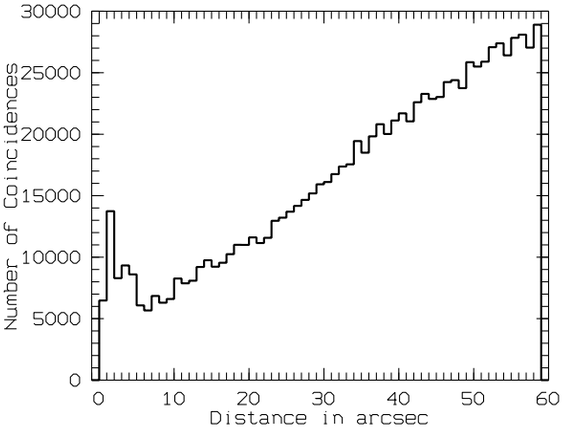

Fig. 1. Coincidence histogram of all source candidates as retrieved by the procedure discussed in Section 3. The confidence of sources found at a distance $D \leq 6$" is not much above 50%.

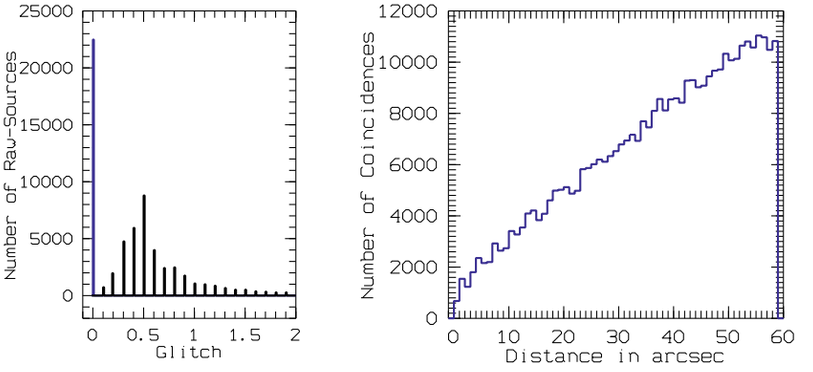

Fig. 2. a) Histogram of the inter-crossing wavelet coefficient which we call "glitch". This function is smooth but shows a singularity at glitch close to zero. (left). b) Coincidence histogram of all sources with glitch ~ 0. Within the statistical limit all those sources can be regarded as spurious.

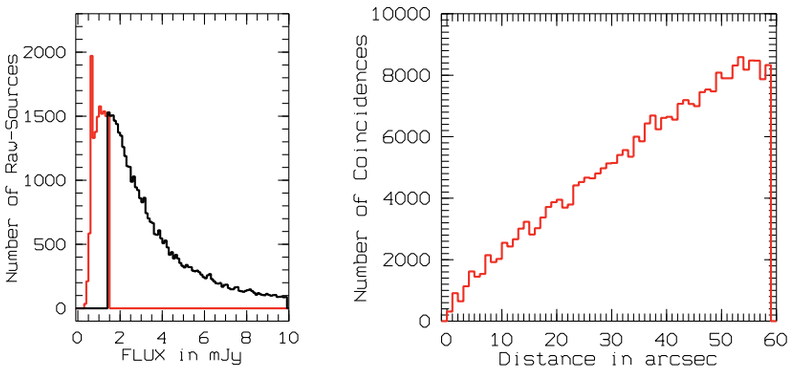

Fig. 3. a) Histogram of the source fluxes. For starring observation the limiting flux is above 1.5 mJy (left). b) Coincidence histogram of all sources with fluxes less than the predicted sensitivity limit. Within the statistical limit all those sources can be regarded as spurious.

We expect to see in the coincidence histogram a peak close to $D \sim 0''$, a secondary peak at $D \sim 12''$ and overlaid a linear function which represents the background. The integral of the first peak divided by the integral of the interpolated background under this peak gives the *confidence* level. In Fig. 1 we show the coincidence histogram of the input catalogue (as retrieved from Section 3). One notice a strong linear background over a small peak centered around $D \sim 2''$. The confidence level is just above 50%. This indicates that still after a careful calibration effort of the images the so far retrieved source candidates have a high probability to be spurious. At this point one could for example identify some of the source candidates by cross correlation with other catalogues, e.g. DENIS, and extract at least some real sources. However, our aim is to provide a catalogue with a confidence level for each source sufficient for further scientific analysis. For example from the wavelet analysis one can relate the inter-crossing coefficients of the different wavelet scales to the physical size of the source [7]. The histogram of this parameter, which we call for simplicity "glitch", is shown in Fig. 2a. It shows a quite smooth distribution but a singularity at glitch ~ 0. Looking at the coincidence histogram (Fig.2b) of source candidates having in at least one pointing glitch ~ 0, proves that they are within all statistical limits spurious.

As second example we investigate the histogram of the retrieved source fluxes (Fig.3a). We find a sharp cut-off at a flux of $\sim$ 1mJy. We plot in Fig. 3b

the coincidence histogram of all source candidates which are found below the expected limiting flux ($\geq$ 1.5 mJy) of ISOCAM starring observations [8] in at least one pointing. Again one notice that all those sources are spurious.

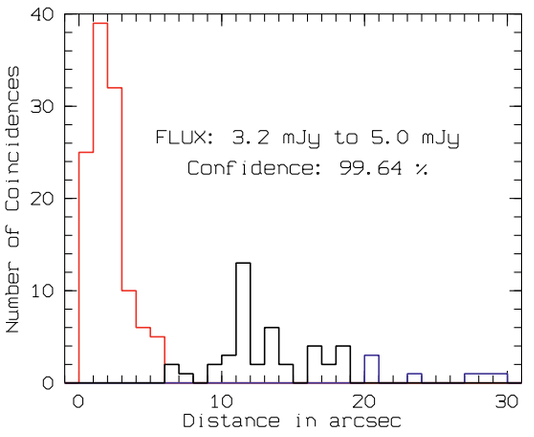

Fig. 4. Coincidence histogram of sources close to the predicted sensitivity limit of starring observations. We applied a method to suppress the background and fine tuned the cut of parameters from the input list of source candidates (see text). The interpolation of sources detected between 20" – 30" to distances $D \leq 6''$ represents the number of spurious detections. We proof that our remaining source candidates have a confidence above 95%.

At this point the background in the coincidence histograms is significantly reduced. It becomes difficult to distinguish real and spurious components of the measured background. We therefore look back to the detector geometrie to find an area and a procedure allowing to suppress the background: Considering the lens wheel jitter, which is ~ 2 pixels, we need to neglect in our analysis the boarder of the detector. Caused by the dead column (which is column 23) we should consider only the detector area up to column (23-2). From the center of the detector (column 15) we are left with a radius of $23 - 2 - 15 = 7$ pixels (42"), which is never influenced by detection problems caused by the boarder or the dead column; also still by considering the lens wheel jitter. We then calculate the coincidence histograms, but with a slightly modified procedure:

1. We select a source S in pointing P_1 which is detected between columns $9 - 15$ and rows $9 - 25$. This is the detector area surely free of boarder problems.

2. We consider only those sources S in P_1 where no further source is detected in a circle with radius of 7 pixels. This should suppress most of the background.
3. We select all pointings P_2 where source S should be re-observed at a nominal position on the detector as defined in 1.
4. In P_2 we measure the distance D from the nominal source position of S to all other source candidates. However since we need to consider once more the lens wheel jitter we measure source distances in P_2 only up to a radius of 5 pixels from the nominal source position of S.

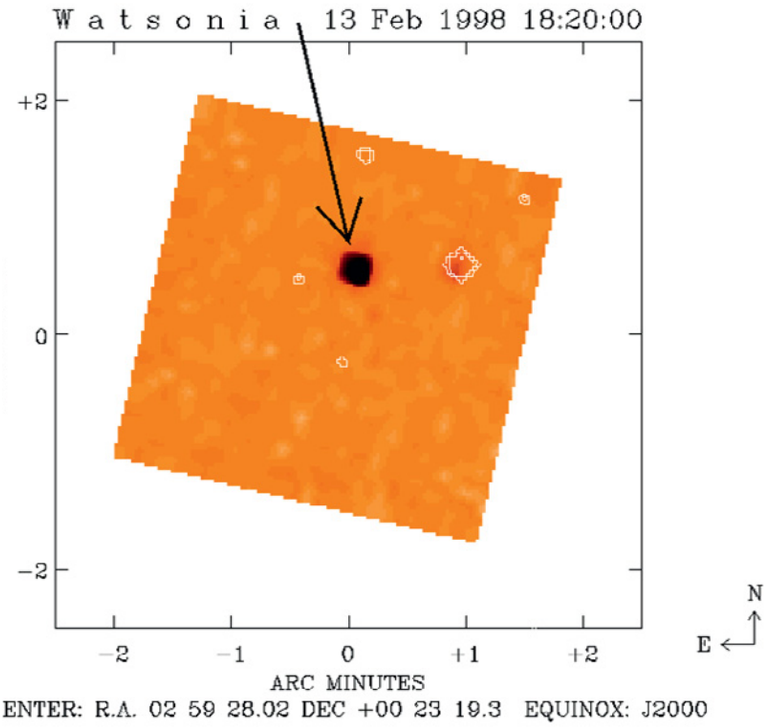

Fig. 5. ISOCAM image observed at 13 Feb 1998, 18:20:00 UTC. Contours represent an overlay of the digitized sky survey. We detect asteroid Watsonia at a flux of $\sim$ 150mJy.

The coincidence histogram should give a peak at $D \leq 1$ pixel (6") of at most real sources and a secondary peak at ~ 2 pixels. The secondary peak is caused by the lens wheel jitter. The coincidences for $D > 20''$ should be

almost free of true background sources except a few. The few remaining real background sources are those which are not detected in P_1 because of different sensitivity limits, e.g. integration times in both images; - suppose the case that only a minimum number of exposures are taken in P_1 but a much larger integration time was spend on P_2. The definition of the confidence level of the sources remains the same as given above. After fine tuning the cut of parameters we show in Fig. 4 the coincidence histogram. We show this only for sources close to the theoretical detection limit (3.2 – 5 mJy) and still calculate a confidence level of the sources around 99.6%.

We so far have used only a pure statistical analysis so that we can apply the retrieved cut of parameters to the full input catalogue of source candidates. If we further extrapolate the number of the remaining sources to the full data base of ISOCAM parallel mode observations we expect a total of ~ 50.000 sources extracted from lw2 observations at a confidence limit well above 95% and at a limiting flux close to the predicted sensitivity limit.

5 Time Variable Sources: Asteroid Watsonia

We are left to discuss time variable source as a contribution to the background structure measured in the coincidence histograms. Together with T.G. Müller, we detected in the parallel mode image observed on the 13 Feb 1998 at 18:20:00 UTC two sources (Fig. 5). One of the source can be identified by a star and the other is a time variable source which coincides with the predicted orbital position of the asteroid *Watsonia*. From the orbital elements [4] a flux of $F_{pre} = 100 \pm 10$mJy is predicted. Considering a colour correction factor of 1.15 we measure in our ISOCAM data a flux of 115 ± 15mJy.

References

1. Cesarsky C., Abergel A., Agnèse P. et al., 1996, A&A 315, L32
2. Kessler M.F., Steinz J.A., Anderegg M.E. et al., 1996, A&A 315, L27
3. Ott S., Pollock A., Siebenmorgen R., *this volume*
4. Müller T.G., Lagerros J., 1998, A&A 340, 338
5. Siebenmorgen R., Abergel A., Altieri B., et al., 1996, A&A 315, L169
6. Siebenmorgen R., Blommaert J., Sauvage M., Starck J.-L., 1999, ISO Handbook Volume III (CAM), SAI – 99 – 057/Dc, http://www.iso.vilspa.esa.es/
7. Starck J.L., Murtagh F., Bijaoui A., Image Processing and Data Analysis: The Multiscale Approach, Cambridge University Press, Cambridge (GB), 1998, (http://www.multiresolution.com)
8. The ISOCAM Team, 1996, "ISOCAM Observer's Manual", ESA/ESTEC

Data Reduction Techniques for the ISOCAM Parallel Survey – Challenges and Solutions

Stephan Ott, Andy Pollock, and Ralf Siebenmorgen

ISO Data Centre, Astrophysics Division, Space Science Department of ESA,
Villafranca del Castillo, P.O. Box 50727, 28080 Madrid, Spain.

Abstract. In its so-called "parallel mode", ISOCAM, the mid-infrared camera on board ESA's Infrared Space Observatory (ISO), continued to observe while other instruments were prime, thus providing a widespread, if uneven, high-sensitivity survey of the sky. Due to the variety of the data and the small number of read-outs usually available, special data reduction algorithms are needed. We present the current state what has been done to overcome the problems involved; outline possible further improvements; and show how other types of ISOCAM observations may benefit from these new techniques.

1 Introduction

During most of ESA's Infrared Space Observatory (ISO) mission [1,2], the mid-infrared camera ISOCAM [3], continued to observe the sky in its so-called "parallel mode" while another instrument was prime.[2]

In parallel mode, 12 images with 2.1 seconds integration time were accumulated on board and downlinked every 25 seconds. In order to avoid saturation of the detector, the optical configuration was adapted to the expected flux level in one of several modes: (ISOCAM team 1996, [5])

- 6" Pixel Field of View, LW2 (5 - 8.5μ): extragalactic mode
- 6" Pixel Field of View, LW4 (5.5 - 8.5μ): galactic mode
- 1.5" Pixel Field of View, LW3 (12 - 18μ): slew mode
- 1.5" Pixel Field of View, LW-CVF (15μ): galactic centre mode
- dark configuration: dark mode

Depending on the prime instrument, ISOCAM observed the sky 10' to 20' from the prime target [6]. Effectively, this permitted an unbiased survey of limited areas of the infrared sky with high sensitivity and 15 times the angular resolution of IRAS, albeit with varying depth and wavelength per field due to the different configurations used and the highly variable time spent per observation — from less than 25 seconds to over 5.5 hours [7,8].

[2] ISO is an ESA project with instruments funded by ESA member states (especially the PI countries: France, Germany, the Netherlands and the United Kingdom) and with the participation of ISAS and NASA.

D. Lemke, M. Stickel, and K. Wilke (Eds.): LNP 548, pp. 283–290, 2000.

2 Data Reduction Challenges

While standard procedures for ISOCAM data reduction [5,9,10] served perfectly well for much of the analysis, the variety of the data and the small number of readouts generally available meant that special attention had to be paid to deglitch and flat-field the data.[3]

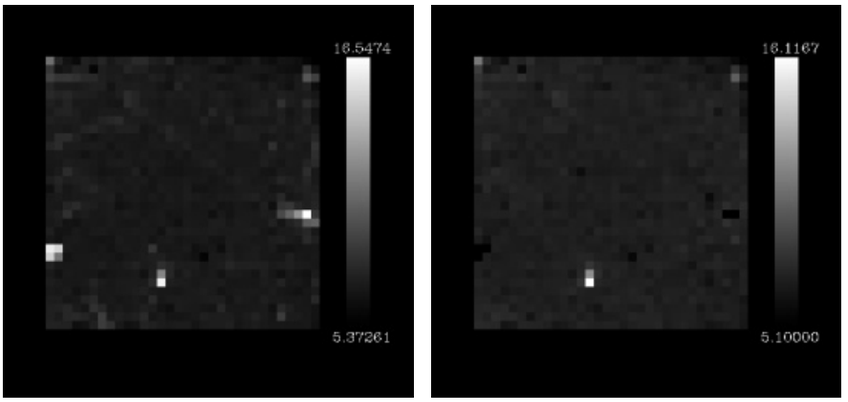

Fig. 1. Left image: Flat-fielded CAM parallel image after multiresolution deglitching. The leftmost bright pixels are due to a glitch, and the rightmost bright pixels are due to an overlay of a strong glitch with a weak source. Only in the middle we see a bona-fide source. Right image: Flat-fielded CAM parallel image after BISC deglitching. Note that six pixels, corresponding to strong glitches, were completely suppressed by BISC due to their high noise.

2.1 Cosmic Ray Suppression

Overview The glitches that result from cosmic-ray impacts are an important – and often dominant – limiting factor for all aspects of ISOCAM data analysis [12]. Standard deglitching techniques [5,11] work on the data vector only and therefore ignore valuable information about

- ISOCAM's current configuration
- our knowledge of temporal glitch distribution
- the current flux level per pixel

Therefore the standard deglitchers have often to rely on badly chosen thresholds, which consequently results in

[3] CIA was used for the standard data reduction steps. CIA is a joint development by the ESA Astrophysics Division and the ISOCAM Consortium. The ISOCAM Consortium is led by the ISOCAM PI, C. Cesarsky.

- high noise level due to un-suppressed glitches
- masked out gradients during stabilisation
- masked out sources
- no deglitching for observations with few read-outs

The last two points especially proved a major obstacle for the calibration of CAM parallel images, as the flux and its associated noise can vary extremely during an observation and pointings with as few as 4 readouts had to be treated.

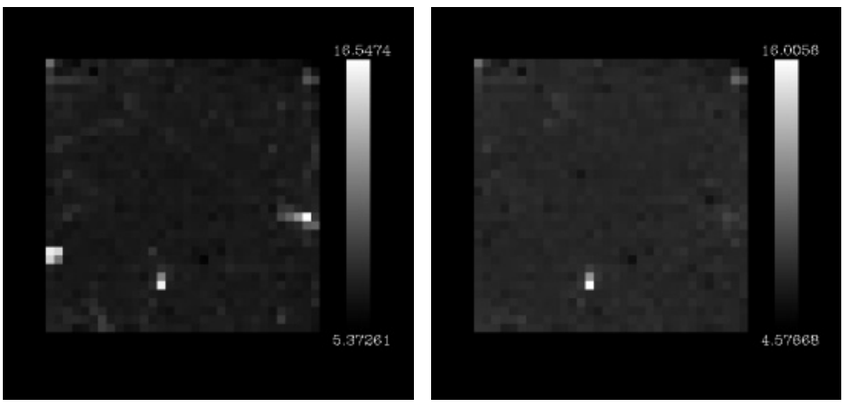

Fig. 2. Flat-fielded CAM parallel image after multiresolution deglitching (left) and after NOSC deglitching (right). Note that the strong glitches at the border of the array have been removed by NOSC.

Best Iterative Sigma Clipping For stabilised data (like faint source or CAM parallel data) the "Best Iterative Sigma Clipping Deglitcher" (BISC) was developed. It is an iterative method, in which the data are first normalized by an estimate of the flux before sigma clipping with a threshold locally determined by the variance of the pixel which is used to calculate a new estimate of the flux; the process being repeated until the flux level does not change significantly. Optionally, this may be followed by a second iteration in which the threshold is globally determined by the variance of the detector array.

This method performs a stringent deglitching, including very good rejection of different types of glitches. However, pixels with high temporal gradients, due to stabilisation effects or cross-talk near strong extended sources, or strong noisy point sources might be masked out and so have to be recovered by the NOSC post-processing step described below.

Normalized Sigma Clipping For CAM parallel data with as few as four readouts the "Normalized Sigma Clipping Deglitcher" (NOSC) was developed.

Standard sigma clipping fails for data with very few samples because even one outlier or glitch significantly increases the variance. Consider, for example, the series of four measurements [-1,1,10,0]. The variance of the four values is 4.4 and although it is obvious that the highest value of 10 is a glitch, its rejection as such would require a 1.7σ criterion to be applied. That would clearly be unacceptable in the vast majority of cases. The trouble is obviously that the original sample does not gave a Gaussian distribution.

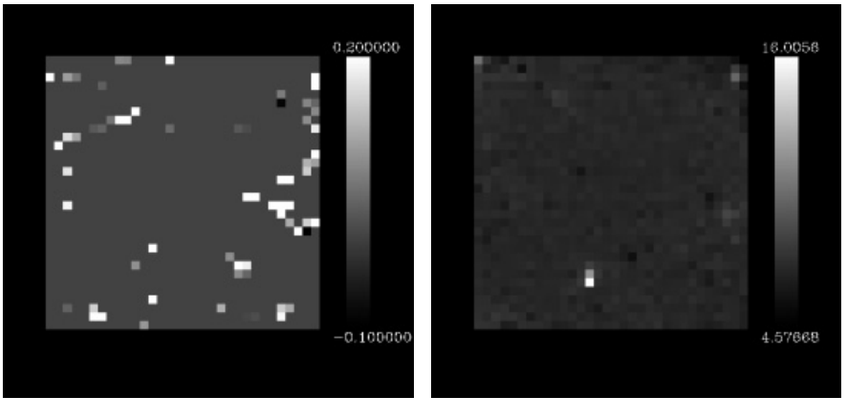

Fig. 3. Left image: Difference between a fully, e.g. BISC and NOSC deglitched, and only NOSC deglitched image. Trails and blobs, due to additional identified glitches are clearly visible. Right image: Flat-fielded CAM parallel image after full deglitching. This image is shown as contour overlay in fig. 2.2.

NOSC avoids this problem by estimating the mean and variance of the complete sample from only its middle 3/4, suitably adjusted, before sigma clipping in the normal way. The clipping stops if the remaining number of readouts falls short of a set limit, which represents the predicted number of good readouts per state[4] for CAM parallel observations (see table 1). Finally, standard clipping is performed.

This method performs a less stringent deglitching than BISC, but, by construction, will not mask out any data points completely. It will also suffer from imperfect glitch rejection if there are more strong glitches within one state than expected.

[4] A state is defined as the finest time division of ISOCAM activities. All CAM and satellite (pointing) parameters are fixed during a state.

Table 1. Rejection Criteria for NOSC Deglitcher

number of readouts	predicted number of good readouts
4 - 5	3
6	4
7 - 8	5
9 - 10	6
> 10	60 %

Deglitching Algorithm Applied to CAM Parallel Survey Data After multiple test-runs, the following deglitching strategy was chosen:

1. BISC deglitching, using 3σ globally determined threshold
2. NOSC deglitching to further improve glitch-rejection and to recover pixels masked out by BISC

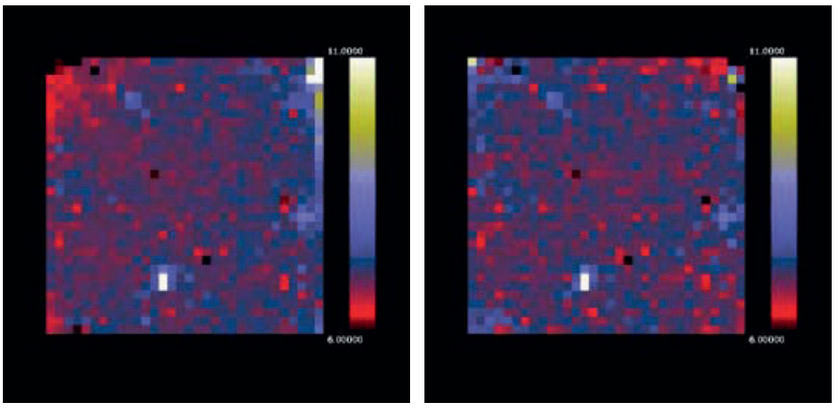

Fig. 4. Left image: CAM parallel image flat-fielded with a library flat-field. Note the low values at the upper-left corners and the bright column to the right, both due to flat-field artifacts. Right image: CAM parallel image flat-fielded with best-fitting master flat-field.

2.2 Flat - Fielding

Due to ISOCAM's lens wheel, selection wheel and filter wheel jitter the flat-field is highly variable at the array borders (in extreme cases up to a factor of 20 for a pixel using the 6" lens). This comprises the limiting factor at the array

borders, thereby reducing the usable area of an observation and diminishing the photometric accuracy. Standard flat-fielding techniques like library flat-fielding [5] will lead to highly inaccurate images at the borders, while sky flat-fielding, needing a raster with a sufficiently high number of pointings, is only applicable for a small percentage of CAM parallel observations.

To overcome this problem, over 100 different sky flat-fields were produced from suitable CAM prime observations. They were grouped into flat-field families, each showing a similar pattern, and merged into one master flat-field per family. At the moment, 11 different master flat-fields have been identified.

For each image, one of the 11 master flat-fields, namely that flat-field that minimizes the RMS at the border is chosen. While more work is needed to refine the master flat-fields, and extended sources at the border of a CAM image could lead to a wrongly selected flat-field, first results show that for the majority of observations with several states the same flat-field is chosen for each state, which indicates a proper treatment. Remaining flat-field errors could be due to the long-term responsive transient, which is an additive factor and gives a significant contribution for poorly illuminated pixels at the edges of the CAM detector.

3 Sample Result

We demonstrate the capabilities of the current CAM parallel processing algorithms for one observation with only 6 read-outs. The overlay with the corresponding digital sky survey image shows that the four discernible infrared sources coincide with stars, and no bogus sources due to unsuppressed glitches were produced. The flux of the detected objects ranges between 6.5 and 36 mJy.

4 Application to Other Observations

While the algorithms described were developped for the CAM Parallel Survey, also other observations can benefit from these new techniques.

Figure 6 demonstrates the advantages of BISC deglitching for a highly redundant faint source raster. (The six visible sources in the middle of the field range between 100 μJy and 1 mJy.)

Figure 7 shows the advantages of flat-fielding with a master flat-field for a short (230 sec.) 2×2 raster observation.

5 Planned Improvements

It is expected that astrometric corrections and the field distortion depend on the exact positioning of ISOCAM's optical elements, which is in case

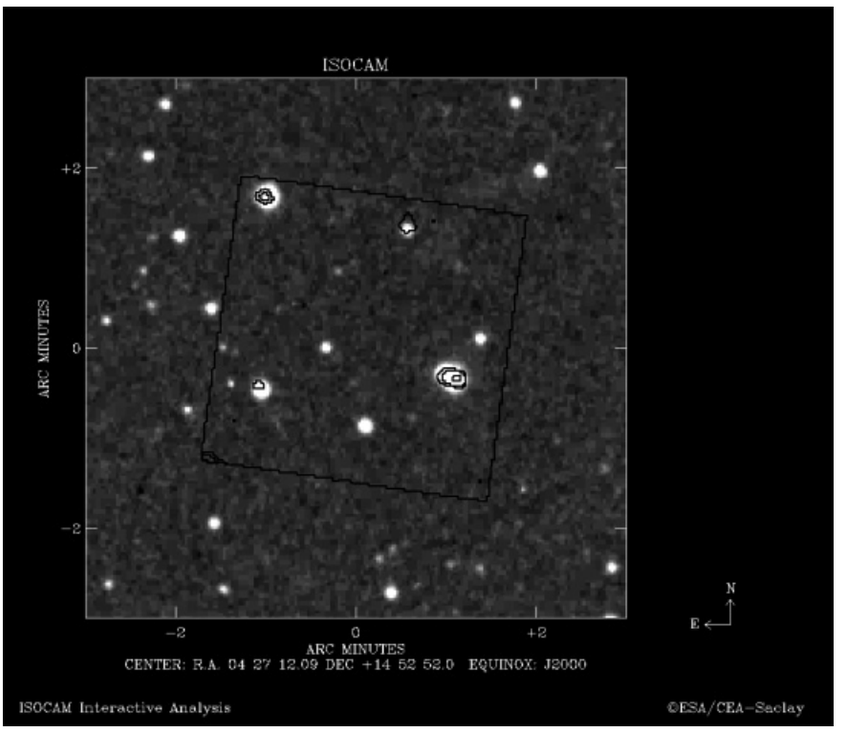

Fig. 5. DSS image overlaid with reduced CAM parallel exposure (contours).

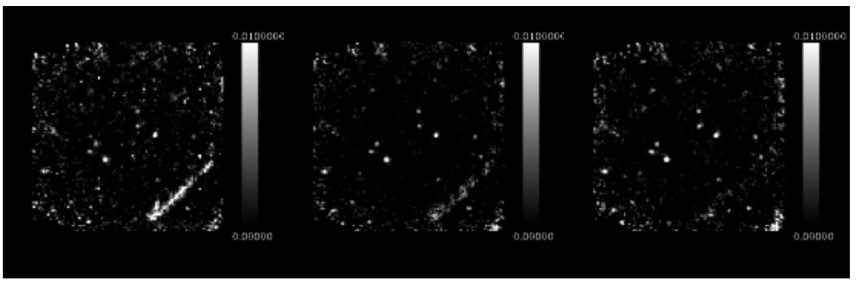

Fig. 6. Left image: CAM survey data after multiresolution deglitching. Middle image: CAM survey data after BISC deglitching. Right image: BISC deglitched data after additional noise rejection. Note the improved rejection of the long diagonal glitch in the lower right corner.

of a sufficiently strong uniform background recognizable by the flat-field. This fact, combined with a posteriori comparison of the astrometry of point sources found by the ISOCAM Parallel Survey with counterparts from other

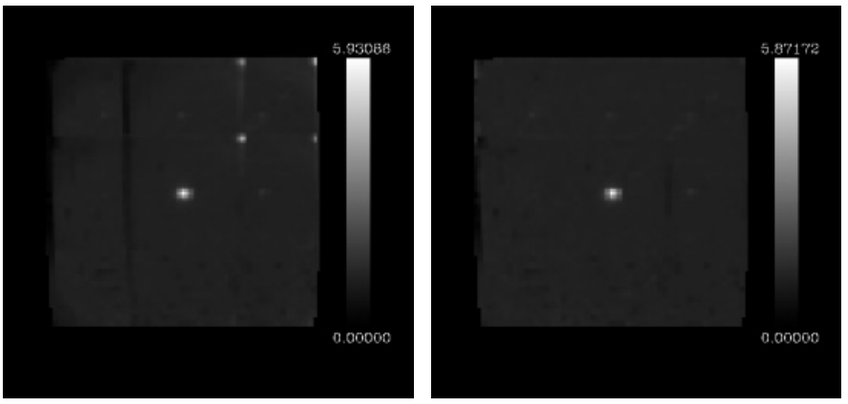

Fig. 7. Left image: CAM raster flat-fielded with a library flat-field. Right image: CAM raster flat-fielded with best-fitting master flat-field. Note that the disappearance of vertical stripes and of the four bright pixels in the upper-right corner.

catalogues should permit an improvement of the position accuracy from 20" to 6".

References

1. Kessler M.F., Steinz J.A., Anderegg M.E. et al., 1996, A&A 315, L27
2. Maldari P., Riedinger J., Estaria P., 1996, ESA Bulletin, Number 86
3. Cesarsky C., Abergel A., Agnése P et al., 1996, A&A 315, L32
4. The ISOCAM Team, 1996, "ISOCAM Observer's Manual", ESA/ESTEC
5. Siebenmorgen R., Blommaert J., Sauvage M., Starck J.-L., 1999, ISO Handbook Volume III (CAM), ESA Document Reference Number SAI-99-057/Dc, http://www.iso.vilspa.esa.es/manuals
6. Leech K., 1998, Infrared Space Observatory Satellite & Data Manual, ESA Document Ref. Number SAI/98-094/Dc, http://www.iso.vilspa.esa.es/manuals
7. Siebenmorgen R., Abergel A., Altieri B., et al., 1996, A&A, L169
8. Siebenmorgen R., Schartel N., Ott S., *this volume*
9. Ott S., Abergel A., Altieri B., et al., 1996, Design and Implementation of CIA, the ISOCAM Interactive Analysis System, ASP Conference series, Vol 125, 1997
10. Delaney M. ed., 1999, ISOCAM Interactive Analysis User's Manual, ESA Document Ref. Number SAI/96-5226/Dc, http://www.iso.vilspa.esa.es/manuals/
11. Claret A., Dzitko H., Engelmann J., Starck J.-L., 1998, Glitch effects in ISOCAM Detectors, Experimental Astronomy, in press, http://www.iso.vilspa.esa.es/users/expl_lib/CAM_list.html
12. Ott S., Metcalfe L., Pollock A, 1999, Innovative Cosmic Ray Rejection in ISOCAM Data, ASP Conference Series, in press

The ISO LWS Parallel Mode

Tanya Lim[1], Florence Vivares[1,2], and Emmanuel Caux[3]

[1] Space Science and Technology Department, Rutherford Appleton Laboratory, CLRC, Chilton, Didcot, OXON, OX11 OQX, UK
[2] SEMA GROUP, Space Systems Division, BP 46, Labége Cedex, France
[3] CESR CNRS-UPS, BP 4346, F-31028 Toulouse Cedex 4, France

Abstract. The ISO Long Wavelength Spectrometer (LWS) parallel mode allowed LWS data to be taken at all times when the LWS was not the prime ISO insrument. Although the data is of a lower quality than that of the prime mode, large regions of the sky have been probed with 10 narrow band photometry points between 46 and 178μm. Detailed below is a description of the current state of the processing, interactive analysis and calibration with estimates of the accuracies obtainable.

1 Introduction

The LWS parallel and serendipity modes are additional to the normal mode of the LWS instrument [2], used during those times when LWS was not the prime instrument. During operations using these modes, the instrument was configured to take data and insert it into the downlinked telemetry stream at a greatly reduced rate compared with prime mode operations. This was done through the 'essential' housekeeping data, a part of the telemetry stream where all the instruments on the satellite downlinked data for the spacecraft control centre to monitor their health. While not observing, some of the LWS housekeeping was not necessary and the LWS parallel and serendipity modes were implemented by replacing this data with detector signal values calculated on board. The space available provided for two values from each detector to be placed in each telemetry format (every 2 sec.). The detector integration time on board was adjusted to provide 1 sec integrations in these modes rather than the 1/2 or 1/4 sec used during prime observations. When another instrument was the prime instrument, the LWS was operating in parallel mode. When no AOT was active the LWS operated in a serendipity mode and this mainly refers to those times when ISO was slewing. The actual configuration of the LWS instrument for the parallel and serendipity modes was identical. These modes were not used until revolution 237 and continued until the end of the ISO mission with a gap between revolutions 380 and 442 when LWS was switched off due to a problem with the interchange wheel. In all more than 100,000 individual pointings were made in parallel mode in over 17,000 individual observations with a total sky coverage of about 1% (see figure 1).

In section 2 we outline the offline processing steps with reference to the processing done on prime mode data and in section 3 we give the status of

D. Lemke, M. Stickel, and K. Wilke (Eds.): LNP 548, pp. 291–298, 2000.

the calibration of both modes and in the following sections we describe the comparisons with other instruments and the interactive analysis packages.

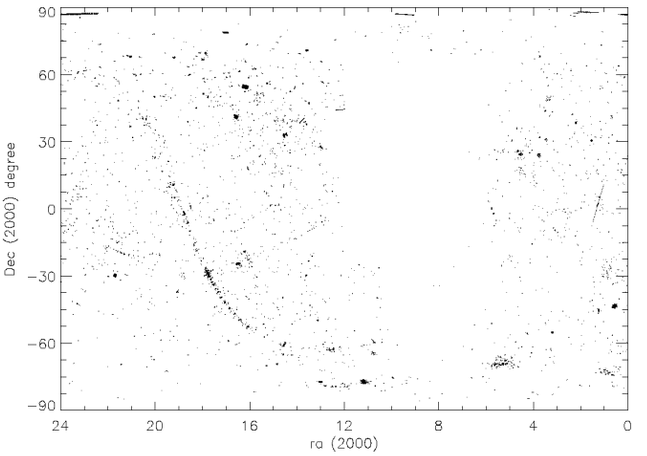

Fig. 1. Sky coverage of parallel mode

2 Processing and Pipeline Calibration

The approach to the processing of parallel and serendipity data is essentially the same as for the prime data and, whenever possible, the same algorithms and calibration files are applied ([5], [1]) i.e. engineering conversions are applied to obtain a photocurrent, then a small adjustment for the difference in slopes, obtained from 1s (parallel/serendipity) and 1/2s (prime mode) ramps, is applied.

Once the photocurrents have been obtained, the next stage is to remove the dark current. For prime mode grating data this is done by measuring dark current values prior to the illuminator flashes which take place at the start and end of each observation and subtracting the average. All dark current measurements were checked for trends and it was found that the dark current has remained at a stable value throughout each revolution of the ISO mission. The rare exception being that transient effects after observing bright sources sometimes led to higher than normal values. A similar monitoring exercise was done with parallel and serendipity data. The dark values which were defined as the mininum photocurrents consistently obtained and these were implemented as one dark current value per detector. These values (see table 1) were found to be lower that those found in prime mode ([5]) and are applied as a fixed dark removal in the parallel/serendipity pipeline.

The calibration of the detector responsivity relies on a simple ratio between the response to the illuminators found at the time of a particluar observation and that used as a reference. This is due to the responsivity of the LWS detectors drifting upwards during a revolution which is known from the inspection of prime mode illuminator flashes. This is a linear drift upwards in responsivity, however a reset by bias boost during the handover period in the middle of a revolution resets the value to that at the start of the revolution, followed by another linear drift in the second part of the revolution ([3]). Both parallel and serendipity observations did not have dedicated illuminator flashes, therefore the responsivity correction could not be applied directly. For each half revolution all illuminator flashes were linearly fitted to obtain responsivity drift coefficients for that revolution. The parallel and serendipity data were then calibrated by using the interpolated response of the detectors. For revolutions where there are no prime mode observations, a standard responsivity drift defined by averaging all revolutions was applied.

In prime mode the grating or FP is moving constantly hence the detector receives a constantly changing signal. In parallel mode the grating remains at a fixed position and therefore it was possible to apply a transient correction to the data. The wavelength determination was done by lookup table as all the data were taken at the grating rest position and this remained stable throughout the ISO mission. Each data point has a bandwidth of one grating resolution element (see table 1). The units of parallel products are $\mathrm{W\,cm^{-2}\,\mu m^{-1}}$ and serendipity products are in $\mathrm{MJy\,sr^{-1}}$ as a correction is made for the beam profiles [4].

Table 1. Parallel mode parameters

Detector	Wavelength (μm)	Resolution Element (μm)	Dark signal ($\times 10^{-16}\mathrm{Wcm^{-2}\mu m^{-1}}$)
SW1	46.2	0.29	4.34
SW2	56.2	0.29	1.89
SW3	66.1	0.29	1.91
SW4	75.7	0.29	0.86
SW5	84.8	0.29	1.21
LW1	102.4	0.60	2.22
LW2	122.1	0.60	2.56
LW3	141.7	0.60	0.29
LW4	160.5	0.60	1.74
LW5	177.9	0.60	1.28

3 Internal Calibration

The parallel mode data can be compared directly to prime mode data when a prime mode observation occurs within a parallel raster and/or at the same pointing as a parallel position. Five L01 observations were selected to provide a direct cross check between parallel and prime mode. All the L01 positions lie within the parallel rasters and two pointings are exactly coincident with one of the raster positions. Figure 2 shows a galactic centre region position where the pointing is the same for the prime and parallel mode observations. For all five positions it is found that the agreement is generally better ($\leq$20%) by comparing the fluxes from each detector at the parallel wavelengths with the prime data at those specific wavelengths. The best agreement was in the position which had the most flux, i.e. the uncertainties in dark current affect the quality of the data. There were no systematic differences between prime and parallel mode, although detector SW1 could be more than a factor of two higher or lower than prime mode. This detector is often affected by transients and has a slow time constant leading to a strong variation of the flux level obtained. For the interpolated positions all other detectors were well within a factor of 2 of prime mode.

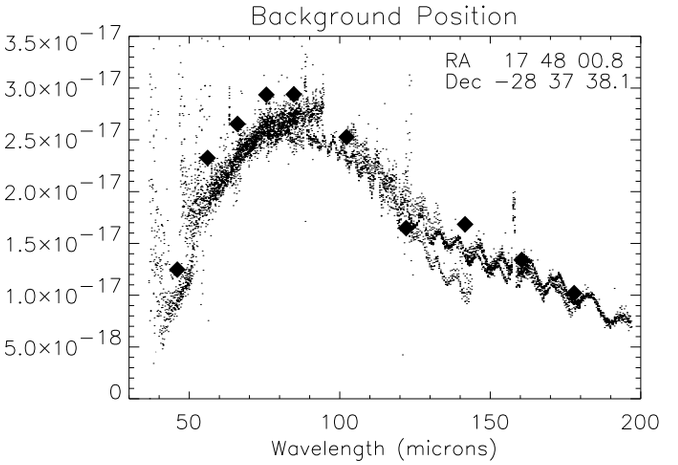

Fig. 2. Parallel mode observation at same position as prime mode

The parallel mode interactive analysis (LPIA) enables the building of a map from constituent product files using linear interpolation to form a uniform grid. Figure 3 shows one example where a map has been generated from 34 parallel observations. The raster pointings superposed on this map are from TDT:31801219. Each individual point from the raster was ratioed with

the nearest point in the map and these were averaged to get one comparison value for that detector per raster observation. All constituent observations were compared to the final map and the ratio for all detectors was always found to be within 20%, with the majority of pointings well within 10%.

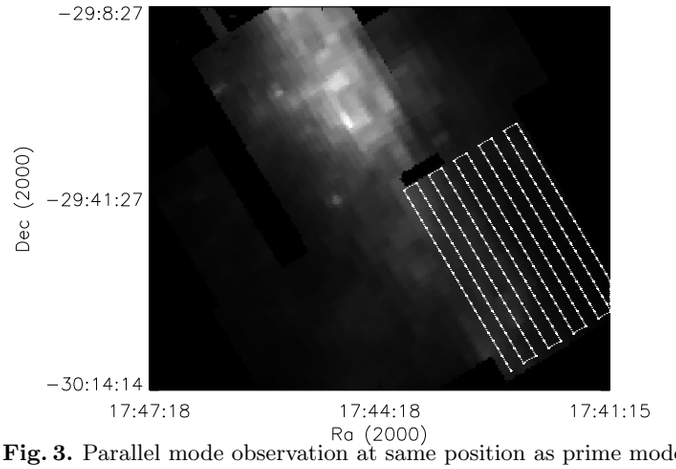

Fig. 3. Parallel mode observation at same position as prime mode

4 Comparison with Other Instruments

In addition to checking the internal calibration, comparisons can be made with IRAS and ISOPHOT. For each of these other instruments comparison is difficult to interpret as the flux obtained for parallel observations is in a very narrow band (one grating resolution element) whereas the other instruments are observing in a broad band. The three main wavelengths for comparison are 60μm, LWS-SW2, LWS-SW3, IRAS, PHOT, 100μm, LWS-LW1, IRAS, PHOT and 178μm LWS-LW5, PHOT, PRONAOS. The Rho Oph region was selected for cross-comparison and figure 4 shows a LWS LW1 parallel image with IRAS 100μm band contours superposed. From this, and similar maps in other bands, the structure of the regions compared is very similar leading to confidence in the relative calibration across the maps.

One important aspect of cross-checking with other instruments, which cannot be done with the internal checks, is to see if the beam shapes used for the conversion from $\mathrm{Wcm^{-2}\mu m^{-1}}$ to $\mathrm{MJysr^{-1}}$ are reasonable. Linear strips were selected across the maps which gave a variation in brightness and structure. Figure 5 shows the fluxes along the profile at 60μm, for SW2(56μm), SW3(66μm) and IRAS. The difference between the instruments at any point along an individual profile, was overall about 10% although SW3 was about

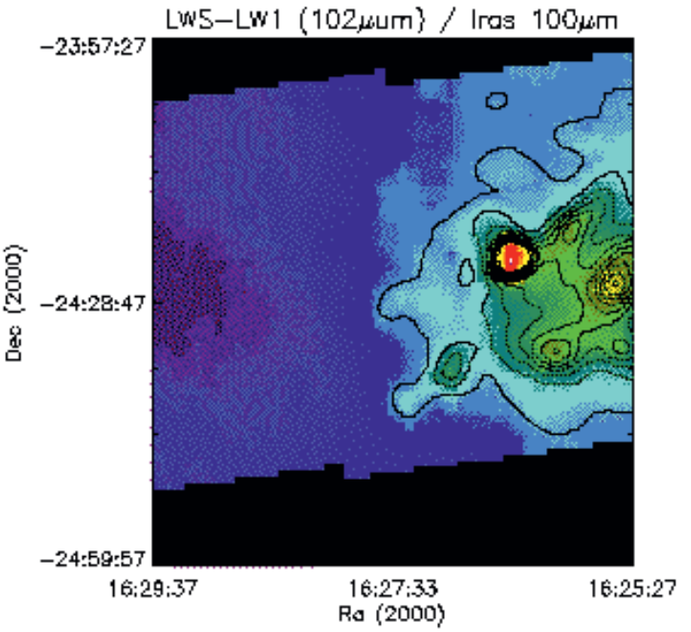

Fig. 4. Parallel mode LW1 map of Rho Oph with IRAS 100μm band contours.

30% higher at the position with the maximum flux. At 60μm the SW2 profile almost exactly matched the IRAS profile and the SW3 profile was always higher indicating that the efective wavelength of the IRAS filter may be nearer the SW2 wavelength than SW3. At 100μm LW1 gave a very good match $\leq$5% difference while SW5(84.8μm) was higher, and LW2(122.1μm) and the PHOT (80-120μm) filter were lower. The comparison with LW2 however is not meaningful as the IRAS 100μm filter only has a 20% transmission at 120μm. LW2 is also the only detector in parallel mode where the wavelength is coincident with a strong line ([NII]).

5 Discussion

The LWS parallel and serendipity mode has successfully completed a partial sky survey consisting of a set of LWS pointings when not prime. A pipeline has been implemented which allows similar processing to prime mode, with a few additions mainly to account for the non-availability of illuminator flashes for parallel and serendipity observations.

There are three main uncertainties in the data. As with prime mode, when looking at faint sources, it is not possible to accurately determine the dark signal which can have a large spread of values. Hence when observing background the derived dark current subtracted from the data may be greater

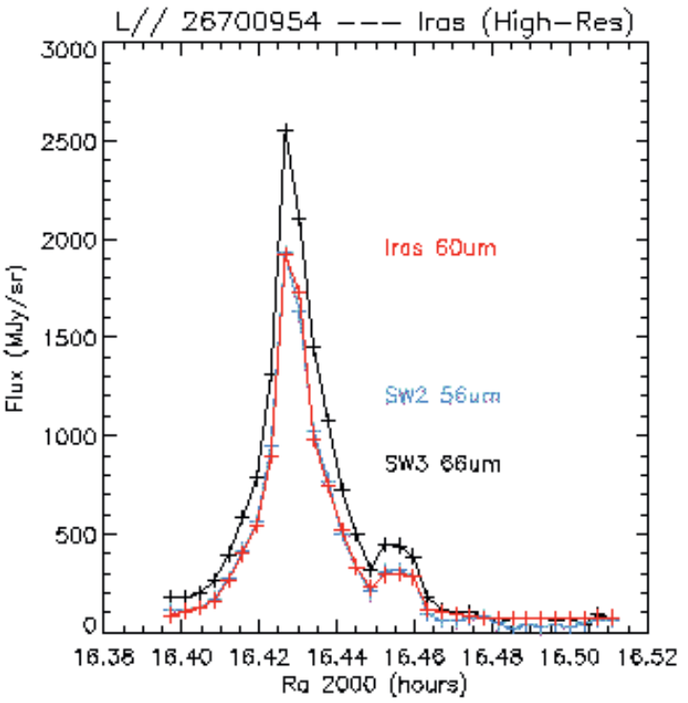

Fig. 5. Comparison of fluxes from different instruments around 60μ taken from a strip through a map of Rho Oph.

than the photocurrent measured from the source, leading to a negative flux. Another aspect is the LWS fringing. This not only leads to fringes observed in full grating spectra on the detectors but also affects the overall flux levels of individual detectors causing the sub-spectra not to match. With only one point per detector available it is difficult to determine to what extent the fringing is affecting the flux obtained at that point. Another difficulty is accurate glitch detection and removal. This is because detection of glitches on individual ramps is not possible due to only the slope being downlinked. In parallel mode there can be several ramps at the same pointing allowing deglitching by comparison, however in serendipity mode there is often only one ramp available at a particular pointing. Glitches which can affect adjacent detectors are often picked up in the point source extraction software and need to be removed by hand.

Despite the overall data set being of lower quality than prime mode, it is well calibrated, matches well with prime mode data and by comparing overlapping rasters, is known to be repeatable. Comparisons with other instruments show consistent results leading to confidence that the output of these modes yields scientifically usable data.

References

1. Burgdorf, M. J., Harwood, A. S. et al. (1998) SPIE, 3349, 359
2. Clegg, P. E., Ade, P. A. R., et al. (1996) A. & A., 315, 38
3. Lim, T. L., Burgdorf, M. J., et al. (1998) SPIE, 3354, 347
4. Lloyd, C., (2000) ESA Sp:ISO Beyond Point Sources, In Print
5. Swinyard, B. M., Burgdorf, M.J., et al. (1998) SPIE, 3354, 888
6. Vivares, F., Lim, T. L., et al. (2000) this volume

ISO-LWS Serendipity Survey and Source Catalogue

Florence Vivarès[1,2], Tanya Lim[1], Tom Day[1], and Emmanuel Caux[3]

[1] Space Science and Technology Department, Rutherford Appleton Laboratory, CLRC, Chilton, Didcot, OXON, OX11 OQX, UK
[2] SEMA GROUP, Space Systems Division, BP 46, Labége Cedex, France
[3] Centre d'Etude Spatiale des Rayonnements 9 avenue du Colonel Roche BP 4346 31028 TOULOUSE Cedex4 FRANCE

Abstract. We present the serendipity mode of ISO-LWS spectrometer. Included is an account of the estimated sky coverage, how the data is calibrated and processed and a description of the end product in the ISO archive.

We focus on the sources that can be extracted from this survey and we present and example of a source seen on both parallel and serendipity mode. Using this example we discuss the scientific quality of Serendipity mode data.

1 LWS Serendipity Mode

During the ISO mission, the ISO-LWS instrument was acquiring data at all times including when another instrument was active and when the satellite was slewing to a new target. At those times when the satellite was stable and another instrument was active the LWS was said to be in parallel mode [1]. At all other times, principally when the satellite was slewing, the LWS was said to be in serendipity mode.

The data acquisition and on-board processing for the two modes is identical with the distinction between the modes being made on the basis of the pointing data. As the data is passed to the ground on the LWS housekeeping telemetry stream, only a limited amount of space was available, hence the ramp integration had to be done on-board. Further savings were made by the use of 1s integrations, rather than the 1/2s integrations used in prime mode.

Differences between parallel and serendipity The main difference between the modes is that in parallel mode the satellite was in a stable pointing configuration allowing a good sampling of the flux at that position. In serendipity mode however the satellite was moving and the speed was constantly varying from zero to the maximum slewing speed of around 7 arc-min/s.

Sky coverage In over 17,000 individual slews (one before each parallel observations), more than 4 000 000 individual pointings were made covering about 10 % of the sky.

D. Lemke, M. Stickel, and K. Wilke (Eds.): LNP 548, pp. 299–306, 2000.

2 Processing

The pipe-line processing for parallel and serendipity modes is very similar (see [1] for a more detailed explanation).

2.1 SPD Processing

Standard processed data (SPD) has the same format for both non-prime modes and is similar to prime mode SPD in that it essentially consists of the set of derived photocurrents from the ramps in a time sequence. However as the ramps are processed on-board, no de-glitching can be done on individual ramps.

Deglitching In serendipity mode the pointing is not stable, hence the expected flux will vary. Therefore unlike parallel mode, deglitching cannot be done using the statistics from a series of similar ramps. However it is important to distinguish glitches from noise and possible sources. This can be achieved by using the LWS ten detector multiplexing i.e. glitches are searched for by comparing the ten detector outputs at the same time. A photocurrent is flagged as a glitch if :

- it is a peak higher than current noise and current flux slope,
- a similar peak does not appears on its neighbours (in wavelengths).

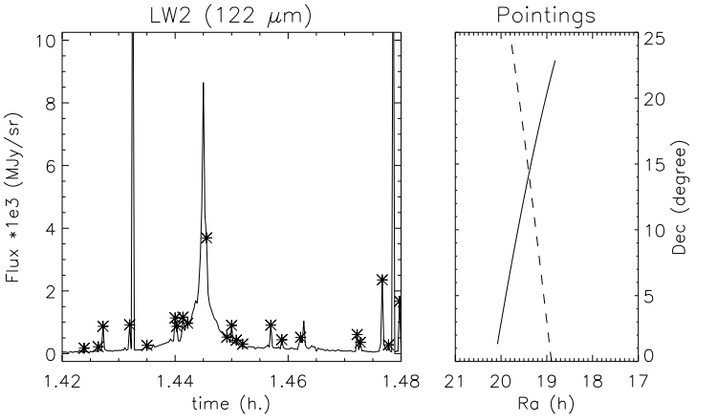

Fig. 1. An example of serendipity time sequence. The glitches are flagged by the star symbol

2.2 Calibration

Calibration is also similar for both parallel (see [1]) and serendipity modes. Two steps are different, transient correction cannot done as we have no model allowing to process non stable sequences, and an additional step is added to have homogeneous flux, flux is converted into MJy/sr.

Beam Profiles The effective beam profiles for serendipity mode are constantly changing as a function of the spacecraft velocity. Therefore the serendipity flux levels are essentially meaningless unless the effective beam is taken into account, hence the serendipity products have units of MJy/sr. As the speed is changing it is possible to have a different beam profile for every sample in a slew and it is not possible to extract the pointing with a good precision (like in parallel mode). The beam estimate is made by using the current knowledge of the LWS beam profile (see table 1) and by taking the central position for the integration, the current speed and the previous and next positions.

Table 1. beam sizes at serendipity wavelengths

Det.	Wavelength	HWHM
SW1	46.02 μm	41.1894 ”
SW2	56.10 μm	43.7922 ”
SW3	66.02 μm	45.4759 ”
SW4	75.61 μm	44.7780 ”
SW5	84.73 μm	44.3239 ”
LW1	102.28 μm	42.7402 ”
LW2	122.05 μm	43.9789 ”
LW3	141.64 μm	40.0549 ”
LW4	160.45 μm	40.7210 ”
LW5	177.87 μm	42.0299 ”

In a slew, speed will usually increase up to around 7 arc-min/sec, then when arriving close to the target, slow down and the satellite is stabilised and acquires its target. Figure 2, shows a series of serendipity slews projected on the sky. The areas shown are the calculated effective beam profile for each central integration position.

Serendipity Calibration The calibration of serendipity mode is done in the same way as parallel mode except that transient correction is not done.

1. remove dark levels and correct for long term drifts,
2. apply parallel/serendipity specific correction to correct for error due to on-board integration,
3. apply standard calibration (divide by filter response, bandwidth),
4. convert in MJy/sr.

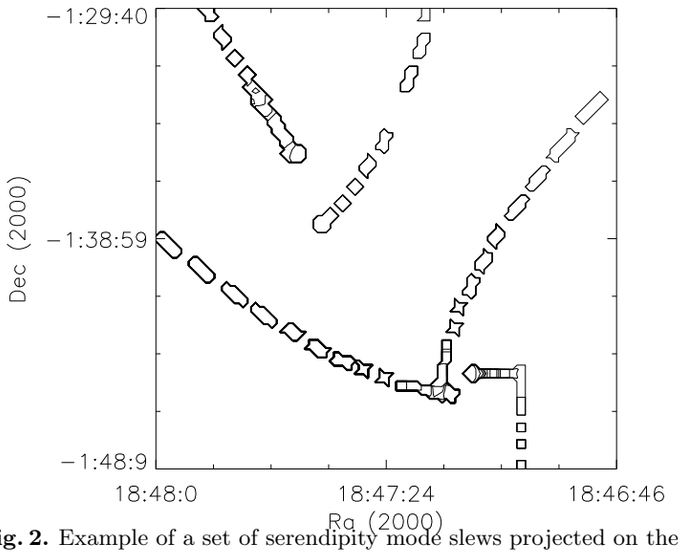

Fig. 2. Example of a set of serendipity mode slews projected on the sky

2.3 Data in Archive

Serendipity products in the archive exist for the two main stages of processing and have similar file formats to prime mode data. Apart from the unit change another important difference with the serendipity product is the addition of speed information (degree/sec).

Units Flux unit of calibrated serendipity data (MJy/sr) is different than this of parallel or prime mode ($Watt/cm^2/\mu m$) to take into account speed variation in time sequence and have homogeneous sequences.

Pointing is presented in same way (Ra, Dec and Roll angle), and for calibrated data, we add speed information ($degree/s$)

Caveat These data must be handled with care. We have same uncertainties than for parallel mode, to which we must add the uncertainty about beam size :

- uncertainty about ramp integration (there no way to decrease it as for parallel mode, as we have no real stable position)
- uncertainty about calibration (see [1])
- uncertainty about effective beam sizes
- uncertainty about effective beam profile and central position : ISO moves are supposed to be quite flat, but some jittering may appear.

In some serendipity slews a "WARNING" field appears in the header. This flags any known problems with pointing, jitters, or other telemetry related problems. Flagged products should be used with care.

3 Validation

As LWS have quite large beam versus the on-target threshold (10 arc-sec.), when the satellite is acquiring a point source before an LWS prime observation, we have often about 5 to 10 seconds of serendipity mode data on same target.

Two examples of the comparison between stabilisation periods and the following prime mode observation are given in figure 3. The serendipity mode points are plotted as * symbols with dashed lines connecting them. The prime mode data points at the serendipity wavelengths are plotted as + symbols with dotted lines connecting them. These two examples indicate that the agreement between serendipity mode during stabilisation and prime mode is very good over the entire dynamic range of LWS. Other cases were checked in a validation exercise and this agreement is almost always within 20% and is often better than 10%.

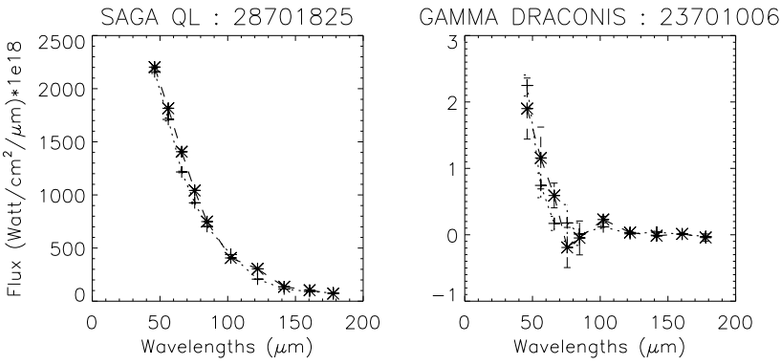

Fig. 3. LWS serendipity mode (dotted line) in the period immediately before a prime mode observation (dashed line)

The detector where differences were most often seen was SW1. This difference is probably due to the different dark current removal methods between serendipity and prime mode. Serendipity observations have a standard low value subtracted, whereas in prime mode a measured value is used which can be high due to the offset FP etalons used as the blank, not being completely opaque. For these observations the standard beam size could be used. We estimate an additional 20% uncertainty due to the effective beam calculation when slewing at speed.

4 Point Source Extraction

The first scientific usage of serendipity mode has been to find point sources, extract their spectra and try and identify them with known sources.

4.1 Principle

Point sources extraction is done on a per revolution basis, with a faint detection threshold :

1. serendipity data are read and averaged so that distance between successive pointing is larger than pointing uncertainty and so that :
   (a) distance between successive pointings is computed from Ra/Dec coordinates which gives speed variation,
   (b) fluxes are averaged, per detector, to have at least 10 arc seconds distance between successive values,
   (c) a deglitching is applyed when move is slow enough to have a time sequence.
2. candidate sources are selected as peaks smaller than LWS beam and appearing on several detectors (at least 3) :
   - a small threshold (per detector) is used (one sigma) because of an important noise in serendipity data. This criterium can't select sources from glitches.
   - the second criterium (the peak must appear on several contiguous detectors) is much more determinant (less than 1% of candidates are remaining)
3. source parameters are estimated (position, uncertainty, fluxes)
   (a) for position and uncertainty, speed is taken into account
   (b) source and background fluxes are estimated interpolating non glitched integrations before and after candidate sources.

4.2 Implementation

As the software read large pieces of data, there are from 10 to more than 100 serendipity products per revolution, this algorithm has been implemented as an additional pipe-line and produces FITS files with candidate sources.

The routines are available in Interactive Analysis package for LWS parallel / serendipity mode, and can be applied manually to data from both modes.

When applied to parallel mode averaged data, sources appearing on several wavelengths are also detected.

4.3 Analysis

The result is a small set of candidate sources (in general no more than 20) per revolution which have to be checked. Several possibilities are available :

- compare with parallel mode (which will have a better resolution)
- compare with IRAS point sources data

As we have tiny bandwidths, it is not expected to find sources not detected by IRAS. What is interesting is the set of fluxes for the ten wavelengths which give a good idea of the spectrum of the source at long wavelengths.

Example In revolution 343, 14 candidates are detected. The fourth one is interesting because a parallel map is available around it. Moreover, if we apply same detection routine to parallel mode, the same source is also detected.

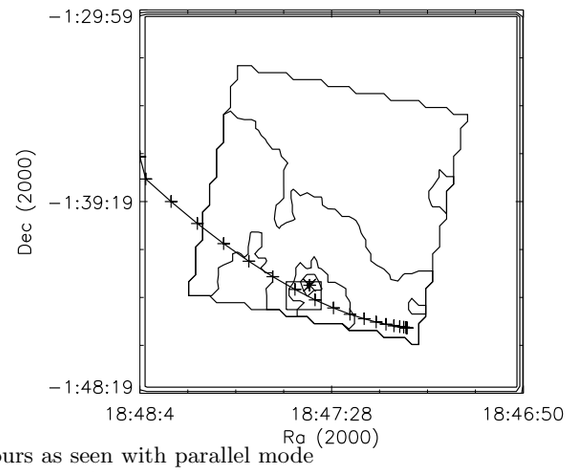

Fig. 4. Contours as seen with parallel mode
Serendipity pointings (full line with "+").
The square shows positions where the source is detected in serendipity mode.
The cross "*" inside the square shows position where the source is detected on parallel mode with same algorithm

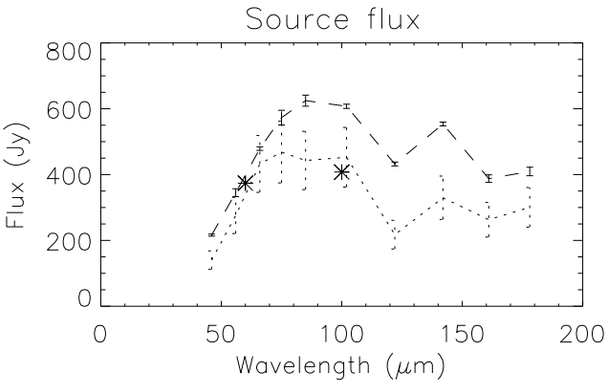

Fig. 5. LWS parallel mode source (dash line),
serendipity mode (dot line),
IRAS fluxes (stars), estimated from IRAS High-Res maps.

We can see from figure 4 that the serendipity slew does not pass exactly through the source, hence the fluxes on the 10 detectors at the closest position are lower that those obtained from the parallel observation. The fluxes from the ten detectors are plotted in figure 3 and the source shape is one expected for a cool source for detectors SW1-LW1. The LW2 detector is the only detector which coincides in wavelength with a bright atomic line (122 μm [NII]). In this observation LW3 is affected by long term transient effects and the serendipity mode fluxes from LW4 and LW5 are close to their dark signal values, hence the large uncertainties in the measurement. However both the serendipity and parallel data sets indicate a flat profile here and this may indeed be real.

For this source we get Iras High-Res map[1] and integrate flux on LWS parallel beam at 60 μm and 100 μm (stars on figure 5). Taking resolution difference into account, we have good matching with IRAS data.

5 Discussion

The processing and calibration of the LWS serendipity mode is now complete and the next stage, which is to extract and identify candidate point sources is now underway. Preliminary results show that the serendipity data is of sufficient quality to enable detection of point sources and hence obtain ten new flux values at the ten LWS detector rest wavelength positions. However this work is at an early stage and there are still many problems with both non-detections and the algorithm failing to detect some sources. The current estimate is that we will be able to identify about 20% of the current list of 6759 candidate sources. The ultimate sensitivity of this survey is not yet known as uncertainties in the specific serendipity calibrations are difficult to predict, hence this will be determined empirically from the data.

References

1. Lim, T. L., Vivarès, F., Caux, E. (2000) this volume

[1] The IRAS High-Res map was kindly provided by IPAC's IRAS support

An ISOPHOT Survey of Pre-stellar Cores

Derek Ward-Thompson[1] and Philippe André[2]

[1] Cardiff University, PO Box 913, 5 The Parade, Cardiff, UK
[2] Service d'Astrophysique, Centre d'Etudes de Saclay, France

Abstract. We present the results of an ISOPHOT study of isolated pre-stellar cores (originally known as pre-protostellar cores). The pre-stellar phase is one in which a dense core in a molecular cloud is gravitationally bound, but contains no embedded luminosity source. This takes place prior to the protostellar Class 0 phase. Hence pre-stellar cores are believed to represent the initial conditions of isolated star formation. They were not detected by IRAS, but have been detected by ISOPHOT at 200 and 170μm, but typically not at 90μm. The lack of detections at 90μm shows that there is no significant quantity of warm dust in these cores. Colour temperature maps can be made by ratio-ing the 170 and 200μm data. An example of this is shown, and an inside-out temperature gradient is observed, confirming the lack of a central protostellar heating source. Subsequently, a modified black-body is fitted to both the ISOPHOT and millimetre/submillimetre data, which allows submillimetre measurements to be converted into more accurate mass estimates.

1 Introduction

The study of the formation of low-mass stars (0.2–2$M_\odot$) has made significant progress, partly due to the ISO satellite, although the process is still not fully understood (for a review, see: [1]). One of the main problems is that there is still debate over the initial conditions which pertain in the clouds from which stars form. The initial form of the radial variation of density, temperature, velocity and magnetic field are all crucial to the protostellar collapse phase of star formation.

The main protostellar collapse phase was identified observationally by [2], and labelled the Class 0 stage. The subsequent Class I stage [3,4] represents the late accretion phase during which the remnant circumstellar envelope material accretes onto the central protostar and disk [5,6]. The final pre-main-sequence stages of Classes II & III [3,4] correspond to the Classical T Tauri (CTT) and Weak-line T Tauri (WTT) stages respectively [7].

These protostellar and pre-main-sequence stages are understood at least in outline. Infall has been reported in Class 0 sources by a number of authors (e.g. [8,9]). However, the manner of the collapse remains a matter for debate. The ideas of inside-out collapse (e.g. [10]) have been disputed by many authors (e.g. [11]), and recently appear to have been disproved observationally [12].

In addition, broad general agreement now appears to be emerging that protostellar accretion occurs at a non-constant rate, which decreases with

D. Lemke, M. Stickel, and K. Wilke (Eds.): LNP 548, pp. 309–316, 2000.

time throughout the accretion phase (e.g. [13,14]), and there are strong indications that a decreasing accretion rate is what is observed throughout the protostellar accretion phase (e.g. [15]). The exact form of the collapse depends almost entirely on the initial conditions [11,16] and a decreasing accretion rate requires a radial density profile which is relatively flat in the centre, and which steepens towards the edge (e.g. [11]).

In this paper we present ISOPHOT observations of objects which are in that phase of evolution which occurs earlier than any of the above-mentioned protostellar stages, and which we originally termed pre-protostellar [17], but now also call pre-stellar for brevity (the two terms refer to the same stage). This may be defined as the phase in which a gravitationally bound core has formed in a molecular cloud, and evolves towards progressively higher degrees of central condensation, eventually leading to protostellar collapse, but no central protostar exists yet in the dense cloud core. Hence pre-stellar (or pre-protostellar) cores are believed to represent the initial conditions for protostellar collapse in regions of low-mass, isolated star formation.

2 Pre-stellar Cores

We selected for study the regions which were identified by Myers and coworkers [18,19,20] from the catalogues of Lynds and others, and which were observed in various transitions of NH_3, CO and other molecules ([20] and references therein). But we selected from these a sub-sample of cores which do not contain IRAS sources [21], on the grounds that these should be at an earlier evolutionary stage, with the cores with IRAS sources having already formed protostars at their centres.

It was shown [17] in a JCMT submillimetre study of some pre-stellar cores, that the cores all appeared to have density profiles which were flat in their centres ($\rho \propto r^{-1}$), and steepened towards their edges ($\rho \propto r^{-2}$). This is qualitatively reminiscent of the profile predicted for a Bonnor-Ebert sphere, or for a thermally supported core interacting with an external UV radiation field (e.g. [22,23]). It is also similar to that predicted for magnetic support of a partially ionised core undergoing slow contraction by ambipolar diffusion (e.g. [24]), and consistent with that predicted by theory to produce a decreasing accretion rate with time (e.g. [11,13]) such as is seen in protostellar sources, as discussed above.

Studies at 1.3-millimetre wavelength [25,26] of a number of pre-stellar cores compared the findings in more detail with various theoretical models, and found that, in the case of L1689B for instance, the inner radial density profile had the form $\rho \propto r^{-(0.4-1.2)}$ (depending on deprojection) within a radius of 4000AU, steepening to $\rho \propto r^{-2}$ outside of this radius. Furthermore, absorption studies by ISOCAM ([27]; see also [28]) showed that at the outer edges (typically >15000AU) pre-stellar cores show very steep profiles indeed ($\rho \propto r^{-(4-5)}$).

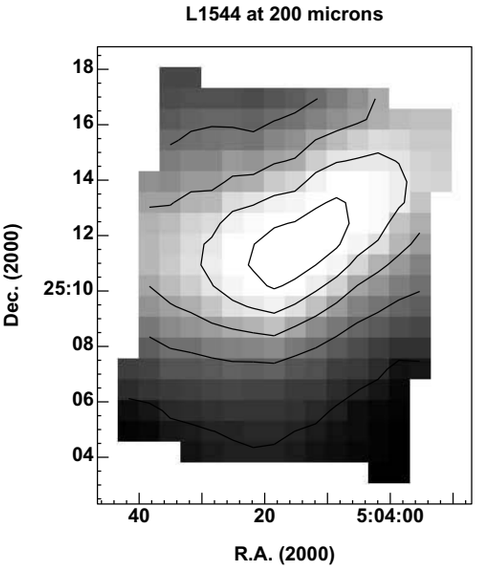

Fig. 1. ISOPHOT 200-μm image of the pre-stellar core L1544. The core is clearly detected and an elongated structure is seen

One of the difficulties associated with studying pre-stellar cores is that they have not previously been detected in the infra-red, either from the ground, or by the IRAS satellite out to 100 μm – this is one of the selection criteria of these sources. However, the spectral energy distributions increase with decreasing wavelength from 1.3 mm to 350 μm [17]. Consequently their spectra must peak between 100 and 350 μm. So we decided to observe pre-stellar cores with the Infrared Space Observatory (ISO) at far-infrared wavelengths from 90 to 200 μm using the photometer instrument ISOPHOT. In this paper we show some results of our ISOPHOT study of these cores. In a subsequent paper we will present the results of our full survey of 18 pre-stellar cores [29].

3 Observations

Our ISOPHOT observations took place during the period 1996 March 10–16 in orbits 114–120, and 1997 August 29–October 8 in orbits 652–692. Sources were observed at each of three wavelengths – 90, 170 & 200 μm. The observations were carried out in the over-sampled mapping mode, PHT32, in which the source is mapped by using the chopper to position the source on the detector array at a series of positions, separated by less than the detector resolution, intermediate between successive spacecraft pointings. A map is built up of a series of such scans in a raster fashion [30].

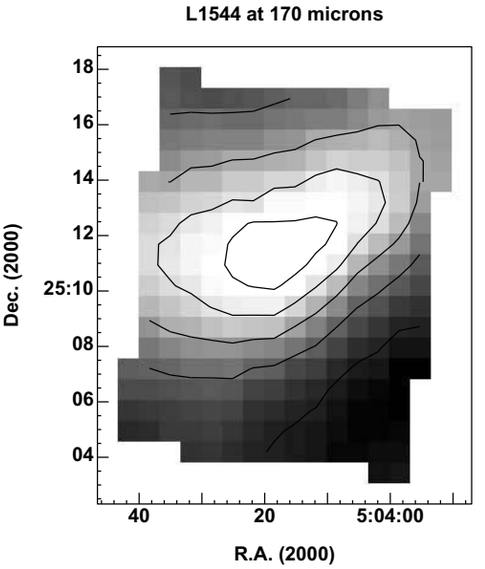

Fig. 2. ISOPHOT 170-μm image of L1544. The core is again clearly detected and very similar structure is seen to that in Figure 1

The filters used were the C_200 filter, which has a peak wavelength response at ∼200 μm and bandwidth FWHM ∼25 μm, the C_160 filter, which actually has a peak wavelength of ∼170 μm and bandwidth FWHM of ∼40 μm, and the C_90 filter, which has a peak wavelength of 90 μm and FWHM ∼30 μm [30]. The C_200 and C_160 filters are associated with the PHT-C200 camera, which has four pixels in a 2×2 array with each pixel 90×90 arcsec square. The C-90 filter is associated with the PHT-C100 camera, which has nine pixels in a 3×3 array with each pixel 45×45 arcsec square. Data reduction was carried out using the PHOT Interactive Analysis (PIA) software version 7.1.

4 Results

Figures 1–3 show ISOPHOT maps of the pre-stellar core L1544, in the Taurus molecular cloud complex, at 200, 170 and 90μm respectively. In Figures 1 and 2 the emission is clearly detected and some structure is seen. However, it can be seen from Figure 3, which is displayed at much lower levels, and with lower dynamic range, that at 90μm the core is not detected by ISO. All that is visible in the map is the low level extended Galactic cirrus emission, as expected in this low latitude region. The lack of any detectable emission associated with L1544 at 90μm shows that the dust which is detected at the longer wavelengths must be very cold.

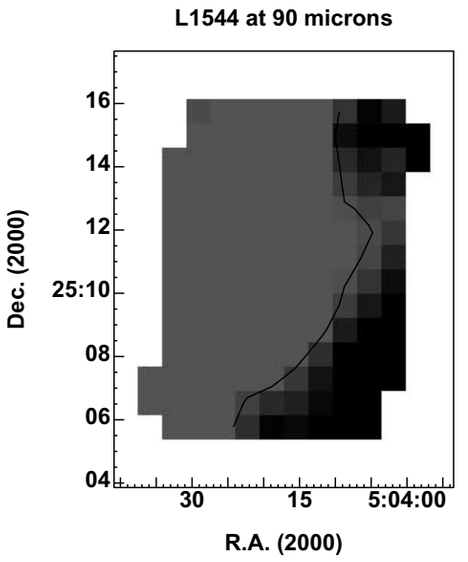

Fig. 3. ISOPHOT 90-μm image of L1544. The core is not detected. The contour is three times lower than the lowest contour in Figure 2

This core is typical of what we see throughout our ISOPHOT sample. Namely, we have detected all but one of the 18 cores at the longest wavelengths, and failed to significantly detect all but one of the cores at 90μm. One core was not detected at any wavelength, and one was detected at all three wavelengths. But the trend is nonetheless for the cores to be detected only at the longer ISOPHOT wavelengths, indicating that they are extremely cold (T<20K, see below).

We can use the ratio of the images at 170 and 200μm to determine the spatial variation of colour temperature across the pre-stellar cores. Figure 4 shows a colour temperature map of the same pre-stellar core L1544. This has been calculated by first removing a background flux density from each of the two input images, and then ratio-ing them. A lookup table was created using the optically thin grey-body assumption with β=2 (see below). The values in the ratio image are then converted into formal colour temperatures. Figure 4 shows that L1544 appears to be colder in its centre than it is towards the edge. This appears to confirm the pre-stellar nature of this core, with no central heating source, and its source of energy being the external inter-stellar radiation field.

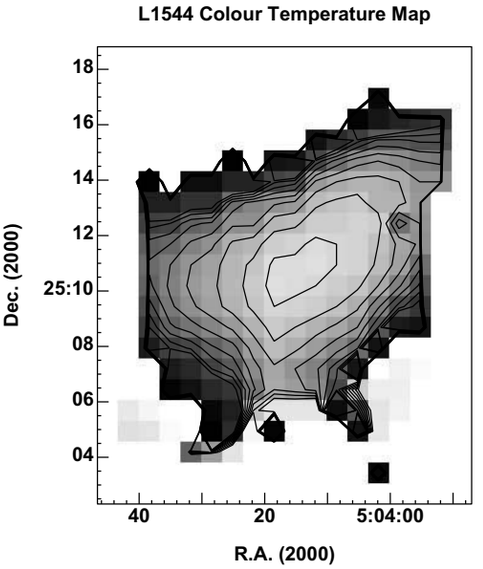

Fig. 4. Colour temperature map of L1544 based on a grey-body fit to the ratio of the 200 and 170μm data. A value of β=2 was used and a suitable background was subtracted. The colour temperature contours run from 19.5K at the centre to 23.5K at the edge (note that colour temperature is not the same as physical temperature)

5 Spectral Energy Distributions

We can measure the flux densities of our pre-stellar cores at 200 & 170μm and estimate upper limits to the flux density at 90μm, and hence construct the spectral energy distribution (SED) of each source. Figure 5 shows a plot of Log(S_ν) against Log(ν) for the same pre-stellar core, L1544, where the flux densities have been measured in its central region. The plot shows the ISOPHOT 90-μm upper limit and 170 & 200-μm detections, as well as the JCMT 850-μm and IRAM 1.3-mm detections.

We have fitted the source with a modified black-body function (often referred to as a grey-body) of the form:

$$S_\nu = \Omega\, B_\nu(T_{\rm d})\,(1 - \exp[-\tau_\nu]) \qquad (1)$$

where $B_\nu(T_{\rm d})$ is the blackbody function, Ω is the solid angle of the source, τ_ν is the optical depth ($=[\nu/\nu_c]^\beta$), ν_c is the critical frequency at which the optical depth is 1, and β is the dust emissivity index. We show one such fit as a solid line on Figure 5, which has T=11K, β=2, which is typical of our sources – all are <20K. Note that the temperature derived from fitting the full SED is less than that which was derived from simply ratio-ing the 170 and 200μm data above. When the data at other wavelengths are taken

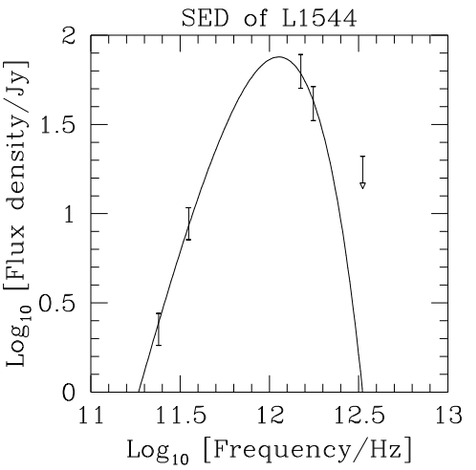

Fig. 5. Spectral energy distribution of the pre-stellar core L1544

into account, chiefly the 90μm upper limit, the best fit temperature decreases from 19K to 11K.

Comparison of Figure 5 with Figure 5(c) of [17] shows the importance of the ISO detections at 170 & 200μm. Whereas previously we could only place upper limits on the temperature of the dust, as constrained by the IRAS upper limits, we can now actually fit the peak of the modified black-body curve to the ISO data and obtain a temperature for the dust. We can also estimate the luminosity of L1544 by integrating under the curve in Figure 5. Doing this, we derive a value of $0.57 L_{\odot}$. Estimating the amount of heating such a core would receive from the inter-stellar radiation field alone [31,32], we derive a range of 0.45–0.75 $L_{\odot}$ for its re-radiated luminosity. Hence L1544 is consistent with having no significant central heating source.

6 Conclusions

We have shown ISOPHOT images of a pre-stellar core, which is typical of our sample of pre-stellar cores on the verge of forming stars. The cores are detected at the longer ISOPHOT wavelengths only, and remain undetected shortward of 100μm. This shows that all of the cores are very cold and typically <20K, indicating that they do not contain embedded, accreting protostars or young stellar objects, but rather are at the pre-collapse phase of evolution. Hence further study of these cores will increase our knowledge of the initial conditions of isolated protostellar collapse. Higher angular resolution observations, such as those provided by FIRST, will be required to carry out a similar study in densely clustered environments.

Acknowledgements

The authors would like to thank the staff of the ISOPHOT Data Centre at the Max Planck Institut fur Astrophysik, Heidelberg, and in particular Martin Haas, for assistance during the data reduction.

References

1. André, P., Ward-Thompson, D., Barsony, M. 2000, in 'Protostars and Planets IV', eds Mannings V., Boss A. P., Russell S. S., in press
2. André, P., Ward-Thompson, D., Barsony, M. 1993, ApJ 406, 122
3. Lada C. J., Wilking B. A., 1984, ApJ, 287, 610
4. Lada C. J., 1987, IAU Symp., 115, 1
5. André, P., 1994, in: 'The Cold Universe', eds Montmerle T., et al., 179, Editions Frontières, Gif-sur-Yvette
6. Ward-Thompson D., 1996, Ap&SS, 239, 151
7. André, P., Montmerle, T. 1994, ApJ 420, 837
8. Zhou S., Evans N. J., Koempe C., Walmsley C. M., 1993, ApJ, 404, 232
9. Ward-Thompson D., Buckley H. D., Greaves J. S., Holland W. S., André P., 1996, MNRAS, 281, L53
10. Shu F. H., Najita J., Galli D., Ostriker E., Lizano S., 1993, in: Levy E. H., Lunine J. I., eds, 'Protostars and Planets III', 3, University of Arizona Press, Tucson
11. Foster P. N., Chevalier R. A., 1993, ApJ, 416, 303
12. Tafalla M., Mardones D., Myers P. C., Caselli P., Bachiller R., Benson P. J., 1998, ApJ, 504, 900
13. Henriksen R. N., André P., Bontemps S., 1997, A&A, 323, 549
14. Safier P. N., McKee C. F., Stahler S. W., 1997, ApJ, 485, 660
15. Bontemps, S., Andre P., Terebey S., Cabrit S., 1996, A&A, 311, 858
16. Whitworth A., Summers D., 1985, MNRAS, 214, 1
17. Ward-Thompson, D., Scott, P., Hills, R.E., André, P., 1994, MNRAS, 268, 276
18. Myers P. C., Benson P. J., 1983, ApJ, 266, 309
19. Myers P. C., Linke R. A., Benson P. J., 1983, ApJ, 264, 517
20. Benson, P.J., Myers, P.C. 1989, ApJS 71, 89
21. Beichman, C.A. et al. 1986, ApJ 307, 337
22. Falgarone E., Puget J.-L., 1985, A&A, 142, 157
23. Chièze J. P., Pineau des Forêts G., 1987, A&A, 183, 98
24. Ciolek, G.E., Mouschovias, T.Ch. 1994, ApJ 425, 142
25. André, P., Ward-Thompson, D., Motte, F. 1996, A&A 314, 625
26. Ward-Thompson, D., Motte F., André, P. 1999, MNRAS, 305, 143
27. Bacmann A., André P., Puget J-L., Abergel A., Bontemps S., Ward-Thompson D., 2000, A&A, in press
28. Abergel A., et al., 1996, A&A, 315, 329
29. Ward-Thompson, D., André, P. 2000, in preparation
30. ISOPHOT Observer's Manual 1994, ESA
31. Mathis J. S., Mezger, P. G., Panagia, N. 1983, A&A, 128, 212
32. Perault M. 1987, Thèse d'Etat, Université de Paris

ISOPHOT Far-Infrared Survey of Nearby Molecular Clouds

Kimmo Lehtinen[1], Kalevi Mattila[1], Dietrich Lemke[2], Lauri Haikala[1,3], and Arto Heikkilä[1]

[1] Observatory, Tähtitorninmäki, P.O. Box 14, 00014 University of Helsinki, Finland
[2] Max-Planck Institut für Astronomie, Königstuhl 17, D-69117, Heidelberg, Germany
[3] Swedish-ESO Submillimetre Telescope, European Southern Observatory, Casilla 19001, Santiago, Chile

Abstract. We present results of a far-infrared molecular cloud mapping program which utilizes the PHT-P photometer and PHT-C cameras of the ISOPHOT instrument. ISO has enabled us to study the emission of very cold dust, $T_{\rm d} < 15\,{\rm K}$. The multi-wavelength observations between 3.6–200 μm allow to discern emission of different grain components, and to construct spectral energy distributions for embedded young stellar objects at far-IR wavelengths where their emission is at maximum. The extension up to 200 μm and the multi-filter coverage of the 60–200 μm wavelength range are essential improvements for study of physical properties of young stellar objects.

1 Introduction

The long wavelength and multi-filter capability of ISOPHOT, combined with its improved sensitivity and spatial resolution over IRAS, is utilized in studying the far-IR emission of molecular clouds and young stellar objects (YSOs): (I) The physical properties (e.g. temperature) of dust grains in molecular clouds, including the presence of different grain populations and differences in their distributions, as well as the presence of very cold dust with $T_{\rm d} < 15\,{\rm K}$. (II) Searches for newly formed embedded stars including the earliest stages of star formation ("pre-protostellar cores"). Analysis of their evolutionary status using the SEDs (spectral energy distributions). The dust distribution and dust properties near the newly formed stars.

2 Observations

The molecular clouds of the survey are listed in Table 1. We have performed both raster mapping and multi-filter photometry. Raster mapping applied the observing template P 22, i.e. a regular two-dimensional grid. For the C100 detector the steps in the satellite coordinate system (Y and Z) were 135" and 90", while for C200 detector they were 180" in both directions. Multi-filter

D. Lemke, M. Stickel, and K. Wilke (Eds.): LNP 548, pp. 317–324, 2000.

Table 1. Clouds included in the survey. The field center is in galactic coordinates. Diameter gives the size of the area mapped with ISOPHOT

Cloud	Field center		Diam.	Remarks	References
	l [°]	b [°]	[arcmin]		
Cha I Centre	297.2	-15.7	39.5	star forming (SF)	[16], [17]
Cha I South	297.3	-16.2	19.5	non-SF	
Thumbprint	302.6	-15.9	12	globule, non-SF	[4], [7], [8]
DC 303.8-14.2	303.8	-14.2	21	globule, SF	[6], [9], [11]
L 1780	359.1	36.7	40	translucent, non-SF	[13], [14]
L 183	6.1	36.7	30	dense, non-SF ?	[18], [19]
R CrA Centre	359.9	-17.9	25	SF	[1]
R CrA South	359.8	-18.4	12	non-SF	[1]
Draco Main	89.8	38.6	69	non-SF	[3]
Draco Rim	91.0	37.5	33×96	non-SF	[3]
L 1642	211.1	-36.5	80	translucent, SF	[5]

photometry was performed on L 183 using the following filters: ISOPHOT-P 3.6, 4.85, 7.3, 11.3, 11.5, 20, and ISOPHOT-C 60, 70, 100, 120, 135, 200. Linear raster scans were performed using observing template P 03 or P 22, with a two way path (2×10 positions) returning to the start position.

3 Results

Thumbprint Nebula (TPN) and DC 303.8-14.2 globules. Morphologically the surface brightness distributions at 100 and 200 μm are similar in TPN and DC 303.8-14.2 (excluding the IRAS source); the surface brightness increases towards the cloud center. No limb brightening is detected in either cloud. For more details we refer to [8] and [9].

DC 303.8-14.2 contains the embedded IRAS source 13036–7644. Fitting it with the footprint matrix for the C100 or C200 camera, fluxes of 12.4 and 53.7 Jy at 100 and 200 µm, respectively, are derived. For the SED of this source see [9].

The emission at 100, 200 and 1300 µm [2] wavelength is expected to originate from "classical" large dust grains which are at an equilibrium temperature with the radiation field, thus we have fitted these flux values with a modified blackbody of the form

$$F_\nu = B_\nu(T_\mathrm{d})\,(1 - \exp(-\tau_\nu))\,\Omega_\mathrm{s}\ . \tag{1}$$

where $B_\nu(T_\mathrm{d})$ is the Planck function at the dust temperature T_d, τ_ν is the optical depth which is assumed to vary with frequency as $\tau_\nu = (\nu/\nu_0)^\beta$, and Ω_s is the solid angle of the emitting region. The value β=2 gives the best fit. The results are $T_\mathrm{d} \approx$20 K, ν_0 corresponding to $\approx$ 184 μm (i.e. the wavelength where the optical depth is unity), and $\Omega_\mathrm{s} \approx$ 23 square arcsec. The IRAS source is classified as a YSO intermediate between Class 0 and I [11].

At 1.3 mm the emission is optically thin, therefore one can estimate the circumstellar dust mass

$$M_{cm} = S_\nu D^2 / R \kappa_\nu B_\nu(T_\mathrm{d}) \; . \tag{2}$$

where D is the distance, R is the dust-to-gas mass ratio and κ_ν is the mass absorption coefficient of the dust. Using D=200 pc, R=1/100 and κ_ν = 1 cm^2 g^{-1} one obtains $M_\mathrm{cm} \approx 0.2\,\mathrm{M}_\odot$, which is similar to the observed circumstellar masses of Class I sources.

Cederblad 110 star formation region in Chamaeleon I. Figure 1 shows contour maps of the Cederblad 110 region. Before ISO, three PMS stars (IRS 2, 4 and 6) [16] and a mm-continuum source (Cha-MMS1) [17] were known to exist in the region. The point sources are embedded in a SW to NE oriented elliptical ridge of emission related to a dense gas clump. We detect all these sources at all four wavelengths, except for IRS 2 at 200 μm.

The residual map at 80 μm shows a rather point-like source, located between IRS 4 and 6, 17σ above the noise. It is a potential new young stellar object. We designate this source as IRS 11. A 6.7 and 14.3 μm ISOCAM survey [15] has recently detected a point source at the same position.

The SED of the Cha-MMS1≡IRS 10 based on ISO results is shown in Fig. 1d. Cha-MMS1 meets all the criteria of a Class 0 object. It coexists with its more advanced neighbours in a small volume (diameter $<$ 0.1 pc) making the core of Cederblad 110 a region of ongoing active star formation [10].

Dark cloud L 183. The 100 and 200 μm maps peak at different positions (see [12], Fig. 1). The temperature map, derived from 100 and 200 μm maps (using $\beta = 2$) is shown in Fig.2. The temperature minimum at the center of the cloud, after subtracting the background emission, is about 12 K.

In Fig. 2 we show three examples of our multi-filter photometry at the center, edge and outskirts of the cloud. Multi-filter photometry between 100-200 μm is well fitted with $I \propto \nu^2 B_\nu(T_\mathrm{d})$ for T_d=12.0–13.7 K. Shorter wavelength bands indicate the presence of warmer dust, even in the direction of the cold core. This is evidence for a different dust population (smaller size).

We have detected two point sources in this cloud. The first one is coincident with the previously known sub-mm continuum source ([18], [19]), and it is located at the temperature minimum of the cloud. It is detected only at 200 μm. The SED of this source is shown in Fig. 3a. The flux densities have

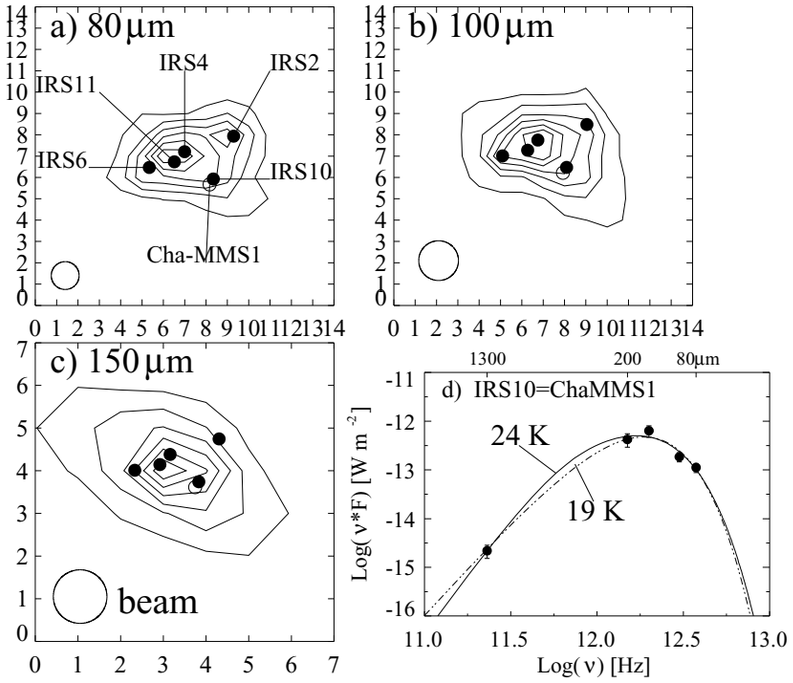

Fig. 1. Contour maps of the Cederblad 110 region at 80 (**a**), 100 (**b**) and 150 µm (**c**). The maps have been deconvolved using a MEM algorithm in the PIA. The filled circles mark the fitted positions of IRS 2, 4, 6, 10 and 11 in the 80 µm map. The open circle marks the position of the mm-continuum source Cha-MMS1a [17]. The axes are along the equatorial coordinates, and the units are map pixels (45 arcsec at 80 and 100 µm, 90 arcsec at 150 µm). Panel **d** shows the spectral energy distribution of Cha-MMS1≡IRS 10. The solid line is a modified blackbody fit with $\beta = 2.0$, and the dotted line is with $\beta = 1.0$. The 1-σ error bars are given

been fitted using (1), and give a dust temperature of about 12 K (see Fig. 3a). In can be seen that our 200 µm point is essential for an accurate estimate of the temperature. The bolometric luminosity of the source, derived by integrating over the fitted blackbody curve, is about 0.06 $L_\odot$. The total (gas + dust) mass of the circumstellar matter, derived using (2), is about 1.1 $M_\odot$. This source is a good canditate for being a pre-protostellar core or a Class 0 object.

The other, previously unknown source, is located at the maximum of the 100 µm surface brightness distribution. At 100 µm it is difficult to separate the fluctuating background and the source, so we consider the derived flux density as an upper limit. The derived color temperature has thus an upper limit of about 13 K. Figure 3b shows the SED and a modified blackbody fit (β=2). By integrating over the blackbody curve we derive a bolometric

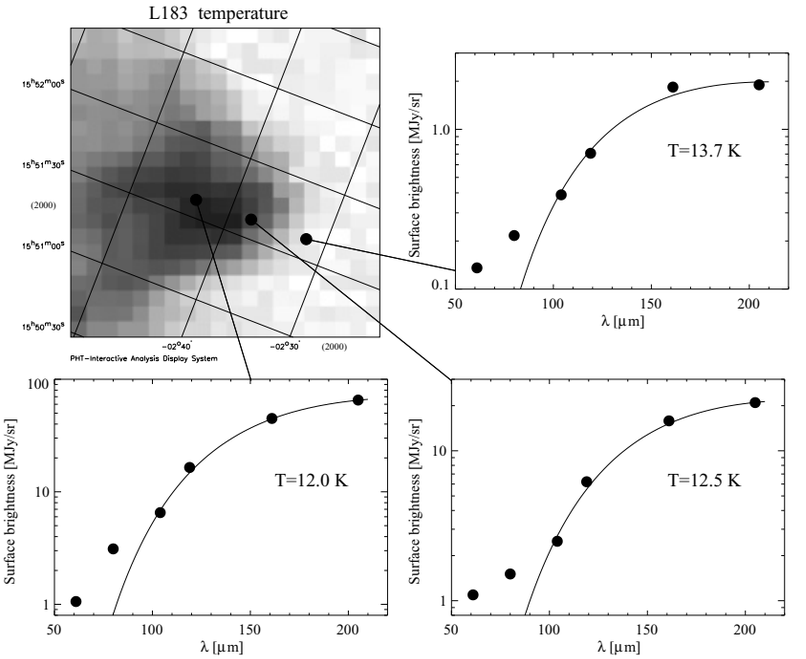

Fig. 2. At upper left is a grayscale map of the dust temperature in L 183, derived from 100 and 200 μm maps. Darker areas are colder. In other panels are shown some examples of our multi-filter photometry at different positions in the cloud. The solid line is a modified blackbody (ν^2 emissivity) fit to the four longest wavelengths. The derived blackbody temperatures are indicated

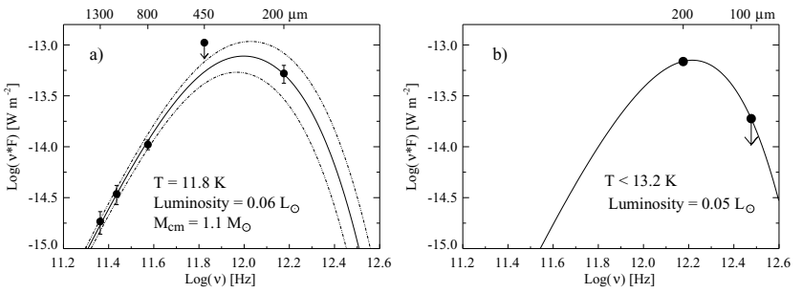

Fig. 3. (**a**) The spectral energy distribution of the possible pre-protostellar core in L 183. The 200 μm flux density value is our ISOPHOT measurement, others are from literature. The solid line is a modified blackbody fit to the data points. The dotted lines are blackbodies which have 1 K higher and lower temperatures than the solid line. (**b**) The spectral energy distribution of the new source in L 183 discovered by us. The solid line is a modified blackbody curve ($\beta = 2$), with a temperature equal to the colour temperature derived from the 100 and 200 μm flux densities

luminosity of about $0.05\,L_{\odot}$. With the present information it is not possible to determine the true nature of this source. It could be a gravitationally bound pre-protostellar clump, or a Class 0 protostar.

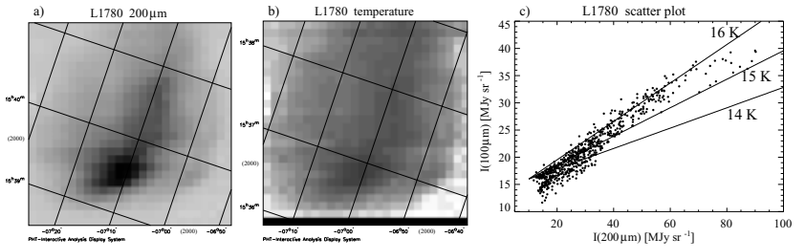

Fig. 4. Grayscale map of 200 μm surface brightness of L 1780 (**a**). Darker areas are brighter. In (**b**) is shown the temperature derived from 100 and 200 μm maps. Darker areas are colder. A scatter plot of 100 and 200 μm surface brightness values, together with relations for a modified blackbody at different temperatures, is shown in (**c**)

Translucent cloud L 1780. Figure 4 shows the 200 μm surface brightness and the temperature maps (ν^2 emissivity) of L 1780. The 100 and 200 μm surface brightness distributions are very similar. Consequently, the dust temperature is rather uniform over the cloud. The temperature minimum, ∼15 K, is located at the western head of the cloud. This is clearly higher than in L 183 or other clouds with higher extinction. In Figure 4c we show a scatter plot for 100 and 200 μm surface brightness, demonstrating how accurately the temperature can be determined.

An extended lower extinction halo around the central core is seen at 100 and 200 μm and also in extinction and optical scattered light [14].

Dark cloud R Corona Australis. Two areas in this cloud were mapped by ISO: The 'active' part (here denoted CrA Center) contains two star clusters with pre-main sequence stars and younger dust enshrouded protostellar objects. The 'quiescent' part (here denoted CrA South) is centrered on a cold molecular cloud core without any signs of star-formation activity.

Contour maps of the 100 μm emission from CrA Center, and the 200 μm emission from Cra South are shown in Figs. 5a and b, respectively. In the CrA Center, the 100 μm peaks in the TY CrA area, while the 200 μm emission reaches its maximum in the Coronet area. CrA South does not contain any point sources. However, a pronounced 200μm excess coincides with the centre of this core, suggesting the presence of a very cold clump ($T_{dust} \approx 12$ K).

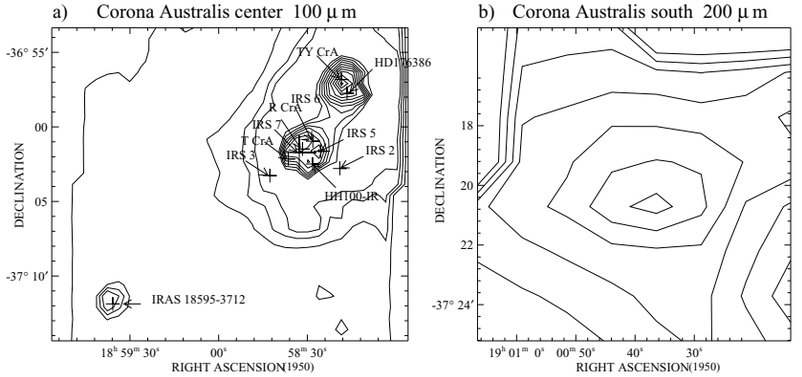

Fig. 5. Contour maps of 100 μm emission from CrA Center (**a**), and of 200 μm emission from CrA South (**b**). Some YSOs in CrA Center are indicated with arrows

4 Conclusions

ISO observations of physically different (dense, translucent, star forming and non-star forming) molecular clouds have given new information about properties of dust grains in these clouds and about YSOs which were born inside these clouds.

In dense dark clouds the minimum dust temperature is found to be rather constant from cloud to cloud, with $T_{\mathrm{d}ust} \approx 12\,\mathrm{K}$. The dust temperature in the translucent cloud L 1780 is rather uniform with a minimum of about 3 K higher than in dark clouds, showing that UV-optical radiation is able to penetrate the cloud while suffering only a modest amount of extinction. Observations of L 183 verify that 100 μm emission does not trace very cold dust. Multi-filter photometry of L 183 shows that at wavelengths longer than about 100 μm the observations are well described by a single modified blackbody emission from "classical" grains, while at shorter wavelengths other grain components start to dominate. This "excess" emission is detected even in the coldest part of the cloud.

We have searched the clouds for protostellar cores and embedded YSOs. In Cederblad 110 we have detected five YSOs which are at different evolutionary phases. One of the YSOs has all the characteristics of a Class 0 object. With the ISO observations we can determine accurately the temperature, and thus the mass of the circumstellar matter of these sources. The dark cloud L 183 shows no signs of star formation at optical, near-IR or even in the IRAS 100 μm observations, but we have detected at 200 μm two point-like sources, both of which are candidates for being pre-protostellar cores.

We have studied the connection of dust distribution and dust properties to the presence of newly-formed stars: e.g. in Cederblad 110 the YSOs are still embedded in their cold parental material which is detected by far-infrared emission.

Acknowledgements

We thank P. Persi, A.R. Marenzi and G. Olofsson for the permission to quote their ISOCAM data before publication.

References

1. Harju J., Haikala L.K., Mattila K. et al. (1993) Large scale structure of the R Coronae Australis cloud core. A&A 278, 569
2. Henning Th., Pfau W., Zinnecker H., Prusti T. (1993) A 1.3-millimeter Survey of Circumstellar Dust around Young Chamaeleon Objects. A&A 276, 129
3. Herbstmeier U., Heithausen A., Mebold U. (1993) Tracing the molecular hydrogen content of the Draco nebula. A&A 272, 514
4. Juvela M., Lehtinen K., Paatero P. (1996) The use of Positive Matrix Factorization in the analysis of molecular line spectra. MNRAS 280, 616–626
5. Laureijs R. J., Mattila K., Schnur, G. (1987) IRAS and optical observations of the high-latitude dust cloud LYNDS 1642. A&A 184, 269
6. Lehtinen K., Higdon J.L. (1999) Centimeter wavelength observations of young stellar objects in the dark cloud DC 303.8-14.2. A&A in press
7. Lehtinen K., Mattila K., Schnur G.F.O, Prusti T. (1995) The Thumbprint nebula: the distribution of molecular gas and dust in a regular Bok globule. A&A 295, 487–503
8. Lehtinen K., Lemke D., Mattila K., Haikala L.K. (1998) Far-infrared ISOPHOT observations and the energy balance of a quiescent globule. A&A 333, 702–708
9. Lehtinen K., Lemke D., Mattila K. (1999) ISOPHOT far-infrared observations of the dark cloud DC 303.8-14.2. In: Cox P., Kessler M F. (Eds.) The Universe as seen by ISO, Paris, France, October 20–23, 1998. ESA SP-427, 695–697
10. Lehtinen K., Haikala L.K., Mattila K., Lemke D. (1999) Far infrared observations of Cederblad 110: A Class 0 protostar and a group of young stellar objects. A&A to be submitted
11. Lehtinen K., Mattila K., Lemke D. (1999) ISO far-infrared observations of the dark cloud DC 303.8-14.2. A&A, in preparation
12. Lemke D. (1998) Observations with ISOPHOT. In: Anderson J. (Ed.) Highlights of Astronomy, Vol. IIB, Kluwer, 1116
13. Mattila K. (1986) Radio observations of CH in three dark nebulae and the correlation of CH with optical extinction and molecular hydrogen. A&A 160, 157
14. Mattila K. (1979) Optical extinction and surface brightness observations of the dark nebulae LYNDS 134 and LYNDS 1778/1780. A&A 78, 253
15. Persi P., Marenzi A.R., Olofsson G. et al. (1999) A&A, to be submitted
16. Prusti T., Clark F.O., Whittet D.C.B. et al. (1991) Infrared objects near Cederblad 110. MNRAS 251, 303
17. Reipurth B., Nyman L.-Å., Chini R. (1996) Protostellar Candidates in Southern Molecular Clouds. A&A 314, 258
18. Ward-Thompson D., Scott P.F., Hills R.E., Andrè P. (1994) A submillimetre continuum survey of pre-protostellar cores. MNRAS 268, 276–290
19. Ward-Thompson D., Motte F., Andrè P. (1999) The initial conditions of isolated star formation - III. Millimetre continuum mapping of pre-stellar cores. MNRAS 305, 143–150

A Deep Survey with ISOCAM of the Chamaeleon I Dark Cloud

Paolo Persi

Istituto Astrofisica Spaziale, CNR, Area di Ricerca Roma Tor Vergata, Via del Fosso del Cavaliere, 00133 Roma, Italy

Abstract. A deep survey at 6.7 and 14.3 μm has been undertaken with the infrared camera (ISOCAM) aboard of the ISO satellite of the southern hemisphere dark cloud Chamaeleon I. A total of 282 mid–IR sources have been detected in an area of 0.59 sq.deg. of the cloud. From an analysis of the ISOCAM colour/magnitude diagram and of the near-infrared colour indices J-K_s vs K_s -$m_{6.7}$, 34 new members of the dark cloud have been found. Several of these newly discovered young stars are relatively faint suggesting a population in Cha I of very low mass stars, probably brown dwarfs in their early contraction phases as shown by the luminosity function derived for 108 members of Cha I.

1 Introduction

The complete census of the young stellar population in molecular clouds and dark clouds is fundamental in understanding the processes of star formation. Due to the strong wavelength dependence of the cloud extinction, this can be obtained with very deep surveys in the infrared spectral region. The infrared camera ISOCAM [1] aboard of the Infrared Space Observatory [2] with its moderate spatial resolution and high sensitivity in the mid–infrared represents a powerful tool to detect very low-luminosity young stellar objects still embedded in their parental cloud. This will allow to extend the study of the luminosity function and the mass distribution (IMF) in molecular clouds, including very low-mass young stars near or below the hydrogen burning limit.

For this purpose, a deep survey with ISOCAM of nearby star forming regions has been conducted as part of the ISO central programme *L-NORDH.SURVEY*, in the two broad band filters LW2(5-8.5 μm) and LW3(12-18 μm), designed to avoid the silicate features at 10 and 20 μm [3], [4]. The list of the observed nearby molecular clouds is reported in Table 1. In summary, the survey was made with a p.f.o.v of 3 or 6 arcsec in raster scanning mode, and the total observed area for the 15 clouds of Table 1, was $\sim$ 3.7 sq deg. at a mean sensitivity limit of approximately 1.3 mJy (1 σ) at 6.7 μm and 2.3 mJy (1 σ) at 14.3 μm.

This program is conducted by the ISOCAM star formation working group, and the results for a few molecular clouds of Table 1 such as R CrA, Serpens, ρOph, and Cha I have been published or submitted for publication in international journals ([5],[6],[7],[8]).

D. Lemke, M. Stickel, and K. Wilke (Eds.): LNP 548, pp. 325–332, 2000.

In the present paper, I report a summary of the results of the ISOCAM survey of the southern hemisphere dark cloud Chamaeleon I (Cha I). A detailed presentation and discussion of the ISOCAM data of this region is given in [8]. In Sect.2 a brief review of the previous observations of Cha I is reported, while in Sect.3 the analysis of the ISOCAM colour/magnitude diagram and the cross-correlation between the ISOCAM data and the DENIS near-IR survey of the region is reported. Finally, in Sect.4 the luminosity function obtained for all the detected members of the dark cloud is discussed and the energy distribution of one of the faintest detected young stellar object is illustrated.

Table 1. List of the ISOCAM Survey of Molecular Clouds

Molec.Cloud	α(2000) h m s	δ(2000) ° ′ ″	Area sq.deg.	No.rasters
NGC 1333	03 28 52	31 21 10	0.19	5
L1551	04 31 39	18 11 09	0.18	6
L1527/TMC1	04 39 50	26 00 10	0.26	5
L1641	05 36 19	-06 22 13	0.02	1
NGC 2023	05 41 37	-02 15 24	0.43	1
LBS23	05 46 11	-00 11 04	0.14	1
NGC 2071	05 46 25	00 23 35	0.28	3
NGC 2068	05 46 37	00 04 44	0.15	1
Cha I	11 07 00	-77 18 19	0.59	5
Cha III	12 52 53	-79 38 18	0.10	1
Cha II	13 00 47	-77 06 09	0.24	1
ρOph	16 28 22	-24 36 36	0.70	9
Serp.	18 29 48	-01 16 04	0.22	4
R CrA	19 00 06	-36 58 17	0.45	4
Cep A	22 56 17	62 02 33	0.17	6

2 Chamaeleon I Dark Cloud

Chamaeleon I is part of a complex of three molecular clouds located in the southern hemisphere. This dark cloud is one of the closest active star forming region. Its distance D=160 pc [9], the high galactic latitude (b$\sim$ -16°) and the

relatively low extinction make this cloud one of the most interesting target to investigate the formation of low-mass stars.

Cha I has a size of approximately $1^\circ \times 2^\circ$, and a total mass of $\sim 450\ M_\odot$ [10], and is characterized by the presence of three bright reflection nebulae (Ced 110,111,and 112) illuminated by Herbig Ae stars, four Herbig-Haro objects and a T-Tauri association [11]. Figure 1 shows the optical and the IRAS image at 100 μm of the region observed with ISOCAM.

In the northern part of the dark cloud, ISOCAM has detected a new Class I source [12] located at the center of a bipolar CO outflow [10] that is probably the engine of this outflow.

The stellar population in Cha I were in the past studied by means of H_α and X-ray surveys, near–IR observations, and IRAS data (see i.e. [13], [14], [15], [16]). All these surveys were limited to the study of pre-main-sequence stars with masses higher than $\sim 0.3 M_\odot$. The presence of a very low-mass young stellar population near or below the hydrogen burning limit (M=$0.08 M_\odot$) was recently found in the central region of Cha I by means of a very deep H_α survey [17], and in the northern part of the cloud using deep near–IR images [12].

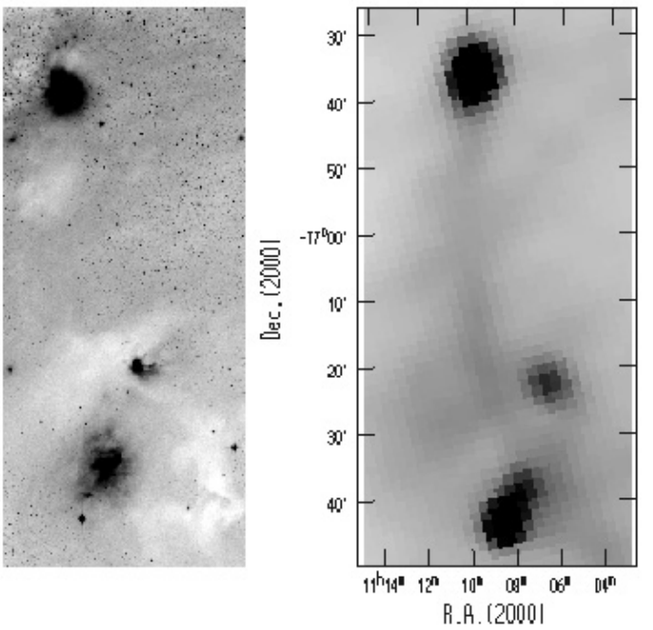

Fig. 1. Optical image (left) and IRAS image at 100 μm (right) of Cha I

3 Results

3.1 ISOCAM Survey

Chamaeleon I has been mapped in five separate but overlapping main rasters for a total of 0.59 sq.deg at 6.7 and 14.3 μm with a p.f.o.v = 6 arcsec. The data analysis of the ISOCAM images, the calibration and the photometry of the detected sources are described in [8]. At the detection limit of $\sim$ 2.0 mJy and 3.9 mJy (3σ) for LW2 and LW3 respectively, a total of 282 sources were found with approximately 37% measured in both filters. All the previously identified members in the region (74 sources) were detected by ISOCAM. For the 103 sources detected at LW2 and LW3, the colour/magnitude plot $m_{14.3}$ versus $m_{6.7}$-$m_{14.3}$ is derived (Fig.2a). This diagram is a powerful tool to distinguish sources with and without IR excess [5], [18]. From Fig.2a, a clear separation between sources with color indeces around zero, in which the mid–IR emission is due to the photosphere of the star, and the sources with a mid–IR excess due mainly to the circumstellar dust material around the young star, can be made.

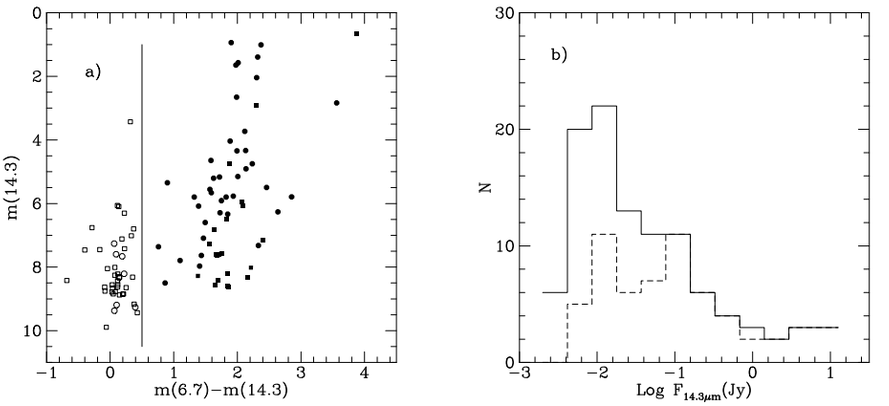

Fig. 2. (**a**)ISOCAM colour/magnitude diagram for the sources detected in Cha I. Filled and open circles are known members of the cloud, while the open and filled squares are new detections. (**b**) Flux distribution at 14.3 μm of all the detected sources (full line) and of the sources with mid–IR excess (dashed line)

Of the 57 sources showing mid–IR excess, 17 are new detections that represent new members of Cha I. The 14.3 μm flux distribution of Fig.2b indicates that the majority of the new sources have a peak around 10 mJy (dashed line in Fig.2b), and are weaker that the previous identified members. In addition a consistent number of faint sources have not mid–IR excess (full line in Fig.2b). As an example in Fig.3 is reported the ISOCAM image at

6.7 μm of the northern part of Cha I. The extended and bright source in Fig.3 coincides with the Herbig Ae star HD 97300 illuminating the reflection nebula Ced 112.

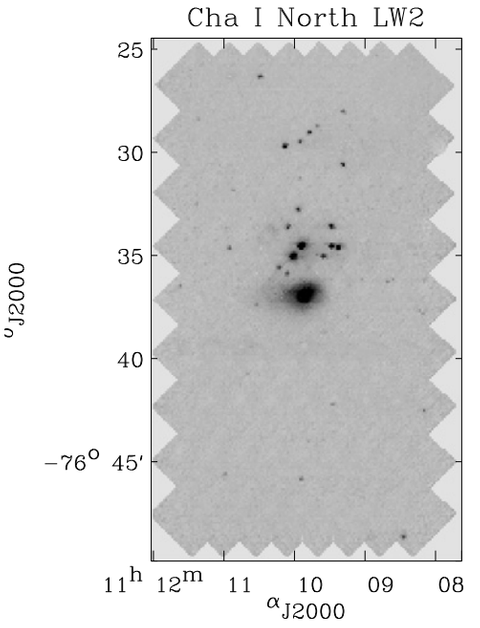

Fig. 3. ISOCAM image at 6.7 μm of the northern part of Cha I

3.2 Comparison Between ISOCAM and DENIS Survey

From the comparison between the DENIS survey of Cha I obtained in the I, J and K_s band [15] and the ISOCAM survey, it is found that 96% of the ISOCAM sources have a near–IR counterpart. Sometimes the identification between ISOCAM and DENIS is uncertain because of the presence of more than one near–IR source surrounding the ISOCAM position that is accurate within ± 5 arcsec. In order to understand the nature of the sources detected only at 6.7 μm, the analysis of the two colour diagram J-K_s vs K_s - $m_{6.7}$ has been made. This diagram illustrated in Fig.4a indicates that all the sources with a mid-IR excess are at the right of the reddening line (dashed line in Fig.4a) determined by a best fit of the identified members of the cloud without IR excess. The slope of this line is consistent with a normal reddening law at

6.7 μm with $A_{6.7} \sim 0.1\ A_K$. At least 24 sources detected only at 6.7 μm and too faint for the LW3 filter show also an intrinsic K_s -$m_{6.7}$ excess (crosses in Fig.4a), and can be considered as new members of Cha I.

The infrared spectral index α_{IR}=dlog(λF_λ)/dlog(λ) computed from 2.2 and 14.3 μm for the members of Cha I results to be well correlated with the colour index K_s - $m_{6.7}$ (Fig4b). This index is normally used to give a classification of young stellar objects [19]. As observed from Fig.4b the majority of these members have an infrared spectral index consistent with that of Class II sources in which the observed flat spectrum is the result of accretion processes in an active circumstellar disk.

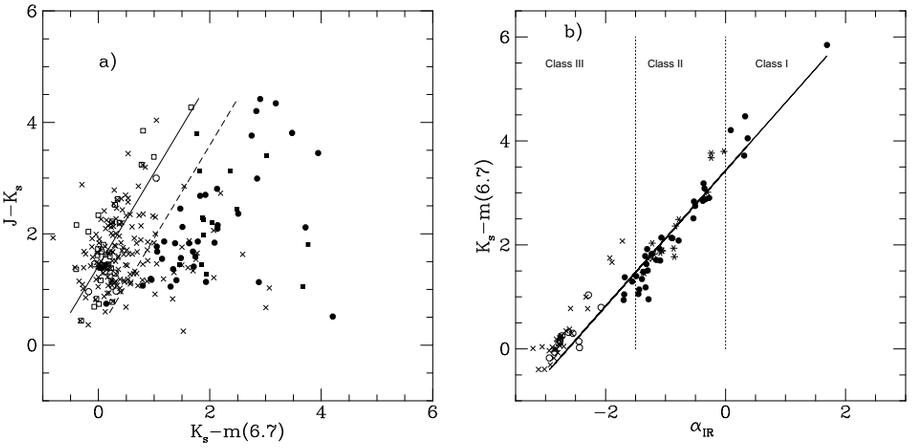

Fig. 4. (**a**) Two colour diagram of the ISOCAM sources. Crosses are sources detected only at LW2. (**b**) K_s-$m_{6.7}$ vs α(IR) plot

4 Luminosity Function

The stellar luminosities have been computed for 108 members of the clouds including the 34 new sources. For the sources observed in the I and J bands the following relationship :

$\log L(L_\odot) = 1.86 - 0.4(\text{J-DM-A}_J) - 0.4\ BC_J$

is used with DM=6.02 (distance modulus), $A_J = 1.41[(\text{I-J}) - (\text{I-J})_0]$, and J the measured magnitude in the J band . The intrinsic colours $(\text{I-J})_0$, the bolometric corrections in J, BC_J, and the reddening law are taken from [20], [21]. For sources not detected in I and J, the correlation found in Cha I between the stellar luminosity and the flux at 6.7 μm has been adopted [8].

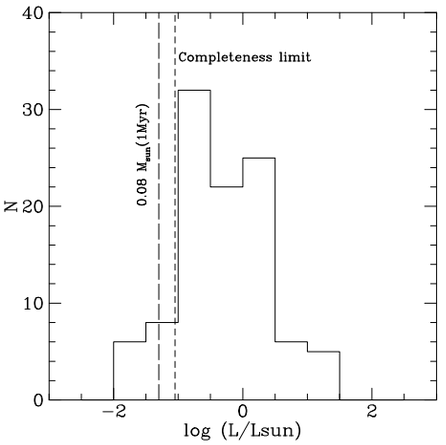

Fig. 5. Luminosity function of 108 members of Chamaeleon I dark cloud

Figure 5 shows the luminosity function (LF) for the 108 members of Chamaeleon I. The completeness limit corresponding to about $0.09 L_{\odot}$ is reported in the figure, together with the brown dwarf limit (dashed line in Fig.5) computed according to the models for an age of 1 million years [22]. The derived LF indicates that a number of young objects below the brown dwarf limit are present in Cha I.

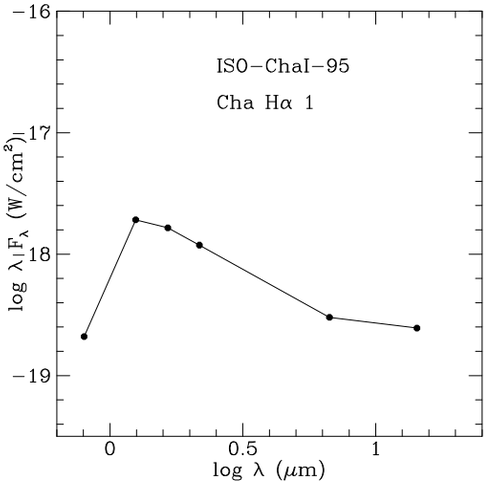

Fig. 6. Energy distribution of the young brown dwarf ISO–ChaI–95

One of this very faint source, ISO–ChaI–95 ([8]), has been identified with the young brown dwarf Cha Hα1 with X-ray emission [17]. Its spectral energy distribution (SED) obtained combining the ISOCAM observations with the near-IR photometry (Fig.6) indicates a prominent mid–IR excess of the source and the lack of the near–IR excess. A model to explain this SED is under study.

In summary, 282 ISOCAM point sources have been found in Cha I, and 34 new members are added to the dark cloud. The majority of the members in Chamaeleon I are Class II sources, and a number of young stars have masses below the brown dwarf limit.

References

1. Cesarsky, C. J., Abergel, A. et al. (1996) Astron.Astrophys. 315, L32
2. Kessler, M. F., Steinz, J.A. et al. (1996) Astron.Astrophys. 315, L27
3. Nordh, L., Olofsson, G. et al. (1998) In:*Star Formation with the Infrared Space Observatory (ISO)* J.L.Yun and R.Liseau (Eds.), ASP Conf.Ser.,vol.132, p.127
4. Olofsson, G., Kaas, A. A. et al. (1999) In: *The Universe as seen by ISO* P.Cox and M.Kessler (Eds.), ESA SP-427, 459
5. Olofsson, G., Huldtgren, M. et al. (1999) Astron.Astrophys. 350, 883
6. Kaas, A. A., Olofsson, G., et al. (1999) In: *The Universe as seen by ISO* P.Cox and M.Kessler (Eds.), ESA SP-427, 493
7. Bontemps, S., Nordh, L., et al. (1999) In: *The Universe as seen by ISO* P.Cox and M.Kessler (Eds.), ESA SP-427, 475
8. Persi, P., Marenzi, A. R., et al. (1999) submitted in Astron.Astrophys.
9. Whittet, D., C., B., Prusti, T., et al. (1997) Astron.Astrophys. 327, 1194
10. Mattila, K., Liljestrom, T., Toriseva, M., (1989) In: *Low mass star formation and pre-main-sequence objects* B.Reipurth (Ed.)ESO Conf.Ser.33, 153
11. Hyland, A. R., Jones, T. J., Mitchell, R. M., (1982) Mon.Not.R.astr.Soc. 201, 1095
12. Persi, P., Marenzi, A. R., et al. (1999) Astron.J. 117, 439
13. Gauvin, L. S., Strom, K. M., (1992) Astrophys.J. 385, 317
14. Lawson, W. A., Feigelson, E. D., Huenemoerder, D. P., (1996) Mon.Not.R.astr.Soc. 280, 1071
15. Cambrésy, L., Copet, E., et al. (1998) Astron.Astrophys. 338, 977
16. Prusti, T., Clark, F., et al. (1991) Mon.Not.R.astr.Soc. 251, 303
17. Comeron, F., Rieke, G. H., Neuhauser, R., (1999) Astron.Astrophys. 343, 477
18. Nordh, L., Olofsson, G., et al. (1996) Astron.Astrophys. 315, L185
19. Lada, C. J., (1987) In: *Star Forming Regions* IAU Symp.115, p.1
20. Kenyon, S.J., Hartmann, L., (1995) Astrophys.J.Suppl. 101, 117
21. Rieke, G. K., Lebofsky, M. J., (1985) Astrophys J. 288, 618
22. D'Antona, F., Mazzitelli, I., (1998) Mem.Soc.Astron.Ital. 68, 807

Search for Very Young Massive Stars

Thomas Henning[1], Randolf Klein[1], Ralf Launhardt[2], Katharina Schreyer[1], and Bringfried Stecklum[3]

[1] Astrophysical Institute and University Observatory (AIU), D-07745 Jena, Schillergässchen 3, Germany
[2] Caltech, Pasadena, CA 91125, USA
[3] Thuringian State Observatory, Sternwarte 5, D-07778 Tautenburg, Germany

Abstract. The paper will review the observational properties of very young massive stars. Strategies to find the earliest stages of massive star formation will be discussed. Results of ISO observations of very young massive stars will be presented including the spectral energy distribution of the massive class 0 object CB 3-mm.

1 Introduction

Stars with masses larger than 8-10 $M_\odot$ play an important role in galactic lifecycles: they dominate the return of mass, momentum, and energy from the stellar component of a galaxy to the interstellar medium. They are strong emitters of ionizing Lyman continuum radiation. During their evolution, massive stars enrich the gas of a galaxy with heavy elements. There are dramatic differences between galaxies with a low or high fraction of luminous O-stars. The global effects of massive star formation can be seen best in the case of ultra-luminous infrared galaxies (ULIRGs) where massive star formation dominates the overall energetics in most objects with luminosities less than 10^{12} $L_\odot$ [24]. The importance of the effect of massive star formation is also well known from observations of HII regions in our own Galaxy and the Magellanic Clouds.

In contrast to the importance of the formation of massive stars to the evolution of galaxies, the birth process is not well understood. Both non-spherical accretion of matter and the coalescence of intermediate-mass stars have been proposed as formation scenarios [18,2]. O and B stars can spend a considerable fraction of their lifetime deeply embedded in their parental molecular cloud cores [1]. In this stage they can only be detected by radio or infrared observations. Very young massive stars are among the most luminous far-infrared sources in our Galaxy. However, the nearest young massive stars are located at larger distances than the closest regions of low-mass star formation, are formed in association with other high- and low-mass stars and strongly influence their environment by stellar winds and radiation pressure. Therefore, high spatial resolution is required for a deeper understanding of massive star formation (see, e.g. [10]).

The strong infrared radiation and the required spatial resolution seems to speak against using the instruments aboard the Infrared Space Observa-

D. Lemke, M. Stickel, and K. Wilke (Eds.): LNP 548, pp. 333–340, 2000.

tory ISO for observations of galactic massive young stellar objects (YSOs). However, the ISO spectrometers provided the first complete infrared spectrum of a massive molecular cloud core — M 17-North [15]. In addition, an infrared spectrum of the LMC protostar region N 160A-IR could be obtained [16]. Furthermore, we could identify the object CB3-mm (LBN 594) as a very good candidate for a prototype massive class 0 object [22].

We will first discuss the observational properties of very young massive stars and discuss the appearance of their earliest phases. Later, we will summarize the results of our ISO observations and discuss in more detail the object CB3-mm.

2 Properties of Very Young Massive Stars

Very young massive stars are characterized by spectral energy distributions (SEDs) which strongly rise in the infrared toward longer wavelengths and peak around 100 μm [6,12]. The fluxes at these far-infrared wavelengths are usually 3-4 orders of magnitude above the free-free emission extrapolated from the radio observations. The objects are internally heated and their SEDs cannot be fitted by a single modified Planck function. In addition, strong molecular ice (H_2O, CO, CO_2) and silicate absorption features are often observed, which points to a high optical depth of the surrounding material. However, there are strong differences of the gas/solid abundance ratios between individual sources indicating enhanced evaporation of ices during the evolution of the objects [34]. The unidentified infrared bands (UIBs) get prominent and can be used as important indicators of massive star formation. In the radio range, the massive YSOs are observed as ultracompact HII regions. Based on the IRAS colours of known ultracompact HII regions, Wood & Churchwell (1989) [35] developed a two-colour selection criterion and selected a total of 1717 embedded massive star candidates from the IRAS Point Source Catalog (see Fig. 1). Later on it turned out that some of these candidates are diffuse HII regions, nearby late B stars or objects not really deeply embedded in molecular cloud cores (see, e.g. [20]).

A compilation of massive YSOs together with molecular line and continuum data can be found in Chan et al. (1996) [5]. Most of the well-known massive YSOs are very bright at far-infrared wavelengths, having fluxes above 500 Jy at 100 μm. We have investigated a number of such objects in much detail during the last years by means of their infrared and millimetre continuum emission, molecular lines indicating the presence of dense cores and outflows, and H_2O maser emission (e.g. [14,32,30]). A detailed study of the temperature and density structure of the envelopes of deeply embedded massive YSOs has been performed recently by van der Tak et al. (2000) [33].

There is the strong expectation that the earliest phases of massive stars are associated with hot molecular cloud cores [20]. An increase of the temperature measured toward the centre of some of these cores indicates that

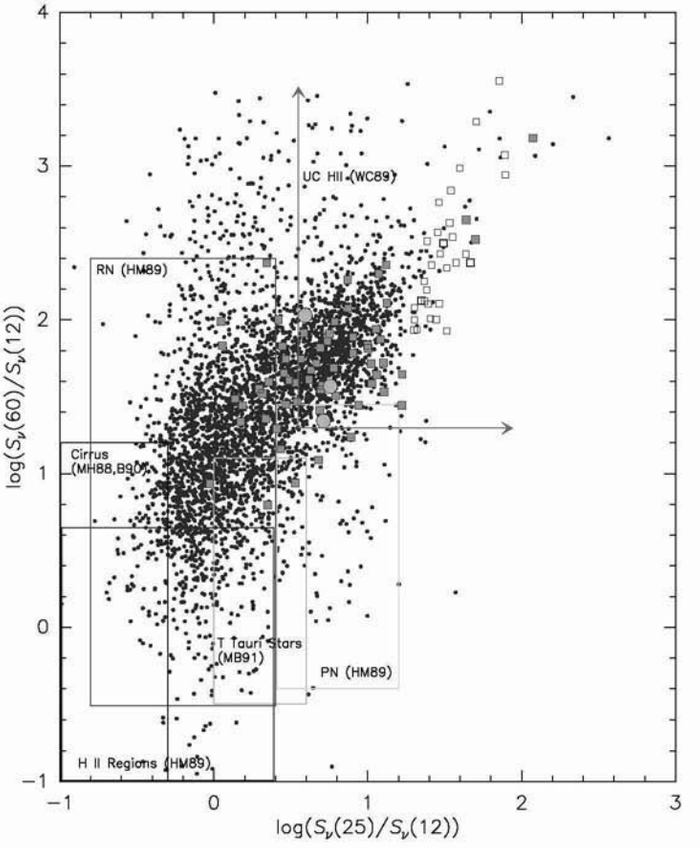

Fig. 1. Colour-colour diagram of luminous IRAS sources together with the colour boxes for planetary nebulae, reflection nebulae, and HII regions [17], T Tauri stars [29], cirrus [26,3], and ultracompact HII regions [35]. The filled squares indicate the positions of our sample of 67 northern IRAS sources. The open squares represent the southern sample compiled by Osterloh et al. (1997) [30]. The three circles stand for the three galaxies with fluxes larger than 500 Jy at 100 μm (M 82, NGC 253, and NGC 4945).

they are internally heated [4]. Some of these objects are characterized by a black body-type SED which is typical of deeply embedded class 0 objects, which have most of their mass still in the envelope and show already outflow activity. Molinari et al. (1998a) [27] detected the prototype massive class 0 object IRAS 23385+6053. Another example of such a source will be discussed in Sect.4. In the earliest stages of the evolution of a massive YSO, the radio emission is expected to be suppressed by the accretion flow [36,13,28,25]. Therefore, these objects should have no detectable, or only weak, thermal emission from ionized gas. Examples are W51:e8, IRAS 23385+6053, G75.78+0.34mm,

G34.24+0.13mm, and NGC6334F:mm (see the review by Garay & Lizano 1999 [11] for references). An effective search for such objects can be performed at mid-infrared wavelengths where one can efficiently discriminate between objects associated with ultracompact HII regions and such objects with suppressed ionized regions by observing both in the mid-infrared continuum and in the [NeII] line (see Fig. 2). We should note that possible other reasons for a low radio free-free mission are the absorption of ionizing UV photons by circumstellar dust grains or the fact that several stars of lower luminosity are the embedded sources.

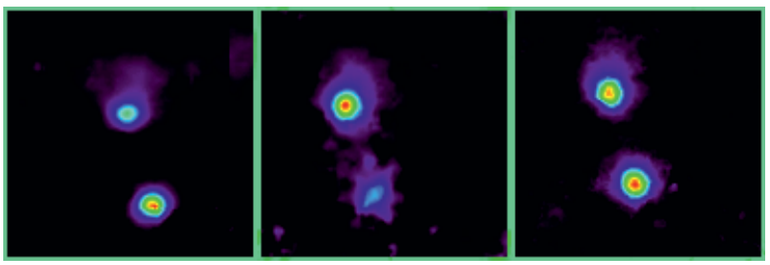

Fig. 2. Mid-infrared observations of the region G345.00-0.22. There are two objects which are equally bright in the continuum, but show very different fluxes in the [NeII] line. Left: nn1 filter 7.91-8.87 μm, Centre: [NeII] filter 12.66-13.03 μm, Right: SiC filter 10.3-13.00 μm. Observations were performed with TIMMI at the 3.6 m telescope of ESO in June 1998.

3 ISO Spectroscopy and Imaging of Massive YSOs

The spectrometers SWS and LWS aboard ISO have been used to obtain a complete infrared spectrum from 2-200 μm of the massive molecular cloud core M 17-North [15]. In addition, ISOCAM CVF spectra were obtained at several positions over the northern part of M 17 [19]. In addition, we obtained an SWS spectrum of the LMC protostar region N 160A-IR [16]. We will not repeat all the material given in the original papers, but will summarize the lessons which have been learned from studying these Rosetta stones. The two objects have only faint near-infrared counterparts because of the high extinction ($A_V \sim$ 40-50 mag from the centre of the cloud cores). Their SEDs rise steeply towards longer wavelengths and have their maxima around 100 μm. The objects are easily detectable by their rather high 1.3 mm continuum fluxes. The SEDs cannot be represented by single blackbody curves or the radiation of isothermal slabs of finite optical depth. The cloud core M 17-North is surrounded by ionized gas and picks up a lot of flux from surrounding sources ($L \sim 2\text{-}6 \cdot 10^4$ $L_\odot$), whereas the central luminosity amounts to only 1500 $L_\odot$.

The SEDs are characterized by the presence of the unidentified infrared bands (UIBs) which share the properties of UIBs observed in the spectra of galactic HII regions. The variations of the UIBs are related to the nature of the radiation field. The analysis of the band spectra favours molecules (e.g. molecules related to the PAHs) over grains as carriers of the bands.

An interesting result of the observations of M17-North and related massive star-forming regions (see, e.g., the region around G 45.45+0.06 [9]). is the detection of strong mid-infrared sources in the fields which are neither associated with a strong near-infrared source nor with a strong millimetre continuum object. Such objects could be good candidates for young stellar objects surrounded by disk-like structures.

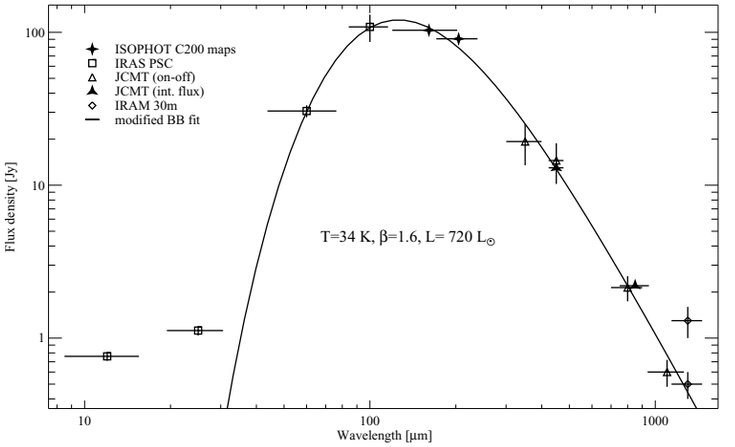

Fig. 3. Spectral energy distribution of CB 3-mm together with a modified blackbody curve (1-exp(-$\tau(\nu)$)) B_ν(T) with $\tau(\nu) \propto \nu^\beta$.

4 The Luminous Protostar CB 3-mm

The millimetre source CB 3-mm resembles in many aspects the prototype massive class 0 object IRAS 23385+6053. The dark cloud CB 3 is associated with the optical nebula LBN 594 and the cold and luminous IRAS point source 00259+5625 (for a discussion of the infrared morphology of the region we refer to Launhardt et al. 1998 [22]. Due to its optical appearance, this object was classified as a Bok globule (CB 3, [7]). However, it turned out that CB 3 is clearly distinguished from "ordinary" low-mass globules by its larger distance, higher mass and other physical parameters (Launhardt & Henning 1997). CB 3 is located at the inner side of the Perseus arm at a

distance of about 2.5 kpc. The compact millimetre source CB 3-mm, located in CB 3, is associated with a well-collimated and very powerful outflow [8,23].

Diffraction-limited photometric maps were obtained with ISOPHOT using the C 200 2x2 array. Together with IRAS and ground-based data a very complete SED of CB 3-mm for wavelengths beyond 25 μm could be obtained. The SED of CB 3-mm can be well represented by a single modified blackbody curve with a temperature of 34 K and a luminosity of 720 $L_{\odot}$ (see Fig. 3). The extinction must be very high in order to produce such an SED. The contribution of transiently heated very small dust grains and of a stellar-like NIR source in the field gets larger at shorter wavelengths. Thus, the SED does not follow a modified black-body curve any longer at these wavelengths. Assuming that the luminosity of CB 3-mm is completely provided by mass accretion and deuterium burning, the mass of the protostar should range between 5 and 10 $M_{\odot}$. It is remarkable that the source is also associated with an H_2O maser [31] which is generally seen as a sign of high-mass star formation. Mid-infrared ISOCAM images show that the cloud core is relatively sharp-edged on the eastern side where diffuse PAH emission and the lack of reddened stars indicate the presence of thin and warm gas.

References

1. Beech, M., Mitalas, R. (1994) Formation and evolution of massive stars. Astrophys. J. Suppl. Ser. 95, 517–534.
2. Bonnell, I. A., Bate, M. R., Zinnecker, H. (1998) On the formation of massive stars. Mon. Not. R. Astron. Soc. 298, 93–102.
3. Boulanger, F., Falgarone, E., Puget, J. L., Helou, G. (1990) Variations in the abundance of transiently heated particles within nearby molecular clouds. Astrophys. J. 364, 136–145.
4. Cesaroni, R., Hofner, P., Walmsley, C. M., Churchwell, E. (1998) Sub-arcsecond structure of hot cores in the NH_3(4,4) line. Astron. Astrophys. 331, 709–725.
5. Chan, S. J., Henning, Th., Schreyer, K. (1996) A catalogue of massive young stellar objects. Astron. Astrophys. Suppl. Ser. 115, 285.
6. Churchwell, E. (1990) Ultracompact HII regions - The impact of newly formed stars on their environment. Astron. Astrophys. Rev. 2, 79–123.
7. Clemens, D. P., Barvainis, R. (1988), A catalog of small, optically selected molecular clouds - Optical, infrared, and millimetre properties. Astrophys. J. Suppl. Ser. 68, 257–286.
8. Codella, C., Bachiller, R. (1999) Molecular outflows in intermediate-mass star-forming regions: the case of CB 3. Astron. Astrophys. 350, 659-671.
9. Feldt, M., Stecklum, B., Henning, Th., Hayward, T. L., Lehmann, Th., Klein, R. (1998) The ultracompact HII region G 45.45+0.06. A pearl necklace in the sky. Astron. Astrophys. 339, 759–772.
10. Feldt, M., Stecklum, B., Henning, Th., Launhardt, R., Hayward, T. L. (1999) High-resolution imaging of ultracompact HII regions. II. G5.89-0.39 revisited. Astron. Astrophys. 346, 243–259.
11. Garay, G., Lizano, S. (1999) Massive stars: their environment and formation. Publ. Astron. Soc. Pacific 11, 1049–1087.

12. Henning, Th. (1990) Formation and early evolution of massive stars. Fund. of Cosmic Physics 4, 321–442.
13. Henning, Th., Pfau, W., Altenhoff, W. J. (1990) Infrared and radio emission from very young massive stellar objects. Astron. Astrophys. 227, 542–552.
14. Henning, Th., Cesaroni, R., Walmsley, M., Pfau, W. (1992) Maser search towards young stellar objects. Astron. Astrophys. Suppl. Ser. 93, 525–538.
15. Henning, Th., Klein, R., Launhardt, R., Pfau, W., Lemke, D. (1998a) The molecular cloud core M17-North: ISO spectroscopy and IR/mm continuum mapping. Astron. Astrophys. 332, 1035–1043.
16. Henning, Th., Klein, R., Chan, J., Fitzpatrick, E.L., Siebenmorgen, R., Stecklum, B. (1998b) The nature of the LMC protostar N 160A-IR. Astron. Astrophys. 338, L51–L54.
17. Hughes, V. A., MacLeod, G.C. (1989), The use of IRAS data to define HII regions. Astron. J. 97, 786-800.
18. Jijina, J., Adams, F. C. (1996) Infall collapse solutions in the inner limit: radiation pressure and the effects on star formation. Astrophys. J. 462, 874–887.
19. Klein, R., Henning, Th., Cesarsky, D. (1999) The molecular cloud core M 17-North: New ISOCAM observations. Astron. Astrophys. 343, L53-L56.
20. Kurtz, S., Cesaroni, R., Churchwell, E., Hofner, P., Walmsley, M. (2000) Hot molecular cores and the earliest phases of high-mass star formation. In: V. Mannings, A. Boss, S. Russell (eds.): Protostars and Planets IV, Arizona Press, Tuscon, in press
21. Launhardt, R., Henning, Th. (1997) Millimetre dust emission from northern Bok globules Astron. Astrophys. 326, 329–346.
22. Launhardt, R., Henning, Th., Klein, R. (1998) Multi-wavelength study of the massive star-forming region LBN 594. In: J. Yun, R. Liseau (eds.): Star formation with the Infrared Space Observatory. ASP Conf. Ser. 132, 119–124.
23. Launhardt, R., Henning, Th., Klein, R. (2000), in preparation.
24. Lutz, D., Spoon, H. W. W., Rigopoulou, D., Moorwood, A. F. M., Genzel, R. (1998) The nature and evolution of ultraluminous infrared galaxies: a mid-infrared spectroscopic survey. Astrophys. J. Lett. 505, L103-L107.
25. Mayra, O., Lizano, S., D'Alessio, P. (1999) Hot molecular cores and the formation of massive stars. Astrophys. J., 525, 808–820.
26. Meurs, E. J. A., Harmon, R. T. (1988) The extragalactic sky viewed by IRAS. Astron. Astrophys. 206, 53–62.
27. Molinari, S., Test, L., Brand, J., Cesaroni, R., Palla, F. (1998a) IRAS 23385+6053: A prototype massive class 0 object. Astrophys. J. 505, L39–L42.
28. Molinari, S., Brand, J., Cesaroni, R., Palla, F., Palumbo, G. G. C. (1998b) A search for precursors of ultracompact HII regions in samples of luminous IRAS sources. II. VLA observations. Astron. Astrophys. 336, 339–351.
29. Morgan, J. A., Bally, J. (1991) Molecular outflows in the L 1641 region of Orion. Astrophys. J. 372, 505-517.
30. Osterloh, M., Henning, Th., Launhardt, R. (1997) Infrared images and millimetre data of cold southern IRAS sources. Astrophys. J. Suppl. Ser. 110, 71–114.
31. Scappini, F., Caselli, P., Palumbo, G.G.C. (1991) A new water maser source in LBN594. Monthly Not. R.A.S. 249, 763–765.
32. Schreyer, K., Henning, Th., Kömpe, C., Harjunpää, P. (1996) NH_3 and HCO^+ towards luminous IRAS sources. Astron. Astrophys. 306, 267–277.

33. van der Tak, F.F.S., Dishoeck, E., Evans II, N.J., Blake, G.A. (2000) Temperature and density structure of the envelopes of deeply embedded massive young stars. Astrophys. J., in press.
34. van Dishoeck, E.F. et al. (1998) ISO observations of gas and dust chemistry in star-forming regions. In: J. Yun, R. Liseau (eds.): Star formation with the Infrared Space Observatory. ASP Conf. Ser. 132, 54–65.
35. Wood, D. O. S., Churchwell, E. (1989) Massive stars embedded in molecular clouds: their population and distribution in the galaxy. Astrophys. J. 340, 265–272.
36. Yorke, H.W. (1986) The dynamical evolution of HII regions - recent theoretical developments. Ann. Rev. Astron. Astrophys. 24, 49-87.

Structure and Evolution of Circumstellar Disks Around Young Stars: New Views from ISO ⋆

Michael R. Meyer[1] ⋆⋆ and Steven V.W. Beckwith[2]

[1] Steward Observatory, The University of Arizona, Tucson, AZ 85721–0065 USA
[2] Space Telescope Science Institute, Baltimore, MD 21218 USA

Abstract. A question central to understanding the origin of our solar system is: how do planets form in circumstellar disks around young stars? Because of the complex nature of the physical processes involved, multi–wavelength observations of large samples will be required in order to obtain a complete answer to this question. Surveys undertaken with ISO have helped to solve pieces of this puzzle in addition to uncovering new mysteries. We review a variety of studies aimed at understanding; i) the physical structure and composition of circumstellar disks commonly found surrounding young stellar objects; and ii) the evolution of circumstellar disks from the active accretion phase to post–planet building debris disks.

1 Introduction

The number of researchers involved in studies of circumstellar disks surrounding young stars has exploded in recent years – and with good reason! Discoveries of giant planets orbiting main sequence stars in the solar neighborhood, of planetary mass companions surrounding pulsars, and of brown dwarf companions to stellar mass objects have brought new urgency and interest in the search to understand the structure and evolution of circumstellar disks. In addition to their fundamental importance as the likely sites of planet formation, circumstellar accretion disks also play an important role in pre–main sequence evolution. Depending on their mass, accretion rates, and lifetimes, such disks could contribute significantly to building up the final mass of a solar type star. They also appear to play a crucial role in regulating stellar angular momentum during the early accretion phase. ISO, the first multi–mode infrared space observatory, devoted a significant fraction of time to object–oriented surveys of stars in order to study their circumstellar disks.

We begin with a review of what was known and unknown about circumstellar disks surrounding pre–main sequence stars when ISO was launched. In section 3, we discuss new results from ISO that shed light on the physical structure and composition of these disks. In section 4, we review several mid– and far–infrared surveys conducted with ISO focussed on the temporal

⋆ ISO is an ESA project with instruments funded by ESA Member States (especially the PI countries: France, Germany, the Netherlands and the United Kingdom) and with the participation of ISAS and NASA.
⋆⋆ Hubble Fellow

D. Lemke, M. Stickel, and K. Wilke (Eds.): LNP 548, pp. 341–352, 2000.

evolution of the disks. Finally in section 5, we summarize these results and comment on progress that will be made in the coming years.

2 Properties of Circumstellar Disks

It is generally accepted that the formation of a circumstellar disk is a common outcome of the star formation process [7]. Observational evidence for the existence of these disks abounds. Many young stars exhibit infrared and millimeter excess emission indicating the presence of large amounts of circumstellar material. Yet in order to provide an optically–thin line of sight toward the central object, a flattened dust distribution is required [38]. Emission–line profiles observed toward young stars provided additional evidence. Red–shifted components of the bi–polar flow are thought to be occulted by a geometrically–thin, optically–thick disk resulting in blue–shifted line profiles [4]. In young stellar objects where the observed flux is dominated by accretion luminosity (e.g. FU Ori eruptive variables) one can observe kinematic signatures of rotation in absorption lines arising in the disk photosphere [53]. However the most compelling evidence comes from direct images of the disks themselves (Figure 1).

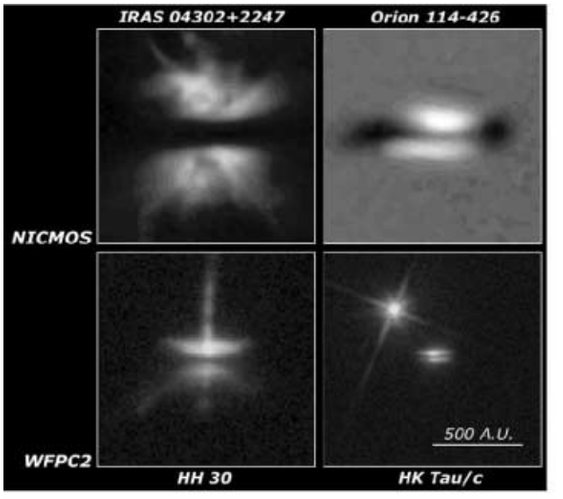

Fig. 1. Optical and infrared images of circumstellar disks seen via scattered light with the Hubble Space Telescope: Images courtesy of NASA, STScI/AURA, and the following authors [44] (upper–left), [34] (upper–right), [8] (lower–left), and [49] (lower–right).

Based on these and other studies over the past 15 years, we have learned a great deal concerning the physical properties of disks. From sub–mm observa-

tions of optically–thin dust emission, estimates of total disk mass (gas+dust) range from 0.1–10^{-3} M_{sun} ([43]; [3]; and [13]). Based on direct images obtained with HST, modeling of spectral energy distributions, and millimeter wave observations of gas disks, sizes are estimated to range from $10 < r < 1000$ AU. Finally, observations of UV/blue excess emission allow one to estimate accretion rates from the disk onto the star [16]. Recent estimates range from 10^{-9} to 10^{-7} M_{sun} yr^{-1} for classical T Tauri stars and $\times$ 100 greater for the FU Ori objects. There is a hint of decreasing accretion rate with age for T Tauri stars found in the Taurus–Auriga and Chamaeleon I complexes [21]. This is consistent with the pioneering studies of the frequency of near–infrared excess emission [50] as a function of stellar age. Near–IR excess emission (1–5 μm) traces dust emission at radii < 0.1 AU and there is a nearly 1:1 correlation between the presence of dust in the inner disk and spectroscopic signatures of accretion [20]. Recent studies which utilize larger statistically significant samples confirm that the timescale for dissipation of inner accretion disks is < 30 Myr [24]. Further, due to the small number of objects found to be evolving from optically–thick to optically–thin disks in the region 0.1–1.0 AU, it appears that the transition time is $< 10^6$ yrs [47]. Finally, there appears to be a connection between the presence/absence of an inner accretion disk and the evolution of stellar angular momentum [14]. This relationship can be understood in terms of a magnetospheric star–disk interaction [39].

Despite the tremendous explosion in our knowledge concerning circumstellar disks surrounding young stars, many fundamental questions remain unanswered. What physical processes control the energy budget as a function of radius in the disk? What is the chemical composition of the dust grains observed? Does the evolution of disks in the planet–forming regions from 0.1–10.0 AU differ from the evolution of the inner accretion disks? ISO has made fundamental contributions toward answering these questions as described below.

3 Physical Structure and Composition

Photometric observations obtained over a broad wavelength range can be a powerful diagnostic of the spatial distribution of circumstellar material. As the temperature of the circumstellar material decreases with radius, progressively longer wavelength emission traces larger radii in the disk (Figure 2). Utilizing the ISOPHOT instrument on–board ISO [30], Beckwith and collaborators set out to conduct a small survey of young star+disk systems in order to search for structure in the SEDs impossible to observe from the ground. They obtained multi–wavelength photometry with 13 filters from 4.9–160 μm for a sample of 14 objects in the Taurus–Auriga and Chamaeleon I dark clouds (d $\sim$ 150 pc). Preliminary results are presented in Figure 3 for a representative sample of objects compared to expected stellar SEDs as well as

a simple model of a geometrically–thin, optically–thick passive reprocessing disk seen face–on [46]. A few general trends are obvious from inspection of these data. First of all, several objects lack significant near–infrared excess emission suggesting the presence of inner holes in the circumstellar dust distribution [36]. An extreme example is CS Cha in which the disk appears to be evacuated to > 0.1 AU. Secondly, it appears that a standard reprocessing (or accretion disk) matches the SEDs between 2–10 μm. Finally, the observed SEDs are flatter and exhibit greater flux in the mid– and far–IR than simply blackbody disk models predict; an additional emission component is required. Similar conclusions have been reached from a multi–wavelength study of the peculiar young star UX Ori [40] utilizing ISOPHOT.

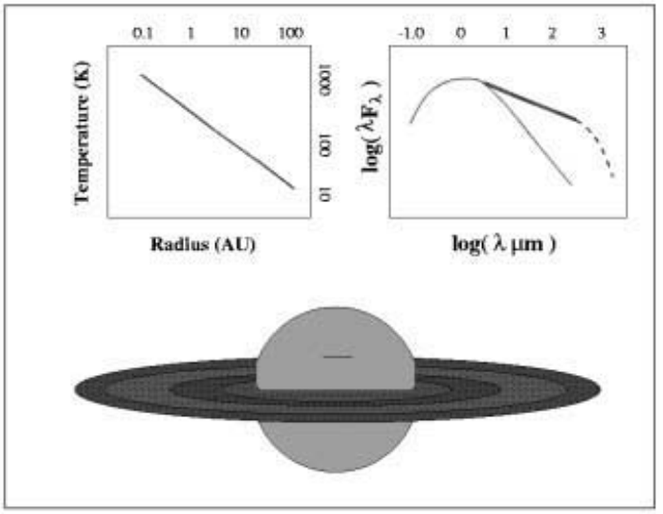

Fig. 2. Schematic representation of an optically–thick, geometrically–thin circumstellar disk model. Viscous accretion and/or reprocessing of stellar photons results in a power–law temperature distribution in the disk [2]. Each radius corresponds to a unique blackbody temperature which is diagnosed using a specific range of wavelengths (see [6]).

What controls the energy budget in these circumstellar disks? For a disk dominated by the dissipation of accretion energy confined to the disk mid–plane, the disk should exhibit a decreasing temperature distribution away from the mid–plane which could produce absorption features in the disk photosphere as observed in the FU Ori objects. For a disk dominated by reprocessing of stellar radiation, there should be a temperature inversion

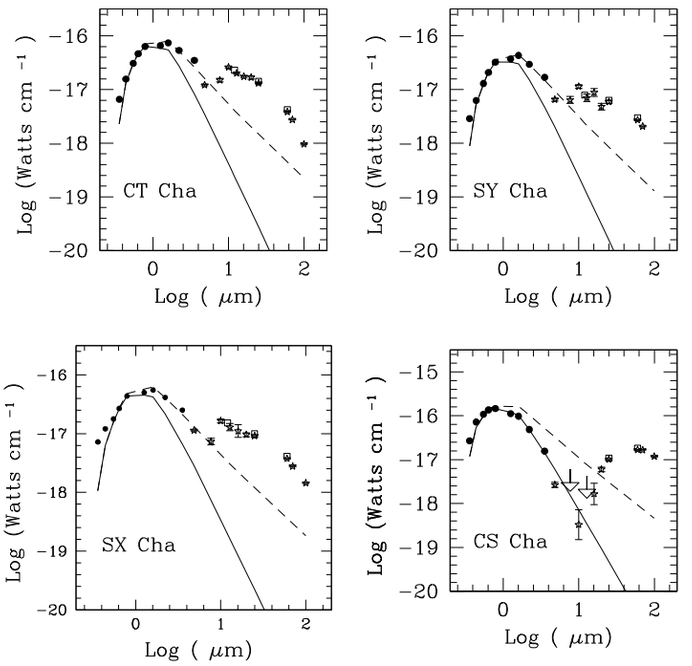

Fig. 3. Dereddened spectral energy distributions where the circles are ground–based photometry, the stars are new ISO photometry, and the squares are IRAS data. Also shown are expected stellar photospheric flux appropriate for the known spectral type of the star (solid line) as well as expected SEDs from a geometrically–thin, optically–thick reprocessing disk viewed face–on (dashed line).

producing emission–lines in a hot, optically–thin disk atmosphere ([9]; [10] (CG97)). A pioneering mid–IR spectral survey of T Tauri star+disk systems [11] found several sources exhibiting 10 μm emission attributed to Si–O stretching modes. In order to investigate inner disk regions as well as understand the heating mechanisms which control disk structure, Natta, Meyer, and Beckwith [42] utilized the PHOT–S module of ISOPHOT, to conduct a low resolution spectrophotometric survey from 2.5–11.7 μm of a sub–set of the T Tauri sample sample described above (see also [17]). *Each star in the sample of nine exhibited some evidence of a 10 μm emission feature.* Using the simple flared–disk atmosphere model of CG97 and adopting a fiducial Si–O feature cross–section (σ_ν/σ_{10}), they fitted these data for the efficiency of converting stellar photons into silicate emission ($\epsilon = \sigma_{10}/\sigma_*$). The results of these fits are shown in Figure 4 where the 10 μm features are compared with the models. The CG97 models successfully reproduce the majority of the observed spectra using a mixture of amorphous olivine and pyroxene grains with sizes < 1 μm. Combining these results with the SEDs described

above suggests that disk atmospheres contribute significantly to the mid– and far–infrared fluxes observed in young star+disk systems.

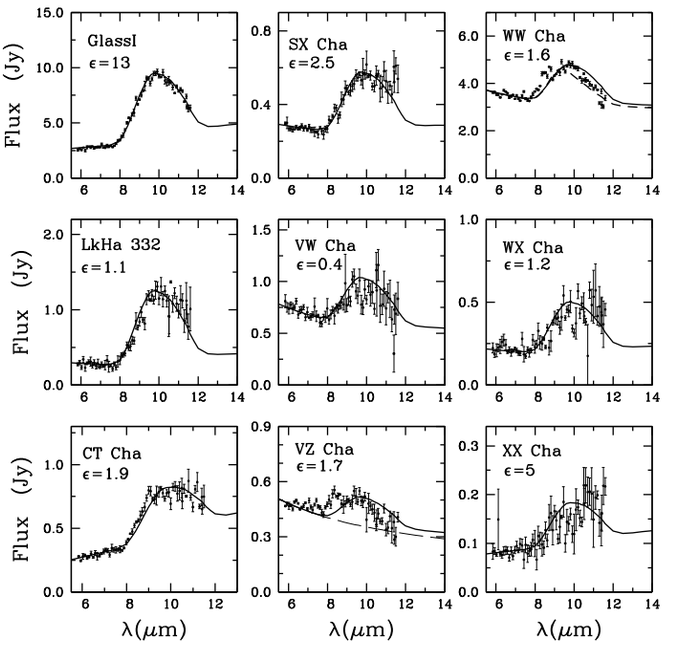

Fig. 4. Model fits to the observed spectra. In each panel, the dots show the observed points while the solid line shows the predicted emission of the superheated disk atmosphere, computed following CG97 for pyroxene grains of 1.2 μm radius. The value of $\epsilon = \sigma_{10}/\sigma_*$ which gives the best fit to the observations is indicated.

Additional surveys undertaken with the SWS instrument on–board ISO have enabled us to ask new questions regarding the dust mineralogy and gas content of these disks. Moderate resolution ($R \sim 1500$) mid–infrared spectroscopy obtained for a sample of young intermediate mass Herbig Ae/Be stars, have revealed the presence of crystalline silicate features in three objects; HD 100546, HD 142527, and HD 179218 ([32]; [31]; and [52]). Similar features have been observed in the disk of β Pictoris [28] as well as in solar system comets [19]. These observations are intriguing because crystalline silicates are not observed in the diffuse interstellar medium. Thus their presence in the circumstellar material surrounding the Herbig stars suggests that amorphous silicate grains were transported into the inner disk region where they could be processed at temperatures > 1500 K. This, along with their observation at characteristic dust temperatures of ~ 300 K, suggests large–scale radial mixing in these disks (however see [37]). Finally, we note that

pioneering observations have detected H_2 toward some young star+disk systems ([51]; [12]). The relative intensities of the S(0) and S(1) lines suggest gas temperatures of $\sim$ 100 K and mass estimates $\sim$ 0.01 M_{sun} comparable to the minimum mass solar nebula [22].

4 Temporal Evolution

While it appears that most young stars form accompanied by a circumstellar disk, it is not clear that all disks form planets. Several factors could play a crucial role in determining the fate of an accretion disk. It has been suggested that disks evolve more quickly around high mass stars ($M_* > 1.0\ M_{sun}$) compared to low mass stars [41]. Stellar companions can also effect the dynamical evolution of disk material [33]. Finally, stellar environment can also play a role [23]. Of course one would like to study disk evolution as a function of all these variables. Here we review the observed correlations of disk properties with time as studied from ISO surveys of stars in clusters with ages determined from evolutionary models as well as surveys of main sequence field stars of uncertain age.

Despite significant advances in our understanding of the evolution of inner accretion disks *very little is known concerning the evolution of outer disks.* At mid–infrared through sub–mm wavelengths (10–1000 μm) observations trace material between 0.1–10 AU. Several surveys have been conducted with ISOPHOT which have made significant contributions to our understanding of outer disks. Meyer et al. [35] observed between 10 and 30 stars in each of five separate clusters and associations at 25 and 60 μm tracing material in the terrestrial planet zone from 0.3–3.0 AU. This survey provides a complete census of optically–thick circumstellar disks at these wavelengths surrounding solar–type stars with ages 1–300 Myr. Despite being a factor of $\times$ 5 more sensitive than IRAS at 60 μm, only four sources were detected with $SNR > 3$ out of a sample of 97 stars. All of the sources detected were members of the Chamaeleon I dark cloud ($\tau < 10$ Myr) including one transition object possessing a large hole in its inner disk. These results suggest that optically–thick outer disks dissipate, or coagulate into larger particles on timescales comparable to the cessation of accretion (c.f. [5]; [26]). A complementary survey undertaken by Spangler et al. [48], observed 300 stars in young clusters and the field at 60 and 90 μm spanning a similar age range. These authors analyze the data in terms of the fractional contribution of the far–infrared emission to the bolometric luminosity of the sources observed ($f = L_{FIR}/L_{bol}$). They plot the mean value of f as a function of cluster age, and find a smooth variation from the youngest stars ($f > 10^{-2}$ at ages $< 10^7$ yrs) to the oldest stars in sample ($f \sim 10^{-5}$ at ages $\sim 10^9$ yrs). Presented in this way, the zodiacal dust disk (within 5 AU) would have a value of $f \sim 10^{-7}$ for the 4.5 Gyr age of our solar system.

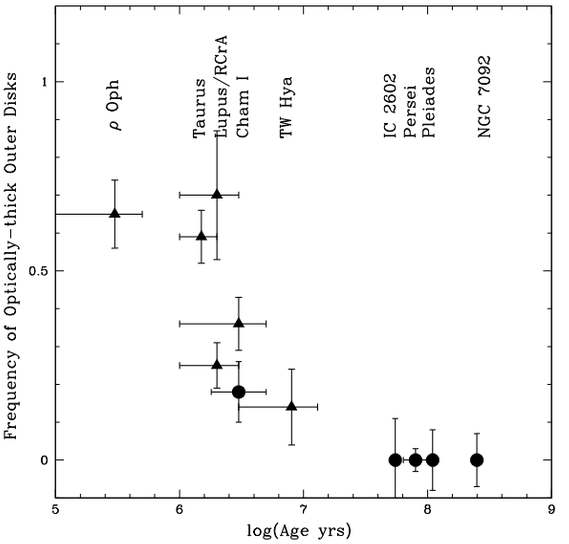

Fig. 5. Frequency of 60 μm detections as a function of cluster age for several star–forming regions observed by IRAS (triangles) and ISO (circles) [35]. Because the ISO observations are $\times$ 5 more sensitive than the IRAS survey, the triangles should be considered lower–limits when compared to the circles. It appears that optically–thick disks from 0.3–3.0 dissipate or coagulate into larger bodies on a timescale comparable to the termination of the main accretion phase in T Tauri disks.

Other relevant surveys include the study of intermediate mass members of the Ursa Major Stream ($\tau \sim 300$ Myrs) [1]. One out of nine stars were detected consistent with a recent estimate of the frequency of IR excess among field main sequence stars [45]. Similar results based on a survey of 38 main sequence stars at 20 μm, tracing the inner–most annuli of these cool outer disks, have also been reported [15]. Finally, Habing et al. [18] present preliminary results concerning their survey of stars in the solar neighborhood. Improving on searches for "Vega phenomenon" objects in the IRAS database, this survey was sensitive to stellar photospheric emission for A–K stars out to a distance of 25 parsecs. Combining ISO observations with improved age estimates for their sample, they report the intriguing result that all stars younger than 300 Myr possess a detectable disk while no stars older than 400 Myr show IR excess emission at 60 μm. They interpret this result as evidence that the era of maximum bombardment documented in our own solar system is a common phenomena in the evolution of circumstellar disks.

5 Summary and Future Work

From this vast array of observational results, a coherent picture is emerging. Most young stars (50–100 %) possess active accretion disks during a significant portion of their PMS evolution. These disks appear to have masses comparable to the minimum mass solar nebula in both gas and dust. Structurally, they posses small inner holes (< 0.05 AU) and flare in their outer regions as expected from hydrostatic equilibrium. Although almost all disks that extend to within 0.1 AU of the stellar surface appear to be actively accreting, the energy budget of the outer regions are dominated by reprocessing of light from the central star. The active accretion phase lasts from 1–10 Myr in most systems, though it can persist longer. The time to transition from optically–thick to optically–thin within 1 AU lasts < 1 Myr. At the same time, outer disks appear to dissipate, or grow into larger bodies (with decreased mass opacity) rendering them optically–thin. The results of Meyer et al. [35] and Spangler et al. [48] appear to be consistent when comparing the frequency of detections in both surveys. Additional data are required in the crucial 10–30 Myr old range order to discern whether or not there is a gradual evolution of dust mass in small particles ($a < 1$ mm) with time, or an abrupt change in disk properties associated with the termination of accretion. Perhaps particle growth in circumstellar disks is inhibited during the active accretion phase? Similarly, further study of stars aged 100–500 Myr is necessary to follow–up the intriguing results of Habing et al. [18]. Is the era of maximum bombardment, thought to be associated with with planet formation, a common phase of dust disk evolution around solar–type stars?

Tremendous observational capabilities, both ground– and space–based, will focus on these problems in the coming decade. With continued improvement in instrumentation, the current generation of 6–10m class telescopes will continue to make astounding discoveries such as the dramatic images of the disk surrounding HR4796A ([29]; [27]). High resolution images obtained from the UV through the near–infrared with HST will have an on–going impact on studies of circumstellar disks [54]. Sub–millimeter telescopes (both single dish surveys and targeted observations with extant and future interferometric arrays) will provide data necessary to obtain a complete understanding of the evolution of dust mass and grain size in circumstellar disks [25]. SIRTF will enable a detailed census of faint debris disks in the solar neighborhood, as well as surveys of unprecedented sensitivity in nearby star–forming regions. SOFIA will prove very complementary to SIRTF, providing higher spatial and spectral resolution. Finally, both ALMA and NGST have as central to their science missions studies of circumstellar disk evolution and planet formation. With the renewed interest in the origins of stars and planets, future work is sure to provide answers to questions that surveys undertaken with ISO have played a key role in defining.

Acknowledgements

We would like to express our thanks to A. Natta, M. Robberto, B. Schulz, J. Stauffer, and D. Backman for their continued collaboration in the analysis and interpretation of ISO data, and to the conference organizers for inviting this contribution. Special thanks to L.A. Hillenbrand for comments on an earlier version of this manuscript. Support for this work was provided by NASA through Hubble Fellowship Grant # HF–01098.01–97A awarded by the Space Telescope Science Institute which is operated by the AURA, Inc., for NASA under contract NAS 5–26555.

References

1. Abraham, P. , Leinert, C. , Burkert, A. , Lemke, D. & Henning, T. 1998, A&A, 338, 91
2. Adams, F. C., Lada, C. J. & Shu, F. H. 1987, ApJ, 312, 788
3. Andre, P. & Montmerle, T. 1994, ApJ, 420, 837
4. Appenzeller, I., Oestreicher, R. & Jankovics, I. 1984, A&A, 141, 108
5. Beckwith, S.V.W., Henning, T., & Nakagawa, Y. 2000, in Protostars and Planets IV, ed. V. Mannings, A. P. Boss & S. S. Russell (Tucson: University of Arizona Press), in press
6. Beckwith, S.V.W. 1999, in The Origin of Stars and Planetary Systems, ed. C. Lada & N. Kylafis, (Dordrecht: Kluwer Academic Publishers), 579
7. Beckwith, S. V. W. & Sargent, A. I. 1996, Nature, 383, 139
8. Burrows, C. J., et al. 1996, ApJ, 473, 437
9. Calvet, N., Magris, G. C., Patino, A. & D'Alessio, P. 1992, Revista Mexicana de Astronomia y Astrofisica, 24, 27
10. Chiang, E. I. & Goldreich, P. 1997, ApJ, 490, 368
11. Cohen, M. & Witteborn, F. C. 1985, ApJ, 294, 345
12. van Dishoeck, E. F., Thi, W. F., Blake, G. A., Mannings, V., Sargent, A. I., Koerner, D. & Mundy, L. G. 1998, ApSS, 255, 77
13. Dutrey, A., Guilloteau, S., Duvert, G., Prato, L., Simon, M., Schuster, K. & Menard, F. 1996, A&A, 309, 493
14. Edwards, S. , et al. 1993, AJ, 106, 372
15. Fajardo-Acosta, S. B., Stencel, R. E., Backman, D. E. & Thakur, N. 1999, ApJ, 520, 215
16. Gullbring, E. , Hartmann, L. , Briceno, C. & Calvet, N. 1998, ApJ, 492, 323
17. Gürtler, J., Schreyer, K., Henning, T. , Lemke, D. & Pfau, W. 1999, A&A, 346, 205
18. Habing, H. J., et al. 1999, Nature, 401, 456
19. Hanner, M. S., Lynch, D. K. & Russell, R. W. 1994, ApJ, 425, 274
20. Hartigan, P. , Edwards, S. & Ghandour, L. 1995, ApJ, 452, 736
21. Hartmann, L. , Calvet, N. , Gullbring, E. & D'Alessio, P. 1998, ApJ, 495, 385
22. Hayashi, C., Nakazawa, K. & Nakagawa, Y. 1985, Protostars and Planets II, 1985 eds. D. Black & M. Shapley, (Tucson: University of Arizona Press), 1100
23. Hillenbrand, L. A., Strom, S. E., Calvet, N. , Merrill, K. M. , Gatley, I. , Makidon, R. B., Meyer, M. R. & Skrutskie, M. F. 1998, AJ, 116, 1816

24. Hillenbrand, L. A. & Meyer, M. R. 1999, American Astronomical Society Meeting, 195, 0209
25. Holland, W. S., et al. 1998, Nature, 392, 788
26. Hollenbach, D., Yorke, H., Johnstone, D. 2000, in Protostars and Planets IV, ed. V. Mannings, A. P. Boss & S. S. Russell (Tucson: University of Arizona Press), in press
27. Jayawardhana, R. , Fisher, S. , Hartmann, L. , Telesco, C. , Pina, R. & Fazio, G. 1998, ApJ, 503, L79
28. Knacke, R. F., Fajardo-Acosta, S. B., Telesco, C. M., Hackwell, J. A., Lynch, D. K. & Russell, R. W. 1993, ApJ, 418, 440
29. Koerner, D. W., Ressler, M. E., Werner, M. W. & Backman, D. E. 1998, ApJ, 503, L83
30. Lemke, D., et al. 1996, A&A, 315, L64
31. Malfait, K., Waelkens, C., Bouwman, J., de Koter, A. & Waters, L. B. F. M. 1999, A&A, 345, 181
32. Malfait, K., Waelkens, C., Waters, L. B. F. M., Vandenbussche, B., Huygen, E. & de Graauw, M. S. 1998, A&A, 332, L25
33. Mathieu, R.D. et al. 2000, in Protostars and Planets IV, ed. V. Mannings, A. P. Boss & S. S. Russell (Tucson: University of Arizona Press), in press
34. McCaughrean, M. J., et al. 1998, ApJ, 492, L157
35. Meyer, M.R., Beckwith, S.V.W., Schulz, B., Stauffer, J.S., & Backman, D. 2000, in preparation.
36. Meyer, M. R., Calvet, N. & Hillenbrand, L. A. 1997, AJ, 114, 288
37. Molster, F. J., et al. 1999, Nature, 401, 563
38. Myers, P. C., Fuller, G. A., Mathieu, R. D., Beichman, C. A., Benson, P. J., Schild, R. E. & Emerson, J. P. 1987, ApJ, 319, 340
39. Najita, N., Edwards, S., Basri, G., & Carr, J. 2000, in Protostars and Planets IV, ed. V. Mannings, A. P. Boss & S. S. Russell (Tucson: University of Arizona Press), in press
40. Natta, A., Prusti, T., Neri, R., Thi, W. F., Grinin, V. P. & Mannings, V. 1999, A&A, 350, 541
41. Natta, A., Grinnin, V., & Mannings, V. 2000, in Protostars and Planets IV, ed. V. Mannings, A. P. Boss & S. S. Russell (Tucson: University of Arizona Press), in press
42. Natta, A., Meyer, M.R., & Beckwith, S.V.W. 2000, ApJ, in press
43. Osterloh, M. & Beckwith, S. V. W. 1995, ApJ, 439, 288
44. Padgett, D. L., Brandner, W. , Stapelfeldt, K. R., Strom, S. E., Terebey, S. & Koerner, D. 1999, AJ, 117, 1490
45. Plets, H. & Vynckier, C. 1999, A&A, 343, 496
46. Robberto, M., Beckwith, S.V.W., Meyer, M.R., Natta, A., in preparation
47. Skrutskie, M. F., Dutkevitch, D. , Strom, S. E., Edwards, S. , Strom, K. M. & Shure, M. A. 1990, AJ, 99, 1187
48. Spangler, C. et al. 1999, The Universe as Seen by ISO, eds. P. Cox & M. Kessler (Noordwijk: ESA Publications Division), 405
49. Stapelfeldt, K. R., Krist, J. E., Menard, F. , Bouvier, J. , Padgett, D. L. & Burrows, C. J. 1998, ApJ, 502, L65
50. Strom, K. M., Strom, S. E., Edwards, S. , Cabrit, S. & Skrutskie, M. F. 1989, AJ, 97, 1451
51. Thi, W. -F. , van Dishoeck, E. F., Blake, G. A., van Zadelhoff, G. -J. & Hogerheijde, M. R. 1999, ApJ, 521, L63

52. Waelkens, C., Malfait, K. & Waters, L. B. F. M. 1998, ApSS, 255, 25
53. Welty, A. D., Strom, S. E., Strom, K. M., Hartmann, L. W., Kenyon, S. J., Grasdalen, G. L. & Stauffer, J. R. 1990, ApJ, 349, 328
54. Weinberger, A. J., Becklin, E. E., Schneider, G., Smith, B. A., Lowrance, P. J., Silverstone, M. D., Zuckerman, B. & Terrile, R. J. 1999, ApJ, 525, L53

Present Results of the ISOGAL Survey of the Inner Galaxy

Alain Omont and the ISOGAL Collaboration

Institut d'Astrophysique de Paris, CNRS, 98bis BD Arago, 75014 Paris

Abstract. ISOGAL[1,2,3] is a 7-15μm survey of $\sim$20 deg^2 in the inner galactic plane. With KJI DENIS data, it allows detailed studies of cold stars and galactic structures in highly obscured regions, with a sensitivity and pixel surface $\sim$100 times better than IRAS. Data reduction is difficult because of strong sources and memory effects of the detectors. A catalogue of $\sim 10^5$ ISOGAL-DENIS sources will be published within a few months. A few fields exemplify the results expected from the $\sim$200 fields observed. ISOGAL provides a practically complete census of mass-losing AGB stars in fields of the inner bulge. Even very weak mass losses are well characterised down to the RGB tip. The determination of the AGB luminosity function and mass loss function is in progress, as well as cross-identifications with OH/IR stars and LPVs, and the analysis of their dust from 5-16μm CVF spectra. The AGB sequence is also quite visible in 7-15μm colour-magnitude diagrams in the galactic disk. Foreground stars and dusty young stars are also numerous. The latter with a few solar masses are detectable through the galactic centre. The combination of ISOGAL and DENIS data allows a detailed estimate of the interstellar extinction.

1 Introduction

ISOGAL is a 7-15μm ISOCAM survey (with 6" pixels and sensitivity below 10 mJy) of $\sim$20 deg^2 in the galactic plane, mostly interior to $|\ell| = 30^o$. In combination with KJI DENIS data, the ISO images allow detailed studies of cold stellar populations and galactic structures in highly obscured regions throughout the inner Galaxy.

Its main scientific goals include :

– A census of bright red giants at very low galactic latitudes, through the Galactic Centre distance ($\sim 10^5$ detections expected).

[1] ISOGAL Co-Investigators include: C. Alard, J. Blommaert, C. Cesarsky, N. Epchtein, M. Felli, P. Fouqué, R. Genzel, G. Gilmore, F.Guglielmo, H. Habing, A. Omont (PI), M. Pérault, S. Price, A. Robin and G.Simon. A number of associate members of the ISOGAL Collaboration have also contributed to the results discussed here. They include : I. Glass, M. Morris, L. Testi and R. Wyse

[2] The ISOGAL data reduction team includes: C. Alard, T. August, J. Blommaert, E. Copet, S. Ganesh, D. Ojha, M. Pérault, F. Schuller, M. Schultheis, G. Simon, J. van Loon and M. Unavane

[3] Many of the results presented here rely on data of the DENIS survey [5]

D. Lemke, M. Stickel, and K. Wilke (Eds.): LNP 548, pp. 353–362, 2000.

– A complete characterisation of the amount of circumstellar dust of those stars which lose mass (on the AGB), and of their proportion with respect to the other red giants.

– The use of the multiwavelength information from ISOGAL+DENIS, which allows characterisation of the small scale interstellar extinction on the observed lines of sight and dereddening of the stellar fluxes, even in very obscured regions.

– The study of the most obscured inner galactic structures, using standard red giants as tracers and overcoming the effects of extinction. Such structures include the inner disk and bulge, the central stellar cluster, the inner spiral arms and the molecular ring, the galactic bar, etc.

– The detection of numerous dusty young stars. When its emission peaks about 15μm, a solar mass star is detectable up to 1-2 kpc, and up to the Galactic Centre for a few solar masses.

– The search for peculiar stellar objects of various kinds with infrared excess. They are either evolved stars (post-AGB, planetary nebulae, binary systems, supergiants, etc.) or young ones (H_2O masers, compact HII regions, B[e] stars, circumstellar disks, open clusters, etc.).

In addition to stellar sources, the study of the diffuse mid-infrared emission at small scale provides valuable information about its carriers (PAHs and dust). In particular, it allows the identification of dense globules and filaments, dark even in the mid-infrared [12], [4]. It also enables us to check the infrared extinction curve along various lines of sight.

Data reduction is particularly difficult because of the high density of strong sources, of memory effects and of short integration times. However, an improved data reduction with the use of CIA ISOCAM software and of a special source extraction is almost complete for all the fields observed. The data quality is acceptable enough (with respect to reliability, completeness and photometric accuracy of the sources) to allow a systematic scientific analysis.

The regions observed ($\sim$20 deg^2) were distributed along the inner galactic disk (mostly within $|\ell| < 30^o$, $|b| < 1^o$), in order to sample it regularly. The central region ($|\ell| < 1.5^o$, $|b| < 0.5^o$) was almost entirely observed, except very close to the Galactic Centre. However, a major problem was to avoid saturation of the ISOCAM detectors. Therefore, observations were performed in $\sim$200 small ℓxb rasters ($\sim$0.1 deg^2) generally avoiding strong IRAS sources (typically 6 - 12 Jy).

More details on the observations and data reduction and quality are given in [9], [10], [11]. Detailed information on the observation parameters and (in particular) on the limits of the fields observed is available on the ISOGAL web server accessible through the IAP server *www-isogal.iap.fr/*. Systematic cross-identifications with near-infrared K,J,I sources of the DENIS survey is a part of the ISOGAL program. Specific DENIS observations of the ISOGAL fields were performed to allow early availability of such data. It is intended

to make public, by mid 2000, a five wavelength catalogue of ISOGAL point sources with their DENIS identification if available ($> 10^5$ sources).

2 Multi-Wavelength Analysis

The simultaneous availability of several wavelengths, both in the near- and middle-infrared ranges, is very powerful in analysing the nature and the properties of detected sources and in disentangling the effects of interstellar extinction.

The five wavelengths at our disposal from DENIS-ISOGAL data (0.8, 1.25, 2.15, 7 and 15 μm) are fairly complementary. They span a wide range of interstellar extinction ($A_\lambda/A_V \sim 0.5$, 0.28, 0.09, 0.04, 0.02, respectively, see Section 3), and a wide range of intrinsic colours generated by various amounts of circumstellar dust. Indeed, in the conditions of ISOGAL lines of sight with very large and various extinction, near-infrared data by themselves are not very useful to characterise the sources and disentangle the various classes. However, JK data are powerful enough to estimate the interstellar extinction, except in the largest cases. The JK data also yield the bolometric fluxes of most DENIS-ISOGAL sources, except for the most dusty ones (see Section 3). On the other hand, 15 μm ISOGAL fluxes are very little affected by extinction and they give a direct view of the amount of circumstellar dust around the sources when combined with shorter wavelengths, especially 7 μm.

The various colour magnitude diagrams (CMD) and colour-colour diagrams that can be generated using various combinations of ISOGAL and DENIS wavelength bands are very useful tools for such practical analysis. The most useful examples are displayed in Figs 1–4.

As discussed in Section 3, K/J–K diagrams (Fig. 2) directly provide estimates of the extinction for most sources (RGB and most AGB sources). They are completed by 7/K–7 or K/K–7 diagrams for very large extinctions. J–K/K–7 and I–J/J–K diagrams are also useful to check and disentangle effects of interstellar and intrinsic reddening and to characterise stars and their photospheric emission. However, it should be stressed that in most ISOGAL lines of sight, only a minority of ISOGAL sources have useful I data, because the I detection is limited to foreground sources. Indeed, the detectability is also reduced in J for large A_V, and even marginally in K for very weak and/or red sources.

I–J can provide useful information, complementary to J–K, to identify and characterise the stars and their photospheric emission. However, I detection is limited to the cases of small extinction, either at large b, or for foreground sources.

The most obvious originality of ISOGAL data is their ability to trace and characterise sources with middle-infrared excess, i.e. sources with various amounts of circumstellar dust. The presence of such dust, even in very small amounts, is always well traced by the 15 μm excess, i.e. by the colours K–

[15] and especially [7]–[15]. Indeed, the latter is often directly related to the mass-loss rate for the warm dust of typical AGB stars, because it is barely sensitive to extinction. Therefore, only small extinction corrections have to be applied.

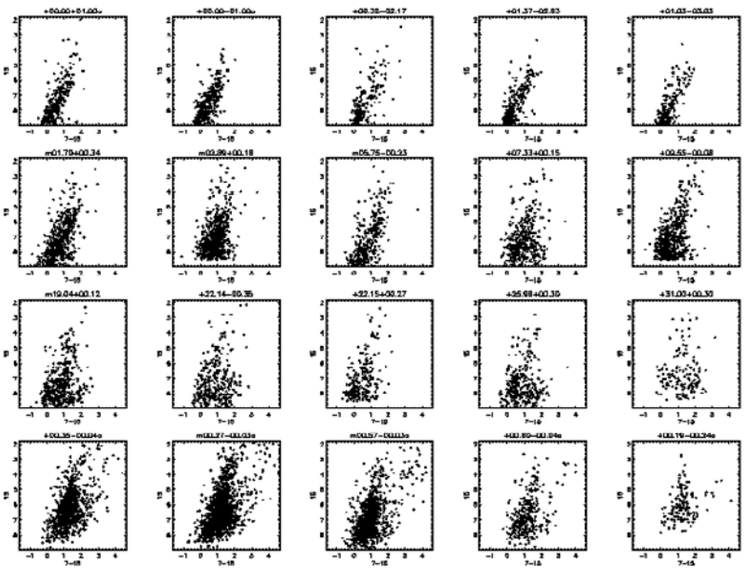

Fig. 1. Typical colour-magnitude diagrams 15/7-15 : first row intermediate bulge; second and third rows galactic disk; fourth row inner bulge (Ganesh et al. in preparation)

The colour-magnitude diagram 15/7–15 thus provides a straightforward view of the nature and the amount of dusty sources of various classes in each ISOGAL field, with even a direct measure of their mass-loss rates for AGB stars. Such diagrams are displayed in Fig. 1 for various typical ISOGAL fields in the Galactic bulge and disk. Their most conspicuous common feature is a sequence of AGB stars with more or less mass loss which are the majority of the sources detected at 15 μm.

The interpretation is simpler in the intermediate bulge with $|b| \leq 1^\circ$ (first row of Fig. 1 ; [7], [9]). There the sequence is particularly well defined and narrow, and it includes more than 90% of the sources. The obvious interpretation is that most stars are luminous red giants (AGB or RGB) at Galactic–Center distance, and the extinction is small. The sources at the beginning of the se-

quence, with practically no 15 μm excess, have the luminosity expected for bulge giants at the tip of the red giant branch (RGB). The 15 μm excess at the other end of the sequence is typical for mass-losing mira variables ($\sim$ a few $10^{-7} M_{\odot}$/yr). The other stars of the sequence are thus "intermediate" AGB stars with very small, but detectable, mass-loss. A few foreground stars are also visible in the diagrams, left of and above the AGB sequence.

The AGB sequence is also conspicuous in 15/7-15 diagrams in all other lines of sight (Fig. 1). Towards the inner bulge ($|\ell| <$ a few degrees, $|b| < 0.5°$, fourth line of Fig. 1), the sequence is broadened towards the right by the very large extinction $\sim$ 20 - 30 (Section 3). Luminous and very cold AGB stars, mainly OH/IR stars, are also more numerous (Section 4). In addition, a new population of luminous young stellar objects is conspicuous in the right part of the diagrams (Section 5).

A similar AGB sequence is also visible in the lines of sight at larger galactic longitudes in the galactic disk. However, these diagrams are made less visible by the broader range of distances among the source distribution, with the absence of a strong peak as, e.g., in the bulge. The percentage of foreground sources (mostly RGB and AGB) is larger, which broadens the diagrams in their left part. Depending on the line of sight, more or less numerous young stars could be present in the lower right part of the diagrams; however, their distinction from AGB stars is not always obvious at the boundary of the AGB sequence.

The diagrams involving one or two near-infrared bands (K,J,I) show similar and complementary information. However, they are much more dependent on the interstellar extinction and on its variations along the line of sight, or even at small scale on the sky. K–15 is again very sensitive to reveal the presence of small amounts of circumstellar dust, mostly in AGB stars, but also in YSOs ; however, it is not always easy to disentangle the large effects of interstellar extinction. The latter is generally traced best by J–K, but K–7 may be useful as well when J is not detected (see Section 3).

3 Infrared Interstellar Extinction

Because of reduced extinction, infrared wavelengths are ideal to trace the highly extincted inner regions of the Galaxy. However, for such large values of A_V, the effects of extinction are still important at near-IR wavelengths, and non negligible in the mid-IR. This allows to use IR reddening or IR counts to determine A_V. It also forces us to correct well for the reddening effects when determining intrinsic IR and bolometric magnitudes. In addition, when the distribution of A_V along a line of sight is known, its determination for a specific star can provide a crude estimate of its distance and, hence, of its luminosity. An early determination of A_V in a few deg^2 around the Galactic Centre was performed by Catchpole et al. [3] from near-IR reddening of red giants (indeed, intermediate AGBs). A similar method was used by omont1 et

al. [1] at the very coarse scale (∼0.7 deg) of the COBE resolution to estimate the extinction towards the bulge from the COBE JK data, assuming that the bulge has a constant JK colour. Cambrésy [2] has implemented a sytematic use of counts of near-IR surveys to map extinction in nearby molecular clouds. We have used the DENIS JK data to extend the method of Catchpole et al. to map extinction in the most extincted part of the bulge (∼30 deg^2; [14]). The method is based on the very well defined relation K_o/J_o–K_o for bulge red giants (zero-extinction curve in Fig. 2). The JK interstellar reddening and hence A_V are thus immediately deduced from JK for each star (Fig. 2). Along each line of sight, the peak of the distribution of J-K is interpreted as the bulge value, and it gives the value of A_V to the bulge in this direction. Of course, this method is only an approximate one because of statistical fluctuations and of the difficulty to disentangle bulge and disk distributions at large ℓ. In addition, the method is not applicable to the largest extinctions ($A_V \geq 25$) where the DENIS J detections are not complete. However, the derived map is quite spectacular. It displays in particular a very flat distribution in galactic latitude b, similar to that known for CO emission, showing that a substantial part of the extinction probably takes place within the bulge. On the other hand, its very rich structure down to a few arcmin scale is probably related to the fractal structure of the interstellar medium in the intervening disk.

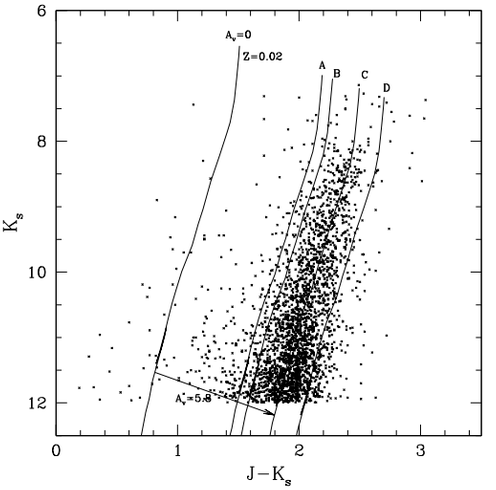

Fig. 2. Colour magnitude diagram (J-K_s) / K_s for the field 0.00+1.0 [9]

Indeed, there are still various uncertainties in the values of the infrared interstellar extinction law. In the near-infrared, proposed values for A_K/A_V differ by as much as 30% (see e.g. [6]). However, the difference is not larger

than 7% for the JK reddening $(A_J–A_K)/A_V$. The situation is still much more uncertain for the mid-IR ISOGAL bands. In particular, Lutz et al. [8] have provided, for the Galactic Center line of sight, much larger values for the extinction in the 7μm region compared to the classical interstellar extinction curve (see e.g. Draine's curve reproduced by Lutz et al.) used by most authors.

ISOGAL results provide a way of checking the extinction value, averaged in the broad band used, in many fields along the galactic disk. The most straightforward way is to measure the ratio J–K/K–[7], assuming a constant value for $J_o–K_o$ for the intermediate AGB and RGB stars detected by ISOGAL. In J–K/K–7 diagrams, most sources follow more or less a straight line with some dispersion. For instance, in a well behaved case (ℓ = -18.63, b = 0.35) studied by Jiang et al. (in preparation), its slope gives $(A_{KS}–\bar{A_7})/(A_J–A_{KS}) \sim 0.37$ for the LW2 ISOCAM filter (5–8.5 μm), which yields $(A_{KS}–\bar{A_7}) \sim 0.06$. Such a value is more compatible with the results of Lutz et al. [8] than with the classical extinction curve (see e.g. Draine's curve reproduced by Lutz et al.). One deduces $\bar{A_7}/A_V \sim 0.027$ and 0.056 for the values of A_K/A_V deduced from Glass [6] (A_K/A_V = 0.089) and Rieke and Lebofsky [13] (A_K/A_V = 0.117), respectively. However, we favour Glass's value for A_{KS}. Let us stress that the resulting value, $\bar{A_7}/A_V \sim 0.03$, is not really in disagreement with either the classical curve or the results of Lutz et al. In other ISOGAL fields the J–K_S/K_S–7 diagrams often tend to display a larger dispersion in the values of K_S–[7], which makes the value of $\bar{A_7}/A_V$ even more uncertain. An estimate of $\bar{A_{15}}/A_V$ from J–K_S/K_S–15 diagrams is practically impossible because of the very large and various values of $(K_S–[15])_o$ for many stars. However, from the behaviour of the diagrams involving [7]–[15] in regions of large extinction, it seems that $\bar{A_{15}}$ is smaller than $\bar{A_7}$.

4 AGB Stars: Mass-loss and Luminosity

As for IRAS 12 μm, AGB stars above the RGB tip are the majority of sources detected at 15 μm by ISOGAL, because they are very luminous, cold and dusty. Their analysis is particularly easy in bulge fields with relatively low extinction, because the distance and the reddening are well defined. We have already analysed in detail the AGB population in several such AGB fields ([9], [7], Ojha et al. in preparation). The case of two fields of Baade's Windows is discussed by I. Glass in these proceedings. We arrived at similar conclusions in a field closer to the Galactic Center (l = 0.00, b = +1.00) with larger extinction and source density [9]. A detailed analysis of the stellar populations is facilitated there by the overwhelming preponderance of bulge stars with a well defined distance and by the relatively low and constant interstellar reddening in front of the whole field studied. As discussed, the latter is determined from the K/J-K colour-magnitude diagram (Fig. 2).

Most DENIS sources are distributed in this diagram in a narrow sequence parallel to the dereddened red giant sequence. The inferred extinction is

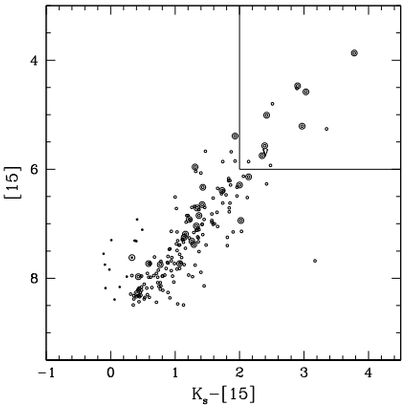

Fig. 3. 15/K_s-[15] colour-colour diagram for the field 0.00+1.0 [9]

$A_v = 6 \pm 1$ mag, quite uniform in the whole field. About 90% of the ISOGAL sources are matched with a near-infrared source of the DENIS survey. The five wavelengths of the ISOGAL+DENIS, together with the relatively low and constant extinction, allow a very good determination of the nature of the sources. Most 15μm sources are distributed along a well defined sequence in the colour-magnitude diagrams LW3/K-LW3 and LW3/LW2-LW3 (Figs. 3,1). They are late M AGB red giants of the bulge, just above the RGB tip. Their large excess at 15μm with respect to 2μm and 7μm cannot be entirely explained by their cold dust photosphere, but implies circumstellar dust with weak mass loss ($\dot{M}_{gas} \sim 10^{-9} - 10^{-7} M_\odot$/yr). These ISOGAL results are the first systematic evidence and study of dust emission at this stage, before the onset of the super-wind phase ($\dot{M}_{gas} \geq 10^{-7}M_\odot$/yr). The systematic evidence of dust at such an early stage of evolution might cast some light on the mechanisms of dust formation and mass-loss generation. A number of more luminous stars are also detected with larger excess at 7 and 15μm. Repeated ISOGAL and DENIS observations show that the majority of them are likely to be long period variables with large amplitude, probably in the super-wind stage ($\dot{M} \geq 10^{-7} M_\odot$/yr). There are also some sources with comparable luminosities, but bluer K-[7] colours and no sign of strong variability. The diagrams 15/(K-15) and 7/(K-7) are particularly useful to distinguish between strong variables with relatively large mass-loss from other ("intermediate") AGB stars (in the early AGB thermal pulse phase). Both populations have similar features in Baade's Windows fields studied by Glass et al. ([7] and in these proceedings). It is thus quite likely that practically all such intermediate AGBs detected in the present field are also some kind of semi-regular LPVs with smaller amplitude and period.

The presence of dust is confirmed by a complementary CVF 5-16μm spectral observation of a 3'x3' sub-field, where $\sim$ 10 spectra display some kind of

silicate 10μm feature and give information about the dust nature (Blommaert et al. in prep.).

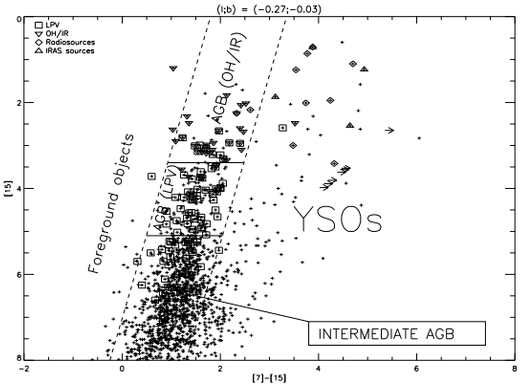

Fig. 4. 15/7–[15] colour-colour diagram for the field -0.27-0.03 (Schuller et al. in preparation)

We have also already begun a systematic study of ISOGAL AGB stars in the inner bulge ($|b| \leq 0.5°$, $|\ell| \leq 1.5°$). The large values of the extinction ($A_V \sim$ 20-30) substantially shifts the 15/(7-15) AGB sequence (Figs. 1,4) and makes dereddening quite important even at 7 or 15 μm. Fig. 4 displays the case of a field close to the Galactic Center (centered at ℓ = -0.27°, b = -0.03°, Schuller et al. in preparation). It is seen that the density of AGB stars is much higher with respect to the intermediate bulge (compare in Fig. 1 to field 0.00+1.00 which is only three times smaller). The AGB sequence again includes intermediate AGBs, and LPVs with large amplitude (miras) identified by I. Glass. It is extended to a number of very red and luminous 15 μm sources, most of which are OH/IR stars. ISOGAL data allows a systematic analysis of the mid-infrared emission of OH/IR stars in the inner bulge (Ortiz et al. in preparation). In particular, their mass-loss rate is estimated from $(K\text{-}[15])_o$ or $([7]\text{-}[15])_o$, and their bolometric luminosity L is determined from the dereddened magnitudes in the DENIS-ISOGAL bands. It is known that L is directly related to the initial mass M_i of the star and hence to its age. The number of the most luminous OH/IR stars thus reflects their formation rate in the inner bulge $\sim 10^7$ yr ago. Preliminary results by Ortiz et al. find this number smaller than in some previous studies of bulge OH/IR stars which lacked their mid-IR fluxes.

5 Young Stars

As discussed by Pérault et al. [12], ISOGAL sources with very large [7]-[15] excess, right to the AGB sequence (Figs. 1,4), are good candidates for being

young stellar objects (YSO) with circumstellar dust. Expected [7]-[15] colours for various classes of YSOs is further discussed by Felli et al. (in preparation) from previous results on IRAS or ISOCAM colours of YSOs. This gives some tentative criteria to distinguish them from AGB stars. The number of such objects, right to the AGB sequence, is quite variable following the ISOGAL fields (Fig 1). They are practically absent from the fields in the intermediate bulge [9]. They are generally not very numerous in typical ISOGAL disk fields (Felli et al. in preparation), but nevertheless present in most of them [12], [15]. It should be remembered that most ISOGAL fields were selected to avoid strong IRAS sources (except in the inner bulge); they are thus biased against most active star forming regions, with a few exceptions. However, for most of the fields, the YSOs are not yet analysed in detail. The number of low mass YSOs is particularly high in the field centered at b = +31.00°, ℓ = +0.30°, in the direction of a well studied molecular cloud (Pérault et al. in preparation).

The number of luminous YSO candidates is spectacularly large in the ISOGAL fields of the central inner bulge (Fig. 1). More details are given in Fig. 4 for the field b = -0.03°, ℓ = -0.27° (Schuller et al. in preparation). A number of the coldest strong 15μm are not even detected at 7μm. The radio identification of all these massive YSO candidates is in progress. A few of the strongest ones are already identified with compact HII regions. A near-IR spectroscopy programme has been proposed with SOFI/NTT to confirm such YSO identification, help to disentangle them from cold AGB stars and to further characterise them

References

1. Arendt R.G. et al., 1994, ApJ 425, 81
2. Cambrésy L. 1999, PhD Thesis, Université Paris 7
3. Catchpole R.M., Whitelock P.A., Glass I.S. 1990, MNRAS 247, 479
4. Egan M.P., Shipman R.F., Price S.D. et al. 1998 ApJ Lett. L494, 199
5. Epchtein N. et al. 1997, Messenger 87, 27
6. Glass I.S. 1999, Infrared Astronomy, Cambridge University Press
7. Glass, I.S., Ganesh, S., Alard, C. et al. 1999, MNRAS 308, 127
8. Lutz D., Feuchtgruber H., Genzel R. et al. 1996, A&A 315, L272
9. Omont A., Ganesh S., Alard C. et al. 1999a, A&A 348, 755
10. Omont A. & The ISOGAL Collaboration 1999, in "Astrophysics with Infrared Surveys: A Prelude to SIRTF", Eds M. Bicaye, C. Beichman, R. Cutri and B. Madore, Pasadena, ASP Conference Series
11. Omont A. et al. 1999b, in 'The Universe as seen by ISO', eds. P. Cox and M.F. Kessler, ESA Special Publications series (SP-427)
12. Pérault M., Omont A., Simon G., et al. 1996 A&A 315, L165
13. Rieke G.H. & Lebofsky M.J. 1985, ApJ 288, 618
14. Schultheis M., Ganesh S., Simon G. et al. 1999, A&A 349, L69
15. Testi L., Felli M., Omont A. et al. 1997, A&A 318, L13

ISOGAL Survey of Baade's Windows

Ian S. Glass[1], David R. Alves[2], and the ISOGAL and MACHO teams

[1] S.A. Astronomical Observatory, PO Box 9, Observatory 7935, South Africa
[2] Space Telescope Science Institute, Baltimore, MD 21218, USA

Abstract. The Baade's Windows of low obscuration towards the inner parts of the Galactic bulge represent ideal places in which to develop an understanding of the ISOGAL colour-magnitude diagrams. Unlike the case for the solar neighbourhood, their contents are at a uniform distance from the Sun, affected only by the finite thickness of the Bulge.

The objects detected in the ISOGAL survey are found to be late-type M-giants at the red giant tip or on the Asymptotic Giant Branch (AGB). The ISOGAL colour-magnitude diagrams show that mass-loss starts at about M4 and increases towards later types. Many non-Miras have mass-loss rates similar to shorter-period Miras.

The visible counterparts of the ISOGAL sources have been identified in the database of the MACHO gravitational lensing survey. A first report of this work is included here. It is found that nearly all the ISOGAL sources are semi-regular variables (SRVs), which are many times more numerous than Miras. Their stellar luminosities increase with period. Based on a simple interpretation of the photometry, mass-loss rates from about 10^{-9} $M_\odot$ yr^{-1} to 10^{-7} $M_\odot$ yr^{-1} are found for SRVs with periods in excess of ∼60 days.

1 Introduction

The ISOGAL survey (see Omont, this volume) has covered a large number of heavily obscured fields in the inner galaxy in the mid-infrared, using the ISOCAM filters LW2 (5.5–8 μm) and LW3 (12–18 μm). Very little information is available concerning individual stars in most of the survey areas and it was decided to include the relatively well-studied Baade's Windows (BW) of low obscuration, namely NGC 6522 (l=+1°, b=–3.8°) and Sgr I (l=1.37°, b=–2.63°), whose A_V is about 1.5, for comparison purposes. The M-type stellar content of the NGC 6522 field has been surveyed by Blanco, McCarthy and Blanco [1] and Blanco [2]. Frogel & Whitford [3] have presented near-IR photometry of many stars. The census of Mira (V amplitude > 2.5 mag) variables in these fields is complete and their periods have been found by Lloyd Evans [4] (photographic infrared) and Glass et al. [5] (*JHKL* region). The K and bolometric magnitudes of the Miras obey period-luminosity relations. No carbon-type AGB stars have been found in these fields.

The results of the ISOGAL BW survey have recently been presented by Glass, Ganesh et al. [6]. In the two ISOGAL fields, each of 15 × 15 arcmin^2,

D. Lemke, M. Stickel, and K. Wilke (Eds.): LNP 548, pp. 363–370, 2000.

a total of 1,193 objects were found. The survey is believed to be complete to a level of 5 mJy in both bands, corresponding to $m_7 = 10.64$ and $m_{15} = 8.99$ mag. The photometric errors are < 0.2 mag for bright sources, rising to $<$ 0.4 mag for faint ones. The sensitivity and spatial resolution of ISOCAM are about two orders of magnitude better than with IRAS. At the faint end, the density of sources approaches the confusion limit.

The principal conclusions of the survey are illustrated by Fig. 1. There is a continuous sequence of increasing m_{15} mag with $m_7 - m_{15}$ colour. Much of the scatter is due to the distribution in depth of the Bulge, as found for the Mira log P – K relation ($\sigma = 0.35$; see Glass et al., [5]). Making use of the known spectral types of many objects, the data are interpreted as evidence for increasing dust emission with increase of stellar luminosity and decrease of temperature. Substantial numbers of stars in these fields have luminosities and mass-loss rates similar to those of the shorter-period Miras.

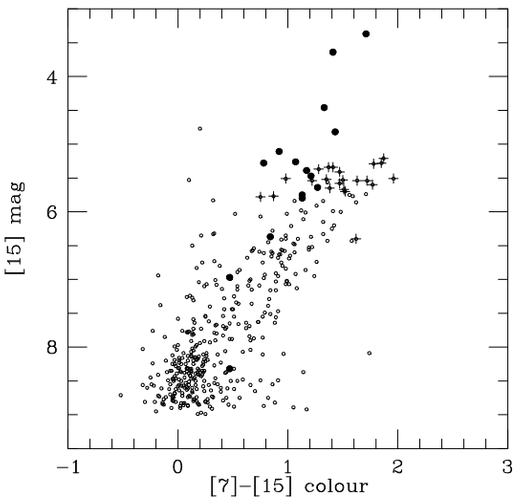

Fig. 1. ISOGAL colour-magnitude diagram for sources detected in the NGC 6522 and Sgr I Baade's Windows. A sequence of increasing 15 μm flux (flux arising in part from dust emission) with $m_7 - m_{15}$ colour (i.e., dust relative to photosphere), starts at the tip of the RGB in the bottom left corner and ends with the Miras at top right (solid points). Many other stars in the diagram, such as those with crosses, have luminosities and mass-loss rates similar to the shorter-period Miras. There is some contamination from foreground stars with small $m_7 - m_{15}$ colour

The ISOGAL 7 μm flux of a late-type star with an optically thin dust shell arises from its photosphere, while the 15 μm flux arises from a combination of the photosphere and the dust. This is illustrated in Fig. 2, an opacity-sampled stellar atmosphere calculation including "astronomical silicate" dust, taken from Aringer et al. [7]. The bandpasses of the ISOCAM LW2 and LW3 filters

are superimposed. It will be noticed that the 7 μm band is hardly affected by dust emission, but exhibits absorption features, probably due to water vapour and SiO. The 15μm band, on the other hand, may be dominated by silicate emission, which can greatly exceed that from the photosphere in this region.

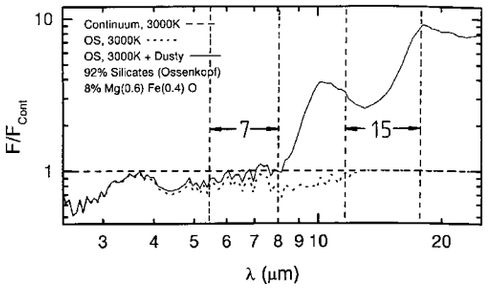

Fig. 2. Model of a 3000K stellar atmosphere with an "astronomical silicate" dust shell, taken from Aringer et al [7], with ISOCAM filter limits marked. The fluxes have been normalized to a 3000 K blackbody. Note that the 7μm ISOGAL filter mainly measures a photospheric flux, while the 15μm filter is mainly sensitive to dust

2 Correlation with MACHO

The Baade's Windows fields form part of the Bulge area that was surveyed nightly for six seasons of $\sim$ 250 days by the MACHO gravitational lensing project. The MACHO observations were made in two bands, v and r, at effective wavelengths around 500 nm and 700 nm, and were transformed using formulae from Alcock et al. [8] to Kron-Cousins V, R. The completeness and sensitivity to small-amplitude variations of MACHO and similar CCD-based surveys is much greater than in all previous work which depended on photographic techniques. In particular, large numbers of small-amplitude SRVs in the solar neighbourhood might be found if data of MACHO quality were available.

Counterparts of the ISOGAL sources were sought within a radius of 3 arcsec of their nominal positions. Since it is known that the ISOGAL sources are red giants, or else very bright early-type stars, only MACHO stars with $V < 13.5 + 4.67(V-R)$ were considered as candidates, with $(V-R)$ taken to be 0.5 in cases where only one colour was available. This left 40,000 objects in the two fields to select from. There were 904 positional matches. The distributions of distance residuals for the two fields, together with, as a test, random matches produced when the MACHO star coordinates were displaced by 15 arcsec, show that spurious matches should not exceed about 10% in

NGC 6522 and about 20% in Sgr I, which is a denser field. Sources which were not matched fell on gaps in the MACHO detector mosaic or, in a few cases, were too bright to be included in the MACHO database. A total of 332 stars had photometry at V, R, 7 μm and 15 μm and these were analysed further.

3 Periods and Light Curves

Almost all the 332 selected counterparts show variability at some level, and may be classified as semi-regular variables. Twenty-eight stars, most of them foreground bright objects, were rejected for saturation effects in their MACHO lightcurves (these included two Miras). Five of the ∼14 known Miras in the ISOGAL fields (see Glass, Ganesh et al. [6]) were recovered; the remaining 7 had already been rejected at the matching stage. Fourier amplitude spectra were calculated for all 332 members of the sample. In general, a short period (15 to 200 days) could be identified, but, for many sources, slower variability, not necessarily periodic, was also evident. Because of the seasonality of the data, each season was also analysed separately and the Fourier amplitude spectra were summed before searching for the most significant periods. Work is continuing on the period-finding, which may still be subject to revision.

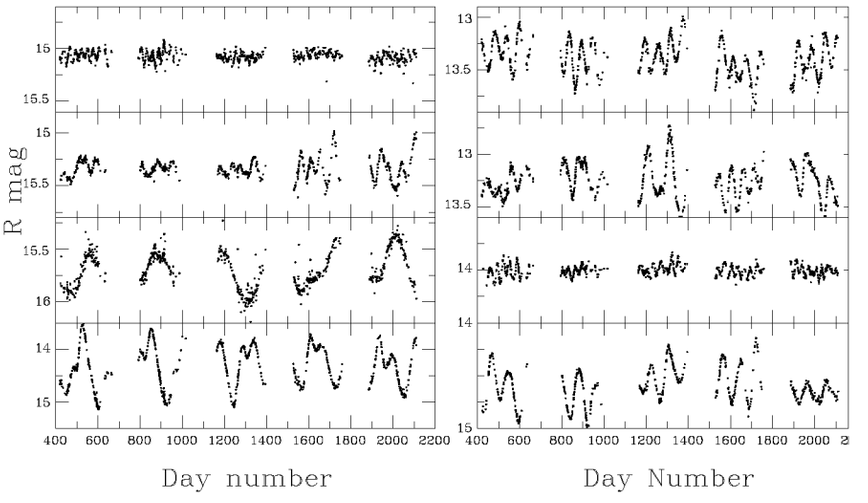

Fig. 3. Sample MACHO light curves of SRVs

The light curves (see Fig. 3) and periods are similar to those found by Wood et al [9] for AGB stars in the Large Magellanic Cloud. As in the LMC, the SRVs outnumber the Miras by a large factor (∼ 20 in this case). However, although most SRV light curves show clear evidence for variability in the 15–200 day range, as stated, only a few also show the longer periods around

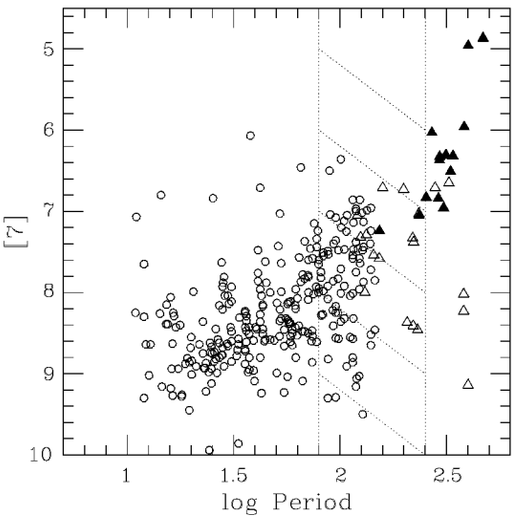

Fig. 4. Log P, m_7 plot for cross-identified objects. The open points are the main periods identified. Open triangles are separately identified long periods and solid triangles are Mira (large-amplitude) variables, some of which were saturated in the MACHO data. Periods for these cases were taken from Glass et al. [5]. The periods in the hatched area may be subject to some revision

300–400 days that seem to be common in the LMC (Type D in Fig. 2 of Wood et al. [9]).

In the log P, m_7 diagram (Fig. 4), a clear period-luminosity correlation is seen for the SRVs (periods below $\log P = 2.2$) with a steeper slope for the Miras. The stars with periods longer than 200 days include the Miras, which do not show simultaneous shorter periods. One star shows a single period of around 300 days and a 7μm luminosity appropriate to a Mira, but is not a Mira. The group of three stars around log $P = 2.35$ and $m_7 = 8.4$ show no evidence for short periods. On the other hand, there are three low points with log $P \sim 2.6$ which clearly show other periods around 50–60 days, allowing them alternative locations in the more heavily populated part of the diagram.

There is no clear period clumping among the SRVs. Instead, there seems to be a continuous progression, apart from the change in slope, in stellar luminosity, from the shortest period SRVs to the Miras. Solar neighbourhood SRVs with periods in the range 100-140 days show Population I kinematics that are similar to those of Miras with $P > 300$ days (Feast [10]), although shorter-period Miras fall into population II. Also, s-process elements are sometimes detected in both these sets of stars (Little, Little-Marenin & Bauer [11]). This has led to suggestions that at least some of the SRVs are related to the long-period Miras, but pulsating in higher overtones.

3.1 Amplitudes and SRV Classifications

The amplitudes of most of the SRVs are below 0.5 mag at R. The five Miras with MACHO light curves have amplitudes in the range 2.5–4. A few of the SRVs in the range 150–200 days have amplitudes of about 1 mag.

About two thirds of the light curves show persistent periodicity without much change in amplitude and could be classified SRa. The remainder, although they usually show persistent periodicity, also show slow random or very long-period level-shifts and are classified as SRb. However, it should be noted that these classsifications are subjective at best.

Kerschbaum & Hron [12] classify O-rich SRVs as "blue" or "red", according to their $V - m_{12}$ and IRAS colours. Probably the blue SRVs correspond to those stars with $m_{15} \geq 8$ and $m_7 - m_{15} \sim 0$, while the red SRVs are more luminous at 15μm and have dust emission (see below).

4 Mass Loss

For an order-of-magnitude estimate of the mass loss associated with a given star, we can estimate its 15 μm flux excess due to dust emission by assuming that the photospheric flux can be extrapolated as a Rayleigh-Jeans tail from the 7 μm measurement, which should be almost entirely free of dust emission. The result is shown in Fig. 5.

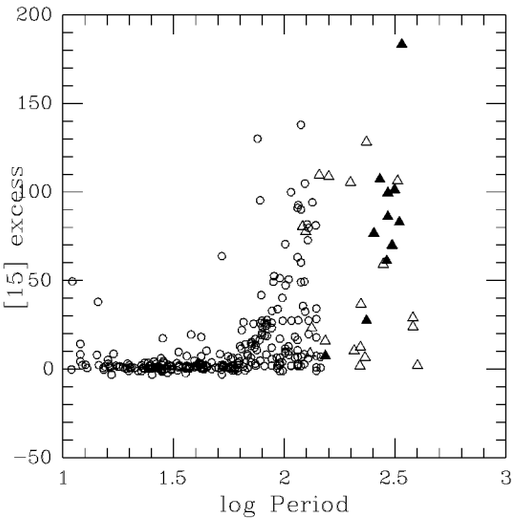

Fig. 5. Excess 15μm fluxes in mJy, beyond what is expected by assuming a Rayleigh-Jeans photospheric energy distribution fitted to the 7μm fluxes, shown plotted against log period. Having a period $P > 60$ days seems to be a necessary, but not a sufficient, condition for significant mass-loss

The mass-loss rates for the SRVs overlap those of the shorter-period Miras and clearly do not depend on amplitude of pulsation. The lack of measurable mass-loss for stars with $P < 60$ days accords with the finding of Kerschbaum, Oloffson & Hron [13] that mass-loss from stars having $0 < P < 75$ days could not be detected in CO radio emission, while those in the range $75 < P < 175$ days had a 50% detection rate.

Jura [14] gives for the mass-loss from an AGB star:

$$\dot{M} = 1.7 \times 10^{-7} v_{15} R_{kpc}^2 L_4^{-1/2} F_{\nu,60} \lambda_{10}^{1/2} M_{\odot} \mathrm{yr}^{-1},$$

where v_{15} is the gas outflow velocity in units of 15 kms^{-1}, determined from CO observations, R is the distance to the star in kpc, L_4 is the stellar luminosity in units of 10^4 $L_{\odot}$, $F_{\nu,60}$ is the flux from the object at 60 μm and λ_{10} is the mean wavelength of light emerging from the star in units of 10 μm. We take v to be 8 km sec^{-1}, the average value determined for semi-regular variables by Kerschbaum, Olofsson & Hron [13], $R \sim 8.2$ kpc, and $L_4 = 0.3$, from the bolometric magnitude of a 200-day Mira (Glass et al. [5]). To relate the given 15 μm flux to the 60 μ flux required, we very tentatively take the relation by Jura [15], intended for carbon stars (but see also the values of Q_{abs} for astronomical silicate grains; Draine & Lee [15]), namely $F_{\nu} \propto \nu^{1.54}$. If the excess 15 μm flux is 100 mJy, we obtain $\dot{\mathrm{M}} = 1.3 \times 10^{-7}$ $M_{\odot}$ yr^{-1}.

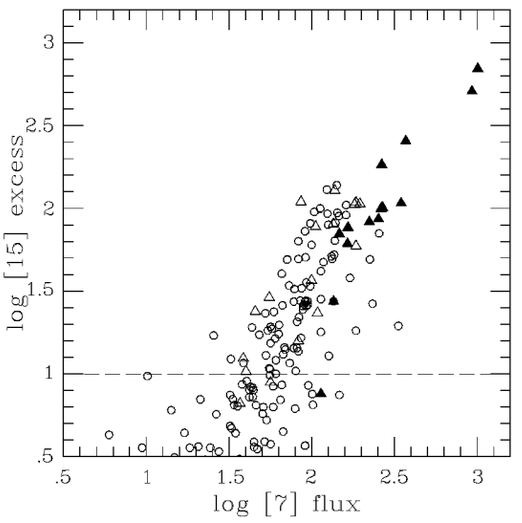

Fig. 6. Log 15μm excess, an indication of mass-loss, vs log 7μm flux, an indication of bolometric mag. Below the dashed line the data may be subject to photometric errors, exaggerated by taking logarithms. The slope is about 2.6

Figure 5 suggests that the lower rate limit of mass-loss that we detect is about two orders of magnitude less than the example discussed, or about $10^{-9}\ M_{\odot}\ \mathrm{yr}^{-1}$ (cf. Omont et al. [17]).

Mass-loss in SRVs is apparently a function of T, L and P. Because high luminosity in LPVs is also associated with low temperatures, it is unclear how these quantities separately affect $\dot{M}$. Considering L as an independent variable, from Fig. 6 we see that mass-loss increases with luminosity according to the approximate relation

$$\dot{M} \propto L^{2.6},$$

where we have assumed that $\dot{M}$ is proportional to the $15\,\mu$m flux excess and the bolometric luminosity of the star is proportional to the $7\,\mu$m flux (note that in the case of Miras dust emission may also contribute to the $7\,\mu$m band, leading to an over-estimate of photospheric luminosity).

Finally, the reader interested in the general properties of SRVs should remember that we have discussed so far only those stars which were detected in both MACHO and both ISOGAL bands. A preliminary glance at the light curves of the stars seen by ISOGAL only at $7\,\mu$m indicates that most of them are also SRVs, but presumably with mass-loss rates too low for $15\,\mu$m detection.

References

1. Blanco V.M., McCarthy M.F., Blanco B.M., 1984, AJ 89, 636
2. Blanco V.M., 1986, AJ, 91, 290
3. Frogel J.A., Whitford A.E., 1987, ApJ, 320, 199
4. Lloyd Evans T., 1976, MNRAS, 174, 169
5. Glass I.S., Whitelock P.A., Catchpole R.M., Feast M.W., 1995 MNRAS, 273, 383
6. Glass I.S., Ganesh S., Alard C., Blommaert J.A.D.L., Gilmore G., Lloyd Evans T., Omont A., Schultheis M. and Simon G., 1999, MNRAS 306, 127
7. Aringer B., Kerschbaum F., Hron J., Posch T., Windsteig W., Jorgensen U.G., Höfner S., 1999 In IAU Symp 191, Asymptotic Giant Branch Stars, ed Le Bertre T., Lèbre A., Waelkens C., Astronomical Society of the Pacific, San Franscisco
8. Alcock C. et al (MACHO collaboration), 1999, PASP (in press)
9. Wood P.R. et al (MACHO collaboration) 1999 In IAU Symp 191, Asymptotic Giant Branch Stars, ed Le Bertre T., Lèbre A., Waelkens C., Astronomical Society of the Pacific, San Franscisco
10. Feast M.W., 1963, MNRAS, 125, 367
11. Little S.J., Little-Marenin I.R., Bauer W.H., 1987, AJ, 97, 981
12. Kerschbaum F., Hron J., 1992, A&A, 263, 97
13. Kerschbaum F., Olofsson H., Hron J., 1996, A&A, 311, 273
14. Jura M., 1987, ApJ, 313, 743
15. Draine B.T., Lee H.M., 1984 ApJ, 285, 89
16. Jura M., 1986, ApJ, 303, 327
17. Omont A. et al., 1999, A&A, 348, 755

The ISOCAM GT Survey of Selected Areas in the Galactic Plane

Martin Burgdorf[1], Martin Cohen[2], Steve Price[3], Michael Egan[3], Stephan Ott[1], Shashikiran Ganesh[4,5], and Christophe Alard[4]

[1] ISO Data Centre, Astrophysics Division, Space Science Department of ESA, Villafranca del Castillo, P.O. Box 50727, 28080 Madrid, Spain.
[2] Radio Astronomy Lab., 601 Campbell Hall, University of California, Berkeley CA 94720, USA.
[3] Phillips Lab./GPOB, 29 Randolph Rd., Hanscom AFB, MA 01731-3010, USA.
[4] Institut d'Astrophysique de Paris, CNRS, 98bis Bd Arago, F-75014 Paris.
[5] Physical Research Laboratory, Navarangpura, Ahmedabad 380009, India.

Abstract. Seven fields in the inner Galactic plane were imaged by the Infrared Space Observatory's camera ISOCAM between April and September 1996 with the objective to observe the large scale properties of the Galaxy. Between 134 and 194 point sources were extracted at 15.0 μm in the $11.6 \times 11.6\,\mathrm{arcmin}^2$ fields, and between 182 and 289 objects at 9.6 μm. The limiting flux for completeness is approximately 10 mJy. For most of the areas there is a good correlation between the observed source counts and the numbers predicted with a multiwavelength model (SKY), originally built to replicate the IRAS 12- and 25-μm point source sky.
At specific Galactic longitudes, however, significantly more sources were detected with ISOCAM than predicted. These discrepancies enable us to probe the mid-infrared populations of the molecular ring and the bulge. Colour histograms are presented as other indicators of the nature of any populations potentially missing from the model.

1 Introduction

The determination of the spatial distribution of stars in our Galaxy is a problem with a long history. A fundamental difficulty in this "classical" stellar statistics is the extinction of star light caused by interstellar dust which limits star counts at visible wavelengths to relatively high Galactic latitudes or small windows near the plane. As this extinction decreases with increasing wavelength, radio and infrared observations were used in order to investigate the Galactic structure at large distances and close to the Galactic plane. These wavelengths, however, probe different Galactic constituents than the visible: Whereas the latter is dominated by ordinary stars, the radio directly traces the distribution of gas, and the mid-infrared preferentially detects dust

D. Lemke, M. Stickel, and K. Wilke (Eds.): LNP 548, pp. 371–378, 2000.

heated by nearby stellar objects. From these observations it was inferred that our Galaxy is a mildly barred spiral.
Detailed characterizations of the global distribution of stars in our Galaxy were studied by using plausible models of the near- and mid-infrared sky. Earlier surveys in the near-infrared, however, suffered either from too low sensitivities or from too coarse resolution to accurately model the structure of the Galaxy. This drawback will be met with the *DE*ep *N*ear *I*nfrared *S*urvey DENIS ([5]) and the 2 *M*icron *A*ll *S*ky *S*urvey 2MASS. At mid-infrared wavelengths our knowledge is mainly based on star counts from the IRAS Point Source Catalog, but unfortunately IRAS data products are often confusion limited along the Galactic plane. This "confusion" degraded IRAS' detection limit over much of the inner plane to fluxes of 1 Jy or greater. Therefore, only the most luminous of stars in the Galactic plane could be detected at large distances by IRAS, biasing the sample.
With the observations discussed in this paper it was possible to check the validity of models for the mid-infrared point source sky at lower fluxes. We chose for the comparison between observation and theory a modified version of the SKY model ([12], [3], [4]). The authors built an ab initio statistical model of the point source sky and tested it extensively against IRAS source counts. [2] extended the model's synthetic spectral library from 2.0 to 35.0 μm. This range covers in particular the ISOCAM filters LW3 and LW7 that were used in our observations.

2 Observations and Data Processing

The observing strategy consisted of sampling a number of critical positions in the Galactic plane with ISOCAM raster scans. The positions of the fields analyzed are given in Table 1.

Table 1. Central positions of the rasters in the GPSURVEY program

OSN	latitude b	longitude l	Revolution number
1	$-0.^\circ1$	$+5.^\circ2$	148
2	$+0.^\circ3$	$+15.^\circ9$	148
3	$+0.^\circ6$	$+28.^\circ1$	152
4	$+0.^\circ3$	$-28.^\circ8$	273
5	$0.^\circ0$	$-15.^\circ7$	289
6	$+0.^\circ1$	$-6.^\circ0$	391
7	$+3.^\circ1$	$0.^\circ0$	301

Each raster consisted of 6×6 images, separated by 100 arcsec in spacecraft y- and z-axis. This way we covered an area of 135 arcmin^2 in an observation of two hours duration. The images were taken with the Astronomical Observation Template CAM01 using filters LW3 and LW7. They cover the wavelength ranges 12-18 μm and 8.5-10.7 μm, respectively. The pixel field of view was 6 arcsec.
The starting point of the data processing was Auto Analysis Results from pipeline version 7. For the extraction of point sources we used an algorithm developed for the ISOGAL project ([1]), an observing program with a similar observing strategy as GPSURVEY ([9]). It contains inter alia corrections for the distortion of the ISOCAM field of view and for transient effects. Spot-checks of the lists produced were then carried out with the ISOCAM Interactive Analysis software ([11]) in order to test the reliability of the source extraction. In each field we detected more sources in filter LW7 than in filter LW3, as expected because of the shorter wavelength. Therefore it was possible to check the completeness of the LW3 source list by means of cross-identification with LW7. We found for 86 % of the sources stronger than 10 mJy in LW3 a counterpart in LW7, hence the source extraction worked in a satisfactory way down to that flux level.

3 Results

Figs. 1 and 2 show the comparison between the ISOCAM observations and the SKY 5 model for all fields that were observed in the Galactic Plane. For observations sequence numbers (OSN's) 1, 3, 4 and 5 we find excellent agreement. OSN 7 samples mainly the bulge population and is not further discussed in this paper (first results from an analysis of ISOCAM data taken in the inner Galactic Bulge can be found in [10]). For OSN's 2 and 6 we find significantly more sources in filter LW7 than the model predicted; at OSN 2 there is also an excess of sources in filter LW3.
For the comparison with the model we only used the inner 64 arcmin^2 of each GPSURVEY field, where 80 percent of the area has been observed in 4 different raster positions. This way we increased the reliability of the source detection and created a dataset with rather homogeneous signal to noise ratio. We considered only sources with fluxes above 10 mJy, hence the lower limit of our survey is at least five times the rms noise. This is the minimum needed to derive a sound number–flux-density relationship ([7]). For fluxes above several hundred mJy the number of sources found is too small to allow reliable statements on their distribution. Besides, the GPSURVEY fields had to be chosen away from bright sources in order to avoid saturation of the detectors, hence objects with very high fluxes might be systematically underrepresented in our samples. The source densities in our fields range between 3600 and 5200 deg^{-2} for LW3 and between 4900 and 7700 deg^{-2} for LW7; this is not far from the formal confusion limit of 8000 deg^{-2} at 15 μm ([8]).

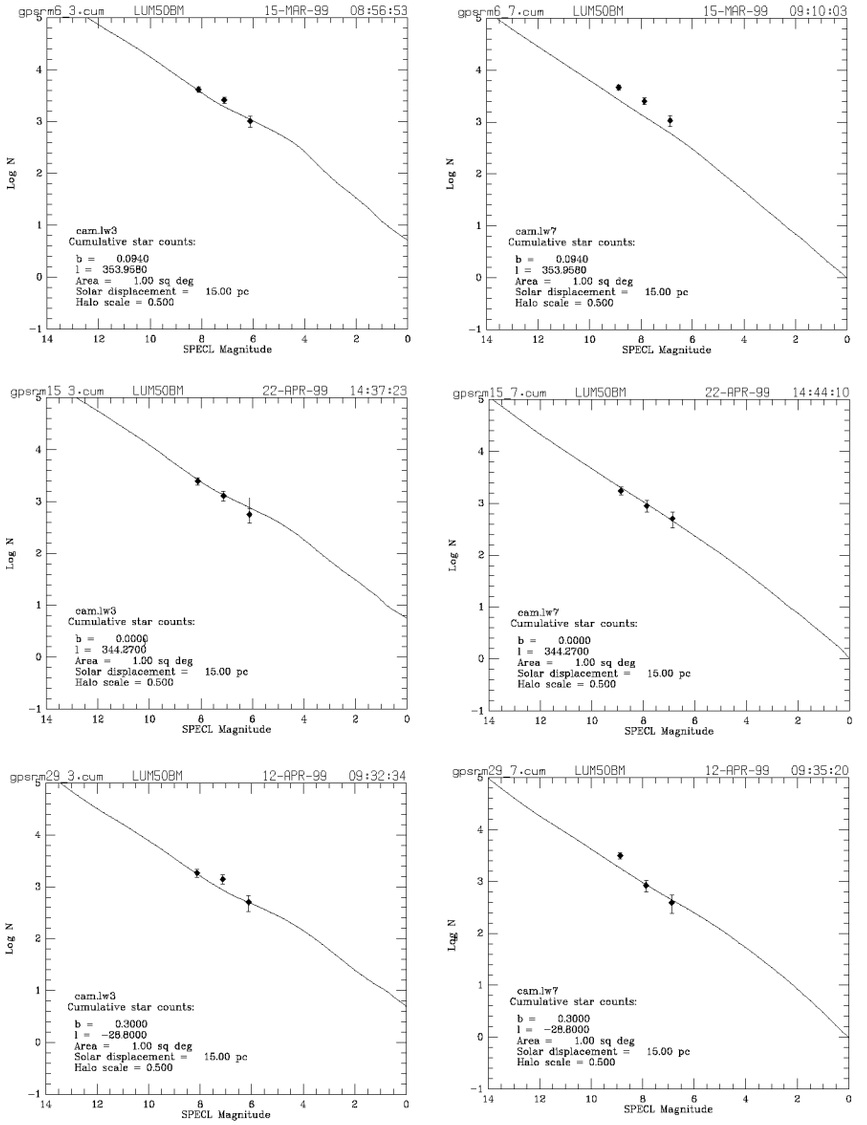

Fig. 1. Comparison of SKY 5 predictions and GPSURVEY observed cumulative star counts at the positions observed at negative longitudes in the Galactic Plane. Poisson error bars are shown, appropriate to the actual number of sources observed in each bin. Diamonds, observed star counts; solid line, total model prediction.

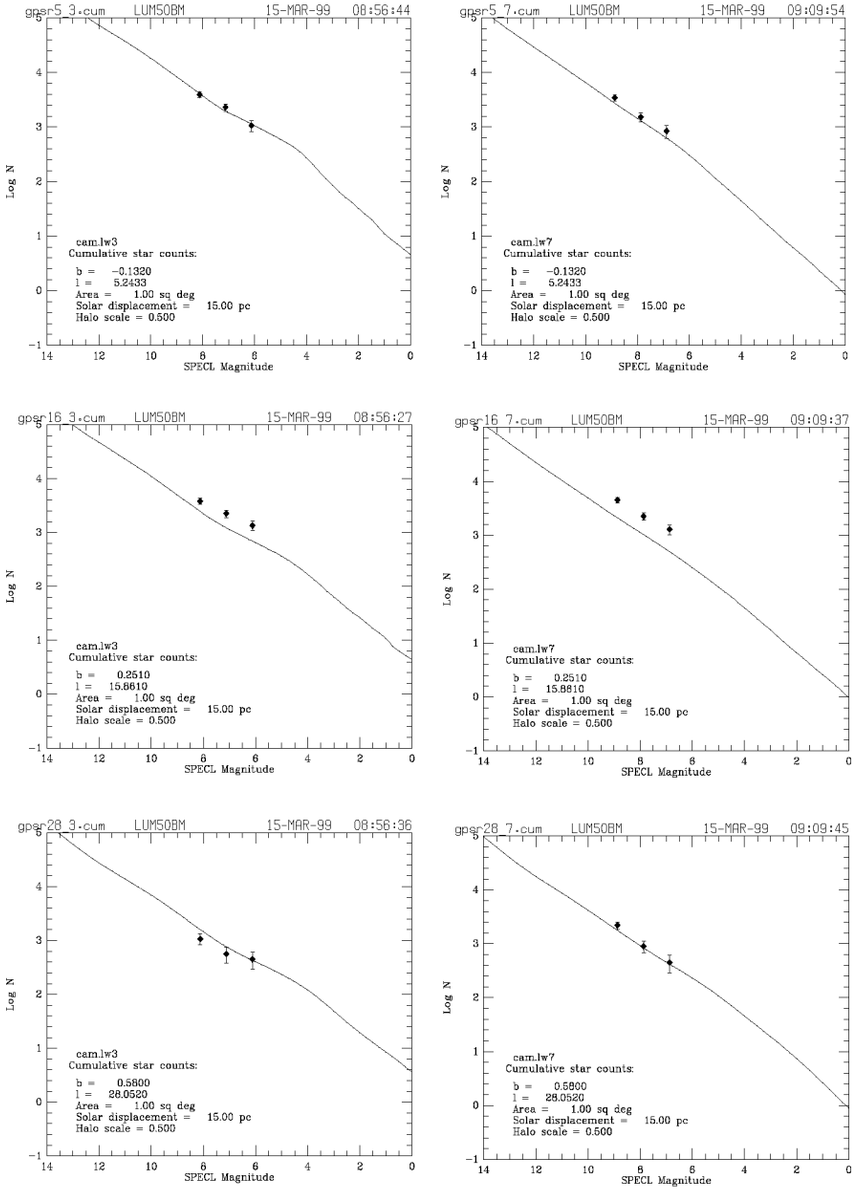

Fig. 2. Comparison of SKY 5 predictions and GPSURVEY observed cumulative star counts as in Fig. 1, but for positive Galactic longitudes.

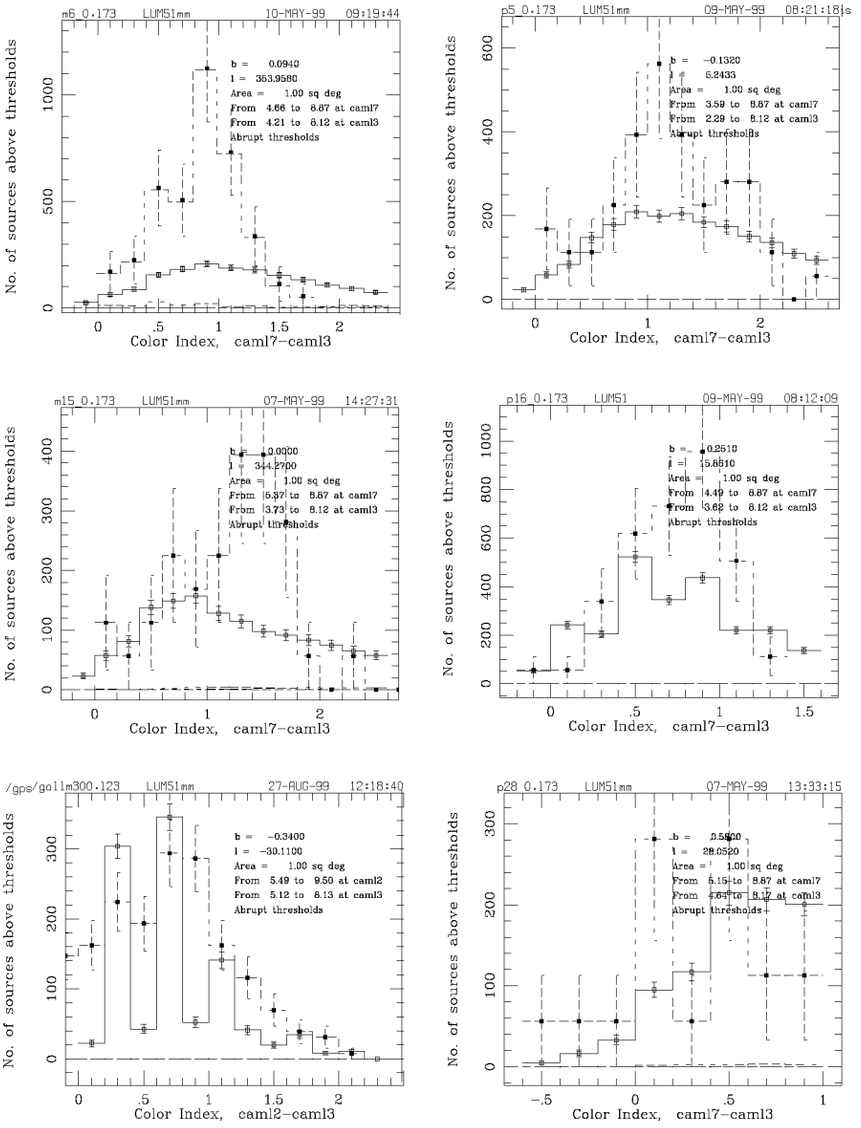

Fig. 3. [9.6]-[15] colour histograms for the fields observed in the Galactic Plane ([6.8]-[15] for $l = -30°$). Solid line, total model prediction; short dashed, observed number of point sources.

Fig. 3 gives the colour histograms for the fields that were observed in the Galactic Plane. The observed source colours agree with the model only at the largest distances from the Galactic Center that we observed. Further towards the interior we find more sources with colour indices [9.6]-[15] ≈ 1 than the model predicts.

4 Conclusions

We extended the range of fluxes S for source counts N in the mid-infrared by two orders of magnitude compared to what was known from IRAS. Because of the high sensitivity and spatial resolution provided by ISOCAM, it became possible to check the predictions in the SKY 5 model for the flux range 10-300 mJy.

From a comparison of the source lists for the two different filters we conclude that we have reached a high level of completeness in the LW3 filter down to 10 mJy. This is in good agreement with the limit found in the ISOGAL fields which were observed with a similar strategy. As the sensitivity of the camera in LW7 is rather similar to the one in LW3, we assume that the completeness limit in this filter is ≈ 10 mJy as well. This is borne out by the $\log N$, $\log S$ slopes which are smooth and essentially constant to this flux limit.

The comparison of the observed source counts with the SKY model showed discrepancies at $l = -6.^\circ 0$ and $l = 15.^\circ 9$. From the colour indices of the excess stars observed we conclude that they must be late type giants: K, M or AGB stars. This finding supports a stick-like bar with a half-length of about 4 kpc in the inner Galaxy more than a ring ([6]).

Extinction does not affect the source counts strongly, even in filter LW7 which is centered on the "Silicate band" at 9.7 μm. The distribution of stars in a two colour diagram generated with observations at 6.8, 9.6 and 15 μm at $l = -6.^\circ 0$ in the Galactic plane suggests an extinction of half a magnitude in LW7. This means that extinction is negligible in LW3 for all the directions probed with this survey.

References

1. Alard C. et al. (2000) in preparation
2. Cohen, M. (1993) A model of the 2-35 micron Point Source Infrared Sky. AJ 105, 1860–1879
3. Cohen, M. (1994) Powerful model for the point source sky: Far-ultraviolet and enhanced midinfrared performance. AJ 107, 582–593
4. Cohen, M. (1995) The displacement of the sun from the galactic plane using IRAS and faust source counts. ApJ 444, 874–878
5. Epchtein, N. (1997) The Deep Near Infrared Survey Of The Southern Sky (DENIS): Progress report, and scientific results overview. The Impact of Near-Infrared Sky Surveys on Galactic and Extragalactic Astronomy. Kluwer, Dordrecht

6. Hammersley, P., Garzón, F. et al. (1997) IR Star Counts In The Inner Disc. The Impact of Near-Infrared Sky Surveys on Galactic and Extragalactic Astronomy. Kluwer, Dordrecht
7. Murdoch, H., Crawford, D. et al. (1973) Maximum-Likelihood Estimation Of The Number–Flux-Density Distribution Of Radio Sources In The Presence Of Noise And Confusion. ApJ 183, 1–13
8. Omont, A., Ganesh, S. et al. (1999) ISOGAL-DENIS detection of red giants with weak mass loss in the Galactic bulge. A&A, 348, 755–767
9. Omont, A. (2000) The ISOGAL survey of the inner Galaxy: Summary of present results. See these proceedings
10. Omont, A., Caillaud, B. et al. (1997) Mass-Losing AGB Stars And Young Stars In The ISOGAL Survey. The Impact of Near-Infrared Sky Surveys on Galactic and Extragalactic Astronomy. Kluwer, Dordrecht
11. Ott, S., Abergel, A. et al. (1997) Design and Implementation of CIA, the ISOCAM Interactive Analysis System. A.S.P. Conf. Ser. 125, San Francisco
12. Wainscoat, R., Cohen, M. et al. (1992) A Model Of The 8-25 Micron Point Source Infrared Sky. ApJ Suppl., 83, 111–146

Extragalactic Surveys Using NICMOS

Marcia Rieke

Steward Observatory, University of Arizona, Tucson, AZ 85721, USA

Abstract. The Near-Infrared Camera and Multi-Object Spectrometer (NICMOS) on the Hubble Space telescope was used for several unbiased deep sky surveys at high galactic latitude. The instrument was also used for directed surveys of quiescent and starburst galaxies. Snapshot surveys of AGNs were also carried out. Of interest to the ISO community was the parallel spectroscopic survey which detected Hα emission at a rate comparable to that for ISOCAM 15μm galaxy detections.

1 Introduction

NICMOS was installed into HST in February of 1997. It includes three cameras for imaging from 0.8μm to 2.5μm at diffraction limited scales for cameras 1 and 2 and at 0.2″/pixel for camera 3, the "wide-field" camera. Camera 3 is also equipped with slitless grisms which enables spectroscopic surveys covering nearly a micron at once. The instrument is most sensitive near 1.6μm where the HST and sky background are at a minimum. NICMOS can be operated when another instrument is prime so areal coverage can be built up in a parallel mode.

2 Deep, Directed Surveys

Two surveys of the north Hubble Deep Field were executed using NICMOS. Thompson et al. (1999) [13] observed one camera 3 field (a net of 49″x49″) for 36 hours at both 1.1μm and 1.6μm. An additional 20 hours were used in observing with a grism covering 1.1μm to 1.9μm. The results from the broadband survey include detections as faint as $\sim$ 4 nJys at 1.6μm. Where the counts are complete, a flattening is seen which suggests that at this depth, corresponding to 1.6×10^9 objects/sr/mag, NICMOS may be coming close to seeing all the galaxies that exist. However, this is far deeper than probed by ISOCAM and is dominated by galaxies where the stellar output is observed. The very small area surveyed must also be kept in mind as this line of sight may not be representative.

Another deep survey was executed by a team led by Mark Dickinson. They surveyed the entire HDF-N at the same two wavelengths as Thompson et al. but only using 3.5 hours of integration per point. A preliminary report of this work is presented in Dickinson (1999) [4]. Dickinson et al. (1999) [5] report on the object J123656.3+621322 which stood out in this survey because of its red color. The flux of this object drops by over a factor of 8

D. Lemke, M. Stickel, and K. Wilke (Eds.): LNP 548, pp. 381–384, 2000.

between 1.1μm and 1.6μm. They model this as either a dusty galaxy with z somewhat greater than 2, a maximally old galaxy at z greater than 3 (and perhaps with some dust) or as a $z > 10$ object whose flux at $\lambda < 1.6$ μm has been suppressed by the intergalactic medium.

The most striking fact about these deep surveys is not that some very red galaxies were found, but how similar galaxies appear in the NICMOS images as compared to the shorter wavelength data. Only a few galaxies appear to have morphologies that vary strongly as a function of wavelength.

NICMOS was also used to observe the HDF-S. See Treu et al. (1998) [15] for a report on an extremely red galaxy found in the test exposures for this project. Stiavelli et al. 1999 report that this is a possible high redshift elliptical.

3 Parallel Surveys

Instruments on HST can gather data in a parallel mode, and NICMOS has been used to conduct a serendipitous survey of high galactic latitudes at 1.6μm and also using the G150 grism covering 1.1μm to 1.9μm. Yan et al. (1998) [16] report on the broadband imaging of 12 fields using camera 3 with exposure times ranging from 0.6 to 3.8 hours. They learned that for a 1.6μm flux of < 0.2μJy, there are a total of 1×10^9 galaxies/sr and the slope of the dN/dmag relation is 0.3, in rough agreement with the deeper but smaller area survey of Thompson et al. Yan et al. also report a deficit of low surface brightness galaxies.

Teplitz et al. (1998) [12] report on parallel observations using the two higher resolution NICMOS cameras. This survey was not as deep as that reported by Yan et al. but took advantage of the good spatial resolution to classify galaxies morphologically. They found that their NICMOS data has a smaller percentage of irregular galaxies than shorter wavelength surveys. They conclude that this is the result of irregulars being relatively blue and at modest ($z < 1$) redshift rather than NICMOS seeing the same galaxies as seen at shorter wavelengths but exhibiting more regular morphologies at longer wavelengths.

A search for high redshift ellipticals in the NIMCOS parallel data was conducted by Treu and Stiavelli (1999) [14]. They combined NICMOS data with optical data either from the ground or HST. They found a deficit of objects that would be examples of galaxies formed in a single burst at very high redshift with only passive evolution since. They did find evidence for populations which must have formed before z∼2.

4 Relationship of Grism Results to ISOCAM Surveys

Potentially of greatest interest to ISO observers was the grism parallel survey with results reported by McCarthy et al. (1999) [7]. The grism used covers

1.1μm to 1.9μm which translates to a redshift range of 0.8 to 1.9 for Hα. The survey covered an area of 58 square arc minutes to a limit of 0.4×10^{-16} ergs/sec/cm^{-2} which corresponds to a volume of 100,000 cubic Mpc, much larger than any previous high redshift Hα survey. The NICMOS parallel survey was also completely unbiased rather than being based on a search for emission-line objects around some known object like a QSO or radio galaxy. McCarthy et al. found a total of 33 objects, essentially all with one emission line which is assumed to be Hα.

Yan et al.(1999) [16] constructed an Hα luminosity function from these data at z$\sim$1.3 and found the Hα luminosity to be 14 times the local value. Removing the three brightest objects to make an approximate correction for AGN leaves a luminosity ten times the local value. Using relations given in Kennicutt (1998) [6], these Hα luminosities can be transformed into far-infrared luminosities. This calculation shows that the peak in the distribution of far-infrared luminosities of the NICMOS grism galaxies is at $8 \times 10^{10} L_{\odot}$ with significant numbers at $\sim 1.4 \times 10^{11} L_{\odot}$.

The overall properties of this survey give 33 galaxies per 58 square arc minutes or 6.7×10^6 galaxies/sr in a range of 0.9 in redshift for 6.1×10^6 galaxies/sr/dz with an average z=1.35. If these galaxies have spectral energy distributions like that of M82 in the Devriendt et al. (1999) [3] compilation, these galaxies would have fluxes of $\sim$ 30 μJy at 15μm and estimating from Tan et al., could comprise as much as 10% of the ISOCAM detections. This is a result very complementary to that reported by D. Rigopoulou at this conference.

5 Object-Oriented Surveys

Because of their limited fields of view, instruments on HST are more frequently used for surveys of particular classes of objects than in unbiased surveys. NICMOS is no exception to this rule, and several classes of galaxy have been studied using NICMOS. Scoville et al. 1999 [9] have imaged a sample of ultraluminous galaxies. They found evidence for nuclear point sources in 7 out of 24 galaxies and $r^{1/4}$ law distributions in 9 out of the 24 objects. Not surprisingly, they also found abundant evidence for nuclear reddening. First results from AGN imaging snapshot surveys are given in Regan and Mulchaey (1999) [8] who find evidence for nuclear bars in only 3 out 12 galaxies in their sample.

A special capability of NICMOS is its ability to take continuum-corrected emission-line images, especially of Pα emission. Böker et al. (1999) [2] used the HST snapshot mode to acquire Pα images of 94 nearby galaxy nuclei using camera 3. They find the nuclear Pα surface brightness is highest in early-type (Sa-Sb) spirals. In the first of what will be a series of papers on nearby starbursts, Alonso-Herrero et al. (1999) [1] report on emission-line imaging of Arp299.

Acknowledgements

The United States National Aeronautics and Space Administration is thanked for travel support, and I also thank the Local Organizing Committee for providing support while I was at Ringberg.

References

1. Alonso-Herrero, A., Rieke, M. J., Rieke, G. H. 1999, Astrophys. Space Sci. 263, 131
2. Böker, T., Calzetti, D., Sparks, W., Axon, D., Bergeron, L., Bushouse, H., Colina, L., Daou, D., Gilmore, D., Holfeltz, S., MacKenty, J., Mazzuca, L., Monroe, B., Najita, J., Noll, K., Nota, A., Ritchie, C., Schultz, A., Sosey, M., Storrs, A., Suchkov, A. 1999 ApJSupp 124 95.
3. Devriendt, J., Guiderdoni, B., Sadat, R. (1999) A&A 350 381.
4. Dickinson, M. (1999) A Complete NICMOS Map of the Hubble Deep Field North. In Holt, S., Smith, E. (Eds) After the Dark Ages: When Galaxies Were Young (the Universe at $2 < z < 5$), 9th Annual October Astrophysics Conference, Maryland, 12-14 Ocotber, 1998. American Institute of Physics Press,New York,122.
5. Dickinson, M., Hanley, C., Elston, R., Eisenhardt, P., Stanford, S., Adelberger, K., Shapley, A., Steidel, C., Papovich, C., Szalay, A., Bershady, M., Conselice, C., Ferguson, H., Fruchter, A. (1999) ApJ in press.
6. Kennicutt, R. (1998) ARA&A 36 189.
7. McCarthy, P., Yan, L., Freudling, W., Teplitz, H., Malumuth, E., Weymann, R., Malkan, M., Fosbury, R., Gardner, J., Storrie-Lombardi, L., Thompson, R., Williams, R., Heap, S. (1999) ApJ 520 548.
8. Regan, M., Mulchaey, J. (1999) AJ 117 2676.
9. Scoville,N., Evans, A., Thompson, R., Rieke, M., Hines, D., Low, F., Dinshaw, N., Surace, J., Armus, L. (1999), ApJ in press.
10. Stiavelli,M., Treu, T., Carollo, C., Rosati, P., Viezzer, R, Casertano, S., Dickinson, M., Ferguson, H., Fruchter, A., Madaui, P., Martin, C., Teplitz, H. (1999) A&A 342 L25.
11. Tan,J., Silk, J., Balland, C. (1999) 522 579.
12. Teplitz, H., gardner, J., Malamuth, E., Heap, S. (1998) ApJ 507 17.
13. Thompson, R., Storrie-Lombardi, L., Weymann, R., Rieke, M., Schneider, G., Stobie, E., Lytle, D. (1999) AJ 117 17.
14. Treu, T., Stiavell, M. (1999) ApJ 523 27.
15. Treu, T., Stiavelli, M., Walker, A., Williams, R., Baum, S., Bernstein, G., Blacker, B., Carollo, C., Casertano, S., Dickinson, M., Demllo, D., Ferguson, H., Fruchter, A., Lucas, R., Mackenty, J., Madau, P., Postman, M. (1998) A&A 340 10.
16. Yan, L., McCarthy, P., Freudling, W., Teplitz, H., Malumuth, E., Weymann, R., Malkan, M. (1999) ApJ 519 L47.
17. Yan, L., McCarthy, P., Storrie-Lombardi, L., Weymann, R. (1998) ApJ 503 L19.

Commissioning Data from the Sloan Digital Sky Survey

David Schlegel

Princeton University, Princeton NJ 08544, USA

Abstract. The Sloan Digital Sky Survey (SDSS) will provide a photometrically and astrometrically calibrated imaging survey of one-quarter of the sky in five bands to a depth of $g \sim 23$ mag and a spectroscopic survey of the 10^6 brightest galaxies and 10^5 brightest quasars. This talk describes the operation of the survey, the data obtained over the year of commissioning, and some of the first science results from this data.

1 Imaging Survey

1.1 The Instrument and Survey Strategy

The SDSS uses a dedicated 2.5-meter altitude-azimuth telescope at Apache Point, New Mexico. The instrument uses a modified f/5.0 Ritchey-Chrétien optical design that provides a nearly distortion-free 3-degree focal plane.

The imaging camera uses 30 2048×2048 SITe/Tektronix CCDs with $0.''4$ pixels. The photometric detectors are arrayed in the focal plane in six columns of five chips each. The sky is imaged in drift-scan mode at the sidereal rate (at the equator). The result is a long "strip" of near-simultaneous five-color data for the six columns. Each column subtends $13.'5$ and is separted by $24.'7$ from its neighbor. The observations are filled in by a second, offset strip to produce a filled "stripe" with 5% lateral overlap.

The sky is necessarily imaged in great circles. The SDSS region covers $10,000$ contiguous square degrees in the Northern Galactic Cap at $|b| > 30^\circ$, adjusted to lie within the minimum of Galactic extinction. Figure 1 plots those great circles over the Schlegel et al. (1998) [8] extinction maps.

The limiting magnitudes for SDSS and for the 2MASS survey are listed in Table 2. Further details about the camera and the filter responses can be found in Gunn et al. (1999) [6].

1.2 Deep Sourthern Survey

In the Southern Galactic Cap, three stripes will be repeatedly observed to produce a survey ~ 2 mag deeper than the main survey (see Table 2), covering ~ 600 square degrees. The equatorial stripe is located at RA=$20.7^h \rightarrow 4^h$,

D. Lemke, M. Stickel, and K. Wilke (Eds.): LNP 548, pp. 385–393, 2000.

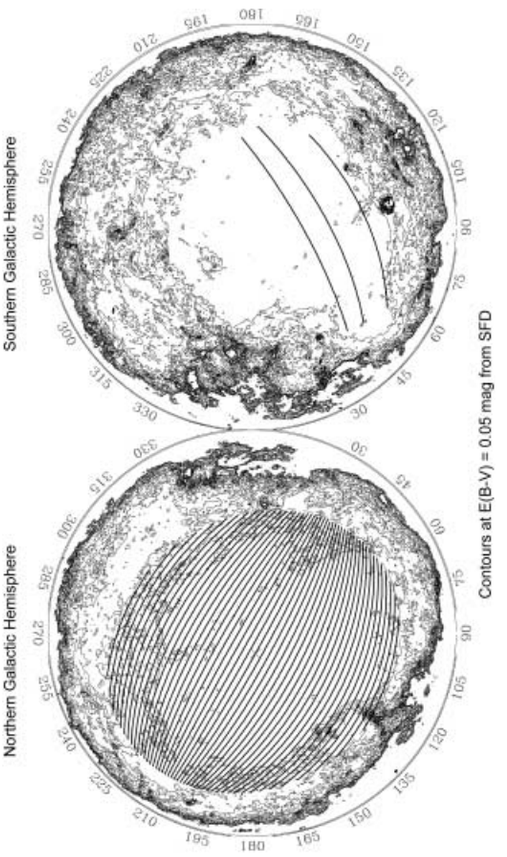

Fig. 1. The SDSS stripes overplotted on the Schlegel et al. (1998) [8] reddening maps.

DEC = $\pm 1.25°$. The other two (non-adjacent) stripes will cover RA=$20.7^h \rightarrow 4^h$, DEC=$-5.°8 \rightarrow -10.° \rightarrow -5.°8$, and RA=$22.4^h \rightarrow 2.3^h$, DEC=$13.°2 \rightarrow 15.° \rightarrow 8.°7$. These 3 stripes are marked on Figure 1. As well as the additional depth, we will have ~ 40 repeated observations allowing the opportunity to thoroughly investigate time-variable phenomena.

1.3 Astrometry

The imaging camera also contains 22 leading and trailing astrometric CCDs that cover the entire width of the camera. These smaller CCDs observe in the magnitude range $r = [4, 15.5]$ mag, allowing a tie-in from bright astrometric

Table 1. Limiting magnitudes for point sources in the SDSS and 2MASS surveys (5:1 signal to noise ratio).

Table 2. SDSS+2MASS Survey Depths

Band	λ_{eff} (Å)	SDSS/2MASS (mag)	Southern Strip (mag)
u	3540	22.0	24.2
g	4920	23.0	25.2
r	6340	22.8	25.0
i	7800	22.0	24.2
z	9290	20.5	22.7
J	12500	15.9	
H	16500	15.2	
K	21600	14.5	

standards and the brightest, unsaturated stars in our imaging survey. We have demonstrated an astrometric accuracy of 80 milli-arcseconds.

Because the sky takes 10 minutes to cross from the r-band to z-band (at the extremes of the focal plane), we are sensitve to finding objects that move on this timescale. The survey is sensitive to motion at 40 A.U. (at opposition), which allows us to identify Kuiper Belt objects.

1.4 Photometric Calibration

The primary photometric calibration for the survey will be done by the 20-inch Photometric Telescope adjacent to the 2.5-meter. This telescope will observe a grid of 140 isolated stars, tied to our three fundamental standards: BD+21°607, BD+26°2606, and BD+17°4708 (see Fukugita et al. 1996 [5]). Each night, the Photometric Telescope alternates between observing patches of the sky in the same strip as the imaging camera, and standard stars at different airmasses to establish absolute calibrations and airmass terms.

1.5 PHOTO Software

As amazing as the SDSS hardware is, the software that automatically reduces the 20 Gb/hour data stream to useful object catalogs is equally impressive. A schematic overview of the software systems appears in Figure 2.

The photometric pipeline (PHOTO; Lupton et al. 2000) reduces all the imaging data. It calculates the point spread functions as a function of time and positions on the CCDs, combines data from the five bands, deblends superposed objects, and measures positions, magnitudes, and shape parameters for all detected objects. The photometric pipeline uses position information

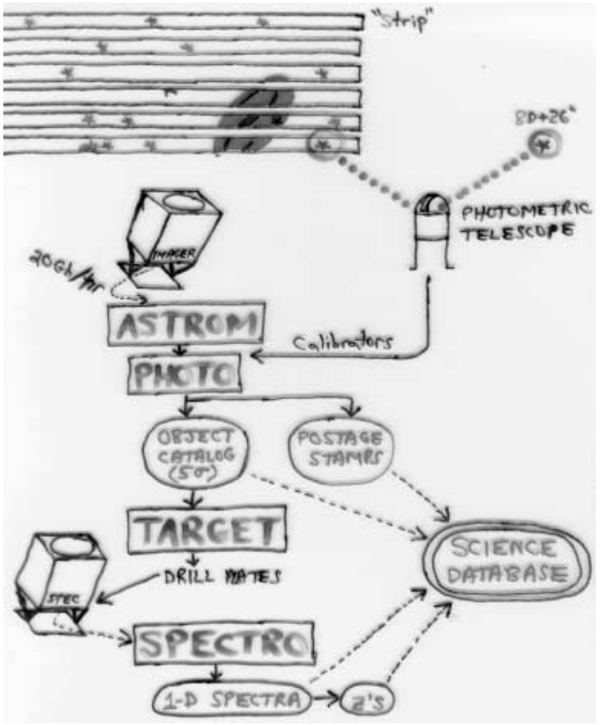

Fig. 2. Overview of SDSS observing strategy.

from the astrometric pipeline and photometric calibrations from the photometric telescope. The outputs are objects catalogs and "postage stamp" images of these objects.

Note that the catalogs list Petrosian (1976) radii and mangitudes because they do not introduce biases with distance or Galactic extinction (as aperature magnitudes would do). These are magnitudes within a radius at which the surface brightness is some fraction of the mean surface brightness within that radius.

Figure 3 presents color-color diagrams for 4 hours of data taken on March 20/21, 1999. Only the ~ 1 million stellar sources at $i < 20.2$ mag are plotted. For clarity, the inner parts of the diagrams are shown as contours, linearly spaced in the density of stars in color-color space. The width of the stellar locus in color space is very much dominated by real differences in stellar colors rather than measurement errors.

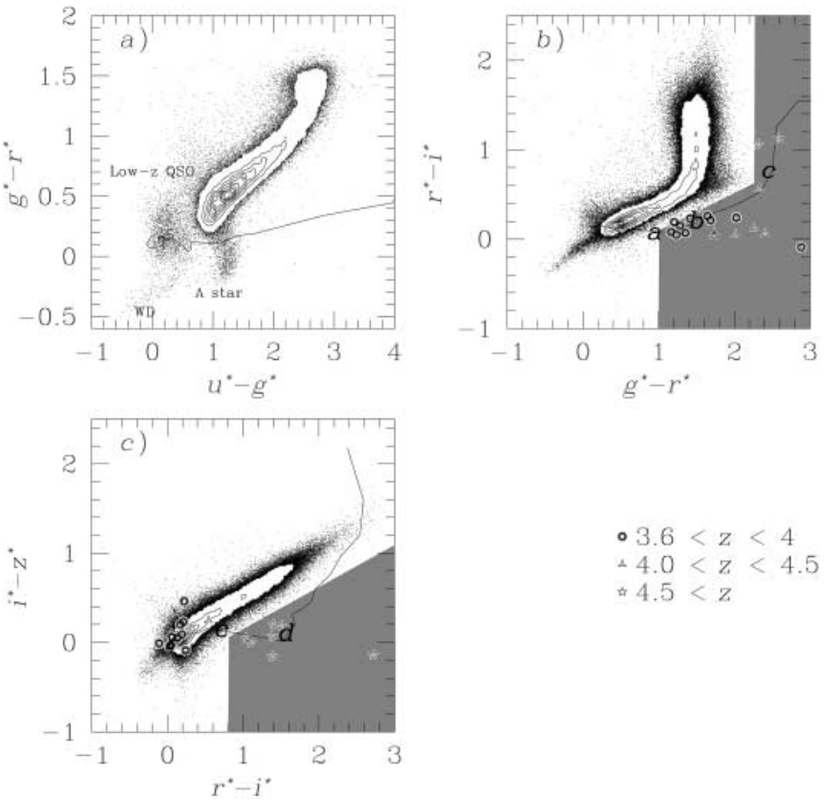

Fig. 3. Color-color diagrams for all stellar objects in 75 square degrees of SDSS imaging data (reproduced from Fan et al. 1999) [3]. The solid line is the median track of simulated quasar colors as a function of redshift, and the symbols denote 24 spectroscopically-confirmed quasars at $z > 3.6$.

2 Spectroscopic Survey

2.1 The Instrument

The goal of the spectroscopic survey is to obtain spectra and redshifts for the million brightest galaxies and 100,000 brightest quasars in the survey area. This will be done with a 640-fiber spectrograph on the same 2.5-meter telescope used for imaging, with the fibers fed to two double spectrographs (four 2048×2048 CCDs). The fibers have a diameter of $3''$, which is a good compromise between collecting much of a galaxy's light and rejecting the night sky. The spectral coverage is $3900-9200$ Å, with a resolution of $\lambda/\Delta\lambda = 1700$. This coverage ensures that the CaII H+K lines are observable at $z = 0$,

and Hα is observable to $z = 0.40$. The total system throughput for the spectrographs is 25%.

The 10,000 deg^2 of the SDSS region will be "tiled" into $\sim 3,000$ circular (overlapping) plates of diameter 3°. Each plate will observe 608 objects and 32 blank sky positions. After objects are selected from the PHOTO outputs (see Figure 2), the appropriate plates are drilled at the U. Washington machine shop and shipped to the telescope. These plates are inserted into cartridges which must be manually(!) plugged before bolting them to the focal plane of the telescope. We have 9 such cartridges, which can all be plugged during the daytime and swapped-out on the telescope during a spectroscopic observing run. A full complement of cartridges requires plugging 5760 fibers by hand.

2.2 Target Selection

PHOTO has detected objects, classified them as point sources or extented, and measured their Petrosian magnitudes. These magnitudes are corrected for Galactic extinction using the Schlegel et al. (1998: SFD) [8] extinction maps to guarantee uniformity of the survey.

From these data, we select two galaxy samples. The main sample of 900,000 galaxies will be selected to a Petrosian limit of $r = 18.1$ mag with a median redshift of $z \sim 0.1$ The second galaxy sample, of 100,000 galaxies, exploits the characteristics of red color and high metallicity of bright red galaxies (BRGs). Strong absorption lines in those galaxies allow our spectrographs to reliably measure their redshifts to $r = 19.5$ mag. Reasonably accurate photometric redshifts can be determined from the PHOTO colors, allowing the selection of a distance-limited sample to $z = 0.45$ [1,2]. Since brightest cluster galaxies have these red colors, this second sample will be used to probe the clustering of high-density regions in the Universe out to moderate redshift.

About 150,000 quasar candidates will be selected from stellar objects that deviate from the stellar locus in color space. In Figure 3, the shaded areas on the $g-r$ vs. $r-i$ and the $r-i$ vs. $i-z$ diagrams represent the selection criteria used to select quasar candidates. This method has proven very successful at identifying quasars, with a success rate of $\sim 65\%$. From the commissioning data, 37 high-redshift ($z > 3.6$) quasars have been published [3,4], with the most distant setting the record at $z = 5.03$!

Finally, the spectroscopic survey will target $\sim 100,000$ sources that will not necessarily define uniform or complete samples. These include $15,000$ ROSAT sources, $12,000$ spectrophotometric standards, $20,000$ reddening standards, and $40,000$ other stars and "serendipity" sources.

2.3 SPECTRO Software

The spectroscopic data are reduced by an automated pipeline, SPECTRO, that returns calibrated spectra, redshifts, and spectral typing. From com-

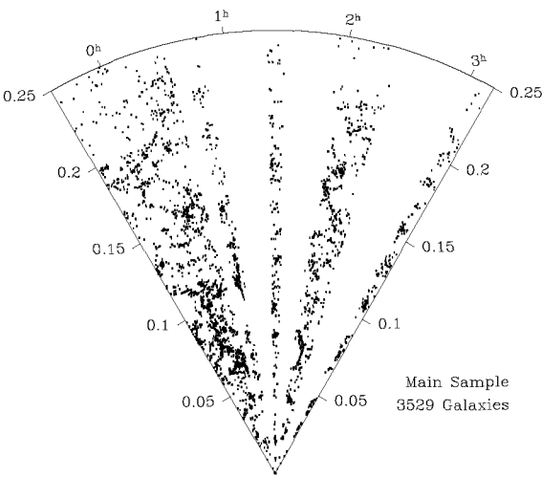

Fig. 4. Redshift-space map for galaxies from 12 SDSS commissioning plates. The RA is labelled, and the slice is 3° wide in declination centered on the equator.

missioning data, redshifts have been shown to be reliable 97% of the time for galaxies. The reliability will likely not be as high for the quasar sample. Figure 4 shows a very preliminary redshift-space map for 3,529 galaxies out to $z = 0.25$. Note that this represents only 0.4% of the final survey!

Table 3. SDSS Timeline

Jan '98	Mirror arrives at Apache Pt., N.M.
May '98	Mosaic camera first light
Sep '98	First long equatorial scan
Jun '99	Spectro-1 first light (320 fibers)
Jun '99	Light baffling complete
Sep '99	First long off-equator scan
	Spectro-1 & Spectro-2 (640 fibers)
Oct '99	"In the can": $\sim 200\text{deg}^2$ science-quality images
	12 spectro plates $\rightarrow$ 7000 spectra
(*Nov-Jan*	*Shutdown to fix secondary mirror*)
Feb '00	Begin survey
Feb '05	End survey

3 Survey Status

The Sloan survey has been many years in the making, and has existed even longer as an idea. However, scientific commissioning only began with first light of the imaging camera in May 1998. In September 1999, we achieved two major goals: (1) the first off-equator imaging scan, with the telescope tracking a great circle to high precision, and (2) spectroscopic plates of 640 objects using both double-spectrographs. With a fix of the damaged secondary mirror now in progress, we expect to begin the survey proper in February 2000. A summary timeline appears in Table 3.

The past year of commissioning has produced a tremendous amount of data and early science results. As of November 1999, SDSS has reduced approximately 450 $\deg^2$ of images and follow-up spectroscopy of 8,000 objects (14 plates). As shown in Figure 3, Fan et al. have greatly increased the list of known high-redshift quasars. Strauss et al. (1999) [9] have reported the discovery of very low mass stars (type L) and the first field methane dwarf (type T). The detection rate shows that SDSS should find several thousand L and T dwarfs. Also, SDSS has found several objects of wierd color that defy classification that may represent new classes of objects.

Further technical details and scientific goals of the SDSS can be found in the on-line Project Book at

`http://www.astro.princeton.edu/PBOOK/welcome.htm`,

which will soon be submitted for publication [10].

Acknowledgements

The SDSS is a joint project of The University of Chicago, Fermilab, the Institute for Advanced Study, the Japan Participation Group, The Johns Hopkins University, Princeton University, the United States Naval Observatory, and the University of Washington. Apache Point Observatory, site of the SDSS, is operated by the Astrophysical Research Consortium. Funding for the project has been provided by the Alfred P. Sloan Foundation, the SDSS member institutions, the National Aeronautics and Space Administration, the National Science Foundation and the U.S. Department of Energy.

References

1. Connonlly, A. J., Csabai, I., Szalay, A. S., Koo, D. C., Kron, R. G., & Munn, J. A. 1995, A. J., 100, 2655
2. Eisenstein, D. et al. 2000, in prep.
3. Fan, X. et al. 1999, A. J., 118, 1
4. Fan, X. et al. 2000, A. J., in press
5. Fukugita, M., Ichikawa, T., Gunn, J. E., Doi, M., Schneider, D. P., & Shimasaku, K. 1996, A. J., 111, 1748
6. Gunn, J. E. et al. 1998, A. J., 116, 3040

7. Lupton, R. et al. 2000, in prep.
8. Schlegel, D. J., Finkbeiner, D. P., & Davis M. 1998 Ap. J., 500, 525 [SFD]
9. Strauss, M. A. et al. 1999, Ap. J., 522, L61
10. York, D. G. et al. 2000, Ap. J., in prep.

Surveys with SIRTF

George H. Rieke

Steward Observatory, University of Arizona, Tucson, AZ 85721, USA

Abstract. NASA will launch the Space Infrared Telescope Facility (SIRTF) at the end of 2001. SIRTF is an 85-cm cryogenically cooled telescope using large format infrared arrays in cameras operating from 3.5 to 160μm and spectrographs from 5 to 40μm and, at very low resolution, from 52 to 99μm. Coincidentally – since no one can be given credit for planning the missions this way – SIRTF generally has strengths where the Infrared Space Observatory had weaknesses and weaknesses where ISO had strengths. The large format, high performance arrays in the SIRTF cameras will allow large area surveys of unprecedented sensitivity. The use of two dimensional arrays in the SIRTF spectrograph allows observation of an entire octave at once, both improving sensitivity and encouraging line surveys over the entire accessible spectral range. Large scale surveys with SIRTF will be encouraged through the "Legacy" program to be selected late in 2000.

1 Introduction

Initiated by NASA in 1983, the Shuttle Infrared Telescope Facility (the original SIRTF) was envisioned as a program on a similar scale to the Hubble Space Telescope and Chandra. Instead, SIRTF became the mission too tough to die, enduring many years of redefinitions, descopes, and even cancellations. The Space Infrared Telescope Facility (SIRTF) now under construction for launch in late 2001 is on the cost scale of former "super Explorer" NASA missions like the Infrared Astronomy Satellite (IRAS) or the Cosmic Background Explorer (COBE). Along the way, SIRTF lost many versatile capabilities, but the original telescope aperture of 85 cm as been retained and advances in infrared detector arrays have increased its sensitivity. At the same time new mission concepts have extended its expected operational lifetime to a required 2.5 years and expected $\sim$ 5 years.

In many ways, the development of the Infrared Space Observatory was more in line with the original plans for SIRTF – both in schedule and in the range of scientific capabilities. Fortunately, events have provided two highly complementary missions. The strengths of SIRTF – near and far infrared imaging, moderate and low resolution spectroscopy with 2-dimensional arrays – augment relatively weak capabilities in ISO, but ISO has provided many of the capabilities missing in SIRTF, such as far infrared and high resolution spectroscopy. Because of its widespread use of large format, high performance infrared arrays, SIRTF is particularly suited to advances in infrared surveys,

D. Lemke, M. Stickel, and K. Wilke (Eds.): LNP 548, pp. 394–401, 2000.

and such applications have received a high priority in the instrument and overall mission design. The potential of SIRTF for surveys is explored in detail in the conference proceedings "Astrophysics with Infrared Surveys: A Prelude to SIRTF" (Bicay et al. 1998 [1]). This paper reviews and updates that information, and in the surrounding context of the results from ISO surveys. I hope that readers will thereby see new possibilities to advance infrared astronomy.

The paper will describe briefly the capabilities of each SIRTF instrument, with an emphasis on surveying, followed by a discussion of the Legacy program.

2 Infrared Array Camera (IRAC)

2.1 Instrument Design

The IRAC is being built under the direction of Principal Investigator G. Fazio at the Harvard-Smithsonian Center for Astrophysics, with Goddard Space Flight Center conducting the engineering, construction, and test. This instrument uses a pair of 256x256 pixel InSb arrays supplied by Raytheon/Santa Barbara Research Corporation at 3.6 and 4.5μm. A pair of Raytheon/SBRC Si:As IBC arrays image at 5.8 and 8μm. All the arrays are of 256x256 format, with pixels projected to 1.2" on the sky and total fields of view of 5.1'. All four arrays view the sky simultaneously, with the 3.6 and 5.8μm channels sharing a single field of view that is split spectrally with a dichroic filter and the 4.5 and 8μm arrays similarly viewing a single field. In addition to reading out the full arrays, there is a 'postage stamp' option where a 32x32 section of the arrays is read out rapidly (20 msec) to allow measurement both of very bright sources and of rapidly time variable phenomena. IRAC includes a shutter to block the sky and measure the array dark currents. When the shutter is closed, stimulators in an integrating sphere can inject signals to verify aliveness and provide flat fielding data.

The relatively closely spaced IRAC spectral bands can provide a number of diagnostics. For example, they can be used on the spectral energy distributions of normal galaxies to obtain photometric redshifts. This type of study depends on the broad spectral maximum in old (and even fairly young) stellar populations due to the dominance of red giants and supergiants in the overall luminosity and particularly the near infrared luminosity. These stars have a H- opacity minimum near 1.6μm and a CO and H_2O opacity maximum between 2.3 and 3μm. As a result, there is a broad, fixed-wavelength near infrared spectral maximum that is shifted through the IRAC bands for $1 < z < 4$, producing a distinct color signature correlated with redshift. Since IRAC has adequate sensitivity to measure such redshifts on galaxies of L* luminosity out to $z \sim 3$, these photometric redshifts should be a powerful tool for locating galaxies of interest for follow up observations from IRAC surveys.

ISO has shown that the mid infrared spectra of normal galaxies are dominated by poly-aromatic hydrocarbon (PAH) features due to transiently heated small interstellar dust grains. Such grains also play an important role in the spectra of other types of source. A very strong PAH feature is located near 8 μm, and will result in a unique signature in the IRAC bands.

The bands are also useful for identifying substellar T-dwarfs. These objects have absorption features due to CH_4 at ~ 3.4 μm and due to CH_4 and H_2O at $\sim 7\mu$m, with an opacity minimum and spectral maximum between them near 4.4μm. This behavior would appear as enhanced emission in the 4.5μm band.

Further information about the IRAC design can be found in Fazio et al. (1998) [2] or at the IRAC homepage at
http://cfa-www.harvard.edu/cfa/oir/Research/irac/firstpage.html.

2.2 Surveying with IRAC

IRAC has a single observing mode in which it integrates, the telescope offsets, and then another integration is obtained ("step-and-integrate"). The small offsets demanded of the spacecraft can be made quickly by switching to a gyro-only control that circumvents the smoothing normally imposed on the spacecraft motions. Efficient surveying can be conducted by using these capabilities for a series of integrations that extend coverage over the sky and at the same time optimize the generation of flat field data from repeated sky observations and provide redundant data on sources to allow removal of cosmic ray and bad pixel effects. All four arrays view the sky and take data simultaneously. Thus, multi-color surveys can be very efficient, requiring only a single pass over a region of sky. However, it is recommended that each region be surveyed at least twice with a time separation of at least an hour to identify asteroids by their motion and to find any other transient phenomena.

3 Infrared Spectrograph (IRS)

3.1 Instrument Design

J. Houck of Cornell University is the Principal Investigator for the IRS, and the instrument construction is at Ball Aerospace. In addition, to save weight and money on the flight hardware, the IRS team is leading the construction of a single integrated warm electronics system for both themselves and for MIPS.

The IRS consists of four modules, each containing an independent spectrograph. Each module has a single 128 x 128 pixel silicon blocked impurity band (BIB) array supplied by Boeing North America. Rather than using mechanisms to change optical parameters but with a single array, each module has a unique optical train to provide a range of capabilities. The slits of

the spectrographs are oriented in "module space"; that is, each is rotated to a unique angle as required to keep the module optics as simple as possible.

The 'short-lo' module is used with a long slit and provides spectral resolution of R = $\lambda/\Delta\lambda \sim 60$ - 120 from 5.3 to 14.2μm. The 7.5-14.2μm octave is measured in first order, while the shorter wavelengths are measured in second order; the slit is divided into two equal lengths for the two wavelength ranges. As with the other IRS modules, the slit width is set to λ/D for the longest wavelength of operation for that module, in this case to 3.6". The scale is set to two pixels across the slit, and the slit length is made as long as possible subject to optical constraints, in this case 30 pixels, or 54.6".

The 'short-hi' module is a cross-dispersed echellette with a resolution of R $\sim$ 600 from 10 to 19.5μm. The slit is λ_{max}/D = 5.3" wide, projected to two pixels. It is only 5 pixels long to allow separation of the orders. Both this module and the short-lo one use Si:As BIB arrays.

The long-lo module is similar in concept to the short-lo, with resolution of R $\sim$ 60 - 120 from 20.6 to 40 μm (first order) and 14.2 to 21.8μm (second order). Each of the two slit portions is 2x30 pixels, projected to 9.7"x 151" on the sky. The long-hi module is similar to the short-hi, with R $\sim$ 600 from 19.3 to 37μm. Its slit is 2x5 pixels, projecting to 11.1"x 22.4" on the sky. Both of the long wavelength modules utilize Si:Sb BIB detector arrays with response to 40μm. This detector type was developed specifically by Cornell and Boeing North America for use in SIRTF. Other than the change in dopant, the arrays are identical to the Si:As BIB arrays used in the short wavelength modules.

To allow centering infrared sources accurately on the IRS slits, the short-lo module has a second optical train that forms images of the sky on a portion of its array. In turn, the imaging region is divided with two spectral filters, at 15 and 23.5μm. The standard observing sequence will be to put a source on one of these "peak-up" regions and centroid on its image to obtain an accurate coordinate in the SIRTF frame of reference. An offset to the desired slit will be computed and communicated to the spacecraft pointing and control system, which will move the telescope to point accurately at the desired object.

Further information about the design of the IRS can be found in Roellig et al. (1998) [4] or at the IRS homepage at
http://astrosun.tn.cornell.edu/SIRTF/irshome.htm.

3.2 Surveying with IRS

IRS will be very effective for surveys in which members of a class of object are observed to obtain a uniform suite of spectra. Such surveys can be conducted at high efficiency because an entire octave of the spectrum is obtained in a single exposure (although multiple exposures should be obtained for reliability). In addition, unless the sources have complex morphologies, the "peak-up" capability will allow rapid location of the sources and accurate spectrophotometry through uniform placement on the center of the slit. In

addition, peaking up can circumvent an otherwise laborious and slow procedure of obtaining infrared images (e.g., with IRAC or MIPS), measuring accurate coordinates, and then scheduling spectral observations with them.

A second operation mode will be implemented for IRS shortly after launch, spectral mapping. In this mode, the pointing and control system will move the telescope slowly in the cross-slit direction across the source. Multiple exposures with IRS will then produce a spectral map of a two-dimensional region on the sky. Spectral mapping will be most useful with the low resolution modules because of their long slits.

4 Multiband Imaging Photometer for SIRTF (MIPS)

4.1 Instrument Design

The MIPS PI is G. Rieke (University of Arizona) and the construction contractor is Ball Aerospace. The instrument is built around three different types of infrared array. A 128x128 pixel Si:As BIB is used for imaging at 24μm, with pixels set to $\lambda/2.3$D = 2.5" and a total field of 5.3' square. This array was developed by the IRS team and Boeing North America and is identical to the arrays in the short-lo and short-hi modules of the IRS except for an anti-reflection coating to maximize the response in the MIPS band. A 32x32 pixel Ge:Ga array is used for imaging at 70μm. In the most common survey mode, the optics will set the pixels to $\lambda/1.7$D = 9.9", again giving a field of 5.3' square. This array was built at the University of Arizona using detector material provided by Lawrence Berkeley National Laboratory and cryogenic readouts made by Hughes Aircraft/Raytheon. The optical design provides an option to double the magnification on this array, providing $\lambda/3.4$D = 4.9" pixels to be used when the maximum possible angular resolution is desired, at the expense of field of view and signal to noise. In addition, this array is used in its coarse pixel mode with a low resolution diffraction grating to allow spectra with R = $\lambda/\Delta\lambda \sim 20$ from 52 to 99μm. The third array is a 2x20 pixel stressed Ge:Ga device, also built at the UA/LBNL/Raytheon. It operates at 160μm and has pixels projected to $\lambda/2.5$D =16", for a field 5.3' in length (cross-scan). The wavelengths of the MIPS imaging bands were selected to provide good sensitivity to luminosity independent of temperature by filling in wavelength space uniformly in a logarithmic sense from the longest IRAC band to 350μm, where sensitive observations can be obtained with large groundbased installations.

To assist in the calibration of the 70 and 160μm data, MIPS includes a scan mirror (based on the design developed for the Short Wavelength Spectrometer (SWS) on ISO, which was kindly provided by T. DeGraauw). The scan mirror allows switching source positions quickly between integrations, so the signals are modulated fast enough to keep the response in the well-behaved 'fast' regime characterized by generation and recombination of charge carriers in the bulk of the detectors. The slow reponse from space

charge effects near the contacts is 'chopped out' to first order. The scan mirror also allows a very efficient surveying mode, and is used to feed the different optical trains to expand the usefulness of the 70μm array. The mirror also provides a cold 'shutter' function, both to measure dark currents and also to allow chopping the diffuse sky brightness against a stable cold reference to allow measurement (total power) of very extended emissions.

In addition to the modulation provided by the scan mirror, a number of additional freatures have been included to assist in the calibration of the MIPS far infrared detectors. The detector readouts operate in a DC-stable mode at the focal plane temperature of $\sim$ 1.5K. The detectors are heat sunk separately from the readouts, and the readouts are cycled continuously, so heat associated with electronic power dissipation does not affect detector response or dark current. The readouts themselves are of the CTIA design so they maintain the detector bias accurately while signal is integrated (unless the readout is saturated). Calibration stimulator signals are mixed periodically with the MIPS science data to track any response changes.

Additional information about the MIPS design can be found in Heim et al. (1998) [3], or at the MIPS homepage at http://mips.as.arizona.edu.

4.2 Surveying with MIPS

The MIPS has four basic operational modes (of which the first two will be implemented at launch and the remainder soon thereafter): 1.) Scan Map; 2.) Photometry and Superresolution; 3.) Spectral Energy Distribution; and 4.) Total Power. Although surveys could be conducted in any of these modes, the first one was conceived for this purpose and should prove particularly powerful.

Scan map observations are conducted by using the SIRTF pointing and control system to scan the telescope boresite at a constant rate in the direction of image motion provided by the MIPS scan mirror. The scan mirror is driven in a ramp that exactly compensates the telescope motion and stabilizes the images on the MIPS arrays. After these arrays have completed a set of integrations, the scan mirror jumps forward to move the fields to new positions on all the arrays and then resumes the motion-compensating ramp for the next set of integrations. The three arrays are arranged in a line along the direction of scan mirror motion, so a source will be observed sequentially by each of them as the telescope scans. Thus, long tracks on the sky can be surveyed in all three colors in a single pass, and without taking any time out to accelerate and decelerate the spacecraft to new pointings.

The normal approach to scan mapping will provide a high level of redundancy in the observations at 24 and 70μm, with 10 independent integrations on each source along the scan track. The redundancy will allow compensation for bad pixels, cosmic ray hits, and any other anomalies in the data. The multiple observations occur on fractional pixel spacings, so once they are

combined into a single image the point spread function will be very well sampled in the scan direction. The array geometry will not be aligned perfectly in scan mirror coordinates, so a single scan will also provide subsampling in the cross-scan direction (an unavoidable 'bug' converted into a feature). The oversampling should help extract the maximal angular resolution from the images, potentially important in studying crowded and confused fields as well as for extracting information about extended source morphology.

It is urged for reliability that each track be scanned at least twice, with at least an hour between observations, to allow removal of asteroids and other transient phenomena from the survey products. At 160μm, the smaller array format results in only a single fully sampled image of each source for a single scan, and a second observation (or more) is even more important as a confirmation.

5 SIRTF Legacy Program

The SIRTF observing time is divided among guaranteed observers (20%), science center director discretionary time (5%), and community time (75%) [beyond 2.5 years, the community portion increases to 80%]. Application is open to astronomers around the world, although NASA can only fund United States investigators.

SIRTF will reveal the infrared sky at a qualitatively new level of depth and areal coverage, but it has a limited cryogenic lifetime. Many of the sources that SIRTF should discover will be beyond detection by any other infrared facility. Therefore, a high priority has been placed on obtaining systematic surveys and providing the results to the general astronomical community as quickly as possible. It is hoped that this information will be assimilated quickly and will lead to many proposals for further SIRTF observations out of the 75% community portion of the mission.

An initial reconnaissance of the infrared sky will be obtained as early as possible in the mission and released as the "First Look Survey." The goal for the FLS is to evaluate aspects of the sky that may influence the optimal planning of other SIRTF observations, but it will also provide the astronomical community with a scientifically valuable set of data.

To encourage community access to large scale, systematic surveys, a "Legacy" program has been established. Legacy proposals should be for a large and coherent body of data that will provide a valuable archival research resource. In addition, the proposals will be ranked on the basis of the scientific use of the data by the proposers. Data obtained under a Legacy program have no proprietary period, but are to be made available to the astronomical community as quickly as possible. No specific time allocation has been made for Legacy programs, but an appropriate effort might be 15-35% of the mission time in the first 2.5 years, with observations concentrated in the first year of this interval. To encourage coherent investigations, Legacy

proposers can specify follow up observations of objects that might be discovered in the initial survey, but the properties of the follow up targets must be specified in the original proposal.

A draft of the Legacy proposal opportunity will be released in April, 2000, with an official release at the end of June. By that time the SIRTF guaranteed time observers will be required to have identified their programs so their targets can be withheld from Legacy proposals. There will be two months to complete proposals and the selections should be announced before the end of the year. The selection will be followed by a workshop with the guaranteed time observers and the SIRTF Science Center at the January, 2002 AAS meeting to coordinate all the programs scheduled for early in the mission.

Further information about SIRTF and the Legacy program can be found at http://sirtf.caltech.edu/.

References

1. Bicay, M. D., Cutri, R. M., & Madore, B. F. (1999) Astrophysics with Infrared Surveys: A Prelude to SIRTF. ASP Conf. Ser., 177
2. Fazio, G. G., et al. (1998) Infrared Array Camera for the Space Infrared Telescope Facility, Proc. SPIE, 3354, 1024 – 1031.
3. Heim, G. B., et al. (1998) Multiband Imaging Photometer for SIRTF. Proc. SPIE, 3356, 985 – 1000.
4. Roellig, T. L. et al. (1998) Infrared Spectrograph for the Space Infrared Telescope Facility, Proc. SPIE, 3354, 1192 – 1203

Extragalactic Spectroscopy with SIRTF/IRS

Bernhard Brandl[1], Vassilis Charmandaris[1], Keven Uchida[1], and Jim Houck[1]

Cornell University, Ithaca NY 14853, USA

Abstract. The Infrared Spectrograph (IRS) is one of the three instruments on board the Space Infrared Telescope Facility (SIRTF) to be launched in December 2001. The IRS will provide high resolution spectra (R≈600) from 10–37 μm and low resolution spectra (R≥60) from 5–40 μm. Its high sensitivity and "spectral mapping"-mode make it a powerful instrument for observing both faint point-like and extended sources. We discuss the performance of the IRS on faint extragalactic targets and present simulated spectra of starbursts and AGNs at high redshift. In addition, we discuss the determination of redshifts from the low resolution spectra.

1 The Infrared Spectrograph

The Infrared Spectrograph (IRS, [4]) will provide the Space Infrared Telescope Facility (SIRTF, [3]) with low and moderate-spectral resolution spectroscopic capabilities from 4 to 40 microns. The IRS (see Fig. 1) is composed of four separate modules, with two of the modules providing R∼50 spectral resolution over 4 to 40 microns and two modules providing R∼600 spectral resolution over 10 to 37 microns.

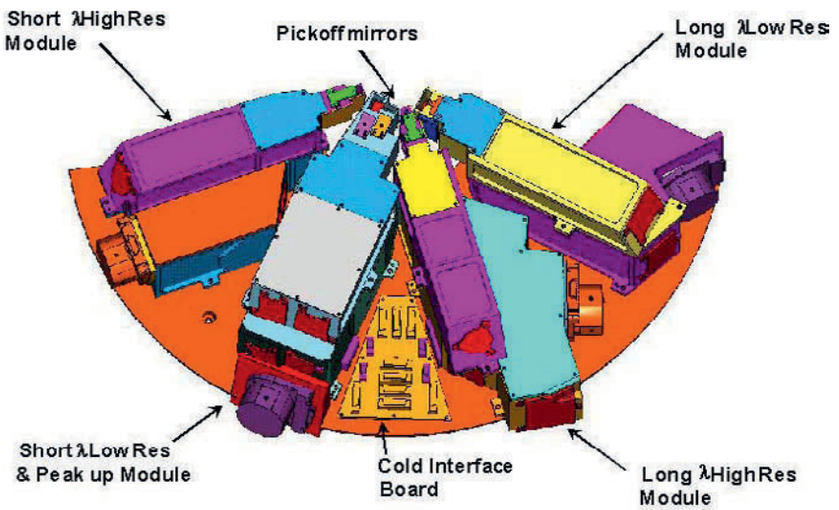

Fig. 1. The 4 IRS modules on their common base plate.

D. Lemke, M. Stickel, and K. Wilke (Eds.): LNP 548, pp. 402–407, 2000.

Table 1. Basic IRS characteristics

Module	Detector (128×128)	Pixel Size (arcsec)	Slit Size (arcsec)	λ (μm)	Resolving Power (R)
Short Low	Si:As	1.8	3.6×54.5	5.3 – 7.5	62-124
”	”	”	”	7.5 – 14	”
Long Low	Si:Sb	4.8	9.7×145.4	14 – 21	62-124
”	”	”	”	21 – 40	”
Short High	Si:As	2.4	4.8×12.1	10 – 19.5	600
Long High	Si:Sb	4.8	9.7×24.2	19 – 37	600

The IRS instrument has no moving parts (“bolt-and-go” philosophy). Each module has its own entrance slit in the focal plane. The low-resolution modules employ long slit designs that allow both spectral and one-dimensional spatial information to be acquired simultaneously on the same detector array. Two small imaging sub-arrays (“peak-up cameras”) in the so-called short-low module (SL) will also allow infrared objects with poorly known positions to be accurately placed into any of the IRS modules’ entrance slits. The high-resolution modules use a cross-dispersed echelle design that gives both spectral and spatial measurements on the same detector array.

2 The IRS Sensitivity

The expected sensitivity of IRS is nearly 10 to 100 times better than that of the Infrared Space Observatory. The theoretical sensitivity plots for the four modules are presented in figures 2 and 3.

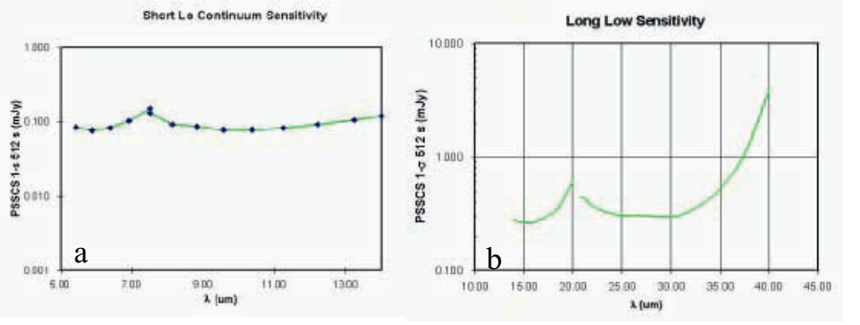

Fig. 2. The theoretical sensitivity plots of the IRS short module (as of 10/99).

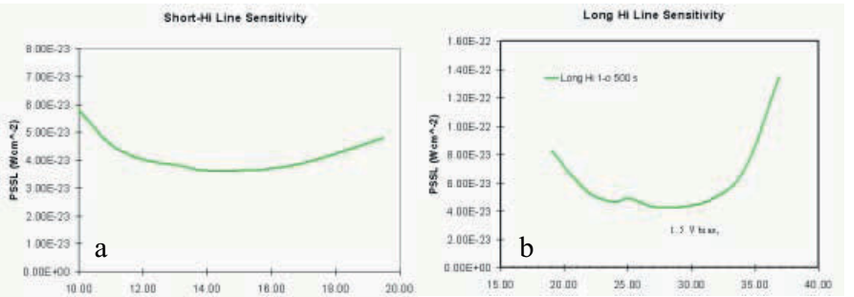

Fig. 3. The theoretical sensitivity plots of the IRS long module (as of 10/99).

The continuum point source (5σ, 500 seconds) sensitivity of the low resolution module is 1 mJy at 10 μm. The line sensitivity of the high resolution module is 3×10^{-18} Wm^{-2} at 15 μm. The two peak-up cameras have a sensitivity of about 0.5 mJy.

The saturation limits in 8 seconds for point (extended) sources are 5 Jy (0.4 Jy arcsec^{-2}) at 10 μm for the low resolution module and 50 Jy (2.1 Jy arcsec^{-2}) at 15 μm for the high resolution module. The 4 s saturation limits for the peak-up cameras are 0.5 Jy for point sources and 40 mJy arcsec^{-2} for extended sources.

3 Extragalactic Science

Two of the main areas of extragalactic research where the IRS will be able to make substantial contributions will be the mid-IR deep surveys as well as the study of the properties of Luminous Infrared Galaxies (LIRGs). LIRGs have been studied since the early 70s, but their importance became evident in 1983 when IRAS revealed tens of thousands of such infrared galaxies galaxies (i.e. [5]). More recently ISO mid-IR deep surveys (i.e. [2]) have shown that the number of galaxies in the distant Universe exceeds model estimates which were derived from optical observations. These mid-IR surveys suggest a strong evolution in galaxy formation, such that more - and perhaps more luminous - galaxies were formed at earlier epochs.

As one can clearly see in Fig. 4 the optical identification of the galaxies with detected mid-IR emission is ambiguous since the spatial resolution in the mid-IR is about an order of magnitude inferior to what can be achieved in the optical.

The combination of superior sensitivity and good spatial resolution of the IRS will make it possible to obtain $5-40\mu$m low-resolution mid-IR spectra of faint sources in relatively short integration times. The distinct spectrum of the mid-IR emission features at 6.2, 7.7 8.6 and 11.3 μm, as well as the presence of the silicate absorption band at 9.7μm (restframe wavelengths), can be

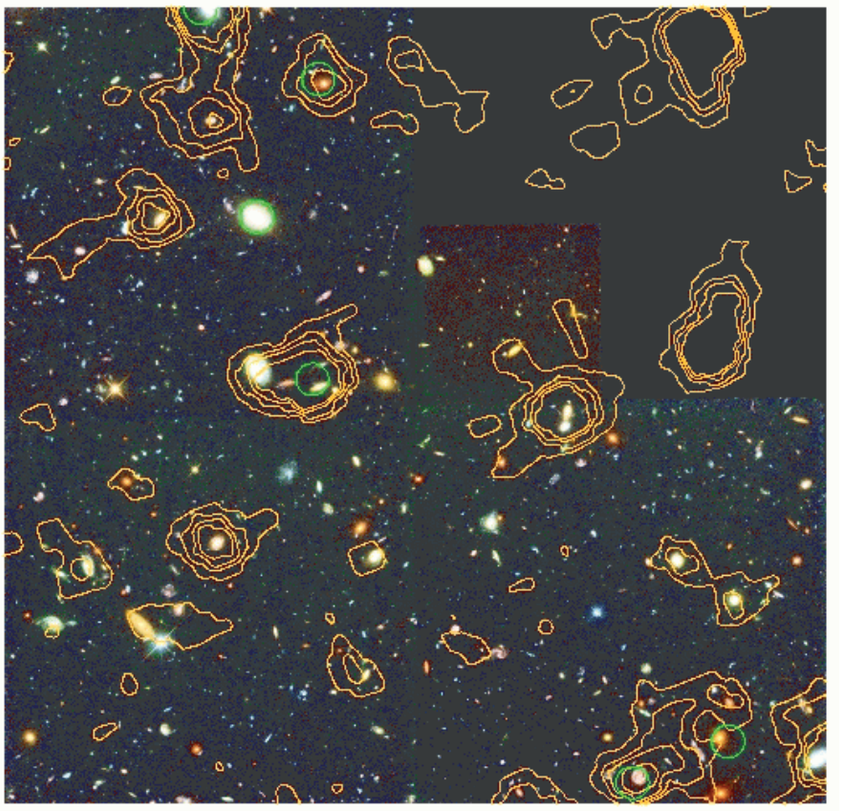

Fig. 4. The HST Hubble Deep Field North with an overlay of the ISOCAM 15 μm contours (yellow lines). The location of 7 μm ISOCAM detections is indicated with green circles [1]

used to directly derive redshifts of individual sources as faint as 0.5 mJy. For illustration we show the simulated IRS spectra of a prototypical starburst (M 82) and active galactic nucleus (NGC 1068) at a redshift of 2 in Fig. 5 and Fig. 6. Please note that the fluxes of the template spectra have been normalized to user-specified values which may differ from the fluxes of M 82 and NGC 1068 if they were at a redshift of $z = 2$. Also note that the specified time is the integration time per module while the full $5 - 40\mu$m is covered by two modules with two settings each.

4 Conclusions

The approach presented here provides an unbiased method of deriving directly the number counts of obscured star forming galaxies as a function

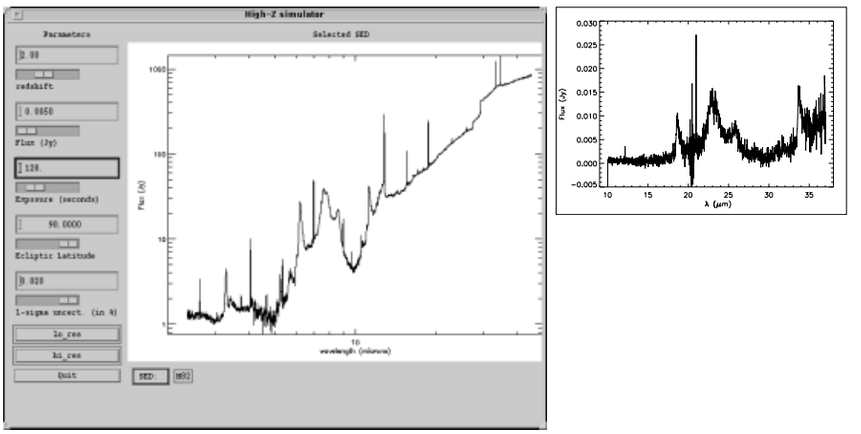

Fig. 5. a) The IRS high-z simulator using as a template the ISO/SWS spectrum of M82. b) The expected IRS high-res spectrum of a starburst with an IRAS 25μm flux of 5mJy located at $z = 2$ after an integration time of 128 seconds. c) The simulated IRS low-res spectrum of the same source.

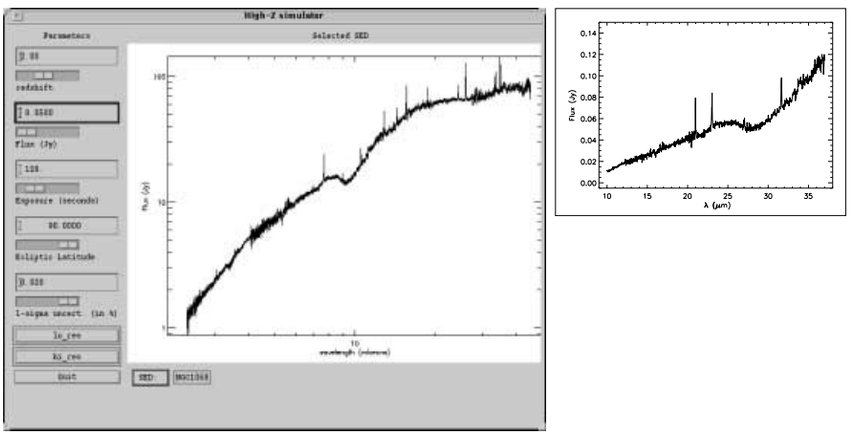

Fig. 6. a) The IRS high-z simulator using as a template the ISO/SWS spectrum of NGC1068. b) The expected IRS high-res spectrum of an AGN with an IRAS 25μm flux of 5mJy located at $z = 2$ after an integration time of 128 seconds. c) The simulated IRS low-res spectrum of the same source.

of redshift to a few tenths of a mJy. Moreover, deep imaging surveys with SIRTF or even beyond will reveal the mid/far-IR colors that can be used for photometric redshift determinations of the faintest IR galaxies. The IRS observations will provide an important calibration sample for these surveys.

More information on the IRS can be found at the following Web-sites:
http://astrosun.tn.cornell.edu/SIRTF/irshome.htm
http://sirtf.caltech.edu/Observing/obs_frame.html.

Acknowledgements

We'd like to thank Dan Weedman and Jeffrey Wolovitz for providing the basis of the IRS simulator program, Jeffrey van Cleve for the sensitivity plots and Eckhard Sturm for providing the ISO-SWS data on M 82 and NGC 1068 prior to publication.

References

1. Aussel, H., Cesarsky, C. J., Elbaz, D., Starck, J. L. (1999) ISOCAM observations of the Hubble Deep Field reduced with the PRETI method. A&A 342, 313–336.
2. Elbaz, D. et al. (1999) Source Counts from the 15 microns ISOCAM Deep Surveys. A&A, (in press) (astro-ph/9910406).
3. Fanson, J.L., G. Fazio, J.R. Houck, T. Kelly, G.H. Rieke, D.J. Tenerelli, M. Whitten (1998) Space Infrared Telescope Facility (SIRTF). Proc. SPIE Vol. 3356, 478–491.
4. Houck, J.R. & J.E. van Cleve (1995) IRS: An infrared spectrograph for SIRTF. Proc. SPIE Vol. 2475, 456–463.
5. Sanders, D.B., Mirabel, I.F. (1996) Luminous Infrared galaxies. ARA&A 34 749–792.

The FIRST Mission

Göran L. Pilbratt

ESA Astrophysics Division, Space Science Department, ESTEC / SCI-SA,
Keplerlaan 1, NL−2201 AZ Noordwijk, The Netherlands
email: gpilbratt@astro.estec.esa.nl

Abstract. The 'Far InfraRed and Submillimetre Telescope', (FIRST), is the fourth cornerstone mission in the European Space Agency (ESA) science programme. It will perform photometry and spectroscopy in the far infrared and submillimetre part of the spectrum, covering approximately the 60−670 μm range.

FIRST will carry a 3.5 metre passively cooled telescope, to be supplied by NASA, and house a science payload complement of two cameras/medium resolution spectrometers (PACS and SPIRE) and a very high resolution heterodyne spectrometer (HIFI) in a superfluid helium cryostat. FIRST will be placed in a transfer trajectory towards its operational orbit around the Earth-Sun L2 point by an Ariane 5 (shared with Planck) in early 2007. Once operational FIRST will offer a minimum of 3 years of routine observations; roughly 2/3 of the available observing time is open to the general astronomical community through a standard competitive proposal procedure.

1 Introduction

The 'Far InfraRed and Submillimetre Telescope' (FIRST) is a multi-user 'observatory type' mission that targets approximately the 60−670 μm wavelength range in the far infrared and submillimetre part of the electromagnetic spectrum, providing observation opportunities for the entire astronomical community. FIRST is one of the original four 'cornerstone' missions in the ESA science 'Horizon 2000' plan.

FIRST is the the only space facility dedicated to the submillimetre and far infrared part of the spectrum. Its vantage point in space provides several decisive advantages, most notably a low and stable background and full access to this part of the spectrum.

2 Science Objectives

The FIRST science objectives target the 'cold' universe. Black-bodies with temperatures between 5 K and 50 K peak in the FIRST wavelength range, and gases with temperatures between 10 K and a few hundred K emit their brightest molecular and atomic emission lines here. Broadband thermal radiation from small dust grains is the most common continuum emission process in this band. These conditions are widespread everywhere from within our own solar system to the most distant reaches of the Universe!

D. Lemke, M. Stickel, and K. Wilke (Eds.): LNP 548, pp. 408–415, 2000.

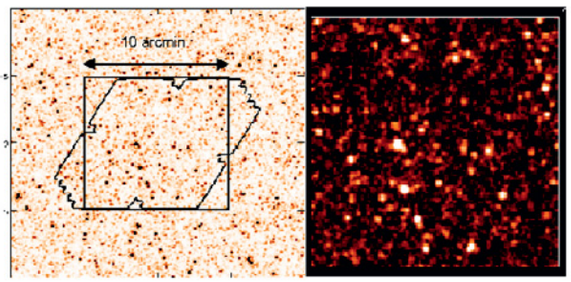

Fig. 1. Simulations are underway to determine optimum instrument configurations and observation strategies for e.g. unbiased deep extragalactic surveys

FIRST – being a unique facility in many ways – has the potential of discovering the earliest epoch proto-galaxies, revealing the cosmologically evolving AGN-starburst symbiosis, and unraveling the mechanisms involved in the formation of stars and planetary system bodies. The key science objectives emphasise (see also [1]) specifically the formation of stars and galaxies, and the interrelation between the two. Example observing programmes with FIRST will include:

- Deep extragalactic broadband photometric surveys in the 100−600 μm FIRST 'prime' wavelength band and related research. The main goals will be a detailed investigation of the formation and evolution of galaxy bulges and elliptical galaxies in the first third of the present age of the Universe (see also Fig. 1).
- Follow-up spectroscopy of especially interesting objects discovered in the survey. The far infrared/submillimetre band contains the brightest cooling lines of interstellar gas, which give very important information on the physical processes and energy production mechanisms (e.g. AGN vs. star formation) in galaxies.
- Detailed studies of the physics and chemistry of the interstellar medium in galaxies, both locally in our own Galaxy as well as in external galaxies, by means of photometric and spectroscopic surveys and detailed observations. This includes implicitly the important question of how stars form out of molecular clouds in various environments.
- Observational astrochemistry (of gas and dust) as a quantitative tool for understanding the stellar/interstellar lifecycle and investigating the physical and chemical processes involved in star formation and early stellar evolution in our own Galaxy. FIRST will provide unique information on most phases of this lifecycle.
- Detailed high resolution spectroscopy of a number of comets and the atmospheres of the cool outer planets and their satellites.

From past experience, it is also clear that the 'discovery potential' is significant when a new capability is being implemented for the first time.

Observations have never been performed in space in the 'prime band' of FIRST. The total absence of (even residual) atmospheric effects – enabling both a much lower background for photometry and full wavelength coverage for spectroscopy – and a cool low emissivity telescope open up a new part of the phase-space of observations. Thus, a space facility is essential in this wavelength range and FIRST will be breaking new ground!

3 Telescope and Science Payload

In order to fully exploit the favourable conditions offered by being in space FIRST will need a precise, stable, very low background telescope, and a complement of very sensitive scientific instruments.

3.1 Telescope Development

The FIRST telescope will be provided by NASA/Jet Propulsion Laboratory (JPL) as part of NASA's involvement in the FIRST mission. The baseline is a Ritchey-Chrétien design with a 3.5 m diameter primary and an 'undersized' secondary. The telescope has a segmented primary mirror made of carbon fibre reinforced plastic (CFRP) structure, with a zerodur secondary that could be precisely machined to correct for low spatial frequency imperfections in the primary. Being protected by a fixed sunshade, the telescope will radiatively cool to an operational temperature of around 80 K in orbit.

An aggressive development programme is underway to optimise the design – including optical, mechanical, thermal, and straylight properties – perfect manufacturing and testing procedures, and control potential detrimental environmental impacts.

3.2 Scientific Instruments

The FIRST science payload has been conceived and optimised with the prime science goals in mind, but in addition it offers a wide range of capabilities for the 'general' observer. Principal Investigator (PI) consortia will provide the instruments to ESA under their own funding, in return for guaranteed observing time.

The PIs and instruments are:

- The Photoconductor Array Camera and Spectrometer (PACS) instrument will be built by a consortium led by A. Poglitsch, MPE, Garching, Germany.
- The Spectral and Photometric Imaging REceiver (SPIRE) instrument will be built by a consortium led by M. Griffin, QMW, London, UK.
- The Heterodyne Instrument for FIRST (HIFI) instrument will be built by a consortium led by Th. de Graauw, SRON, Groningen, The Netherlands.

PACS is a photoconductor detector array camera and spectrometer instrument. It employs two 25×16 Ge:Ga detector arrays together covering the 60−210 μm band. The two arrays are appropriately stressed and operated at slightly different temperatures in order to optimise sensitivity for their respective wavelength coverage. The stress mechanism is pictured in Fig. 2.

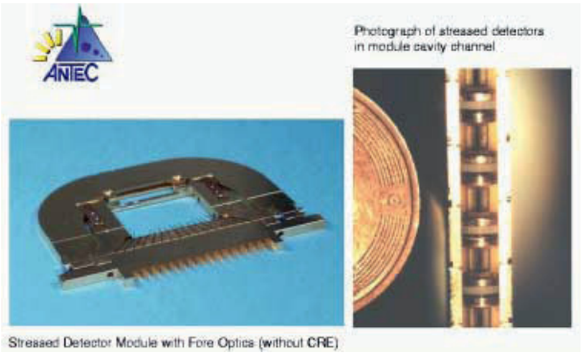

Fig. 2. To the left a 1×16 array of PACS detectors in the stress module, a complete array is made up of 25 such modules. To the right a close-up of a section of a stress module, showing individual detectors

PACS has three defined photometric bands with $R \sim 2$. The short wavelength 'blue' array covers the 60−90 and 90−130 μm bands, while the 'red' array covers the 130−210 μm band. The pixel sizes of the two arrays (3.4″ and 6.8″, respectively) have been chosen to provide full sampling of the telescope point spread function at 90 and 180 μm. In the photometry mode PACS will perform imaging simultaneously in two bands, one of the 'blue' bands as well as the 'red' band, covering roughly 1′× 1.5′ and 2′× 3′ on the sky respectively.

As a spectrometer PACS covers 57−210 μm in three contiguous bands. It provides a velocity resolution in the range 150−200 km^{-1} with an instantaneous coverage of ∼1500 km^{-1}, and 25 pixels on the sky approximately covering 1′× 1′.

SPIRE is a bolometer detector array camera comprising an imaging photometer and a symmetrical Mach-Zender imaging spectrometer. SPIRE has been designed to maximise mapping speed. In its broadband ($R \sim 3$) photometry mode it simultaneously images a 4′×4′ (possibly even 4′×8′) field on the sky in three colours centred on 250, 350, and 500 μm. The exact band centres are still subject to fine tuning.

There are presently three detector technologies being considered for SPIRE. The CEA-SAp/LIR proposal utilises silicon grids with resonant absorbers and ion implanted thermometer readouts with CMOS cryogenic readout electronics and multiplexers.

The NASA-GSFC/NIST array technology employs silicon 'pop-up' detectors (SPUDs) and transition edge superconductor (TES) sensors, with squid readouts and multiplexers.

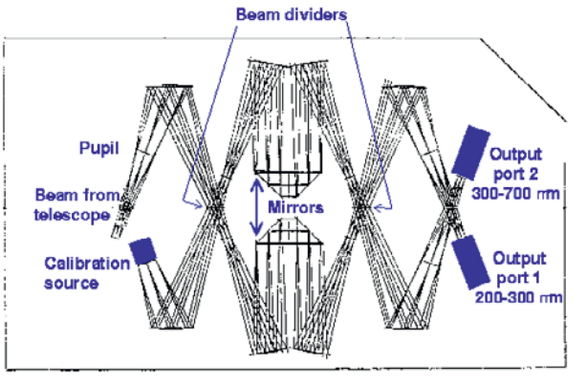

Fig. 3. The SPIRE spectrometer employs a dual Mach-Zender configuration, note the use of both input ports

The third alternative is more similar to the the currently in use SCUBA instrument on the JCMT. It employs spider-web bolometers with NTD Ge temperature sensors, with each pixel being fed by a single-mode $2F\lambda$ feedhorn, and JFET readout electronics operating at around 100 K.

The first two technologies would provide SPIRE with fully sampled ($0.5F\lambda$) arrays, if the $4' \times 8'$ field of view is realised this means a total of 3712 detectors, if the third alternative is selected the number of detectors is reduced to 289.

The SPIRE spectrometer is based on a Mach-Zender configuration with novel broad-band beam dividers (see Fig. 3). Both input ports are used at all times, the signal port accepts the beam from the telescope while the second port accepts a signal from a calibration source, the level of which is chosen to balance the power from the telescope in the signal beam. The two output ports have detector arrays dedicated for 200−300 and 300−600 μm respectively. The maximum resolution will be in the range 100−1000 at a wavelength of 250 μm, and the field of view $2.6'$ (square or circular).

HIFI is a heterodyne receiver instrument which combines the high spectral resolving power capability (0.3−300 km^{-1}) of the radio heterodyne technique with the low noise detection offered by superconductor - insulator - superconductor (SIS) and hot electron bolometer (HEB) mixers.

The focal plane unit (FPU, see Fig. 4), houses seven mixer subunits, each one equipped with two orthogonally polarised mixers. Bands 1−5 utilise SIS mixers that together cover approximately 500−1250 GHz without any gaps in the frequency coverage. Bands 6 and 7 utilise HEB mixers, and target the 1410−1910 and 2400−2700 GHz bands, respectively. The FPU also houses the optics that feeds the mixers the signal from the telescope and combines it with the appropriate local oscillator (LO) signal, as well as provides a chopper and the capability to view internal calibration loads.

The LO signal is generated by a source unit located in the spacecraft service module (SVM, see Sect. 4). By means of waveguides it is fed to the LO unit, located on the outside of the cryostat vessel, where it is ampli-

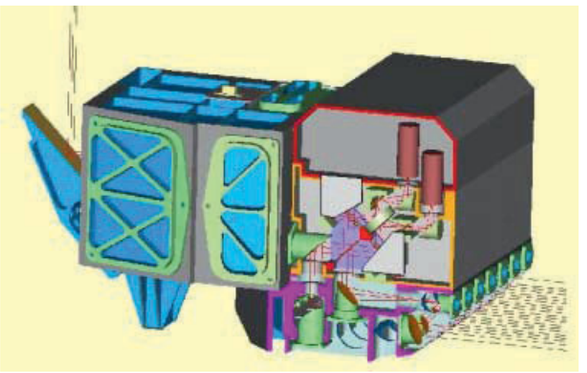

Fig. 4. The HIFI focal plane unit. The M3 mirror on the left feeds the telescope signal via the common optics unit to the mixer unit on the right, where the seven mixer subunits and the optics combining the signal from the telescope with the local oscillator signal entering from the right

fied, multiplied and subsequently quasioptically fed to the FPU. The SVM also houses the wideband acoustoptic spectrometers and the high resolution digital autocorrelators.

4 Spacecraft and Orbit

Studies have shown that the now well proven ISO cryostat technology can be used to advantage also for FIRST. The FIRST configuration shown in Fig. 5 (see also [2], [3]) envisages a payload module based on ISO cryostat technology and has been used to establish payload interfaces and study mission design.

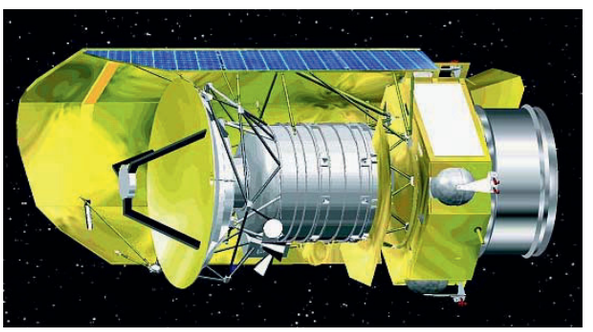

Fig. 5. Artist's impression of FIRST in space performing routine science operations

This FIRST concept is modular, consisting of a payload module (PLM), comprising the superfluid helium cryostat – housing the optical bench with the instrument FPUs – which supports the telescope, star trackers, and some payload associated equipment; and the service module (SVM), which provides the 'infrastructure' and houses the 'warm' payload electronics. It measures approximately 7.5 m in height, 4.5 m in width, and has an approximate launch mass of 3200 kg.

FIRST will share an Ariane 5 launcher with Planck; both satellites will be injected into a transfer trajectory towards the second Lagrangian point (L2) in the Sun-Earth system, and subsequently operate independently. L2 is situated 1.5 million km away from the Earth in the anti-sunward direction. It offers a stable thermal environment with good sky visibility. The transfer to the operational orbit will last approximately 4 months, after which FIRST will go into the routine science operations phase for a minimum duration of 3 years.

5 Observing Time

The FIRST observation time will be shared between guaranteed and open time. The guaranteed time (approximately one third of the total time) will be defined by the guaranteed time holders. The open time will be allocated to the general community on the basis of calls for observing time. A small amount of the open time will be reserved for targets that could not have been foreseen at the time of a proposal deadline.

Given the science objectives of the FIRST mission it is clear that key projects in the form of large spatial and spectral surveys will constitute very important elements of the observing programme, requiring a substantial fraction of the available time of the overall mission. It is envisaged that early in the mission significant time will be spent on several key programmes for which a special call for observing time is envisaged.

6 Science Operations

FIRST will be a multi-user observatory open to the general astronomical community. The scientific operations concept is being designed to this effect, including providing an interface to the community at large to keep abreast with FIRST developments as they take place – especially with respect to its predicted scientific capabilities and procedures for applying for observing time – and to provide user support.

The scientific operations of FIRST will be conducted in a novel 'decentralised' manner. The proposed ground segment concept (see also [4]) comprises five elements:

- a FIRST Science Centre (FSC), provided by ESA,
- three dedicated Instrument Control Centres (ICCs), one for each instrument, provided by their PIs,
- a Mission Operations Centre (MOC), provided by ESA.

In addition it is foreseen that the NASA Infrared Processing and Analysis Center (IPAC) will become a sixth element. The ground segment elements will be united by dedicated computer links into a coherent science ground

segment. These computer links are part of the FIRST Integrated Network and Data Archive System (FINDAS) for which the FSC is responsible. The FSC acts as the single-point interface to the science community and outside world in general.

All scientific data will be archived and made available through FINDAS, together with software tools to produce 'standard' data products and to further process the data interactively.

7 Status and Schedule

FIRST is presently in a pre-phase B development phase. The instrument consortia are in the process of finalising the instrument designs in order to start building the first test models. Industrial studies are being carried out to further define payload and telescope interfaces, and to refine the cryostat and telescope designs.

The current planning envisages issuing the Invitation to Tender (ITT) for phases B/C/D to industry in September 2000, and to start phase B – the detailed design phase – in summer 2001. A series of milestones, including instrument and telescope flight model deliveries in 2004, will lead to a launch in 2007.

More information can be found on the ESA Astrophysics FIRST World Wide Web site at URL `http://astro.estec.esa.nl/FIRST`.

Acknowledgements

This paper has been written on behalf of the large number of people who either currently are working on one or more of the many aspects of the FIRST mission – in ESA, the scientific community, and industry – or who have been doing so in the past.

References

1. Pilbratt G.L. 1998, 'The FIRST ESA Cornerstone Mission' *Proc. of SPIE* 3356, 452−461
2. Schupp J., Moßbacher B., Seidel A. 1998, 'The FIRST PLM based on a HeII cryostat' *Proc. of 1998 Space Cryogenics Workshop,* ESA WPP−157, 107−110
3. Collaudin B., Paßvogel Th. 1998, 'The FIRST and Planck 'carrier' missions: Description of the cryogenic systems' *Proc. of 1998 Space Cryogenics Workshop,* ESA WPP−157, 111−122
4. Bauer O.H., Estaria P., King K.J., Pilbratt G., Robson A., Roelfsema, P.R., Schaap H. 1998, 'FIRST Ground Segment and Science Operations Concept' *Proc. of SPIE* 3349, 312−318

Stratospheric Observatory for Infrared Astronomy (SOFIA)

Eric E. Becklin[1,2] and Jochen M.M. Horn[1]

[1] Division of Astronomy and Astrophysics, University of California, Los Angeles, 405 Hilgard Avenue, Los Angeles, CA 90024
[2] Universities Space Research Association, NASA Ames Research Center, MS T3B, Moffett Field, CA 94035-1000

Abstract. The joint US and German SOFIA project to develop and operate a 2.5-meter infrared airborne telescope in a Boeing 747-SP is now well into development. Work on the aircraft and the telescope has started. First science flights will begin in 2003 with 20% of the observing time assigned to German investigators. The observatory is expected to operate for over 20 years. The sensitivity, characteristics and science instrument complement are discussed. SOFIA will have instrumentation that will allow astronomical surveys that were not possible on the KAO. A future SOFIA project related to astrochemistry is discussed.

1 Introduction

The Stratospheric Observatory For Infrared Astronomy (SOFIA) is NASA's and DLR's premier observatory for infrared and submillimeter astronomy into the next century. A Boeing 747-SP aircraft will carry a 2.5-meter telescope designed to make sensitive infrared measurements of a wide range of astronomical objects. It will fly at and above 12.5 km, where the telescope collects radiation in the wavelength range from the 0.3 micrometers to 1.6 millimeters.

The telescope and 20% of operations will be supplied by Germany through contracts managed by DLR. A team led by the Universities Space Research Association (USRA) has been selected by NASA to design and develop the airborne platform; and to assemble, test, and operate the SOFIA observatory.

The development of the science instruments to be attached to the SOFIA telescope will be the responsibility of the US and German science communities. In the US, science instruments will be designed and built at universities and national centers through a USRA peer review process.

2 SOFIA First Light Instruments

A total of ten instruments have been selected and recommended for development. The selection includes four Facility Class (FI) Science Instruments (AIRES, HAWC, FORCAST, and FLITECAM), five Principal Investigator Class (PI) Science Instruments, and one Special Purpose Principal Investigator Class (SI) Science Instrument.

D. Lemke, M. Stickel, and K. Wilke (Eds.): LNP 548, pp. 416–422, 2000.

SOFIA First Light Instruments

Name	Class	PI	Institute	Type of Instrument
AIRES	FI	E. Erickson	NASA−ARC	Echelle Spectrometer 40 to 110 μm, R$\simeq$10,000
HAWC	FI	D.A. Harper	Univ. of Chicago	Far Infrared Bolometer Camera 30−300 μm
FORCAST	FI	T. Herter	Cornell	Mid IR Camera 5−40 μm
FLITECAM	FI	I. McLean	UCLA	Near IR Test Camera 1−5 μm
EXES	PI	J.Lacy	Univ. of Texas	Echelon Spectrometer 5−28 μm,R=1500 & R=100,000
CASIMIR	PI	J. Zmuidzinas	Caltech	Heterodyne Spectrometer 250−600 μm
SAFIRE	PI	H. Moseley	NASA-GFC	Imaging Fabry-Perot Bolometer Array Spectrometer 145−655 μm,R=1000−10,000
FIFI LS	PI	A. Poglitsch	MPE, Garching	Field Imaging Far IR Line Spectrometer 40−350 μm
GREAT	PI	R. Guesten	MPIfR, KOSMA DLR−WS	Heterodyne Spectrometer 75−250 μm
HOPI	SI	E. Dunham	Lowell Observatory	Visible Occultation CCD Photometer/Imager

3 First Light Expected in 2002

SOFIA will see first light in 2002, and is planned to make more than 140 scientific flights per year of at least 8 hours duration . SOFIA is expected to operate for at least 20 years, primarily from Moffett Field in California, but occasionally from other bases around the world, especially in the Southern Hemisphere. SOFIA will fly above 12.5 km, where the typical water vapor column density is less than 10 μm.

The SOFIA Science and Mission Operations Center (SSMOC), to be operated by USRA, will be located at NASA Ames Research Center at Moffett Field, in the same hangar housing SOFIA. The SOFIA Program will support approximately 50 investigation teams per year. SOFIA is primarily for use by the US and German science communities, but it is also open to the international science community. 76% of the observations will be allocated by a USA peer-review process (managed by USRA), 19% will be allocated by a German peer-review process, and 5% will be allocated at the discretion of the USRA Observatory Director. The USRA Investigator Program is currently being formulated. There will be a mix of Key Projects, Surveys, Service Observations, and Small Investigations. The latter would be awarded annually; the first two investigation modes could be multi-year projects. The program will also support the development of US science instruments for SOFIA. Some of these instruments will be facility instruments, which will be supported by the SSMOC for use by general investigators. General investigators may also use PI science instruments, but support will be limited.

Work on SOFIA is presently being carried out in Germany and the U.S. The primary mirror (Fig. 1 left) has been ground, annealed and shipped to REOSC in France for polishing and lightweighting by 80 per cent. The aircraft (Fig. 1 right) has undergone pre-modification test flights to verify and document its performance. The flight tests indicate that SOFIA's performance is significantly better than its predecessor's, the Kuiper Airborne Observatory (KAO).

Fig. 1. *Left: The SOFIA primary mirror is now light weighted by 80 % and is being polished at REOSC in France. Right: The SOFIA 747-SP aircraft, originally dedicated as the 'Clipper Lindbergh'.*

Detailed tests and analysis have resulted in several design changes. The telescope will now be built with a hydrostatic bearing rather than an air bearing. Changes in the aircraft door design have also led to improved telescope and aircraft performance.

4 Science Potential

SOFIA will provide a sensitive platform with high spatial resolution for both imaging and spectroscopy at all infrared wavelengths, including those longer than the 200 μm limit of the Infrared Space Observatory (ISO) and Space Infrared Telescope Facility (SIRTF). Fig. 2 and Fig. 3 show a comparison to other missions.

With the parameters given under SOFIA Characteristics, and the atmospheric transmission at flight altitudes given in Traub & Stier (1976) [7], see Fig. 4, we calculate that the background limited NEFD at 100 μm in a 30% band should be about 400 mJy Hz$^{-1/2}$ and at 450 μm about 300 mJy Hz$^{-1/2}$. The corresponding 1-σ noise in an hour integration should be 7 mJy at 100 μm and 5 mJy at 450 μm. The 1-σ line flux limit in 1 hour should be about 4×10^{-18} Wm^{-2} at a resolution of 10^3 at 100 μm.

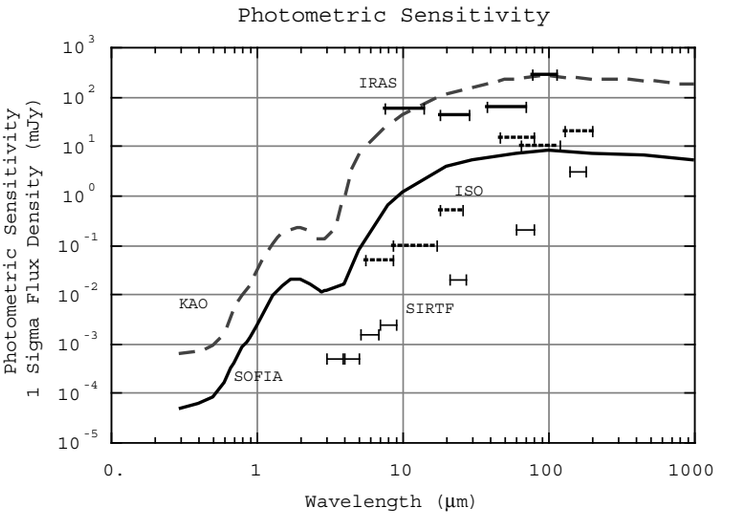

Fig. 2. SOFIA photometric point source sensitivities are shown compared with KAO, IRAS, ISO, and SIRTF.

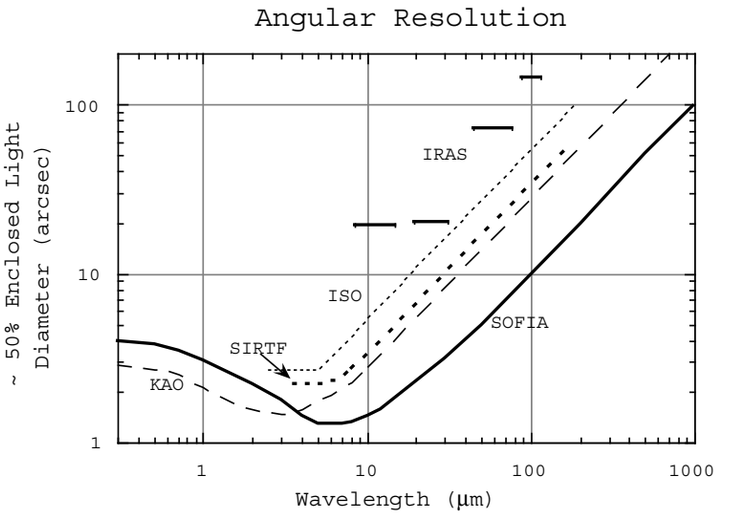

Fig. 3. SOFIA spatial resolution compared with KAO, IRAS, ISO, and SIRTF.

SOFIA Characteristics

Nominal Operational Wavelength Range	0.3 to 1600 μm
Primary Mirror Diameter	2.7 meters
System Clear Aperture Diameter	2.5 meters
Nominal System f-ratio	19.6
Primary Mirror f-ratio	1.28
Telescope's Unvignetted Elevation Range	20−60 degrees
Unvignetted Field-of-View Diameter	8 arcmin
Maximum Chop Throw on Sky	± 4 arc min (unvignetted)
Diffraction-Limited Wavelengths	$\geq 15\,\mu$m
Recovery Air Temp in Cavity (and Optics Temp)	240K
Image Quality of Telescope Optics (at 0.6 μm)	1.5 arcsec on-axis (80% encircled energy)
Optical Configuration	Bent Cassegrain with chopping secondary mirror and flat folding tertiary.
Chopper Frequencies	1 to 20 Hz for 2-point square wave chop
Pointing Stability	$\lesssim 0.''8$ rms for first light
Pointing Accuracy	$\lesssim 1''$ if on-axis Focal Plane tracking $=3''$ if on-axis Fine-Field tracking
Total Emissivity of Telescope (Goal)	15% at 10 μm with dichroic tertiary 10% at 10 μm with aluminized tertiary
Chopped Image Quality due to coma for $\pm 4'$ Chop Throw	$=9.''1$ for 80% encircled energy diameter $=5.''8$ for 50% encircled energy diameter

5 Surveys with SOFIA

SOFIA has the opportunity to obtain airborne surveys for infrared astronomy. Some surveys will be encouraged by the operations center. Below we give an example.

Line Surveys with SOFIA

The variety of instruments on SOFIA makes it possible to conduct molecular line surveys in wavelength regions which are not accessible from ground. From ground based observatories such surveys have been performed by e. g. Blake et al. (1986) [2] from 247 - 263 GHz, Schilke et al. (1997a) [4] from 325 - 360 GHz and Schilke (1997b) [5] from 607 - 725 GHz, and Serabyn & Weisstein (1995) [6] carried out a survey from 190 - 900 GHz with 200 MHz resolution.

A study is ongoing to determine the feasibility of a similar project for SOFIA, covering almost the entire region from 30 - 330 μm which is inaccessible from ground-based observatories. The German PI-class heterodyne spectrometer GREAT, operating in two bands, one at 2.7 THz and the other from 1.6 - 2.0 THz (188 - 150 μm) with a resolution of about 10^6 will be es-

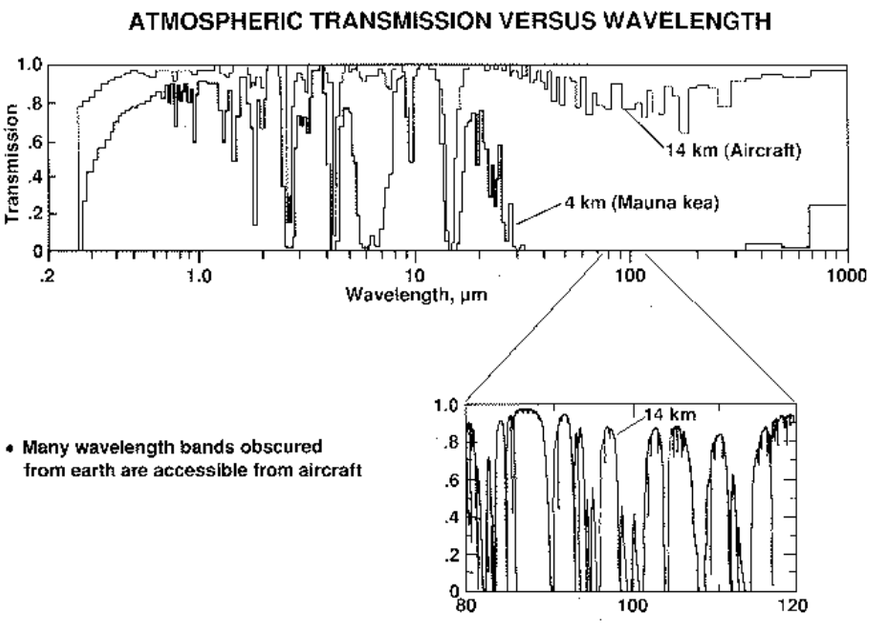

Fig. 4. *Atmospheric Transmission vs. Wavelength in the Infrared. The figure shows computed atmospheric transmission (Traub & Stier 1976) [7] as a function of wavelength for aircraft (14 km) and mountaintop (4 km) altitudes. The absorption is largely due to water vapor, Fig. from Erickson (1995) [1].*

pecially useful for line survey studies, see e. g. Graf et al. (1998) [3] . With GREAT, the beam size for the 150 - 188 μm range with SOFIA is of similar size as with the CSO survey conducted by Schilke et al. (1997a) [4].

The 325 - 360 GHz and 607 - 725 GHz surveys show typical lower limits for 3-σ line intensities of about 0.3 K and 1 K respectively. Using Hot Electron Bolometers (HEBs) for the 1.6 - 2.0 THz range of GREAT, one can estimate that the total integration time for this 400 GHz range should not exceed 20 hours in order to detect 3-σ lines at a level of 1.5 K. The SOFIA survey should be similar to the lower frequency surveys since the lines should be stronger for higher frequencies. Advantage has been taken of the fact that the 1.6 - 2.0 THz band of GREAT will have two polarisations in each of the two beams, so that simultaneous observations at two different frequencies are possible.

The wavelength ranges adjacent to the one from GREAT (150 - 188 μm) can be covered by CASIMIR which is another PI-class heterodyne spectrometer with a resolution of $R \geq 10^6$ and by the FI-instrument AIRES, a grating

spectrometer with $R \geq 10^4$. With CASIMIR the range from 188 - 330 μm becomes accessible and with AIRES the range from 40 - 110 μm.

The atmospheric transmission at SOFIA's operating altitudes gives access to almost all molecular rotational transitions up to the lightest hydrids in the wavelength range from 30 - 330 μm. The first light instruments can cover this range with only small gaps from 30 - 40 μm and from 110 - 150 μm. Those gaps however could be filled with future instruments and/or upgrades of existing instruments.

Acknowledgements

We like to thank Juleen Moon and Jackie Davidson for their contribution to this paper.

References

1. Erickson, E.F. 1995, SOFIA: The Next Generation Airborne Observatory , Space Sci. Reviews, 74, pp. 91-100
2. Blake, G. A., Sutton, E. C., Masson, C. R., Phillips, T. G. 1986, ApJS, 60, 257
3. Graf U. U., Haas S., Honingh C. E., Jacobs K., Schieder R., Stutzki J., 1997, Proc. of the SPIE, Vol. 3357, 159
4. Schilke, P., Groessbeck, T. D., Blake G. A., Phillips, T. G., 1997a, ApJS, 108, 301
5. Schilke, P., 1997b, Proceedings of the ESA Symposium 'The Far Infrared and Submillimetre Universe', 15-17 April 1997, Grenoble, France, ESA SP-401
6. Serabyn E. & Weisstein E. W., 1995, ApJ, 451, 238
7. Traub, W.A. and Stier, M. 1976, Theoretical Atmospheric Transmission in the Mid- and Far-Infrared at Four Altitudes, Applied Optics, 15, 364

X-ray Surveys of the Obscured Universe

Günther Hasinger[1,2]

[1] Astrophysikalisches Institut Potsdam, An der Sternwarte 16, 14482 Potsdam
[2] Universität Potsdam, Am Neuen Palais 10, 14469 Potsdam

Abstract. Deep X-ray surveys have shown that the cosmic X-ray background (XRB) is largely due to accretion onto supermassive black holes, integrated over cosmic time. However, the characteristic hard spectrum of the XRB can only be explained if most AGN spectra are heavily absorbed. The absorbed AGN will suffer severe extinction and therefore, unlike classical QSOs, will not be prominent at optical wavelengths. Most of the accretion power is being absorbed by gas and dust and will have to be reradiated in the FIR/sub-mm band. AGN could therefore contribute a substantial fraction to the recently discovered cosmic FIR/sub-mm background. Here it is shown that a number of high-redshift absorbed X-ray sources selected in the *ROSAT* Deep Survey of the Lockman Hole have broad-band spectral energy distributions very similar to the local ULIRG NGC6240, lending additional support to the background models for the obscured universe.

1 Echos from the Past

All cosmic processes like the Big Bang, the formation and evolution of galaxies, the creation and the growth of massive Black Holes and the heating of the Universe due to large-scale clustering will imprint characteristic radiation patterns on the electromagnetic spectrum of the universe. The structure of the Universe at the epoch of decoupling is frozen into the 2.7 K Cosmic Microwave Background (CMB). Star and galaxy light, produced after the Dark Ages by thermonuclear fusion, is mainly confined to the near-infrared, optical and ultraviolet spectral bands. Active black holes in galactic nuclei (AGN), which accrete matter and efficiently convert gravitational energy into radiation, typically shine in a very broad energy band, from radio to gamma wavelengths. The role of dust is also very important: it absorbs optical, UV and X-ray light, is warmed up and re-radiates the energy in the far-infrared band. The extragalactic background radiation, i.e. the total cosmic energy density spectrum, therefore gives a fossil record of all radiation processes in the universe, integrated over cosmic time.

In the recent years, the extragalactic background spectrum has been determined with relatively high precision over a very broad range of the electromagnetic spectrum, apart from some inaccessible regions. Figure 1 shows a compilation of most recent determinations of the cosmic energy density spectrum from radio waves to high-energy gamma rays – the "Echos from the Past". Apart from the CMB peak, which clearly dominates the energy

D. Lemke, M. Stickel, and K. Wilke (Eds.): LNP 548, pp. 423–432, 2000.

budget of the universe, three distinct components can be identified in the spectral energy distribution: the Cosmic Far-Infrared Background (CIB), the Cosmic Optical/UV Background (COB) and the Cosmic X-ray/Gamma-ray Background (CXB).

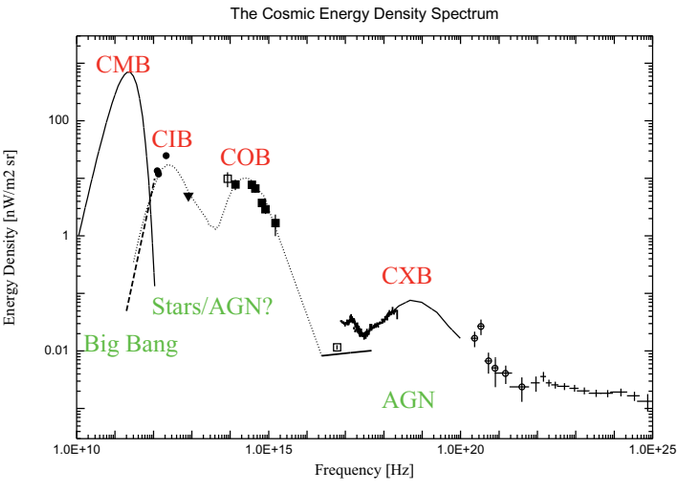

Fig. 1. The cosmic energy density spectrum from radio waves to high energy gamma rays in a νI_ν representation, where a horizontal line corresponds to equal radiation power per decade of energy. The FIR to UV data are from (left to right) [35,13,22,45,33,2]. The dotted line shows one of the models in [9] extrapolated from the visual to the EUV range. The X-ray/gamma-ray data are from [18,46,30,17,25,42].

The cosmic X-ray background (CXB) radiation was the first extragalactic background emission to be announced [14]. In the seventies, X–ray satellites like *UHURU*, *ARIEL V* and *HEAO–1*, which were able to scan the whole sky, produced high-quality XRB maps revealing a large degree of isotropy which immediately led to the conclusion that the origin of the XRB has to be mainly extragalactic and might therefore be of cosmological interest. Gamma-ray satellites like *SAS-3*, *COS-B* and finally the Compton Gamma Ray Observatory extended the background measurements to the highest-energy gamma rays (see [19] for a review). The energy spectrum of the CXB has a characteristic hump at about 30 keV and a long tail towards higher energies. At energies below 1 keV diffuse galactic emission starts to dominate the sky. At 1/4 keV a large fraction of the background determined by shadowing experiments has been resolved by deep *ROSAT* surveys [46,18].

In the sub-mm to UV range the extragalactic background light is completely swamped by other background components, i.e. the CMB, the interplanetary dust emission, the interstellar dust emission, scattering from

the interplanetary dust (zodiacal light), galactic starlight and scattering by interstellar dust. In the far-infrared range different groups have recently detected the long-sought residual cosmic far-infrared background (CIB) signal [35,22,13] by carefully modelling the other components in the high-frequency tail of the Cosmic Microwave Background (see fig. 1).

In the near-infrared to UV band, on the other hand, the Hubble Space Telescope Deep Field images are so sensitive, that one can safely assume that most of the Cosmic Optical Background (COB) has been resolved into discrete sources [33]. In the mid-infrared range the bright zodiacal light does not allow a direct detection of the extragalactic background light and one has to resort to galaxy population synthesis models and relatively uncertain upper limits [9]. At higher frequencies, in the extreme ultraviolet range, the interstellar absorption basically inhibits the detection of the extragalactic light and the background level can only be estimated by interpolating between the UV and the soft X-ray measurements.

The extragalactic background light seems to be dominated by two distinct humps, one in the optical/near-infrared range (COB), which could very well be produced by the red-shifted star light in all of the distant galaxies, and another one in the FIR/sub-mm range (CIB), which is very likely produced by dust emission in distant galaxies. The fact that the dust peak contains at least as much or even more energy than the stellar peak indicates that a large amount of light in the early universe had to be absorbed by dust. However, what fraction of the dust is heated by starlight or by AGN accretion power remains to be determined.

2 Deep X-ray Surveys

The X-ray range is one of the few regions of the electromagnetic spectrum, where on one hand the sky emission is dominated by the extragalactic background and on the other hand modern imaging telescopes are sensitive enough to resolve a substantial fraction of the background into discrete sources. The aim of deep X-ray surveys is to resolve as much of the background as possible, then to obtain reliable optical identifications and redshifts of the X-ray sources and finally for all classes of objects to determine luminosity functions and their cosmological evolution (see e.g. [31]). Since the emitted light, integrated over cosmic time can be compared directly to the total X-ray background, important constraints on the cosmological evolution and possible residual diffuse intergalactic emission can be obtained.

A large number of deep, medium-deep and shallower surveys have been performed with *ROSAT* (see [21] for a review). The *ROSAT* Deep Surveys in the Lockman Hole (see 2a) have so far been the deepest X-ray observations ever performed (until the deep *Chandra* and *XMM* surveys will be completed). They reach a source density of ~ 1000 sources deg^{-2} at the faintest flux limit,

where 70–80% of the soft X–ray background has been resolved into discrete sources [20].

Deep R-band images have been obtained at the Keck telescope. In the Lockman Hole Deep survey most optical counterparts have magnitudes in the range R=18–23. With the excellent HRI positions typically only one or two counterparts are within the X–ray error circle. Spectra of the optical counterparts of the X-ray sources were mostly obtained with the Keck telescope. Currently 85 out of 91 X–ray sources are spectroscopically identified. About 80% of those turned out to be active galactic nuclei [38], among them the highest redshift X–ray selected QSO at z=4.45 [39]. Most AGN are luminous QSOs and Sy1 galaxies with broad emission lines. However about 16% show only narrow emission lines and are classified as Seyfert 2 galaxies [21].

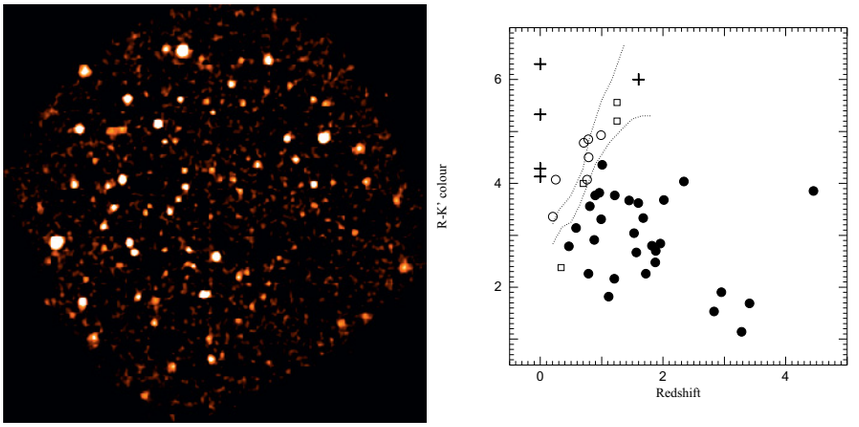

Fig. 2. Left: The *ROSAT* Deep HRI Survey in the Lockman Hole [20]; the size of the image is about 35 arcmin across. **Right:** R-K colours against redshift for X-ray sources in the Lockman Hole marked with different symbols: filled circles are broad-line AGN, open circles are narrow-line AGN (Sy 2), open squares are clusters and groups of galaxies. Plus signs are optical/NIR counterparts without spectroscopic identifications, for the ROSAT source 14Z with a photometric redshift $z_{ph} \approx 1.6$. The dotted lines correspond to unevolved spectral models for E (upper) and S_b (lower) galaxies [5].

There is a group of X-ray sources in the Lockman Hole, which have optical counterparts fainter than R=24, for which optical spectroscopy was not possible, even with the Keck telescope. For these one has to resort to NIR photometry and photometric redshifts. It turns out that the spectroscopically unidentified objects typically have very red R-K colours [21,23]. Figure 2b shows a correlation diagram between the R-K colours and redshifts for different types of objects identified in the Lockman Hole in comparison with normal galaxy colours predicted from evolutionary models. The colours of

type-1 AGN are relatively blue and scatter widely, while type-2 AGN and cluster galaxies show on average much redder colours, correlating well with redshift in the region expected for normal galaxies. This indicates that the optical colours of type-2 AGN are dominated by the light from the host galaxy, probably because the optical nucleus is obscured. A population of heavily obscured AGN is thus already showing up in the soft X-ray band. Based on R-K colours and photometric redshifts it is likely that the as yet unidentified sources are dust shrouded AGN in the redshift range 1-2.

There is, however, an interesting dichotomy in the redshift distribution of the sources. Unobscured objects (solid circles) are found to $z \approx 4.5$, while the obscured objects (open circles, pluses) are restricted to $z < 2$. There is a "negative K-correction effect" for obscured objects at soft X-rays: at higher redshifts it is easier to detect obscured X-ray sources, because their unobscured rest-frame hard X-ray emission is shifted into the observed soft X-ray band. The fact that we do not find obscured objects at high redshifts could indicate a dependence of obscuration on intrisic source luminosity. High luminosity X-ray sources to some degree could be able to "clean out" their environment from obscuring material.

3 Hard X-ray Population Synthesis Models

The X–ray background has a significantly harder spectrum than that of local unobscured AGN. This led to the assumption that a large fraction of the background flux is due to obscured AGN, as originally proposed by Setti and Woltjer [41]. Models following the unified AGN schemes, assuming an appropriate mixture of absorbed and unabsorbed AGN spectra folded with cosmological AGN evolution models, can in principle explain the shape of the background spectrum over the whole X–ray band (e.g. [29,27,8]), but gave problems with a number of new observational constraints [15]. Apart from the AGN cosmological evolution [31], the distribution of absorption column densities among different types of AGN and as a function of redshift is one of the major uncertainties. The standard X–ray background population synthesis models (e.g. [8]) assume that the absorption distribution, which has been determined observationally only for local Seyfert galaxies, is independent of X–ray luminosity and redshift. In particular, the fraction of type-2 QSOs, obscured high-luminosity X-ray sources, should be as high as that of Seyfert-2 galaxies. This assumption, however, has been proven wrong by recent observations (see e.g. fig. 2b, [31,15]). The current X-ray background models therefore still have rather limited predictive power.

A significant improvement in our understanding of the hard X-ray background is to be expected from optical identifications of complete samples of sources selected at faint fluxes in the hard X–ray band. Deep Surveys performed with *ASCA* [16,32] and *BeppoSAX* [12] have recently resolved about 30% of the harder X-ray background, but due to very limited angular reso-

lution their optical identification is tedious and in the case of faint optical counterparts almost impossible. Upcoming deep surveys with the *Chandra* observatory (*AXAF*) and *XMM* with very high sensitivity and good positional accuracy in the hard band together with optical identifications from the VLT and the Keck telescopes are expected to yield a solid statistical basis to disentangle these various effects and lead to a new, unambiguous population synthesis for the X–ray background.

An immediate consequence of the obscured background models is that the radiation produced by accretion processes in AGN emerges completely unabsorbed only at energies well above 10 keV, thus producing the observed maximum of the XRB energy density at ~ 30 keV. Comparison between the background energy density at 30 keV and at 1 keV leads to the suggestion that most (80–90%) of the accretion power in the universe might be absorbed, implying a very large solid angle of the obscuring material as seen from the central source. Fabian et al. [10] suggest that circumnuclear starburst regions are responsible for the large covering factor. They may be both triggering and obscuring most of the nuclear activity. Recently Fabian and Iwasawa [11] have shown that these AGN background synthesis models can explain the mass distribution of dark remnant black holes in the centers of nearby galaxies by conventional accretion which is largely hidden by obscuration.

4 Predictions for Other Wavebands

The obscured background synthesis models has important consequences for the current attempts to understand black hole and galaxy formation and evolution. The absorbed AGN will suffer severe extinction and therefore, unlike classical QSOs, would not be prominent at optical wavelengths. The light of the optical counterparts of distant absorbed X-ray sources should therefore be dominated by the host galaxy, which indeed seems to be the case for a significant number of faint X-ray sources (see fig 2b).

If most of the accretion power is being absorbed by gas and dust, it will have to be reradiated in the FIR range and be redshifted into the sub–mm band. AGN could therefore contribute a substantial fraction to the cosmic FIR/sub–mm background which has already partly been resolved by deep SCUBA surveys. The background population synthesis models have recently been used by Almaini et al. [1] to predict the AGN contribution to the sub–mm background and source counts. Depending on the assumptions about cosmology and AGN space density at high redshifts they predict that a substantial fraction of the sub–mm source counts at the current SCUBA flux limit could be associated with active galactic nuclei. Interestingly, the first optical identifications of SCUBA sources indicate a significant AGN contribution [3].

Another, largely independent line of arguments leads to the conclusion that accretion processes may produce an important contribution to the ex-

tragalactic background light. Dynamical studies [28] come to the conclusion that massive dark objects, most likely dormant black holes, are ubiquitous in nearby galaxies. There is a correlation between the black hole mass and the bulge mass of a galaxy: $M_{BH} \approx 6 \times 10^{-3} M_{Bulge}$. Since gravitational energy release through standard accretion of matter onto a black hole is producing radiation about 100 times more efficiently than the thermonuclear fusion processes in stars, the total amount of light produced by accretion in the universe should be of the same order of magnitude as that produced by stars. A more detailed treatment following this argument comes to the conclusion that the bolometric AGN contribution should be about 1/5 of the stellar light in the universe [11].

5 NGC 6240 – Representative of the Obscured Universe?

The ultraluminous IRAS galaxy NGC 6420 is a starburst galaxy with a double nucleus [36] with some evidence for a weak active nucleus. Its position in the mid-infrared diagnostic diagram based on ISO spectroscopy [24] indicates that its bolometric luminosity, which is dominated by the far-infrared dust emission, should be mainly heated by star formation processes. Recently, however, *BeppoSAX* hard X-ray spectroscopy revealed an underlying very luminous, though heavily obscured active galactic nucleus, which could well be responsible for the major fraction of the bolometric luminosity. Figure 3 shows the spectral energy distribution (SED) of NGC 6240 in a νF_ν representation from the radio to the hard X-ray band. The SED peaks in the far-infrared dust band and shows the mid-infrared policyclic aromatic hydrocarbonic emission bands as well as the synchrotron radio emission typical for starburst galaxies. The optical starlight peak is lower than the dust emission peak - similar to the overall extragalactic energy distribution. In the hard X-ray range the nonthermal AGN continuum emission is severely absorbed below 15 keV and strong reprocessed iron line is seen. The UV to soft X-ray nuclear continuum is completely obscured.

The SEDs of three AGN from the *ROSAT* deep survey in the Lockman Hole, which have been observed over a broad wavelength range from radio to X-rays have been superposed on this diagram. These are (see [38,23]): 32A, a QSO/Sy1 at z=1.33 (crosses), 12A a Sy2 at z=0.99 (filled circles) and 14Z, a very red object, probably a Sy2 galaxy, with $z_{ph} \approx 1.6$ [34]. The radio detections and upper limits at 20cm and 6cm are from [37] and [7]. The upper limit in the millimeter-range for 14Z has been obtained with IRAM [4]. In the X-ray range the *ROSAT PSPC* spectra of these three sources have been fitted with a power law with galactic or intrinsic absorption. For a comparison on the same absolute scale the Lockman SEDs have been shifted to the redshift of NGC 6240 and scaled by the square of their luminosity distances.

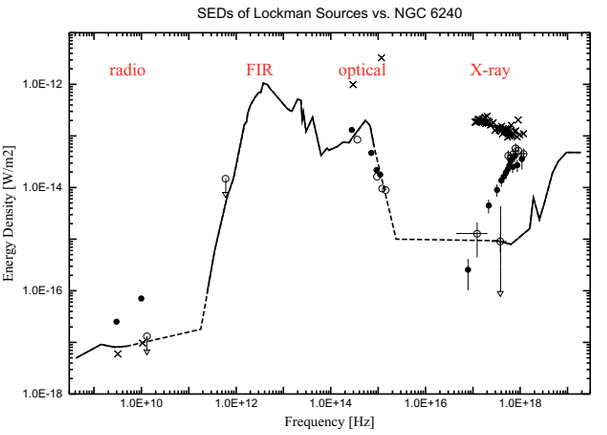

Fig. 3. Spectral energy distribution of the ultraluminous IRAS galaxy (ULIRG) NGC 6240 from radio to hard X-ray frequencies (thick solid line, dashed in unobserved portions) [48,26,44], compared to the spectral energy distribution of three high-redshift X-ray sources from the *ROSAT* Deep Survey [38,23]: 12A (filled circles), 14Z (open circles) and 32A (crosses). The latter SEDs have been normalised to the redshift of NGC 6240 (see text).

The two absorbed *ROSAT* sources (12A and 14Z) have SEDs surprisingly similar to NGC 6240. The galaxy 12A may have a relatively stronger starburst component, indicated by its higher radio luminosity. The main difference lies in the X-ray range, where the luminosity at hard X-ray energies is very similar for all 3 sources, while the intrinsic absorption is clearly different: N_H is about $10^{24} cm^{-2}$ for NGC6420, $3 \cdot 10^{22} cm^{-2}$ for 14Z and $10^{22} cm^{-2}$ for 12A. In contrast, the SED for the radio-quiet QSO 32A, while fitting relatively well to the other sources in the radio band, is clearly dominated by the unobscured light of the active nucleus in the optical and X-ray range.

This figure is a nice illustration of the obscured AGN model for the X-ray background and its potential relevance to the FIR/sub-mm background, since it shows that X-ray-selected high-redshift AGN can indeed have SEDs similar to local ULIRGS. Unfortunately there are no observations yet, which are sensitive enough both in the X-ray band and in the sub-mm band to obtain a better quantitative estimate of the fraction of the far-infrared background produced by AGN. Future joint sub–mm/X–ray deep surveys will therefore be a very powerful tool to disentangle the different processes dominating the universe at high redshift.

Acknowledgements

I thank my collaborators in various projects, in particular F. Bertoldi, P. Ciliegi, R. Giacconi, I. Lehmann, M. Schmidt, T. Soifer, D. Thompson, J.

Trümper, G. Wilson and G. Zamorani for the permission to show some material in advance of publication. This research has made use of the NASA/IPAC Extragalactic Database (NED) which is operated by the Jet Propulsion Laboratory, California Institute of Technology, under contract with the National Aeronautics and Space Administration. This work has been supported in part by DLR grant 50 OR 9908 0.

References

1. Almaini O., Lawrence A., Boyle B., 1999, MNRAS 305, L59
2. Armand C., et al., 1994, A&A 284, 12
3. Barger A.J., et al., 1999, AJ117, 2656
4. Bertoldi F., et al., 2000 (in prep.)
5. Bruzual A.G. & Charlot S., 1993, ApJ 405, 538
6. Cen R., Ostriker J., 1999, ApJ 514, 1
7. Ciliegi P., et al., 2000 (in prep.)
8. Comastri A., et al., A&A 296, 1
9. Dwek E., et al., 1998, ApJ 508, 106
10. Fabian A.C. et al., 1998, MNRAS 297, L11
11. Fabian A.C., Iwasawa K., 1999, MNRAS 303, L34
12. Fiore F. et al., 1999, MNRAS 306, L55
13. Fixsen D.J., et al., 1998, ApJ 508, 123
14. Giacconi, R. et al., 1962, Phys.Rev.Letters 9, 439
15. Gilli R., Risaliti G. & Salvati M., 1999, A&A 347, 424
16. Georgantopoulos I. et al., 1997, MNRAS 291, 203
17. Gruber D.E., in *The X–ray Background* X. Barcons & A.C. Fabian eds, (Cambridge University Press), p.45 (1992).
18. Hasinger G., et al., 1993, A&A 295, 1
19. Hasinger G., 1996, A&AS 120C, 607
20. Hasinger G., et al., 1998, A&A 329, 482
21. Hasinger G. et al., 1999, astro-ph/9901103
22. Hauser M.G., et al., 1998, ApJ 508, 25
23. Lehmann, I., et al., 1999, A&A (in press), astro-ph/9911484
24. Lutz D., et al., 1996, A&A 315, L137
25. Kappadath, S.C., et al., 1996, A&AS 120C, 619
26. Klaas U., et al., 1997, A&A 325, L21
27. Madau P. et al., 1994, MNRAS 283 1388
28. Magorrian J. et al., 1998, AJ 115, 2285
29. Matt G. & Fabian A.C., 1994, MNRAS 267 187
30. Miyaji T. et al., 1998, A&A 334, L13
31. Miyaji T. et al., 2000, A&A 353, 25
32. Ogasaka Y. et al. 1998, AN 319, 43
33. Pozzetti L. et al., 1998, MNRAS 298, 1133
34. Pozzetti L. 1999, priv. comm.
35. Puget J.-L. et al., 1996, A&A 308, L5
36. Rafanelli P., et al. 1997, A&A 327, 901
37. de Ruiter H. et al., 1997, A&A 319, 7
38. Schmidt M. et al. 1998, A&A, 329, 495

39. Schneider D. et al., 1998, AJ 115, 1230
40. Snowden S.L., et al., 1997, ApJ 485, 125
41. Setti G. and Woltjer L. 1989, A&A 224, L21
42. Sreekumar P., et al., 1998, ApJ 494, 523
43. Tegmark M., et al., 1997, ApJ 474, 1
44. Vignati P., et al., 1999, A&A 349, 57
45. Völk H. 1998, priv. comm.
46. Warwick R. S., Roberts T. P, 1998, AN 319, 59
47. Zdziarski A.A., et al., 1995, ApJ 438, L63
48. NASA Extragalactic Database